A three-dimensional numerical investigation of the thermo-hydro-mechanical behaviour of a large-scale prototype repository.

Philip James Vardon

Geoenvironmental Research Centre

Cardiff School of Engineering

Cardiff University

Thesis submitted in candidature for the degree of Doctor of Philosophy

at Cardiff University

July 2009

CARDIFF
UNIVERSITY

PRIFYSGOL
CAERDYᴅ

UMI Number: U585221

UMI®

Dissertation Publishing

ProQuest®

Acknowledgements

Summary

This thesis describes the modelling of the thermo-hydro-mechanical behaviour of a large-scale experiment, carried out at SKB's underground research laboratory in Äspö, Sweden. The experiment, known as the Prototype Repository Project, was constructed in highly fractured granite rock and is scheduled to last 20 years. Results from the experiment are collected systematically by SKB from the initial rock characterisation to the highly instrumented installed material.

The model applied is the thermo-hydro-mechanical model previously developed at the Geoenvironmental Research Centre (GRC). The GRC's current model was extended to successfully accommodate three-dimensional THM behaviour, including the development of a high-performance computing algorithm using both multi-threaded and message-passing programming paradigms to enable simulations to be completed in significantly reduced time.

Model simulations have been conducted of both the pre-placement stage of the experiment and the post-placement operational phase. The results of the pre-placement phase have been used to aid the calibration of the simulation and provide confidence in the development of the operational phase simulation. In the pre-placement phase simulation, a pragmatic approach using a combination of an effective continuum model and a number of key discontinuities was employed. A domain of $100 \times 100 \times 160m$ was used, discretised into over 550,000 finite-elements. The simulations were able to reproduce three-dimensional highly anisotropic flow conditions shown in the experimental results.

The post-placement operational stage was then simulated in three-dimensions using the same rock domain as for the pre-placement analyses, including the buffer material, and discretised into over 920,000 elements. A number of key features, including the anisotropic hydraulic behaviour, were captured. It was concluded that the geological conditions, backfill re-saturation and buffer re-saturation, including the micro-structural effects of the bentonite, are all important to the simulation of a high-level waste repository. Long term simulation results were also presented.

A number of aspects were explored using two-dimensional analyses, including the macro/micro-structural interactions of the bentonite buffer. A time-dependant form of the hydraulic conductivity relationship was developed and yielded significantly improved results in long-term analyses. The behaviour of a fracture intersecting a deposition-hole was also investigated highlighting the importance of discrete fractures on hydration behaviour.

Contents

Nomenclature

a	Parameter for the SWRC defined in table 5.1
a	Constant used in van Genuchten equation
$[a]$	Matrix of coefficients
A	System matrix as defined in figure 4.2
A_1	Parameter for thermal conductivity relationship defined in table 5.1
A_2	Parameter for thermal conductivity relationship defined in table 5.1
A_s	Defined in equation (3.115)
A_T	Defined in equation (3.116)
$\mathbf{A}$	Matrix defined in equation (3.201)
$\mathbf{A_p}$	Plastic modulus, defined in equation (3.137)
b	Parameter for the SWRCs defined in tables 5.1 and 5.3
b	Constant used in van Genuchten equation
b	Vector of coefficients as defined in figure 4.2
$[b]$	Matrix of coefficients
b_x, b_y, b_z	Body forces in Cartesian coordinate system
$\mathbf{b}$	Vector of body forces
$\mathbf{B}$	Shape function/strain matrix defined in equation (3.188)
$\mathbf{B}$	Matrix defined in equation (3.201)
B_w	Bandwidth of an interconnect
C	Subscript defining value as corrector
C_{aa}	Defined in equation (3.68)
C_{al}	Defined in equation (3.66)
C_{aT}	Defined in equation (3.67)
C_{au}	Defined in equation (3.69)

C_{la} — Defined in equation (3.48)

C_{ll} — Defined in equation (3.46)

C_{lT} — Defined in equation (3.47)

C_{lu} — Defined in equation (3.49)

C_{pda} — Specific heat capacity of dry air

C_{pl} — Specific heat capacity of liquid

C_{ps} — Specific heat capacity of solid particles

C_{pv} — Specific heat capacity of water vapour

C_{Ta} — Defined in equation (3.92)

C_{Tl} — Defined in equation (3.90)

C_{TT} — Defined in equation (3.91)

C_{Tu} — Defined in equation (3.93)

C_{ua} — Defined in equation (3.144)

C_{ul} — Defined in equation (3.142)

C_{uT} — Defined in equation (3.143)

C_{uu} — Defined in equation (3.145)

$\mathbf{C}$ — Matrix defined in equation (3.201)

$\mathbf{C_{aa}}$ — Defined in equation (3.180)

$\mathbf{C_{al}}$ — Defined in equation (3.178)

$\mathbf{C_{aT}}$ — Defined in equation (3.179)

$\mathbf{C_{au}}$ — Defined in equation (3.181)

$\mathbf{C_{la}}$ — Defined in equation (3.162)

$\mathbf{C_{ll}}$ — Defined in equation (3.160)

$\mathbf{C_{lT}}$ — Defined in equation (3.161)

$\mathbf{C_{lu}}$ — Defined in equation (3.163)

$\mathbf{C_{Ta}}$ — Defined in equation (3.171)

$\mathbf{C_{Tl}}$ — Defined in equation (3.169)

$\mathbf{C_{TT}}$ — Defined in equation (3.170)

$\mathbf{C_{Tu}}$ — Defined in equation (3.172)

$\mathbf{C_{ua}}$ — Defined in equation (3.197)

$\mathbf{C_{ul}}$ — Defined in equation (3.195)

$\mathbf{C_{uT}}$ — Defined in equation (3.196)

$\mathbf{C_{uu}}$ — Defined in equation (3.198)

dx — Parameter for thermal conductivity relationship defined in table 5.1

D	Amount of data in bytes
D_{atms}	Molecular diffusivity of vapour through air
$\mathbf{D}$	Elasticity matrix
$\mathbf{D_{ep}}$	Elasto-plastic stress-strain matrix
e	Void ratio
E	Young's modulus
E_n	Efficiency for n number of processing cores
E_{ss}	Sink/source term
f	Flow area factor
F	Applied force
F_1	Yield function as defined in equation (3.121)
F_2	Yield function as defined in equation (3.123)
F_p	Floating point operations per second undertaken by a specific processor
$\mathbf{f_a}$	Defined in equation (3.184)
$\mathbf{f_l}$	Defined in equation (3.167)
$\mathbf{f_T}$	Defined in equation (3.176)
$\mathbf{f_u}$	Defined in equation (3.199)
$\mathbf{F}_h$	Approximate heat flux normal to the boundary surface
g	Gravitational constant
G	Shear modulus
G_s	Specific weight
h	Relative humidity
H_c	Heat capacity of the soil
H_s	Henry's volumetric coefficient of solubility
i	Iteration level
J_a	Defined in equation (3.72)
J_l	Defined in equation (3.53)
J_T	Defined in equation (3.97)
k	Constant related to the cohesion of the soil defined in equation (3.122)
k_{init}	Initial hydraulic conductivity of pellets
k_{inf}	Saturated hydraulic conductivity of pellets
k_l	Intrinsic permeability of pore liquid
k_a	Effective permeability of pore air
K	Bulk modulus

K_a	Unsaturated conductivity of pore air
K_{aa}	Defined in equation (3.71)
K_{al}	Defined in equation (3.70)
K_l	Unsaturated hydraulic conductivity
K_m	Modified hydraulic conductivity due to micro/macro effects
K_{la}	Defined in equation (3.52)
K_{ll}	Defined in equation (3.50)
K_{lT}	Defined in equation (3.51)
K_{pel}	Unsaturated hydraulic conductivity of pellets
K_{sat}	Saturated hydraulic conductivity
K_{swell}	Hydraulic conductivity of a swelling soil
K_{Ta}	Defined in equation (3.96)
K_{Tl}	Defined in equation (3.94)
K_{TT}	Defined in equation (3.95)
K_{va}	Defined in equation (3.157)
K_{vl}	Defined in equation (3.155)
K_{vT}	Defined in equation (3.156)
$\mathbf{K_{aa}}$	Defined in equation (3.183)
$\mathbf{K_{al}}$	Defined in equation (3.182)
$\mathbf{K_{la}}$	Defined in equation (3.166)
$\mathbf{K_{ll}}$	Defined in equation (3.164)
$\mathbf{K_{lT}}$	Defined in equation (3.165)
$\mathbf{K_{Ta}}$	Defined in equation (3.175)
$\mathbf{K_{Tl}}$	Defined in equation (3.173)
$\mathbf{K_{TT}}$	Defined in equation (3.174)
L	Latent heat of vapourisation
L	Latency of a communication over an interconnect
M	Slope of the critical state line
M	Preconditioner for BiCG solver as defined in figure 4.2
$\mathbf{m}$	Unit vector
n	Porosity
n	Number of processing cores
n_0	Initial porosity
n_{calcs}	Number of individual calculations defined in equation (4.4)

n_{proc}	Number of processing cores defined in equation (4.4)
$\underline{n}$	Direction cosine normal to the surface defined in equation (3.153)
N_s, N_r	Shape functions
$N(s)$	Intercept of the normal compression line for a soil at suction s
$N(0)$	Intercept of the normal compression line for the saturated soil
$\mathbf{N}$	Matrix of shape functions
p	Net mean stress
p_{atms}	Atmospheric pressure
p_i	Initial net mean stress
p_i	Search direction at iteration i for BiCG solver as defined in figure 4.2
$\tilde{p}_i$	Search direction at iteration i for BiCG solver as defined in figure 4.2
p_i	Search direction for BiCG solver as defined in figure 4.2
p_c	Reference stress
p_s	Parameter controlling suction effect on cohesion
p_0	Preconsolidation stress at suction s
p_0^*	Preconsolidation stress of saturated soil
P_0	Air entry value
P_g	Gas pressure
P_l	Liquid pressure
P_s	Parameter for modified van Genutchen equation, defined in equation (5.11)
$\mathbf{P}$	Strain matrix
q	Deviatoric stress
q_i	Vector to update residuals at iteration i for BiCG solver as defined in figure 4.2
$\tilde{q}_i$	Vector to update residuals at iteration i for BiCG solver as defined in figure 4.2
$\mathbf{Q}$	Heat flux per unit area
Q_1	Plastic potential function for LC yield surface defined in equation (3.124)
Q_2	Plastic potential function for SI yield surface defined in equation (3.125)
r	Parameter controlling the maximum stiffness of the soil
r_i	Residual at iteration i for BiCG solver as defined in figure 4.2
$\tilde{r}_i$	Residual at iteration i for BiCG solver as defined in figure 4.2
R_Ω	Residual error introduced due to approximation
R_{da}	Specific gas constant for dry air

R_v	Specific gas constant for water vapour
s	Suction at temperature T
s_i	Initial suction
s_m	Matrix suction
s_o	Osmotic suction
s_r	Suction at reference temperature T_r
s_t	Total suction
s_0	Critical value of suction - suction hardening parameter
S_a	Degree of saturation of pore air
S_l	Degree of saturation of pore water
S_{labs}	Degree of saturation of absorbed pore water
S_{lA}	Degree of saturation at point A in figure 5.11
S_{lfree}	Degree of saturation of free pore water
S_n	Speed-up for n number of processing cores
t	Time
T	Temperature
T	Transmissivity
T_0	Reference temperature for the SWRC defined in table 5.1
T_{calc}	Estimated walltime of calculation defined in equation (4.4)
T_{comm}	Estimated walltime of communication defined in equation (4.5)
T_n	Walltime of computation for n number of processing cores
T_r	Reference temperature
$\hat{T}$	Approximate value of temperature
$\hat{T}_r$	Approximate traction defined in equation (3.192)
$(\nabla T)_a / \nabla T$	Ratio of the microscopic temperature gradient in pore space to the macroscopic temperature gradient
$\mathbf{T}_s$	Temperature vector defined in equation (3.158)
$\dot{\mathbf{T}}_s$	Time differential of temperature defined in equation (3.200)
$\mathbf{TL}_{abs}$	Matrix of absolute tolerances
$\mathbf{TL}_{rel}$	Matrix of relative tolerances
u_a	Pore-air pressure
u_{da}	Partial pressure of dry air
u_l	Pore-water pressure
u_v	Partial pressure of water vapour

$\hat{u}_a$	Approximate value of pore-air pressure
$\hat{u}_l$	Approximate value of pore-water pressure
u_{var}	Defined in equation (3.146)
$\hat{u}_{var}$	Defined in equation (3.146)
$\mathbf{u}$	Displacement vector
$\mathbf{u}_{as}$	Pore-air pressure vector defined in equation (3.158)
$\mathbf{u}_{ls}$	Pore-water pressure vector defined in equation (3.158)
$\mathbf{u}_s$	Displacement vector defined in equation (3.158)
$\hat{\mathbf{u}}$	Approximate value of displacement
$\dot{\mathbf{u}}_{as}$	Vector of time differentials of pore-air pressure defined in equation (3.200)
$\dot{\mathbf{u}}_{ls}$	Vector of time differentials of pore-water pressure defined in equation (3.200)
$\mathbf{u}_{ls}$	Vector of time differentials of displacement defined in equation (3.200)
v	Specific volume
v_0	Initial specific volume
v_s	Specific volume due to suction changes
v_v	Mass flow factor
V_s	Volume of solids
$\mathbf{v_a}$	Velocity of air
$\mathbf{v_l}$	Velocity of liquid
$\mathbf{v_v}$	Equivalent velocity of water vapour, in terms of liquid water velocity
$\hat{\mathbf{v}}_{fn}$	Approximate velocity of free air normal to the boundary surface
$\hat{\mathbf{v}}_{an}$	Approximate velocity of dissolved air normal to the boundary surface
$\underline{\hat{\mathbf{v}}}_{ln}$	Approximate liquid velocity normal to the boundary surface
$\underline{\hat{\mathbf{v}}}_{va}$	Approximate pressure vapour velocity normal to the boundary surface
$\underline{\hat{\mathbf{v}}}_{vd}$	Approximate diffusive vapour velocity normal to the boundary surface
w	Water content
x_0	Parameter for thermal conductivity relationship defined in table 5.1
x_i	Solution at iteration i for BiCG solver as defined in figure 4.2
x, y, z	Global Cartesian coordinates
z_i	Solution of preconditioner at iteration i for BiCG solver as defined in figure 4.2
$\tilde{z}_i$	Solution of preconditioner at iteration i for BiCG solver as defined in figure 4.2
α	Parameter for the SWRC defined in table 5.1

α	Coefficient defining the rate of time dependent change in the hydraulic conductivity defined in equation (5.7a)
α_i	Multiple for the update of the residuals at iteration i for BiCG solver as defined in figure 4.2
α_q	Parameter for non-associated flow rule
α_T	Coefficient of thermal expansion
β	Parameter controlling the rate of increase of soil stiffness with suction
β_i	Multiple for the update of the search directions at iteration i for BiCG solver as defined in figure 4.2
β_l	Parameter for SWRC defined in equation (8.1)
β_p	Coefficient representing the rate of pellet homogenisation defined in equation (5.14)
χ_1, χ_2	Plastic multipliers determined through plastic consistency conditions
δ	Material parameter for use in the SWRC, defined in equation (5.1)
∂V	Incremental volume
ϵ	Total strain
ϵ	Strain vector
ϵ^e	Elastic component of strain
ϵ^p	Plastic component of strain
ϵ_q^e	Elastic component of strain due to deviatoric stress changes
ϵ_q^p	Plastic component of strain due to deviatoric stress changes
ϵ_p^e	Elastic component of strain due to mean stress changes
ϵ_s^e	Elastic component of strain due to suction changes
ϵ_T^e	Elastic component of strain due to temperature changes
ϵ_v	Volumetric strain
ϵ_v^p	Total volumetric plastic strain
ϵ_{vp}^p	Volumetric plastic strain due to stress changes
ϵ_{vs}^p	Volumetric plastic strain due to suction changes
ϕ	Variable vector
ϕ_l	Defined in equation (3.203)
ϕ'	Angle of friction for saturated soils
γ_l	Unit weight of liquid
Γ_e	Element boundary surface
η	Parameter for the SWRC defined in table 5.1

η_1	Factor in vapour transfer equation defined in equation (5.10)
η_2	Factor in vapour transfer equation defined in equation (5.10)
κ	Stiffness parameter for changes in net mean stress in the elastic region
κ_s	Stiffness parameter for changes in suction in the elastic region
λ	Coefficient of thermal conductivity of saturated soil
λ_{vg}	Parameter for modified van Genutchen equation, defined in equation (5.11)
λ_{sw}	Parameter for the SWRC defined in table 5.1
λ_s	Stiffness parameter for changes in suction for virgin states of the soil
λ_{s_vg}	Parameter for modified van Genutchen equation, defined in equation (5.11)
λ_T	Coefficient of thermal conductivity of unsaturated soil
$\lambda(0)$	Stiffness parameter for changes in net mean stress for virgin states of saturated soil
$\lambda(s)$	Stiffness parameter for changes in net mean stress for virgin states of the soil
μ_a	Absolute viscosity of air
μ_l	Absolute viscosity of pore liquid
θ	Volumetric water content
θ_a	Volumetric air content
θ_l	Volumetric liquid content
θ_{res}	Residual water content
θ_{sat}	Saturated water content
θ_v	Volumetric vapour content
ϑ	Defined in equation (3.203)
ρ_i	To define the multiple for the update of the search directions at iteration i for BiCG solver as defined in figure 4.2
ρ_0	Denisty of saturated water vapour
ρ_b	Bulk density
ρ_d	Dry density
ρ_{da}	Density of dry air
ρ_l	Density of liquid water
ρ_s	Density of solid particles
ρ_v	Density of water vapour
σ	Total stress
σ'	Effective stress

σ''	Net stress
$\sigma_1, \sigma_2, \sigma_3$	Principle stresses
$\sigma_x, \sigma_y, \sigma_z$	Normal stresses
$\tau_{xy}, \tau_{yz}, \tau_{zx}$	Shear stresses
τ_v	Tortuosity factor
υ	Poisson's ratio
ϖ	Integration constant defined in equation (3.202)
ψ	Capillary potential
∇	Gradient operator
ω_{abs}	Proportion of pore-water absorbed
ω_{abs}^{max}	Maximum proportion of pore-water absorbed
ω_{pel}	Effect of homogenisation on the hydraulic conductivity of pelletised bentonite
Ω	Heat contact of moist soil
Ω^e	Element domain
ξ	Surface energy at temperature T
ξ_r	Surface energy at temperature T_r
ζ	Residual force defined in equation (3.208)

1

Introduction

1.1 Introduction

There is a general global consensus that climate change is occurring and that the cause is anthropologically produced greenhouse gases such as carbon dioxide (United Nations, 1998). Moreover natural resources are being consumed at a faster rate than ever before and projected reserves are diminishing. In addition, global population growth and expanding demands of both developed and developing countries has led to high demand for resources, in particular energy, with global tensions meaning energy security is an important issue for most countries (UNEP, 2009a; UNEP, 2009b, WWF, 2008). Therefore, sustainable development, energy security and low carbon technologies are seen as important issues for society (UNEP, 2009b).

Renewable energy is seen to have potential to solve many of these issues but as an industry, in terms of production of energy on a large-scale comparable to traditional power stations, it is not mature (IEA, 2008). Ongoing technical concerns related to intermittency and power

distribution via national grid facilities still exist (e.g. House of Lords, 2008). Therefore, interest into new-build nuclear power has increased recently, with the possible advent of new power stations being operational by 2020 (DTI, 2006). However, the public in the UK remains generally sceptical to nuclear power and the nuclear legacy including work into nuclear waste disposal. Therefore, it is recognised that the problem of radioactive waste is both technical and social (CoRWM, 2006). Nuclear waste production will also increase over the next few decades due to the decommissioning process of existing power stations. This thesis is generally concerned with the disposal of high-level nuclear waste. Moreover, this thesis is produced against a background of existing, or legacy, nuclear waste existing in significant quantities and the continuing production of radioactive waste through, in the main, nuclear power generation activities.

High-level nuclear waste, containing 92% of the radioactivity in less than 2% of the volume (CoRWM, 2006), exists throughout the world in significant quantities with deep geological disposal being the primary disposal proposition (CoRWM, 2006). Understanding the behaviour of these geological disposal repository systems, including the thermo-hydro-mechanical behaviour, is essential for the assessment of safety. This thesis presents a numerical investigation into the thermo-hydro-mechanical behaviour in the near-field of a repository system. In particular, a large-scale experiment, the Prototype Repository Project (Johannesson et al., 2007), is simulated with the aim to further understanding of the processes occurring.

Background information related to the nuclear industry in the UK, including likely future developments gained from government policy is first presented in section 1.2, with an introduction to nuclear waste highlighting the wastes produced and the overarching principles adopted regarding the disposal of the wastes following in section 1.3. High-level nuclear waste disposal is then discussed in section 1.4 including a brief review of the UK's progress towards a disposal strategy. Deep geological disposal, and in particular the multi-barrier disposal concept are outlined in section 1.5, with particular reference to a full scale experimental repository, the Prototype Repository Project (PRP), in section 1.6. The role of the safety case, computation and numerical simulation and experimentation are outlined in sections 1.7, 1.8 and 1.9. The outline of the study is contained in section 1.10, including the objectives

of the study. An overview of the research background and study scope and limitations are contained in sections 1.11 and 1.12. An overview of the work contained in this thesis is contained in 1.13.

1.2 Background to the nuclear industry in the UK

Currently the nuclear industry provides around 20% of the UK's electricity supply, but with all active sites due to be decommissioned by 2035 and the majority by 2023 (CoRWM, 2006), without a programme of new build this percentage will rapidly reduce. The accident in Chernobyl in 1986 and the possession of a nuclear arsenal, in particular, have given rise to a public perception that nuclear power is dangerous. In addition, domestically produced oil and gas with lower capital costs, the privatisation of power generation and competitive pricing led to a decline in the planning and construction of nuclear power stations (BERR, 2008).

More recently, with higher hydro-carbon prices and concern over carbon-dioxide emissions nuclear power has rejoined the power production agenda. The UK has signed and ratified the Kyoto Protocol (United Nations, 1998) committing it to the reduction of greenhouse gasses to 8% below the 1990 levels for the European Union nations. Further to this the Climate Change Act (2008) informed by the Energy White Paper (DTI, 2003) commits the UK to an 80% reduction on 1990 greenhouse gas levels by 2050.

Power production in the UK accounted for nearly 40% of the carbon dioxide emissions in 2006 and was the biggest single contributor, with transport approximately 20% and manufacturing, industry and construction at approximately 15% (Defra, 2008a). Therefore it is essential that carbon dioxide from power generation is reduced to allow the UK to meet carbon dioxide reduction targets laid out in legislation.

In 2003 the UK government's opinion on nuclear power was that it:

> '...is currently an important source of carbon-free electricity. However, its
>
> current economics make it an unattractive option for new, carbon-free generating
>
> capacity and there are also important issues of nuclear waste to be resolved.'
>
> (DTI, 2003)

This opinion was updated in 2006 by the new Energy Review (DTI, 2006) which states that nuclear power is currently an important source of low carbon power generation and that a programme of replacement is required. In addition, it states that due to high hydrocarbon prices, the introduction of carbon pricing would make nuclear power economically viable. The review also concluded that investment and construction of new power stations must be undertaken by private industry and only facilitated by government policy.

1.3 Nuclear waste

Nuclear waste is categorised via its properties, with each category having different requirements and criteria in the method by which it is dealt, ensuring that they do not pose too great an environmental or health risk. These radioactive products have great variation in the level of radioactivity, heat production and longevity. Unfortunately there is no general international consensus on how to categorise these wastes. In the UK the wastes are categorised as follows (CoRWM, 2006):

- Spent Nuclear Fuel (SNF) - this is a mixture of plutonium, uranium and waste materials. This can be reprocessed to extract the plutonium and uranium. This can be largely considered HLW.

- High Level Waste (HLW) - very radioactive, mainly fission products and generates a great deal of heat, less than 2% by volume 92% of radioactivity.

- Intermediate Level Waste (ILW) - less radioactive than HLW, does not generate sufficient heat for this to be taken into account of during long-term management but can require significant shielding.

- Low Level Waste (LLW) - less radioactive than ILW and consist of redundant equipment and soil, concrete and steel arising from decommissioning.

- Very Low Level Waste (VLLW) - less radioactive than LLW and is disposed of in small concentrations in conventional landfill sites.

There is no allowance for the longevity within these categorisations. However, the waste remains highly radioactive for thousands of years depending on the exact make-up and reactions that may occur. When referring to categories of waste in this work it will be by the

above definitions. In this thesis only the disposal of HLW is considered and the remainder of this work, therefore, concentrates upon this part of the nuclear waste inventory.

The civilian nuclear power industry in the UK has a projected $1,300m^3$ of HLW (up to 2010) and in addition to the HLW the UK will also have approximately $8,150m^3$ of SNF and a total of approximately $478,000m^3$ of higher activity waste e.g. HLW, ILW, some LLW that cannot be disposed of at the Drigg facility and SNF, arising by 2120 (CoRWM 2006). In the context of general waste production these amounts are small, with the UK producing 29 million tonnes of municipal waste in 2005 (Parliamentary Office of Science and Technology, 2005).

The International Atomic Energy Agency (IAEA) as part of the Radioactive Waste Safety Standards (RADWASS) published a high level document outlining the principles of radioactive waste management. In which they state:

> *'Responsible radioactive waste management requires the implementation of measures that will afford protection of human health and the environment since improperly managed radioactive waste could result in adverse effects to human health or the environment now and in the future.'* (IAEA, 1995)

A series of nine governing principles in the management of this waste is set out in order to achieve such an aim, which are:

i. Protection of human health: radioactive waste shall be managed in such a way as to secure an acceptable level of protection for human health.

ii. Protection of the environment: radioactive waste shall be managed in such a way as to provide an acceptable level of protection of the environment.

iii. Protection beyond national borders: radioactive waste shall be managed in such a way as to assure that possible effects on human health and the environment beyond national borders will be taken into account.

iv. Protection of future generations: radioactive waste shall be managed in such a way that predicted impacts on the health of future generations will not be greater than relevant levels of impact that are acceptable today.

v. Burdens on future generations: radioactive waste shall be managed in such a way that will not impose undue burdens on future generations.

vi. National legal framework: radioactive waste shall be managed within an appropriate national legal framework including clear allocation of responsibilities and provision for independent regulatory functions.

vii. Control of radioactive waste generation: generation of radioactive waste shall be kept to the minimum practicable.

viii. Radioactive waste generation and management interdependencies: interdependencies among all steps in radioactive waste generation and management shall be appropriately taken into account.

ix. Safety of facilities: The safety of facilities for radioactive waste management shall be appropriately assured during their lifetime.

Governments and agencies responsible for the management of nuclear and other radioactive waste must demonstrate that the concepts by which they intend to manage the waste are appropriate and safe. This builds scientific confidence in the technical understanding/feasibility and may also improve the public perception of methods (CoRWM, 2006).

1.4 High-level nuclear waste disposal

High-Level Waste (HLW) generally occurs in the form of solid or liquid and is stored in interim storage in the short to medium term, i.e. ≈50 years. This allows for some of the heat generative capacity to be reduced and therefore reduces the technical challenge to long-term disposal. Storage of liquid waste has certain longer-term security issues, e.g. corrosion of tanks. Hence to reduce the long-term storage risks and for ease of handling for long-term disposal the waste is encapsulated, in the UK normally via vitrification (Bayliss and Langley, 2003; CoRWM, 2006).

It is anticipated that after interim storage a permanent disposal method will be used to allow passive long-term storage for the waste. There are many broad concepts that have been contemplated and these are itemised below (World Nuclear Association, 2008).

- Long-term above ground storage

- Long-term below ground storage

- Disposal in outer space

- Deep boreholes

- Rock-melting

- Disposal at subduction zones

- Sea disposal

- Sub-seabed disposal

- Disposal in ice sheets

- Direct Injection

- Repositories (near-surface or deep)

- Store and wait

The only concept to have gained international consensus and scientific support is deep geological disposal (CoRWM, 2006). This concept yields control over the waste, predictability of the behaviour and the environment and the long-term viability of prospective sites. For example The Geological Society (1999) state 'only deep geological disposal can provide a long-term, safe and sustainable solution for radioactive waste'.

Following from the principles of generational equity and long-term safety there is a general consensus that the problem of HLW disposal should be tackled in the present time, as opposed to the *store and wait* method, awaiting better technology and techniques. The Principles of Radioactive Waste Management (IAEA, 1995) states that the burden of disposal should not be left for future generations although some actions such as maintaining and monitoring facilities is reasonable.

However, some environmental groups, such as Greenpeace, remain opposed to the repository solution as they believe that monitoring and maintaining these repositories is an unacceptable risk to place on future generations (Greenpeace, 2007). They advocate the *store and wait*

solution until a proven solution is found (Greenpeace, 2008).

Many countries produce nuclear waste and consequently there is wide interest in research and development of a realistic, cost-effective, safe solution. The scientific consensus that deep geological disposal is the prime proposal has led to many research programs and governmental interest. This work whilst tackling some of the technical aspects also is about building confidence in that the processes are understood.

1.4.1 Nuclear waste disposal in the UK

At present the UK's strategy, undertaken by the Nuclear Decommissioning Authority (NDA), is to make the HLW, much of it currently in liquid form, passively safe (NDA, 2006). To this end, vitrification of the liquid waste and encasing the resultant glass in robust stainless steel canisters is being undertaken (NDA, 2006). It is then destined for interim storage, generally at Sellafield, until a more permanent solution has been found (NDA, 2006; CoRWM, 2006). There are 20 nuclear sites in the UK awaiting decommissioning (NDA, 2006). The Energy Act (2004) lays out how the nuclear industry is to deal with such large quantities of waste in the UK.

The Committee on Radioactive Waste Management (CoRWM) was asked by the UK government in 2003 to oversee a review into the long-term management of the UK's higher activity waste. CoRWM (2006) published a report of their findings and conclude with a series of recommendations. They recommended to the Government that:

> '*Within the present state of knowledge, CoRWM considers geological disposal to be the best available approach for the long-term management of all the material categorised as waste in the CoRWM inventory when compared with the risks associated with other methods of management. The aim should be to progress to disposal as soon as practicable, consistent with developing and maintaining public and stakeholder confidence.*'

In addition the Royal Society stated that '*The confidence that could be placed in geological disposal in UK sites has been understated.*' (Royal Society, 2006).

Later in 2006 the Government (UK Government, 2006) published a response where they

accepted CoRWM's recommendations and state:

'In particular, Government accepts that geological disposal coupled with safe and secure interim storage is the way forward for the long-term management of the UKs higher activity wastes. As CoRWMs report observes, geological disposal is the approach being adopted in the majority of other nuclear nations, including in Belgium, France, Finland, Germany, Japan, Sweden, Switzerland and the US. CoRWMs work has shown that this is also the appropriate way forward for the UK. Nevertheless, securing geological disposal represents a major challenge and will require commitment over many decades.'

Following consultation, the Government published a white paper 'Managing Radioactive Waste Safely: A Framework for Implementing Geological Disposal' in June 2008 (Defra *et al.*, 2008). The main aspects of the Government's approach for implementation were set out including the technical framework for implementation, the support of ongoing research and a framework for site selection.

1.5   Deep geological disposal - Swedish System

As previously discussed the most likely option for the UK and the rest of the world for disposal of nuclear waste is deep geological disposal. As part of this many countries are developing full systems for the management of nuclear waste from interim storage to final disposal. One of the most advanced countries in this respect is Sweden. Svensk Karnbranslehantering AB (SKB), the Swedish Nuclear Fuel and Waste Management Company, have established a system, known as the Swedish System, for managing radioactive waste that includes a central interim storage facility for spent nuclear fuel, an encapsulation plant and a final repository (SKB, 2008a). The storage facility, Clab, exists in Oskarshamn and a repository for operational waste, i.e. not high-level, exists in Forsmark. The encapsulation plant is due to be built adjacent to Clab so that the operation and some facilities may be shared (SKB, 2008a). An integral part of the Swedish System is the KBS-3 multi-barrier concept for repository disposal. This requires the high-level waste to be encapsulated in copper, placed in a repository at approximately $500m$ depth in bedrock, embedded in clay and sealed. (SKB, 2008a).

The research and development program is advanced and includes the Hard Rock Laboratory (HRL) at Äspö for field scale tests, including practical and scientific tests, both short and long-term (SKB, 2007). The Prototype Repository Project, in particular, offers engineers a chance to understand the field scale challenges and theory validation in a realistic environment. SKB applied for a permit for the plant to encapsulate HLW in November 2006 and is due to apply for a permit for the final repository in 2010 (SKB, 2009).

1.5.1 Disposal concept (KBS-3)

The current Swedish disposal concept is the KBS-3 system which stands for Nuclear Fuel Safety (KBS) and three barriers (3). Many countries and research programmes have adopted this concept as a reference concept. The Swedish system entails that the waste is contained by a number of barriers and deposited in bedrock at approximately $500m$ depth. The barrier system is illustrated in figure 1.1 and consists of the following (SKB, 2003):

- Canister - The copper canister isolates the fuel from the surroundings and is designed so that no radionuclides can escape until corrosion occurs. Copper is known to corrode very slowly in the conditions expected in a repository. A cast iron insert will protect the canister from mechanical stresses (SKB, 2003).

- Buffer - The canister is deposited in a bentonite clay buffer. The buffer allows small movements in the rock to occur, swells when adsorbing water and acts to greatly retard any radionuclide release from the canister. The bentonite swelling property allows the material to 'self-heal' and hold the canister in place. The buffer and canister represent the near-field, engineered barriers (SKB, 2003).

- Bedrock - The rock protects the buffer and canister, retards any radionuclide release and provides a stable chemical environment (SKB, 2003).

The barriers as a whole are intended to stop, in the short term, and vastly retard, in the long-term, the migration of radionuclides to the biosphere (SKB, 2008b). SKB have proposed both the KBS-3V and the KBS-3H systems whereby canisters are inserted into deposition-holes drilled vertically and horizontally respectively.
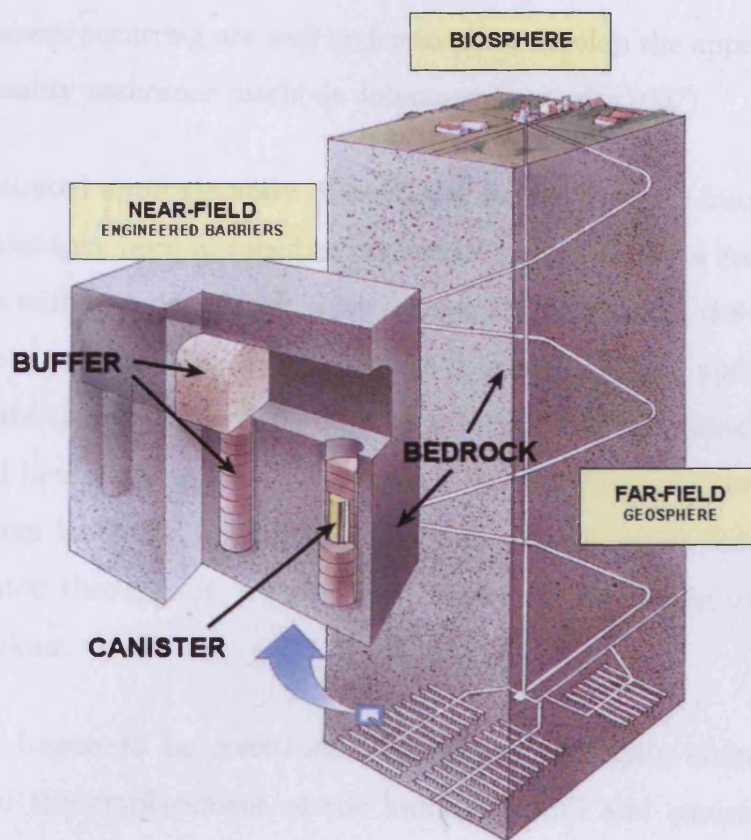
Figure 1.1. KBS-3 concept for disposal. (after SKB, 2003)

1.6 Prototype Repository Project

As part of the ongoing research programme a full scale test of the KBS-3 repository concept has been undertaken at the Hard Rock Laboratory (HRL) at Äspö. The project is unique in the fact that it offers for the first time the integration of all aspects of the repository concept, includes multiple deposition-holes and is intended to be operational for at least 20 years (Svemar and Pusch, 2000).

The project builds upon over two decades of research in this area of deep geological disposal, and extends the capability of previous experimental work investigating various aspects of the disposal strategy. This is the first time that all aspects of the repository system have been investigated at the same time and in an integrated manner. The project aims to simulate a future KBS-3 deep geological repository, in as realistic conditions as possible, in respect to design, installation, geometry, materials, construction and environment. The exception is that the HLW is simulated by use of heaters (Svemar and Pusch, 2000). Additionally, the main aims of the project are to compare experimental and simulated results to investigate

whether the processes occurring are well understood, to develop the appropriate engineering standards and quality assurance methods Johannesson *et al.* (2007).

The project is situated approximately 450m below sea level and in fractured granite rock. Six deposition-holes have been included in two sections separated by a concrete plug, so that the outer section with two deposition-holes can be removed before the end of the project. After the repository construction, emplacement of the buffer material and canisters including heaters to simulate the heat flux from HLW, the tunnel was backfilled with a mixture of crushed rock and bentonite. A heat flux regime was implemented based on the reducing heat flux likely from HLW and begun sequentially in each deposition-hole. The project was highly instrumented throughout, with sensors measuring the temperature, hydraulic and mechanical behaviour.

The project was begun to be constructed and the rock highly characterised prior to emplacement and the emplacement of the buffer, backfill and canisters was begun in September 2001 and finished in June 2003. The project is ongoing and intends to provide results for at least 20 years, although it must be noted that a number of sensors have failed as the project progresses.

1.7 Safety case

The safety case is essentially the method by which the safety of a facility is substantiated and confidence in the overall performance is gained. It contains outputs of safety assessments, supporting evidence and reasoning on the robustness and reliability of the repository. Any weaknesses or unknowns will be identified and the methods to overcome them outlined. Both quantitative and qualitative evidence will be included along with all relevant information (IAEA, 2006; Defra, 2008b).

Safety assessment is part of the safety case and is the systematic process of analysing hazards and risk associated with the facility. Quantification of performance and risk is essential to this part and are inherently site specific. Specifically commissioned work and a more general body of scientific knowledge is drawn upon to undertake the process. An output of safety assessment may be to identify where further research should be undertaken (Defra, 2008b). The post-closure safety assessment will include both generic and site specific

studies, assessment reports including numerical analyses, study of natural analogues and a demonstration of compliance with requirements (Defra, 2008b).

To experimentally assess the long-term viability of the deep geological repository concept over the design timescales of many thousand years is impractical. Therefore, naturally occurring phenomena that have been in existence for the timescales required and that reflect some of the properties required or contain the materials to be utilised can be examined. These are known as natural analogues.

A good summary of the use of natural analogues in relation to geological disposal of radioactive wastes is presented by Miller *et al.* (2000). It is noted, however, that no natural analogue completely describes a deep geological repository for various reasons, e.g. dissimilar mineralogy of ores/waste, clays or host rocks, variation in size of deposits. For example there are no known clay deposits at an appropriate temperature that contain metallic elements that are likely to corrode and therefore generate gas.

Site specific assessment includes both experimental and numerical results. Numerical assessment of the repository backed up with experimental evidence is one method used in safety assessment, used to build confidence that the major physical processes have been understood. Confidence in numerical assessment must be built-up via the simulation of experimental work. A wide range of experimental work has been undertaken at both laboratory scale and field-scale, so that the processes and materials used can be characterised.

1.8 Computational/numerical simulation

The ability to simulate, via computation, requires an understanding of the various underlying processes. It is well accepted that numerical simulation can be used to illustrate technical understanding, via development of conceptual models and validation with experimental data. Numerical simulation can then be used to test various scenarios at a fraction of real cost and predict future behaviour. Computer modelling is also non-destructive; data can be easily produced at all locations and can be gained in reduced time periods compared to experimentation. However, it is critical that models are correctly understood and used only in relevant circumstances, otherwise important processes may be omitted from simulations and incorrect results found.

1.9 Experimentation

Much experimental work has been undertaken at various scales, both within the laboratory to characterise various phenomena in detail and at field-scale to investigate both physical and practical processes. A brief summary of some selected experiments on the behaviour of the engineered barrier is contained in table 1.1 for laboratory work and table 1.2 for underground research laboratories. Further details are given in chapter 2.

Authors	Year	Details
Villar *et al.*	1996	Thermo-hydraulic experiments on compacted bentonite with a variety of initial water contents and heating regimes.
Börgesson *et al.*	1996	Reported a range of mechanical and hydro-mechanical tests, including iso-thermal swelling, shear tests, triaxial tests and hydraulic conductivity tests.
Villar *et al.*	1999	Investigated the mechanical response of compacted bentonite
Lloret *et al.*	2003	in an odeometer under constant suction.
Villar *et al.*	2003/ 2005	Investigated hydration of compacted bentonite both isothermally and under a temperature gradient.
Romero *et al.*	2005	Investigated thermo-hydro-mechanical behaviour of two clays via temperature and suction controlled odeometers.
Delage *et al.*	2006	Observed time dependant change in the pore structure of MX-80 bentonite using MIPS.
Hoffmann *et al.*	2007	Hydraulic and hydro-mechanical response of bentonite pellets. Material evolution was found to be critical.
Villar *et al.*	2008	Longterm experiment into the thermo-hydraulic behaviour of compacted bentonite, this paper reports results from 8 years.

Table 1.1. Summary of selected experiments in relation to the engineered barrier system.

Site	Country	Details
HADES URF	Belgium	Investigating many aspects of HLW disposal in a Boom clay deposit, including various aspects of the thermal-hydraulic response.
Whiteshell URL	Canada	Situated in granitic rock contained many experiments on buffer material in full size. Contained the first long-term test of 6.5 years.
Grimsel Test Site	Switzerland	Situated in granite rock contains many experiments into radionuclide transport, near-field processes and engineering feasibility.
Stripa	Sweden	A number of tests were undertaken aimed to investigate rock characterisation, groundwater flow and engineered barriers in granite rock. Fractures in rock were found to be key in predicting flow.
Äspö Hard Rock Laboratory	Sweden	Constructed in granitic rock was designed to address real-scale uncertainty in the bedrock, buffer behaviour and practical engineering issues.

Table 1.2. Summary of selected underground research facilities.

1.10 Study outline

In the context of deep geological disposal and large scale experimentation the Prototype Repository Project (PRP) is being undertaken in Äspö, Sweden by SKB and is yielding a set of unique results both in terms of physical scale and length of time. This represents an opportunity to review past and current work and undertake numerical simulation of this project to try and further understand the physical behaviour of such systems. The PRP was introduced in section 1.6 and is detailed in chapter 6 including an overview of experimental results. This experiment is key within world-wide experimental programmes, building on over two decades experience, and tests a full repository concept at full-scale. A key aspect of this project, which is likely to be apparent in many disposal concepts in crystalline rock, is the fractured nature of the rock and three-dimensional nature of the geometry. There is a need to identify the fractures, analyse their behaviour and include their behaviour in any numerical simulation. Any simulation capable of including the major features of this

project will need to be three-dimensional due to the experiment geometry and anisotropic flow conditions in the fractured rock. The PRP utilises heaters to simulate the heating potential of high-level nuclear waste and a highly-swelling clay is used as a buffer material. Therefore, thermal, hydraulic and mechanical effects have been observed and through many experimental programmes these processes are known to be coupled. Numerical studies to simulate the behaviour of the PRP have been undertaken (e.g. Melhuish, 2004) and this work aims to expand upon this existing body of work.

1.10.1 Objectives

The main objectives of this study are to:

i. Produce a three-dimensional thermo-hydro-mechanical model of the Prototype Repository Project.

- Formulate a computational algorithm so that large-scale long-term simulations may be undertaken in a reasonable time. High-performance computer facilities may be used if appropriate.

- Develop existing material models to take account of rock fractures;

- Develop existing material models to take account of time dependent micro-structural behaviour of buffer materials;

ii. Compare with experimental field data.

iii. Evaluate numerical and experimental results.

1.11 Current research background

This work is undertaken at the Geoenvironmental Research Centre at Cardiff University where considerable research, including the development of the numerical computer code COMPASS, has been performed prior to the study. This section provides the context to this work, and is not intended to replace more detailed reviews of literature in chapter 2 or the theoretical formulation in chapter 3.

A two-dimensional solution of heat and mass transfer in unsaturated soil was presented by Thomas (1985) and developed including material non-linearity and a variety of time stepping

schemes (Thomas 1987, 1988a, 1988b, Thomas and Rees, 1988, 1990). The principle of mass conservation was employed for moisture flow and the conservation of energy used for heat transfer. Moisture vapour transport was assumed to be diffusive following de Vries (1958) and latent heat transfer was incorporated via the approach of Luikov (1966).

Ewen and Thomas (1987) undertook an experimental work consisting of an unsaturated sand surrounding a heating rod. A variety of moisture contents and heat fluxes were used. A numerical formulation in terms of moisture content and temperature and a simulation of the work was carried out by Ewen and Thomas (1989) including vapour transport via a diffusive mechanism.

Thomas and King (1991) presented a theoretical heat and moisture formulation cast in terms of capillary potential and temperature and found good agreement with the Ewen and Thomas (1987) experiments. Thomas and Sansom (1995) extended this formulation to include elevated pore-air pressures and validated via comparison to experimental works on sand and clay. This formulation was presented in three-dimensions including work on pre and post-processing, visualisation and parallel computation by Sloper (1997) and Thomas et al. (1998).

Deformation was introduced examining seasonal ground movements (Thomas and Rees, 1990, 1993), with an isothermal coupled moisture-mechanical numerical model presented by Thomas et al. (1992) utilising that non-linear elastic state-surface approach of Lloret and Alonso (1985). This model was applied to seasonal ground movements in Thomas and Zhou (1995). An elasto-plastic coupled thermo-hydro-mechanical (THM) model was presented by Thomas and He (1994) using the elasto-plastic model of Alonso et al. (1990) and this was further developed to include some behaviour of expansive clays by Thomas and Cleall (1999).

THM models of large scale experiments were presented by Mitchell (2002), Thomas et al. (2003), Melhuish (2004) and Cleall et al. (2006) and included investigation into the micro-structural behaviour of bentonite when re-saturating. The hydraulic conductivity of bentonite was modified so that micro-macro behaviour could be included. It is worth noting that this inflow rate was slow in the cases simulated by Mitchell (2002) and Thomas et

al. (2003). Melhuish (2004) modelled the PRP and this thesis follows directly from this work.

In addition other theoretical developments include non-reactive chemical and contaminant transport (Thomas and Cleall, 1997); two-dimensional couple moisture and reactive multi-chemical solute transport (Hashm, 1999); and coupled thermo-hydro-chemical-mechanical including reactive multi-chemical transport (Cleall *et al.*, 2007a, 2007b). However, these developments were beyond the scope of this work.

1.12 Scope and limitations

The scope of the work undertaken in this thesis and in particular the limitations that are anticipated are listed below:

- Numerical approximation is used to find a solution to the system of coupled differential equations. In particular, the finite-element method is used to provide a spatial solution and the finite-difference method used to provide a temporal solution.

- Within the definition of the behaviour of each material, anisotropy has not been allowed for in the theoretical formulation. Therefore known anisotropy, for example in some soil stress-strain behaviour, cannot be included in numerical simulations. However, multiple materials can be defined and utilised so that overall system heterogeneity can be included.

- Soil hysteresis behaviour such as found in the moisture retention behaviour in wetting/drying paths has not been included in the model. This is due in part to a lack of experimental evidence and a complex wetting/drying path.

- The temperature range that the theoretical model has been formed for and therefore valid over is from 0 to $100°C$. For the PRP experiment both the design and experimental results so far indicate that this range will not be exceeded.

- The constitutive relationships presented in the theoretical formulation were developed for slightly and moderately swelling soils.

- Vapour transport is assumed to be diffusive. At higher-temperatures, elevated air-pressure gradients may occur, leading to increased vapour movement. This has not been included in the theoretical formulation.

- It is acknowledged that chemical/geochemical and biological processes among others may have an impact on the behaviour of the PRP but the study of these processes is beyond the scope of this work.

1.13 Overview of thesis

Chapter 2 contains a selective review of the current literature salient to the work contained in the remainder of thesis, including a review of the state-of-the-art coupled thermo-hydro-mechanical modelling and experimentation into aspects of high-level nuclear waste disposal.

The theory and numerical formulation are presented in chapter 3 with the computational formulation and performance contained in chapter 4. Here, the literature pertinent to computational optimisation of coupled finite element models is reviewed and a number of algorithms suggested to increase performance. This implementation is defined and performance of improvements analysed.

Model development and validation work is presented in chapter 5 with special attention paid to the micro-structural behaviour of the compacted bentonite both in compacted blocks and pelletised form. In particular the time-dependent behaviour of highly-compacted bentonitic material is introduced and a framework outlined so that it may be included in porous media models. This is validated against available experimental work.

A full-size mock-up experiment of a HLW repository named the Prototype Repository Project is introduced in detail in chapter 6, including an outline of the experimental results and synthesis of the behaviour exhibited.

Chapters 7 and 8 present the numerical simulation work that aims to comprehensively simulate the Prototype Repository Project. A suite of models are presented from small scale work designed to test material parameter selection and material relations to full size coupled analyses intending to simulate the whole repository. Finally, predictions for the long-term behaviour are presented.

Concluding remarks and suggestions for further work are presented in chapter 9.

1.14 References

Alonso, E.E., Gens, A., Josa, A., (1990) "A constitutive model for partially saturated soils", *Géotechnique*, **40**(3), 405-430.

Bayliss, C.R., Langley, K.E., (2003) *Nuclear decommissioning, waste management, and environmental site remediation*, Elsevier.

Department for Business, Enterprise & Regulatory Reform (BERR), (2008) *Meeting the energy challenge, a white paper on nuclear power*, Cm 7296, Stationery Office, London.

Börgesson, L., Karnland, O., Johannesson, L-E., (1996) "Modelling of the physical behaviour of clay barriers close to water saturation", *Engineering Geology*, **41**, 127-144.

Cleall, P.J., Melhuish, T.A., Thomas, H.R., (2006) "Modelling the three-dimensional behaviour of a prototype nuclear waste repository", *Engineering Geology*, **85**(2), 212-220.

Cleall, P.J., Seetharam, S.C., Thomas, H.R., (2007a) "Inclusion of some aspects of chemical behaviour of unsaturated soil in thermo/hydro/chemical/mechanical models. I: Model development" *ASCE Journal of Engineering Mechanics*, **133**(3), 338-347.

Cleall, P.J., Seetharam, S.C., Thomas, H.R., (2007b) "Inclusion of some aspects of chemical behaviour of unsaturated soil in thermo/hydro/chemical/mechanical models. II: Application and transport of soluble salts in compacted bentonite" *ASCE Journal of Engineering Mechanics*, **133**(3), 348-356.

Climate Change Act, (2008) c.27, HMSO, London.

CoRWM, (2006) *Managing our radioactive waste safely, CoRWM's recommendations to Geovernment*, Committee on Radioactive Waste Management.

Defra, (2008a) *e-digest statistics about: Climate change* [WWW] <URL:http://www.defra.gov.uk/environment /statistics/globatmos/index.htm> [Accessed 26th January 2009].

Defra, (2008b) *Managing radioactive waste safely - Regulatory scrutiny and control: Production of safety case* [WWW] <URL:http://www.defra.gov.uk/environment /radioactivity/mrws/safety/> [Accessed 13th May 2009].

Defra, BERR and the devolved administrations for Wales and Northern Ireland (2008) *Managing Radioactive Waste Safely: A framework for implementing geological disposal*, Cm 7386, Stationery Office, London.

Delage, P., Marcial, D., Cui, Y.J., Ruiz, X., (2006) "Ageing effects in a compacted bentonite: a microstructure approach", *Géotechnique*, **56**(5), 291-304.

de Vries, D.A., (1958) "Simultaneous transfer of heat and moisture in porous media", Transactions of the American Geophysics Union, **39**(5), 909-916.

DTI, (2003) *Energy white paper: Our energy future - creating a low carbon economy*, Cm 5761, The Stationary Office, London.

DTI, (2006) *The energy challenge, energy review: A report*, Cm 6887, Department of Trade and Industry, London.

Energy Act, (2004) c.20, HMSO, London.

Ewen, J., Thomas, H.R., (1987) "The thermal probe - a new method and its use on an unsaturated sand", *Géotechnique*, **37**(1), 91-105.

Ewen, J., Thomas, H.R., (1989) "Heating unsaturated medium sand", *Géotechnique*, **39**(3), 455-470.

The Geological Society, (1999) *Geosciences verdict on radioactive waste disposal*, News Release PR26/99, The Geological Society, London.

Greenpeace, (2007) *Climate Change - Nuclear not the answer*, Greenpeace Briefing.

Greenpeace, (2008) *End the nuclear age* [WWW] <URL:http://www.greenpeace.org/ international/campaigns/ nuclear> [Accessed 20th December 2008].

Hashm, A.A., (1999) "A study of the transport of a selection of heavy metals in unsaturated soils", *PhD Thesis*, Cardiff University, Cardiff.

Hoffmann, C., Alonso E.E., Romero, E., (2007) "Hydro-mechanical behaviour of bentonite pellet mixtures", *Physics & Chemistry of the Earth*, **32**, 832-849.

House of Lords, (2008) *The economics of renewable energy, volume I: report*, Select Committee on Economic Affairs, 4th Report of Session 200708, Authority of the House of Lords, The Stationery Office, London.

IAEA, (1995) *The principles of radioactive waste management.* Safety Series No. 111-F, Safety Fundamentals, International Atomic Energy Agency, Vienna.

IAEA, (2006) *Geological disposal of radioactive waste: Safety requirements*, IAEA Safety Standards Series No. WS-R-4, International Atomic Eenergy Agency, Vienna.

International Energy Agency (IAE), (2008) *Deploying Renewables: Principles for Effective Policies*, OECD Publishing.

Johannesson, L-E., Börgesson, L., Goudarzi, R., Sandèn, T., Gunnarsson, D., Svemar, C., (2007) "Prototype repository: A full scale experiment at Äspö HRL", *Physics and Chemistry of the Earth*, **32**, 58-76.

Lloret, A., Alonso, E.E., (1985) "State surfaces for partially saturated soils", *Proceedings of the 11th International Conference of Soil Mechanics and Foundation Engineering*, San Francisco, **2**, 557-562.

Lloret, A., Villar, M.V., Sánchez, M., Gens, A., Pintado, X., Alonso, E.E., (2003) "Mechanical behaviour of heavily compacted bentonite under high suction changes", *Géotechnique*, **53**(1), 27-40.

Luikov, A.V., (1966), *Heat and mass transfer in capillary porous bodies*, Pergamon Press, Oxford.

Melhuish, T.A., (2004) "An investigation of the three-dimensional thermo/hydro/mechanical behaviour of large scale in-situ experiments" *PhD Thesis*, Cardiff University, Cardiff.

Miller, W., Alexander, R., Chapman, N., McKinley, I., Smellie, J., (2000) *Geological disposal of radioactive wastes and natural analogues, Lessons from nature and archaeology*, Pergamon, Oxford.

Mitchell, H.P., (2002) "An investigation into the thermo/hydro/mechanical interactions involved in high level nuclear waste disposal" *PhD Thesis*, University of Wales, Cardiff.

NDA, (2006) *Strategy*, Nuclear Decommissioning Authority.

Parliamentary Office of Science and Technology, (2005) *Postnote: Recycling household waste*, Number 252, The Parliamentary Office of Science and Technology, London.

Romero, E., Villar, M.V., Lloret, A., (2005) "Thermo-hydro-mechanical behaviour of two heavily overconsolidated clays", *Engineering Geology*, **81**, 255-268.

Royal Society, (2006) *The long-term management of radioactive waste: the work of the committee on radioactive waste management*, Policy document 01/06, Royal Society, London, UK.

SKB, (2003) *Deep repository for spent nuclear fuel*, SKB, Stockholm.

SKB, (2007) *RD&D 2007, Programme for research, development and demonstration of methods for the management and disposal of nuclear waste*, SKB, TR-07-12, Stockholm.

SKB, (2008a) *Our Facilities - SKB* [WWW] <URL:http://www.skb.se/templates/SKBPage___8738.aspx> [accessed 10th July 2008].

SKB, (2008b) "Äspö Hard Rock Laboratory" [WWW] <URL:http://www.skb.se/templates/ SKBPage___8855.aspx> [accessed 10th July 2008].

SKB, (2009) *Permits, EIA and consultations* [WWW] <URL:http://www.skb.se/Templates/ Standard___16764.aspx> [Accessed 26th January 2009].

Sloper, N.J., (1997) "The development of a new three dimensional numerical model for fully coupled heat, moisture and air flow in unsaturated soil incorporating scientific visualisation and parallel computing techniques", *PhD Thesis*, University of Wales, Cardiff.

Svemar, C., Pusch, R., (2000) *Äspö Hard Rock Laboratory, Prototype Repository, Project description*, SKB, IPR-00-30, Stockholm.

Thomas, H.R., (1985) "Modelling two-dimensional heat and moisture transfer in unsaturated soils, including gravity effects", *International Journal of Analytical Methods in Geomechanics*, **9**, 573-588.

Thomas, H.R., (1987) "Non-linear analysis of heat and moisture transfer in partly saturated soil", Journal of Engineering Mechanics, *American Society of Civil Engineering*, **113**, 1163-1180.

Thomas, H.R., (1988a) "A non-linear analysis of two-dimensional heat and moisture transfer in partly saturated soil", *International Journal of Analytical Methods in Geomechanics*, **12**, 31-44.

Thomas, H.R., (1988b) "The influence of non-linear thermal parameters on moisture content distributions in unsaturated soil", *International Journal of Analytical Methods in Engineering*, **26**, 263-279.

Thomas, H.R., Cleall, P.J., (1997) "Chemico-osmotic effects on the behaviour of unsaturated expansive clays", *Geoenvironmental engineering, Contaminated ground; fate of pollutants and remediation*, Yong, R.N., Thomas, H.R., (eds.), Thomas Telford, London, 272-277.

Thomas, H.R., Cleall, P.J., (1999) "Inclusion of expansive clay behaviour in coupled thermo hydraulic mechanical models", *International Journal of Engineering Geology*, **54**, 93-108.

Thomas, H.R., Cleall, P.J., Chandler, N., Dixon, D., Mitchell, H.P., (2003) "Water infiltration into a large-scale in-situ experiment in an underground research laboratory", Géotechnique, **53**(2), 207-224.

Thomas, H.R., He, Y., (1994) "An elasto-plastic analysis of the thermo/hydraulic/mechanical behaviour of unsaturated soil", *Proceedings of the 8th International Conference on Computer Methods and Advances in Geomechanics*, Morgantown, Siriwardane, H.J., Zaman, M.M., (eds.), Balkema, Rotterdam, 1171-1176.

Thomas, H.R., King, S.D., (1991) "Coupled temperature/capillary potential variations in unsaturated soil", *Journal of Engineering Mechanics, American Society of Civil Engineers*, **117**(11), 2475-2491.

Thomas, H.R., Rees, S.W., (1988) "The use of Lee's algorithm in the analysis of some ground heat and mass transfer problems", *Proceedings of the 6th International Conference on Numerical Methods in Geomechanics*, Innsbruck.

Thomas, H.R., Rees, S.W., (1990) "An examination of the performance of a 3-level time stepping algorithm - Coupled heat and mass transfer computing", *Proceedings of the 1st International Conference, Advances in Computer Methods in Heat Transfer*, Southampton.

Thomas, H.R., Rees, S.W., (1993) "The numerical simulation of seasonal soil drying in an unsaturated clay soil", *International Journal of Numerical & Analytical Methods in Geomechanics*, **17**(1), 119-132.

Thomas, H.R., Rees, S.W., Sloper, N.J., (1998) "Three-dimensional heat, moisture and air transfer in unsaturated soils", *International Journal of Numerical & Analytical Methods in Geomechanics*, **22**(2), 75-95.

Thomas, H.R., Sansom, M.R., (1995) "Fully coupled analysis of heat, moisture and air transfer in unsaturated soil", Journal of Engineering Mechanics., *American Society of Civil Engineering*, **121**(3), 392-405.

Thomas, H.R., Zhou, Z., (1995) "A comparison of field measured and numerically simulated seasonal ground movement in unsaturated clay", *International Journal for Numerical and Analytical Methods in Geomechanics*, **19**, 249-265.

Thomas, H.R., Zhou, Z., He, Y., (1992) "Analysis of consolidation of unsaturated soils", *Proceedings of the 2nd Czechoslovak Conference on Numerical Methods in Geomechanics*, Prague, Dolezalova, M., (ed.), **1**, 242-247.

UK Government and the devolved administrations, (2006) *Response to the report and recommendations from the committee on radioactive waste management (CoRWM)*, PB 12303, Department for Environment, Food and Rural Affairs, UK.

United Nations, (1998) *Kyoto protocol to the United Nations framework convention on climate change*, United Nations.

United Nations Environment Programme (UNEP), (2009a) *From conflict to peacebuilding. The role of natural resources and the environment*, UNEP.

United Nations Environment Programme (UNEP), (2009b) *Global trends in sustainable energy investment*, UNEP.

Villar, M.V., (1999) "Investigation of the behaviour of bentonite by means of suction-controlled oedometer tests", *Engineering Geology*, **54**, 67-73.

Villar, M.V., Cuevas, J., Martín, P.L., (1996) "Effects of heat/water flow interaction on compacted bentonite: Preliminary results", *Engineering Geology*, **41**, 257-267.

Villar, M.V., Martín, P.L., Barcala, J.M., (2005) *Infiltration tests at isothermal conditions and under thermal gradient*, CIEMAT, Technical report CIEMAT/DMA/M2140/1/05.

Villar, M.V., Sánchez, M., Lloret, A., Gens, A., Romero, E., (2003) "Experimental and numerical study of the T-H-M behaviour of compacted bentonite in small-scale tests", *Advances in Understanding Engineered Clay Barriers* Alonso, E., Ledesma, A., (eds.), 323-335.

Villar, M.V., Sánchez, M., Gens, A., (2008) "Behaviour of a bentonite barrier in the laboratory: Experimental results up to 8 years and numerical simulation", *Physics & Chemistry of the Earth* **33**, S476-S485.

World Nuclear Association, (2008) *Waste Management in the Nuclear Fuel Cycle* [WWW] <URL:http://www.world-nuclear.org/info/inf04.html> [Accessed 2nd December 2008].

WWF, (2008) *Living planet report 2008*, WWF International, Gland, Switzerland.

2

Selective Literature Review

2.1 Introduction

The study of flow and deformation within porous material, in particular, soils has been of interest for many years. Hence, many of the processes are well established. The flows and deformation within partially saturated soils are more complex than in saturated soils and it is the interactions between the flows and deformations that determine the behaviour. This field has been of particular interest in relation to the long-term disposal of High-Level Nuclear Waste (HLW). There are a number of research programmes, including numerical investigation and experimental, both laboratory and field scale, into the processes involved.

In the engineered buffer and the immediately surrounding rock matrix of a high-level nuclear waste repository, termed the near-field (NF), the key processes include the thermal, hydraulic and mechanical behaviour and how these interact. These processes are impacted by the unsaturated conditions and as such the gas phase must be considered. In addition, it is likely that chemical, geochemical and biological phenomena may impact on some of these

processes, in particular, the micro-structural behaviour of the soil. However, this is beyond the scope of this work.

A number of reviews exist in the fields of Thermo-Hydraulic-Mechanical (THM) coupled behaviour in relation to buffer materials (e.g. Cleall, 1998) and flow within fractured material (e.g. Jing, 2003). This review summarises the salient elements of previous work and concentrates upon recent developments within this field.

Numerical modelling is intrinsically coupled to developments in computers and computational techniques. However, this review is concerned with the understanding of geomechanics of the problem, with a review of overall computational trends, including high-performance computing, contained within chapter 4. Geomechanical modelling is utilised in performance assessment and formulation of the safety case, which in turn utilises long-term comparison with natural phenomena termed natural analogues and the quantification of uncertainty, risk and reliability.

Section 2.2 contains a review of models of coupled heat, moisture, air flow and deformation of an unsaturated soil, with section 2.3 reviewing the same processes in fractured rock. Experimentation on various aspects of nuclear waste disposal in particular on the buffer materials and engineered barrier systems is reviewed in section 2.4 and concluding remarks are presented in section 2.5.

2.2 Coupled thermo-hydro-mechanical behaviour in unsaturated soil

A number of comprehensive studies have been undertaken of various aspects of THM behaviour (e.g. Thomas, 1980; Alonso et al., 1987; Fredlund and Rahardjo, 1993; Delage and Graham, 1996; Cleall, 1998; Mitchell, 2002; Melhuish, 2004) and as such only the salient developments have been discussed along with more recent developments. The derivation of THM models for unsaturated soils have originated from two distinct directions, the first from analysis of consolidation behaviour (hydro-mechanical) and the second from the analysis of the flow behaviour (hydraulic, thermo-hydraulic). The formulation of flow behaviour tends to follow two general approaches, a thermodynamic approach and a mechanistic approach. In general terms the thermodynamic approach tends to be more rigorous, but is difficult to

use in terms of parameter definition, whereas the mechanistic approach tends to have more easily determinable parameters.

Biot (1941) established a three-dimensional theory for consolidation of a linear-elastic isotropic soil. The deformation of the soil was shown to be a function of the stress and pore-water-pressure and as such is consistent with the effective stress theory (Terzaghi, 1936). Bishop (1959, 1960) extended the effective stress concept for unsaturated soils and formed a single effective stress variable for unsaturated soils:

$$\sigma' = (\sigma - u_a) + \chi(u_a - u_l) \tag{2.1}$$

where χ is a parameter relating to the degree of saturation and varies between zero and one for a dry and saturated soil respectively.

This proposal was investigated by many researchers (Jennings and Burland, 1962; Bishop and Blight, 1963; Aitchison, 1965; Burland, 1965) and it was concluded that effective stress in this form could explain shear strength adequately but was not able to describe the volume change behaviour. Coleman (1962) suggested the use of three stress-state variables where all three have an impact on volume change, net mean stress (p), matric suction (s) and deviatoric stress (q). Bishop and Blight (1963) use all three stress-states to describe the soil stress-state but link only net stress and matric suction to volume change. These stresses can be defined as:

$$\sigma'' = \sigma - u_a \tag{2.2}$$

$$s = u_a - u_l \tag{2.3}$$

$$q = \sqrt{\frac{1}{2}\left[(\sigma_1 - \sigma_2)^2 + (\sigma_2 - \sigma_3)^2 + (\sigma_3 - \sigma_1)^2\right]} \tag{2.4}$$

Barden (1965) proposed a consolidation model for unsaturated clay. Four partial differential equations were formed in terms of pore-air-pressure, pore-water-pressure, unsaturated fluid conductivity and porosity. The Bishop (1959, 1960) principle of effective stress was used to govern the deformation. Matyas and Radhakrishna (1968) undertook a series of oedometer and triaxial tests and related changes in degree of saturation and void ratio to two independent stress parameters: net stress and matric suction, via the state surface approach. Such state surfaces were found to be unique for monotonic loading and increases

in the degree of saturation. Barden *et al.* (1969) confirmed these findings.

An early important mechanistic model for heat and moisture flow was that of Philip and de Vries (1957) whereby moisture transport in a porous media was described by a single equation for both liquid and vapour. Liquid flow was described by Darcy's Law and included heat surface energy effects via the model proposed by Edelfsen and Anderson (1943) and vapour flow was considered to be diffusive. Later, de Vries (1958) modified the proposed model to include local thermodynamic equilibrium for vapour and liquid, including consideration of phase change.

Using a thermodynamics approach Luikov (1966) presented a significant work on the flow of heat and mass through porous media. Flow processes were mixed in the governing equations and coefficients were interdependent, hence hard to determine. Whitaker (1977) then proposed a set of constitutive equations, similar to those of Luikov (1966), but formed for each phase. A volume averaging technique was then used to yield a solvable set of equations. Pollock (1986) defined three non-linear partial differential equations based on Whitaker (1977) in terms of temperature, degree of saturation and total gas pressure and applied them to a one-dimensional model of a nuclear waste repository over 1000 years.

Other models of note include: Dakshanamurthy and Fredlund (1981) for the one-dimensional heat, moisture and air transport in an unsaturated soil; Couvillion and Hartley (1986) investigating thermally induced drying fronts in unsaturated sandy soil; Fredlund and Hasan (1979), extending the Terzaghi (1936, 1943) approach to unsaturated conditions; Lloret and Alonso (1980) using a coupled one-dimensional model for water, air and deformation, utilising the state-surface approach based on the work of Matyas and Radhakrishna (1968); Chang and Duncan (1983) formed a fluid and elasto-plastic deformation model; Thomas (1985) presented a two-dimensional heat and moisture transfer model; Geraminegad and Saxena (1986) proposed a coupled thermo-elastic model for heat, moisture and air flow and volume change due to pore-pressure; with Lloret *et al.* (1987) and Alonso *et al.* (1988) presenting a model with all terms coupled for flow and deformation.

Experimental work was undertaken by Lloret and Alonso (1985) who performed a series of

confined and isotropic compression tests and proposed a number of functions to describe
the state-surfaces, and Ewen and Thomas (1987) who investigated the drying of a sand.
Ewen and Thomas (1989) modelled the sand drying experiment using a two dimensional
finite element method. A heat and mass transfer model based upon the capillary potential
and temperature was proposed by Thomas and King (1991), with Thomas and Sansom
(1995) then presenting a coupled heat, moisture and air transfer model, where the air was
considered to be a binary mix of dry air and vapour, with all terms coupled to other processes.

A number of limitations were identified with elastic state-surface models:

- Only include wetting induced swelling and collapse if loading is monotonic.

- Only include elastic deformation.

- Do not include the influence of deviatoric stress on volumetric deformation.

The development of elasto-plastic relationships was designed to overcome some of the
limitations of elastic constitutive modelling. In general, elasto-plastic models are able to
include both elastic and plastic deformation and link shear and volumetric behaviour. A
number of models have been proposed for unsaturated soils: Alonso *et al.* (1990); Kohgo *et
al.* (1993a); Wheeler and Sivakumar (1995); and Bonelli and Poulain (1995).

Of particular note is the work of Alonso *et al.* (1990) who formed the so called Barcelona
Basic Model (BBM) by means of an extension of the Modified Cam-Clay (MCC) model,
using three stress-states to define the stress as Coleman (1962). All three of the stress-states:
suction, net stress and deviatoric stress, are used to describe volume change. The salient
features of the model in addition to the elastic models are:

- The soil stiffness changes in response to suction change.

- Irrecoverable (plastic) volumetric strains occur due to wetting collapse.

- The amount of wetting collapse is linked to the level of net stress.

As with the MCC an elastic region is defined, in this case bound by two yield surfaces in net
stress - shear stress - suction $(p - q - s)$ space. In isotropic stress space, the yield curves are
the load collapse (LC) curve and the suction increase (SI) curve, which are extended into

full $p - q - s$ stress space assuming that the MCC is valid for any suction and the SI remains parallel to the q axis to form the yield surfaces. These are explained in more detail in chapter 3. A constitutive equation for specific volume change was proposed by Alonso *et al.* (1990) where the plastic stiffness due to stress change is an asymptotic function of the suction.

Experimental evidence for the existence of the LC curve is available e.g. Josa (1988), Wheeler and Sivakumar (1995), Cui and Delage (1996), all of which exhibited a shape similar to that predicted by Alonso *et al.* (1990). Josa *et al.* (1992) proposed an expression that included a maximum amount of wetting collapse possible, while Wheeler and Sivakumar (1995) presented results from triaxially tested Kaolin under controlled-suction and proposed a series of expressions. However, evidence for the existence and form of the SI curve is less strong. Yong *et al.* (1971) and Josa *et al.* (1987) showed plastic strains for kaolin under a drying-wetting cycle. But due to a lack of further evidence the assumption that the yield surface is independent of stress-states p and q was made, along with the shape: a straight line parallel to the p axis.

An elasto-plastic framework was established by Gens and Alonso (1992) for unsaturated expansive clays using double structure mechanical behaviour. Cui *et al.* (2002) used the same basic concepts and added a critical swelling curve (CSC), allowing for the hydro-mechanical behaviour of a highly compacted swelling clay. This model included only six parameters, but was limited to the prediction of volume change behaviour for isotropic and odeometric stress conditions.

Other models exist that use other stress-state variables than the three discussed here (Kohgo *et al.*, 1993a, 1993b; Jommi and di Prisco, 1994; Kato *et al.*, 1995; Bolzon *et al.*, 1996) and are reviewed elsewhere (Wheeler and Karube, 1996; Gens, 1995). In general more complex stress-states are proposed in an attempt to simplify elasto-plastic formulations.

Thomas and He (1995, 1998) present a coupled thermal, hydraulic and mechanical model for partially saturated soil where all terms are coupled. Multiphase flow based on Thomas and Sansom (1995) was implemented. In the first paper (Thomas and He, 1995) a state-surface approach was implemented for mechanical behaviour (Lloret and Alonso, 1985), whereas in

the second (Thomas and He, 1998) an elasto-plastic model was implemented (Alonso *et al.*, 1990). Thermal deformation was included in both models, using a function of expansion, which can be either constant or a function of temperature and net mean stress. This model has been validated (e.g. Thomas *et al.*, 1994a, 1994b) against a series of experimental work.

Other models have been proposed including aspects such as the variation of the degree of saturation with deformation, inclusion of hydraulic hysteresis behaviour, describing yield by a single surface and modifying the transition from unsaturated to saturated behaviour (Gallipoli *et al.*, 2003a, 2003b; Wheeler *et al.*, 2003).

2.2.1 Expansive clays - bentonite

Expansive clays, in particular bentonite, are of interest for example in waste isolation and material models have been modified to attempt to include the behaviour. Pusch *et al.* (1990) describes the structure of bentonite, stating that the micro-structure is made up of stacks of smectite flakes with interlamellar water. In particular, the authors state that attention must be given to hydrating processes and how equilibrium between bulk and interlamellar water is achieved.

Kanno *et al.* (1996) investigated both experimentally and numerically the movement of moisture in a highly compacted bentonite under temperature gradients with a maximum time of 200 hours. The proposed model was based on Thomas and King (1991) and Ewen and Thomas (1989) models. Good correlation was observed between the numerical and experimental results.

Thomas and Cleall (1999) extended the thermo-hydro-mechanical model presented by Thomas and He (1998) to expansive soils, including the effects of non-reactive chemical solute transport on the deformation behaviour and a double porosity model. This approach was found to be able to produce the largest strains in an unconfined sample. A dual porosity model for expansive clays was proposed by Alonso *et al.* (1999), combining previous models: Alonso *et al.* (1990) defining the macro-structural mechanical behaviour; and Gens and Alonso (1992) to define the behaviour of the micro-structure. The coupling between these models was defined from drying and wetting functions. Suction controlled tests showed that

the behaviour was able to be qualitatively captured. A model for the heat, liquid and gas flow and deformation of expansive soils is presented by Navarro and Alonso (2000). A double porosity model for the liquid transfer between the micro and macro-pores was introduced. The deformation behaviour was included via an elasto-plastic model (Alonso *et al.*, 1990).

Thomas *et al.* (2003) present a simulation of a large-scale long-term infiltration experiment in an almost intact granitic host rock. Consequently the inflow was slow and it was found that due to micro-structural change a conventional hydraulic conductivity could not be used. A modification was suggested and found to yield good correlation. Kröhn (2003) provides some commentary on conceptual micro-structural models for bentonites and compares a hydraulic diffusion model with a hydraulic model using Darcian flow.

Development of theoretical THM behaviour has been less prolific in recent times and material characterisation and modelling experimental tests have been the recent focus of attention. Alonso *et al.* (2005) present a comparison of modelling approaches of various teams for the FEBEX large scale experiment. The conclusions were that the buffer behaviour could not be replicated without a fully coupled THM model, specifically including water phase change and vapour transport. A discussion of the behaviour and modelling of the fractured rock is also included and discussed later.

Alonso and Hoffmann (2007) presented work based upon bentonite pellet characterisation laboratory experiments presented by Hoffmann *et al.* (2007) on the field behaviour of such bentonite pellets in a large scale experiment. It was shown that hydraulic conductivities alter by many orders of magnitudes as hydration progresses and behaviour can be irregular, although displacements were of the correct magnitude.

Singh (2007) presented an experimental and numerical study on the flow vapour in highly compacted kaolin and bentonite. The flow of vapour and liquid was investigated subject to thermal and hydraulic gradients, both independently and together. A modification to the Philip and de Vries vapour law was proposed, and a reasonable fit with experimental data was found. However, it is advocated that further work be undertaken. A numerical study considering gas flow at elevated temperatures through highly compacted bentonite

was presented by Siddiqua (2008). The Luikov (1966) approach is utilised modifying an existing coupled thermo-hydraulic-mechanical code to include the high temperature effects. A pore-gas constitutive equation is proposed as opposed to dry air transfer and thermal osmosis is included. Improved results were found when considering experimental results at high temperatures compared to the Thomas and He (1995) approach.

2.2.2 Chemical and biological processes

Although in general beyond the scope of this work, a brief outline of the inclusion of further processes is given. A compendium of analytical models is given by van Genutchen and Alves (1982), whereby a number of solutions for various boundary conditions, radioactive decay and linear adsorption were outlined. These models are only useful for finding the solutions of controlled laboratory tests and validating numerical models and cannot be used for more complex problems.

Coupling moisture and chemical transport has been undertaken, for example Jennings *et al.* (1982) who presented a technique for modelling the groundwater transport of a multi-component chemical solution. A number of chemical processes could be included although redox reactions, precipitation and dissolution could not be accommodated and the pH is assumed constant. A more complete hydro-chemical model was presented by Yeh and Tripathi (1991) where a two-dimensional, finite-element model was presented. The chemical processes of complexation, dissolution/precipitation, adsorption/desorption, ion exchange, redox and acid/base reactions were all included and could be undertaken simultaneously. Geochemical models, to predict the concentrations of ions, the complexes formed and the species saturation among other geochemical activities have been studied, with a number of models formed. Of particular note is MINTEQA2 (Allison *et al.*, 1991) developed from a previous geochemical model and developed for application to nuclear waste disposal. Thomas *et al.* (1997) presented a coupled moisture and reactive transport model. It is noted that the kinetics of reactions are ignored in this model.

Thermal effects are important, especially in unsaturated soils, where the moisture regime is affected by phase change, with liquid moisture causing advection of chemicals and moisture vapour flows not causing advective transport, with the exception of dissolved gas. Wu and

Chieng (1995) proposed a model to include these effects using Philip and de Vries (1957) for moisture flow, Thomas (1985) for heat transfer and Yeh and Tripathi (1991) for reactive chemical transport.

Olivella *et al.* (1995) presented a coupled brine, heat, gas and deformation model. As such, the inclusion of solubility controlled dissolution/precipitation was the only chemical phenomena included. A non-reactive chemical and contaminant transport was presented as part of a chemical-hydraulic-mechanical model by Thomas and Cleall (1997) and extended into a coupled thermo-hydro-chemical-mechanical model by Thomas and Cleall (1999), also mentioned in the previous section. Seetharam (2003) presented a coupled thermo-hydro-chemical-mechanical model and including reactive multi-chemical transport. Cleall *et al.* (2007a, 2007b) update the work including geochemical reactions via the use of Allison *et al.* (1991), and provide application problems. In addition, Thomas and Seetharam (2008) presented a first attempt to include biological processes into a thermo-hydro-chemical-mechanical framework and integrate results into a health impact model.

2.2.3 Conclusions

The review in this section presented a brief overview of the progress in the simulation of coupled heat, moisture, air and deformation in unsaturated soils. This has led in general to established rules for flow processes which are included in current models and some consensus on deformation models. More recently work has been undertaken on highly compacted clay materials including elevated temperatures. Modifications to existing theory to allow the inclusion of certain phenomena has been undertaken in a mechanistic manner and included into existing models. The same processes in fractured rock are examined in the next section with the coupling of these flows with deformation reviewed later. In addition, the inclusion of chemical, geochemical and biological aspects has been briefly reviewed although in general are beyond the scope of this work.

2.3 Coupled thermo-hydro-mechanical behaviour in fractured rock

Low permeability fractured rocks are of interest in waste barriers for toxic and radioactive waste (e.g. Wang *et al.*, 1982; Neuman and Simpson, 1985). In this section the behaviour of fractured media, i.e. rock, as opposed to homogenous or slightly heterogeneous porous

media has been analysed. Thorough reviews of flow in fractured media exist (e.g. Bear *et al.*, 1993; National Research Council, 1996, 2001; Hudson and Harrison, 1997; Berkowitz, 2002; Jing, 2003; Neuman, 2005), therefore only a brief outline of the salient points is given here. All approaches recognise that the flow processes are generally the same as in porous media and it is the pathway of flow that causes any major differences along with fundamental differences in the stress/strain behaviour. Mechanical behaviour of intact rock prior to a peak yield, where the rock fractures, can be generally described in an elastic manner (Hudson and Harrison, 1997) and failure can be described by criteria such as Mohr-Coulomb. When fractured however the rock behaves differently and failure is localised along fractures (Hudson and Harrison, 1997). In addition, when extrapolating from a single fracture to a real system the behaviour becomes vastly more complex.

Discontinuities or fractures in a rock mass are defined by Hudson and Harrison (1997) as a separation in the rock continuum having zero tensile strength. These discontinuities have been formed over, usually, millions of years and a variety of stress-states and thermal conditions. As such, they can be described as naturally occurring, as opposed to manufactured materials, and characterisation prior to engineering works is required (Jing, 2003). It is likely that these fractures will have a large influence over strength, deformability and permeability, including anisotropic properties such as fracture orientations (Hudson and Harrison, 1997). Fractured rock masses are usually characterised in terms of fracture size, density, orientation, aperture and spatial correlation (National Research Council, 1996).

The processes for the couplings of heat, moisture and air in fractured rock can be generally assumed to be the same as in porous media and it is the heterogeneity that governs differences (Jing, 2003). A compendium of thermal-hydraulic models in fractured rock (Wang *et al.*, 1982) reviews a number of computer codes to simulate thermohydrological flow in fractured rock. In general the assumption is that the fractures affect the hydraulic flowpath (Neretneicks *et al.*, 1982; Neretnieks, 1989; Berkowitz, 2002) and consequently the heat transfer is effected by convection. Conduction processes remain the same albeit affected by the variety of materials present in the system.

Flow in a single fracture through rock has been investigated and experimental data has

been produced both in the laboratory and in the field that illustrates classical smooth parallel plate theory is not adequate to predict flow in fractures (e.g. Tsang, 1984; Ravan and Gale, 1985; Rasmuson and Neretnieks, 1986). Fracture roughness has been conjected as key to understanding flow, for example Meheust and Schmittbuhl (2001) show that fracture roughness heterogeneity can enhance or inhibit flow. Tsang (1984) stated that fractures resisted flow proportionally to the inverse of the cube of the aperture as in parallel plate theory, but added that tortuosity and connectivity are highly important to flow in a real fracture. Brown (1989) concludes that by considering tortuosity, the microscopic behaviour can be described at a macroscopic level by Darcy's Law for fluid flow in a fracture. In addition, properties such as surface roughness can affect the mechanical performance (Hudson and Harrison, 1997) and led to models such as the bi-linear failure criterion whereby the local surface roughness has an impact on the friction angle until a level of stress is exceeded whereby only the bulk rock properties are used (Patton, 1966).

Bonnet states that systems of fractures are inherently three-dimensional and extrapolating one-dimensional or two-dimensional experimental data is non-trivial (Bonnet *et al.*, 2001). This paper provides dialogue on how to characterise fractures over various scales. Berkowitz (2002) reiterates that scale is important both in simulation and measurement. Field scale experiments which include fracture networks show highly preferential flow paths and in some cases only 0.1% of the fractures were found to contribute to flow in the large scale (Neretnieks, 1993). Deterministic data as to locations of specific fractures can be transformed from two-dimensions to three-dimensions using stereological techniques (e.g. Warburton, 1980) and use of simplifications including fractures being treated as discs.

A number of large field-scale experiments on fracture flow have been undertaken in Underground Research Laboratories (URLs) designed for the experimentation on deep geological disposal of nuclear waste. These are described in more detail in section 2.4.

The mechanical field in fractured rock has been studied by many researchers including Goodman *et al.* (1968), Zienkiewicz and Pande (1977), Brady and Bray (1978) and Goodman (1989). In general an elastic approach is taken, with various methods employed allowing for fractures. The finite element method has been usually used but is limited in that only small

scale deformations are supported. The distinct element method which allows movement and rotation of blocks may be used (Cundall, 1980) but yields large numerical problems. Huang *et al.* (1995) suggested an expression for the deformation behaviour of a rock mass intersected by three intersecting sets of joints at non-orthogonal directions derived from the rock and joint properties.

In general hydro-mechanical coupling in fractured rock relates to the effect on rock permeability from the changing in fracture aperture due to stress change (Hudson and Harrison, 1997; Clifford *et al.*, 1997). Wei and Hudson (1998) apply this method in the near field of a problem where stress change is likely and apply an equivalent continuum model in the far field where stress change is unlikely and the effect of preferential flow reduced.

Millard *et al.* (1995) compare a number of both discrete and continuum THM models applied to fractured rock, as part of the DECOVALEX project, an international project comparing experimental and numerical THM results. It was found that there is little variation between model types in the temperature field, stress fields show similar results with a greater variation from the discrete fracture models but hydraulically large differences are found, with discrete fracture models being more accurate but computationally expensive. Further to Millard *et al.* (1995) a compendium of work from the DECOVALEX project, all in relation to THM processes in fractured rock, has been published by Stephansson *et al.* (1996). In addition to the processes already discussed in this section, thermal and hydraulic induced damage and fracturing are discussed and it is stated that these processes can change the bulk rock properties, for example increase the ability for fluid to flow.

Alonso *et al.* (2005) presents a comparison of modelling approaches for the FEBEX large scale experiment also as part of the DECOVALEX project. For the behaviour of the fractured rock it is concluded that correct geological characterisation is key and also in this case the existence of fractures is not that important, attributed to the high permeability of the rock compared to the buffer.

Guvanasen and Chan (2000) present a model for deformation, groundwater flow, heat transport. Biot's consolidation theory is used for the deformation and a joint element is

proposed to simulate normal, lateral deformations including dilatency, contraction and hysteresis. The paper highlighted non-isothermal flow could affect flow in fractured media.

With fractured rock it is important to understand the information that is required from the modelling before resolving upon a modelling technique (Berkowitz, 2002). The required resolution of results is critical and will impact upon the method and consequently on the analytical time and resources required. Modelling the hydraulic behaviour of a fractured rock mass, for example, largely falls into two groups; namely discrete fracture modelling and continuum modelling or a combination of the two techniques (Berkowitz, 2002; Neuman, 2005). Continuum models consider an effective continuum, with an averaging of material properties allowing the bulk properties of a region to be captured. Discrete fracture models explicitly include fractures and the remaining material matrix in the domain. In general they are able to capture the flow effects from the fractures but are computationally expensive to run and hard to determine properties at any real scale.

Berkowitz *et al.* (1988), for example, examine a continuum model and a model where fractures and porous blocks are represented discretely for fractured porous media in both flow and contaminant transport fields. The results are compared and good correlation is found except in a single location. They conclude that in certain circumstances a single continuum model can be appropriate. Carrera *et al.* (1990) also successfully modelled the flow through a fractured block as a single continuum. However Neuman (2005) states that while flow can successfully be modelled by a continuum rarely can both flow and transport. Modification such as dual porosity models such as proposed by Bibby (1981) offer some appreciation of flow paths whereas hydraulic conductivity tensors (e.g. Hsieh and Neuman, 1985) allow some anisotropy to be included.

Discrete fracture modelling falls into two general categories, statistical and deterministic. Within deterministic fracture modelling work has been undertaken to understand the behaviour of a single fracture (e.g. Brown, 1987, 1989) and the behaviour of deterministic Discrete Fracture Networks (DFNs) (e.g. Smith and Schwartz, 1984). Statistical modelling allows statistical information about fracture networks e.g. size, correlation and distribution, to be input into random functions to allow DFNs to be generated (e.g. Neuman 1987,

1988). Specialist computer codes exist to generate fracture networks from statistical fracture information (e.g. FracMan, 2008).

Hybrid models attempt to include the benefits of both types of models while reducing the weaknesses of both. Berkowitz (2002) states that given the amount of data generally available a combination of modelling techniques might be appropriate. The data available may only be able to identify the key hydraulic features or the features in a certain location. Carrera and Martinez-Landa (2000) illustrate that a small number of fractures can dominate flow conditions. If these are identified the remainder of the model may be modelled as a continuum. Neuman (2005) states that a continuum with a either a small number of discrete fractures or statistical information about fractures may be used to simulate a fractured system. Wei and Hudson (1993) present a hybrid model where flow occurs in the near field in fractures and in a continuum in the far field.

Meshless methods, such as described by Belytchko *et al.* (1996), have been used to allow the propagation of fractures and is flexible in the treatment of fractures. However, the finite element method is still more powerful in terms of computing performance (Jing and Hudson, 2002). In addition, Moës *et al.* (1999) introduces a method to allow the propagation of cracks with the finite element method without the need to re-mesh, by introducing discontinuous shape functions. Nodes adjacent to fracture locations are 'enriched' where required to describe the fracture and its propagation.

2.3.1 Conclusions

The coupled flow of heat, moisture, air and deformation through fractured rock has been reviewed in this section. It was shown that the processes that govern the flow remain the same as in porous media, but the flowpath and resistance alter the flow behaviour. Flow behaviour through a single fracture was shown to be affected by fracture aperture and surface properties. Techniques to convert this behaviour into models that can describe real three-dimensional systems have been described, in particular continuum, discrete and hybrid models.

2.4 Experimentation

An overview of nuclear waste disposal is given in section 1.4. Experimental programmes have been instigated in many countries to i) determine whether deep geological disposal is viable, ii) the designs proposed are suitable and iii) to inform performance assessment. Work has been undertaken to test many phenomena and materials over different scales and time periods.

Both the buffer materials, which are manufactured so can be generically characterised; and bedrock, which must be analysed in a site specific manner, must be investigated. How these materials interact is also of consideration. Experiments in the laboratory are able to be controlled and conducted in a cost effective manner, but are limited in scale and realism. Field tests hold many more unknowns in terms of boundary conditions and materials but are more realistic in terms of scale and comparison to a final repository. Therefore both sets of experimentation are useful. Detailed reviews of experimentation have been carried out (e.g. Pusch, 2001; Mitchell, 2002) so a selected few are presented here, salient to this work, along with more recent developments.

2.4.1 Laboratory

Laboratory tests have been used to study in detail the behaviour of the materials within potential repositories. They are generally of a small size and can be well controlled. Material behaviour is analysed and the results obtained can be used to test and validate conceptual and numerical models. A major difficulty in carrying out this work is the length of time required for some of the processes to occur and the high values of variables predicted to occur in nuclear waste repositories. A selection of key studies is presented here although it is acknowledged that there are many others.

Villar *et al.* (1996) undertook a series of thermo-hydraulic experiments on compacted bentonite blocks; a number of different initial water contents and a variety of different heating regimes were tested, with time periods varying from approximately 750 hours to 4,000 hours. A porous plate hydration mechanism and inserted heating rod allowed both temperature and hydraulic gradients to be controlled. The conclusions were that with the power and water contents considered the temperature was independent of the water content;

the hydration process was largely independent of the thermal gradient, under 2,500 hours; water content distribution is related to the thermal gradient; hydration rate is linked to initial water content and a density redistribution occurs due to the swelling pressures from hydration. In addition, a high saline content was found near to the heater, which may cause canister corrosion in a waste repository. This indicates a vapour transport, liquid hydration regime being present.

A number of other thermo-hydraulic tests undertaken in the same laboratory have been reported (e.g. Villar *et al.*, 2003, 2005) whereby hydration both isothermally and with a temperature gradient on a variety of test cells was undertaken. Interestingly, an almost steady-state condition existed in both temperature and relative humidity at the end of the tests with both a thermal and hydraulic gradient.

Ongoing work into long-term thermo-hydraulic experiments on bentonite columns was reported by Villar *et al.* (2008). This paper showed results, after 8 years, for a long-term experiment with the inclusion of both thermal and hydraulic gradients. This time scale in a laboratory experiment is unprecedented and has led to some interesting results, including that the column was not fully saturated even after 8 years.

Villar (1999) and Lloret *et al.* (2003) report a series of odeometer tests on highly-compacted bentonite with controlled suction. A series of stress paths were followed each with either fixed suction and varying stress, or fixed stress and varying suction. This allows an assessment of how independent stress variables affect the volume change characteristics in highly-compacted bentonite samples. The existing stress levels of either suction or applied stress affect the volume change characteristics of the material.

The thermo-hydro-mechanical behaviour of two over consolidated clays, including a Spanish bentonite, is presented by Romero *et al.* (2005) via the use of suction and temperature controlled odeometers. Strains are seen to depend on initial water content, confining stress, dry density and temperature. In fact, temperature was seen to effect the swelling responses to the two clays in opposing manners, with elevated temperature reducing the swelling strain for the bentonite.

A range of mechanical and hydro-mechanical tests including iso-thermal swelling, shear tests, hydraulic conductivity tests and triaxial tests are reported by Börgesson *et al.* (1996). These tests are reported individually in Börgesson *et al.* (1988); Börgesson (1990, 1992, 1993). Additional triaxial tests were reported in Börgesson *et al.* (1995). Initial modelling work is also undertaken, with a comprehensive report written including a variety of scenarios and experimental results parameterised for numerical models (Börgesson and Hernelind, 1999).

A time-dependent phenomenon, named ageing, has been observed by Delage *et al.* (2006). Testing of the pore-structure of compacted manufactured bentonite over times up to 100 days using non-wetting Mercury Intrusion Porosimetry tests led to the observation that the bentonite pore-structure is evolving without the application of thermal, hydraulic or mechanical gradients.

The experimental testing of pelletised bentonite is limited. In addition, the manner in which pellets can be used is more varied than compacted bentonite blocks and as such representative experiments for any particular application are scarce. Imbert and Villar (2006) published experimental results for a mixture of bentonite pellets and powder. It is reported that an initial swelling pressure is found during hydration and this pressure then reduced, a process attributed to a collapse of the macrostructure. This pattern is similar for all densities, although the initial density and initial water content affect the quantitative behaviour.

Hoffmann *et al.* (2007) report initial experimentation upon compacted pellets, without the inclusion of powder. Both single size samples of pellets and samples including a distribution of sizes were tested in a variety of manners. The pore-size distribution, hydraulic conductivity, water retention properties and some mechanical properties were reported for two different water pressures. A key finding was that the material evolution during saturation is critical in determining the behaviour.

Johannesson *et al.* (1999) reported a collection of experimental work on bentonite/rock

mixtures of various proportions. Mata (2003) presents a comprehensive test programme for a 30%/70% mixture including standard hydraulic conductivity tests and odeometer tests at a variety of strengths of saline solution. All tests were isothermal. A wide range of hydraulic conductivities were found in samples indicating that this material has a large structural variation. Mechanical results, however, were more consistent.

An investigation into vapour conductivity was undertaken by Singh (2007). Both kaolin and bentonite were tested with a thermal gradient and then a hydraulic and thermal gradient applied. The water content and chloride ion content was determined. This indicated a cycle of liquid hydration from the hydraulic gradient and vapour movement by means of the thermal gradient. The rate of vapour movement was found to be substantially and quantifiably lower than predicted by the theory proposed by Philip and de Vries (1957).

2.4.2 Large/Field scale

A number of major uncertainties exist, such as the behaviour of the buffer material at full scale, its interaction with the rock and the installation of canisters, that can only be resolved at a full or realistic scale. Large scale experimentation undertaken at representative conditions is essential for accurate predictions and 'upscaling' of the findings from experimental work. The processes and techniques whereby material is excavated and emplaced in a repository structure will have an impact on the repository structure and the processes that occur within it. The volumes of material and timescales may also be larger than commonly found in a laboratory and hence may be more realistic. However, the cost associated with these underground research laboratories (URLs) is great and repetition of experiments uncommon. URLs can be used either to host experiments to understand more about the generic disposal concept or used to characterise a specific location, with the aim to build a repository in close proximity or convert the URL into a repository. In addition, URLs provide an opportunity to understand the practical issues associated with repository construction, installation and operation. Table 2.1 contains a list of the main URLs both past and present. An overview of some salient URLs and some experiments contained within them is also presented.

Country	Location	Name	Type	Host formation	Experiments	Period
Belgium	Mol	HADES URF	S (purpose-built)	Soft clay	TCHMR+D	Since 1980
Canada	Pinawa, Manitoba	Whiteshell URL	G (purpose-built)	Granite	TCHM	Since 1984
Czech Republic	Prbam	Shaft 16	G (galleries in U mine)	Granite	Characterisation	Late 1990s
Finland	Olkiluoto	Research Tunnel	G (in VLJ repository)	Granite	HM+D	Since 1993
France	Fanay Augres/Tenelles	Fanay	G (galleries in U mine)	Granite	TCHM	1980-1990
	Amelie	Amelie	G (galleries in K mine)	Bedded Salt	TM+D	1986-1994
	Tournemire	Tournemire Research Tunnel	G (railway and test galleries)	Shale	CHM	Since 1990
	Bure	Bure URL	S (purpose built)	Shale	Under construction	Since 2000
Gernmany	Asse	Asse Salt Mine	G (test galleries in K/salt mine)	Domed salt	TCHMR + D	1977-1995 Now sealing
	Gorleben	Gorleben	S (purpose built)	Domed salt	Characterisation	Since 1997
	Konrad	Konrad	S (test galleries in Fe mine)	Shale Shale	CHM	Since 1980
	Morsleben	ERAM	S (test galleries in K/salt mine)	Domed salt	D	Since 1981
Hungary	Pécs	Pécs	G (galleries in U mine)	Shale	Characterisation	1995-1999
Japan	Tono	Tono	G (galleries in U mine)	Sandstone	CHM	Since 1986
	Kamaishi	Kamaishi	G (galleries in Fe-Cu mine)	Granite	Characterisation	1988-1998
	Mizunami	MIU	G (purpose built)	Granite	Under development	
	Honorobe	Honorobe	G (purpose built)	Sedimentary rocks	Under development	
Sweden	Stripa	Stripa	G (galleries in Fe mine)	Granite	TCHM	1976-1992
	Äspö	HRL	G (purpose built)	Granite	TCHM+D	Since 1990
Switzerland	Grimsel	GTS	G (dam tunnel)	Granite	TCHM	Since 1983
	Mont Terri	Mont Terri URL	G (highway and test galleries)	Shale	TCHM	Since 1995
UK	Sellafield	RCF	S	Tuff	Characterisation	Stopped 1997
USA	Nevada Test Site	Climax	G (galleries in mine)	Granite	D	1978-1983
	Nevada Test Site	G-Tunnel	G (tunnel)	Tuff	THM	1979-1990
	Lyons, Kansas	Project Salt Vault	G (galleries in mine)	Bedded salt	TM	1965-1968
	Carlsbad, New Mexico	WIPP	S (TRU repository)	Bedded salt	TCHMR+D	Since 1982
	Yucca Mountain, Nevada	ESF	S (purpose built)	Tuff	TCHM+D	Since 1993
	Yucca Mountain, Nevada	Busted Butte	G (purpose built)	Tuffs	CHM	Since 1997

Table 2.1. Main past and present URLs (IAEA, 2001).

2.4.2.1   HADES URF, Belgium

A comprehensive overview of the work undertaken at the HADES URF site in Mol, Belgium is contained in Bastiaens (2007). The site is operated by SCK-CEN, the Belgium Nuclear Research Centre and situated in a Boom Clay formation approximately $100m$ thick, which is seen as the primary barrier in the Belgium disposal concept. A diagram summarising the construction history is contained in figure 2.4.2.1. A ground freezing technique was used in the shaft construction at various locations where needed.
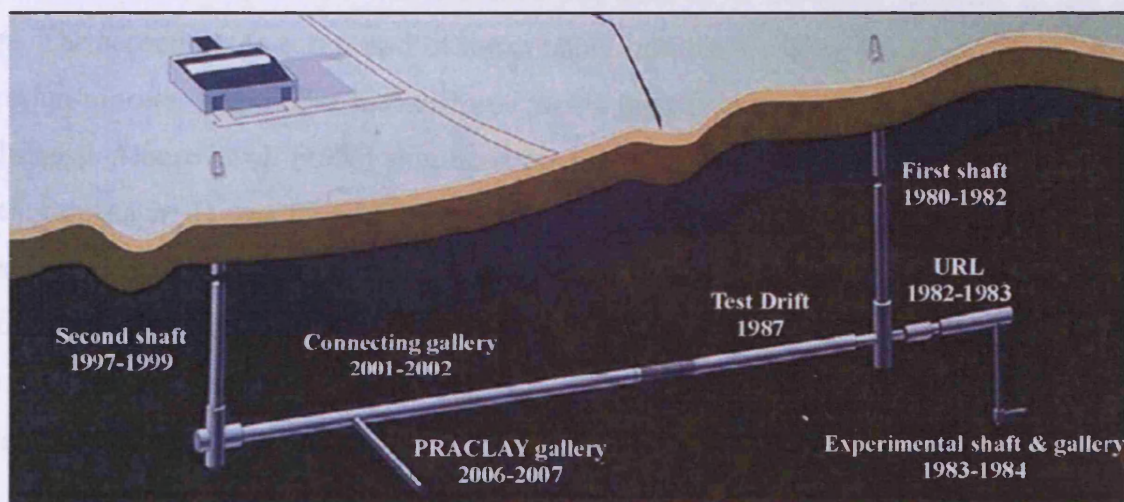
Figure 2.1. Construction history of HADES URF (Bastiaens, 2007).

A large number of experimental tests have been conducted in HADES URF from 1991 until today. The hydraulic and thermal response of the clay layer is seen as critical to the successful design of a repository with a design using this concept. Three of the experiments are reviewed below.

BACCHUS

The BACkfilling Control experiment for High level wastes in Underground Storage (BACCHUS) was designed to investigate the thermal properties of Boom Clay and the thermo-hydraulic properties in a highly compacted clay material. An overview of the project is given by Bastiaens (2007) with details found in Bernier and Neerdael (1996) for BACCHUS 1 and Alonso et al. (1995) for BACCHUS 2. The project comprises a heater surrounded

by a buffer material and sealed at the top. BACCHUS 1 was undertaken in 1988 with a clay-sand-graphite mixture for the buffer and recompacted Boom Clay for the sealing plug. There were no internal measurements in the buffer, but there were thermal, hydraulic and mechanical measurements in the massif.

BACCHUS 2 (Alonso *et al.*, 1995), undertaken from 1993, was designed to optimise the installation procedure for a clay buffer. It was made up of Boom Clay pellets and Boom Clay powder and was used as part of a validation exercise for a hydro-mechanical numerical model. No thermal load was present. The material was allowed to naturally saturate in the first stage. The second stage comprised of water being injected under pressure to accelerate the hydration process. The buffer material was highly instrumented for both pore-pressures and total stress. Alonso *et al.* (1995) simulated the first phase by both a state surface and elasto-plastic approach. It was found that both approaches were able to simulate the hydraulic phase well. It was concluded that the elasto-plastic approach predicted better radial stresses although it was difficult to establish this as the experiment was non-symmetrical and had been modelled symmetrically. It was noted that the elasto-plastic model was also based on a large number of poorly defined parameters which would affect predictive capacity.

CACTUS

The THM behaviour of Boom Clay under a thermal load at near real scale was investigated in the ChAracterisation of Clay under Thermal loading in Underground Storage (CACTUS) project in 1989 (Bernier and Neerdael, 1996). This project was undertaken to understand the near-field behaviour and to propose a conceptual model for the THM behaviour. Two experiments were undertaken, the first with a falling power output and the second a constant power. In both tests similar conclusions were drawn. Pore-water-pressures were found to increase due to heating and then dissipate falling to a reduced equilibrium level with the opposite occurring in the cooling cycles.

PRACLAY

The PReliminary demonstration test for CLAY disposal of highly radioactive waste (PRACLAY) is intended to further knowledge of the disposal of HLW in clay while not

being specific to any repository design. As previously mentioned the Belgium concept relies on the Boom Clay as the major barrier and it is the early THM behaviour of this clay that this project is set to investigate. A 45m gallery contains the three experiments: the gallery and crossing test, the heater test and the plug test. The project is under construction (Bastiaens, 2007).

2.4.2.2 Whiteshell URL, Canada

The Whiteshell/Lac du Bonnet URL, situated in granitic rock, located in Manitoba, Canada was operated by Atomic Energy of Canada Limited (AECL). It opened in 1982 to study the feasibility of safe disposal of HLW via deep geological disposal. Currently, it is in the initial stages of decommissioning. Several large scale in-situ tests have been undertaken at the URL (AECL, 2008).

Buffer/Container Experiment

The buffer/container experiment (Graham *et al.*, 1997; Dixon *et al.*, 2002) was designed to test the effect of heat on the performance of a large scale buffer. It was found that it was difficult to separate the effects of heat and water intake, so the Isothermal Test was designed. The Buffer/Container Experiment was monitored for 2.5 years. Temperature, water content, hydraulic pressure and total pressure both within the buffer and inside the host rock were monitored. Water was taken into the buffer from the rock and redistributed within the buffer due to temperature effects. The temperature also increased hydraulic pressures in the host rock. The buffer was found to have shrunk adjacent to the heaters and swollen where water content had increased.

Isothermal Test

The Isothermal Test was a large-scale experiment designed to investigate the rate of water uptake into a compacted sand/bentonite buffer material (Chandler, 2000; Dixon *et al.*, 2002). The test was monitored for a period of 6.5 years prior to removal, hence was the first truly long-term field-scale test. A 35% reduction in water supply in comparison with pre-emplacement conditions was noted, impacting the prediction of saturation time for the buffer material. Thomas *et al.* (2003) reported a simulation exercise of the Isothermal

Test finding that a 'conventional' hydraulic conductivity/degree-of-saturation relationship was inadequate to describe the behaviour of bentonite, in particular the expansion of the micro-structure. By forming a relationship reducing the pores available for water flow as the micro-structure expands yielded a significant result; both the pattern and rate of water uptake were significantly different and improved in comparison with experimental results.

Tunnel Sealing Experiment

The Tunnel Sealing Experiment was designed to investigate the performance of two bulkhead materials and is described by Guo and Dixon (2006). The first bulkhead was manufactured from highly compacted sand/bentonite blocks and the second high-performance concrete. A permeable sand was placed between the two bulkheads with hydraulic control. In the first phase the water pressure was raised to $4MPa$ and a second stage of heated water with a maximum of $65°C$ was undertaken. A passive cooling stage followed and the THM behaviour was monitored. Guo and Dixon (2006) undertook a series of THM simulations of the Tunnel Sealing Experiment. It was found that the temperature could be well simulated in the rock mass but the bulkheads were found experimentally to have a lower temperature than simulated. This was attributed to air being released from solution and reducing thermal conduction and micro-structural changes in the materials. The hydraulic response was reasonably simulated and the quantitative deformation could not be well simulated. Melhuish (2004) presented a series of simulations of the Tunnel Sealing Experiment. It was found that the thermal and hydraulic behaviour could be well captured, although the micro-structural changes in the clay bulkhead were important to consider and could delay full saturation significantly.

2.4.2.3   Grimsel Test Site, Switzerland

The Grimsel Test Site (GTS) is situated in granite rock in Switzerland, $1730m$ above sea level and $450m$ below ground level. Constructed in 1983 and having over $1km$ of tunnels a large number of experiments have been undertaken including work into radionuclide transport, near-field processes and engineering feasibility (Nagra, 2005).

FEBEX

The Full-scale high-level waste Engineered Barrier system EXperiment (FEBEX) was designed to test the feasibility of manufacturing and installing an engineering barrier system and to develop models and methods to assess the THM and thermo-hydro-geochemical behaviour of the engineered barrier system. The test consisted of two parts, an in-situ test; and a mock-up test, whereby a full-size engineered barrier was assembled in laboratory conditions. A confining structure, hydration mechanism and heating capability where the same conditions as the in-situ test were attempted to be created. Both tests were highly instrumented throughout. The main conclusions were that the feasibility of constructing a full-scale barrier system had been demonstrated, full saturation had been achieved in the outermost bentonite rings after 5 years and bentonite saturation was uniform in relation to the rock (GTS, 2008).

2.4.2.4   Stripa, Sweden

The Stripa project was an URL based in a disused iron mine in crystalline granite rock in central Sweden. Managed by SKB, the project was funded by the Organisation for Economic Co-operation and Development (OECD) and directed by representatives from a number of countries. The project started in 1980 and finished in 1992. The aims were to develop instruments and procedures to characterise repository sites, understand the groundwater flow and solute transport and to design engineered barriers to contribute to waste isolation. A number of experiments were undertaken including the Buffer Mass Test (BMT), to test the ability for bentonite to seal rocks, and grout injection tests to test the ability of grout to seal fractured zones (Fairhurst *et al.*, 1993).

Buffer Mass Test

The BMT consisted of a six $160mm$ diameter holes drilled vertically into the floor of the Stripa mine. Heaters were surrounded by highly-compacted bentonite and the THM material behaviour monitored. The water flow could be measured from the rock matrix but mainly occurred through the fractures. This in turn meant that highly anisotropic flow conditions were observed in the drilled holes. Gray (1993) comments that where the water was supplied via fractured rock there was almost unlimited quantities available. Uplift pressures from

bentonite was found to be resisted by backfill material.

2.4.2.5   Äspö Hard Rock Laboratory, Sweden

The Hard Rock Laboratory (HRL) was constructed to address real-scale uncertainty, buffer behaviour and practical issues. The specific aims were to (SKB, 2008):

- Develop and test methods of the investigation of the bedrock.

- Continue developing and testing methods to adapt a repository to local rock conditions.

- Increase scientific understanding of the security of a repository.

- Develop, test and demonstrate technology that will be used in a repository.

The HRL is located in Äspö, Sweden. The tunnel complex is made up of a vertical shaft and a helixical tunnel, shown in figure 2.2, containing many experiments. Figure 2.3 highlights the main experiments and in particular the Canister Retrieval Test (CRT) and the Prototype Repository Project (PRP) which is described in detail in chapter 6.

Backfill and Plug Test Project

The aim of the Backfill and Plug Test Project was to investigate the behaviour of a full size repository tunnel backfilled with compacted backfill material along with a confining plug. The behaviour investigated was hydro-mechanical as no thermal sources were included (Gunnarsson et al., 2001). A special backfilling compaction tool compacted the fill into layers and the backfill was instrumented. The hydro-mechanical behaviour of the backfill was tested along with backfill installation techniques and plug installation techniques and performance. The project began in 1996, with the installation completed in 1999 and wetting began in late 1999 through a system of filter mats. The backfill was completely water saturated by 2003 and tests on the saturated behaviour have been undertaken since then (SKB, 2007).

Canister Retrieval Test

The Canister Retrieval Test (CRT) is a full size KBS-3V deposition hole including a heater to simulate the radioactive waste heat output inside a copper/steel canister. The KBS-3V
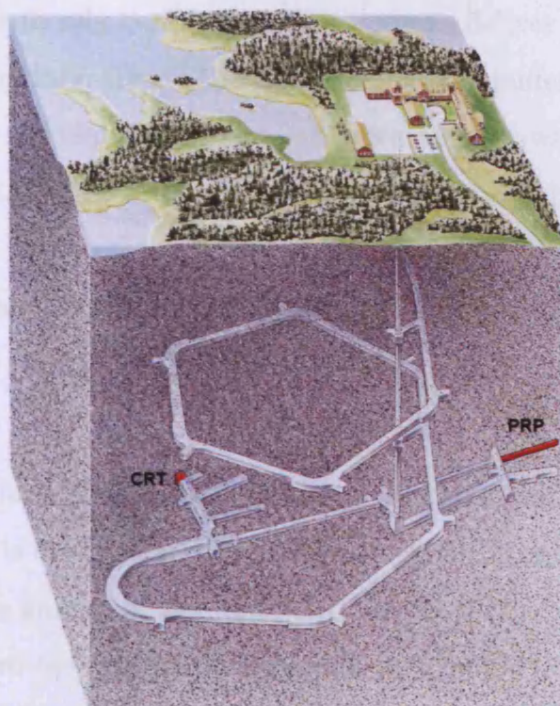
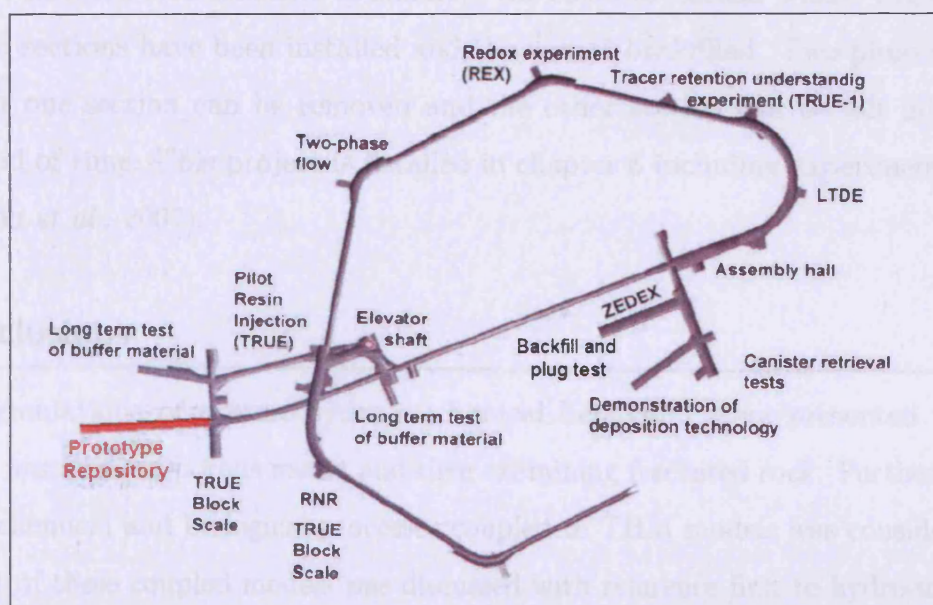**Figure 2.2.** Underground view of the HRL at Äspö (after SKB, 2008).

Figure 2.3. Location of experiments within the PRP, (Dahlström, 1998).

concept is described in detail in chapter 1. In addition the hydraulic phase was controlled by the inclusion of hydraulically conductive filter mats to deliver a controllable hydraulic regime on the buffer boundary. The THM behaviour in the buffer and the near field rock was monitored and 'post-mortem' data was taken when the test was being dismantled. The emplacement was undertaken in 2000, the heater and hydraulic boundary switched on in 2000. The retrieval was initiated in January 2006. A high level of instrumentation and 'post-mortem' data is available (Börgesson, 2005; SKB, 2007; THERESA, 2008).

Temperature Buffer Test

This test is also a single full size KBS-3 single deposition hole, but differs in approach from the other tests in that it is designed to test buffer behaviour at temperatures **above** $100°C$. It is situated in the same gallery of the Äspö HRL as the CRT. Two heaters are situated above each other separated by a bentonite block and surrounded by bentonite as the KBS-3 concept. Artificial water pressure is applied via a sand filled slot (SKB, 2007).

Prototype Repository Project

The Prototype Repository Project (PRP) is a full size mock-up experiment of a repository with heaters inserted into canisters to simulate the effect of nuclear waste. Six deposition holes in two sections have been installed and the tunnel backfilled. Two plugs have been cast so that one section can be removed and the other section can be left in-situ for a longer period of time. This project is detailed in chapter 6 including experimental results (Johannesson *et al.*, 2007).

2.5 Conclusions

Coupled formulations of thermo-hydro-mechanical behaviour were presented first with reference to unsaturated porous media and then examining fractured rock. Furthermore, the addition of chemical and biological processes coupled to THM models was considered. The development of these coupled models was discussed with reference first to hydro-mechanical models such as consolidation models and the development of independent stress-states to describe the stress-state of the soil and secondly to thermo-hydraulic models. Both thermodynamic and mechanistic approaches were introduced with the mechanistic approach

deemed to have more easily determinable material parameters. The development of elasto-plastic mechanical models was discussed as well as the coupling of all processes. Salient aspects of fractured rock influencing the material behaviour were reviewed. The general processes are thought to be the same as in porous media, but fractures usually act as preferential flowpaths with physical characteristics of the fractures, such as roughness, affecting the flow characteristics. Many models are available for both porous media and fractured rock, although it is clear that more research is needed to ensure that material behaviour is well represented.

Experimentation on buffer materials both in the laboratory and in-situ is reviewed. The experiments range from small laboratory desk-top experiments to large scale in-situ experiments situated in dedicated underground laboratories, with a range of time from a few hours to several years. Both are useful in terms of control and realism and building confidence in material behaviour understanding. A number of key experiments were highlighted including the Hard Rock Laboratory in Äspö, Sweden where the Prototype Repository Project is located.

2.6 References

AECL, (2008) *Nuclear Science - Whiteshell Laboratories.* [WWW] <URL:http://www.aecl.ca/ Science/WL.htm> [Accessed 7th December 2008].

Aitchison, G.D., (1965) "Discussion", *Proceedings of the 6th International Conference on Soil Mechanics and Foundation Engineering*, **3**, 318-321.

Allison J.D., Brown, D.S., Novo-Gradac, K.J., (1991) *MINTEQA2/PRODEFA2, a geochemical assessment model for environmental systems: Version 3.0 user's manual*, Environment Research Laboratory, US Environmental Protection Agency, US EPA, Athens, Georgia.

Alonso, E.E., Alcoverro, J., Coste, F., Malinsky, L., Merrien-Soukatchoff, V., Kadiri, I., Nowak, T., Shao, H., Nguyen, T.S., Selvadurai, A.P.S., Armand, G., Sobolik, S.R., Itamura, M., Stone, C.M., Webb, S.W., Rejeb, A., Tijani, M., Maouche, Z., Kobayashi, A., Kurikami, H., Ito, A., Sugita, Y., Chijimatsu, M., Börgesson, L., Hernelind, J., Rutqvist, J., Tsang, C-F., Jussila, P., (2005) "The FEBEX benchmark test: case definition and comparison of modelling approaches", *International Journal of Rock Mechanics & Mining Sciences* **42**, 611-638.

Alonso, E.E., Battle, F., Gens, A., Lloret, A., (1988) "Consolidation analysis of partially saturated soils - Application to earthdam construction", *Proceedings of the 6th International Conference on Numerical Methods in Geomechanics*, Rotterdam, **2**, 1303-1308.

Alonso, E.E., Gens, A., Hight, D.W., (1987) "Special problem soils. General report", *Proceedings of the 9th European Conference on Soil Mechanics & Foundation Engineering*, Dublin, **3**, 1087-1146.

Alonso, E.E., Gens, A., Josa, A., (1990) "A constitutive model for partially saturated soils", *Géotechnique*, **40**(3), 405-430.

Alonso E.E., Hoffmann, C., (2007) "Modelling the field behaviour of a granular expansive barrier", *Physics & Chemistry of the Earth*, **32**, 850-865.

Alonso, E.E., Lloret, A., Gens, A., Delahaye, C.H., Vanaut, J., Volckaert, G., (1995) "Coupled analysis of a backfill hydration test", *Proceedings of the International Workshop on 'Hydro-Thermo-Mechanics of Engineered Clay Barriers & Geological Barriers'*, Montreal, Quebec.

Alonso, E.E., Vaunat, J., Gens, A., (1999) "Modelling the mechanical behaviour of expansive clays", *Engineering Geology*, **54**, 173-183.

Barden, L., (1965) "Consolidation of compacted and unsaturated clays", *Géotechnique*, **15**(3), 267-286.

Barden, L., Madedor, A.O., Sides, G.R., (1969) "Volume change characteristics of unsaturated clay", *Journal of Soil Mechanics & Foundation Engineering, American Society of Civil Engineers*, **95**(1), 33-51.

Bastiaens, W., (2007) *The HADES Underground Research Facility. RWMC FY2006 Consultation 2 Task 2.1*. Mol, Belgium: SCK-CEN.

Bear, J., Tsang, C-F., de Marsily, G., (1993) *Flow and contaminant transport in fractured rock*, Academic Press, San Diego.

Belytchko, T., Krongauz, Y., Organ, D., Fleming, M., Krysl, P., (1996) "Meshless methods: an overview and recent developments", *Computer Methods in Applied Mechanics & Engineering*, **139**, 3-47.

Berkowitz, B., (2002) "Characterizing flow and transport in fractured geological media: A review", *Advances in Water Resources*, **25**, 861-884.

Berkowitz, B., Bear, J., Braester, C., (1988) "Continuum models for contaminant transport in fractured porous formations", *Water Resources Research* **24**(8), 1225-1236.

Bernier, F., Neerdael, B., (1996) "Overview of in-situ thermomechanical experiments in clay: Concept, results and interpretation", *Engineering Geology*, **41**, 51-64.

Bibby, R., (1981) "Mass transport of solutes in dual-porosity media", *Water Resources Research*, **17**(4), 1075-1081.

Biot, M.A., (1941) "General theory of three-dimensional consolidation", *Journal of Applied Physics*, **12**(2), 115-164.

Bishop, A.W., (1959) "The principle of effective stress", lecture delivered in Oslo, Norway, 1955, *published in Teknisk Ukeblad*, **106**(39), 859-863.

Bishop, A.W., (1960) "The measurement of pore pressure in the triaxial test", *Pore Pressure and Suction in Soils*, Butterworths, London.

Bishop, A.W., Blight, G.E., (1963) "Some aspects of effective stresses in saturated and partly saturated soils", *Géotechnique*, **13**(3), 177-197.

Bolzon, G., Schrefler, B.A, Zienkiewicz, O.C., (1996) "Elasto-plastic soil constitutive laws generalise to partially saturated states", *Géotechnique*, **46**(2), 279-289.

Bonelli, S., Poulain, D., (1995) "Unsaturated elasto-plastic model applied to homogeneous earth dam behaviour", *Proceedings of the 1st International Conference on Unsaturated Soils*, Alonso, E.E., Delage, P., (eds.), Paris, A.A. Balkema, **1**, 265-271.

Bonnet, E., Bour, O., Odling, N.E., Davy, P., Main, I., Cowie, P., Berkowitz, B.. (2001) "Scaling of fracture systems in geological media" *Reviews of Geophysics*, **39**(3), 347-384.

Börgesson, L., (1990) *Laboratory and theoretical work in modelling the drained and undrained behaviour of buffer materials*, SKB, Interim Report, Stockholm.

Börgesson, L., (1992) *Interaction between rock, bentonite buffer, and canister. FEM calculation of some mechanical effects on the canister in different disposal concepts*, SKB, TR-92-30, Stockholm.

Börgesson, L., (1993), *Modelling of the physical behaviour of water saturated clay barriers. Improved material model*, SKB, Arbetsrapport FoU 93-49, Stockholm.

Börgesson, L., (2005) *Canister Retrieval Test, Compilation made for the EBS Task Force*, Clay Technology AB.

Börgesson, L., Hernelind, J., (1999) *Preliminary modelling of the water saturation phase of the buffer and backfill materials*, SKB, IPR-00-11, Stockholm.

Börgesson, L., Hökmark, H., Karnland, O., (1988) *Rheological properties of sodium smectite clay*, SKB, TR-88-30, Stockholm.

Börgesson, L., Johannesson, Sandén, T., Hernelind, J., (1995) *Modelling of the physical behaviour of water saturated clay barriers, Laboratory tests, material models and finite element application*, SKB, PR 44-93-009, Stockholm.

Börgesson, L., Karnland, O., Johannesson, L-E., (1996) "Modelling of the physical behaviour of clay barriers close to water saturation", *Engineering Geology*, **41**, 127-144.

Brady, B.H.G., Bray, J.W., (1978) "The boundary element method for determining stress and displacements around long openings in a triaxial stress field", *International Journal of Rock Mechanics & Mining Sciences & Geomechanical Abstracts*, **15**, 21-8.

Brown, S.R., (1987) "Fluid flow through rock joints: the effect of surface roughness", *Journal of Geophysical Research*, **92B**, 1337-1347.

Brown, S.R., (1989) "Transport of fluid and electric current through a single fracture", *Journal of Geophysical Research*, **94**(B7), 9429-9438.

Burland, J.B., (1965) "Some aspects of mechanical behaviour of partly saturated soils", *Moisture Equilibrium and Moisture Changes in Soils Beneath Covered Areas*, Butterworths, Sydney, 270-278.

Carrera, J., Heredia, J., Vomvoris, S., Hufschmied, P., (1990) "Modeling of flow in a small fractured monzonitic gneiss block", *Hydrogeology of low permeability environments, hydrogeology, selected papers*. Neuman, S.P., Neretnieks, I., (eds.), **2**, Verlag Heinz Heise, Hannover, 115-167.

Carrera, J., Martinez-Landa, L., (2000) "Mixed discrete-continuum models: a summary of experiences in test interpretation and model predictions", *Geophysical monograph* **122**, 251-265.

Chandler, N., (2000) *Water inflow calculations for the isothermal buffer-rock-concrete plug interaction test*, Nuclear Waste Management Division Report 06819-REP-01200-10046-R00, Ontario Power Generation, Ontario.

Chang, C.S., Duncan, J.M., (1983) "Consolidation analysis for partially saturated clay by using an elasto-plastic effective stress-strain model", *International Journal for Numerical and Analytical Methods in Geomechanics*, **7**, 30-56.

Cleall, P.J., (1998) "An investigation of the thermo/hydraulic/mechanical behaviour of unsaturated soils, including expansive clays", *PhD Thesis*, University of Wales, Cardiff.

Cleall, P.J., Melhuish, T.A., Thomas, H.R., (2006) "Modelling the three-dimensional behaviour of a prototype nuclear waste repository", *Engineering Geology*, **85**(2), 212-220.

Cleall, P.J., Seetharam, S.C., Thomas, H.R., (2007a) "Inclusion of some aspects of chemical behaviour of unsaturated soil in thermo/hydro/chemical/mechanical models. I: Model development" *ASCE Journal of Engineering Mechanics*, **133**(3), 338-347.

Cleall, P.J., Seetharam, S.C., Thomas, H.R., (2007b) "Inclusion of some aspects of chemical behaviour of unsaturated soil in thermo/hydro/chemical/mechanical models. II: Application and transport of soluble salts in compacted bentonite" *ASCE Journal of Engineering Mechanics* **133**(3), 348-356.

Clifford, D.J., Hatcher, P.G., Botto, R.E., Muntean, J.V., Michels, B., Anderson, K.B., Liao, Q.H., Hencher, S.R., (1997) "Numerical modelling of the hydro-mechanical behaviour of fractured rock masses", *International Journal of Rock Mechanics & Mining Sciences & Geomechanics Abstracts*, **34**(3), 428-428.

Coleman, J.D., (1962) "Stress strain relations for partly saturated soil", *Correspondence to Géotechnique*, **12**(4), 348-350.

CoRWM, (2006) *Managing our radioactive waste safely, CoRWM's recommendations to Geovernment*, Committee on Radioactive Waste Management, CoRWM.

Couvillion, R.J., Hartley, J.G., (1986) "Drying front movement near low intensity impermeable underground heat sources", *Journal of Heat Transfer, American Society of Mechanical Engineers*, **108**, 182-189.

Cui, Y.J., Delage, P., (1996) "Yielding and plastic behaviour of an unsaturated compacted silt", *Géotechnique*, **46**(2), 291-311.

Cui, Y.J., Yahia-Aissa, M., Delage, P., (2002) "A model for the volume change of heavily compacted swelling clays", *Engineering Geology*, **64**, 233-250.

Cundall, P.A., (1980) *UDEC - A generalized distinct element program for modelling jointed rock*. U.S. Army European Research Office and Defense Nuclear Agency, contract DATA 37-79-C-0548.

Dahlström, L-O., (1998) *Äspö HRL - Test plan for the Prototype Repository*, SKB, HRL-98-24, Stockholm.

Dakshanamurthy, V., Fredlund, D.G., (1981) "A mathematical model for predicting moisture flow in an unsaturated soil under hydraulic and temperature gradients", *Water Resources Research*, **17**(3), 714-722.

Delage, P., Marcial, D., Cui, Y.J., Ruiz, X., (2006) "Ageing effects in a compacted bentonite: a microstructure approach", *Géotechnique*, **56**(5), 291-304.

Delage, P., Graham, J., (1996) "Mechanical behaviour of unsaturated soils: Understanding the behaviour of unsaturated soils requires reliable conceptual models", *Proceedings of the 1st International Conference on Unsaturated Soils*, Alonso E.E., Delage, P., (eds.), Paris, A.A. Balkema, **3**, 1223-1258.

de Vries, D.A., (1958) "Simultaneous transfer of heat and moisture in porous media", *Transactions of the American Geophysics Union*, **39**(5), 909-916.

Dixon, D., Chandler, N., Graham, J., Gray, M.N., (2002) "Two large-scale sealing tests conducted at Atomic

Energy of Canadas underground research laboratory: the buffercontainer experiment and the isothermal test", *Canadian Geotechnical Journal*, **39**, 503-518.

Edlefsen, N.E., Andersen, A.B.C., (1943) "Thermodynamics of soil moisture", *Hilgardia*, **15**(2), 31-298.

Ewen, J., Thomas, H.R., (1987) "The thermal probe - a new method and its use on an unsaturated sand", *Géotechnique*, **37**, 91-105.

Ewen, J., Thomas, H.R., (1989) "Heating unsaturated medium sand", *Géotechnique*, **39**(3), 455-470.

Fairhurst, C., Gera, F., Gnirk, P., Gary, M., Stillborg, B., (1993) *OECD/NEA International Stripa Project 1980-1992, Overview Volume I, Executive Summary*, SKB, Stockholm.

FracMan, (2008) *FracMan software and consulting* [WWW] <URL:http://fracman.golder.com/> [Accessed 20th December 2008].

Fredlund, D.G., Hasan, J.U., (1979) "One-dimensional consolidation theory: unsaturated soils", *Canadian Geotechnical Journal*, **16**, 521-531.

Fredlund, D.G., Rahardjo, H., (1993) "Soil Mechanics for Unsaturated Soils", *John Wiley & Sons Inc*, New York.

Gallipoli, D., Wheeler, S.J., Karstunen, M., (2003a) "Modelling the variation of degree of saturation in a deformable unsaturated soil", *Géotechnique*, **53**(1), 105-112.

Gallipoli, D., Gens, A., Sharma, R., Vaunat, J., (2003b) "An elasto-plastic model for unsaturated soil incorporating the effects of suction and degree of saturation on mechanical behaviour", *Géotechnique*, **53**(1), 123-135.

Gens, A., (1995) "Constitutive modelling: application to compacted soils", *Proceedings of the 1st International Conference on Unsaturated Soils*, Alonso, E.E., Delage, P., (eds.), Paris, A.A. Balkema, **1**, 1179-1200.

Gens, A., Alonso, E.E., (1992) "A framework for the behaviour of unsaturated expansive clays", *Canadian Geotechnical Journal*, **29**, 1013-1032.

Geraminegad, M., Saxena, S., (1986) "A coupled thermoelastic model for saturated-unsaturated porous media", *Géotechnique*, **36**(4), 539-550.

Goodman, R.E., (1989) *Introduction to Rock Mechanics*, Second Edition, John Wiley and Sons, London.

Goodman, R.E., Taylor, R.L., Brekke, T.L., (1968) "A model for the mechanics of jointed rock", *Journal of the Soil Mechanics & Foundations Division, ASCE*, **94**(3), 637-660.

Graham, J., Chandler, N.A., Dixon, D.A., Roach, P.J., To, T., Wan, A.W.L., (1997). *The Buffer/Container Experiment: Results, synthesis, issues*. Report AECL-11746, COG-97-46-I. Atomic Energy Canada Limited, Ontario.

Gray, M., (1993) *OECD/NEA International Stripa Project 1980-1992, Overview Volume III, Engineered Barriers*, SKB, Stockholm.

GTS, (2008) *Full-Scale High-Level Waste Engineered Barrier System Experiment (FEBEX) - Introduction* [WWW] <http://www.grimsel.com/febex/febex_intro_1.htm > [Accessed 20th December 2008].

Gunnarsson, D., Börgesson, L. Hökmark, H., Johannesson, L.E. Sandén, T., (2001) *Äspö HRL - Report on the installation of the Backfill and Plug Test*, SKB, IPR-01-17, Stockholm.

Guo, R., Dixon, D., (2006) "Thermohydromechanical simulations of the natural cooling stage of the Tunnel Sealing Experiment". *Engineering Geology*, **85**, 313-331.

Guvanasen, V., Chan, T., (2000) "A three-dimensional numerical model for thermohydromechanical deformation with hysteresis in a fractured rock mass", *International Journal of Rock Mechanics & Mining Sciences*, **37**, 89-106.

Hoffmann, C., Alonso E.E., Romero, E., (2007) "Hydro-mechanical behaviour of bentonite pellet mixtures", *Physics & Chemistry of the Earth*, **32**, 832-849.

Hsieh, P.A., Neuman, S.P., (1985) "Field determination of the three dimensional hydraulic conductivity tensor of anisotropic media: 1. Theory", *Water Resources Research*, **21**(11), 1655-1665.

Huang, T.H., Chang, C.S., Yang, Z.Y., (1995) "Elastic moduli for fractured rock mass", *Rock Mechanics and Rock Engineering*, 28(3), 135-144.

Hudson, J.A., Harrison, J.P., (1997) *Engineering rock mechanics: an introduction to the principles.* Elsevier Ltd., Oxford.

Imbert, C., Villar, M.V., (2006) "Hydro-mechanical response of a bentonite pellets/powder mixture upon infiltration", *Applied Clay Science*, **32**, 197-209.

International Atomic Energy Agency, (2001) *The use of scientific and technical results from underground research laboratory investigations for the geological disposal of radioactive waste*, IAEA, Vienna.

Jennings, J.E., Burland, J.B., (1962) "Limitations to the use of effective stresses in partly saturated soils", *Géotechnique*, **12**(2), 125-144.

Jennings, A.A., Kirkner, D.J., Theis, T.L., (1982) "Multicomponent equilibrium chemistry in groundwater quality models", *Water Resources Research*, **18**(4), 1089-1096.

Jing, L., Hudson, J.A., (2002) "Numerical methods in rock mechanics", *International Journal of Rock Mechanics & Mining Sciences*, **39**, 409-427.

Jing, L., (2003) "A review of techniques, advances and outstanding issues in numerical modelling for rock mechanics and rock engineering". *International Journal of Rock Mechanics & Mining Sciences* **40**, 283-353.

Johannesson, L-E., Börgesson, L., Goudarzi, R., Sandèn, T., Gunnarsson, D., Svemar, C., (2007) "Prototype repository: A full scale experiment at Äspö HRL", *Physics and Chemistry of the Earth*, **32**, 58-76.

Johannesson, L-E., Börgesson, L., Sandén, T., (1999) *Äspö HRL - Backfill materials based on crushed rock (part 2). Geotechnical properties determined in laboratory*, SKB, IPR-99-23, Stockholm.

Jommi, C., di Prisco, C., (1994) "Un semplice approcio teorico per la modellazione del comportamento meccanico di terreni granulari parcialmente saturi", *Conf. Il ruolo dei fluidi nei problemi di ingegneria geotecnica*, Mondovi, 167-188, (in Italian).

Josa, A., (1988) "Un modelo elastoplastico para suelos no saturados", *PhD Thesis*, Universitat Politechnica de Catalunya, Barcelona.

Josa, A., Alonso, E.E., Lloret, A., Gens, A., (1987), "Stress-strain behaviour of partially saturated soils", *Proceedings of the 9th European Conference on Soil Mechanics & Foundation Engineering*, Dublin, **2**, 561-564.

Josa, A., Balmaceda, A., Gens, A., Alonso, E.E., (1992) "An elastoplastic model for partially saturate soils

exhibiting a maximum of collapse", *Proceedings of the 3rd International Conference on Computational Plasticity*, Barcelona, **1**, 815-826.

Kanno, T., Kato, K., Yamagata, J., (1996) "Moisture movement under a temperature gradient in highly compacted bentonite", *Engineering Geology*, **41**, 287-300.

Kato, S., Matsuoka, H., Sun, D.A., (1995) "A constitutive model for unsaturated soil based on extended SMP", *Proceedings of the 1st International Conference on Unsaturated Soils*, Alonso E.E., Delage, P., (eds.), Paris, A.A. Balkema, **2**, 739-744.

Kohgo, Y., Nakano, M., Miyazaki, T., (1993a) "Theoretical aspects of constitutive modelling for unsaturated soils", *Soils & Foundations*, **33**(4), 49-63.

Kohgo, Y., Nakano, M., Miyazaki, T., (1993b) "Verification of the generalised elasto-plastic model for unsaturated soil", *Soils & Foundations*, **33**(4), 64-73.

Kröhn, K.P., (2003) "New conceptual models for the resaturation of bentonite", *Applied Clay Science*, **23**, 25-33.

Lloret, A., Alonso, E.E., (1980) "Consolidation of unsaturated soils including swelling and collapse behaviour", *Géotechnique*, **30**(4), 449-477.

Lloret, A., Alonso, E.E., (1985) "State surfaces for partially saturated soils", *Proceedings of the 11th International Conference of Soil Mechanics & Foundation Engineering*, San Francisco, **2**, 557-562.

Lloret, A., Gens, A., Battle, F., Alonso, E.E., (1987) "Flow and deformation analysis of partially saturated soils", *Proceedings of the 9th European Conference on Soil Mechanics & Foundation Engineering*, Dublin, **2**, 565-568.

Lloret, A., Villar, M.V., Sánchez, M., Gens, A., Pintado, X., Alonso, E.E., (2003) "Mechanical behaviour of heavily compacted bentonite under high suction changes", *Géotechnique*, **53**(1), 27-40.

Luikov, A.V., (1966), *Heat and mass transfer in capillary porous bodies*, Pergamon Press, Oxford.

Mata, C., (2003) "Hydraulic behaviour of bentonite based mixtures in engineered barriers: The Backfill and Plug Test at the Äspö HRL (Sweden)", *PhD Thesis*, Technical University of Catalonia.

Matyas, E.L., Radhakrishna, H.S., (1968) "Volume change characteristics of partially saturated soils", *Géotechnique*, **18**(4), 432-448.

Meheust. Y., Schmittbuhl. J., (2001) "Geometrical heterogeneities and permeability anisotropy of rough fractures", *Journal of Geophysical Research*, **106**(B2), 2089-2102.

Melhuish, T.A., (2004) "An investigation of the three-dimensional thermo/hydro/mechanical behaviour of large scale in-situ experiments", *PhD Thesis*, Cardiff University, Cardiff.

Millard, A., Durin, M., Stietel, A., Thoraval, A., Vuillod, E., Baroudi, H., Plas, F., Bougnoux, A., Vouille. G., Kobayashi, A., Hara, K., Fujita, T., Ohnishi, Y., (1995) "Discrete and continuum approaches to simulate the thermo-hydro-mechanical couplings in a large, fractured rock mass", *International Journal of Rock Mechanics & Mining Science & Geomechanics Abstracts*, **32**, 409-434.

Mitchell, H.P., (2002) "An investigation into the thermo/hydro/mechanical interactions involved in high level nuclear waste disposal" *PhD Thesis*, University of Wales, Cardiff.

Moës, N., Dolbow, J., Belytschko, T., (1999) "A finite element method for crack growth without remeshing", *International Journal of Numerical Methods in Engineering*, **46**, 131-50.

Nagra, (2005) *Grimsel Test Site, research on safe geological disposal of radioactive waste*, National Cooperative for the Disposal of Radioactive Waste, Nagra, Wettingen.

National Research Council, (1996) *Rock fractures and fluid flow: contemporary understanding and applications*, National Academy Press, Washington DC.

National Research Council, (2001) *Conceptual models of flow and transport in the fractured vadose zone*. National Academy Press, Washington DC.

Navarro, V., Alonso, E.E., (2000) "Modelling swelling soils for disposal barriers", *Computers and Geotechnics*, **27**(1), 19-43.

Neretnieks, I., (1989) *Solute transport in fractured rock - applications to radionuclide waste repositories*, Swedish Nuclear Fuel and Waste Management Company, SKB, Stockholm.

Neretnieks, I., (1993) "Solute transport in fractured rock: applications to radionuclide waste repositories.", *Flow and contaminant transport in fractured rock*, Bear, J., Tsang, C-F., de Marsily, G., (eds.) Academic Press, San Diego, 39-127.

Neretnieks, I., Ericksen, T., Tahtinen, P., (1982) "Tracer movement in a single fissure in granitic rock: Some experimental results and their interpretation", *Water Resources Research*, **18**(4), 849-858.

Neuman, S.P., (1987) "Stochastic continuum representation of fractured rock permeability as an alternative to the REV and fracture network concepts", *Rock Mechanics, Proceedings of the 28th US Symposium*, Farmer, I.W., Daemen, J.J.K., Desai, C.S., Glass, C.E., Neuman, S.P., (eds.), Tucson, Arizona, A.A. Balkema, 533-561.

Neuman, S.P., (1988) *A proposed conceptual framework and methodology for investigating flow and transport in Swedish crystalline rocks*, SKB, Working Report AR 88-37, Stockholm.

Neuman, S.P., (2005) "Trends, prospects and challenges in quantifying flow and transport through fractured rocks" *Hydrogeology Journal*, **13**, 124-147.

Neuman, S.P., Simpson, E.S., (eds), (1985) "Hydrogeology of rocks of low permeability", *Memoirs of the International Association of Hydrogeology, Proceedings of the 17th IAH Congress*, **XVII**, Arizona.

Olivella, S., Gens, A., Carrera, J., Alonso, E.E., (1995) "Numerical formulation for a simulator (CODE_BRIGHT) for the coupled analysis of saline media", *Engineering Computations*, **13**(7), 87-112.

Patton, F.D., (1966) "Multiple modes of shear failure in rocks", *Proceedings of First Congress of International Society of Rock Mechanics*, Portugal, **1**, 509-513.

Philip, J.R., de Vries, D.A., (1957) "Moisture movements in porous materials under temperature gradients", *Transactions of the American Geophysical Union*, **38**(2), 222-232.

Pollock, D.W., (1986) "Simulation of fluid and energy processes associated with high level radioactive waste disposal in unsaturated alluvium", *Water Resources Research*, **22**(5), 765-775.

Pusch, R., (2001) *The buffer and backfill handbook, Part 2: Materials and techniques*, SKB, TR-02-12, Stockholm.

Pusch, R., Karnland, O., Hokmark, H., (1990) *GMM: a general microstructural model for qualitative and quantitative studies of smectite clays*, SKB, Technical Report, SKB-90-43, Stockholm.

Rasmuson, A., Neretnieks, I., (1986) "Radionuclide transport in fast channels in crystalline rock", *Water Resources Research*, **22**, 1247-56.

Raven, K.G., Gale, J.E., (1985) "Water flow in a natural rock fracture as a function of stress and sample size", *International Journal of Rock Mechanics & Mining Science & Geomechanics Abstracts*, **22**(4), 251-261.

Romero, E., Villar, M.V., Lloret, A., (2005) "Thermo-hydro-mechanical behaviour of two heavily overconsolidated clays", *Engineering Geology*, **81**, 255-268.

Sansom, M.R., (1995) "A fully coupled numerical analysis of mass, air and heat transfer in unsaturated soil", *PhD Thesis*, School of Engineering, University of Wales, Cardiff.

Seetharam, S.C., (2003) "An investigation of the thermo/hydro/chemical/mechanical behaviour of unsaturated soils" *PhD Thesis*, Cardiff University, Cardiff.

Siddiqua, S., (2008) "An investigation of the influence of elevated temperatures on the thermal-hydraulic-mechanical response of unsaturated soils", *PhD Thesis*, Cardiff University, Cardiff.

Singh, R.M., (2007) "An experimental and numerical investigation of heat and mass movement in unsaturated clays", *PhD Thesis*, Cardiff University, Cardiff.

SKB, (2007) *Äspö Hard Rock Laboratory, Status Report, October-December 2006*, SKB, IPR-07-04, Stockholm.

SKB, (2008) "Äspö Hard Rock Laboratory" [WWW] <URL:http://www.skb.se/templates/ SKBPage____8855. aspx>[Accessed 10th July 2008].

Smith, L., Schwartz, F.W., (1984) "An analysis of the influence of fracture geometry on mass transport in fractured media", *Water Resources Research*, **20**(9), 1241-1252.

Stephansson, O., Jing, L., Tsang, C-F., (1996) *Coupled Thermo-Hydro-Mechanical processes of fractured media, Mathematical and experimental studies, recent developments of DECOVALEX project for radioactive waste repositories*, Elsevier, Amsterdam.

Terzaghi, K., (1936) "The shearing resistance of saturated soils and the angle of plates between the planes of shear", *Proceedings of the 1st ICSMFE*, Harvard, **1**, 54-56.

Terzaghi, K., (1943) *Theoretical soil mechanics*, Wiley, New York.

THERESA, (2008) *THERESA project, Interface benchmark (1-D) large scale test, description of the Canister Retrieval Test (CRT)*, Unpublished report.

Thomas, H.R., (1980) "Finite element analysis of shrinkage stresses in building materials", *PhD Thesis*, University College, Swansea.

Thomas, H.R., (1985) "Modelling two-dimensional heat and moisture transfer in unsaturated soils, including gravity effects", *International Journal of Analytical Methods in Geomechanics*, **9**, 573-588.

Thomas, H.R., Cleall, P.J., (1997) "Chemico-osmotic effects on the behaviour of unsaturated expansive clays", *Geoenvironmental engineering, Contaminated ground; fate of pollutants and remediation*, Yong, R.N., Thomas, H.R., eds., Thomas Telford, London, 272-277.

Thomas, H.R., Cleall, P.J., (1999) "Inclusion of expansive clay behaviour in coupled thermo hydraulic mechanical models", *Engineering Geology*, **54**, 93-108.

Thomas, H.R., Cleall, P.J., Chandler, N., Dixon, D., Mitchell, H.P., (2003) "Water infiltration into a large-scale in-situ experiment in an underground research laboratory", *Géotechnique*, **53**(2), 207-224.

Thomas, H.R., He, Y., (1995) "Analysis of coupled heat, moisture and air transfer in a deformable unsaturated soil", *Géotechnique*, **45**(4), 677-689.

Thomas, H.R., He, Y., (1998) "Modelling the behaviour of unsaturated soil using an elasto plastic constitutive relationship", *Géotechnique*, **48**(5), 589-603.

Thomas, H.R., He, Y., Ramesh, A., Zhou, Z., Villar, M.V., Cuevas, J., (1994a) "Heating unsaturated clay - An experimental and numerical investigation", *Proceedings of the 3rd International Conference on Numerical Methods in Geotechnical Engineering, Manchester, Numerical Methods in Geotechnical Engineering*, Smith, I.M., (ed.), A.A. Balkema, 181-186.

Thomas, H.R., King, S.D., (1991) "Coupled temperature/capillary potential variations in unsaturated soil", *Journal of Engineering Mechanics, American Society of Civil Engineers*, **117**(11), 2475-2491.

Thomas, H.R., Sansom, M.R., (1995) "A fully coupled analysis of heat, moisture and air transfer in unsaturated soil", *Journal of Engineering Mechanics, American Society of Civil Engineering*, **12**(3), 392-405.

Thomas, H.R., Sansom, M.R., Volckaert, G., Jacobs, P., Kumnam, M., (1994b) "An experimental and numerical investigation of the hydration of compacted powdered Boom clay", *Proceedings of the 3rd International Conference on Numerical Methods in Geotechnical Engineering, Manchester, Numerical Methods in Geotechnical Engineering*, Smith, I.M., (ed.), A.A. Balkema, 135-142.

Thomas, H.R., Seetharam, S.C., (2008) "On the inclusion of some biological impacts and influences in coupled transport phenomena in unsaturated soil", *Proceedings of the 12th International Conference of International Association for Computer Methods & Advances in Geomechanics (IACMAG)*, Goa, 2172-2180.

Thomas, H.R., Yong, R.N., Hashm, A.A., (1997) "Numerical modelling of contaminant transport in unsaturated soils", *Geoenvironmental Engineering, Contaminated ground: fate of pollutants and remediation*, Yong, R.N., Thomas, H.R., (eds.), 278-283.

Tsang, Y,W., (1984) "Effect of tortuosity on fluid flow through a single fracture", *Water Resources Research*, **20**(9), 1209-1215.

van Genutchen, M.T., Alves, W.J., (1982) *Analytical solutions of the one-dimensional convective-dispersive solute transport equation*, US Department of Argriculture, technical bulletin 1661.

Villar, M.V., (1999) "Investigation of the behaviour of bentonite by means of suction-controlled oedometer tests", *Engineering Geology*, **54**, 67-73.

Villar, M.V., Cuevas, J., Martín, P.L., (1996) "Effects of heat/water flow interaction on compacted bentonite: Preliminary results", *Engineering Geology*, **41**, 257-267.

Villar, M.V., Martín, P.L., Barcala, J.M., (2005) *Infiltration tests at isothermal conditions and under thermal gradient*, CIEMAT, Technical report CIEMAT/DMA/M2140/1/05.

Villar, M.V., Sánchez, M., Lloret, A., Gens, A., Romero, E., (2003) "Experimental and numerical study of the T-H-M behaviour of compacted bentonite in small-scale tests", *Advances in Understanding Engineered Clay Barriers* Alonso, E., Ledesma, A., (eds.), 323-335.

Villar, M.V., Sánchez, M., Gens, A., (2008) "Behaviour of a bentonite barrier in the laboratory: Experimental results up to 8 years and numerical simulation", *Physics & Chemistry of the Earth* **33**, S476-S485.

Wang, J.S.Y., Tsang, C-F., Sterbentz, R.A., (1982) "The state of the art of numerical modeling of thermohydrologic flow in fractured rock masses", *Environmental Geology*, 4(4), 133-199.

Warburton, P.M., (1980) "A stereological interpretation of joint trace data", *International Journal of Rock Mechanics & Mining Science & Geomechanics Abstracts*, **17**, 181-90.

Wei, L., Hudson, J.A., (1993) "A coupled discrete-continuum approach for modelling water flow in fractured rocks", *Géotechnique*, **43**, 21-36.

Wei, L., Hudson, J.A., (1998) "A hybrid discrete-continuum approach to model hydro-mechanical behaviour of jointed rocks", *Engineering Geology*, **49**, 317-325.

Wheeler, S.J., Karube, D., (1996) "Constitutive modelling", *Proceedings of the 1st International Conference on Unsaturated Soils*, Alonso E.E., Delage, P., (eds.), Paris, A.A. Balkema, **3**, 1323-1356.

Wheeler, S.J., Sharma, R.S., Buisson, M.S.R., (2003) "Coupling of hydraulic hysteresis and stress-strain behaviour in unsaturated soil", *Géotechnique*, **53**(1), 41-54.

Wheeler, S.J., Sivakumar, V., (1995) "An elasto-plastic critical state framework for unsaturated soil", *Géotechnique*, **45**(1), 35-53.

Whitaker, S., (1977) "Simultaneous heat, mass and momentum transfer in porous media: A theory of drying", *Advances in Heat Transfer*, **14**, 119-203.

Winberg, A., Andersson, P., Poteri, A., Cvetkovic, V., Dershowitz, W., Hermanson, J., Gómez-Hernández, J.J., Hautojärvi, A., Billaux, D., Tullborg, E.V., Holton, D., Meier, P., Medina, A., (2003) *Final report of the TRUE Block Scale project. 4. Synthesis of flow, transport and retention in the block scale*, SKB. TR-02-16, Stockholm.

Wu, X., Chieng, S.T., (1995) "Modeling multicomponent reactive chemical transport in nonisothermal unsaturated/saturated soils. I: Mathematical model development", *Transactions of the American Society of Agricultural Engineers*, **38**(3), 817-826.

Yeh, G.T., Tripathi, V.S., (1991) "A model for simulating transport of reactive multispecies components: Model development and demonstration", *Water Resources Research*, **27**(12), 3075-3094.

Yong, R.N., Japp, R.D., How, G., (1971) "Shear strength of partially saturated clays", *Proceedings of the 4th Asian Regional Conference on Soil Mechanics & Foundation Engineering*, Bangkok, 2(12), 183-187.

Zienkiewicz, O.C., Pande, G.N., (1977) "Time dependent multilaminate model of rocks - a numerical study of deformation and failure of rock masses", *International Journal for Numerical & Analytical Methods in Geomechanics*, **1**, 219-247.

3

Theoretical and Numerical Formulation

3.1 Introduction

The theoretical and numerical formulation are presented in this chapter. The majority of this formulation has been presented previously (Cleall, 1998; Mitchell, 2002; Melhuish, 2004). A formulation is presented for the Thermo-Hydro-Mechanical (THM) behaviour of an unsaturated soil, considered to be a porous media. The flow variables of liquid and air are considered via a mass balance approach, heat flow is considered by the conservation of energy approach and the mechanical formulation is based upon the stress equilibrium approach. The mechanical formulation has been developed here in three-dimensional form to match analyses undertaken later in this work. A numerical formulation is developed based upon the finite-element method spatially and the finite-difference method temporally.

General aspects of the theoretical formulation are presented in section 3.2 including the basic assumptions and the primary variables. The governing equation describing the moisture transfer is developed in section 3.3 based upon the principle of conservation of mass and

treating water as a two phase flow process. Air transfer is considered in section 3.4 considering air to be a binary mixture of dry air and water vapour. Air is considered to be found both as bulk air and air dissolved in the water phase. The governing equation of heat transfer is presented in section 3.5 based upon the conservation of energy and identifying conduction, convection and radiation as the main modes of transfer. Finally, the mechanical formulation is detailed in section 3.6, using an elasto-plastic model with two yield surfaces and treating the suction as a stress-variable. The numerical formulation is presented in section 3.8; with spatial discretisation described in section 3.9 and temporal discretisation described in section 3.10. A summary of the theoretical formulation is presented in section 3.7 and the main conclusions are given in section 3.11.

3.2 Theoretical formulation - General

Soil is considered to be a three-phase porous medium, consisting of a solid soil skeleton, pore-water and pore-air, which is made up of dry air and water vapour. In the following formulation the flow of moisture, air and heat energy in a deformable porous media are considered. In particular, governing differential equations are developed for moisture, dry air, heat and deformation. These governing equations are expressed in terms of four primary variables, namely:

  i. Pore-water-pressure, u_l

  ii. Pore-air-pressure, u_a

  iii. Temperature, T

  iv. Displacement, $\mathbf{u}$

The behaviour of all these variables are included within coupled thermo-hydro-mechanical (THM) formulation. Liquid and vapour water transfer are considered utilising the principle of conservation of mass, as is the transfer of pore air. The pore air is considered a binary mixture of dry air and water vapour. Heat transfer is governed by the conservation of energy, taking into account conduction, convection and the phase change via the latent heat of vapourisation. Radiation is assumed negligible. The mechanical behaviour is governed by a constitutive relationship developed using an elasto-plastic relationship for a slightly

swelling soil via consideration of stress equilibrium. All of the governing equations are then developed in a three-dimensional form.

3.3 Moisture Transfer

Moisture is found in both liquid and vapour form within unsaturated soil at the temperatures considered in this work ($10°C < T < 90°C$). Transfer of moisture can be described as a two phase flow process, comprising both liquid and vapour form. The volumetric water content, θ, is defined as the sum of these phases:

$$\theta = \theta_l + \theta_v \tag{3.1}$$

where θ_l is the volumetric liquid content and θ_v is the volumetric vapour content. The conservation of mass for each phase may be considered separately.

The principle of local thermodynamic equilibrium dictates that at any point the volumetric liquid water and water vapour are in equilibrium (de Vries, 1958). This principle is used to define the following relationship:

$$\theta_v = \frac{(n - \theta_l)\,\rho_v}{\rho_l} \tag{3.2}$$

where, n is the porosity, ρ_v is the density of water vapour and ρ_l is the density of the liquid water.

Considering the liquid water phase, the principle of conservation of mass demands that the time derivative of the liquid content is equal to the spatial gradient of the liquid flux, with the inclusion of a sink/source term allowing for phase change gives:

$$\rho_l \frac{\partial\left(\theta_l \partial V\right)}{\partial t} = -\rho_l \partial V \,\nabla \cdot \mathbf{v_l} - \rho_l \partial V E_{ss} \tag{3.3}$$

where ∂V is the incremental volume, t is the time, ∇ is the gradient operator, $\mathbf{v_l}$ is the velocity of liquid and E_{ss} is a sink/source term.

Using the principle of conservation of mass similarly for the vapour phase, the time derivative of the vapour content is equal to the spatial gradient of the vapour flux with an equal and opposite sink/source term to the liquid water allowing for the change of state. This is

expressed as:

$$\rho_l \frac{\partial\left(\theta_v \partial V\right)}{\partial t} = -\rho_l \partial V \bigtriangledown \cdot \mathbf{v_v} - \partial V \bigtriangledown \cdot \left(\rho_v \mathbf{v_a}\right) + \rho_l \partial V E_{ss} \qquad (3.4)$$

where, $\mathbf{v_v}$ is the equivalent velocity of vapour and $\mathbf{v_a}$ is the velocity of pore air. The volumetric air content, θ_a, (including dry air and vapour) can be expressed as:

$$\theta_a = (n - \theta_l) \qquad (3.5)$$

Substituting equations (3.2) and (3.5) into equation (3.4), the law of conservation of mass for water vapour flow can be written as:

$$\frac{\partial\left(\rho_v \theta_a \partial V\right)}{\partial t} = -\rho_l \partial V \bigtriangledown \cdot \mathbf{v_v} - \partial V \bigtriangledown \cdot \left(\rho_v \mathbf{v_a}\right) + \rho_l \partial V E_{ss} \qquad (3.6)$$

Summing the respective equations for liquid and vapour conservation of mass, equations (3.3) and (3.6), gives the moisture conservation of mass:

$$\rho_l \frac{\partial\left(\theta_l \partial V\right)}{\partial t} + \frac{\partial\left(\rho_v \theta_a \partial V\right)}{\partial t} = -\rho_l \partial V \bigtriangledown \cdot \mathbf{v_l} - \rho_l \partial V \bigtriangledown \cdot \left(\mathbf{v_v}\right) - \partial V \bigtriangledown \cdot \left(\rho_v \mathbf{v_a}\right) \qquad (3.7)$$

The volumetric liquid and air contents may be expressed in terms of porosity and degree of saturation:

$$\theta_l = n S_l \qquad (3.8)$$

$$\theta_a = n S_a \qquad (3.9)$$

where S_l and S_a are the degrees of saturation of pore water and pore air respectively. The incremental volume, ∂V is defined as the summation of the volumes of the solid and the void:

$$\partial V = (1 + e)\, \partial V_s \qquad (3.10)$$

where e is the void ratio, and V_s is the volume of the solids. Substitution of equations (3.8), (3.9) and (3.10) into equation (3.7) produces:

$$\rho_l \frac{\partial\left(n S_l \left(1 + e\right) \partial V_s\right)}{\partial t} + \frac{\partial\left(\rho_v n S_a \left(1 + e\right) \partial V_s\right)}{\partial t} + \rho_l \left(1 + e\right) \partial V_s \bigtriangledown \cdot \mathbf{v_l} +$$

$$\rho_l \left(1 + e\right) \partial V_s \bigtriangledown \cdot \mathbf{v_v} + \left(1 + e\right) \partial V_s \bigtriangledown \cdot \left(\rho_v \mathbf{v_a}\right) = 0 \quad (3.11)$$

It is assumed that the volume of the solid remains constant, hence ∂V_s can be eliminated, by definition $n = e/(1 + e)$ and dividing by $(1 + e)$, equation (3.11) becomes:

$$\frac{\rho_l}{(1 + e)} \frac{\partial\left(e S_l\right)}{\partial t} + \frac{1}{(1 + e)} \frac{\partial\left(\rho_v e S_a\right)}{\partial t} + \rho_l \bigtriangledown \cdot \mathbf{v_l} + \rho_l \bigtriangledown \cdot \mathbf{v_v} + \bigtriangledown \cdot \left(\rho_v \mathbf{v_a}\right) = 0 \qquad (3.12)$$

Inspection of the spatial derivative terms of equation (3.12) reveal that the moisture flux includes:

i. A liquid flux.

ii. A component of vapour flux due to vapour pressure gradients.

iii. A component of vapour flux due to the bulk flow of vapour arising from the movement of pore air.

By further inspection of equation (3.12) it can be seen these fluxes governing the movement of water are defined by the velocities of the liquid, vapour and air phases. The flow rates and laws that govern them are discussed below.

3.3.1 Mechanisms of liquid water flow

Many concepts have been used to describe the flow of water through unsaturated soil (Mitchell, 1993; Fredlund and Rahardjo, 1993). The mechanisms that have been found to be appropriate are:

i. Pressure head.

ii. Elevation head.

iii. Thermal gradients.

iv. Electrical gradients.

The first three of these mechanisms are considered within this work and the fourth is not.

Hydraulic head is found from combining the pressure and elevation heads and is described by Darcy (1856) to be a potential for water flow. Darcy's Law (1856) can be used to present this potential for unsaturated soils as Childs (1969) and Neilson (1986). For multiphase flow in unsaturated media Darcy's Law can be expressed as:

$$\mathbf{v_l} = -\frac{k_l}{\mu_l}\left[\nabla\frac{u_l}{\gamma_l} + \nabla z\right] = -K_l\left[\nabla\frac{u_l}{\gamma_l} + \nabla z\right] \tag{3.13}$$

where $\mathbf{v_l}$ is the liquid velocity due to the pressure and elevation heads, k_l is the intrinsic permeability, μ_l is the absolute viscosity, γ_l is the unit weight of the liquid, z is the elevation and K_l is the unsaturated hydraulic conductivity. The temperature strongly influences the

absolute viscosity. Kaye and Laby (1973) presented a relationship between the dynamic viscosity of liquid water and the absolute temperature valid in the range $0°C < T < 100°C$:

$$\mu_l\,(T) = 661.2\,(T - 229)^{-1.562} \times 10^{-3} \pm 0.5\% \qquad (Ns/m^2) \qquad (3.14)$$

Unsaturated hydraulic conductivity of a soil is influenced by a number of factors, the fabric of the soil, degree of saturation and turbulence of the flow. The major influence of the soil fabric is the amount of pore volume that can be used for flow and in addition, turbulence may be neglected if the flow is slow. A number of approaches have been adopted, where the 'standard' approach, generally used for largely inert materials, flow is hypothesised to be able to flow through all water filled pores, therefore:

$$K_l = K_l\,(S_l) \qquad (3.15)$$

Another approach for materials with a high smectite content (e.g. bentonite clay) has been hypothesised by Mitchell (2002) and Thomas $et~al.$ (2003) where the interaction of the macro/micro-structure may have a pronounced effect. Mitchell proposed that as water enters a material such as this, the majority of the water becomes adsorbed within the micro-pores and becomes unavailable for further flow. The micro-pores swell as a result, and dependant upon the degree of mechanical restraint, this swelling may lead to a reduction in the size of the macro-pores (Pusch, 1998). The macro-pores contain the water available for flow, hence the reduction in size would 'choke' moisture flow and reduce the effective hydraulic conductivity of the material.

Mitchell (2002) modified the hydraulic conductivity to allow for micro/macro interaction, proposing a number of relationships. Following Thomas $et~al.$ (2003a) who adopted an approach of Mitchell (2002) and the assumption that 94% of the water present in the clay may be adsorbed and not available for flow (Pusch $et~al.$, 1990), a first approximation of a hydraulic conductivity relationship, varying exponentially with the amount of free water within the soil, was proposed:

$$K_m = K_l\,[S_a + 0.06S_l\,(exp\,\{-100\,(1 - 0.06)\,S_l\})] \qquad (3.16)$$

where K_l is the unsaturated hydraulic conductivity from the 'standard' unsaturated hydraulic conductivity relationship. K_m is the unsaturated hydraulic conductivity relationship taking

into account macro/micro-structure interactions.

Matyas and Radhakrishna (1968) proposed that the degree of liquid saturation is a function of the initial void ratio, the initial liquid saturation, and the stress parameters: net stress, deviatoric stress and suction. Alonso *et al.* (1988) found that the effect of stress upon the degree of saturation to be relatively insignificant. If the initial void ratio of a soil sample is controlled and the sample is confined the degree of saturation can be expressed in terms of the suction, s:

$$S_l = S_l(s) \tag{3.17}$$

Soil suction can be expressed as the free energy state of soil water (Edlefsen and Anderson, 1943; Fredlund and Rahardjo, 1993). The surface energy, ξ, was also expressed by Edlefsen and Anderson (1943) as a function of temperature:

$$\xi = 0.1171 - 0.0001516T \qquad (J/m^2) \tag{3.18}$$

Therefore, if a relationship between suction and degree of saturation at a reference temperature, T_r, is known, the suction at any temperature and degree of saturation can be found:

$$s = \frac{\xi}{\xi_r} s_r \tag{3.19}$$

where ξ_r and s_r are the surface energy and the suction at reference temperature, T_r, and ξ and s are the surface energy and suction at the temperature, T.

If the dependence of soil suction on temperature is incorporated in the partial time differential of equation (3.17), the variation of degree of saturation in respect to time can be expressed as:

$$\frac{\partial S_l}{\partial t} = \frac{\partial S_l}{\partial s} \frac{\partial s}{\partial t} + \frac{\partial S_l}{\partial T} \frac{\partial T}{\partial t} \tag{3.20}$$

Fredlund and Rahardjo (1993) define the matric suction as the difference between the pore air pressure and the pore liquid pressure, expressed as:

$$s = u_a - u_l \tag{3.21}$$

Other forms of suction, such as osmotic, are neglected as changes in these variables due to changes in the other primary variables will not be significant.

The degree of saturation can then be expressed in terms of the primary variables by substituting equation (3.21) into equation (3.20):

$$\frac{\partial S_l}{\partial t} = \frac{\partial S_l}{\partial s}\frac{\partial u_a}{\partial t} + \frac{\partial S_l}{\partial T}\frac{\partial T}{\partial t} - \frac{\partial S_l}{\partial s}\frac{\partial u_l}{\partial t} \tag{3.22}$$

3.3.2 Mechanisms of water vapour flow

The main mechanisms that contribute to the flow of vapour are:

i. Pressure flow

ii. Diffusive flow.

The flow of bulk air, considered to be a binary mix of dry air and water vapour (Pollock, 1986) is dealt with utilising a generalised Darcy's Law (Carman, 1956; Alonso et al., 1988). Diffusive flow behaviour is represented by diffusive vapour flow theory for unsaturated soil, proposed by Philip and de Vries (1957).

Considering only the bulk air phase, the primary driving mechanism is the pore-air-pressure gradient, with elevation providing only a negligible contribution (Fredlund and Rahardjo, 1993). Therefore, a generalised Darcy's Law for flow in unsaturated soil can be described as:

$$\mathbf{v_a} = -\frac{k_a}{\mu_a}\,\nabla\, u_a = -K_a\,\nabla\, u_a \tag{3.23}$$

where $\mathbf{v_a}$ is the velocity of pore air, k_a is the effective permeability of pore air, μ_a is the absolute viscosity of pore air and K_a is the unsaturated conductivity of pore air.

As shown in section 3.3.1 two mass properties must be used to describe unsaturated conductivity. For consistency K_a is considered to be a function of void ratio, e and degree of pore air saturation, S_a (Fredlund and Rahardjo, 1993).

Philip and de Vries (1957) proposed a vapour flow law for the velocity of vapour through an unsaturated soil:

$$\mathbf{v_v} = -\frac{D_{atms}v_v\tau_v\theta_a}{\rho_l}\,\nabla\,\rho_v \tag{3.24}$$

where $\mathbf{v_v}$ is the vapour velocity, D_{atms} is the molecular diffusivity of vapour through air, v_v is a mass flow factor, τ_v is a tortuosity factor and $\nabla\rho_v$ is the spatial vapour density gradient.

The expression utilised by Philip and de Vries (1957) for the molecular diffusivity of vapour through air, within the temperature range 293-343 K, was proposed by Krischer and Rohnalter (1940):

$$D_{atms} = 5.893 \times 10^{-6} \frac{T^{2.3}}{u_a} \qquad (3.25)$$

Philip and de Vries (1957) exercised an expression proposed by Partington (1949) for the mass flow factor, who showed that for steady state diffusion in a closed system between an evapourating source and a condensing sink:

$$v_v = \frac{u_a}{u_a - u_v} \qquad (3.26)$$

where u_v is the partial pressure of vapour and can be calculated by the thermodynamic relationship:

$$u_v = \rho_v R_v T \qquad (3.27)$$

where R_v is the specific gas constant for water vapour (Kaye and Laby, 1973).

Philip and de Vries (1957) recognised that the mass flow factor predicted in equation (3.26) may not be valid for non-stationary conditions, but would predict a correct order of magnitude and that under normal soil temperatures the value is close to 1.

A thermodynamic relationship was proposed by Edlefsen and Anderson (1943), known as the psychrometric law, showing the density of water vapour to be:

$$\rho_v = \rho_0 h = \rho_0 exp \left(\frac{\psi g}{R_v T} \right) \qquad (kg/m^3) \qquad (3.28)$$

where ρ_0 is the density of saturated water vapour, h is the relative humidity, g is the gravitational constant and ψ is the capillary potential defined as:

$$\psi = \frac{u_l - u_a}{\gamma_l} \qquad (m) \qquad (3.29)$$

Ewen and Thomas (1989) presented a relationship fitted to standard data (Mayhew and Rogers, 1976) for the density of saturated water vapour:

$$\rho_0 = \frac{1}{194.4 \exp \left(-0.06374 \left(T - 273 \right) + 0.1634 \times 10^{-3} \left(T - 273 \right)^2 \right)} \qquad (3.30)$$

From equation (3.28) and with substitution from equation (3.21) for suction, the gradient of vapour density may be expressed as:

$$\nabla \rho_v = \left(h \frac{\partial \rho_0}{\partial T} + \rho_0 \frac{\partial h}{\partial T} \right) \nabla T + \left(\rho_0 \frac{\partial h}{\partial s} \right) \nabla u_a - \left(\rho_0 \frac{\partial h}{\partial s} \right) \nabla u_l \qquad (3.31)$$

assuming that the density of saturated water vapour is dependent on temperature whilst relative humidity is dependent upon both suction and temperature.

The time derivative, with the same assumption, can be shown to yield:

$$\frac{\partial \rho_v}{\partial t} = \left(h \frac{\partial \rho_0}{\partial T} + \rho_0 \frac{\partial h}{\partial T} \right) \frac{\partial T}{\partial t} + \left(\rho_0 \frac{\partial h}{\partial s} \right) \frac{\partial u_a}{\partial t} - \left(\rho_0 \frac{\partial h}{\partial s} \right) \frac{\partial u_l}{\partial t} \qquad (3.32)$$

By substituting equation 3.31 into equation 3.24 gives:

$$\mathbf{v_v} = \frac{D_{atms} v_v \tau_v \theta_a}{\rho_l} \left(\rho_0 \frac{\partial h}{\partial s} \right) \bigtriangledown u_l - \frac{D_{atms} v_v \tau_v \theta_a}{\rho_l} \left(h \frac{\partial \rho_0}{\partial T} + \rho_0 \frac{\partial h}{\partial T} \right) \bigtriangledown T$$
$$- \frac{D_{atms} v_v \tau_v \theta_a}{\rho_l} \left(\rho_0 \frac{\partial h}{\partial s} \right) \bigtriangledown u_a \quad (3.33)$$

In experimental tests undertaken by Philip and de Vries (1957) the theory shown in equation (3.33) did not fully capture behaviour of vapour flows at increased temperature gradients. This led to two refinements in the temperature gradient term. A flow area factor, f, was included to allow for a reduction of the vapour flow when higher moisture contents reduce the available flow area. A microscopic pore temperature gradient factor, $(\bigtriangledown T)_a / (\bigtriangledown T)$, was also introduced and is the ratio of the average temperature gradient in the air filled pores to the overall temperature gradient. This factor allows microscopic temperature gradients in the fluid filled pores, which may be much higher than the macroscopic temperature gradients across the whole sample. Heat flow paths shared between sections of solid and fluid paths give rise to this effect. Modifying equation (3.33) to include the aforementioned factors gives:

$$\mathbf{v_v} = \frac{D_{atms} v_v \tau_v \theta_a}{\rho_l} \left(\rho_0 \frac{\partial h}{\partial s} \right) \bigtriangledown u_l - \frac{D_{atms} v_v \tau_v \theta_a}{\rho_l} f \frac{(\bigtriangledown T)_a}{\bigtriangledown T} \left(h \frac{\partial \rho_0}{\partial T} + \rho_0 \frac{\partial h}{\partial T} \right) \bigtriangledown T$$
$$- \frac{D_{atms} v_v \tau_v \theta_a}{\rho_l} \left(\rho_0 \frac{\partial h}{\partial s} \right) \bigtriangledown u_a \quad (3.34)$$

Two alterations to the flow area factor of Philip and de Vries (1957) equation were proposed by Ewen and Thomas (1989). The flow area factor had not been applied to the moisture term, but assuming vapour velocity is proportional to vapour density the factor should appear in both temperature and moisture terms. The second alteration is that the reduction in velocity due to a reduction in flow area, predicted by the equation, was not shown experimentally by Philip and de Vries. Ewen and Thomas suggested the form of the flow area factor is modified to be in terms of the porosity so that this phenomenon is not predicted

by the equation. It is noted, however, that at saturation no vapour movement would occur. Adopting these suggestions, vapour velocity can be written as:

$$\mathbf{v_v} = \frac{D_{atms}v_v n}{\rho_l}\left(\rho_0\frac{\partial h}{\partial s}\right)\bigtriangledown u_l - \frac{D_{atms}v_v n}{\rho_l}\frac{(\bigtriangledown T)_a}{\bigtriangledown T}\left(h\frac{\partial \rho_0}{\partial T}+\rho_0\frac{\partial h}{\partial T}\right)\bigtriangledown T$$
$$-\frac{D_{atms}v_v n}{\rho_l}\left(\rho_0\frac{\partial h}{\partial s}\right)\bigtriangledown u_a \quad (3.35)$$

where $(\bigtriangledown T)_a / (\bigtriangledown T)$ is derived form the work of Preece (1975) for Washington Sand (de Vries, 1966).

It should be noted that the experimental work, above, was conducted on a dense cohesionless material, medium sand. It is acknowledged that the application of an approach validated for a sand requires further research and development when considering the movement of vapour in a cohesive soil, such as a bentonite buffer material. The form of the vapour flow factor, especially, may need to be re-evaluated as a consequence of such work. The importance of such statements is further enhanced when considering the case of highly swelling, densely compacted clay. Furthermore, the application of the original Philip and de Vries (1957) approach, given the mechanistic (constitutive) formulation, may require close re-examination in the context of the latter material. An initial experimental and numerical study was undertaken by Singh (2007) into vapour flow in high-density clays with temperature and hydraulic gradients. It was proposed by Singh to include two material dependant factors in equation (3.34), which can then be expressed as:

$$\mathbf{v_v} = \eta_2\frac{D_{atms}v_v T_v \theta_a}{\rho_l}\left(\rho_0\frac{\partial h}{\partial s}\right)\bigtriangledown u_l - \eta_1\frac{D_{atms}v_v T_v \theta_a}{\rho_l}f\frac{(\bigtriangledown T)_a}{\bigtriangledown T}\left(h\frac{\partial \rho_0}{\partial T}+\rho_0\frac{\partial h}{\partial T}\right)\bigtriangledown T$$
$$-\eta_2\frac{D_{atms}v_v T_v \theta_a}{\rho_l}\left(\rho_0\frac{\partial h}{\partial s}\right)\bigtriangledown u_a \quad (3.36)$$

where η_1 and η_2 are material dependant factors. For MX-80 bentonite these were initially predicted to be 0.17 and 0.60 respectively. However, it was concluded by Singh (2007) that both further experimental and numerical work is required to characterise the behaviour of high-density clays.

3.3.3 Governing differential equations for water flow

The two previous sections have shown the flow components for the liquid and vapour phase respectively. In this section these flow laws are incorporated into the equation of mass

conservation, detailed in equation (3.12). The resulting equation is then restructured in terms of the primary variables to produce the governing equation.

With the expansion of the first two terms of equation (3.12), again recognising $n = e/(1 + e)$ and with the substitution of $S_a = 1 - S_l$ equation (3.12) can be expressed as:

$$\rho_l n \frac{\partial S_l}{\partial t} + \frac{\rho_l S_l}{(1+e)} \frac{\partial e}{\partial t} + \frac{\rho_v (1 - S_l)}{(1+e)} \frac{\partial e}{\partial t} + (1 - S_l) n \frac{\partial \rho_v}{\partial t} - \rho_v n \frac{\partial S_l}{\partial t} + \rho_l \nabla \cdot \mathbf{v_l} + \rho_l \nabla \cdot \mathbf{v_v} + \nabla \cdot (\rho_v \mathbf{v_a}) = 0$$

(3.37)

Grouping all similar terms gives:

$$n (\rho_l - \rho_v) \frac{\partial S_l}{\partial t} + n (1 - S_l) \frac{\partial \rho_v}{\partial t} + \left[\frac{\rho_l S_l + \rho_v (1 - S_l)}{(1+e)} \right] \frac{\partial e}{\partial t} + \rho_l \nabla \cdot \mathbf{v_l} + \rho_l \nabla \cdot \mathbf{v_v} + \nabla \cdot (\rho_v \mathbf{v_a}) = 0$$

(3.38)

Considering the third term, it can be seen that:

$$\frac{\partial e}{(1+e) \partial t} = \frac{\partial \varepsilon_v}{\partial t}$$

(3.39)

where ε_v is the volumetric strain, the rate of change of void ratio with respect to the initial volume. With this substitution, equation (3.38) yields:

$$n (\rho_l - \rho_v) \frac{\partial S_l}{\partial t} + n (1 - S_l) \frac{\partial \rho_v}{\partial t} + [\rho_l S_l + \rho_v (1 - S_l)] \frac{\partial \varepsilon_v}{\partial t} + \rho_l \nabla \cdot \mathbf{v_l} + \rho_l \nabla \cdot \mathbf{v_v} + \nabla \cdot (\rho_v \mathbf{v_a}) = 0$$

(3.40)

The first term of equation (3.40) including substitution from equation (3.22) can be expressed as:

$$n (\rho_l - \rho_v) \frac{\partial S_l}{\partial t} = -n (\rho_l - \rho_v) \frac{\partial S_l}{\partial s} \frac{\partial u_l}{\partial t} + n (\rho_l - \rho_v) \frac{\partial S_l}{\partial T} \frac{\partial T}{\partial t} + n (\rho_l - \rho_v) \frac{\partial S_l}{\partial s} \frac{\partial u_a}{\partial t} \quad (3.41)$$

Including substitution from equation (3.32) the second term can be expressed as:

$$n (1 - S_l) \frac{\partial \rho_v}{\partial t} = n (1 - S_l) \left[\left(h \frac{\partial \rho_0}{\partial T} + \rho_0 \frac{\partial h}{\partial T} \right) \frac{\partial T}{\partial t} + \left(\rho_0 \frac{\partial h}{\partial s} \right) \frac{\partial u_a}{\partial t} - \left(\rho_0 \frac{\partial h}{\partial s} \right) \frac{\partial u_l}{\partial t} \right] \quad (3.42)$$

It can be shown that $\frac{\partial \varepsilon_v}{\partial t}$ can be expressed as:

$$\frac{\partial \varepsilon_v}{\partial t} = (1 + e) \frac{\partial n}{\partial t} = \mathbf{m}^T \frac{\partial \varepsilon}{\partial t} = \mathbf{m}^T \mathbf{P} \frac{\partial \mathbf{u}}{\partial t}$$

(3.43)

where ε is the strain vector and $\mathbf{u}$ is the vector of displacments. The strain matrix, $\mathbf{P}$, and the vector $\mathbf{m}$ will be defined in section 3.6. With this substitution, the third term can be shown to be:

$$(S_l \rho_l + (1 - S_l) \rho_v) \frac{\partial \varepsilon_v}{\partial t} = ((S_l \rho_l + (1 - S_l) \rho_v) \mathbf{m}^T \mathbf{P} \frac{\partial \mathbf{u}}{\partial t}$$

(3.44)

Substituting equations (3.41), (3.42) and (3.44) for the first, second and third terms respectively, and equations (3.13), (3.23) and (3.35) for $\mathbf{v_l}$, $\mathbf{v_a}$ and $\mathbf{v_v}$ respectively, into equation (3.40) yields the governing equation for water transfer in terms of the primary variables:

$$C_{ll}\frac{\partial u_l}{\partial t}+C_{lT}\frac{\partial T}{\partial t}+C_{la}\frac{\partial u_a}{\partial t}+C_{lu}\frac{\partial \mathbf{u}}{\partial t} = \nabla\cdot[K_{ll}\nabla u_l]+\nabla\cdot[K_{lT}\nabla T]+\nabla\cdot[K_{la}\nabla u_a]+J_l \quad (3.45)$$

where:

$$C_{ll} = -n\left(\rho_l - \rho_v\right)\frac{\partial S_l}{\partial s} - n\left(1 - S_l\right)\rho_0\frac{\partial h}{\partial s} \quad (3.46)$$

$$C_{lT} = n\left(\rho_l - \rho_v\right)\frac{\partial S_l}{\partial T} + n\left(1 - S_l\right)\left(h\frac{\partial \rho_0}{\partial T} + \rho_0\frac{\partial h}{\partial T}\right) \quad (3.47)$$

$$C_{la} = n\left(\rho_l - \rho_v\right)\frac{\partial S_l}{\partial s} + n\left(1 - S_l\right)\rho_0\frac{\partial h}{\partial s} \quad (3.48)$$

$$C_{lu} = \left(\left(S_l\rho_l + \left(1 - S_l\right)\rho_v\right)\mathbf{m}^T\mathbf{P}\right) \quad (3.49)$$

$$K_{ll} = \rho_l\left[\frac{K_l}{\gamma_l} - \frac{D_{atms}v_v n}{\rho_l}\left(\rho_0\frac{\partial h}{\partial s}\right)\right] \quad (3.50)$$

$$K_{lT} = \rho_l\frac{D_{atms}v_v n\left(\nabla T\right)_a}{\rho_l\nabla T}\left(h\frac{\partial \rho_0}{\partial T} + \rho_0\frac{\partial h}{\partial T}\right) \quad (3.51)$$

$$K_{la} = \rho_v K_a + \rho_l\left[\frac{D_{atms}v_v n}{\rho_l}\left(\rho_0\frac{\partial h}{\partial s}\right)\right] \quad (3.52)$$

$$J_l = \rho_l\nabla\cdot\left(K_l\nabla z\right) \quad (3.53)$$

3.4 Dry Air Transfer

Dry air is considered to exist in two main forms in unsaturated soils, bulk air and dissolved air (Fredlund and Rahardjo, 1993). Henry's Law governs the proportion of dry air dissolved in the pore liquid. The dissolved air flow is coupled with the pore-liquid flow and the bulk air flow is driven by the air pressure gradient.

Conservation of mass indicates that the temporal derivative of the dry air content and the spatial derivative of the dry air flux must be equal, yielding:

$$\frac{\partial\left(\left[\theta_a + H_s\theta_l\right]\rho_{da}\partial V\right)}{\partial t} = -\partial V\nabla\cdot\left[\rho_{da}\left(\mathbf{v_a} + H_s\mathbf{v_l}\right)\right] \quad (3.54)$$

where H_s is Henry's volumetric coefficient of solubility and ρ_{da} is the density of dry air. Substituting equations (3.8), (3.9) and (3.10) into equation (3.54), eliminating constant ∂V_s

and substituting $n(1+e) = e$ and $S_a = 1 - S_l$, yields:

$$\frac{\partial\left(\left[1 - S_l + H_s S_l\right]\rho_{da}e\right)}{\partial t} + (1+e)\,\triangledown\cdot\left[\rho_{da}\left(\mathbf{v_a} + H_s\mathbf{v_l}\right)\right] = 0 \qquad (3.55)$$

Expanding the first term of equation (3.55) gives:

$$\frac{\partial\left(\left[1 - S_l + H_s S_l\right]\rho_{da}e\right)}{\partial t} =$$
$$\rho_{da}\left(1 - S_l + H_s S_l\right)\frac{\partial e}{\partial t} + e\left(1 - S_l + H_s S_l\right)\frac{\partial \rho_{da}}{\partial t} - e\rho_{da}\frac{\partial S_l}{\partial t} + e\rho_{da}H_s\frac{\partial S_l}{\partial t} \qquad (3.56)$$

Rearranging similar terms gives:

$$\frac{\partial\left(\left[1 - S_l + H_s S_l\right]\rho_{da}e\right)}{\partial t} =$$
$$\rho_{da}\left(1 - S_l + H_s S_l\right)\frac{\partial e}{\partial t} + e\left(1 - S_l + H_s S_l\right)\frac{\partial \rho_{da}}{\partial t} - e\rho_{da}\left(H_s - 1\right)\frac{\partial S_l}{\partial t} \qquad (3.57)$$

Substituting equation (3.57) into equation (3.55), dividing the resultant by $(1+e)$ and recognising $e/(1+e) = n$, yields:

$$\rho_{da}\frac{\left(1 - S_l + H_s S_l\right)}{(1+e)}\frac{\partial e}{\partial t} + n\left(1 - S_l + H_s S_l\right)\frac{\partial \rho_{da}}{\partial t} + n\rho_{da}\left(H_s - 1\right)\frac{\partial S_l}{\partial t} + \triangledown\cdot\left[\rho_{da}\left(\mathbf{v_a} + H_s\mathbf{v_l}\right)\right]$$
$$(3.58)$$

Substituting equation (3.43) into equation (3.39) and then into equation (3.58) yields:

$$\rho_{da}\left(1 - S_l + H_s S_l\right)\mathbf{m}^T\mathbf{P}\frac{\partial\mathbf{u}}{\partial t} + n\left(1 - S_l + H_s S_l\right)\frac{\partial \rho_{da}}{\partial t} +$$
$$n\rho_{da}\left(H_s - 1\right)\frac{\partial S_l}{\partial t} + \triangledown\cdot\left[\rho_{da}\left(\mathbf{v_a} + H_s\mathbf{v_l}\right)\right] = 0 \qquad (3.59)$$

Thomas and Samson (1995) present a method to find the dry density of air in terms of the primary variables. The bulk gaseous phase in soil is considered to be a binary mixture of dry air and water vapour. This phase has been found to, within a sufficiant degree of accuracy, obey the laws of ideal gases (Geraminegad and Saxena, 1986) and the partial pressures can be expressed as:

$$u_{da} = \rho_{da}R_{da}T \qquad (3.60)$$

and:

$$u_v = \rho_v R_v T \qquad (3.61)$$

where R_{da} and R_v are the specific gas constants of dry air and water vapour respectively. The air pressure can be found by application of Dalton's law of partial pressures:

$$u_a = u_{da} + u_v \qquad (3.62)$$

The dry air density can then be found with the substitution of equations (3.60) and (3.61) into equation (3.62), yielding:

$$\rho_{da} = \frac{u_a}{R_{da}T} - \frac{\rho_v R_v}{R_{da}} \tag{3.63}$$

The partial derivative, with respect to time, below is completed with the assumption that $(R_{da} \approx R_a)$. The last term can be calculated from equation (3.32):

$$\frac{\partial \rho_{da}}{\partial t} = \frac{1}{R_{da}} \frac{\partial u_a}{\partial t} - \frac{\rho_a}{T} \frac{\partial T}{\partial t} - \frac{R_v}{R_{da}} \frac{\partial \rho_v}{\partial t} \tag{3.64}$$

To determine the governing equation in terms of the primary variables, equations (3.13), (3.22), (3.23) and (3.64) and substituted into equation (3.59):

$$C_{al} \frac{\partial u_l}{\partial t} + C_{aT} \frac{\partial T}{\partial t} + C_{aa} \frac{\partial u_a}{\partial t} + C_{au} \frac{\partial \mathbf{u}}{\partial t} = \nabla \cdot [K_{al} \nabla u_l] + \nabla \cdot [K_{aa} \nabla u_a] + J_a \tag{3.65}$$

where:

$$C_{al} = -n\rho_{da} (H_s - 1) \frac{\partial S_l}{\partial s} + n (S_a + H_s S_l) \frac{\partial R_v}{\partial R_{da}} \left(\rho_0 \frac{\partial h}{\partial s} \right) \tag{3.66}$$

$$C_{aT} = n\rho_{da} (H_s - 1) \frac{\partial S_l}{\partial T} - n (S_a + H_s S_l) \left(\frac{\rho_a}{T} - \frac{R_v}{R_{da}} \left(h \frac{\partial \rho_0}{\partial T} + \rho_0 \frac{\partial h}{\partial T} \right) \right) \tag{3.67}$$

$$C_{aa} = n\rho_{da} (H_s - 1) \frac{\partial S_l}{\partial s} + n (S_a + H_s S_l) \left(\frac{1}{R_{da}T} - \frac{R_v}{R_{da}} \rho_0 \frac{\partial h}{\partial s} \right) \tag{3.68}$$

$$C_{au} = \rho_{da} (S_a + H_s S_l) \mathbf{m}^T \mathbf{P} \tag{3.69}$$

$$K_{al} = \frac{\rho_{da} H_s}{\gamma_l} K_l \tag{3.70}$$

$$K_{aa} = \rho_{da} K_a \tag{3.71}$$

$$J_a = \rho_{da} H_s \nabla \cdot (K_l \nabla z) \tag{3.72}$$

3.5 Heat Transfer

The primary modes of heat transfer are identified by Jakob (1949) as conduction, convection and radiation. The formulation adopted here assumes radiation effects to be negligible (Mitchell, 1993).

Conservation of energy dictates that the temporal derivative of the heat content, Ω, is equal to the spatial derivative of the heat flux, $\mathbf{Q}$, expressed as:

$$\frac{\partial (\Omega \partial V)}{\partial t} = - \nabla \cdot \mathbf{Q} (\partial V) \tag{3.73}$$

The heat content for a partially saturated soil, per unit volume, may be assumed to be the sum of the product of the heat storage capacity with temperature and the change of enthalpy due to phase change and characterised by the latent heat of vapourisation. This gives:

$$\Omega = H_c \left(T - T_r \right) + L n S_a \rho_v \tag{3.74}$$

where L is the latent heat of vapourisation. The heat capacity at reference temperature, T_r, was presented by Ewen and Thomas (1989) as:

$$H_c = \left(1 - n \right) C_{ps} \rho_s + n \left(C_{pl} S_l \rho_l + C_{pv} S_a \rho_v + C_{pda} S_a \rho_{da} \right) \tag{3.75}$$

where C_{ps}, C_{pl}, C_{pv} and C_{pda} are the specific heat capacities of the solid, liquid, vapour and dry air respectively and ρ_s is the density of the solid.

Thomas and He (1995) define the heat flux as:

$$\mathbf{Q} = -\lambda_T \triangledown T + \left(\mathbf{v_v} \rho_l + \mathbf{v_a} \rho_v \right) L + \left(C_{pl} \mathbf{v_l} \rho_l + C_{pv} \mathbf{v_v} \rho_l + C_{pv} \mathbf{v_a} \rho_v + C_{pda} \mathbf{v_a} \rho_{da} \right) \left(T - T_r \right) \tag{3.76}$$

where λ_T is the coefficient of thermal conductivity. The key modes of heat transportation can be seen in equation (3.76) where the first term describes the conduction and the last convection. The second term discribes the latent heat flow associated with vapour movement.

Following the approach of Thomas and King (1991) the coefficient of thermal conductivity for an unsaturated soil is considered a function of the degree of saturation:

$$\lambda_T = \lambda_T \left(S_l \right) \tag{3.77}$$

The law of conservation of energy as defined in equation (3.73), with the substitution of equations (3.74) and (3.76), can be expressed as:

$$\frac{\partial}{\partial t} \left[\left(H_c \left(T - T_r \right) + L n S_a \rho_v \right) \partial V \right] =$$
$$- \triangledown \cdot \left[\begin{array}{l} - \lambda \triangledown T + L \left(\mathbf{v_v} \rho_l + \mathbf{v_a} \rho_v \right) \\ + \left(C_{pl} \mathbf{v_l} \rho_l + C_{pv} \mathbf{v_v} \rho_l + C_{pv} \mathbf{v_a} \rho_v + C_{pda} \mathbf{v_a} \rho_{da} \right) \left(T - T_r \right) \end{array} \right] \partial V \tag{3.78}$$

Substituting equation (3.10) into equation (3.78) and cancelling the ∂V_s terms, yields:

$$\frac{\partial}{\partial t}\left[(H_c\,(T - T_r) + LnS_a\rho_v)\,(1 + e)\right] =$$

$$-\nabla \cdot \left[\begin{array}{l} -\lambda\,\nabla\,T + L\,(\mathbf{v_v}\rho_l + \mathbf{v_a}\rho_v) \\[6pt] + (C_{pl}\mathbf{v_l}\rho_l + C_{pv}\mathbf{v_v}\rho_l + C_{pv}\mathbf{v_a}\rho_v + C_{pda}\mathbf{v_a}\rho_{da})\,(T - T_r) \end{array}\right](1 + e) \quad (3.79)$$

The first term of equation (3.79) can be expanded, yielding:

$$\frac{\partial}{\partial t}\left[H_c\,(T - T_r)\,(1 + e)\right] = (T - T_r)\frac{\partial}{\partial t}\left[H_c\,(1 + e)\right] + H_c\,(1 + e)\frac{\partial T}{\partial t} \quad (3.80)$$

Substituting equation (3.75) into the first term on the right hand side of equation 3.80 and rearranging yields:

$$(T - T_r)\frac{\partial}{\partial t}\left[H_c\,(1 + e)\right] =$$

$$(T - T_r)\frac{\partial}{\partial t}\left[(C_{ps}\rho_s + n\,(-C_{ps}\rho_s + C_{pl}S_l\rho_l + C_{pv}S_a\rho_v + C_{pda}S_a\rho_{da}))\,(1 + e)\right] \quad (3.81)$$

Expanding further and recognising $n\,(1 + e) = e$ yields:

$$(T - T_r)\frac{\partial}{\partial t}\left[H_c\,(1 + e)\right] =$$

$$(T - T_r)\left[\begin{array}{l} C_{ps}\rho_s\dfrac{\partial e}{\partial t} + (-C_{ps}\rho_s + C_{pl}S_l\rho_l + C_{pv}S_a\rho_v + C_{pda}S_a\rho_{da})\dfrac{\partial e}{\partial t} \\[10pt] + e\left(\begin{array}{l} C_{pl}\rho_l\dfrac{\partial S_l}{\partial t} - C_{pv}\rho_v\dfrac{\partial S_l}{\partial t} + C_{pv}\,(1 - S_l)\dfrac{\partial \rho_v}{\partial t} \\[8pt] + C_{pda}\,(1 - S_l)\dfrac{\partial \rho_{da}}{\partial t} - C_{pda}\rho_{da}\dfrac{\partial S_l}{\partial t} \end{array}\right) \end{array}\right] \quad (3.82)$$

Noting that $\frac{\partial e}{\partial t} = (1 + e)^2\frac{\partial n}{\partial t}$ and rearranging, grouping like terms gives:

$$(T - T_r)\frac{\partial}{\partial t}\left[H_c\,(1 + e)\right] =$$

$$(T - T_r)\left[\begin{array}{l} (C_{pl}S_l\rho_l + C_{pv}S_a\rho_v + C_{pda}S_a\rho_{da})\,(1 + e)^2\dfrac{\partial n}{\partial t} \\[10pt] + e\,(C_{pl}\rho_l - C_{pv}\rho_v - C_{pda}\rho_{da})\dfrac{\partial S_l}{\partial t} + eC_{pv}\,(1 - S_l)\dfrac{\partial \rho_v}{\partial t} + eC_{pda}\,(1 - S_l)\dfrac{\partial \rho_{da}}{\partial t} \end{array}\right]$$

$$(3.83)$$

The second term on the right hand side of equation (3.80) is already expressed in terms of the primary variables. Considering the second term of equation (3.79) and substituting $n\,(1 + e) = e$ yields:

$$\frac{\partial}{\partial t}\left[LnS_a\rho_v\,(1 + e)\right] = \frac{\partial}{\partial t}\left[LeS_a\rho_v\right] \quad (3.84)$$

Expanding yields:

$$\frac{\partial}{\partial t}[LeS_a\rho_v] = L(1 - S_l)e\frac{\partial \rho_v}{\partial t} - Le\rho_v\frac{\partial s_l}{\partial t} + L(1 - S_l)\rho_v\frac{\partial e}{\partial t} \qquad (3.85)$$

Again recognising that $\frac{\partial e}{\partial t} = (1 + e)^2 \frac{\partial n}{\partial t}$ and rearranging gives:

$$\frac{\partial}{\partial t}[LeS_a\rho_v] = L(1 - S_l)e\frac{\partial \rho_v}{\partial t} - Le\rho_v\frac{\partial S_l}{\partial t} + L(1 - S_l)\rho_v(1 + e)^2\frac{\partial n}{\partial t} \qquad (3.86)$$

Substituting equations (3.80), (3.83) and (3.86) into equation (3.79) yields the governing equation for heat flow:

$$(T - T_r)\left[\begin{array}{l} ((C_{pl}S_l\rho_l + C_{pv}S_a\rho_v + C_{pda}S_a\rho_{da})(1 + e)^2)\frac{\partial n}{\partial t} \\[2mm] + e(C_{pl}\rho_l - C_{pv}\rho_v - C_{pda}\rho_{da})\frac{\partial S_l}{\partial t} + eC_{pv}(1 - S_l)\frac{\partial \rho_v}{\partial t} + eC_{pda}(1 - S_l)\frac{\partial \rho_{da}}{\partial t} \end{array}\right]$$

$$+ H_c(1 + e)\frac{\partial T}{\partial t} + L(1 - S_l)e\frac{\partial \rho_v}{\partial t} - Le\rho_v\frac{\partial S_l}{\partial t} + L(1 - S_l)\rho_v(1 + e)^2\frac{\partial n}{\partial t}$$

$$= -\nabla\left[\begin{array}{l} -\lambda\nabla T + L(\mathbf{v_v}\rho_l + \mathbf{v_a}\rho_v) \\[2mm] + (C_{pl}\mathbf{v_l}\rho_l + C_{pv}\mathbf{v_v}\rho_l + C_{pv}\mathbf{v_a}\rho_v + C_{pda}\mathbf{v_a}\rho_{da})(T - T_r) \end{array}\right](1 + e) \qquad (3.87)$$

Dividing equation (3.87) by $(1 + e)$ and substituting $e/(1 + e) = n$ yields:

$$(T - T_r)\left[\begin{array}{l} (-C_{ps}\rho_s + C_{pl}S_l\rho_l + C_{pv}S_a\rho_v + C_{pda}S_a\rho_{da})(1 + e)\frac{\partial n}{\partial t} \\[2mm] + n(C_{pl}\rho_l - C_{pv}\rho_v - C_{pda}\rho_{da})\frac{\partial S_l}{\partial t} + nC_{pv}(1 - S_l)\frac{\partial \rho_v}{\partial t} + nC_{pda}(1 - S_l)\frac{\partial \rho_{da}}{\partial t} \end{array}\right]$$

$$+ H_c\frac{\partial T}{\partial t} + L(1 - S_l)n\frac{\partial \rho_v}{\partial t} - Ln\rho_v\frac{\partial S_l}{\partial t} + L(1 - S_l)\rho_v(1 + e)\frac{\partial n}{\partial t}$$

$$= -\nabla\left[\begin{array}{l} -\lambda\nabla T + L(\mathbf{v_v}\rho_l + \mathbf{v_a}\rho_v) \\[2mm] + (C_{pl}\mathbf{v_l}\rho_l + C_{pv}\mathbf{v_v}\rho_l + C_{pv}\mathbf{v_a}\rho_v + C_{pda}\mathbf{v_a}\rho_{da})(T - T_r) \end{array}\right] \qquad (3.88)$$

Substituting the derivatives with respect to time of porosity, equation (3.43): degree of liquid saturation, equation (3.22); vapour density, equation (3.32); and dry air density, equation (3.64), into the left hand side of governing equation (3.88); and equations (3.13), (3.23) and (3.35) for the velocity terms of liquid, air and vapour respectively, yield;

$$C_{Tl}\frac{\partial u_l}{\partial T} + C_{TT}\frac{\partial T}{\partial t} + C_{Ta}\frac{\partial u_a}{\partial T} + C_{Tu}\frac{\partial \mathbf{u}}{\partial T} = \nabla\cdot[K_{Tl}\nabla u_l] + \nabla\cdot[K_{TT}\nabla T] + \nabla\cdot[K_{Ta}\nabla u_a] + J_T$$

$$(3.89)$$

where:

$$C_{Tl} = \left[\begin{array}{l} -\left(C_{pl}\rho_l n - C_{pv}\rho_v n - C_{pda}\rho_{da}n\right)\dfrac{\partial S_l}{\partial s} - C_{pv}S_a n \left(\rho_0 \dfrac{\partial h}{\partial s}\right) \\[3mm] + C_{pda}S_a n \dfrac{R_v}{R_{da}} \left(\rho_0 \dfrac{\partial h}{\partial s}\right) \end{array} \right](T - T_r)$$

$$+ Ln\rho_v \frac{\partial S_l}{\partial s} - LnS_a \left(\rho_0 \frac{\partial h}{\partial s}\right) \quad (3.90)$$

$$C_{TT} = H_c + \left[\begin{array}{l} \left(C_{pl}\rho_l n - C_{pv}\rho_v n - C_{pda}\rho_{da}n\right)\dfrac{\partial S_l}{\partial T} + C_{pv}S_a n \left(h\dfrac{\partial \rho_0}{\partial T} + \rho_0 \dfrac{\partial h}{\partial T}\right) \\[3mm] + C_{pda}S_a n \left(-\dfrac{\rho_a}{T} - \dfrac{R_v}{R_{da}}\left(h\dfrac{\partial \rho_0}{\partial T} + \rho_0 \dfrac{\partial h}{\partial T}\right)\right) \end{array} \right](T - T_r)$$

$$- Ln\rho_v \frac{\partial S_l}{\partial T} + LnS_a \left(h\frac{\partial \rho_0}{\partial T} + \rho_0 \frac{\partial h}{\partial T}\right) \quad (3.91)$$

$$C_{Ta} = \left[\begin{array}{l} \left(C_{pl}\rho_l n - C_{pv}\rho_v n - C_{pda}\rho_{da}n\right)\dfrac{\partial S_l}{\partial s} + C_{pv}S_a n \left(\rho_0 \dfrac{\partial h}{\partial s}\right) \\[3mm] + C_{pda}S_a n \left(\dfrac{1}{R_{da}T} - \dfrac{R_v}{R_{da}}\left(\rho_0 \dfrac{\partial h}{\partial s}\right)\right) \end{array} \right](T - T_r)$$

$$- Ln\rho_v \frac{\partial S_l}{\partial s} + LnS_a \left(\rho_0 \frac{\partial h}{\partial s}\right) \quad (3.92)$$

$$C_{Tu} = \left[\left(C_{pl}S_l\rho_l + C_{pv}S_a\rho_v + C_{pda}S_a\rho_{da}\right)\mathbf{m}^T\mathbf{P}\right](T - T_r) + LS_a\rho_v\mathbf{m}^T\mathbf{P} \quad (3.93)$$

$$K_{Tl} = -L\rho_l \frac{D_{atms}v_v n}{\rho_l}\left(\rho_0 \frac{\partial h}{\partial s}\right) + (T - T_r)\rho_l \left(\frac{C_{pl}K_l}{\gamma_l} - C_{pv}\frac{D_{atms}v_v n}{\rho_l}\left(\rho_0 \frac{\partial h}{\partial s}\right)\right) \quad (3.94)$$

$$K_{TT} = \lambda_T + L\rho_l \frac{D_{atms}v_v n (\nabla T)_a}{\rho_l \nabla T}\left(h\frac{\partial \rho_0}{\partial T} + \rho_0 \frac{\partial h}{\partial T}\right)$$

$$+ (T - T_r)\rho_l C_{pl}\left(h\frac{\partial \rho_0}{\partial T} + \rho_0 \frac{\partial h}{\partial T}\right) \quad (3.95)$$

$$K_{Ta} = L\rho_l \frac{D_{atms}v_v n}{\rho_l}\left(\rho_0 \frac{\partial h}{\partial s}\right) + L\rho_v K_a$$

$$+ (T - T_r)\left(\rho_l C_{pv}\frac{D_{atms}v_v n}{\rho_l}\left(\rho_0 \frac{\partial h}{\partial s}\right) + \rho_v C_{pv}K_a + \rho_{da}C_{pda}K_a\right) \quad (3.96)$$

$$J_T = (T - T_r)C_{pl}\rho_l \nabla (k_l \nabla z) \quad (3.97)$$

3.6 Deformation

The deformation behaviour of soils is represented in this work by use of an elasto-plastic constitutive model. The model was initially developed by Alonso et $al.$ (1990) and named the Barcelona Basic Model (BBM). The majority of this formulation has been previously presented (Thomas and He, 1998; Cleall, 1998; Mitchell, 2002; Melhuish, 2004) and where matrices are explicitly written, the three-dimensional form is presented. The model has also been formulated for 2D and axisymmetric problems.

It is assumed that deformation (hence volume changes) are a result of applied stress, suction and temperature changes.

It has been stated that the stress-state of a soil in relation to volume change behaviour can be described by two independent stress-state parameters (Fredlund and Rahardjo, 1993). The BBM uses this assumption and uses the two independent stress-state variables, net stress, σ'', and suction, s. The net stress can be defined as:

$$\sigma'' = \sigma - u_a \qquad (3.98)$$

where σ is defined as the total stress. The total stress is given a tension positive sign convention but the pore pressures (u_l and u_a) are given a compression positive sign convention. Suction is defined in equation (3.21).

For three-dimensional stress-states the stress invarients used to define the volume change behaviour are the net-mean stress, p, and suction, s,, with the deviatoric stress, q, utilised for the shear deformation behaviour. The net-mean stress and deviatoric stress are defined below for three-dimensional stress-states:

$$p = \frac{\sigma''_1 + \sigma''_2 + \sigma''_3}{3} \qquad (3.99)$$

$$q = \sqrt{\frac{1}{2}\left[(\sigma_1 - \sigma_2)^2 + (\sigma_2 - \sigma_3)^2 + (\sigma_3 - \sigma_1)^2\right]} \qquad (3.100)$$

A three dimensional soil element with incremental unit dimension under a system of stresses and forces is shown in Figure 3.1 with two types of external forces; body forces acting through the centroid of the element and surface forces acting on the boundary surface of

the element. The system is assumed to follow the thermodynamic law of local equilibrium, whereby the processes are occurring at such a rate that any local point can be described as being in equilibrium.
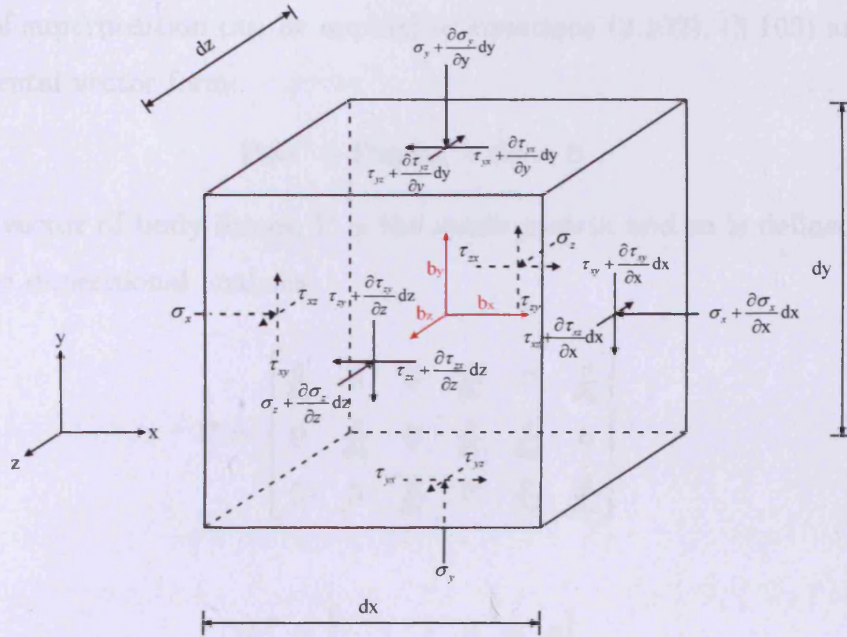
Figure 3.1. Stresses and forces on a soil element of infinitesimal dimensions (after Fredlund and Rahardjo, 1993)

According to Newton's First Law and given that the local equilibrium condition applies the resultant force acting in any direction must be zero. For the x direction:

$$\left(\sigma_x \frac{\partial \sigma_x}{\partial x} dx\right) dz + \left(\tau_{zx} \frac{\partial \tau_{zx}}{\partial z} dz\right) dx + \left(\tau_{yx} \frac{\partial \tau_{yx}}{\partial y} dy\right) dx - \sigma_x dx - \tau_{zx} dx - \tau_{xy} dx + b_x dx dz = 0$$

$$(3.101)$$

Substituting in the total stress equation (3.98) and rearranging yields:

$$\left(\frac{\partial \sigma_x''}{\partial x} + \frac{\partial u_a}{\partial x} + \frac{\partial \tau_{zx}}{\partial z} + \frac{\partial \tau_{yx}}{\partial y} + b_x\right) dx dz = 0$$

$$(3.102)$$

Since $dxdz$ may not necessarily equal zero, equation (3.102) reduces to:

$$\frac{\partial \sigma_x''}{\partial x} + \frac{\partial u_a}{\partial x} + \frac{\partial \tau_{zx}}{\partial z} + \frac{\partial \tau_{yx}}{\partial y} + b_x = 0$$

$$(3.103)$$

In the same manner for the y and z directions:

$$\frac{\partial \sigma_y''}{\partial y} + \frac{\partial u_a}{\partial y} + \frac{\partial \tau_{xy}}{\partial x} + \frac{\partial \tau_{zy}}{\partial z} + b_y = 0 \qquad (3.104)$$

$$\frac{\partial \sigma_z''}{\partial z} + \frac{\partial u_a}{\partial z} + \frac{\partial \tau_{yz}}{\partial y} + \frac{\partial \tau_{xz}}{\partial x} + b_z = 0 \qquad (3.105)$$

The principle of superposition can be applied to equations (3.102), (3.103) and (3.104) to give, in incremental vector form:

$$\mathbf{P}d\sigma'' + \mathbf{P}\mathbf{m}du_a + d\mathbf{b} = 0 \qquad (3.106)$$

where $\mathbf{b}$ is the vector of body forces, $\mathbf{P}$ is the strain matrix and $\mathbf{m}$ is defined in equation (3.108) for three dimensional analysis:

$$\mathbf{P} = \begin{bmatrix} \frac{\partial}{\partial x} & 0 & 0 & \frac{\partial}{\partial z} & 0 & \frac{\partial}{\partial y} \\ 0 & \frac{\partial}{\partial z} & 0 & \frac{\partial}{\partial x} & \frac{\partial}{\partial y} & o \\ 0 & 0 & \frac{\partial}{\partial y} & 0 & \frac{\partial}{\partial z} & \frac{\partial}{\partial x} \end{bmatrix} \qquad (3.107)$$

$$\mathbf{m}^T = \begin{bmatrix} 1 & 1 & 1 & 0 & 0 & 0 \end{bmatrix} \qquad (3.108)$$

3.6.1 Elasto-plastic constitutive relationships

A soil that exhibits elasto-plastic behaviour produces both recoverable (elastic) and irrecoverable (plastic) strains. The total strain may be defined as:

$$d\varepsilon = d\varepsilon^e + d\varepsilon^p \qquad (3.109)$$

where $d\varepsilon^e$ is the incremental elastic strain and $d\varepsilon^p$ is the incremental plastic strain.

To form a constitutive elasto-plastic model a series of relationships are required. These are defined below (Britto and Gunn, 1987; Owen and Hinton, 1980):

i. A constitutive elastic relationship.

ii. A yield function, defining the yield surface in stress space.

iii. A flow rule, defining the direction and magnitude of strains produced during yielding.

iv. A hardening law, defining the relationship between plastic strain and material hardening.

3.6.1.1 Material behaviour under elastic condition

The approach taken by Wang (1953) has been extended by Alonso *et al.* (1988) and Thomas and He (1995) so that the incremental volumetric elastic strain can be written as:

$$d\varepsilon^e = d\varepsilon_p^e + d\varepsilon_s^e + d\varepsilon_T^e \tag{3.110}$$

where the subscripts p, s and T represent components due to mean stress, suction and temperature respectively.

The elastic stress-strain relationship can be described from a generalised Hooke's law:

$$d\sigma'' = \mathbf{D} \left(d\varepsilon - d\varepsilon_s^e - d\varepsilon_T^e - d\varepsilon^p \right) \tag{3.111}$$

where $\mathbf{D}$ is the elasticity matrix.

It is assumed that elastic deformation of unsaturated soils is due to changes in the net stress and the suction under isothermal conditions, (Alonso *et al.*, 1990). Suction changes are also assumed to only produce volumetric strains. At a constant suction, it can be shown that elastic deformation follows unload and reload curves as illustrated in figure 3.2, where v is the specific volume. This behaviour may be idealised and is shown in figure 3.3. The slope of the idealised compression curve (for virgin soils) has a value of $-\lambda$ and the slope of the idealised recompression curve a value of $-\kappa$.

It was shown by Alonso *et al.*, (1990) that the change in specific volume due to incremental stress change can be expressed as:

$$dv = -\kappa \frac{dp}{p} \tag{3.112}$$

This can be used to develop the elastic volumetric strain due to net stress changes:

$$d\varepsilon_p^e = \frac{dv}{v} = -\frac{\kappa}{v}\frac{dp}{p} \tag{3.113}$$

In addition, Alonso *et al.* (1990) showed that the change in specific volume due to suction change at a given stress could be expressed as:

$$dv_s = -\kappa_s \frac{ds}{(s + p_{atms})} \tag{3.114}$$
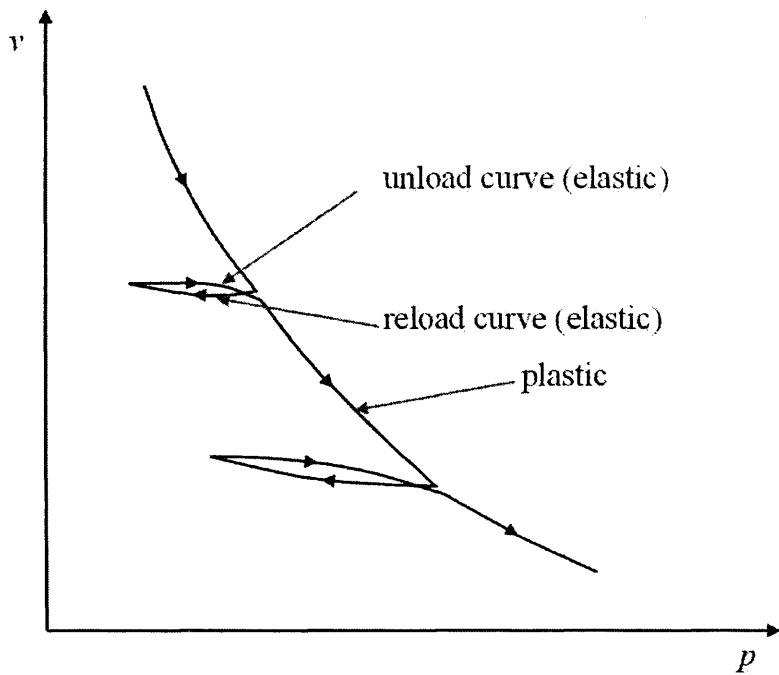
Figure 3.2. Characteristic isotropic compression and recompression curves (Cleall, 1998).
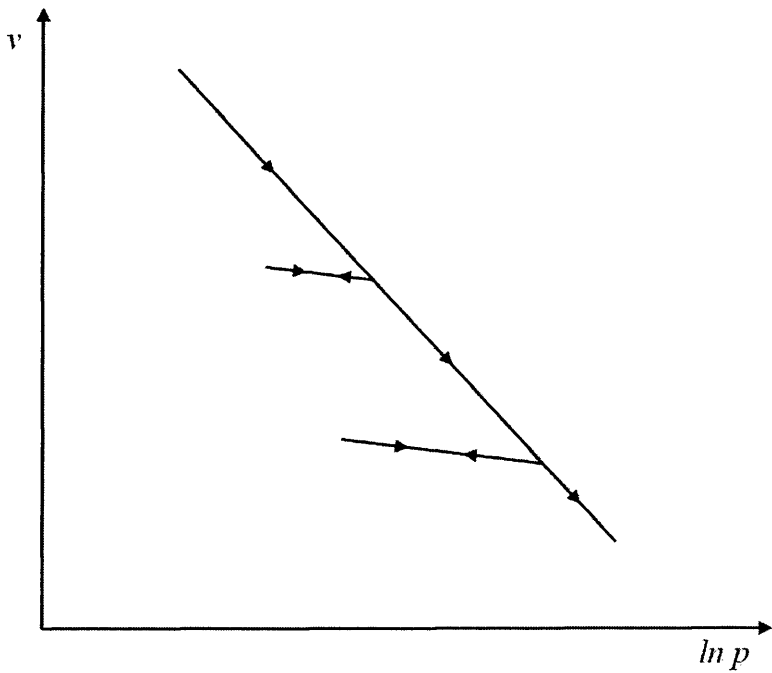
Figure 3.3. Idealised compression and recompression curves (Cleall, 1998).

where κ_s is the slope of the volume-suction curve, in volume-ln suction space, in the elastic region. Atmospheric pressure, p_{atms}, is included to avoid infinite strain as suction tends to zero.

The elastic volumetric component of strain due to suction change is defined as:

$$d\varepsilon_s^e = -\frac{\kappa_s}{v}\frac{ds}{(s + p_{atms})} = A_s ds \tag{3.115}$$

The dependence of suction on temperature was highlighted in section 3.3, hence the strain component due to temperature should include contributions from both thermal expansion and suction change due to temperature (Wang, 1953). This can be expressed as:

$$d\varepsilon_T^e = \left(\frac{\alpha_T}{v_0}dT + A_s\frac{\partial s}{\partial T}dT\right) = \left(A_T + A_s\frac{\partial s}{\partial T}\right)dT \tag{3.116}$$

where α_T is the coefficient of thermal expansion and v_0 is the initial specific volume. The deviatoric strain component, caused by changes in deviatoric stress, is described by Wood (1990) as:

$$d\varepsilon_q^e = \frac{1}{3G}dq \tag{3.117}$$

where q is the deviatoric stress and G is the shear modulus.

3.6.1.2   Yield function

The yield criteria determine when the material starts to yield. The BBM utilises two yield functions, the load-collapse (LC) curve and the suction-increase (SI) curve. The LC curve is such that yielding occurs when stress reaches a critical value, the pre-consolidation stress, p_0. Yield is indicated to occur by the SI curve when suction reaches a critical value, s_0. The LC curve for three-dimensional consolidation, at uniform suction, can be expressed as:

$$F(p, p_0) = p - p_0 = 0 \tag{3.118}$$

The preconsolidation stress is a function of suction. The collapse and swelling behaviour of the soil during wetting and drying is determined by the following relationship, illustrated in figure 3.4 in v-ln p space:

$$\left(\frac{p_0}{p_c}\right) = \left(\frac{p_0^*}{p_c}\right)^{\left(\frac{\lambda(0)-\kappa}{\lambda(s)-\kappa}\right)} \tag{3.119}$$

where p_0^* is the effective pre-consolidation stress of a saturated soil, p_c is a reference stress, $\lambda(s)$ is the stiffness parameter for changes in net mean stress for virgin states of the soil

and $\lambda(0)$ is the stiffness parameter for changes in net mean stress for the virgin state of soil at saturation. An asymptotic expression predicting $\lambda(s)$ was proposed by Alonso $et\ al.$ (1990) as:

$$\lambda(s) = \lambda(0)\left[(1-r)e^{(-\beta s)} + r\right] \tag{3.120}$$

where r controls the maximum stiffness of the soil and β controls the rate of stiffness increase with suction. Alonso $et\ al.$ (1990) extended this model to include the triaxial stress states, and proposed the following LC yield function, also shown graphically in figure 3.5. The yield surface is also valid for three-dimensional stress conditions as the stress-states used, p and q, are invarient in both triaxial and three-dimensional stress conditions.

$$F_1\left(p, q, s, p_0^*\right) = q^2 - M^2\left(p + p_s\right)\left(p_0 - p\right) = 0 \tag{3.121}$$

where M is the slope of the critical state line and p_s is a parameter describing how the cohesion of the soil changes with suction. If the cohesion increases linearly with suction this parameter can be described as:

$$p_s = ks \tag{3.122}$$

where k is a constant.

The SI yield function indicates that yield occurs when suction reaches a critical value, s_0, which is the maximum previously achieved suction and remains parallel to the q-axis when $q > 0$. It is also shown graphically on figure 3.5 and mathematically this was expressed by Alonso $et\ al.$ (1990) as:

$$F_2\left(s, s_o\right) = s - s_0 = 0 \tag{3.123}$$

3.6.1.3   Flow rule

As yield occurs the plastic strain increment is related to the stress gradient by definition of a flow rule. It is assumed that the plastic strain is proportional to the outward normal of a plastic potential function. If the yield function is used as the plastic potential function the flow is termed as associated, otherwise the flow is termed non-associated. Alonso $et\ al.$ (1990) proposed an associated SI plastic flow rule for the SI yield surface and a non-associated plastic flow rule for the LC yield surface. Conventional critical state models often overestimate K_0 (Gens and Potts, 1982), hence Alonso $et\ al.$ (1990) proposed the
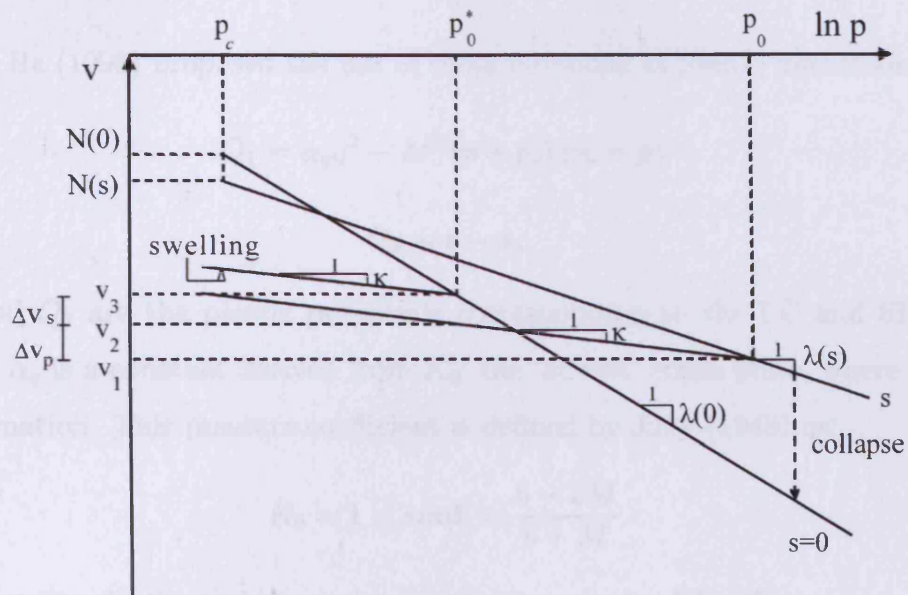
Figure 3.4. Compression curves for saturated and unsaturated soils (after Alonso *et al.*, 1990).
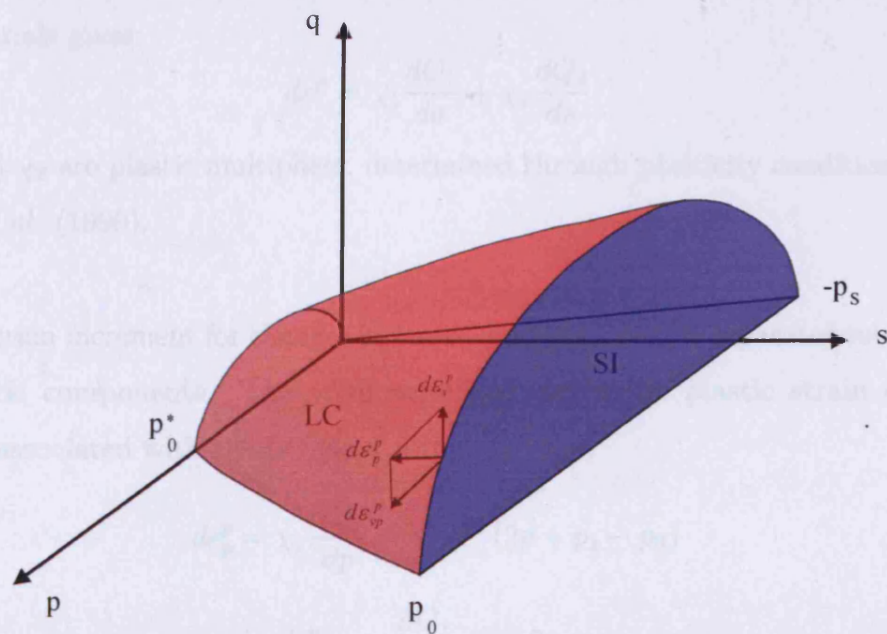

Figure 3.5. Three-dimensional view of yield surfaces in p, q, s stress space (after Alonso *et al.*, 1990) where SI curve is shown in blue and LC curve is shown in red.

introduction of a parameter, α_q.

Thomas and He (1998) proposed the use of these functions as plastic potentials:

$$Q_1 = \alpha_q q^2 - M^2 \left(p + p_s \right) \left(p_0 - p \right) \tag{3.124}$$

$$Q_2 = s - s_0 \tag{3.125}$$

where Q_1 and Q_2 are the plastic potentials corresponding to the LC and SI flow rules respectively. α_q is a constant derived from K_0, the 'at rest' stress state, where there is no lateral deformation. This pressure coefficient is defined by Jaky (1948) as:

$$K_0 = 1 - sin\phi' = \frac{6 - 2M}{6 + M} \tag{3.126}$$

Assuming that the elastic strain increment is zero, α_q can be defined as:

$$\alpha_q = \frac{M \left(M - 9 \right) \left(M - 3 \right)}{6 \left(6 - M \right)} \frac{1}{\left(1 - \frac{\kappa}{\lambda(0)} \right)} \tag{3.127}$$

Dividing the plastic strain increment into components due to net stress changes and suction changes and assuming that the strain increment is proportional to the stress gradient of the plastic potentials gives:

$$d\varepsilon^p = \chi_1 \frac{dQ_1}{d\sigma} + \chi_2 \frac{dQ_2}{ds} \tag{3.128}$$

where χ_1 and χ_2 are plastic multipliers, determined through plasticity conditions as defined by Alonso *et al.* (1990).

The plastic strain increment for changes in stress conditions can be separated into volumetric and deviatoric components. The volumetric and deviatoric plastic strain components respectively associated with the LC yield surface, F_1 are:

$$d\varepsilon_p^p = \chi_1 \frac{\partial Q_1}{\partial p} = \chi_1 M^2 \left(2p + p_s - p_0 \right) \tag{3.129}$$

$$d\varepsilon_q^p = \chi_1 \frac{\partial Q_1}{\partial q} = \chi_1 2\alpha_q q \tag{3.130}$$

The volumetric plastic strain increment associated with the SI yield surface, F_2 is:

$$d\varepsilon_s^p = \chi_2 \frac{dQ_2}{ds} = \chi_2 \tag{3.131}$$

3.6.1.4 Hardening Laws

Strain hardening occurs during plastic deformation. Following yielding the stress level at which further plastic deformation occurs depends on the amount of plastic strain. Josa *et al.* (1987) found that it was possible to couple the hardening of two yield surfaces. The yield surfaces are controlled by the parameters p_0^* and s_0 and depend upon the plastic volumetric strain increment, $d\varepsilon_v^p$, defined as:

$$d\varepsilon_v^p = d\varepsilon_p^p + d\varepsilon_s^p \tag{3.132}$$

Alonso *et al.* (1990) gave the hardening laws for yield surfaces F_1 and F_2 as:

$$\frac{dp_0^*}{p_0^*} = \frac{v}{\lambda(0) - \kappa} d\varepsilon_v^p \tag{3.133}$$

$$\frac{ds_0}{s_0} = \frac{v}{\lambda_s - \kappa_s} d\varepsilon_v^p \tag{3.134}$$

where λ_s is the stiffness parameter for changes in suction for suction virgin soil states.

3.6.2 Governing equation for deformation

Section 3.6.1.1 shows that the elastic strain increment can be related to the stress increment by application of the incremental elastic constitutive matrix $\mathbf{D}$. This matrix must be modified if it is to take into account plastic deformation. Following the approach taken by Owen and Hinton (1980) the constitutive incremental elasto-plastic stress-strain formulation can take the form of:

$$d\sigma'' = \mathbf{D_{ep}} d\varepsilon_p \tag{3.135}$$

Mitchell (2002) defined the matrix $\mathbf{D_{ep}}$ as:

$$\mathbf{D_{ep}} = \mathbf{D} - \frac{\mathbf{D}\frac{\partial Q_1}{\partial \sigma}\frac{\partial F_1}{\partial \sigma}\mathbf{D}}{\mathbf{A_p} + \left(\frac{\partial Q_1}{\partial \sigma}\right)^T \mathbf{D}\frac{\partial F_1}{\partial \sigma}} \tag{3.136}$$

where $\mathbf{A_p}$ is the plastic modulus defined as:

$$\mathbf{A_p} = M^2 \left(p + p_s\right) \frac{\lambda(0) - \kappa}{\lambda(s) - \kappa} p_0 \frac{v}{\lambda(0) - \kappa} \left(M^2 \left(2p + p_s - p_0\right)\right) \tag{3.137}$$

The stress-strain relationship expressed in elastic form in equation (3.111) can be written for elasto-plastic behaviour as:

$$d\sigma'' = \mathbf{D_{ep}} \left(d\varepsilon - d\varepsilon_s^e - d\varepsilon_T^e - d\varepsilon_s^p\right) \tag{3.138}$$

Substituting equations (3.115) and (3.116) into equation (3.138) gives:

$$d\sigma'' = \mathbf{D_{ep}} \left(d\varepsilon - A_s ds - \left(A_T + A_s \frac{\partial s}{\partial T} \right) dT - d\varepsilon_s^p \right) \tag{3.139}$$

Rewriting the stress equilibrium equation (3.105) with substition from equation (3.139) gives:

$$\mathbf{P} \left(\mathbf{D_{ep}} \left(\mathbf{P}^T d\mathbf{u} + A_s du_l - \left(A_T + A_s \frac{\partial s}{\partial T} \right) - A_s du_a - d\varepsilon_s^p \right) \right) + \mathbf{P m} du_a + d\mathbf{b} = 0 \tag{3.140}$$

The governing equation can then be written in concise form as:

$$C_{ul} du_l + C_{uT} dT + C_{ua} du_a + C_{uu} d\mathbf{u} - \mathbf{P D_{ep}} d\varepsilon_s^p + d\mathbf{b} = 0 \tag{3.141}$$

where:

$$C_{ul} = \mathbf{P D_{ep}} A_s \tag{3.142}$$

$$C_{uT} = \mathbf{P D_{ep}} \left(-A_T - A_s \frac{\partial s}{\partial T} \right) \tag{3.143}$$

$$C_{ua} = -\mathbf{P D_{ep}} A_s + \mathbf{m P} \tag{3.144}$$

$$C_{uu} = \mathbf{P D_{ep}} \mathbf{P}^T \tag{3.145}$$

3.7 Summary

The governing equations for moisture transfer, dry air transfer, heat transfer and deformation have been presented in terms of four primary variables: pore water pressure (u_l), pore air pressure (u_a), temperature (T) and deformation $(\mathbf{u})$. For reference they are shown below in concise form.

Moisture transfer:

$$C_{ll} \frac{\partial u_l}{\partial t} + C_{lT} \frac{\partial T}{\partial t} + C_{la} \frac{\partial u_a}{\partial t} + C_{lu} \frac{\partial \mathbf{u}}{\partial t} = \nabla \cdot [K_{ll} \nabla u_l] + \nabla \cdot [K_{lT} \nabla T] + \nabla \cdot [K_{la} \nabla u_a] + J_l$$

Dry air transfer:

$$C_{al} \frac{\partial u_l}{\partial t} + C_{aT} \frac{\partial T}{\partial t} + C_{aa} \frac{\partial u_a}{\partial t} + C_{au} \frac{\partial \mathbf{u}}{\partial t} = \nabla \cdot [K_{al} \nabla u_l] + \nabla \cdot [K_{aa} \nabla u_a] + J_a$$

Heat transfer:

$$C_{Tl} \frac{\partial u_l}{\partial T} + C_{TT} \frac{\partial T}{\partial t} + C_{Ta} \frac{\partial u_a}{\partial T} + C_{Tu} \frac{\partial \mathbf{u}}{\partial T} = \nabla \cdot [K_{Tl} \nabla u_l] + \nabla \cdot [K_{TT} \nabla T] + \nabla \cdot [K_{Ta} \nabla u_a] + J_T$$

Deformation:

$$C_{ul} du_l + C_{uT} dT + C_{ua} du_a + C_{uu} d\mathbf{u} - \mathbf{P D_{ep}} d\varepsilon_s^p + d\mathbf{b} = 0$$

3.8 Numerical formulation - General

The governing equations for the flow of moisture, air and heat in a deformable material are described in the previous sections. A direct analytical solution is prevented by the level of complexity, therefore, a numerical solution is required. The finite-element method (FEM) is employed to spatially discretise the system of equations, whereas a finite difference scheme is used to achieve temporal discretisation.

3.9 Spatial discretisation

In the work presented here the spatial discretisation is undertaken using a Galerkin weighted residual finite-element approach. The features of this approach are well documented (e.g. Zienkiewicz and Taylor, 1991) and have been found to be effective and robust for the type of coupled equations described in section 3.2 (Thomas and He, 1995; Thomas et al., 1998; Cleall, 1998). Detailed description of this method is also available elsewhere (e.g. Thomas and He, 1995; Thomas et al., 1998), hence only a summary is presented here. For the work considered in this thesis both linear three-noded isoparametric triangular elements used in axi-symmetric analyses and linear isoparametric four-noded tetrahedral elements, for three-dimensional analyses, have been used. A Galerkin weighted residual method has been used to minimise the spatial residual error, resulting from nodal estimations by use of the shape functions. A mid-interval implicit forward-difference time integration scheme is used to find a temporal solution.

3.9.1 Spatial discretisation of the governing equations for flow variables

The process of spatial discretisation of flow variables is similar for each of them, therefore only a single case, moisture flow, is presented to avoid repetition.

The primary variables and spatial derivatives can be approximated using shape functions. For a n_{node} noded element this yields:

$$u_{var} \approx \hat{u}_{var} = \sum_{s=1}^{n_{node}} N_s \hat{u}_{vars} \tag{3.146}$$

$$\nabla \hat{u}_{var} = \sum_{s=1}^{n_{node}} \left(\nabla N_s \right) \hat{u}_{vars} \tag{3.147}$$

where $\hat{u}_{var}$ is any one of the primary variables, $[u_l, T, u_a, \mathbf{u}]$, N_s is the shape function, the subscript, $_s$, indicates nodal points and the modifier, $\hat{\ }$, donates approximate form.

The governing equation for moisture flow, with substitution for the primary variables from equations (3.146) and (3.147), may be written as:

$$\begin{bmatrix} -C_{ll}\dfrac{\partial \hat{u}_l}{\partial t} - C_{lT}\dfrac{\partial \hat{T}}{\partial t} - C_{la}\dfrac{\partial \hat{u}_a}{\partial t} - C_{lu}\dfrac{\partial \hat{\mathbf{u}}}{\partial t} \\ + \nabla \left[K_{ll} \nabla \hat{u}_l\right] + \nabla \left[K_{lT} \nabla \hat{T}\right] + \nabla \left[K_{la} \nabla \hat{u}_a\right] + J_l \end{bmatrix} R_\Omega = 0 \qquad (3.148)$$

where R_Ω is the residual error due to the approximations of the primary variables.

The Galerkin weighted residual approach is used to minimise the error over the elemental volume, for example:

$$\int_{\Omega^e} N_r \begin{bmatrix} -C_{ll}\dfrac{\partial \hat{u}_l}{\partial t} - C_{lT}\dfrac{\partial \hat{T}}{\partial t} - C_{la}\dfrac{\partial \hat{u}_a}{\partial t} - C_{lu}\dfrac{\partial \hat{\mathbf{u}}}{\partial t} \\ + \nabla \left[K_{ll} \nabla \hat{u}_l\right] + \nabla \left[K_{lT} \nabla \hat{T}\right] + \nabla \left[K_{la} \nabla \hat{u}_a\right] + J_l \end{bmatrix} d\Omega^e = 0 \qquad (3.149)$$

where Ω^e represents the elemental volume.

Integrating equation (3.149) by parts yields the weak form. The fifth and eight terms, for example, including substitution from section 3.2, can be expressed as:

$$\int_{\Omega^e} N_r \left[\nabla \left(K_{ll} \nabla \hat{u}_l\right)\right] d\Omega^e = \int_{\Omega^e} \nabla \left(N_r K_{ll} \nabla \hat{u}_l\right) d\Omega^e - \int_{\Omega^e} K_{ll} \nabla \hat{u}_l \nabla N_r d\Omega^e \qquad (3.150)$$

and:

$$\begin{aligned} \int_{\Omega^e} N_r \left[J_l\right] d\Omega^e &= \int_{\Omega^e} N_r \rho_l \nabla \left[K_l \nabla z\right] d\Omega^e \\ &= \int_{\Omega^e} \nabla \left(N_r \rho_l K_l \nabla z\right) d\Omega^e - \int_{\Omega^e} K_l \rho_l \nabla z \nabla N_r d\Omega^e \end{aligned} \qquad (3.151)$$

Treating all terms in this way, equation (3.149) yields:

$$\int_{\Omega^e} \begin{bmatrix} \nabla \left(N_r K_{ll} \nabla \hat{u}_l\right) - K_{ll} \nabla \hat{u}_l \nabla N_r + \nabla \left(N_r K_{lT} \nabla \hat{T}\right) - K_{lT} \nabla \hat{T} \nabla N_r \\ + \nabla \left(N_r K_{la} \nabla \hat{u}_a\right) - K_{la} \nabla \hat{u}_a \nabla N_r + \nabla \left(N_r \rho_l K_l \nabla z\right) - K_l \rho_l \nabla z \nabla N_r \\ + N_r \left[-C_{ll}\dfrac{\partial \hat{u}_l}{\partial t} - C_{lT}\dfrac{\partial \hat{T}}{\partial t} - C_{la}\dfrac{\partial \hat{u}_a}{\partial t} - C_{lu}\dfrac{\partial \hat{\mathbf{u}}}{\partial t}\right] \end{bmatrix} d\Omega^e = 0$$

$$(3.152)$$

Employing the Gauss-Green Divergence theorem, the second order differential terms are reduced to first order and surface integrals are introduced. These surface integrals cancel on all adjacent elements, leaving the contribution to be only at the limits of the domain. This yields:

$$\int_{\Omega^e} \begin{bmatrix} - K_{ll} \bigtriangledown \hat{u}_l \bigtriangledown N_r - K_{lT} \bigtriangledown \hat{T} \bigtriangledown N_r \\ - K_{la} \bigtriangledown \hat{u}_a \bigtriangledown N_r - K_l \rho_l \bigtriangledown z \bigtriangledown N_r \\ - N_r \begin{bmatrix} C_{ll} \dfrac{\partial \hat{u}_l}{\partial t} + C_{lT} \dfrac{\partial \hat{T}}{\partial t} \\ + C_{la} \dfrac{\partial \hat{u}_a}{\partial t} + C_{lu} \dfrac{\partial \hat{u}}{\partial t} \end{bmatrix} \end{bmatrix} d\Omega^e + \int_{\Gamma^e} N_r \begin{bmatrix} K_{ll} \bigtriangledown \hat{u}_l + K_{lT} \bigtriangledown \hat{T} \\ + K_{la} \bigtriangledown \hat{u}_a + K_l \rho_l \bigtriangledown z \end{bmatrix} \underline{n} d\Gamma^e = 0$$

(3.153)

where Γ^e is the element boundary surface and $\underline{n}$ is the direction cosine normal to the surface. The surface integral in equation (3.153) in physical terms is the sum of the liquid and vapour fluxes normal to the boundary surface and may be expressed, with appropriate substitution from section 3.2, as:

$$\int_{\Gamma^e} N_r \left[K_{ll} \bigtriangledown \hat{u}_l + K_{lT} \bigtriangledown \hat{T} + K_{la} \bigtriangledown \hat{u}_a + K_l \rho_l \bigtriangledown z \right] \underline{n} d\Gamma^e$$

$$= \int_{\Gamma^e} N_r \left[\rho_l K_l \left(\frac{1}{\gamma_l} \right) + \rho_l \left(K_{vl} \bigtriangledown \hat{u}_l + K_{vT} \bigtriangledown \hat{T} + K_{va} \bigtriangledown \hat{u}_a \right) + \rho_v \left(K_a \bigtriangledown \hat{u}_a \right) \right] \underline{n} d\Gamma^e$$

$$= \int_{\Gamma^e} \mathbf{N}^T \left[\rho_l \hat{\underline{v}}_{ln} + \rho_l \hat{\underline{v}}_{vd} + \rho_v \hat{\underline{v}}_{va} \right] d\Gamma^e$$

(3.154)

where $\hat{\underline{v}}_{ln}$ is the approximate liquid velocity normal to the boundary surface, $\hat{\underline{v}}_{vd}$ is the approximate diffusive vapour velocity normal to the boundary surface, $\hat{\underline{v}}_{va}$ is the approximate pressure vapour velocity normal to the boundary surface and:

$$K_{vl} = \frac{D_{atms} v_v n}{\rho_l} \left(\rho_0 \frac{\partial h}{\partial s} \right)$$

(3.155)

$$K_{vT} = -\frac{D_{atms} v_v n}{\rho_l} \frac{(\bigtriangledown T)_a}{\bigtriangledown T} \left(h \frac{\partial \rho_0}{\partial T} + \rho_0 \frac{\partial h}{\partial T} \right)$$

(3.156)

$$K_{va} = -\frac{D_{atms} v_v n}{\rho_l} \left(\rho_0 \frac{\partial h}{\partial s} \right)$$

(3.157)

Introducing the expressions for the derivatives of the primary variables and expressing in vector form yields:

$$\int_{\Omega^e} \left[K_{ll} \bigtriangledown \mathbf{N}^T \bigtriangledown \mathbf{N} \right] d\Omega^e \mathbf{u_{ls}} + \int_{\Omega^e} \left[K_{lT} \bigtriangledown \mathbf{N}^T \bigtriangledown \mathbf{N} \right] d\Omega^e \mathbf{T}_s + \int_{\Omega^e} \left[K_{la} \bigtriangledown \mathbf{N}^T \bigtriangledown \mathbf{N} \right] d\Omega^e \mathbf{u_{as}}$$

$$+ \int_{\Omega^e} \left[C_{ll} \mathbf{N}^T \mathbf{N} \right] d\Omega^e \frac{\partial \mathbf{u_{ls}}}{\partial t} + \int_{\Omega^e} \left[C_{lT} \mathbf{N}^T \mathbf{N} \right] d\Omega^e \frac{\partial \mathbf{T}_s}{\partial t} + \int_{\Omega^e} \left[C_{la} \mathbf{N}^T \mathbf{N} \right] d\Omega^e \frac{\partial \mathbf{u_{as}}}{\partial t}$$

$$+ \int_{\Omega^e} \left[C_{lu} \mathbf{N}^T \mathbf{N} \right] d\Omega^e \frac{\partial \mathbf{u}_s}{\partial t} + \int_{\Omega^e} \left[K_l \rho_l \bigtriangledown \mathbf{N}^T \bigtriangledown z \right] d\Omega^e$$

$$- \int_{\Gamma^e} \mathbf{N}^T \left[\rho_l \hat{\underline{v}}_{ln} + \rho_l \hat{\underline{v}}_{vd} + \rho_v \hat{\underline{v}}_{va} \right] d\Gamma^e = 0$$

$$(3.158)$$

where $\mathbf{N}$ is the matrix of shape functions, $\mathbf{u_{ls}}$ is the vector of pore-water pressure values at nodes, $\mathbf{T}_s$ is the vector of temperature values at nodes, $\mathbf{u_{as}}$ is the vector of pore-air pressure values at nodes and $\mathbf{u}_s$ is the vector of displacements at nodes.

This can be expressed in concise form as:

$$\mathbf{C_{ll}} \frac{\partial \mathbf{u_{ls}}}{\partial t} + \mathbf{C_{lT}} \frac{\partial \mathbf{T}_s}{\partial t} + \mathbf{C_{la}} \frac{\partial \mathbf{u_{as}}}{\partial t} + \mathbf{C_{lu}} \frac{\partial \mathbf{u}_s}{\partial t} + \mathbf{K_{ll}} \mathbf{u_{ls}} + \mathbf{K_{lT}} \mathbf{T}_s + \mathbf{K_{la}} \mathbf{u_{as}} = \mathbf{f_l} \qquad (3.159)$$

where:

$$\mathbf{C_{ll}} = \sum_{e=1}^{m} \int_{\Omega^e} \left[C_{ll} \mathbf{N}^T \mathbf{N} \right] d\Omega^e \qquad (3.160)$$

$$\mathbf{C_{lT}} = \sum_{e=1}^{m} \int_{\Omega^e} \left[C_{lT} \mathbf{N}^T \mathbf{N} \right] d\Omega^e \qquad (3.161)$$

$$\mathbf{C_{la}} = \sum_{e=1}^{m} \int_{\Omega^e} \left[C_{la} \mathbf{N}^T \mathbf{N} \right] d\Omega^e \qquad (3.162)$$

$$\mathbf{C_{lu}} = \sum_{e=1}^{m} \int_{\Omega^e} \left[C_{lu} \mathbf{N}^T \mathbf{N} \right] d\Omega^e \qquad (3.163)$$

$$\mathbf{K_{ll}} = \sum_{e=1}^{m} \int_{\Omega^e} \left[K_{ll} \bigtriangledown \mathbf{N}^T \bigtriangledown \mathbf{N} \right] d\Omega^e \qquad (3.164)$$

$$\mathbf{K_{lT}} = \sum_{e=1}^{m} \int_{\Omega^e} \left[K_{lT} \bigtriangledown \mathbf{N}^T \bigtriangledown \mathbf{N} \right] d\Omega^e \qquad (3.165)$$

$$\mathbf{K_{la}} = \sum_{e=1}^{m} \int_{\Omega^e} \left[K_{la} \bigtriangledown \mathbf{N}^T \bigtriangledown \mathbf{N} \right] d\Omega^e \qquad (3.166)$$

$$\mathbf{f_l} = \sum_{e=1}^{m} \int_{\Omega^e} \left[K_l \rho_l \bigtriangledown \mathbf{N}^T \bigtriangledown z \right] d\Omega^e - \sum_{e=1}^{m} \int_{\Gamma^e} \mathbf{N}^T m \left[\rho_l \hat{\underline{v}}_{ln} + \rho_l \hat{\underline{v}}_{vd} + \rho_v \hat{\underline{v}}_{va} \right] d\Gamma^e \qquad (3.167)$$

This process can be replicated for the other flow variables, $[T, u_a]$, producing for:

Heat transfer

$$\mathbf{C_{Tl}}\frac{\partial \mathbf{u}_{ls}}{\partial t} + \mathbf{C_{TT}}\frac{\partial \mathbf{T}_s}{\partial t} + \mathbf{C_{Ta}}\frac{\partial \mathbf{u}_{as}}{\partial t} + \mathbf{C_{Tu}}\frac{\partial \mathbf{u}_s}{\partial t} + \mathbf{K_{Tl}}\mathbf{u}_{ls} + \mathbf{K_{TT}}\mathbf{T}_s + \mathbf{K_{Ta}}\mathbf{u}_{as} = \mathbf{f_T} \quad (3.168)$$

where:

$$\mathbf{C_{Tl}} = \sum_{e=1}^{m}\int_{\Omega^e}\left[C_{Tl}\mathbf{N}^T\mathbf{N}\right]d\Omega^e \quad (3.169)$$

$$\mathbf{C_{TT}} = \sum_{e=1}^{m}\int_{\Omega^e}\left[C_{TT}\mathbf{N}^T\mathbf{N}\right]d\Omega^e \quad (3.170)$$

$$\mathbf{C_{Ta}} = \sum_{e=1}^{m}\int_{\Omega^e}\left[C_{Ta}\mathbf{N}^T\mathbf{N}\right]d\Omega^e \quad (3.171)$$

$$\mathbf{C_{Tu}} = \sum_{e=1}^{m}\int_{\Omega^e}\left[C_{Tu}\mathbf{N}^T\mathbf{N}\right]d\Omega^e \quad (3.172)$$

$$\mathbf{K_{Tl}} = \sum_{e=1}^{m}\int_{\Omega^e}\left[K_{Tl}\bigtriangledown\mathbf{N}^T\bigtriangledown\mathbf{N}\right]d\Omega^e \quad (3.173)$$

$$\mathbf{K_{TT}} = \sum_{e=1}^{m}\int_{\Omega^e}\left[K_{TT}\bigtriangledown\mathbf{N}^T\bigtriangledown\mathbf{N}\right]d\Omega^e \quad (3.174)$$

$$\mathbf{K_{Ta}} = \sum_{e=1}^{m}\int_{\Omega^e}\left[K_{Ta}\bigtriangledown\mathbf{N}^T\bigtriangledown\mathbf{N}\right]d\Omega^e \quad (3.175)$$

$$\mathbf{f_T} = \sum_{e=1}^{m}\int_{\Omega^e}\left[C_{pl}\rho_l k_l\bigtriangledown\mathbf{N}^T\bigtriangledown z\right]d\Omega^e - \sum_{e=1}^{m}\int_{\Gamma^e}\mathbf{N}^T\left[\mathbf{F}_h\right]d\Gamma^e \quad (3.176)$$

where $\mathbf{F}_h$ is the approximate heat flux normal to the boundary surface.

Air transfer

$$\mathbf{C_{al}}\frac{\partial \mathbf{u}_{ls}}{\partial t} + \mathbf{C_{aT}}\frac{\partial \mathbf{T}_s}{\partial t} + \mathbf{C_{aa}}\frac{\partial \mathbf{u}_{as}}{\partial t} + \mathbf{C_{au}}\frac{\partial \mathbf{u}_s}{\partial t} + \mathbf{K_{al}}\mathbf{u}_{ls} + \mathbf{K_{aa}}\mathbf{u}_{as} = \mathbf{f_a} \quad (3.177)$$

where:

$$\mathbf{C_{al}} = \sum_{e=1}^{m}\int_{\Omega^e}\left[C_{al}\mathbf{N}^T\mathbf{N}\right]d\Omega^e \quad (3.178)$$

$$\mathbf{C_{aT}} = \sum_{e=1}^{m} \int_{\Omega^e} \left[C_{aT} \mathbf{N}^T \mathbf{N} \right] d\Omega^e \tag{3.179}$$

$$\mathbf{C_{aa}} = \sum_{e=1}^{m} \int_{\Omega^e} \left[C_{aa} \mathbf{N}^T \mathbf{N} \right] d\Omega^e \tag{3.180}$$

$$\mathbf{C_{au}} = \sum_{e=1}^{m} \int_{\Omega^e} \left[C_{au} \mathbf{N}^T \mathbf{N} \right] d\Omega^e \tag{3.181}$$

$$\mathbf{K_{al}} = \sum_{e=1}^{m} \int_{\Omega^e} \left[K_{al} \triangledown \mathbf{N}^T \triangledown \mathbf{N} \right] d\Omega^e \tag{3.182}$$

$$\mathbf{K_{aa}} = \sum_{e=1}^{m} \int_{\Omega^e} \left[K_{aa} \triangledown \mathbf{N}^T \triangledown \mathbf{N} \right] d\Omega^e \tag{3.183}$$

$$\mathbf{f_a} = \sum_{e=1}^{m} \int_{\Omega^e} \left[k_l \rho_{da} \triangledown \mathbf{N}^T \triangledown z \right] d\Omega^e - \sum_{e=1}^{m} \int_{\Gamma^e} \mathbf{N}^T \rho_{da} \left(\mathbf{\hat{\underline{v}}}_{fn} + \mathbf{\hat{\underline{v}}}_{an} \right) d\Gamma^e \tag{3.184}$$

The approximate velocities of free and dissolved air flux normal to the boundary surface are included as $\mathbf{\hat{\underline{v}}}_{fn}$ and $\mathbf{\hat{\underline{v}}}_{an}$ respectively.

3.9.2 Spatial discretisation of the governing equations for displacement variables

The general method of spatial discretisation for displacement variables is the same as for flow variables, described in the section 3.9. This process, for an elasto-plastic framework, as described in section 3.2, is summarised below.

The governing equation for displacement, with substitution from equations (3.146) and (3.147), can be expressed using the shape function approach as:

$$C_{ul} d\hat{u}_l + C_{uT} d\hat{T} + C_{ua} d\hat{u}_a + C_{uu} d\hat{u} - \mathbf{PD_{ep}} d\varepsilon_s^p + d\mathbf{b} = R_\Omega \tag{3.185}$$

The Galerkin weighted residual method is used to minimise error over the elemental volume:

$$\int_{\Omega^e} N_r \left[C_{ul} d\hat{u}_l + C_{uT} d\hat{T} + C_{ua} d\hat{u}_a + C_{uu} d\hat{u} - \mathbf{PD_{ep}} d\varepsilon_s^p + d\mathbf{b} \right] d\Omega^e = 0 \tag{3.186}$$

Integrating by parts and with substitution from section 3.2, yields the weak form and by example of the first term:

$$\int_{\Omega^e} N_r C_{ul} d\hat{u}_l d\Omega^e$$

$$= \int_{\Omega^e} N_r \left[\mathbf{P} \mathbf{D_{ep}} A_s \right] d\hat{u}_l d\Omega^e \tag{3.187}$$

$$= - \int_{\Omega^e} \left[\mathbf{P} N_r \left(\mathbf{D_{ep}} A_s \right) d\hat{u}_l \right] d\Omega^e + \int_{\Omega^e} \mathbf{P} \left[N_r \mathbf{D_{ep}} A_s \right] d\hat{u}_l d\Omega^e$$

where $\mathbf{P} N_r$ can be expressed as:

$$\mathbf{B} = \begin{bmatrix} \frac{\partial N_r}{\partial x} & 0 & 0 & \frac{\partial N_r}{\partial z} & 0 & \frac{\partial N_r}{\partial y} \\ 0 & \frac{\partial N_r}{\partial z} & 0 & \frac{\partial N_r}{\partial x} & \frac{\partial N_r}{\partial y} & o \\ 0 & 0 & \frac{\partial N_r}{\partial y} & 0 & \frac{\partial N_r}{\partial z} & \frac{\partial N_r}{\partial x} \end{bmatrix} \tag{3.188}$$

The second term of equation (3.186) then yields:

$$\int_{\Omega^e} N_r C_{uT} d\hat{T} d\Omega^e$$

$$= \int_{\Omega^e} N_r \left[\mathbf{P} \mathbf{D_{ep}} \left(-A_T - A_s \frac{\partial S_r}{\partial t} \right) \right] d\hat{T} d\Omega^e$$

$$= - \int_{\Omega^e} \left[\mathbf{B} \mathbf{D_{ep}} \left(-A_T - A_s \frac{\partial S_r}{\partial t} \right) d\hat{T} \right] d\Omega^e + \int_{\Omega^e} \mathbf{P} \left[N_r \mathbf{D_{ep}} \left(-A_T - A_s \frac{\partial S_r}{\partial t} \right) d\hat{T} \right] d\Omega^e \tag{3.189}$$

Expressing equation (3.186) in the weak form gives:

$$- \int_{\Omega^e} \left[\mathbf{B} \left(\mathbf{D_{ep}} A_s \right) d\hat{u}_l \right] d\Omega^e + \int_{\Omega^e} \mathbf{P} \left[N_r \mathbf{D_{ep}} A_s \right] d\hat{u}_l d\Omega^e$$

$$- \int_{\Omega^e} \left[\mathbf{B} \mathbf{D_{ep}} \left(-A_T - A_s \frac{\partial S_r}{\partial t} \right) d\hat{T} \right] d\Omega^e + \int_{\Omega^e} \mathbf{P} \left[N_r \mathbf{D_{ep}} \left(-A_T - A_s \frac{\partial S_r}{\partial t} \right) d\hat{T} \right] d\Omega^e$$

$$- \int_{\Omega^e} \left[\mathbf{B} \left(-\mathbf{D_{ep}} A_s - \mathbf{m} \right) d\hat{u}_a \right] d\Omega^e + \int_{\Omega^e} \mathbf{P} \left[N_r \left(-\mathbf{D_{ep}} A_s - \mathbf{m} \right) d\hat{u}_a \right] d\Omega^e$$

$$- \int_{\Omega^e} \left[\mathbf{B} \mathbf{D_{ep}} \mathbf{P}^T d\hat{u} \right] d\Omega^e + \int_{\Omega^e} \mathbf{P} \left[N_r \mathbf{D_{ep}} \mathbf{P}^T d\hat{u} \right] d\Omega^e$$

$$+ \int_{\Omega^e} \left[\mathbf{B} \mathbf{D_{ep}} \varepsilon_s^p \right] d\Omega^e - \int_{\Omega^e} \mathbf{P} \left[N_r \mathbf{D_{ep}} \varepsilon_s^p \right] d\Omega^e + \int_{\Omega^e} N_r d\mathbf{b} d\Omega^e = 0 \tag{3.190}$$

The Gauss Green divergence theorem may be applied to equation (3.190) producing the

surface integrals, yielding:

$$-\int_{\Omega^e} [\mathbf{B}\left(\mathbf{D}_{\mathbf{ep}}A_s\right)d\hat{u}_l]\,d\Omega^e + \int_{\Gamma^e} [N_r\mathbf{D}_{\mathbf{ep}}A_s]\,d\hat{u}_l\underline{n}d\Gamma^e$$

$$-\int_{\Omega^e} \left[\mathbf{B}\mathbf{D}_{\mathbf{ep}}\left(-A_T - A_s\frac{\partial S_r}{\partial t}\right)d\hat{T}\right]d\Omega^e + \int_{\Gamma^e} \left[N_r\mathbf{D}_{\mathbf{ep}}\left(-A_T - A_s\frac{\partial S_r}{\partial t}\right)d\hat{T}\right]\underline{n}d\Gamma^e$$

$$-\int_{\Omega^e} [\mathbf{B}\left(-\mathbf{D}_{\mathbf{ep}}A_s - \mathbf{m}\right)d\hat{u}_a]\,d\Omega^e + \int_{\Gamma^e} [N_r\left(-\mathbf{D}_{\mathbf{ep}}A_s - \mathbf{m}\right)d\hat{u}_a]\,\underline{n}d\Gamma^e$$

$$-\int_{\Omega^e} [\mathbf{B}\mathbf{D}_{\mathbf{ep}}\mathbf{P}^T d\hat{u}]\,d\Omega^e + \int_{\Gamma^e} [N_r\mathbf{D}_{\mathbf{ep}}\mathbf{P}^T d\hat{u}]\,\underline{n}d\Gamma^e$$

$$+\int_{\Omega^e} [\mathbf{B}\mathbf{D}_{\mathbf{ep}}\varepsilon_s^p]\,d\Omega^e - \int_{\Gamma^e} [N_r\mathbf{D}_{\mathbf{ep}}\varepsilon_s^p]\,\underline{n}d\Gamma^e + \int_{\Omega^e} N_r d\mathbf{b}d\Omega^e = 0$$

$$(3.191)$$

The surface integral equation (3.191) may be simplified to:

$$\int_{\Gamma^e} [N_r\mathbf{D}_{\mathbf{ep}}A_s]\,d\hat{u}_l\underline{n}d\Gamma^e + \int_{\Gamma^e} \left[N_r\mathbf{D}_{\mathbf{ep}}\left(-A_T - A_s\frac{\partial S_r}{\partial t}\right)d\hat{T}\right]\underline{n}d\Gamma^e$$

$$+\int_{\Gamma^e} [N_r\left(-\mathbf{D}_{\mathbf{ep}}A_s - \mathbf{m}\right)d\hat{u}_a]\,\underline{n}d\Gamma^e + \int_{\Gamma^e} [N_r\mathbf{D}_{\mathbf{ep}}\mathbf{P}^T d\hat{u}]\,\underline{n}d\Gamma^e - \int_{\Gamma^e} [N_r\mathbf{D}_{\mathbf{ep}}\varepsilon_s^p]\,\underline{n}d\Gamma^e$$

$$= \int_{\Gamma^e} N_r \begin{bmatrix} \mathbf{D}_{\mathbf{ep}}A_s\left(d\hat{u}_l - d\hat{u}_a\right) - \mathbf{m}d\hat{u}_a + \mathbf{D}_{\mathbf{ep}}\left(-A_T - A_s\frac{\partial S_r}{\partial t}\right)d\hat{T} \\ + \mathbf{D}_{\mathbf{ep}}\mathbf{P}^T d\hat{u} + \mathbf{D}_{\mathbf{ep}}\varepsilon_s^p \end{bmatrix}\underline{n}d\Gamma^e = \int_{\Gamma^e} N_r\hat{\underline{T}}_r d\Gamma^e$$

$$(3.192)$$

where $\hat{\underline{T}}_r$ is the approximate traction.

Introducing the shape function derivatives from equation (3.147) into equation (3.191) yields:

$$-\int_{\Omega^e} [\mathbf{B}\left(\mathbf{D}_{\mathbf{ep}}A_s\right)\mathbf{N}]\,d\Omega^e d\mathbf{u}_{ls} + \int_{\Omega^e} \left[\mathbf{B}\mathbf{D}_{\mathbf{ep}}\left(-A_T - A_s\frac{\partial S_r}{\partial t}\right)\mathbf{N}\right]d\Omega^e d\mathbf{T}_s$$

$$-\int_{\Omega^e} [\mathbf{B}\left(-\mathbf{D}_{\mathbf{ep}}A_s - \mathbf{m}\right)\mathbf{N}]\,d\Omega^e d\mathbf{u}_{as} + \int_{\Omega^e} [\mathbf{B}\mathbf{D}_{\mathbf{ep}}\mathbf{B}^T]\,d\Omega^e d\mathbf{u}_s \qquad (3.193)$$

$$+\int_{\Omega^e} [\mathbf{B}\mathbf{D}_{\mathbf{ep}}\varepsilon_s^p]\,d\Omega^e + \int_{\Omega^e} \mathbf{N}^T d\mathbf{b}d\Omega^e + \int_{\Gamma^e} N_r\hat{\underline{T}}_r d\Gamma^e = 0$$

Equation (3.193) must be used in incremental form for transient analysis, found by multiplying the constants by the gradient of time. Doing this and expressing in concise matrix form yields:

$$\mathbf{C}_{\mathbf{ul}}\frac{\partial \mathbf{u}_{ls}}{\partial t} + \mathbf{C}_{\mathbf{uT}}\frac{\partial \mathbf{T}_s}{\partial t} + \mathbf{C}_{\mathbf{ua}}\frac{\partial \mathbf{u}_{as}}{\partial t} + \mathbf{C}_{\mathbf{uu}}\frac{\partial \mathbf{u}_s}{\partial t} = \mathbf{f_u} \qquad (3.194)$$

$$\mathbf{C}_{\mathbf{ul}} = \sum_{e=1}^{m} \int_{\Omega^e} [\mathbf{B}\left(\mathbf{D}_{\mathbf{ep}}A_s\right)\mathbf{N}]\,\bigtriangledown td\Omega^e \qquad (3.195)$$

$$\mathbf{C_{uT}} = \sum_{e=1}^{m} \int_{\Omega^e} \left[\mathbf{BD_{ep}} \left(-A_T - A_s \frac{\partial S_r}{\partial t} \right) \mathbf{N} \right] \bigtriangledown t d\Omega^e \qquad (3.196)$$

$$\mathbf{C_{ua}} = \sum_{e=1}^{m} \int_{\Omega^e} \left[\mathbf{B} \left(-\mathbf{D_{ep}} A_s - \mathbf{m} \right) \mathbf{N} \right] \bigtriangledown t d\Omega^e \qquad (3.197)$$

$$\mathbf{C_{uu}} = \sum_{e=1}^{m} \int_{\Omega^e} \mathbf{BD_{ep}} \mathbf{B}^T \bigtriangledown t d\Omega^e \qquad (3.198)$$

$$\mathbf{f_u} = \sum_{e=1}^{m} \left[\int_{\Omega^e} [\mathbf{BD_{ep}} \varepsilon_s^p] d\Omega^e + \int_{\Omega^e} \mathbf{N}^T d\mathbf{b} d\Omega^e + \int_{\Gamma^e} N_r \hat{\underline{T}}_r d\Gamma^e \right] \qquad (3.199)$$

3.10 Temporal discretisation

To determine the values of the primary variables over time, a temporally discrete numerical formulation is used. In this case a fully implicit mid-interval forward-difference time-stepping algorithm was employed. This has been found to produce good results for this class of equations (Cook, 1981; Thomas *et al.*, 1998).

Expressing the spatially discretised governing equations in matrix form gives:

$$\begin{bmatrix} \mathbf{K_{ll}} & \mathbf{K_{lT}} & \mathbf{K_{la}} & 0 \\ \mathbf{K_{Tl}} & \mathbf{K_{TT}} & \mathbf{K_{Ta}} & 0 \\ \mathbf{K_{al}} & 0 & \mathbf{K_{aa}} & 0 \\ 0 & 0 & 0 & 0 \end{bmatrix} \begin{bmatrix} \mathbf{u}_{ls} \\ \mathbf{T}_s \\ \mathbf{u}_{as} \\ \mathbf{u}_s \end{bmatrix} + \begin{bmatrix} \mathbf{C_{ll}} & \mathbf{C_{lT}} & \mathbf{C_{la}} & \mathbf{C_{lu}} \\ \mathbf{C_{Tl}} & \mathbf{C_{TT}} & \mathbf{C_{Ta}} & \mathbf{C_{Tu}} \\ \mathbf{C_{al}} & \mathbf{C_{aT}} & \mathbf{C_{aa}} & \mathbf{C_{au}} \\ \mathbf{C_{ul}} & \mathbf{C_{uT}} & \mathbf{C_{ua}} & \mathbf{C_{uu}} \end{bmatrix} \begin{bmatrix} \dot{\mathbf{u}}_{ls} \\ \dot{\mathbf{T}}_s \\ \dot{\mathbf{u}}_{as} \\ \dot{\mathbf{u}}_s \end{bmatrix} + \begin{bmatrix} \mathbf{f}_l \\ \mathbf{f}_T \\ \mathbf{f}_a \\ \mathbf{f}_u \end{bmatrix} = 0 \qquad (3.200)$$

where $\left[\dot{\mathbf{u}}_{ls}, \dot{\mathbf{T}}_s, \dot{\mathbf{u}}_{as}, \dot{\mathbf{u}}_s \right]$ are time differentials of the primary variable vectors. Equation (3.200) can be expressed as:

$$\mathbf{A}\phi + \mathbf{B}\frac{\partial \phi}{\partial t} + \mathbf{C} = \{0\} \qquad (3.201)$$

where $\mathbf{A}$, $\mathbf{B}$ and $\mathbf{C}$ are the matrices of coefficients and ϕ is the vector of variables.

The general form of a forward-difference time-stepping algorithm can be expressed as:

$$\mathbf{A}^{\phi_l} \left[\varpi \phi^{n+1} + (1 - \varpi) \phi^n \right] + \mathbf{B}^{\phi_l} \left[\frac{\phi^{n+1} - \phi^n}{\Delta t} \right] + \mathbf{C}^{\phi_l} = \{0\} \qquad (3.202)$$

where ϖ represents a constant controlling the integration scheme, varying from 1, for implicit, 0.5 for Crank-Nicholson and 0 for explicit time integration schemes: and the superscript

ϕ_l represents the level at which the matrices of coefficients are evaluated, which can be generally expressed as:

$$\phi_l = \vartheta\,(n+1) + (1-\vartheta)\,(n) \tag{3.203}$$

where ϑ is a constant, which controls the interval for which matrices $\mathbf{A}$, $\mathbf{B}$ and $\mathbf{C}$ are evaluated. In this case, a fully implicit, mid-interval algorithm is used, hence ϖ and ϑ take the values of 1 and 0.5 respectively.

With substitution of these constants into equation (3.202) yields:

$$\mathbf{A}^{n+1/2}\phi^{n+1} + \mathbf{B}^{n+1/2}\left[\frac{\phi^{n+1} - \phi^n}{\Delta t}\right] + \mathbf{C}^{n+1/2} = \{0\} \tag{3.204}$$

This can be rearranged giving:

$$\phi^{n+1} = \left[\mathbf{A}^{n+1/2} + \frac{\mathbf{B}^{n+1/2}}{\Delta t}\right]^{-1}\left[\frac{\mathbf{B}^{n+1/2}\phi^n}{\Delta t} - \mathbf{C}^{n+1/2}\right] \tag{3.205}$$

Equation (3.205) indicates that vector ϕ^{n+1} can be evaluated if matrices $\mathbf{A}$, $\mathbf{B}$ and $\mathbf{C}$ can be evaluated at time interval $^{n+1/2}$. To achieve this, a predictor-corrector algorithm is utilised. This takes the form of:

i. Matrices $\mathbf{A}$, $\mathbf{B}$ and $\mathbf{C}$ are evaluated at time ^{n}. This is the predictor.

ii. An estimate of matrices $\mathbf{A}$, $\mathbf{B}$ and $\mathbf{C}$ is made for time $^{n+1/2}$ using the predictor and the values from the previous time-step. This is the corrector.

iii. If the analysis includes an elasto-plastic element, the stress conditions are checked for yielding. If the displacements are such that the stress produced is on or outside the yield surfaces, plastic strain is produced and hardening parameters are evaluated.

iv. Convergence is checked by either of the following conditions:

$$\left|\phi_{iC}^{n+1} - \phi_{(i-1)C}^{n+1}\right| < \mathbf{TL}_{abs} \tag{3.206}$$

$$\left|\frac{\phi_{iC}^{n+1} - \phi_{(i-1)C}^{n+1}}{\phi_{(i-1)C}^{n+1}}\right| < \mathbf{TL}_{rel} \tag{3.207}$$

where i is the iteration level, C denotes that the corrector has been used and $\mathbf{TL}_{abs}$ and $\mathbf{TL}_{rel}$ are matrices of absolute and relative tolerances. The residual force is found from stress equilibrium and can be calculated as (Owen and Hinton, 1980):

$$\int_\Omega \mathbf{B}^T \Delta\,\sigma d\Omega - \Delta F = \zeta \tag{3.208}$$

where $\triangle F$ is the increment of applied force. This residual must be below a set tolerance.

v. If either a converged solution has not occurred, or the residual stress is too great the algorithm returns to step 2 where the corrector becomes the new predictor. If, however, convergence has been achieved and the residual force is below the tolerance the analysis moves to the next time step and the process is repeated.

The amount of predictor-corrector iterations used is dependent upon the simulation conditions, the variable gradients and material parameters, and the size of the time step. To provide an time efficient solution a variable time step is allowed. If more predictor-corrector iterations than a specified value is required then the time-step size is reduced and conversely if less iterations are required than a specified value the time-step size is increased.

This model has been incorporated into a computer code COMPASS, the COde for Modelling PArtially Saturated Soils, which has been incrementally developed at the Geoenvironmental Research Centre (GRC), Cardiff University (Thomas et al., 1998).

3.11 Conclusions

A theoretical and numerical approximation for the transient solution of coupled thermo-hydro-mechanical behaviour has been presented. The governing equations for moisture transfer, dry air transfer, heat transfer and deformation have been presented in terms of four primary variables. The spatial and temporal discretisation of these governing equations have been achieved using the finite-element method and a fully implicit mid-interval forward-difference algorithm respectively.

3.12 References

Alonso, E.E., Battle, F., Gens, A., Lloret, A., (1988) "Consolidation analysis of partially saturated soils-Application to earthdam construction", *Numerical Methods in Geomechanics (Innsbruck 1988)*, 1303-1308.

Alonso, E.E., Gens, A., Josa, A., (1990) "A constitutive model for partially saturated soils", Géotechnique, **40**(3), 405-430.

Britto, A.M., Gunn, M.G., (1987) *Critical state soil mechanics via finite elements*, Ellis Horwood Ltd., Chichester.

Carman, P.C., (1956) *Flow of gases through porous media*, Butterworths Scientific Publications, London.

Cleall, P.J., (1998) "An investigation of the thermo/hydraulic/mechanical behaviour of unsaturated soils, including expansive clays", *PhD Thesis*, Cardiff University, Cardiff.

Cook, R.D., (1981) *Concepts and applications of finite element analysis*, John Wiley & Sons, New York.

Childs, E.C., (1969) *An introduction to the physical basis of soil water phenomena*, John Wiley & Sons, New York.

Darcy, H., (1856) *Les Fontaines Publiques de la Ville de Dijon*, Dalmont, Paris.

de Vries, D.A., (1958) "Simultaneous transfer of heat and moisture in porous media" *Transactions of the American Geophysical Union*, **39**(5), 909-916.

de Vries, D.A., (1966) *Physics of plant environment*, 2nd Edition, North Holland Publishing Company, Amsterdam, 215-235.

Edlefsen, N.E., Andersen, A.B.C., (1943) "Thermodynamics of soil moisture", *Hilgardia*, **15**(2), 31-298.

Ewen, J., Thomas, H.R., (1989) "Heating unsaturated medium sand", *Géotechnique*, **39**(3), 455-470.

Fredlund, D.G., Rahardjo, H., (1993) *Soil Mechanics for Unsaturated Soils*, John Wiley & Sons, New York.

Gens, A., Potts, D.M., (1982) "Application of critical state models to the prediction of the behaviour of a normally consolidated low plasticity clay", *Proceedings of the 1st International Symposium on Numerical Modelling and Geomechanics*, Zurich, 312-323.

Geraminegad, M., Saxena, S., (1986) *Finite elements in plasticity: Theory and practice*, Pineridge Press, Swansea.

Jakob, M., (1949) *Heat transfer: Vol 1*, John Wiley & Sons, New York.

Jaky, J., (1948) "Pressure in soils", *Proceedings of the 2nd International Conference on Soil Mechanics and Foundation Engineering*, **1**, 103-107.

Josa, A., Alonso, E.E., Lloret, A., Gens, A., (1987) "Stress-strain behaviour of partially saturated soils", *Proceedings of the 9th European Conference on Soil Mechanics and Foundation Engineering*, Dublin, **2**, 561-564.

Kaye, G.W.C., Laby, T.M., (1973) *Tables of physical and chemical constants*, 14th Edition, Longmans, London.

Krischer, D., Rohnalter, H., (1940) "Warmeleitung und Dampfdiffusion in feutchen Gutern", *Verein Duetscher Ingenieure Forschungsheft*, **402**(11), 1-18.

Matyas, E.L., Radhakrishna, H.S., (1968) "Volume change characteristics of partially saturated soils", *Géotechnique*, **18**(4), 432-448.

Mayhew, Y.R., Rogers, G.F.C., (1976) *Thermodynamic and transport properties of fluids*, 2nd Edition, Blackwell, Oxford.

Melhuish, T.A., (2004) "An investigation of the three-dimensional thermo/hydro/mechanical behaviour of large scale in-situ experiments" *PhD Thesis*, Cardiff University.

Mitchell, J.K., (1993) *Fundamentals of soil behaviour*, John Wiley & Sons, New York.

Mitchell, H.P., (2002) "An investigation into the thermo/hydro/mechanical interactions involved in high level nuclear waste disposal" *PhD Thesis*, University of Wales, Cardiff.

Nielson, D.R., Van Genuchen, M., Biggar, J.W., (1986) "Water flow and solute transport processes in the unsaturated zone", *Water Resources Research*, **22**(9S), 89S-108S.

Owen, D.R.J., Hinton, E., (1980) *Finite elements in plasticity: theory and practice*, Pineridge Press, Swansea.

Partington, J.R., (1949) *Advanced Treatise on Physical Chemistry, Volume One*, Longmans, London.

Pollock, D.W., (1986) "Simulation of fluid flow and energy transport processes associated with high-level radio active waste disposal in unsaturated alluvium", *Water Resources Research*, **22**(5), 765-775.

Philip J.R., de Vries D.A., (1957) "Moisture movements in porous materials under temperature gradients" *Transactions of the American Geophysical Union*, **38**(2), 222-232.

Preece, R.J., (1975) *The measurement and calculation of physical properties of cable bedding sands. Part 2; specific thermal capacity, thermal conductivity and temperature ratio across 'air' filled pores*, Central Electricity General Board, Laboratory Note No. RD/L/N 231/74, London.

Pusch, R., (1998) "Microstructural evolution of buffer clay", *Proceedings of workshop on microstructural modelling of natural and artificially prepared clay soils with special emphasis on the use of clays for waste isolation*, Lund, 31-38.

Pusch, R., Karnland, O., Hokmark, H., (1990) *GMM: a general microstructural model for qualitative and quantitative studies of smectite clays*, SKB, Technical Report, SKB-90-43, Stockholm.

Singh, R.M., (2007) "An experimental and numerical investigation of heat and mass movement in unsaturated clays", *PhD Thesis*, Cardiff University, Cardiff.

Thomas, H.R., Cleall, P.J., Chandler, N., Dixon, D., Mitchell, H.P., (2003) "Water infiltration into a large-scale in-situ experiment in an underground research laboratory", *Géotechnique*, **53**(2), 207-224.

Thomas, H.R., King, S.D., (1991) "Coupled temperature/capillary potential variations in unsaturated soil", *Journal of Engineering Mechanics, American Society of Civil Engineers*, **117**(11), 2475-2491.

Thomas, H.R., He, Y., (1995) "Analysis of coupled heat, moisture and air transfer in a deformable soil", *Géotechnique*, **45**(4), 677-689.

Thomas, H.R., He, Y., (1998) "Modelling the behaviour of unsaturated soil using an elasto plastic constitutive relationship", *Géotechnique*, **48**(5), 589-603.

Thomas, H.R., He, Y., Onofrei, C., (1998) "An examination of the validation of a model of the hydro/thermo/mechanical behaviour of engineered clay barriers", *International Journal of Numerical and Analytical Methods in Geomechanics*, **22**, 49-71.

Thomas, H.R., Samson, M.R., (1995) "A fully coupled analysis of heat, moisture and air transfer in unsaturated soil", *Journal of Engineering Mechanics, American Society of Civil Engineering*, **12**(3), 392-405.

Wang, C., (1953) *Applied Elasticity*, McGraw-Hill, New York.

Wood, D.M., (1990) *Soil behaviour and critical state soil mechanics*, Cambridge University Press, Cambridge.

Zienkiewicz, O.C., Taylor, R.L., (1989) *The finite element method*, 4th edition, McGraw Hill, New York.

4

Computational Formulation and Performance

4.1 Introduction

In computationally expensive applications, such as the THM modelling of large-scale problems described in this thesis, it is essential to find an efficient solution in terms of time to undertake the analysis. These analyses may, using a single processor, take a significant time, i.e. weeks or months (Melhuish, 2004). This time is likely to be prohibitive and it is worth the investment in development time to minimise the analysis time.

In this chapter the computational performance of the implemented numerical model is analysed within the context of large spatial and temporal simulations. Methods of reducing the time taken to execute a simulation were explored. It is logical to take the simplest and easiest method to save time that allows the required quality of results to be found. In many cases this, therefore, involves the simplification of the model, often geometrically for example via the identification of lines of symmetry, so that the domain can be split or reduced in dimensionality, or a coarsening of the results required. If however, as in the

case of the problem addressed in this work, there is inherent three-dimensionality and the resolution of the results required is high, this cannot be done and methods of increasing the amount of computation undertaken in a given time are sought. These may take the form of one or more of the following: improved hardware, better algorithms, fast solvers, optimisation of computer codes or parallel computation. The best and most appropriate hardware available, within constraints e.g. economic, should be sought. The remainder can be grouped into two main groups, i) serial optimisation and ii) high performance computing (HPC). Serial optimisation involves forming all aspects of the computational code: writing, compilation and execution in a streamlined way such that the code performs at or close to its optimum. Care must be taken to ensure that sufficient accuracy is maintained. HPC, in this work is considered to be parallel computing, where multiple processors are used to undertake these simulations and parallel computational algorithms are used to distribute the work across these processors, thereby decreasing the overall analysis time in comparison to a single processor.

Considerable time has been spent on this issue in this field, for example Owen (2000), but due to the evolving computer market the 'goalposts' are constantly moving. It is also true that efficient solutions are largely dependant upon the type of problem (Barrett *et al.*, 1995).

The type of analysis undertaken is examined and characterised in section 4.2 including a definition of a series of benchmark simulations based upon the Prototype Repository Project. It is seen that forming matrices and solving the resultant system are the dominant computational activities undertaken. Serial optimisation is discussed in section 4.3 and in particular looking at the effects of differing solvers, algorithms and optimisation of the computational code are considered. A number of optimisations are implemented and time savings noted.

Section 4.4 presents the a review of parallel computing including hardware evolution, available architectures, programming paradigms and HPC resources used, aiming to reduce the execution time of a simulation. The formation of parallel algorithms is contained in section 4.5, with the performance of these algorithms presented in section 4.6. The performance is assessed against the best serial performance to give an indication of real time reduction, as opposed to algorithm efficiency. A brief discussion of pre and post-processing is contained in section 4.7 and finally conclusions are presented in section 4.8.

4.2 Analysis characterisation

Problems considered in this study, can be expressed as equation (3.205) and rearranged into a system of linear equations;

$$[a] \, \phi^{n+1} = [b] \tag{4.1}$$

where $[a]$ and $[b]$ are matrices of coefficients. To solve this there are two main sections of calculation:

i. Forming the matrices.

ii. Solving the system of equations.

The matrix formation is a relatively simple operation with well defined numerical operations. The scope for the serial optimisation is limited, but is easily parallelisable with synchronisation only required at the start and the end of the process. However, with the solution techniques used in the study many synchronisation points are required. The time taken for a solution to be found for these equations is reliant upon the size of the problem considered, the solver implemented and the computational system used.

The size of the system matrix, often stored using Compressed Row Storage (CRS), a method whereby only non-zeros are stored with accompanying vectors to describe the location, is dependant upon the complexity of the geometry, the connectivity, and the processes that are being considered. The maximum size is the square of the number of active freedoms, but is generally much less than this, i.e. sparse. Table 4.1 gives the sizes of example problems that have been produced and are referred to later, along with the number of freedoms, the size of the system matrix and the sparsity.

The amount of computational work that is required to calculate the system matrix is largely dependent upon the number of elements in the system and is proportional to the square of the number of freedoms, but the amount of computation required to solve the system of equations is dependent upon manipulation of the system matrix. With different solution techniques differing manipulations takes place. Traditionally, matrix-matrix multiplication is undertaken, meaning that the number of calculations required is proportional to the cube of the number of freedoms. With more complex problems, the solution of the system of

equations becomes the dominant component of the analysis as the number of manipulations increases. Various techniques exist to reduce the amount of manipulation required to obtain a solution.

When analyses to be undertaken become large, the amount of storage required, i.e. computer memory, may exceed the amount available, leading to some compromises having to be made. Some calculations may have to be repeated to allow the memory that they have used to be utilised for other information, or information can be distributed into other memory, either attached to another processor, or to slower memory, e.g. page files.

The benchmark simulation has been based on the Prototype Repository Project (PRP), introduced in chapter 1 and described fully in chapter 6. Key features of this project are the implicit three-dimensionality of the fractured rock mass containing the experiment; the high resolution of results required in and around the experiment; the large spatial domain required; and the long time scales needed. This makes it a prime candidate for consideration via HPC techniques. Moreover, this experiment has been previously attempted to be simulated and it was found that the time taken to run analyses was prohibitive (Melhuish, 2004).

Number of elements	Number of freedoms	Square of number of freedoms (a)	Size of system matrix (b)	Sparsity of system matrix (a/b)
100,000	99,534	9.91×10^9	8.63×10^6	1,148.3
350,000	371,172	1.38×10^{11}	3.23×10^7	4,272.4
500,000	527,388	2.78×10^{11}	4.56×10^7	6,096.5

Table 4.1. Characterisation of example analyses with differing number of elements (Vardon *et al.*, 2009).

Specifically, the simulations are of a rock mass, including the effect of fractures in an effective continuum model, containing a repository structure. This repository is made up of a tunnel and 6 deposition-holes. The model domain is $100m \times 100m \times 160m$, the initial conditions in

the rock are hydrostatic with the outer rock boundary maintained at hydrostatic pressure. Buffer material is considered to be in the deposition-holes, with an initial suction of $50 MPa$, the backfill material in the tunnel is considered to have an initial suction of $1 MPa$. The heat production from the canisters is simulated via a heat flux of $100 W/m^2/K$.

4.3 Serial optimisation

Optimisation in serial is the easiest way to form a more time efficient code. Any parallel codes must be compared to the best serial optimisation, not merely the parallel algorithm run in serial. Therefore before any parallelism is considered, the algorithms used, the type of solver and other optimisations within the code must be considered. Each of these may also affect the accuracy obtained and this must be monitored at the same time to ensure equal performance.

4.3.1 Algorithm

The main algorithm within COMPASS is shown in figure 4.1a where NP is the number of processors, n is the identification number of a processor and NE is the number of finite-elements. The major aspects are described as the *Initialisation*, the *System Matrix Build*, the *Iterative Solver* and the *End*. Of these, while the *Initialisation* and *End* sections are largely serial and are only undertaken once per analysis the *System Matrix Build* and the *Iterative Solver* section are undertaken for each iteration of each time step. These latter sections make up the majority of the run time, although time spent in the initialisation phase can be significant.

The *System Matrix Build* loops through the number of elements in the domain and populates matrices [a] and [b] from equation 4.1. It is easily parallelisable and requires only data which is available at the start of the loop so no communication is necessary. The *Iterative Solver* section solves the system of linear equations posed in equation 4.1 by use of a preconditioned Bi-Conjugate Gradient (BiCG) solver. This has serial speed advantages, as well as maintaining sparsity in the system matrix, vastly reducing storage required over direct solvers (Barrett *et al.*, 1995). However, this method requires full knowledge of vectors throughout the solver, hence is more complicated to parallelise (Duff and van der Vorst, 1999). More details of the solver are presented below.
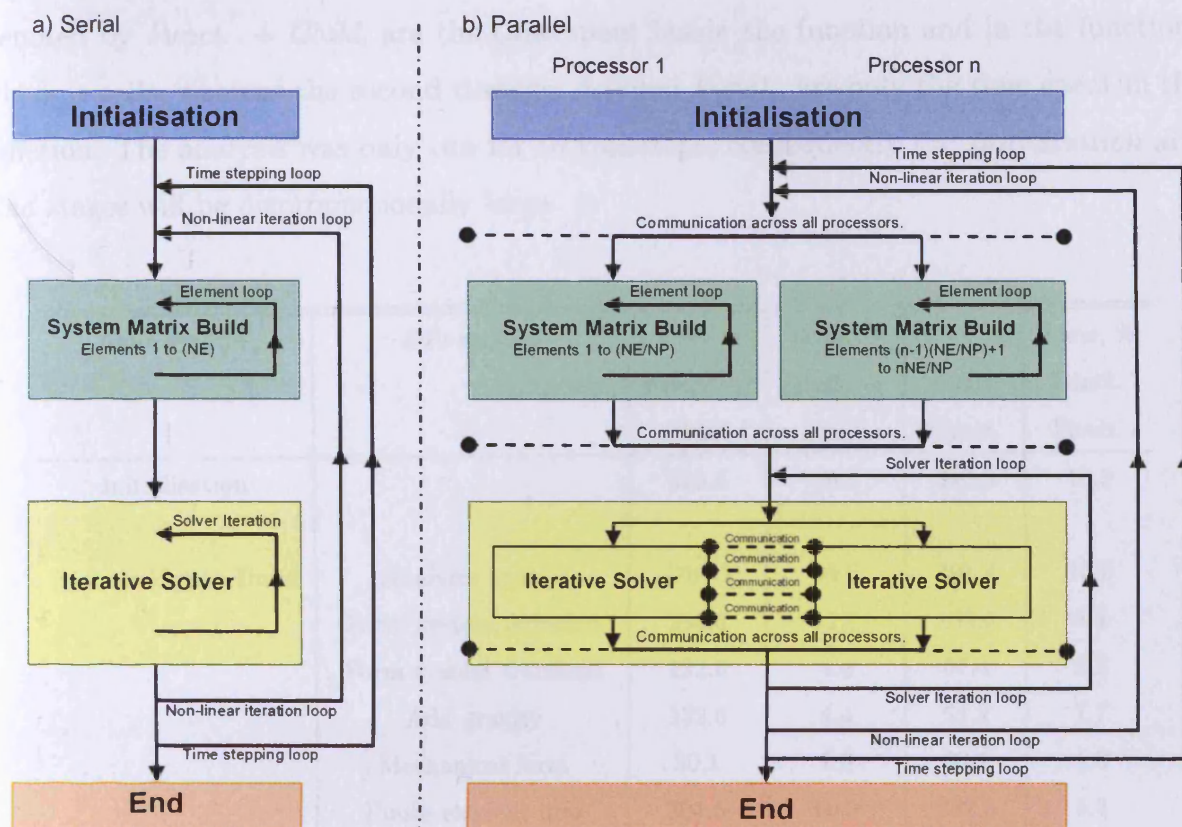
Figure 4.1. COMPASS algorithm in a) serial and b) parallel.

The amount of work required for the *System Matrix Build* and each iteration of the *Iterative Solver* is proportional to the number of freedoms in the simulation. The total size of the system matrix, including zero elements, is the square of the number of freedoms. The solver undertakes a number of vector-vector multiplication operations and two matrix-vector multiplications per iteration. A matrix-vector multiplication has an average of 520 times more calculations than a vector multiplication operation, based on the figures in table 4.1.

The algorithm should be analysed to understand exactly where time is spent. With the results of this analysis it can be identified where to spend effort in reducing computation, for example repetitive calculations may be removed from the algorithm and the values stored in memory. When simulations are using a large amount of memory there is a speed/storage compromise to be made. In this study the code has been profiled using tools available via Microsoft Windows (Prep, Profile and PList) for a number of simulations and optimisation has been undertaken. A brief example is given below in table 4.2, where the first timings,

denoted by *Funct. + Child*, are the time spent inside the function and in the functions which it calls, whereas the second timings, denoted *Funct.*, are only the time spent in the function. The analysis was only run for 10 timesteps, consequently the *Initialisation* and *End* stages will be disproportionally large.

Main section	Sub-section	Time, s Funct. + Child	Time, % Funct. + Child	Time, s Funct. Funct.	Time, % Funct. Funct.
Initialisation		310.5	10.3	310.5	10.3
System Matrix Build	Analysis control	2704.2	89.7	301.4	10.0
	Form system diffusion	334.6	11.1	132.6	4.4
	Form system transient	132.6	4.4	87.4	2.9
	Add gravity	132.6	4.4	51.2	1.7
	Mechanical form	30.1	1.0	30.1	1.0
	Finite-element info	301.5	10.0	262.3	8.7
	Assemble system matrix	413.0	13.7	413.0	13.7
Solver	BiCG solver	651.2	21.6	590.9	19.6
	Pre-conditioner	57.3	1.9	57.3	1.9

Total time = 3014.7 seconds

Table 4.2. Results from code profiling.

During optimisation a number of code modifications were performed and the code re-profiled. In addition the code was timed un-instrumented, i.e. fully compiler optimised to establish whether benefits had been made. The results of these modifications can be seen in table 4.3 with the time saving, in reference to the original that has been achieved. The total time saving is 30% which is significant. In addition, none of the improvements have altered the ability of the code to be parallelised.

Alteration	Time saving of total time, %	Notes/Comments
Gravity calculated in form system transient	4.1	Largely repeated calculations.
Changed finite-element info so values are in memory	16.0	Many repeated calculations. Will monitor when problem size becomes large.
Changed initial guess in solver	7.3	Better guess therefore less work to be undertaken.
Removed some syntax checks	2.6	By using pre-processor some are not required. Time saving will be small when the amount of timesteps increases.

Table 4.3. Serial optimisations undertaken.

4.3.2 Solvers

The two main types of solvers for the type of tightly coupled problem considered in this study can be categorised as direct and iterative solvers (Duff and van der Vorst, 1999), although it should be stated that this is a simplification and that in some cases direct solvers may use iterative techniques to improve performance and iterative solvers may use direct preconditioners to improve performance.

In this work a Krylov subspace, iterative solver has been selected, appropriate for the non-symmetric nature of the coupled THM equations (Owen, 2000). Owen showed how these could be implemented resulting in reduced time over direct solvers, and further speed-up could be achieved via parallelisation. For THM problems a Bi-Conjugate Gradient (BiCG) solver was found to be the most appropriate and numerically robust.

Figure 4.2 shows the original BiCG solver in a computational pseudocode (Barrett et $al.$ 1994) where A is a matrix, M is a pre-conditioner, i is an integer counter, α, β and ρ are real numbers and the remainder are vector quantities.

Pseudocode for Bi-Congugate Gradient Solver

Compute $r_0 = b - Ax_0$ for an initial guess x_0
Choose $\tilde{r}_0$ (for example $\tilde{r}_0 = r_0$)
for $i = 1, 2, \ldots$
  solve $Mz_{i-1} = r_{i-1}$
  solve $M^T\tilde{z}_{i-1} = \tilde{r}_{i-1}$
  $\rho_{i-1} = z_{i-1}^T \tilde{r}_{i-1}$
  if $\rho_{i-1} = 0$ then method fails
  if $i = 1$
      $p_i = z_{i-1}$
      $\tilde{p}_i = \tilde{z}_{i-1}$
  else
      $\beta_{i-1} = \rho_{i-1}/\rho_{i-2}$
      $p_i = z_{i-1} + \beta_{i-1}p_{i-1}$
      $\tilde{p}_i = \tilde{z}_{i-1} + \beta_{i-1}\tilde{p}_{i-1}$
  end if
  $q_i = Ap_i$
  $\tilde{q}_i = A\tilde{p}_i$
  $\alpha_i = \rho_{i-1}/\tilde{p}_i^T q_i$
  $x_i = x_{i-1} + \alpha_i p_i$
  $r_i = r_{i-1} + \alpha_i q_i$
  $\tilde{r}_i = \tilde{r}_{i-1} + \alpha_i \tilde{q}_i$
end

Figure 4.2. Pseudocode for the BiCG solver (Barrett *et al.* 1995).

The main aspects of this solver are that it solves a close system of equations directly, the preconditioner stage, then the Krylov subspace is found iteratively and that it is suitable for solving non-symmetric matrices, due to the fact that there are two 'search' directions to reduce the residual to within a predefined limit. Although there are other forms of the algorithm (e.g. Rybarczyk *et al.*, 2006), this is the most simple in terms of amount of calculation. It can be noticed that this algorithm is made up of 9 vector operations, based on a multiplication of each value in the vector, and 2 matrix-vector operations.

The main serial way of improving the time taken in this algorithm is by selecting an appropriate preconditioner, which is normally a 'nearby' mathematical system. However, the preconditioner also plays a part in the numerical stability of the analysis. In this case a Jacobi preconditioner, which is effectively a vector-vector multiplication, is used for simplicity and ease of parallelisation and good performance for this type of problem (Owen, 2000).

4.3.3 Compilation and programming style optimisation

Good programming technique and good use of compilers can ensure that computational efficiency is optimum for a certain algorithm. However, good programming for performance and good programming for clarity of understanding for the future are not necessarily synonymous. It is important to understand what the compiler will do automatically and what it is necessary for the programmer to do explicitly. The main methods of undertaking serial optimisation are:

- Compiler options - compilers allow a series of optimisations and options that allow the compiler to automatically alter the way the code is transferred into an executable program. There is some influence on accuracy with more aggressive optimisations. Pipelining is a technique that can be used to take full advantage of the amount of instructions a processor can perform simultaneously, instructions can be reordered so that this can be performed optimally. Some compliers may also have processor specific options which allow a code to be compiled specifically for execution on certain processors.

- Reduce cache misses - data is stored in a specific way in memory and cache. The order of accessing this data, for example in loops, can be controlled to take advantage of this. Some compilers are able to do this, but in some cases it is necessary for the programmer to do this.

- Inlining loops - Some loops may be inlined, i.e. joined, which aids performance in terms of complementary instructions and reducing cache misses.

- Eliminate repetition - repeated calculations can be eliminated and data stored in memory. There is a compromise between memory storage and repeating calculations.

4.4   High Performance Computing (HPC) - Parallel computing

High Performance Computing can take many forms, for example distributed (grid) computing or parallel computing. Distributed computing is best suited for a high through-put of analyses, i.e. where a single analysis can easily be completed on a commodity computer (i.e. a PC) but the volume of analyses required is prohibitive. Parallel computing is most suitable for the solution of a single analysis where the time taken and/or memory is prohibitive. The type of problem considered in this study is of the second variety and as such in this thesis the term High Performance Computing is used meaning parallel computing.

4.4.1   Evolution of hardware, with particular reference to HPC

Trends in computer architectures and programming paradigms both past and projecting forward give insight into how a code may be formulated with a view to maintaining performance. It is of obvious importance to look towards the future particularly when the speed of developments in computer hardware and architectures are considered when deciding how to formulate a high performance code. For the time and economic investment to be worthwhile the code must perform well for a number of years.

Graham et al. (2004) show that over the 16 years prior to 2004, processor speed improved by 59% per year in terms of MFLOPS. It is noted that for this increase to be maintained beyond 2004, manufacturers will need to include several processing units on the same chip. Memory bandwidth has only increased by 23% per year since 1995 and memory latencies decreased by 5.5% per year. The bandwidth of interconnects is increasing at 26% per year, on average over the last 14 years, and the latencies improving at 15% per year. Therefore the bottleneck is quickly becoming the communication since comparatively the bandwidth and latencies are increasing compared to the processing speeds. For Krylov subspace methods, such as the BiCG solver, the communication is seen as the bottleneck (Yang and Brent, 2002 and Demmel et al. 2007).

Intel (2006) predict that their transistor density will increase in line with Moore's Law and that their micro-architecture progression, i.e. the number of cores on a processor, will double every two years. Consequently the progression from multi-core to many-core is likely

to happen within the foreseeable future. To take advantage of the continuation of Moore's Law parallel computation is becoming a necessity.

The cost of parallel computing is also becoming vastly reduced. Commodity computers are now commonly supplied with multiple processing units that can be utilised for small scale parallel computation. Graham et al. (2004) note that HPC systems based upon commodity-processors, defined as processors built for the mass market, i.e. a workstation, are roughly an order of magnitude more cost effective than custom-processor based systems in terms of providing the same computing power and now provide over 85% of the TOP500 list (TOP500, August 2008).

4.4.2 Architectures

The historical definitions for types of parallel computers (Flynn, 1972) are outdated (van de Steen and Dongarra, 1996). To reflect this architectures are referred to here as shared-memory, where multiple processors have access to a single memory block, or distributed-memory, where each processor has its own block of memory. A third architecture is now common due to multi-core processors, where a limited number of processing cores have access to a single block of memory forming a node, with a machine made up of a number of nodes. This configuration is sometimes termed hybrid architecture. A variety of other architectures have been produced over time but recently most manufacturers have conformed to these. An additional impact on the HPC market is the switch to commodity based machines. In the past HPC machine vendors have used specifically designed equipment, including the processors, to form their machines.

4.4.2.1 Distributed memory architecture

Distributed memory HPC machines are made up of processors each with its own private memory. They are connected together via an interconnect and allowed to explicitly pass data to each other to allow the successful execution of a single program. The advantage of such systems is the simplicity. There is no shared bus between the processors and memory, therefore the processor can use the full bandwidth with no interference from other processors. With no shared bus, there is no limit on the amount of processors able to be connected to the bus, so hardware scalability is much simpler. No processors are able to overwrite data being

used by other processors and there are no cache coherency problems, i.e. where local data stored in cache is not current. The main disadvantage is that when data is required by one processing unit that belongs to another communication can be more difficult. Messages must be passed, which have a time overhead attached to both sending and receiving them. Figure 4.3 shows a schematic of a distributed memory implementation including the processors, memory, bus and interconnect/network.
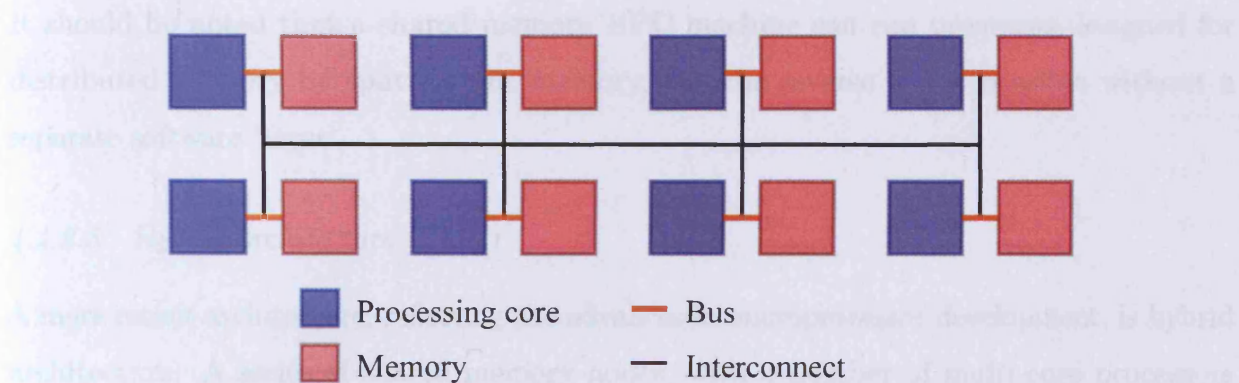
Figure 4.3. Schematic of distributed memory architecture.

4.4.2.2 Shared memory architecture

Shared memory architectures allow multiple processors to be connected to a single memory block via a shared bus. The advantage of this architecture is that no explicit messages are passed, hence little wasted time.
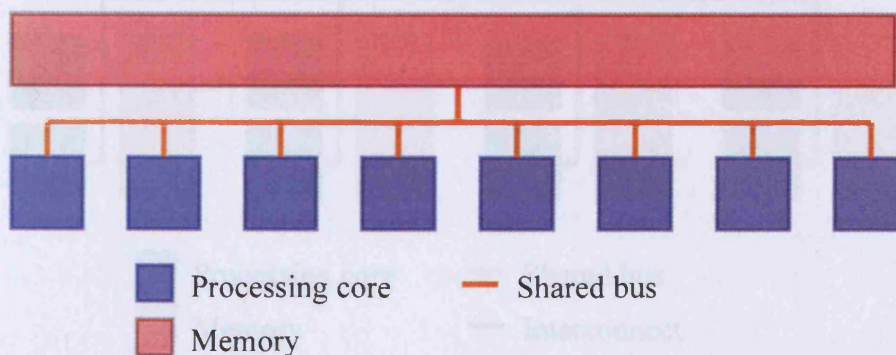
Figure 4.4. Schematic of shared memory architecture.

The disadvantages of the approach include the limitation of the bus bandwidth, which means that a maximum amount of information may be transferred to and from memory and hence limits the amount of processors that can be used. Using cache increases the amount of processors, reducing bus contention, but care must be taken to ensure cache coherency. A schematic of shared memory architecture is shown in figure 4.4, noting the reliance on the shared bus.

It should be noted that a shared memory HPC machine can run programs designed for distributed memory by splitting the memory, but the reverse is not possible without a separate software 'layer'.

4.4.2.3 Hybrid architecture

A more recent architecture, reflecting the advances in microprocessor development, is hybrid architecture. A series of shared memory nodes, with a number of multi-core processors accessing the same shared memory, are added together to form a larger HPC machine. This enables HPC machines to take advantage of small-scale shared memory architecture speeds, due to no message-passing, however the amount of cores should be low enough not to cause a problem to the current bus designs.

Processing core   — Shared bus
Memory   — Interconnect
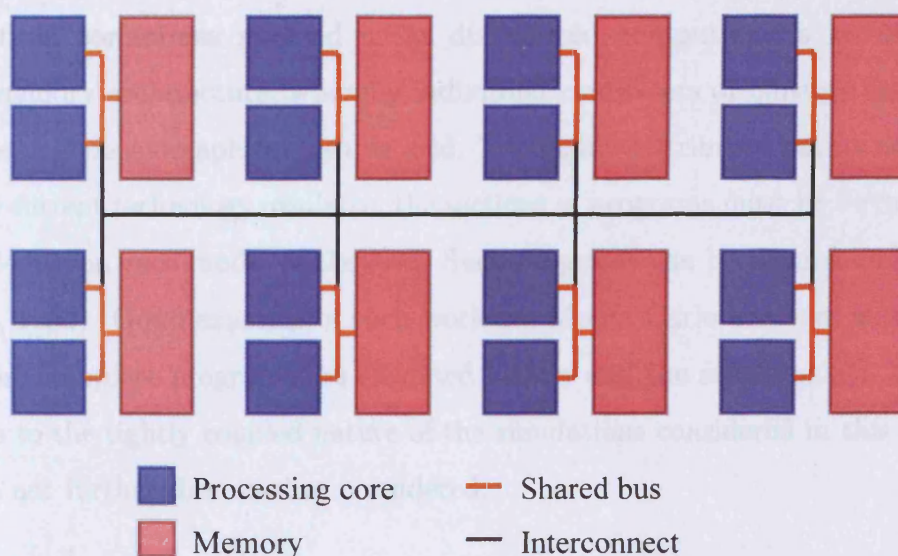
Figure 4.5. Schematic of hybrid memory architecture.

In addition, as the number of cores on a processor increases, the investment into new 'on chip' bus technology will increase and such problems may be reduced. These machines also take advantage of the scalability offered by distributed memory. All of the top 10 HPC machines in the world (TOP500, August 2008) utilise this style of architecture. However, the top HPC machine uses this architecture with the addition of cell accelerators, extra chips attached to the main processing nodes, with a reduced instruction set. Figure 4.5 illustrates the hybrid architecture.

4.4.2.4   Commodity/Proprietary equipment

The majority of HPC machines now produced are made from commodity processors. Over 85% of the worlds fastest 500 computers use commodity processors. The exceptions are the Power processors, led by IBM, which maintain a 13.6% share and Cray who maintain a 0.20% share. This noted, half of the top 10 use Power and Cray processors (TOP500, 2008). This may be due to the financial burden of large purpose build machines, which can be reduced by using commodity parts. The largest machines, it can be argued, can still take advantage of specialist technology where budgetary restraints may be less, whereas it is sufficient for the remainder to use commodity parts.

4.4.2.5   Grid computing

Grid computing, sometimes referred to as distributed computing, is an extension of distributed memory architecture, whereby individual computers or clusters can execute a program across a wide geographical area, or grid. The highly distributed nature of this means that with the current technology available, the sections of programs must be virtually able to run independently on each 'node' of the grid. Such programs can be termed *embarrassingly parallel* (Fox, 1992). Good example of such work are Monte Carlo analyses and sensitivity analyses where complete programs are executed locally and the solutions can be centrally collated. Due to the tightly coupled nature of the simulations considered in this thesis, grid computing is not further discussed or considered.

4.4.3   Programming paradigms

Programming paradigms generally reflect hardware, as this enables the programmer to obtain the highest level of performance. Historically, there have been many parallel programming

paradigms with many manufacturers producing compiler directive based extensions to standard languages. Some consensus has been made recently, in terms of how parallel programming is undertaken and much effort has been made to standardise this. There are two main styles of parallel programming which reflect the two main architectures:

- Message-passing, a common implementation is MPI (Message Passing Interface, 2009)

- Multi-threaded, a common implementation is OpenMP (OpenMP, 2009)

These paradigms can be used together to form a hybrid paradigm suitable for use on hybrid architectures. Usefully, programs designed for hybrid use can be designed so that on distributed memory architecture they revert to message-passing only and on the shared memory architecture revert to multi-threaded operation.

4.4.3.1   Message-passing

Message-passing protocols allow one processor to send a message to another. In general, this means that a message is sent by one processor and received by another. However, in some implementations there are one-sided communications, whereby a processor can read from or place data to another processor memory. In a programming paradigm such as Message Passing Interface (MPI) this simple concept is built into a series of functionalities, which allow more complex tasks to be undertaken. Sending and receiving can also be made to block other commands, or be buffered and synchronisations across processors can be made. This is designed for distributed memory HPC machines, but will also work on shared memory machines by effectively splitting the memory into private sections. Message-passing has a time overhead attached to it and as such parallel programs are likely to have a limit to how scalable they are, depending upon how much information is needed to be passed. Each processor runs a program, in MPI the same program, which contains all the commands that it needs to execute. Care must be taken so that a program does not stall, termed hanging, for example when all processors are waiting to receive data at the same time.

4.4.3.2   Multi-threaded

Multi-threading is a parallel programming tool that allows a single program to use multiple processors to access the same memory. A single master thread is run which controls the

program and other threads, normally contained on other processing cores, are spawned and killed when required. OpenMP is an implementation of this, which enables the programmer, via compiler directives, to control the actions of the threads. Functionality such as automatic work sharing is given to the programmer, which allows flexibility in execution. Difficulties occur during a so called *race condition* (Netzer and Miller, 1992) when a value is dependant on the timing of the execution of instructions carried out by different threads. The programmer must be careful to avoid this while ensuring that work can be shared across processors to gain a performance advantage.

4.4.4   HPC resources available/used

During this study a number of different computing and HPC resources have been used and these are summarised in table 4.4. The newest machine, procured late 2007 and online mid 2008 was the Bull machine, named Merlin. While the processing power per core is greater than the others, it is not by a large margin. However, the interconnect is vastly superior with a 20 times increase in bandwidth and a low latency, in the order of $1.4\mu s$.

4.5   Parallel algorithm/formulation

There are a number of general parallel computation methods that split the computational work into sections. These are generally considered in terms of the granularity of the parallelisation. In a very coarse grained parallelisation, sections of the computation can be undertaken with little or no communication, i.e. embarrassingly parallel. Medium granularity can be described as a problem where sections of simulation can be undertaken independent of others with little communication. Domain decomposition (Quarteroni and Valli, 1999) is an example of this where sections of the domain are solved independently, with some overlapping of solution space and the overlapping space is then compared, ensuring convergence. This is likely to involve many iterations for a highly active or non-linear system. Much care must be taken when splitting a domain in terms of limiting iterations for convergence and computational work-balancing. Another example is where a more general coarse solution can be solved and then more complex, refined solutions determined locally, i.e. a subgrid. A very fine grained parallelisation is required where the impact of a calculation has a large effect on other areas. In the calculations occurring in this study the material parameters depend on the results of the last iteration and are highly non-linear

Name	Vendor	Processors	Number of cores	Interconnect	Memory
Merlin	Bull	Intel 3GHz Xeon (Harpertown/ Seaburg)	2048 (8 per node)	InfiniBand Connect-X (20Gbps)	2GB per core
HP *	HP	Intel 3GHz Xeon (Woodcrest)	32 (4 per node)	InfiniBand (10Gbps)	2GB per core
Raptor	SUN	AMD 2.6GHz Opteron	2048 (4 per node)	Gigabit Ethernet	2GB per core
COMA	Compusys	AMD 2.2GHz (max) Opteron	228 (2-8 per node)	Myrinet	1GB per core
WESC	SGI	MIPs 600MHz R14000	32	Ethernet	512MB per core

*Only available temporarily

Table 4.4. The specifications of HPC machines used.

and the domain can be highly active with steep variable gradients and changing material parameters. Also, the different coupled phenomena will have significantly varying levels of influence both spatially and temporally during an analysis.

As mentioned earlier, to form an efficient parallel algorithm the sections of the analysis where most computational effort is spent must be identified. This has been undertaken for a number of cases and on a number of computers with some example results given above in section 4.2.

4.5.1 Matrix build parallel algorithm

A parallel formulation has been implemented for the *Matrix build* section where work balancing is trivial and the amount of communication compared to computation is low. The matrix build loops through all elements and calculates their contribution to the matrices $[a]$ and $[b]$ shown in equation (4.1). The work required for each element is almost identical and assuming that on the HPC machine executing the program all processors are identical there is no need for dynamic work balancing. The number of elements is divided by the number of processors and the work is divided. By undertaking the work balancing in this manner, some time may be lost at the end of the loop, should any of the processors complete the allocated work slowly, but some gains may be made due to information stored in arrays being current in cache.
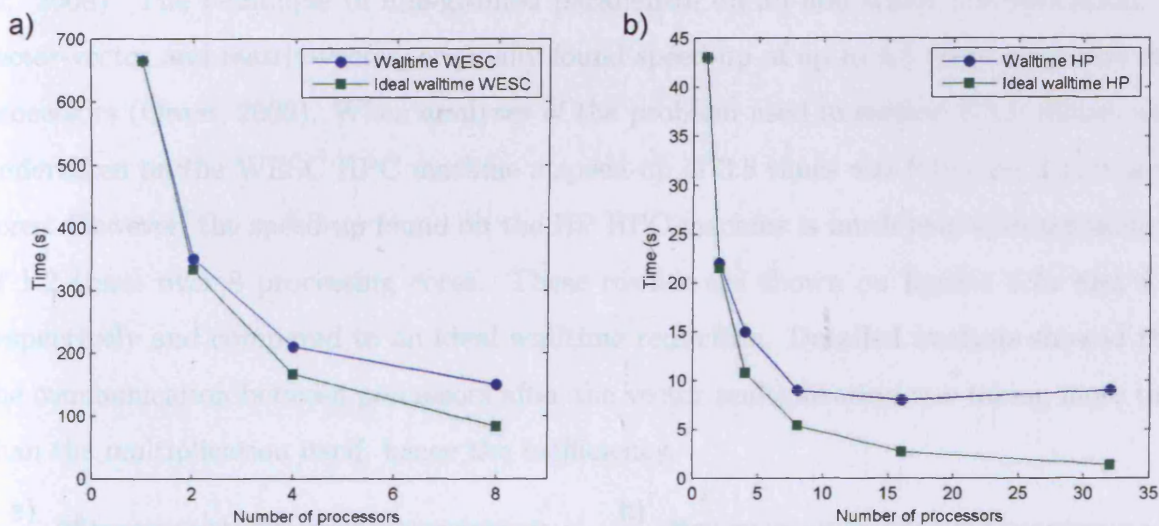
Figure 4.6. Results of the parallel implementation of the *Matrix build* section on (a) WESC and (b) HP HPC machines.

This implementation was tested on both the WESC and the HP HPC machines and the results reported in Vardon *et al.* (2008). The analysis that was run was the 100,000 finite-element problem with details given in table 4.1 and details of the HPC machines are shown on table 4.4. It was shown that this implementation works well on both parallel machines, especially when comparing to the ideal reduction, i.e. the time for a single processor divided by the number of processors. Figure 4.6 shows these results for (a) WESC and (b) HP machines. The reduction in walltime is significant on both machines, although it is noticed that above 16 processors the algorithm does not scale. This is due to

the communication times which are influenced by both latencies and bandwidth, and the comparison of communication time to calculation time, whereby the calculation is much reduced. Should an improved interconnect be used this scaling should also improve. In addition, a larger analysis would be affected comparatively less by the communication latency. It is worth remarking on the difference in execution time between the two machines, the HP machine executing in serial is faster than the fastest time with 8-cores of the WESC machine.

4.5.2 Solver parallel algorithm

Owen (2000) established a parallel implementation for the solver but it has been found that this implementation is not viable on modern HPC machines, reported in (Vardon *et al.*, 2008). The technique of fine-grained parallelism on all non-scalar multiplication, i.e. vector-vector and matrix-vector, originally found speed-up of up to 4.5 times when run on 8 processors (Owen, 2000). When analyses of the problem used in section 4.5.1, above, were undertaken on the WESC HPC machine a speed-up of 3.5 times was found on 8 processing cores. However, the speed-up found on the HP HPC machine is much less, with a maximum of 1.2 times over 8 processing cores. These results are shown on figures 4.7a and 4.7b respectively and compared to an ideal walltime reduction. Detailed analysis showed that the communication between processors after the vector multiplication was taking more time than the multiplication itself, hence the inefficiency.
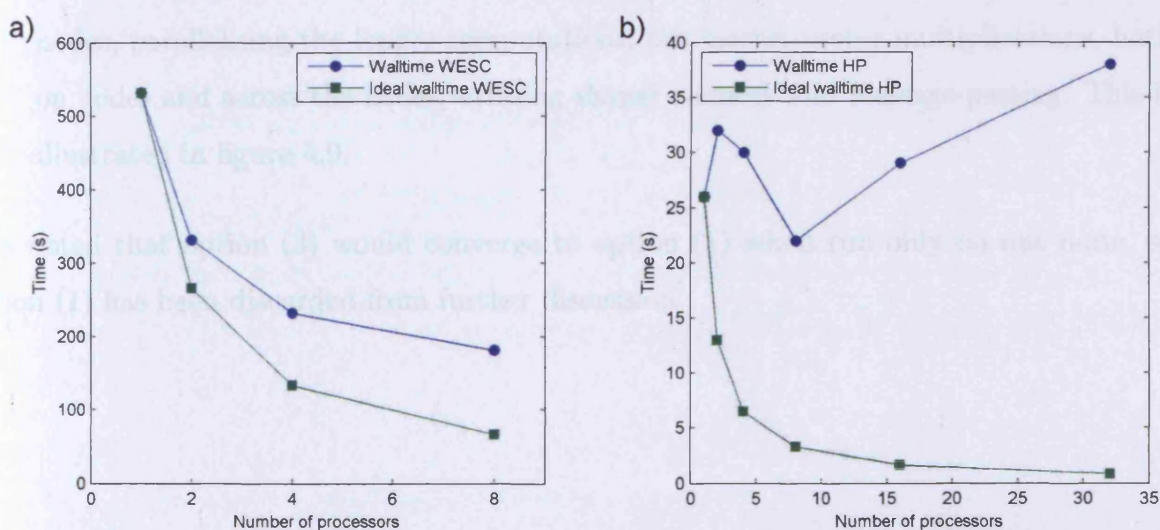
Figure 4.7. Results of the parallel implementation of the *Iterative Solver* section on (a) WESC and (b) HP HPC machines.

The considerations taken in developing this new parallelisation were that the solver must be portable and some consideration must be given to future HPC machine architecture developments. It was noted that the HPC machines that were available were utilising commodity processors and were a hybrid style and that for small scale modelling work it is convenient to use desktop computers. This work concentrates on larger scale analyses and is designed for the hybrid commodity processor based machines, but acknowledges that in the future it could be transferred to desktop computers when multi-core architectures including fast interconnects are common. The solutions that were considered are:

i. **Shared memory** - Removing all message-passing and hence communication time. This is likely to increase parallel performance. The restriction of such a scheme on commodity based HPC machines is that the number of processing cores available is commonly less than 8.

ii. **Overlapping communication with computation** - This approach can be implemented for the BiCG algorithm so that communication and computation can be carried out at the same time. Figure 4.8 illustrates this via a section of pseudocode. The communication of q_i is overlapped with the computation of $\tilde{q}_i$ and the communication of $\tilde{q}_i$ is overlapped with the computation of α_i, x_i and r_i.

iii. **Multi-level parallelism** - The proposed algorithm reflects the hybrid architecture, parallelising the shorter computations, the vector-vector operations, on shared memory nodes, parallelising the longer computations, the matrix-vector multiplications, both on nodes and across the nodes, utilising shared memory and message-passing. This is illustrated in figure 4.9.

It is noted that option (3) would converge to option (1) when run only on one node, so option (1) has been discarded from further discussion.

$$
\begin{aligned}
&\textit{threads on a single processor} \\
&\quad \textit{thread 1} \qquad\qquad\qquad \textit{thread 2} \\
&\qquad\quad . \qquad\qquad\qquad\qquad\quad . \\
&\qquad\quad . \qquad\qquad\qquad\qquad\quad . \\
&\qquad\quad . \qquad\qquad\qquad\qquad\quad . \\
&q_i = A p_i \qquad\qquad\qquad\qquad\; . \\
&\tilde{q}_i = A \tilde{p}_i \qquad\qquad \textit{send and recieve } q_i \\
&\quad \textit{syncronise across processors} \\
&\alpha_i = \rho_{i-1}/\tilde{p}_i^T q_i \qquad \textit{send and recieve } \tilde{q}_i \\
&x_i = x_{i-1} + \alpha_i p_i \qquad\qquad\quad . \\
&r_i = r_{i-1} + \alpha_i q_i \qquad\qquad\quad . \\
&\quad \textit{syncronise across processors} \\
&\tilde{r}_i = \tilde{r}_{i-1} + \alpha_i \tilde{q}_i \qquad\qquad\quad . \\
&\qquad\quad . \qquad\qquad\qquad\qquad\quad . \\
&\qquad\quad . \qquad\qquad\qquad\qquad\quad .
\end{aligned}
$$

Figure 4.8. Pseudocode of multi-threading, overlapping communication with computation.

$$
\begin{aligned}
&\textit{threads on processor 1} \qquad\quad \textit{threads on processor n} \\
&\textit{thread 1} \qquad \textit{thread n} \qquad\quad \textit{thread 1} \qquad \textit{thread n} \\
&\quad . \qquad\qquad . \qquad\qquad\qquad . \qquad\qquad . \\
&\quad . \qquad\qquad . \qquad\qquad\qquad . \qquad\qquad . \\
&\quad . \qquad\qquad . \qquad\qquad\qquad . \qquad\qquad .
\end{aligned}
$$

matrix - vector multiplication across all threads/processors

e.g. $q_i = A p_i$

communication across processors

vector-vector operation	vector-vector multiplication
across threads on single processor	across threads on single processor
e.g. $\alpha_i = \rho_{i-1}/\tilde{p}_i^T q_i$	e.g. $\alpha_i = \rho_{i-1}/\tilde{p}_j^T q_i$

Figure 4.9. Section of pseudocode illustrating using a multi-level parallelism.

4.5.2.1   Overlapping communication with computation

This technique may be in opposition to normal serial optimising techniques where combining loops inline to undertake more calculation per loop cycle aids performance. Therefore this technique must be compared to the inlined version of the algorithm and it is likely to be slower running on a single processor. White and Bova (1999) state that although conceptually there is no reason why communication cannot be overlapped with computation in a standard MPI implementation, none of the implementations tested by them were able to do this. However, Mao et al. (2006) suggest that using a multi-threaded model, with a thread for computation, such an overlap can be achieved.

Determining which vectors can be passed overlapping with calculation times relies on careful analysis of the algorithm, shown in figure 4.2, as to where the variable is next used. In addition, care must be taken to ensure that other variables that are required are not waiting to be communicated. Figure 4.10 shows the peusdocode of the BiCG algorithm with the key calculation components, for iterations greater that one, i.e. the majority of time spent in the solver. The calculations and communications have been identified and possible overlaps shown. The horizontal lines represent stages where all communication must be completed before the calculation can begin. Where the calculation results are required in the next step, e.g. α_i, no overlap is possible and communication follows calculation. In addition, the algorithm has been slightly reordered so that more overlaps are possible. It is clear from the figure that a relatively even amount of calculation and communication events will occur. Therefore knowledge of the amount of time that both communication and calculation will take is critical to evaluate the possible performance gain, including whether all or some operations should be parallelised. A theoretical analysis can be carried out, in section 4.6.3.1, to determine suitable implementations.

4.5.2.2   Multi-level parallelism

The implementation of the multi-level parallelisation in the BiCG solver is shown in figure 4.11 for the full pseudocode. The nine vector-vector operations are shown to be only formed in parallel on shared-memory nodes and the two matrix-vector multiplications are shown to be undertaken in parallel over both shared-memory nodes and across nodes, using distributed memory.

Pseudocode	Communication	Overlap
for $i = .., 2, ...$		
$\quad$ solve $M^T \tilde{z}_{i-1} = \tilde{r}_{i-1}$	x_{i-1}	
$\quad$ solve $M z_{i-1} = r_{i-1}$	$\tilde{r}_{i-1}$	
$\quad \rho_{i-1} = z_{i-1}^T \tilde{r}_{i-1}$	r_{i-1}	
	ρ_{i-1}	
$\quad \beta_{i-1} = \rho_{i-1}/\rho_{i-2}$		
$\quad p_i = z_{i-1} + \beta_{i-1} p_{i-1}$		
$\quad \tilde{p}_i = \tilde{z}_{i-1} + \beta_{i-1}\tilde{p}_{i-1}$	p_i	
$\quad q_i = A p_i$	$\tilde{p}_i$	
$\quad \tilde{q}_i = A\tilde{p}_i$	q_i	
$\quad \alpha_i = \rho_{i-1}/\tilde{p}_i^T q_i$		
	α_i	
$\quad \tilde{r}_i = \tilde{r}_{i-1} + \alpha_i \tilde{q}_i$		
$\quad r_i = r_{i-1} + \alpha_i q_i$	$\tilde{r}_i$	
$\quad x_i = x_{i-1} + \alpha_i p_i$	r_i	
end		

Figure 4.10. Pseudocode of BiCG solver including details of overlapping communication with computation.

Pseudocode	Shared memory parallel	Distributed memory parallel
Compute $r_0 = b - Ax_0$ for an initial guess x_0		
Choose $\tilde{r}_0 \ (\tilde{r}_0 = r_0)$		
for $i = 1, 2, ...$		
$\quad$ solve $M z_{i-1} = r_{i-1}$		
$\quad$ solve $M^T \tilde{z}_{i-1} = \tilde{r}_{i-1}$		
$\quad \rho_{i-1} = z_{i-1}^T \tilde{r}_{i-1}$		
$\quad$ **if** $\rho_{i-1} = 0$ then method fails		
$\quad$ **if** $i = 1$		
$\quad\quad p_i = z_{i-1}$		
$\quad\quad \tilde{p}_i = \tilde{z}_{i-1}$		
$\quad$ **else**		
$\quad\quad \beta_{i-1} = \rho_{i-1}/\rho_{i-2}$		
$\quad\quad p_i = z_{i-1} + \beta_{i-1} p_{i-1}$		
$\quad\quad \tilde{p}_i = \tilde{z}_{i-1} + \beta_{i-1}\tilde{p}_{i-1}$		
$\quad$ **end if**		
$\quad q_i = A p_i$		
$\quad \tilde{q}_i = A\tilde{p}_i$		
$\quad \alpha_i = \rho_{i-1}/\tilde{p}_i^T q_i$		
$\quad x_i = x_{i-1} + \alpha_i p_i$		
$\quad r_i = r_{i-1} + \alpha_i q_i$		
$\quad \tilde{r}_i = \tilde{r}_{i-1} + \alpha_i \tilde{q}_i$		
end		

Figure 4.11. Pseudocode of BiCG solver including details of multi-level parallelism.

4.6 Performance

In this section approximate theoretical performances and also practical analysis are compared to see how a technique performs for a given problem or hardware. The validity of the techniques can then be seen and the impact of future developments considered. It is worth noting that to give a useful comparison the algorithms must be compared with the *best* serial algorithm, not the same algorithm run in serial (Kumar and Gupta, 1994). This is certainly the case as the interest lies in the best time performance, not merely how the computer is performing in parallel. The resultant comparisons are, however, likely to show lower performance using this method.

4.6.1 Scalability / numerics used

For analyses of computational performance, two metrics commonly used are: speed-up S_n and efficiency E_n, for n number of processing cores. These are defined as;

$$S_n = \frac{T_1}{T_n} \tag{4.2}$$

$$E_n = \frac{S_n}{n} \tag{4.3}$$

where, in this study, T_1 is the walltime of the best serial computation and T_n is the time taken for a parallel computation with n processing cores (Kumar and Gupta, 1994).

4.6.2 Benchmarks for computational analysis

To enable the comparison of computational implementations a benchmark simulation has been established. This has been discretised into a number of different elements. The purpose of this is to establish patterns in the performance of the computations and not an investigation into the results, however the problem considered is representative of a typical analysis undertaken in this study. This benchmark has been defined in more detail in section 4.2.

4.6.3 Theoretical analysis of the algorithm performance

A theoretical analysis of the computational times is initially presented, followed by an analysis of the performance of the algorithms on various HPC machines. Results are

presented for the two most modern HPC machines that access was available for, i.e. Merlin and Raptor, whose general description can be found in table 4.4.

The times taken for the computation and communication times are predicted here. The calculations have been designed to be simple and easy to understand and give a general impression as to whether the approaches are likely to provide useful speed-up and efficiencies prior to implementation and testing. There are a number of performance models that can be used to model performance of message-passing, e.g. Hockney, LogP (Pješivac-Grbović *et al.*, 2007). In this case a Hockney model is used (Hockney, 1994) to predict the time taken for a message to be passed. Other models may be more complex and sophisticated, but this is used for simplicity. It is worth noting that the bandwidth and latencies achieved can be largely affected by the size of message that is being passed (Pješivac-Grbović *et al.*, 2007), which has been included in their performance model but is not been considered here for simplicity. This means that the communication times discussed here are likely to be an underestimate.

The approach taken estimates the time taken for the sections of computation, assuming that a processor can maintain maximum efficiency. The time for the calculations can be approximated as;

$$T_{calc} = n_{calcs} / (F_p \times n_{proc})$$
$$T_{calc} = n_{calcs} / (F_p \times n_{proc}) \tag{4.4}$$

where T_{calc} is the time taken, in seconds, for the calculation to be undertaken, n_{calcs} is the number of individual calculations, or specifically additions or multiplications, that need to be undertaken, F_p are the floating point operations per second on an individual processor and n_{proc} are the number of processors. and the time taken for communications can be approximated, using the Hockney performance model, as;

$$T_{com} = D/B_w + L \tag{4.5}$$

where T_{com} is the time taken, in seconds, for the communication, D is the amount of data in bytes, B_w is the bandwidth and L is the latency involved in a communication.

4.6.3.1   Overlapping communication with computation.

In this analysis the following calculations and considerations are considered, 9 vector-vector multiplications and 2 matrix-vector multiplications with communication undertaken whenever any of these calculations are undertaken in parallel. Two cases are considered, one with 100,000 finite-elements and the other with 500,000 finite-elements as defined in table 4.1.

The analysis is first undertaken for Raptor. The vector-vector multiplications in the 100,000 element problem could theoretically be completed in $0.036ms$ or $36\mu s$ and the matrix-vector multiplications undertaken in $3.3ms$ on a single processing core. For communication times, either a real number or a real vector had to be communicated. Again for the 100,000 element problem, assuming maximum bandwidth and zero latency the vectors could be communicated in $6.4ms$ between two cores and the real numbers in virtually no time. The amount of data to be transferred to and from each core remains constant, although the total amount of data increases which may saturate the shared bus. Also, there will be latency so realistically total communication time will increase for more cores. Table 4.5 shows the results of calculations for both Raptor and Merlin and for both 100,000 and 500,000 element simulations. It should be remembered from section 4.3.2 that the BiCG solver implemented in this work has nine vector-vector operations and two matrix-vector multiplications.

Machine	Raptor		Merlin	
Number of elements	100,000	500,000	100,000	500,000
Vector-vector operation	$0.036ms$	$0.19ms$	$0.031ms$	$0.03ms$
Matrix-vector multiplication	$3.1ms$	$16.3ms$	$2.7ms$	$14.2ms$
Communication of vector	$6.4ms$	$33.6ms$	$0.318ms$	$1.6ms$

Table 4.5. Theoretical minimum times for various aspects of the solver.

While slightly unrealistic and certainly an underestimation, these calculations reveal some interesting factors: i) it is not worth overlapping a vector communication with a vector-vector multiply as the communication will take longer than the serial calculation, ii) there is scope to overlap vector communication with matrix-vector multiplies, iii) the times are small and hence factors such as memory access and other architecture dependant factors are likely to affect the time. Therefore, the vector-vector operations should not be parallelised when using a message-passing parallelisation with both the HPC machines considered.

Reliance of overlapping communication with the longest calculation times, the matrix-vector multiplications, relies on the algorithm being able to be manipulated in this manner. In the case of the BiCG solver, only a single vector communication could be masked in this manner. Consequently only a single vector-vector operation would be able to be parallelised without taking more time and only two communication operations would be masked. This represents a theoretical time saving of 0.6% for two cores. This method is not likely to be able to increase the performance of the solver by any significant amount in comparison with normal MPI and therefore is not considered further.

4.6.3.2 Multi-level parallelism, coarse/fine grained.

Each of the 9 vector-vector multiplications are calculated to be carried out over the number of threads used. This is likely to be the number of cores that are available with access to the same memory. For Raptor there are four cores that can access the same memory and with Merlin, eight. There is likely to be some effects due to accessing the memory across the shared bus by many cores, but this is not taken into account in this analysis. No communication time has been included for these operations.

The matrix-vector multiplication has been calculated based on the number of cores being used and also the number of nodes. Communication time is added based upon the number of nodes used.

Initial calculations indicate that this method would have potential. Therefore a more reasonable approach has been taken including latencies and non-peak calculation times to try and gain more a reasonable representation of reality. To allow for sustained performance

instead of peak a factor of 1.4, determined from values quoted in the TOP500 (TOP500, August 2008), is included in the calculation times and a latency of 0.2 ms for Raptor and 0.01 ms for Merlin is used. The results are shown on figure 4.12 for (a) Merlin and (b) Raptor for a 100,000 element simulation.
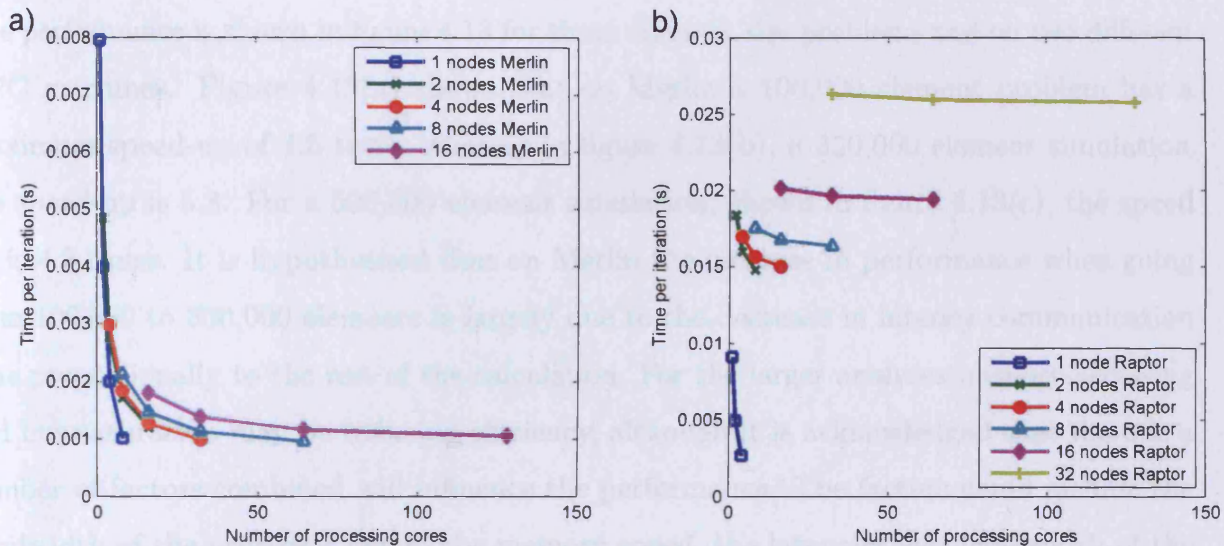
Figure 4.12. Estimates of computational time for a single iteration of the *Iterative solver* for (a) Merlin and (b) Raptor.

For Raptor this method only works theoretically for a single node, whereby as soon as message-passing is used the analysis becomes inefficient. However, the communication times predicted here are likely to be less conservative than the calculation times, which may be many times more conservative. Therefore this will be tested to see if this is the case. The proportionally lower communication times predicted on Merlin have the consequence that for the 100,000 element simulation an 8-noded, 8-threaded solution is the fastest.

These simple calculations illustrate that parallel implementations are critically dependent upon the hardware that is used. In this case it is shown that theoretically the communication times are the bottleneck to the performance of the code and that by using an HPC machine, which has a fast communication speed compared to calculation speed, good efficiency and time increases can be found.

4.6.4 Analysis of the implemented algorithm

Implementation of the proposed algorithm has only been carried out for the multi-level parallelisation option due to the conclusion from the theoretical section that *overlapping communication with computation* would not offer any scalable speed-up.

The performance is shown in figure 4.13 for three different size problems and on two different HPC machines. Figure 4.13(a) shows that on Merlin a 100,000 element problem has a maximum speed-up of 4.5 times whereas in figure 4.13(b), a 350,000 element simulation, the speed-up is 5.8. For a 500,000 element simulation, shown in figure 4.13(c), the speed up is 4.2 times. It is hypothesised that on Merlin the increase in performance when going from 100,000 to 350,000 elements is largely due to the decrease in latency communication time proportionally to the rest of the calculation. For the larger analyses memory accessing and bus saturation may be reducing efficiency, although it is acknowledged that there is a number of factors combined will influence the performance. The factors could include the bandwidth of the processor bus to the memory speed, the latencies and bandwidth of the interconnect and the size and speed of all parts of the memory structure. It is noted on figures 4.13(b) and (c) the efficiency of moving from 1 to 2 cores on a single node is much higher than moving from 4 to 8 cores. However, there are still speed increases by using all cores on the node, compared with using less, albeit with a lower efficiency. Unexpectedly, it is shown on figure 4.13(b) that by increasing the amount of nodes and using the same overall amount of processing cores, the time is reduced. The opposite was expected as a larger overhead is encountered from message-passing than multithreading. However, it is more complex in figure 4.13(c), where a certain amount of repeatable unevenness is found. On Raptor the maximum speed-ups remain largely constant at approximately 3 times. In figure 4.13(d) it is seen that on a single node a 3.3 times speed-up on 4 processing cores is achieved. However, when moving to more nodes the overhead attached to message-passing is too great and this then increases with the amount of nodes. This overhead is also reduced for larger amounts of elements on Raptor, noting the proportionally smaller gaps between nodes on figure 4.13(e) and (f) than figure 4.13(d).
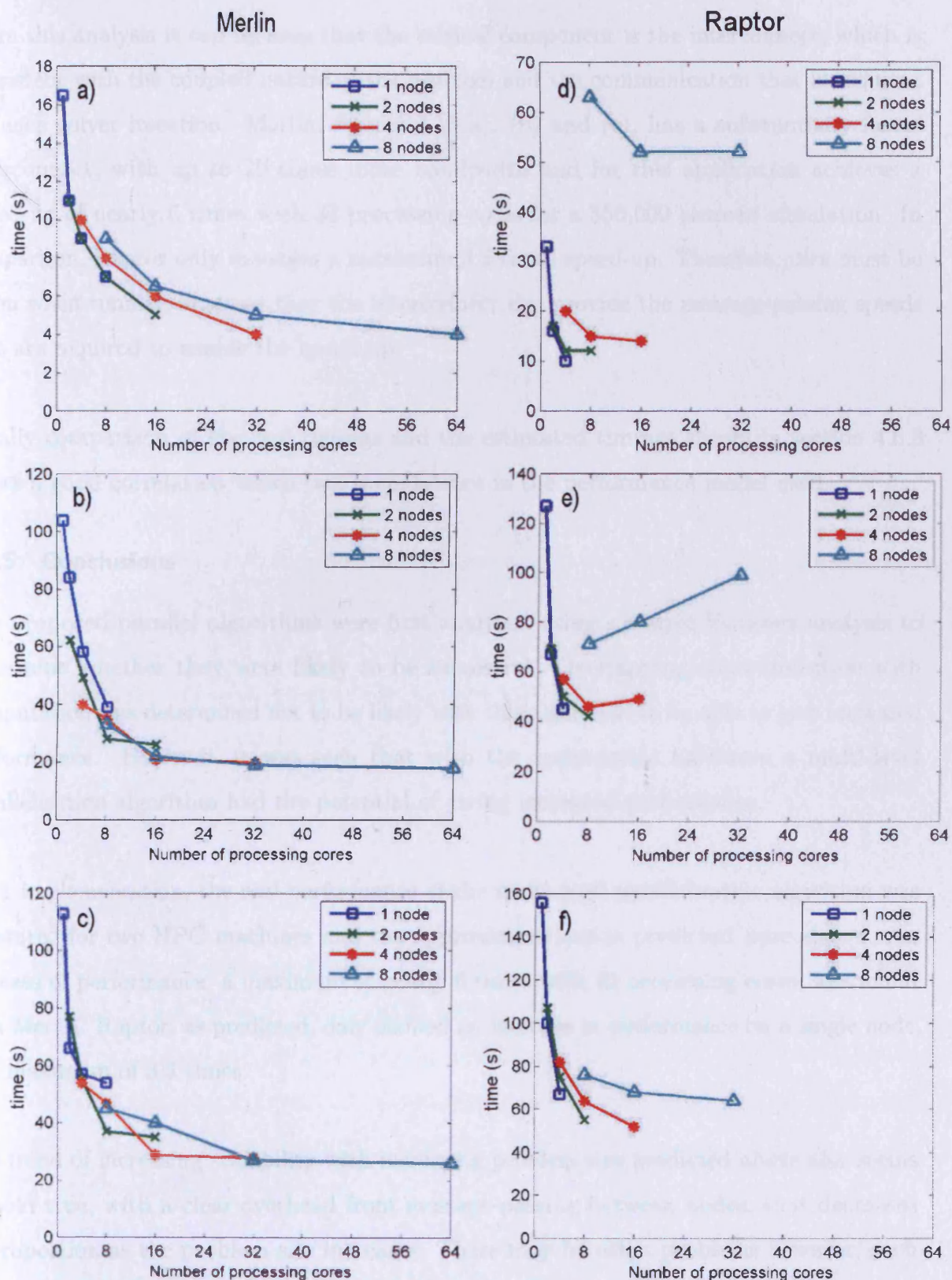
Figure 4.13. Results for two HPC machines with various sized problems. Results (a),(b) and (c) are undertaken on Merlin and have 100,000, 350,000 and 500,000 elements respectively. Results (d), (e) and (f) are undertaken on Raptor.

From this analysis it can be seen that the critical component is the interconnect, which is consistent with the coupled nature of the problem and the communication that is required for each solver iteration. Merlin, figures 4.13(a), (b) and (c), has a substantially faster interconnect, with up to 20 times more bandwidth and for this application achieves a speed-up of nearly 6 times with 32 processing cores for a 350,000 element simulation. In comparison, Raptor only manages a maximum 3.3 times speed-up. Therefore, care must be taken when running analyses that the interconnect can provide the message-passing speeds that are required to enable the speed-up.

Finally comparison of the real timings and the estimated timings shown in section 4.6.3 shows a good correlation which builds confidence in the performance model used.

4.6.5 Conclusions

The proposed parallel algorithms were first analysed using a simple Hockney analysis to determine whether they were likely to be successful. Overlapping communication with computation was determined not to be likely with this algorithm to be able to give increased performance. However, it was seen that with the appropriate hardware a multi-level parallelisation algorithm had the potential of giving increased performance.

After implementation, the real performance of the multi-level parallelisation algorithm was measured for two HPC machines and the approximate trends predicted were shown. An increase of performance, a maximum of nearly 6 times with 32 processing cores, was found with Merlin. Raptor, as predicted, only showed an increase in performance on a single node, of a maximum of 3.3 times.

The trend of increasing scalability with increasing problem size predicted above also seems to hold true, with a clear overhead from message-passing between nodes, that decreases in proportion as the problem size increases. There may be other problems however, such as memory storage and increased bus traffic, for large problem sizes that is indicated by performance tailing off for increasing on-node cores.

4.7 Pre-/Post-processing

While undertaking the analyses is the most demanding in terms of computational effort, attention must be taken in pre and post-processing. Pre-processing is all the work that is undertaken prior to the analysis, including setting up geometry, applying initial and boundary conditions and mesh generation. Post-processing is the process of taking analysis results and turning them into something recognisable. This may be aimed at others in the scientific community or for communicating complex ideas easily to lay-people. It is important to undertake appropriate techniques to enable efficient and useful pre- and post-processing.

4.7.1 Pre-processing

For simple analyses, such as one-dimensional small samples, the problem set-up and the finite-element discretisation may be undertaken manually. For more complicated geometries software that is able to draw the geometric domain and then convert this automatically into a finite-element mesh is required. In this case a software that has full three-dimensional drawing capability and can separate lines, surfaces and volumes, is able to hold information on these entities and then turn this into a finite-element mesh is required. A program that is able to undertake this task is GiD (GiD, 2006). In this study COMPASS has been integrated with GiD to allow efficient pre-processing.

4.7.2 Post-processing

There are many visualisation techniques, from simple graphs tracking a process over time, at a specific location, to three-dimensional stereoscopic visualisations with colour-maps representing processes. Including many processes on the same plot is difficult and hence multiple plots measuring different processes simultaneously are required. Finite-elements implicitly estimate the solution over the whole volume by calculating a numerical estimation at nodes or Gauss-points. This means that unless a node or gauss-point coincides with a point of interest interpolation must be carried out. This may be done by a computer which uses the finite-element solutions to estimate a full three-dimensional solution. It is this solution that is presented in contour plots or similar. Again the same software, GiD, has been used to undertake post-processing.

Finally, an active stereoscopic projector is available at the Geoenvironmental Research Centre (GRC), Cardiff University, to allow a user to see the results in full three-dimensions. This allows complex information to be able to seen and understood easily. This is a powerful tool in aiding complex model understanding. While this tool cannot be used in a standard document it can be invaluable in finding the salient information to provide in two-dimensional form with trends and anomalies being easily spotted. The system includes a stereoscopic workstation, a Christie Digital Mirage projector and an Active Stereo Wall. The user views the images with the use of LCD shutter glasses.

4.8 Conclusion

In this chapter the computational formulation and algorithms of the numerical formulation have been considered with particular reference to large-scale spatial and temporal analyses. The analyses that are undertaken are analysed in terms of the calculations required and the time taken to undertake them. A number of serial optimisations are presented saving approximately 30% of the runtime.

High Performance Computing is shown to have the potential to be able to reduce analysis times further, and a brief discussion of HPC techniques and hardware available is presented, both for current technology and trends so that future developments can be predicted. It was found that most HPC architectures that are being implemented today are formed of many small shared memory nodes, with up to 8 processing cores each, named in this work, hybrid architecture. Therefore, they are neither distributed or shared memory. In addition it was stated that programming paradigms suitable for both shared and distributed memory exist and these may be used together on hybrid architectures.

A new parallel formulation has been proposed, for both the matrix-build and the iterative solver sections of the code. The matrix build section is easily parallelised and is efficient on both historical and modern parallel HPC machines. An existing parallel implementation for the iterative solver was examined and was found to work well on a historical HPC machine but was inefficient on modern machines. A new parallelisation technique was proposed using fine-grained multi-threaded parallelism on single shared-memory nodes and coarse-grained message-passing parallelism across distributed memory nodes. It was shown theoretically

and experimentally that this hybrid modelling strategy can provide significant speed-up for an iterative Krylov sub-space solver. This is contemporary with current architectures and the trend of increasing the number of cores seems set to continue and as such scalability is likely to increase, removing more message-passing. An almost 6 times speed-up was found, although 32 cores were required to do this.

The numerical processor has been fully integrated with a pre- and post-processor. This enables complex geometries and conditions, especially in three-dimensions, to be accurately discretised and the results more easily visualised. It also allows simulation results to be more easily interrogated and understood.

The ability to handle large, three-dimensional, complex geometries and undertake these analyses in reasonable time allows more realistic simulations, such as the simulations considered in this thesis, to be undertaken that otherwise would be beyond computing capabilities.

4.9 References

Barrett, R., Berry, M., Chan, T.F., Demmel, J., Donato, J., Dongara, J., Eijkhout, V., Pozo, R., Romine, C., Van der Vorst, H., (1995) *Templates for the solution of linear systems: building blocks for iterative methods*, John Wiley Press, New York.

Demmel, J., Hoemmen, M.F., Mohiyuddin, M., Yelick, K..A., (2007) *Avoiding Communication in Computing Krylov Subspaces*, EECS Department, University of California, Berkeley, Technical Report No. UCB/EECS-2007-123.

Duff, I.S., van der Vorst, H.A., (1999) *Developments and trends in the parallel solution of Linear Systems*, CERFACS, Technical Report TR/PA/99/10.

Flynn, M., (1972) "Some computer organizations and their effectiveness", *IEEE Transactions on Computers*, **C-21**(9), 948-960.

Fox, G.C., (1992) "Lessons from Massively Parallel Applications on Message Passing Computers", *Compcon Spring '92. Thirty-Seventh IEEE Computer Society International Conference, Digest of Papers*, San Francisco, USA.

GiD, (2006) "GiD The personal pre and post processor", [WWW] <URL:http://gid.cimne. upc.es/> [Accessed 30th August 2008]

Graham, S.L., Snir, M., Patterson, C.A., editors, (2004) *Getting up to speed: The Future of Supercomputing.* National Research Council, National Academies Press, USA.

Hockney, R., (1994) "The communication challenge for MPP: Intel Paragon and Meiko CS-2", *Parallel Computing*, **20**(3):389398.

Intel (2006) *White paper - Intel architecture and silicon cadence. The catalyst for industry innovation.*

Kumar, V., Gupta, A., (1994) "Analyzing Scalability of Parallel Algorithms and Architectures", *Journal of Parallel and Distributed Computing*, **22**(3):379-391.

Mao, J., Song, B., Wu, Y., Yang, G., (2006) "Overlapping communication and computation in MPI by multithreading", *Proceedings of the 2006 International Conference on Parallel & Distributed Processing Techniques and Applications (PDPTA'06)*, 52-57, Las Vegas, USA.

Melhuish, T.A., (2004) "An investigation of the three-dimensional thermo/hydro/mechanical behaviour of large scale in-situ experiments", *PhD Thesis*, Cardiff University, Cardiff.

Message Passing Interface, (2009) [WWW] <URL:http://www-unix.mcs.anl.gov/mpi/> [Accessed 3rd March 2009]

Netzer, R.H.B., Miller, B.P., (1992) "What are race conditions? Some issues and formalization", *In ACM Letters on Programming Languages and Systems*, **1**(1).

OpenMP (2009) "The OpenMP API Specification for Parallel Programming" [WWW] <URL:http://openmp. org/wp/> [Accessed 3rd March 2009]

Owen, D.H., (2000) *Preconditioned parallel iterative solution methods for coupled finite element analyses*, PhD Thesis, University of Wales, Cardiff.

Pješivac-Grbović, J., Angskun, T., Bosilca, G., Fagg, G.E., Dongarra, E.G.J.J., (2007) "Performance Analysis of MPI Collective Operations", *Cluster Computing*, **10**(2):127-143.

Quarteroni, A., Valli, A., (1999) *Domain Decomposition Methods for Partial Differential Equations*, Oxford University Press, UK.

Rybarczyk, A., Szulc, M., Wencel, J., (2006) "The CCM based implementation of the parallel variant of BiCG algorithm suitable for massively parallel computing", *Proceedings of the International Symposium on Parallel Computing in Electrical Engineering (PARELEC'06)*, Bialystok, Poland.

TOP500, (2008) "TOP 500 Supercomputer sites", [WWW] <URL:http://www.top500.org/> [Accessed 25th August 2008]

van de Steen, A.J., Dongarra, J.J., (1996) *Overview of Recent Supercomputers*, 6th edition, Technical report, Department of Computer Science, University of Tennessee, Knoxville.

Vardon, P.J., Cleall, P.J., Thomas, H.R., Philp, R., (2008) "Three-Dimensional Field-Scale Coupled Thermo-Hydro-Mechanical Modelling", *Proceedings of the 12th International Conference of the International Association for Computer Methods and Advances in Geomechanics*, Goa, India.

Vardon, P.J., Banicescu, I., Cleall, P.J., Thomas, H.R., Philp, R.N., (2009) "Coupled thermo-hydro-mechanical modelling: A new parallel approach", *Accepted for publication in the PDSEC-09 workshop of the IPDPS 2009 conference*, Rome.

White, J.B., Bova, S.W., (1999) "Where's the overlap?", *Proceedings of Third MPI Developer's and User's Conference, MPIDC '99*, Atlanta, USA.

Yang, L.T., Brent, R.P., (2002) "The improved BiCG method for large and sparse linear systems on parallel distributed memory architectures", *Proceedings of the International Parallel and Distributed Processing Symposium (IPDPS'02)*, Florida, USA.

5

Material Model Development and Validation

5.1 Introduction

In chapter 3, theoretical and numerical formulations have been presented for a model to describe the THM behaviour of a deformable porous media. In the context of this study the materials considered for use as buffer materials in nuclear waste repositories are typically described as bentonites. These montmorillonite rich clays have a number of specific properties that make them particularly suitable for consideration as candidate buffer materials. Some of these properties are the swelling and self-healing nature, the low permeability and the ability to sorb radio-nuclides. While these properties may be beneficial, they must also be taken into consideration in any numerical simulation. Of particular concern is the ability of compacted bentonite to swell, effectively altering the micro-structure and reducing the pores in which moisture transport can occur (Thomas *et al.*, 2003). This has previously been considered via modification of the hydraulic conductivity, formulated as a function of both degree of saturation and free-water and has been used with some success in cases where infiltration is slow (Thomas *et al.*, 2003; Thomas *et al.*, 2009). Both small-scale and

large-scale tests on bentonitic materials similar to those proposed as buffer materials for nuclear-waste have been and continue to be undertaken, a number of which are detailed in chapter 2.

Highly-compacted bentonite pellets are also used as part of the design concept for nuclear waste repositories. They are installed in the gap between the bentonite blocks and the host rock and designed to swell and become largely homogenous with the remainder of the buffer. However, this behaviour is likely to have a strong effect on the hydraulic behaviour, with the pellets initially presenting little barrier to flow and then decreasing in permeability with hydration and time.

From the behaviour of a number of tests it can be seen that the behaviour of bentonite changes over time. It is hypothesised in this chapter that this occurs due to micro-structural changes. This chapter firstly in section 5.2 analyses the structure of bentonitic materials via existing literature including identification of time-dependent processes. To represent this behaviour an approach is proposed and formulated in section 5.3. These model developments are then tested against small-scale experimental work in section 5.4 examining various aspects of the approach compared to a 'standard' approach.

The behaviour of highly-compacted bentonite pellets is investigated in section 5.5 including identification of properties that are likely to affect the hydraulic conductivity. A material model is proposed in section 5.6 and formulated into a hydraulic conductivity relationship. A field-scale test including both compacted bentonite and pelletised bentonite is simulated in section 5.7 including both the proposed material models. Concluding remarks are given in section 5.8.

5.2 Structure of compacted bentonite

Bentonite is a material composed of clay minerals from the smectite group. The smectite group is characterised by a three-layer crystalline structure and a tendancy to swell when exposed to water. A wide variety of bentonites exist and consequently the physical and chemical properties vary. Commercial bentonites contain typically at least 60% smectite, (usually more than 70%) the remainder being made up of other clay minerals such as kaolinite and non-clay minerals such as quartz and calcite. In addition the most common

smectite clay mineral in commercial bentonites is montmorillonite. A feature of bentonites is that some of the Silicon and Aluminium cations within the clay lattice are replaced by lower valency cations such as sodium and calcium, termed exchangeable cations, which have a large impact in terms of physical and chemical properties. For example sodium bentonites, where the dominant exchangeable cations are sodium, have high swelling characteristics whereas calcium bentonites exhibit much lower swelling potentials and often are termed non-swelling bentonites (Inglethorpe et al., 1993). The MX-80 bentonite considered for much of this study is an industrial Wyoming montmorillonite-dominated sodium bentonite and the FEBEX bentonite considered in one of the experiments simulated has been found to have similar cation exchange properties although a slightly lower percentage of sodium cations (Huertas et al., 2001; Lloret et al., 2003).

The pore-structure of compacted bentonite has been investigated in a variety of ways, e.g. Mercury Intrusion Porosimetry (MIP) and Electron Microscopy. A sample MIP test result is shown in figure 5.1 (Delage et al., 2006) where the quantity of mercury entering pores is measured in terms of both cumulative and density functions. The amount of mercury intruded into the sample void ratio is recorded against the entrance pore radius for the cumulative measurement and the density function is the rate of change of the intruded void ratio to the log of the entrance pore size. It can be clearly seen by the bi-modal shape that there are two main pore-size groups, a larger pore size, approximately $2\mu m$, termed a macro-pore and a smaller pore size, approximately $0.01\mu m$, termed a micro-pore. The exact sizes and distributions are affected by the water content, compaction and load-path history (Delage et al., 2006).

A conceptual representation of the structure of montmorillonite, which dominates bentonites composition, is presented in figure 5.2 illustrating the multilevel structure. The structure of the compacted bentonite is also affected by the fact that it is manufactured and not in a virgin state as may be found in a naturally formed bentonite deposit. The process of manufacture typically begins with a dried and ground bentonite powder. This powder is then wetted to the required water content and compacted, generally in layers, to the required density. Consequently, the compacted bentonite cannot be considered to be a mature material with the micro-structure in a final state. Moreover the micro-structure is likely to be affected by the manufacture process itself.
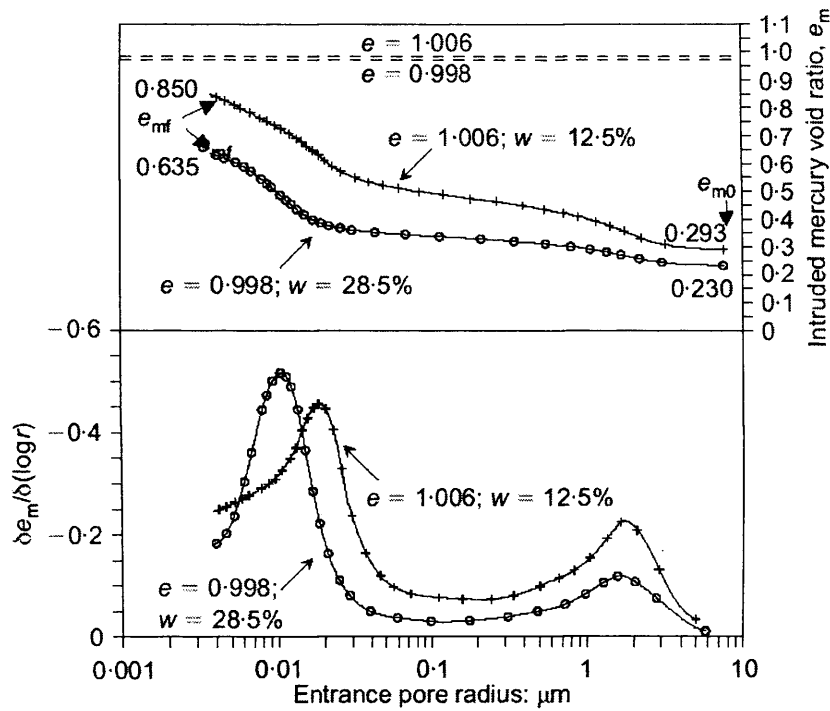
Figure 5.1. MIP test results for MX-80 sample compacted and aged for 1 day with $e = 0.998 - 1.006$ (Delage *et al.*, 2006).

5.2.1 Properties affecting hydraulic conductivity

The two main properties affecting the hydraulic conductivity are i) the amount of voids that are available for flow of water, the free voids and ii) the degree of saturation of these voids, i.e. the amount by volume of the voids that contain fluid not air (Fredlund and Rahardjo, 1993; Thomas *et al.*, 2003). The hydraulic behaviour of a soil that does not swell is well understood, as the proportion of free voids does not change (e.g. ISO 17313, 2004; ISO 11275, 2004). Pusch *et al.* (1990) stated that a proportion of the water that is held in the soil may be absorbed into the micro-structure and be unavailable for flow. If this material is restrained from expanding then the swelling particles would reduce the size of the macro-pores where flow can easily occur (Pusch, 1998). The real uncertainty that exists is how a soil moves from an equilibrium hydration state to another after wetting. The first equilibrium state is defined as where, say, 94% of the water is contained within the micro-structure and 6% in the macrostructure. After wetting a non-equilibrium state occurs where free water has just moved into the soil and the new water is occupying the macropores as free water. The soil state then moves onto another new equilibrium state where, say, 94% of the existing water and the additional water has been absorbed into the microsturcture.
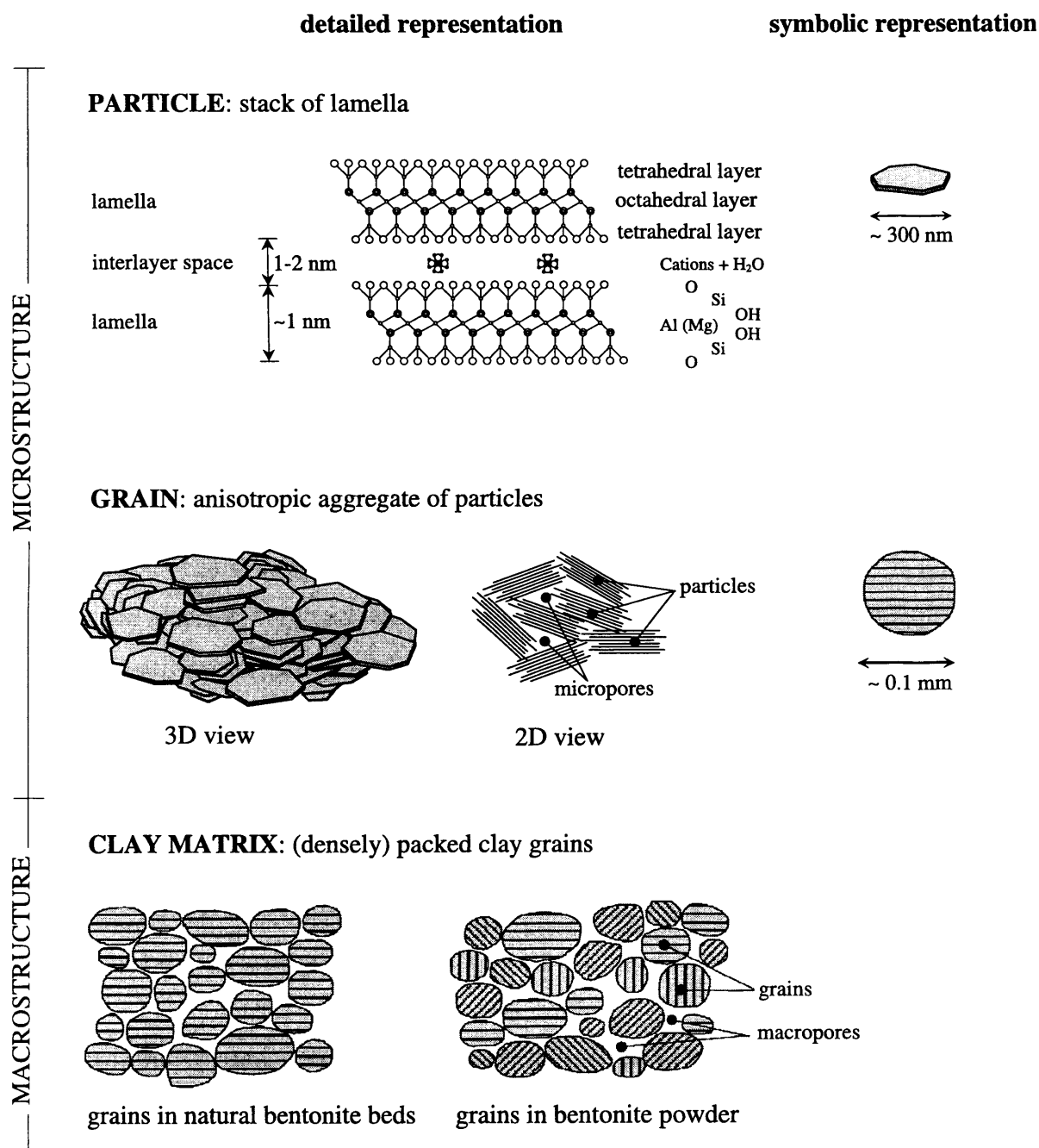
Figure 5.2. The structure of montmorillonite on different scales (Kröhn, 2003 after Karnland, 1998; Pusch and Young, 2003).

5.2.2 Time-dependent processes

A number of processes and conditions have been established as being time-dependent and involved in changing the pore-structure, these include:

- **Equilibrium** - A proportion of the free water that enters a sample of bentonite may be absorbed into the micro-structure and this process will take a period of time. It has been suggested by Tang and Cui (2005) that this could take a number of months and Dueck (2008) found that a 10g sample of MX-80 bentonite could take 10 days for the swelling pressure to fully develop.

- **Availability of water** - It should be noted that for the micro-structure to swell water must be available to it, either from the surrounding materials or from within the bentonite material itself.

- **Aging** - Bentonite manufactured from powder as described above changes over time. This process has been observed, using MIP tests, by Delage *et al.* (2006). It was found that such changes were still occurring after 90 days, which was the maximum time of the data published. The quantity of larger entry pores (the macro-pores) was found to reduce over time after production.

- **Preferential flowpaths / piping** - If flow rates are locally high then erosion of material may take place and a preferential flowpath may develop, be maintained, or increase.

- **Confined or unconfined state** - The degree to which the soil is confined will affect the pore structure after swelling. If well confined the macro-pores will be greatly reduced, but if largely unconfined the overall volume of the soil will increase and the macro-pores will remain more intact (Cui *et al.*, 2008).

Kröhn (2003) provided some commentary on the variety of conceptual models and how the flow and absorption rates may affect the micro-structure and went on to propose a vapour diffusion model. Figure 5.3 shows Kröhn's conceptual diagrams on how the comparative flow and hydration rate may affect the absorbed water content in the bentonite. A source of water is shown to be found in the Excavated Disturbed Zone (EDZ) of the host rock. The location of the canister is shown schematically with the initial solid-pore-interlayer spaces

shown adjacent to the canister as areas representing the total volumes. Adjacent to the hydration source the post-hydration situation is shown in the same manner. The interlayer space is the micro-pores where the water can be absorbed during the hydration and swelling process. In figure 5.3a low hydration-to-flow behaviour is shown, whereby the pores in which flow can occur are only negligibly modified by the flow process and in figure 5.3b the interlayer space has swollen restricting the pores available for flow. The vapour diffusion model proposed by Kröhn has been disregarded in this study due to experimental results that suggest that changes in injection pressure change the rate of hydration (Pusch and Yong, 2003). Pusch and Yong describe the saturation of bentonite by means of three special boundary states, one saturated via a water vapour source (RH=100%), one saturated with zero pore-water pressure and the third under pressurised condition. They discuss the key differences in the micro-structural changes in these states. In essence, Kröhn's conceptual diagrams match with the two ends of these states whereby the *very low hydration to flow rate* diagram describes the pressurised boundary condition and the *very high hydration to flow rate* diagram describes the water vapour boundary condition. However, Pusch and Yong (2003) conclude that the process is 'diffusion-like' and pressure does not affect the 'hydration rate to more than a few centimetres depth'. It is interesting to note that experimental evidence from large scale tests such as the Prototype Repository Project suggest that where water pressure is maintained high saturation occurs relatively quickly and where pressure is low saturation is not reached (Goudarzi and Johannesson, 2007), such differing responses cannot be described purely by diffusion. Ideally, the range of these states should be able to be described by a single approach governing the behaviour of the material and the changes in the micro-structure.
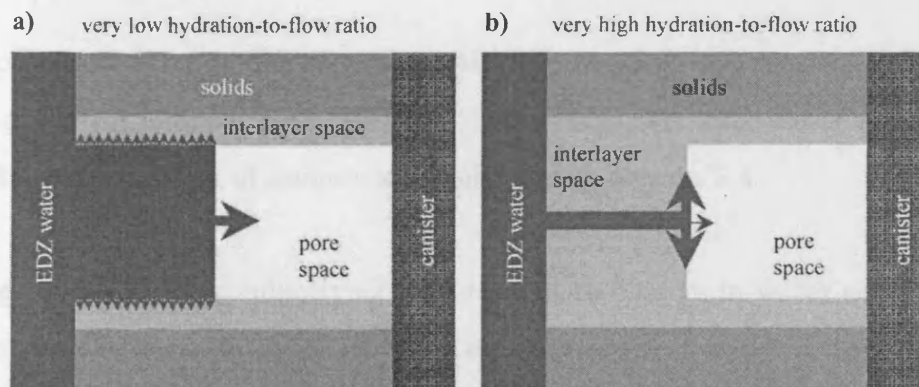
Figure 5.3. Effect of the hydration rate on the water distribution in the bentonite (Kröhn, 2003).

5.3 Proposed approach for representing the hydration of bentonite materials

Based on the preceding discussion in section 5.2 a conceptual model for the hydration of a confined sample allowing for changing absorption over time is presented in this section. The following assumptions have been made:

- The water that is available for flow is contained within the macro-pores.

- The volume of water absorbed into the micro-structure is equivalent in volume to the loss of macro-pore.

- The sample starts in an equilibrium condition.

The macro-pores are the largest of the pores and as such present the least barrier to flow, due to the lower capillary forces that they generate. In addition, the larger pores are more likely to be connected in the soil structure to form a network that moisture can flow through. The concept of free-water and absorbed water is discussed in some detail by Pusch (1998) and Thomas *et al.* (2003). If fully confined, the overall volume of the sample must remain the same. In addition the volume of solids and total volume of pores is assumed to be the same, although the formation of gels within the micro-structure (Pusch, 1998) makes this assumption more complex and it is acknowledged that further work should be undertaken to gain more detailed knowledge of this process. Here, it is assumed that the sample manufacturing processes has occurred at some time prior to the experimentation. This would indicate that the majority of time-dependent processes would have been complete.

It is hypothesised that at full saturation the macro-pores are restricted from reducing any further due to internal pore-pressures developing; this hypothesis will be tested via consideration of a number of numerical simulations in section 5.4.

The change of hydraulic conductivity with respect to change in water content, degree-of-saturation or relative humidity needs to be established. It is useful at this point to define two possible states of the soil. The first, *state* **A**, where the soil is in equilibrium and the second, *state* **B**, where the soil is not in equilibrium and time-dependent change is occurring. This is shown in figure 5.4 where an idealised soil model is shown. The *Initial* and *Final*

states shown for both wetting and drying are in *state* **A** whereas *state* **B** is the state between these two points starting with the *Instantaneous change* and finishing when the final state is reached.

The change of hydraulic conductivity can be considered to take two forms:

i. An instantaneous change, *state **A** to state **B*** - the instantaneous change in hydraulic conductivity related to the water content. The is analogous to the change in hydraulic conductivity due to a change in water content in a non-swelling soil. It is shown in figure 5.4 that this is due to the change in the amount of free water.

ii. A transient change, *state **B** to state **A*** - the time-dependent change in hydraulic conductivity that would occur if water is allowed to absorb into or desorb from the micro-structure.

For this model the instantaneous change is determined as the change that would occur if the material was not a swelling material which has been determined experimentally. This relationship is based upon the free-water filling the available voids and being available for flow to occur. The equilibrium position is that a proportion of the volume of voids that are water saturated are in the micro-structure and not available for flow. A time-dependency needs to be established. Initially, due to a lack of experimental data, a linear relationship is proposed whereby the proportion of water absorbed increases at a rate proportional to saturation until the maximum is reached.

Idealised soil model

Proportional to total volume

Proportional to total voids
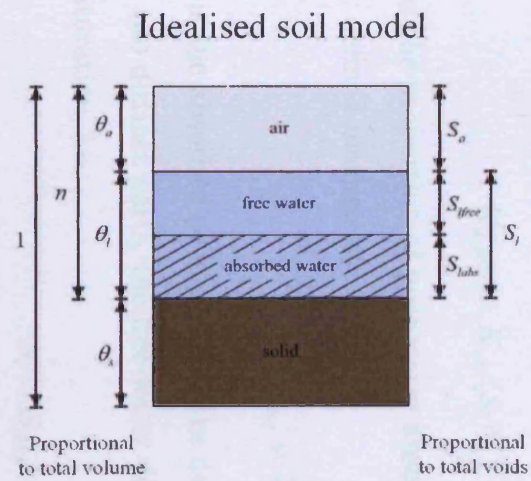
S_l degree of saturation of liquid

θ_l volumetric water content

n porosity

$\theta_s + \theta_l + \theta_a = 1$

$n = \theta_l + \theta_a$

$S_l = \dfrac{\theta_l}{n}$

$S_l = S_{lfree} + S_{labs}$

$\omega_{abs} = \dfrac{S_{labs}}{S_l}$

Wetting

Initial state (**A**)

Instantaneous change

Intermediate state (**B**)

Temporal change

Final state (**A**)

water added to macro-pores

water absorbed into microstructure

$\omega_{abs} = \omega_{abs}^{max}$

$\omega_{abs} < \omega_{abs}^{max}$

$\omega_{abs} = \omega_{abs}^{max}$

Drying

Initial state (**A**)

Instantaneous change

Intermediate state (**B**)

Temporal change

Final state (**A**)

water removed from macro-pores

water desorbed to macro-pores

$\omega_{abs} = \omega_{abs}^{max}$

$\omega_{abs} > \omega_{abs}^{max}$

$\omega_{abs} = \omega_{abs}^{max}$
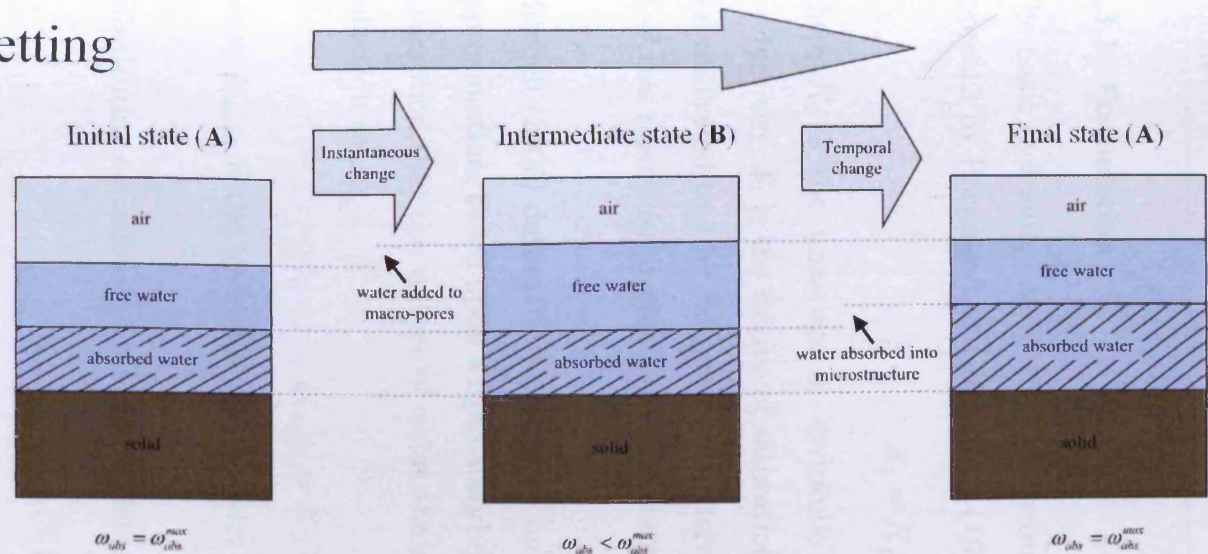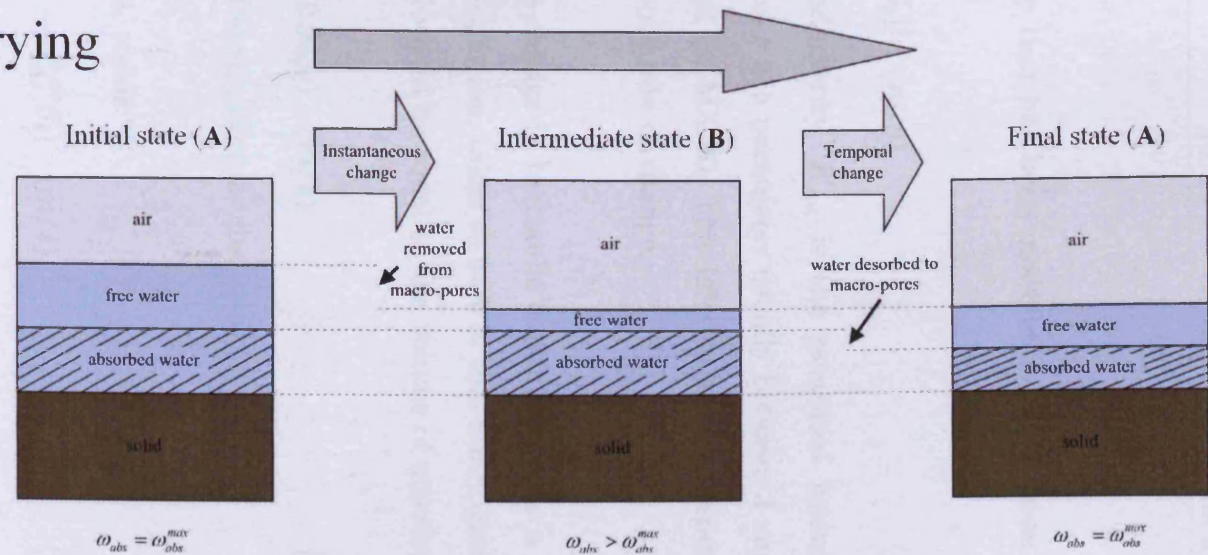
Figure 5.4. Conceptual model of wetting and drying behaviour of a swelling soil.

5.3.1 Formulation

The basic hydraulic conductivity relationship that has been modified is based upon the approach by Börgesson and Hernelind (1999):

$$K_l = K_{sat}(S_l)^\delta \quad (m/s) \tag{5.1}$$

where K_l is the unsaturated hydraulic conductivity, K_{sat} is the saturated hydraulic conductivity, S_l is the degree of saturation and δ is a parameter usually between 3 and 10 and calibrated to 3 by Börgesson and Hernelind for MX-80. The differential with respect to S_l of this relationship provides the instantaneous rate of change.

Mitchell (2002) defined a relationship for the change in hydraulic conductivity, as a first approximation, based upon a fixed absorbed proportion, taken as 94% in that study, and the assumption that the volume of water absorbed would be equal to the volume of macro-pore reduction as:

$$K_{swell} = K_l(1 - 0.94S_l) \quad (m/s) \tag{5.2}$$

where K_{swell} is the hydraulic conductivity at the equilibrium condition.

Substituting equation (5.1) into equation (5.2), yields:

$$K_{swell} = K_{sat}(S_l)^\delta(1 - \omega_{abs}^{max}S_l) \quad (m/s) \tag{5.3}$$

where ω_{abs}^{max} is the maximum proportion of pore-water absorbed. However, allowing for time-dependent processes in the absorption of pore-water into the micro-pores equation (5.3) can be re-written as:

$$K_{swell} = K_{sat}(S_l)^\delta(1 - \omega_{abs}S_l) \quad (m/s) \tag{5.4}$$

where ω_{abs} is the proportion of pore-water absorbed, is time-dependent and varies between 0 and ω_{abs}^{max}, defined mathematically as:

$$\omega_{abs} = \frac{S_{labs}}{S_l} \tag{5.5}$$

where S_{labs} is the absorbed proportion of the degree of saturation, S_l, which is shown to be made up of two distinct parts, the free-water degree of saturation, S_{lfree}, and the absorbed degree of saturation, i.e.:

$$S_l = S_{labs} + S_{lfree} \tag{5.6}$$

The full range of hydraulic conductivities available depending on the percentage of pore-water absorbed and the degree of saturation is schematically shown in figure 5.5.
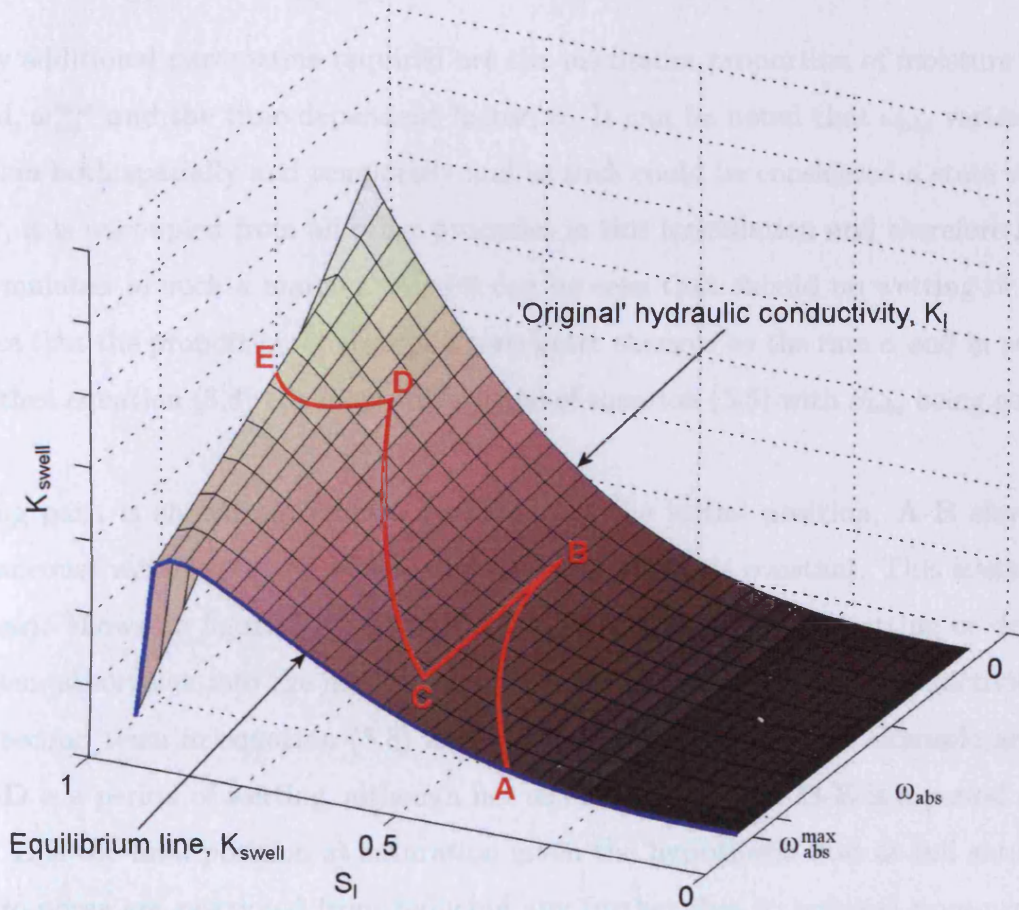
Figure 5.5. Proposed hydraulic conductivity, K_{swell}, against degree of saturation, S_l and percentage of moisture absorbed, ω_{abs}.

The equilibrium line, as defined by K_{swell} in equation (5.2) is the lower limit to hydraulic conductivity at any moisture content and K_l from equation (5.1) is the upper limit.

To address the temporal change between these two limits a function is proposed for the absorption rate as:

$$\frac{\partial S_{labs}}{\partial t} = S_l \cdot \alpha \qquad where \quad S_{labs} < \omega_{abs}^{max} S_l \quad \& \quad S_l < 1 \tag{5.7a}$$

$$\frac{\partial S_{labs}}{\partial t} = 0 \qquad where \quad S_{labs} = \omega_{abs}^{max} S_l \quad or \quad S_l = 1 \tag{5.7b}$$

This is applied to the proportion of absorbed pore-water such that the following equation can be formed:

$$\frac{\partial \omega_{abs}}{\partial t} = \alpha - \frac{S_{labs}}{S_l^2}\frac{\partial S_l}{\partial t} \qquad where \quad \omega_{abs} < \omega_{abs}^{max} \quad \& \quad S_l < 1 \qquad (5.8)$$

The only additional parameters required are the maximum proportion of moisture that is absorbed, ω_{abs}^{max} and the time-dependent factor, α. It can be noted that ω_{abs} varies across the domain both spatially and temporally and as such could be considered a state variable. However, it is uncoupled from all other processes in this formulation and therefore has not been formulated in such a manner. Also it can be seen that should no wetting or drying take place that the proportion of absorbed pore-water changes by the rate α and in addition, if $\alpha = 0$ then equation (5.8) is a simple differential of equation (5.5) with S_{labs} being constant.

A wetting path is shown on figure 5.5 where **A** is the initial position, **A-B** shows fast (instantaneous) wetting, i.e. S_l is increasing and S_{labs} remains constant. This is similar to the scenario shown in figure 5.3a. **B-C** is a period of time when no wetting or drying is undertaken, absorption into the micro-structure occurs and the hydraulic conductivity falls, i.e. the second term in equation (5.8) is zero. This is an the extreme example as figure 5.3b. **C-D** is a period of wetting, although not as fast as **A-B** and **D-E** is a period of slow wetting. **E** is the final position at saturation given the hypothesis that at full saturation the macro-pores are restricted from reducing any further due to internal pore-pressures developing.

5.4 Simulation of the Temperature Gradient Test

Simulation of a small scale test has been undertaken to test and calibrate this relationship. A large scale test is also undertaken at the end of section 5.5 to enable both this relationship and a relationship for pelletised bentonite, proposed in section 5.6, to be tested together.

The Temperature Gradient Test (TGT) was undertaken by CIEMAT (Villar *et al.*, 2005) and consisted of a $40cm$ long and $7cm$ in diameter sample of compacted bentonite. The samples were hydrated from the top end and in the case of the TGT heated from the bottom. Temperature and relative humidity were measured. A schematic diagram of the test is shown in figure 5.6, including the sensor locations.

70mm

400mm

Boundary Conditions
T = atmospheric (as recorded)
u_t = 1.2 MPa (after 65 hours)
impermeable before 65 hours

Sensor HR1

Boundary Conditions
Heat loss = 2.3 W/m^2/K
Impermeable

Initial Conditions
T = 25°C
u_t = -118 MPa

Sensor HR2

Sensor HR3

Boundary Conditions
T = 100°C
Impermeable
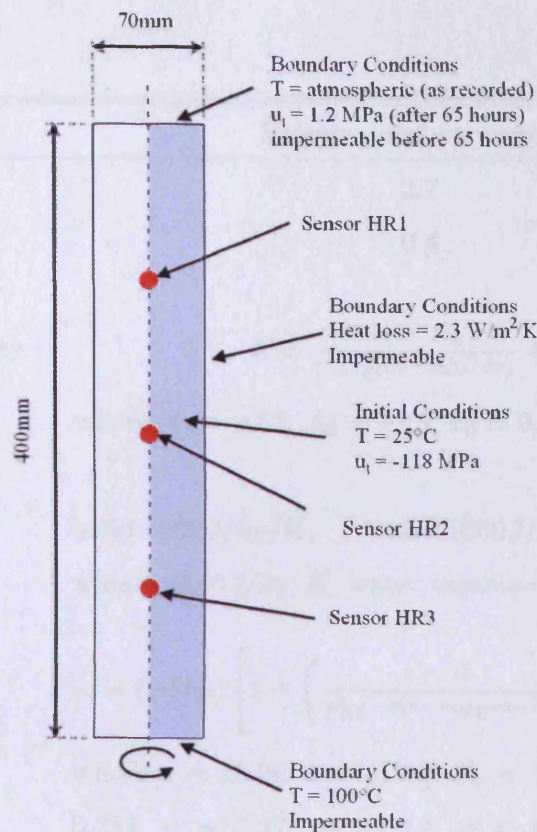
Figure 5.6. Schematic diagram of the TGT.

5.4.1 Initial and boundary conditions

In all of the simulation cases the initial and boundary conditions are as shown on figure 5.6. Specifically, the initial conditions are uniform with a temperature of $25°C$ (measured) and a pore-water pressure of $-118MPa$, converted from the measured relative humidity via the psychrometric law. At the radial boundary there is a heat loss of $2.3W/m^2/K$, calculated from the PTFE casing and foam insulation, both $15mm$ thick and having thermal conductivities of 0.25 and $0.4W/m/K$ respectively. In addition, the radial boundary is prescribed as being hydraulically impermeable. At the base of the sample the temperature is fixed at $100°C$ and is also impermeable. At the top end atmospheric temperature was maintained (and recorded) and a pore-water pressure of $1.2MPa$ applied after 65 hours and impermeable before (Villar *et al.*, 2005; THERESA, 2007) boundary conditions to reflect these conditions were applied. The material relationships and parameters are summarised in table 5.1.

Parameter	Relation and parameters
Specific gravity	2.7
Porosity	0.4
Thermal conductivity	$\lambda = \dfrac{A_1 - A_2}{1 + e^{(S_r - x_0)/(dx)}} + A_2$
	where $A_1 = 0.57$, $A_2 = 1.15$, $x_0 = 0.65$ and $dx = 0.10$
Heat capacities	solid=$800 J/kg/K$, air=$1000 J/kg/K$, liquid water=$4180 J/kg/K$, water vapour=$1870 J/kg/K$
SRWC	$w = (a+bn)\left[1 + \left(\dfrac{s}{P_0 e^{-\eta(n-n_0)} e^{-\alpha(T-T_0)}}\right)^{\frac{1}{1-\lambda_{sw}}}\right]^{-\lambda_{sw}}$
	where $a = 10.96$, $b = 41.89$, $P_0 = 12.68 MPa$, $\lambda_{sw} = 0.211$, $\eta = 7.97$, $n_0 = 0.4$, $\alpha = 0.00647 °C^{-1}$ and $T_0 = 20°C$
Hydraulic conductivity	see table 5.2

Table 5.1. Table of material parameters for the TGT, material relationships and parameters after Villar *et al.* (2005).

5.4.2 Vapour flow law

As discussed in Melhuish (2004) the Philip and de Vries approach to vapour transfer (Philip and de Vries, 1957) in high density clays results in an over prediction of drying due to temperature. In the Philip and de Vries approach the velocity of vapour is expressed as:

$$\mathbf{v_v} = \frac{D_{atms} v_v \tau_v \theta_a}{\rho_l}\left(\rho_0 \frac{\partial h}{\partial s}\right)\nabla s - \frac{D_{atms} v_v \tau_v \theta_a}{\rho_l}\left(h\frac{\partial \rho_0}{\partial T} + \rho_0 \frac{\partial h}{\partial T}\right)\nabla T \qquad (5.9)$$

Melhuish included two empirical factors into this equation to allow for some micro-structural effects yielding an expression of vapour velocity of:

$$\mathbf{v_v} = \eta_2\frac{D_{atms} v_v \tau_v \theta_a}{\rho_l}\left(\rho_0 \frac{\partial h}{\partial s}\right)\nabla s - \eta_1\frac{D_{atms} v_v \tau_v \theta_a}{\rho_l}\left(h\frac{\partial \rho_0}{\partial T} + \rho_0 \frac{\partial h}{\partial T}\right)\nabla T \qquad (5.10)$$

Melhuish utilised a small scale experiment using a temperature gradient to calibrate these

factors and showed that using the factors as $\eta_1 = 0.5$ and $\eta_2 = 1.5$ yielded improved results.

This was experimentally investigated by Singh (2007) for MX-80 and the factors were predicted as a first estimate, due to limited experimental results, as $\eta_1 = 0.17$ and $\eta_2 = 0.6$.

In this work the factors for the vapour flow law have been calibrated for the TGT test. A factor of 0.1 for both components of vapour was found to yield appropriate amounts of drying. It is noted that it is difficult to separate the moisture flow into the constitutive vapour and liquid phases and that the calibration of the vapour law will impact the prediction of the hydraulic conductivity. In this sense more experiments such as undertaken by Singh (2007) where the vapour and liquid flow can be separated, by examination of ions, should be undertaken. However, sensitivity analyses suggest that the vapour flow laws govern the initial drying that is found in the experiment and the modified hydraulic conductivity impacts most greatly on the long term behaviour of the sample. In addition, as the calibration of η_1 is close to that found experimentally and that η_2 is of less importance due to the lower magnitude of the differential some confidence is gained.

5.4.3 Analyses

A series of analyses have been undertaken and are summarised in table 5.2. The saturated hydraulic conductivities are 1.9×10^{-14} m/s, as quoted by Villar *et al.* (2005), for all but the *Analysis 2*. This simulation is shown in figure 5.7a where a saturated hydraulic conductivity of 0.5×10^{-14} m/s is used as a best attempt to calibrate for the results at the dry end of the sample. It is acknowledged that this may not be best modelling practice but has been included for completeness to show how these effects may be partially masked by numerical calibration.

Analyses 3 and 4 show the proposed approach and differ as to whether at saturation the hydraulic conductivity is fixed (equation 5.7b) or is allowed to reduce over time to equation (5.2).

All analyses utilised an axisymmetric mesh, with 100 even sized 4-noded quadrilateral isoparametric elements, which has been checked for numerical convergence, and an initial

Analysis	Hydraulic Conductivity relationship	K_{sat} value, m/s	Comments
1	equation (5.1)	1.9×10^{-14}	K_{sat} quoted by Villar *et al.*, (2005).
2	equation (5.1)	0.5×10^{-14}	Best numerical calibration of K_{sat}.
3	equation (5.4)	1.9×10^{-14}	K_{sat} quoted by Villar *et al.*, (2005). K is allowed to reduce at full saturation as equation (5.7a).
4	equation (5.4)	1.9×10^{-14}	K_{sat} quoted by Villar *et al.*, (2005). K fixed at full saturation as equations (5.7a and b).

Table 5.2. Summary of analyses carried out on TGT.

timestep of 100 seconds that was found to yield converged results. The timestep was allowed to increase and decrease depending on how readily convergence was reached. For all analyses approximately 200 timesteps were required to simulate the 3 year experiment.

Figure 5.7a shows the results of a simulation of the experiment using Börgesson and Hernelind (1999) relationship for the unsaturated hydraulic conductivity, *Analyses 1 and 2*; and figure 5.7b shows the results based on the proposed approach, *Analyses 3 and 4*.

The results show that at the 'dry' end both *Analyses 3 and 4* seem to simulate the quantitative and qualitative results well with the important aspect for long term analyses that the final gradients are reasonable. Even the calibrated *Analysis 2* which is quantitatively reasonable at the dry end shows an increased gradient that would mean longer term results would not be reasonable. At the 'wet' end the original hydraulic conductivity relationship, *Analysis 1*, and the modified relationship with fixed hydraulic conductivity at saturation, *Analysis 4*, seem to maintain a good fit with the experimental results.

At the 'dry' end of the sample the gradients of the water content with respect to space are high in the simulations. This indicates that the degree of acceptable variation away from the experimental data is much larger than at the 'wet' end. More calibration could be undertaken of the vapour laws to gain a closer match to the 'dry' end but many more experimental results would be needed to give confidence to this. Moreover, it would be useful to gain repeatable experimental results to see the inherent variability of the experimental results.

It is seen that the proposed, time-dependent relationship gives better qualitative and quantitative results. It can also be seen that the hypothesis that the hydraulic conductivities should be maintained at saturation gives improved results at the 'wet' end. Importantly the gradients of the relative humidity (and moisture content) with respect to time at the end of the analysis are much improved which gives more confidence to long term predictive simulations.

It may be possible with further detailed micro-structural analysis of the bentonite, for example with high powered x-ray or other techniques that can analyse the micro-structure at the nano-scale, to have a coupled hydro-mechanical model which deals with both the macro and micro-structure in a time-dependent manner and then utilise this data to form a similar relationship. This would be more satisfactory for coupled THM simulations, but beyond the work undertaken here.

5.4.4   Conclusions

A modified form of the hydraulic conductivity relationship has been proposed for materials where the micro-structure changes over time in response to change in degree of saturation. This is of relevance for high density swelling clays that are proposed to be used in waste isolation. A small scale experiment has been utilised to compare this relationship against a standard, non-time-dependent relationship. The nature of the results is good, with improvement in absolute values and perhaps more importantly, the temporal gradients, especially at the later stages. This gives some more confidence in longer term predictions made using numerical simulation.
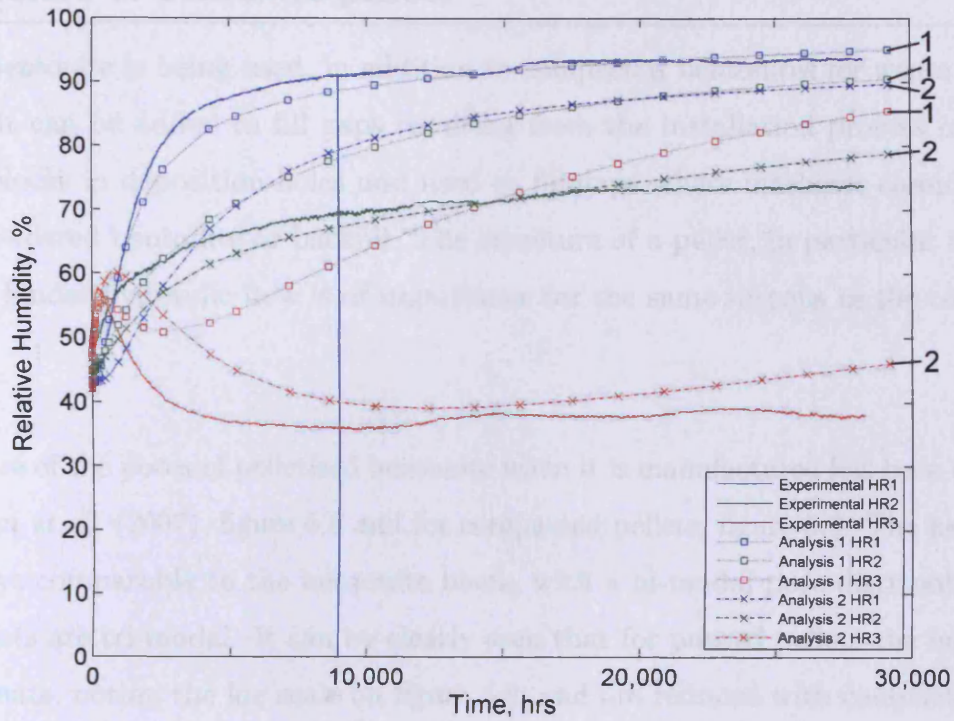
(a) Original Börgesson and Hernelind (1999) relationship, analyses 1 and 2.
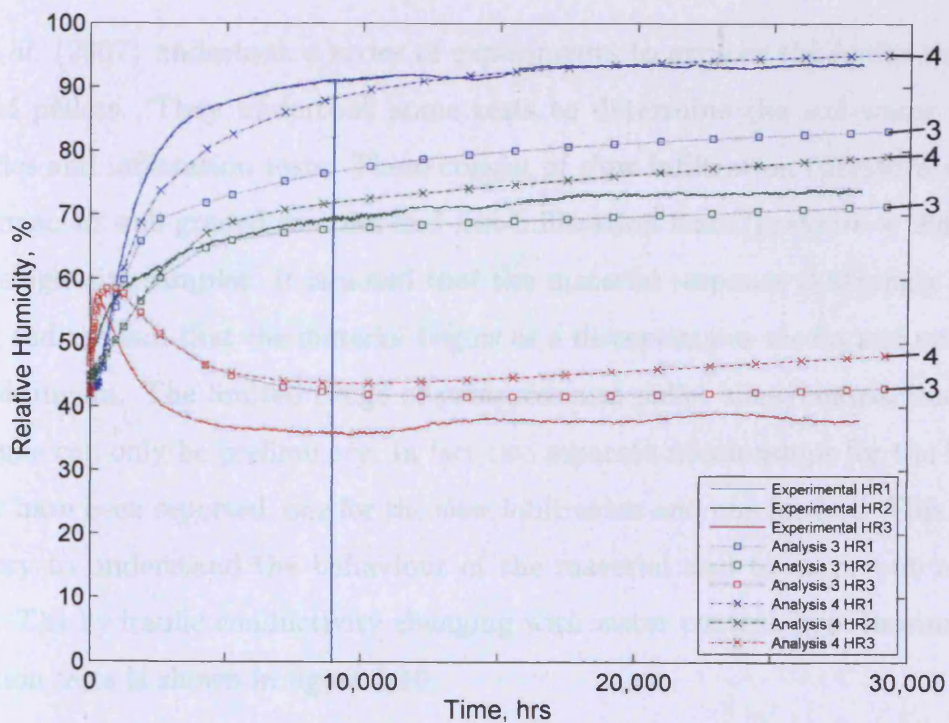
(b) Proposed relationship, analyses 3 and 4.

Figure 5.7. Experimental and numerical results from the TGT.

5.5 Structure of bentonite pellets

Pelletised bentonite is being used, in addition to compacted bentonites for waste isolation purposes. It can be added to fill gaps resulting from the installation process of placing bentonite blocks in deposition-holes and used to fill gaps where machines cannot readily compact powdered bentonite or backfill. The structure of a pellet, in particular its ability to allow or hinder hydraulic flow is of importance for the same reasons as the compacted bentonite.

The structure of the pores of pelletised bentonite when it is manufactured has been described by Hoffmann *et al.* (2007), figure 5.8 and for compacted pellets, figure 5.9. The pellet itself is qualitative comparable to the bentonite block, with a bi-modal pore distribution. The poured pellets are tri-modal. It can be clearly seen that for poured pellets the inter-pellet pores dominate, noting the log scale on figure 5.8, and are reduced with compaction. The larger pores will dominate the ability for the material to resist water flow and it is these that are most easy to change due to swelling.

Hoffman *et al.* (2007) undertook a series of experiments to explore the hydro-mechanical behaviour of pellets. They undertook some tests to determine the soil-water retention characteristics and infiltration tests. These consist of slow-infiltration (pressure $= 20kPa$) tests on compacted well-graded samples and fast-infiltration tests (pressure $= 200kPa$) on compacted single size samples. It is noted that the material response is strongly linked to the swelling and the fact that the material begins as a discontinuous media and evolves into a pseudo-continuum. The limited range of pressures and pellet sizes/compactions means that the results can only be preliminary. In fact two separate relationships for the hydraulic conductivity have been reported, one for the slow infiltration and one for fast. This is clearly unsatisfactory to understand the behaviour of the material and to carry out numerical simulations. The hydraulic conductivity changing with water content hypothesised for the fast infiltration tests is shown in figure 5.10.
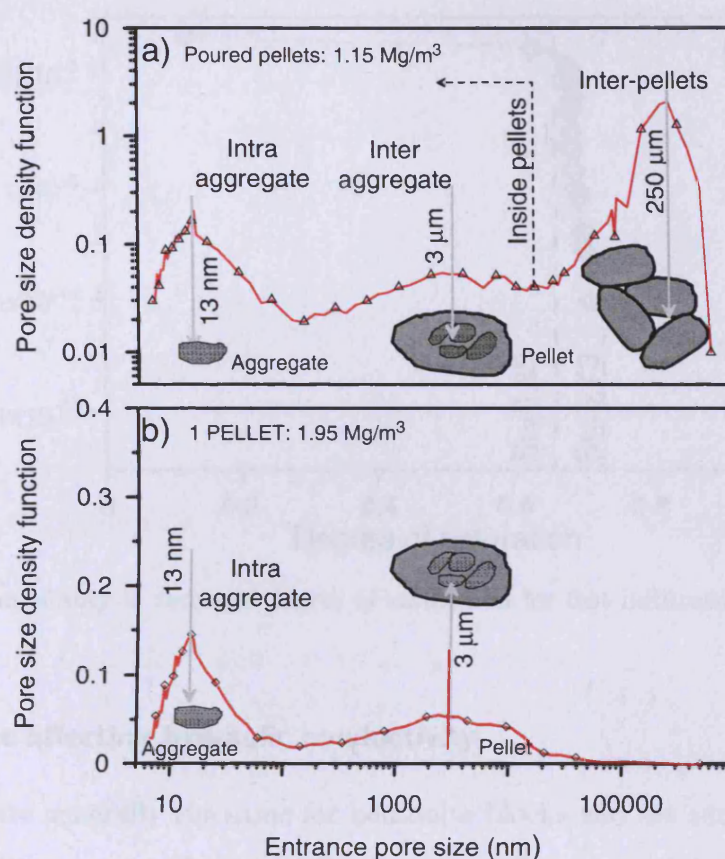
Figure 5.8. MIP results for poured pellets and the results for a single pellet (Hoffmann *et al.*, 2007).
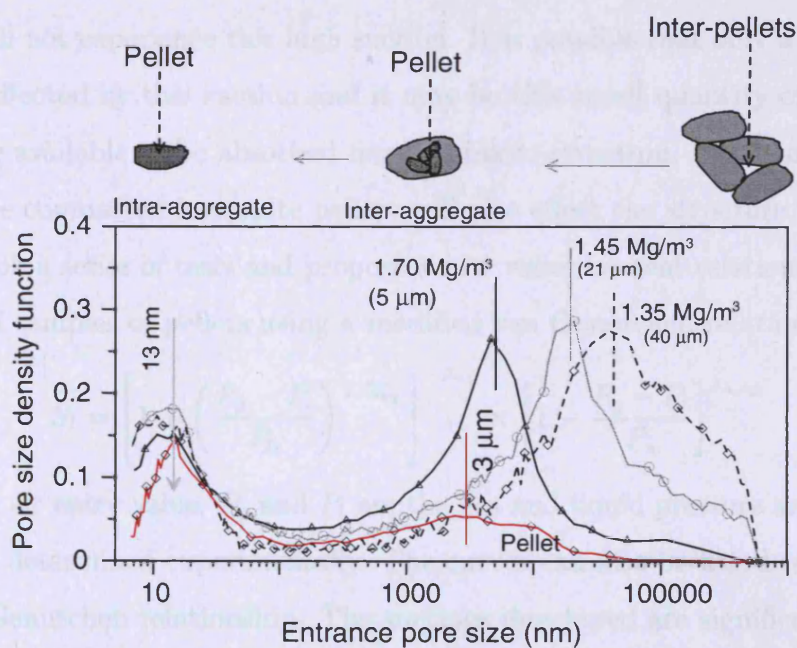
Figure 5.9. MIP results for pellets compacted to different densities, including the results for a single pellet (Hoffmann *et al.*, 2007).
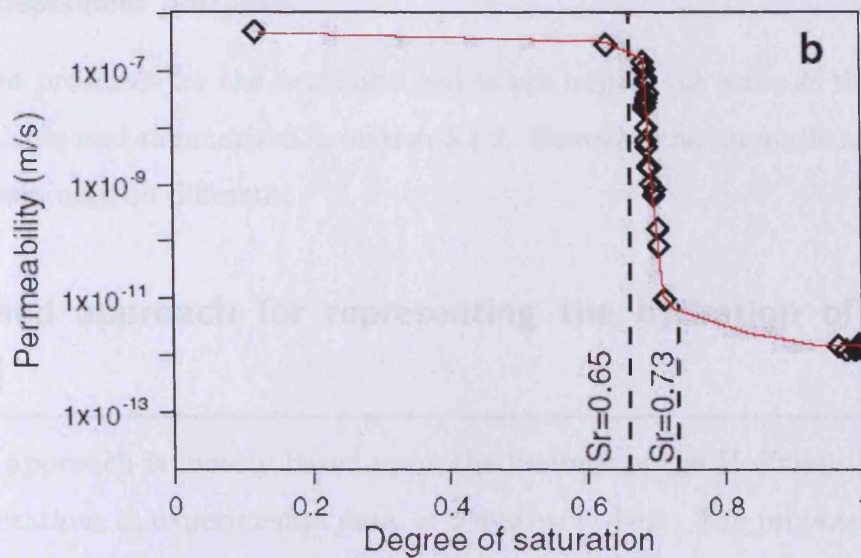
Figure 5.10. Permeability in terms of degree of saturation for fast infiltration tests (Hofmann *et al.*, 2007).

5.5.1   Properties affecting hydraulic conductivity

These properties are generally the same for bentonite blocks and are summarised in section 5.2.1. However, with poured pellets, initially the inter-pellet pores are likely to dominate the behaviour so that other pores may be neglected somewhat. In addition, the high suctions that develop in the micro-pores will not be uniform across the pore structure and a majority of the water will not experience this high suction. It is possible that only a small amount of water will be affected by this suction and it may be this small quantity of water that will interact and be available to be absorbed into the micro-structure. The compaction process used to produce compacted bentonite pellets will also effect the structure. Hoffmann *et al.* (2007) undertook a series of tests and propose a new water content relationship for different dry densities of samples of pellets using a modified van Genutchen relationship:

$$S_l = \left[1 + \left(\frac{P_g - P_l}{P_0} \right)^{\frac{1}{1-\lambda_{vg}}} \right]^{-\lambda_{vg}} \times \left[1 - \frac{P_g - P_l}{P_s} \right]^{\lambda_{s\_vg}} \tag{5.11}$$

where P_0 is the air entry value, P_g and P_l are the gas and liquid pressure and the remaining parameters are determined experimentally. The curves can also be fitted reasonably to the standard van Genutchen relationship. The suctions developed are significantly lower than of a compacted bentonite block of the same water content. It is noted that the tests are limited, undertaken on compacted samples and it is unclear whether these are single size or graded samples.

5.5.2 Time-dependent processes

Time-dependent processes for the bentonite pellets are largely the same as those identified for bentonite blocks and summarised in section 5.2.2. However, the timescale and magnitude of these processes may be different.

5.6 Proposed approach for representing the hydration of bentonite pellets

The proposed approach is loosely based upon the findings of the Hoffmann *et al.* (2007), but due to limitations in experimental data, is tentative at best. The proposed approach is based on the following main assumptions:

- The inter-pellet pores dominate the hydraulic conductivity during the saturation process.

- An initial hydraulic conductivity exists based upon the mean pellet size, pellet size distribution and compaction of the pellets.

- A final hydraulic conductivity exists which is based upon the final continuum structure.

- Only monotonic wetting paths are considered.

- The pellets behaviour is dependant upon degree-of-saturation and time.

The key differences between this approach and the approach presented for the hydraulic conductivity of bentonite blocks is that the behaviour here is characterised by the distinctly discrete material turning into a pseudo-continuum. The water for flow is likely to be held in the inter-pellet pores initially and then in the macro-pores some time into the saturation process.

Two extreme cases can be defined:

i. Rapid wetting - The sample reaches saturation very quickly, with the hydraulic conductivity remaining at the initial high value due to the existence of inter-pellet pores. After this initial rapid saturation the hydraulic conductivity progressively reduces as the pellets swell and become homogenous.

ii. Very slow wetting - The sample wets slowly and the pellets are able to swell as much as the supply of water allows. The minimum hydraulic conductivity is reached much before saturation.

In reality most wetting situations will be between these two extreme cases.

A simple model is proposed to try to capture the various aspects of the material behaviour identified above. The proposed model for hydraulic conductivity is shown schematically in figure 5.11. The key aspects are point **A** which is the minimum water content where the hydraulic conductivity changes; this is close to the initial water content. Point **B** is the minimum hydraulic conductivity. Line **1** is the slow infiltration line, showing extreme case ii, once the threshold **A** is past the conductivity reduces with water content. Any temporal effects are not noticed as the infiltration is too slow. Line **3** is the opposite situation, representing extreme case i, where infiltration happens almost instantaneously and the hydraulic conductivity reduces at saturation to the minimum. Line **2** represents the evolution of hydraulic conductivity with the degree of saturation when the hydration conditions are between the extreme cases of i and ii.
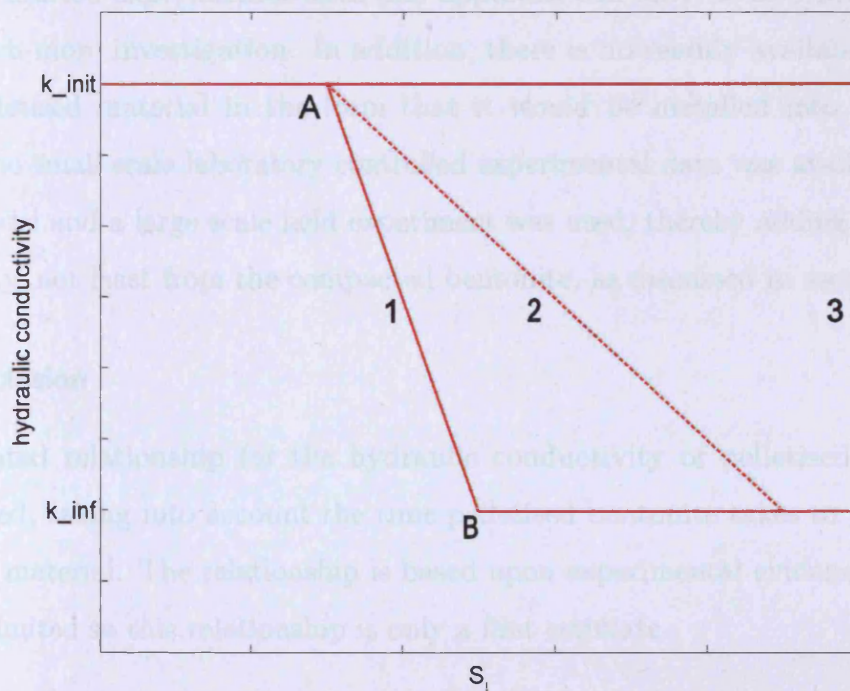
Figure 5.11. Proposed hydraulic conductivity.

5.6.1 Formulation

The formulation requires four variables only, the initial hydraulic conductivity, k_{init}, the final conductivity, k_{inf}, the degree of saturation at point **A**, $S_{l\mathbf{A}}$, and an absorption rate, coefficient β_p. The following relationship for the hydraulic conductivity of the pellets is proposed:

$$K_{pel} = k_{init} - (k_{init} - k_{inf})\omega_{pel} \qquad (5.12)$$

and can be rearranged to yield:

$$K_{pel} = (1 - \omega_{pel})k_{init} - k_{inf}\omega_{pel} \qquad (5.13)$$

The term ω_{pel} is defined to represent the influence of homogenisation on the hydraulic conductivity that has occurred, this term varies between 1 and 0. In this case, as a first estimate, a time-dependent function which governs the rate at which the homogenisation occurs is proposed:

$$\frac{\partial \omega_{pel}}{\partial t} = \beta_p \qquad where \quad S_l > S_{l\mathbf{A}} \qquad (5.14)$$

Due to very limited experimental data this approach can only be as a first estimate and requires much more investigation. In addition, there is no readily available experimental data on pelletised material in the form that it would be installed into the PRP. This means that no small scale laboratory controlled experimental data was available to test the proposed model and a large scale field experiment was used, thereby adding a large amount of uncertainty, not least from the compacted bentonite, as discussed in section 5.2.

5.6.2 Conclusion

An unsaturated relationship for the hydraulic conductivity of pelletised bentonite has been proposed, taking into account the time pelletised bentonite takes to become a more homogenous material. The relationship is based upon experimental evidence, however this evidence is limited so this relationship is only a first estimate.

5.7 Analysis of Canister Retrieval Test

Due to a lack of data from experiments considering just highly-compressed bentonite pellets, tests using both compacted bentonite and bentonite pellets have been examined. Generally these are large scale tests as pellets are used to aid the emplacement of the large bentonite blocks. Both the new hydraulic conductivity relationships found above and the original Börgesson and Hernelind (1999) relationship will be utilised.

The Canister Retrieval Test (CRT) is such a test that uses both compacted bentonite and pellets. The CRT has been performed in the Äspö Hard Rock Laboratory (HRL) in Sweden and operated by SKB. The test comprises a full size mock-up high-level nuclear-waste canister including a heater and a moisture injection system on the rock boundary, whereby the pore-water pressure can be controlled. The aim of the test was to demonstrate the recoverability of canisters after bentonite hydration. In addition, the test was used to study the field-scale THM behaviour of the buffer materials in a deposition-hole. MX-80 bentonite was used in the test and mechanical restraint used at the top of the deposition-hole as opposed to backfill. Details of the test can be found in Thorsager *et al.* (2002).

It is noted that the set-up of this deposition-hole follows the KBS-3 disposal concept and is therefore identical to that found in the PRP, with the exception of the artificial hydration system described below. Therefore this test may indicate the likely ability of the proposed material models to simulate the behaviour in the PRP.

5.7.1 Domain

An axisymmetric domain has been used due to the radial symmetry of the system. It must be noted that there was a small influence in the temperature field due to a nearby test at approximately 900 days. However, this increase was small, approximately $4°C$ at the rock surface and therefore has not been included for simplicity. The domain consists of the buffer material, including the pellets and the compacted buffer blocks, as the hydraulic boundary conditions are controlled by hydraulic mats. These mats were placed at the rock pellet interface and provided water to the buffer material at a pre-defined pressure. Temperatures have been measured at the boundary allowing the thermal boundary conditions to be defined. The domain is shown in figure 5.12.

5.7.2 Material parameters

The material parameters used, with the exception of the hydraulic conductivities described in detail in this chapter, have been summarised in table 5.3. The bentonite is MX-80, a Wyoming industrial bentonite; the material parameters are described in detail in chapter 8. The vapour flow law, described in section 5.4.2 for the Spanish bentonite used in the TGT, has been used for this test with the same parameters. The initial porosities and specific gravities have been averaged following data provided in THERESA (2008) giving the porosity as 0.36 for bentonite blocks and 0.61 for the pellets, and the specific gravity as 2.78 for both the bentonite blocks and the pellets. Thermal conductivity has been assumed the same for both pellets and bentonite blocks due to a lack of experimental data for the pellets with three linear relationships fitted to experimental data depending upon the degree-of-saturation following the approach of Melhuish (2004) and Börgesson and Hernelind (1999). A van Genutchen SWRC is fitted to experimental data following experimental work of Börgesson and Hernelind (1999) for the bentonite blocks and Hoffmann *et al.* (2007) for the pellets. The mechanical parameters are based upon experimental data and given in detail in chapter 8.

5.7.3 Initial and boundary conditions

The initial thermal conditions were as measured (THERESA, 2008, citing Goudarzi *et al.*, 2006). The initial hydraulic conditions are in general from measured results (THERESA, 2008, citing Goudarzi *et al.*, 2006) and converted into pore-water pressure via the psychrometric law. Determining the initial pore-water pressure in the pelletised bentonite region is more complex. The pellets were installed and then the remaining voids filled with water before the concrete plug was cast. Therefore the pore-water pressure would be lower than that of a region just filled with pelletised bentonite. However, as no sensors were installed in this region it is difficult to assess. A first estimate of $-1 MPa$ has been made. In addition, this region is small so this assumption should not affect the pore-water pressure distribution greatly, but will mean that the hydraulic conductivity will begin reducing as per the hydraulic conductivity relationship defined in equation (5.13).

Parameter	Relation and parameters
Specific gravity	2.78
Porosity of bentonite blocks	0.36
Porosity of bentonite pellets	0.61
Thermal conductivity	$\lambda = 0.3 \quad \text{if} \quad S_r < 0.2$ $\lambda = 0.3 + 1.5(S_r - 0.2) \quad \text{if} \quad 0.2 < S_r < 0.8$ $\lambda = 1.2 + 0.5(S_r - 0.8) \quad \text{if} \quad S_r > 0.8$
Heat capacities	solid=$800J/kg/K$, air=$1000J/kg/K$, liquid water=$4180J/kg/K$, water vapour=$1870J/kg/K$
SRWC	$\theta_l = nS_l = \theta_{res} + \dfrac{\theta_{sat} - \theta_{res}}{\left[1 + \left(\frac{1000\alpha s}{\rho_l g}\right)^b\right]^{(1-1/b)}}$ where $\theta_{res} = 0.0001$, $\theta_{sat} = n$, $\alpha = 1.25 \times 10^{-7}$ and $b = 1.75$ for the bentonite blocks and $\theta_{res} = 0.0001$, $\theta_{sat} = n$, $\alpha = 7 \times 10^{-6}$ and $b = 1.3$ for the pellets
Hydraulic conductivity	equation (5.4) for the bentonite blocks equation (5.13) for the bentonite pellets
Mechanical properties	$\kappa = 0.025$, $\lambda(0) = 0.238$, $r = 0.9$, $\beta = 1.0$, $p_c = 0.1MPa$, $p_0^* = 45MPa$, $\kappa_s = 0.075$, $\lambda_s = 0.075$, $s_0 = 500MPa$, $G = 10MPa$, $k = 0$, $M = 0.358$, $\alpha_T = 1 \times 10^{-4}K^{-1}$

Table 5.3. Table of material parameters for the CRT, material relationships and parameters after THERESA, (2008).

The temperature is fixed at the top of the concrete plug and along the rock/pellet interface at the measured values. Following the experimental conditions a heat flux is applied on the canister/buffer boundary as shown in table 5.4a and a hydraulic pressure is applied on the rock/pellet interface as shown in table 5.4b. Deformation is fixed at zero in the radial direction at the rock/pellet interface and the vertical canister/buffer boundary and fixed at zero in the vertical direction at the top of the concrete plug and the top and bottom canister/buffer interfaces. The initial and boundary conditions are illustrated in figure 5.12.

Discretised mesh

Rock edge
Boundary conditions:
   Temperature: as recorded.
   Pore-water-pressure: as applied
   Displacement: dr=0

Top of concrete
Boundary conditions:
   Temperature: 288K
   Pore-water-pressure: 0MPa
   Displacement: dz=0

Buffer material
Initial conditions:
   Temperature: 289K
   Pore-water-pressure: -50MPa
   Stress: 0MPa

Canister top
   Heat flux: As applied
   Deformation: dz=0

Canister side
   Heat flux: As applied
   Deformation: dr=0

Canister bottom
   Heat flux: As applied
   Deformation: dz=0

Pellets material
Initial conditions:
   Temperature: 289K
   Pore-water-pressure: -1MPa (first est.)
   Stress: 0MPa

Figure 5.12. Domain and mesh for simulation of the CRT, including initial and boundary conditions.

	(a)
time	Heater power
(days)	(kW)
0	0
1	0.7
18	1.7
110	2.6
375	0
376	2.6
494	0
501	2.6
684	2.1
1134	1.6
1596	1.15
1811	0
1979	2
2002	0

	(b)
time	Pore-water pressure
(days)	(MPa)
0	0
679	0
714	0.8
805	0.4
819	0.8
1598	0
1877	0

Table 5.4. Variable boundary conditions where (a) is the heater power boundary condition at the canister and (b) is the hydraulic boundary condition at rock/buffer edge, after THERESA (2008) citing Thorsager *et al.* (2002).

5.7.4 Results

The results are presented in figures 5.13a using the Börgesson and Hernelind (1999) relationship for unsaturated hydraulic conductivity for both the pellets and buffer blocks and in figure 5.13b using the proposed hydraulic conductivity relationships presented in this chapter.

In figure 5.13a it can be seen that in the numerical simulation the general trends in the short term, i.e. less than 1,000 days, correlate well with the experimental results. There are some differences in the sensors closest to the canister, i.e. W119, but this is attributed to water filling the small interior void initially; post 100 days the gradients are similar.

After 1,000 days, the gradients increase quickly in the numerical values and the sample is fully saturated at approximately 2,000 days. However, experimentally the gradients are shown to reduce and reach an almost steady-state by about 1,800 days. This is particularly noticeable in the sensors located where the bentonite saturated slowly. Moreover, this experiment was hydrated using artificial hydration therefore it is likely that more of the bentonite will hydrate slowly in realistic conditions, therefore increasing the importance of this phenomena.

The numerical behaviour of the proposed unsaturated hydraulic conductivity relationships, shown in figure 5.13b, exhibits a similar response in the short term (less than 1,000 days), but shows a much improved qualitative and quantitative correlation post 1,000 days. There is still some overestimation of re-saturation, which may indicate that the linear function assumed does not fully allow for the micro-structural change and may be improved. However, more experimental evidence would be required to assume a more complex function. In addition, a calibration of parameters may be undertaken. Full saturation is reached in this case after approximately 3,500 days, representing an increase in time of 75%.

This improved ability to predict the long term response would prove useful to long-term performance assessment as saturation effects corrosion rates and gas production.

5.7.5   Conclusions

Without any available experimentation on pelletised bentonite in the form that it is proposed to be used in the PRP validation of the proposed model is difficult. However, this said, a simulation was undertaken using a full size field experiment, the Canister Retrieval Test (CRT), utilising both highly compacted bentonite and bentonite pellets. An improved correlation to the CRT experimental results was found from the numerical simulation, with particular benefit at the later stages where a 'standard' unsaturated hydraulic conductivity relationship leads to the prediction of full saturation earlier than indicated experimentally. This has particular benefit in performance assessment.
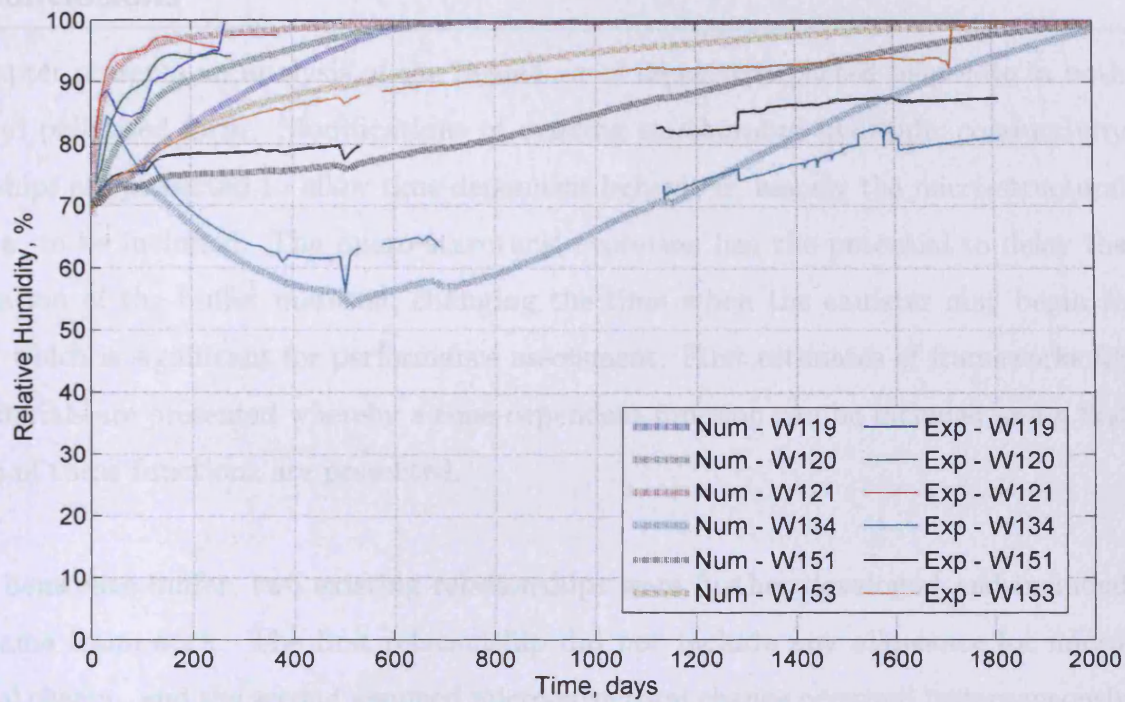
(a) Original Börgesson and Hernelind (1999) unsaturated hydraulic conductivity relationship.
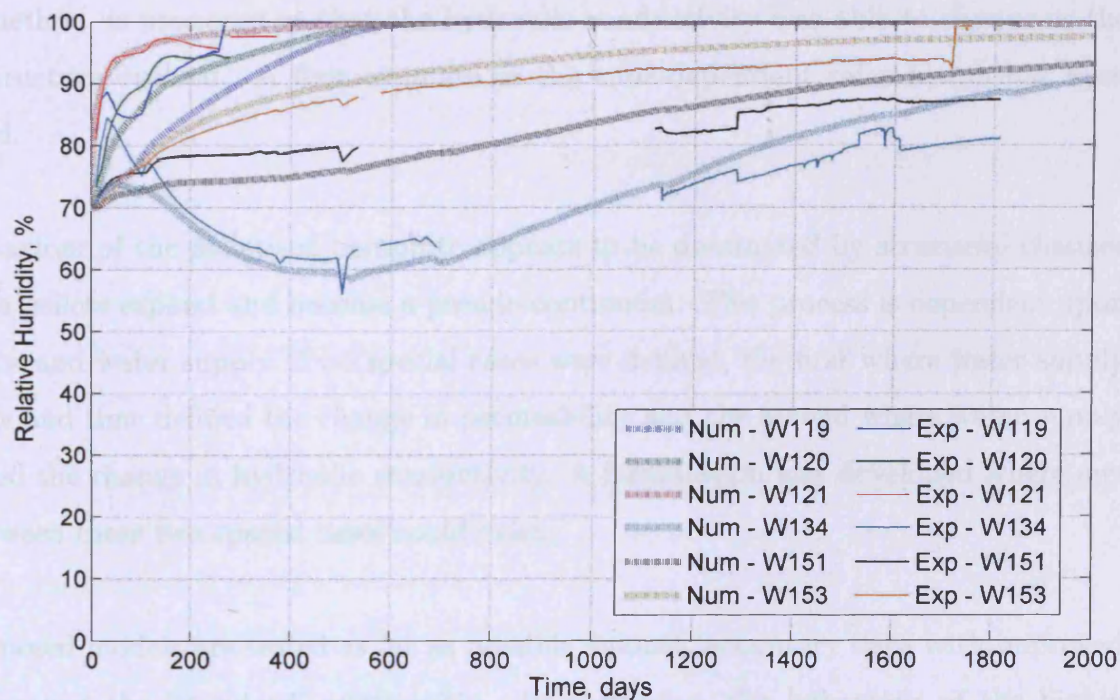
(b) Proposed unsaturated hydraulic conductivity relationships.

Figure 5.13. Experimental and numerical results from the CRT, experimental results from THERESA (2008) citing Goudarzi *et al.* (2006).

5.8 Conclusions

This chapter presents an analysis of the behaviour of highly-compacted bentonite in both block and pelletised form. Modifications of existing unsaturated hydraulic conductivity relationships are presented to allow time-dependent behaviour, namely the micro-structural evolution, to be included. The micro-sturctural evolution has the potential to delay the re-saturation of the buffer material, changing the time when the canister may begin to corrode, which is significant for performance assessment. First estimates of frameworks for both materials are presented whereby a time-dependent function can be included and a first estimate of these functions are presented.

For the bentonite buffer, two existing relationships were further developed and included in the same framework. The first relationship did not include any allowance for micro-structural change, and the second assumed micro-structural change occurred instantaneously. A method of including both relationships in a single framework, where both relationships are included as the limits to the framework, and incuding a time-dependent formulation in the method, is proposed so that the hydraulic conductivity was able to change as the micro-structure evolved. A first estimate of the time-dependent relationship has been proposed.

The behaviour of the pelletised bentonite appears to be dominated by structural changes when the pellets expand and become a pseudo-continuum. This process is dependent upon both time and water supply. Two special cases were defined, the first where water supply was large and time defined the change in permeability and the second where water supply controlled the change in hydraulic conductivity. A formulation was developed where any case between these two special cases could exist.

The proposed models are tested as far as possible against laboratory data with improved results against the 'standard' relationship. In particular, the behaviour of the highly compacted bentonite in the long term is improved whereby the gradients of saturation were improved which may in turn yield significantly improved long term predictions. However, there are no appropriate laboratory experiments available for the pelletised bentonite

material. Therefore, a large-scale experiment, the Canister Retrieval Test, including both highly compacted bentonite and compacted pelletised bentonite was simulated and improved correlation of numerical and experimental results was found, especially in the long term where the 'standard' unsaturated hydraulic conductivity relationship predicts saturation earlier than indicated experimentally. This would prove significant in performance assessment.

5.9 References

Börgesson, L., Hernelind, J., (1999) *Preliminary modelling of the water saturation phase of the buffer and backfill materials*, SKB, IPR-00-11, Stockholm.

Cui, Y.J., Tang, A.M., Loiseau, C., Delage, P., (2008) "Determining the unsaturated hydraulic conductivity of a compacted sandbentonite mixture under constant-volume and free-swell conditions", *Physics and Chemistry of the Earth*, **33**, S462-S471.

Delage, P., Marcial, D., Cui, Y.J., Ruiz, X., (2006) "Ageing effects in a compacted bentonite: a microstructure approach", *Géotechnique*, **56**(5), 291-304.

Dueck, A., (2008) "Laboratory results from hydro-mechanical tests on a water unsaturated bentonite" *Engineering Geology*, **97**, 15-24.

Fredlund, D.G., Rahardjo, H., (1993) "Soil Mechanics for Unsaturated Soils", *John Wiley & Sons Inc*, New York.

Goudarzi, R., Börgesson, L., Röshoff, K., Edelman, M., (2006) *Sensors data report (Period 001026-060501), Canister retrieval test, Report no.12*, SKB, Stockholm.

Goudarzi, R., Johannesson, L-E., (2007) *Äspö Hard Rock Laboratory, Prototype Repository, Sensors data report (Period 010917-070601) Report No:17*, SKB, IPR-07-19, Stockholm.

Hoffmann, C., Alonso E.E., Romero, E., (2007) "Hydro-mechanical behaviour of bentonite pellet mixtures", *Physics and Chemistry of the Earth*, **32**, 832-849.

Huertas, F.J., Carretero, P., Delgado, J., Linares, J., Samper, J., (2001) "An experimental study on the ion-exchange behavior of the smectite of Cabo de Gata (Almería, Spain): FEBEX Bentonite", *Journal of Colloid and Interface Science*, **239**, 409-416.

Inglethorpe, S.D.J., Morgan, D.J., Highley, D.E., Bloodworth, A.J., (1993) *Industrial minerals laboratory manual, Bentonite*, British Geological Survey, Technical Report WG/93/20, Nottingham.

ISO 11275, (2004) *Soil quality - Determination of unsaturated hydraulic conductivity and water-retention characteristic - Wind's evaporation method*, International Organization for Standardization, Geneva.

ISO 17313, (2004) *Soil quality - Determination of hydraulic conductivity of saturated porous materials using a flexible wall permeameter*, International Organization for Standardization, Geneva.

Karnland, O., (1998) *Bentonite swelling pressure in strong NaCl solutions*, POSIVA, Report 98-01, Olkiluoto.

Kröhn, K.P., (2003) "New conceptual models for the resaturation of bentonite", *Applied Clay Science*, **23**, 25-33.

Lloret, A., Villar, M.V., Sánchez, M., Gens, A., Pintado, X., Alonso, E.E., (2003) "Mechanical behaviour of heavily compacted bentonite under high suction changes", *Géotechnique*, **53**(1), 27-40.

Melhuish, T.A., (2004) "An investigation of the three-dimensional thermo/hydro/ mechanical behaviour of large scale in-situ experiments", *PhD Thesis*, Cardiff University.

Mitchell, H.P., (2002) "An investigation into the thermo/hydro/mechanical interactions involved in high level nuclear waste disposal", *PhD Thesis*, University of Wales, Cardiff, U.K.

Philip J.R., de Vries D.A., (1957) "Moisture movements in porous materials under temperature gradients", *Transactions of the American Geophysical Union*, **38**(2), 222-232.

Pusch, R., (1998) "Microstructural evolution of buffer clay", *In Proceedings of workshop on microstructural modelling of natural and artificially prepared clay soils with special emphasis on the use of clays for waste isolation*, Lund, 31-38.

Pusch, R., Karnland, O., Hokmark, H., (1990) *GMM: a general microstructural model for qualitative and quantitative studies of smectite clays*, SKB, Technical Report, SKB-90-43, Stockholm.

Pusch, R., Yong, R., (2003) "Water saturation and retention of hydrophilic clay buffermicrostructural aspects", *Applied Clay Science*, **23**, 61-68.

Singh, R.M., (2007) "An experimental and numerical investigation of heat and mass movement in unsaturated clays", *PhD Thesis*, Cardiff University.

Tang, A-M., Cui, Y-J., (2005) "Controlling suction by the vapour equilibrium technique at different temperatures and its application in determining the water retention properties of MX80 clay", *Canadian Geotechnical Journal*, **42**, 287-296.

THERESA, (2007), *Specification of laboratory benchmark 2, Infiltration tests under isothermal and under thermal gradient performed by CIEMAT*, Unpublished report.

THERESA, (2008) *THERESA project, Interface benchmark (1-D), Large scale test case, Description of the Canister Retrieval Test (CRT)*, Unpublished report.

Thomas, H.R., Cleall, P.J., Chandler, N., Dixon, D., Mitchell, H.P., (2003) "Water infiltration into a large-scale in-situ experiment in an underground research laboratory", *Géotechnique*, **53**(2), 207-224.

Thomas, H.R., Cleall, P.J., Dixon, D., Mitchell, H.P., (2009) "The coupled thermal-hydraulic-mechanical behaviour of a large-scale in situ heating experiment", *Géotechnique*, **59**(4), 401-413.

Thorsager, P., Börgesson, L., Johannesson, L., Sandén, T., (2002) *Canister Retrieval Test, Report on installation*, SKB, IPR-02-30, Stockholm.

Villar, M.V., Martín, P.L., Barcala, J.M. (2005) *Infiltration tests at isothermal conditions and under thermal gradient*, CIEMAT, Technical Report CIEMAT/DMA /M2140/1/05, Madrid.

6

Prototype Repository Project

6.1 Introduction

The Prototype Repository Project (PRP), as introduced in chapter 1, is a unique full-scale experiment designed to investigate the thermo-hydro-mechanical behaviour of high level nuclear waste repository. The experiment is designed to be more realistic than previous experiments and integrate all aspects of the multi-barrier repository system including realistic setting within a real rock mass at realistic depth. Consequently the experiment exhibits three-dimensional behaviour. In addition the timescale that the project is designed for, up to 20 years, is unique and may yield important information regarding time-dependent behaviour.

The Prototype Repository Project (PRP) was constructed in the Hard Rock Laboratory (HRL) in Äspö, Sweden with funding from the European Union and is operated by Svens Kärnbränslehantering AB (SKB). The project is an integral part of SKB's research programme and is specifically designed to test, on full scale, the Swedish KBS-3V disposal concept for High Level Nuclear Waste, see chapter 1. Importantly the experiment is situated

in fractured rock that exhibits anisotropic flow phenomena. This rock mass has been characterised via boreholes and hydraulic tests.

It is important that the salient aspects of the PRP are described so that the modelling approach, assumptions and numerically simulated results can be assessed. The design, rock characterisation, installation and operation may also all influence, to some extent, the behaviour of the project. The extent and limits of the information gathered at the various stages of the project are identified and have been summarised in this chapter to enable an awareness of the available information.

The numerical simulation of this project is important to understand whether the main physical processes occurring have been understood and the information gathered before and during the project are sufficient. This in turn is important so that performance assessment can be carried out and the safety case produced.

In section 6.2 the background to the PRP is described including the project aims, key dates and geometry. The pre-placement period of the tunnel, post construction, but prior to the installation of the canisters and buffer/backfill material is described in section 6.3. The placement stage is described in section 6.4, with section 6.5 containing information about the post-placement stage including the locations of sensors in the project. A summary of key results is presented in section 6.6 and the concluding remarks are presented in section 6.7.

6.2 Background

The Prototype Repository Project aims to tackle and demonstrate many technical and practical issues and is part of a comprehensive research and development program on the KBS-3 disposal concept. The project uses as realistic conditions as possible with the exception of the nuclear waste which is simulated by the use of heaters. The experiment is expected to last up to 20 years. The high level of instrumentation throughout should enable an accurate picture of the thermo-hydro-mechanical processes occurring within the repository.

6.2.1 Aims

Svemar and Pusch (2000) describe the aims of the PRP as to:

- *'investigate, on a full scale, the integrated performance of engineered barriers and near-field rock of a simulated deep repository in crystalline rock with respect to heat evolution, mechanics, water permeation, water chemistry, gas evolution and microbial processes under natural and realistic conditions..'*

Johannesson *et al.* (2007) elaborates and states that the main aims also include, to:

- *'compare results with model predictions and assumptions'*

- *'develop, test and demonstrate appropriate engineering standards and quality assurance methods.'*

- *'simulate appropriate parts of the repository design and construction process'*

The project will be monitored for up to 20 years to provide long term knowledge of repository behaviour under realistic conditions.

6.2.2 Length of project and key dates

The project is intended to have a duration of twenty years. For the short term behaviour however the installation time-line is critical including when bentonite blocks and backfill were installed and when the heaters were switched on. Table 6.1 summarises the key dates and activities. The power is planned to be reduced by $30W$ per year from the end of this chart, following the original plan (Goudarzi and Johannesson, 2007).

6.2.3 Location and geometry

The Prototype Repository Project is well described by both Svemar and Pusch (2000) and Johannesson (2007). It is located at the edge of the HRL facility at -450m below sea level as described in chapter 2. An artistic impression of the PRP and surrounding tunnels is presented in figure 6.1 and a schematic of the repository itself is shown in figure 6.2. It is made up of two sections, one with four deposition holes and the second with two, spaced 6m apart and drilled vertically. The deposition holes are filled sequentially with high density bentonite blocks. The bentonite is an industrial Na-bentonite manufactured into a powder

Section 1		Section 2	
Activity	Date	Activity	Date
Start backfilling	3/9/2001		
Start heating canister 1	17/9/2001		
Start heating canister 2	24/9/2001		
Start heating canister 3	11/10/2001		
Start heating canister 4	22/10/2001		
Finish backfilling	20/11/2001		
Cast plug	14/12/2001		
Decreased power (-20W)	17/9/2002		
Decreased power (-40W)	5/9/2003		
		Start backfilling	29/4/2003
		Start heating canister 5	8/5/2003
		Start heating canister 6	23/5/2003
		Finished backfilling	25/6/2003
		Cast plug	11/9/2003
Decreased power (-30W)	8/9/2004	Decreased power (-30W)	8/9/2004
Power switched off to all canisters	2/12/2004	Power switched off to all canisters	2/12/2004
Tunnel drainage opened	6/12/2004	Tunnel drainage opened	6/12/2004
Power switched on to all canisters*	15/12/2004	Power switched on to all canisters	15/12/2004
		Power switched off to canister 6	6/9/2005
		Power switched on to canister 6	2/11/2005
Decreased power (-30W)	2/12/2005	Decreased power (-30W)	2/12/2005

*Not canister 2

Table 6.1. Key dates for the PRP (Goudarzi and Johannesson, 2007).
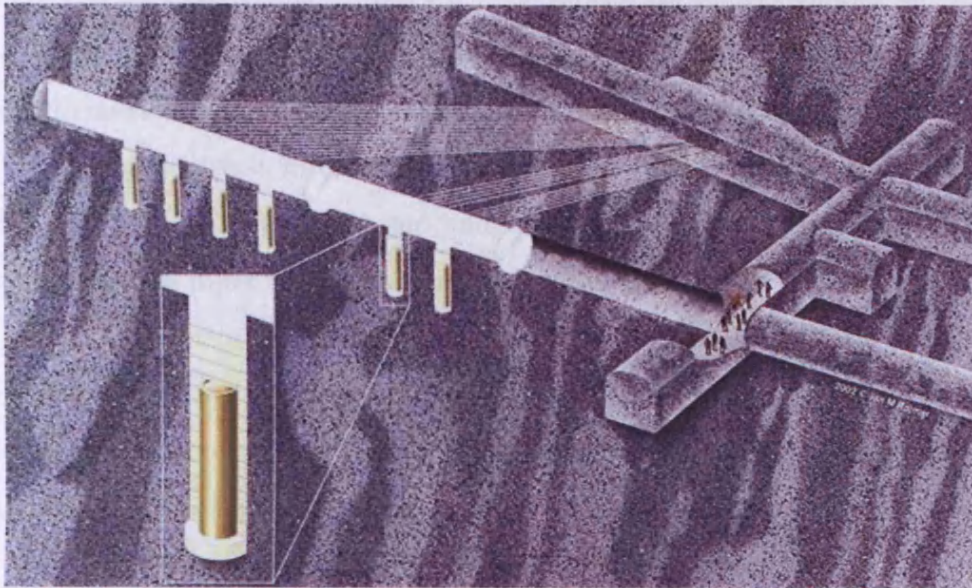
Figure 6.1. Artistic view of PRP and adjoining tunnels (Johannesson *et al.*, 2007).
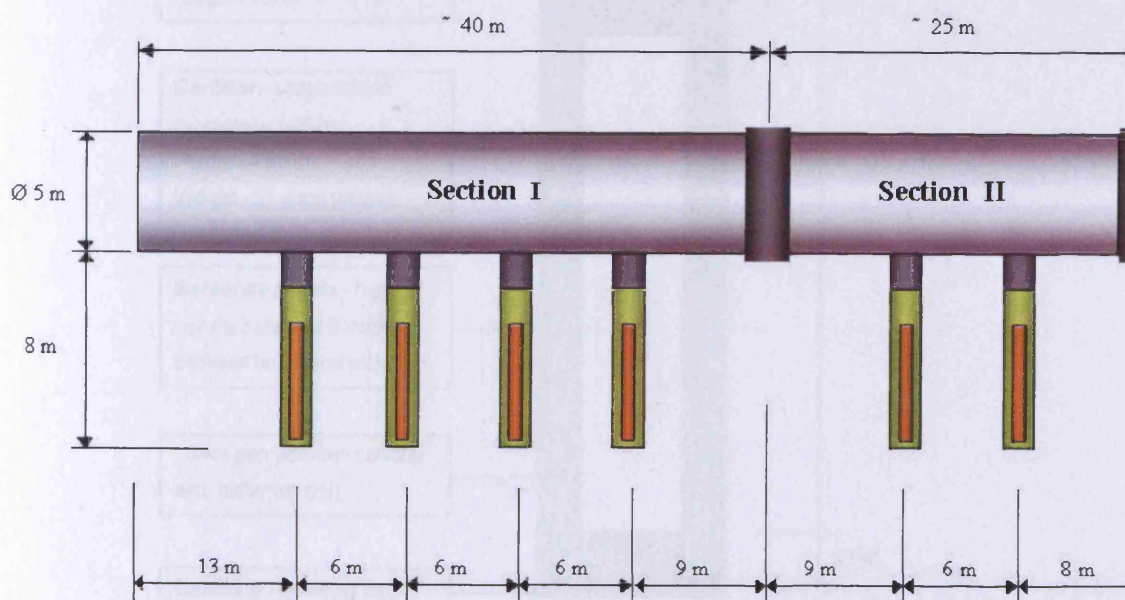
Figure 6.2. Schematic of the PRP project (after SKB, 2008).

near the original source in Wyomming, USA and named MX-80. It is then compacted into blocks of the correct dimensions in Sweden. The blocks are either cylinder sections, placed above and below the waste canister or ring sections surrounding the canister, see figure 6.3, a detailed schematic of the filled deposition hole. Where a cylinder is placed on the ring below, a gap exists, which is filled with brick shape blocks. Between the bentonite blocks and the canister is initially a 10mm gap and between the bentonite and the rock is a gap, mean 50mm, which is filled with high density bentonite pellets. The tunnel and remaining 1000mm of the deposition holes contain backfill which is a crushed rock and bentonite mix (70/30% by weight). A concrete plug was constructed between the two sections and another isolating the project from the rest of the tunnel complex. The plugs were designed to withstand the stresses and pressures that the system was likely to create.
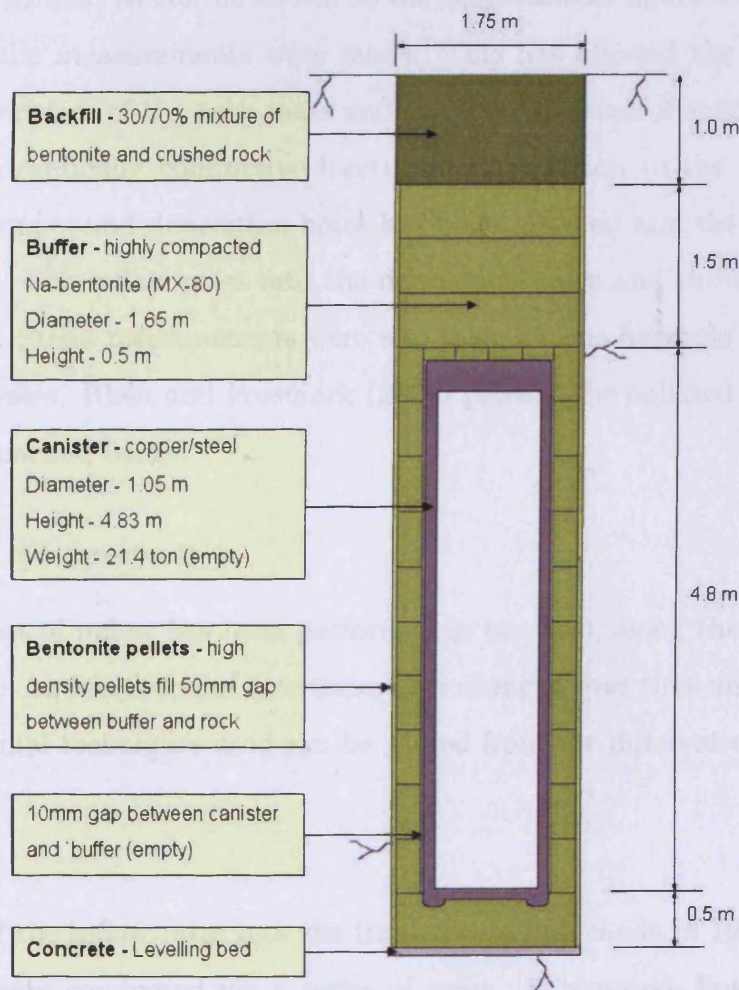
Figure 6.3. Details of KBS-3V deposition hole, (after Melhuish, 2004).

6.3 Pre-placement

The pre-placement stage of the project starts with the construction of the tunnel and finishes when emplacement of buffer material, backfill and canisters begins. The measurements taken during this time period enable the rock to be characterised, numerical models to be calibrated and give an indication of initial conditions. Chapter 7 presents the simulation of the pre-placement stage including calibration for pre-placement results to give initial conditions to post-placement simulation.

6.3.1 Initial experimentation

The rock surrounding the PRP has been characterised at relatively high resolution. 39 boreholes were drilled, as can be shown in the schematic in figure 6.4, and in 33 of these detailed hydraulic measurements were made. This has allowed the observation of both general characteristics of the rock mass and the identification of specific features, such as local highly hydraulically conductive fractures. In addition to the use of boreholes the surface of the tunnel and deposition holes has been mapped and the hydraulically active areas identified. The inflow rates into the deposition-holes and tunnel sections have also been monitored. Stress measurements were also taken in one borehole to gain knowledge of the existing stresses. Rhén and Forsmark (2001) present the collated data and the salient points are summarised below.

6.3.1.1 Inflow measurements

The measurement of inflow has been performed in two sets, along the tunnel and into the deposition-holes. An indication of how these have changed over time and also the sensitivity of the experimental techniques used can be gained from the different results.

Tunnel

Measurement of the inflow rates into the tunnel were first made in 1997 and then in 1999 and 2000 and were conducted via a series of weirs. It is noted, however, that the weir locations did vary, which makes it hard to directly compare data and that the continuous variation of inflow against tunnel chainage is not known due to this methodology. Figure 6.5 shows the repository design with the chainages and weir locations. Table 6.2 contains

the raw data and figure 6.6 shows this data graphically. The values have been averaged to allow comparison and this includes the 1997 values although the weir placements were slightly different. The raw data is also included to allow the range of data to be seen. It is acknowledged that this range is approximate due to both the differences in measured data, the temporal nature of the inflow and the small data set. It can clearly be seen that the variability of flow with respect to location in the tunnel is large and variation with time is less but still occurs, and this must be acknowledged when comparing model simulation data.

Deposition-holes

Flows into the deposition holes were measured in different ways to gain insight into where the flow was coming from. A number of measurements of the total inflow was made, then measurements using diapers were undertaken, shown in figure 6.7 with a sample of the results shown in figure 6.8 for deposition-hole 3, where the x-axis is the circumference of the deposition-hole and the y-axis is the height. The results are shown overlying a fracture map of the deposition-hole. However, there is a degree of uncertainty with the results, both in the variation of results and also inherent to the methods. In general, it is acknowledged that most of the results contain some leakage from the tunnel floor (Rhén and Forsmark, 2001). Even though some of the diaper strips have been disregarded due to being deemed to show leakage from the tunnel flow, there is a general trend that a higher flow rate is found towards the top of the holes, see figure 6.8, indicating that there may still remain some leakage, or preferential flowpath, connected to the tunnel. Table 6.3 contains the results from the total inflow measurements, with some variation in technique and isolation. Rhén and Forsmark (2001) state that some minor leakage from the tunnel floor is included in these measurements except to borehole 3 and boreholes 5 and 6 for the values in bold shown. These same results are shown in figure 6.9 highlighting the variation in measurement and the average result. The most important feature of this measurement is that the inflow into DH-1 is much greater than into any of the others.
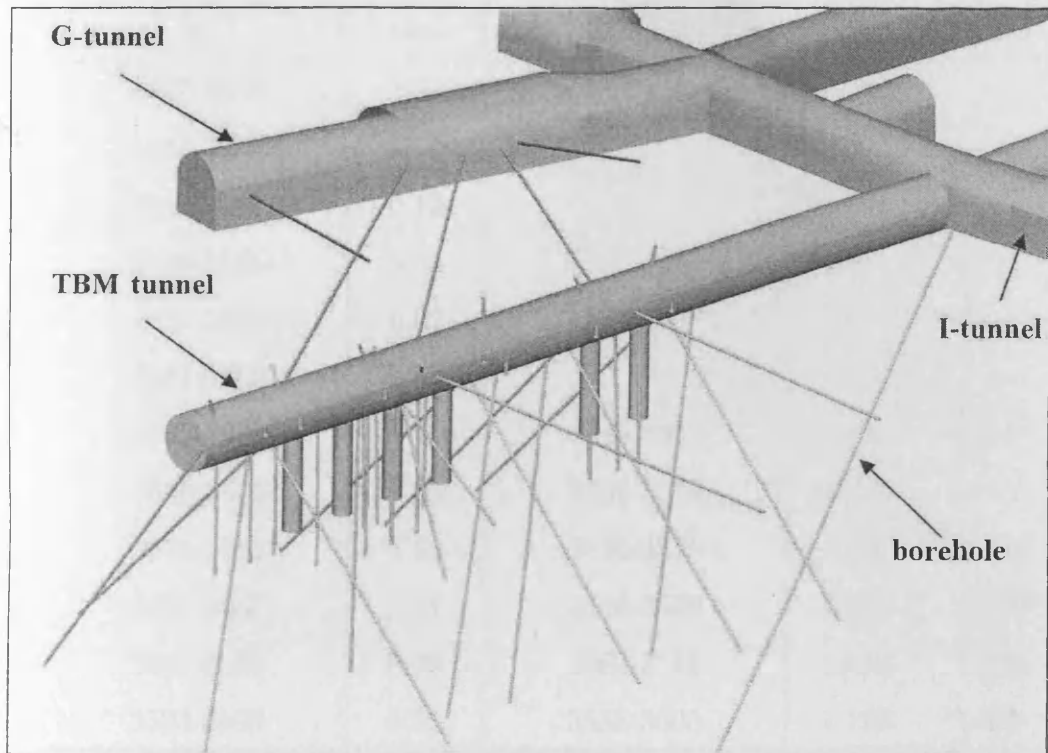
Figure 6.4. Boreholes used for the characterisation of the rock mass (Rhén and Forsmark, 2001).
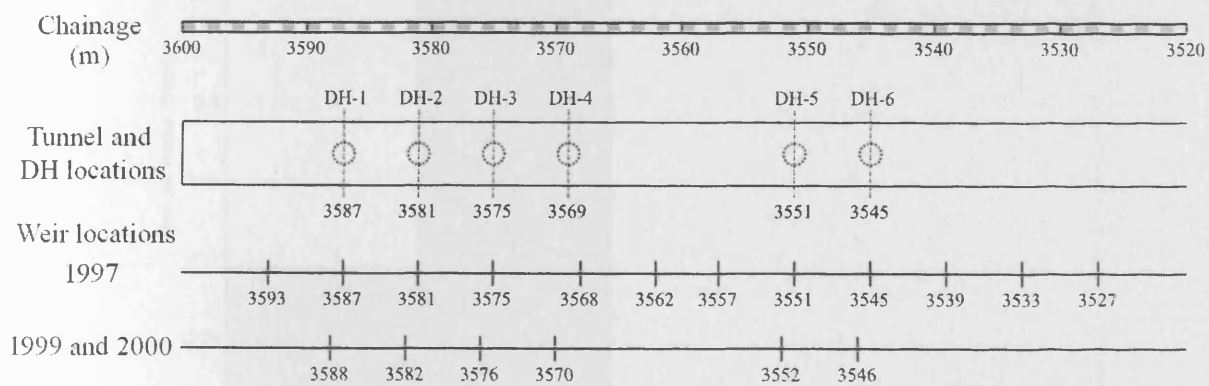
Figure 6.5. Chainage and weir locations for flow measurement along tunnel.

Weir Sections 1997, m	Q 1997, l/min	Weir Sections 1999/ 2000, m	Q 1999, l/min	Q 2000, l/min
3527-3533	0.20	-	-	-
3533-3539	1.17	-	-	-
3539-3545	0.12	-	-	-
3545-3551	0.03	-	-	-
3551-3557	0.02	-	-	-
3557-3562	0.05	-	-	-
3562-3568	0.10	3546-3552	0.001	0.006
3568-3575	0.05	3552-3570	0.100	0.110
3575-3581	1.56	3570-3576	0.000	0.000
3581-3587	1.61	3576-3582	2.000	1.320
3587-3593	0.29	3582-3588	1.490	1.820
3593-3600	0.93	3588-3600	1.120	1.080

Table 6.2. Measured inflow into the tunnel (Goudarzi and Johannesson, 2006).
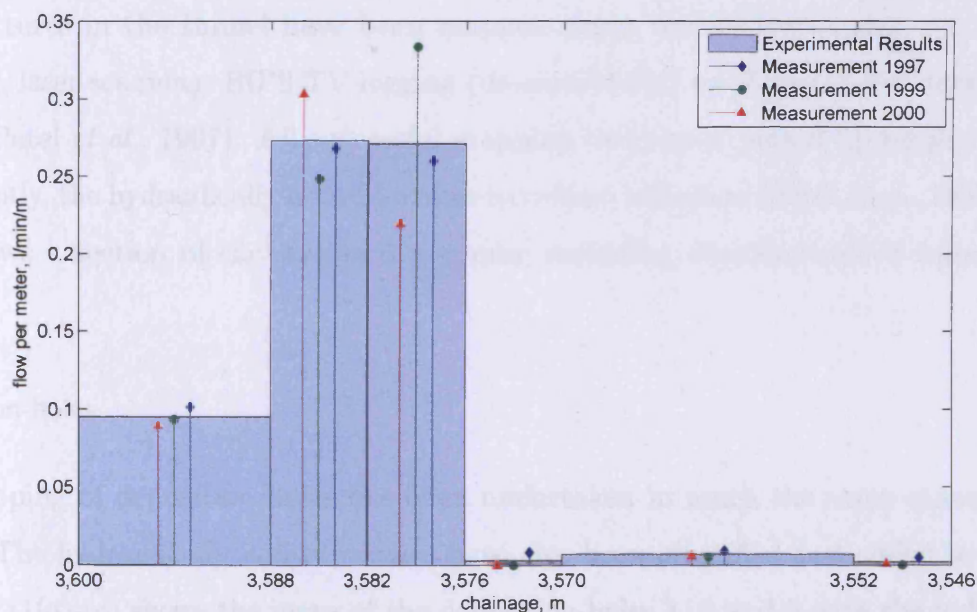
Figure 6.6. Tunnel inflow measurements quoted as flow rate per metre (after Rhén and Forsmark, 2001).
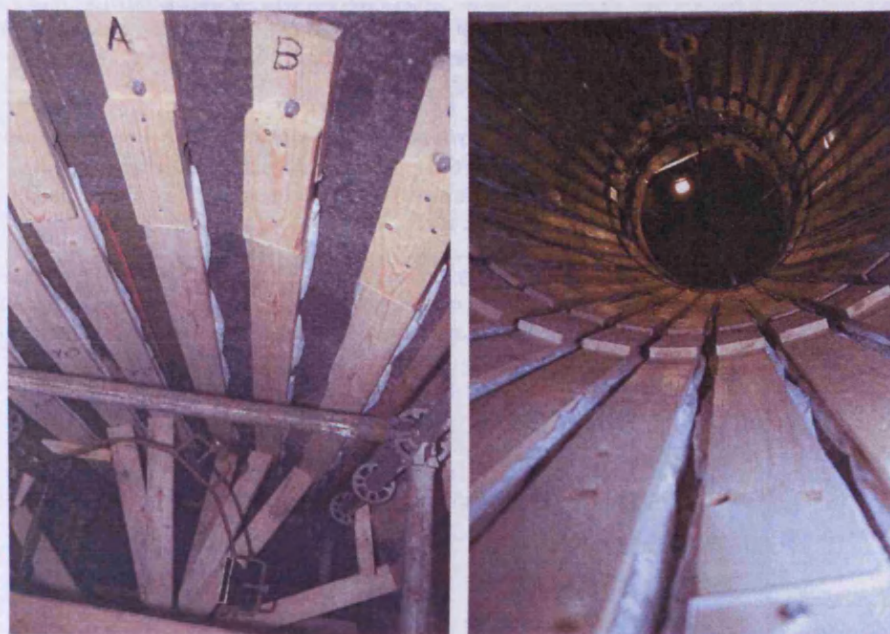
Figure 6.7. Photograph of diaper measurements being made (Rhén and Forsmark, 2001).

6.3.1.2   Fracture mapping

Tunnel

The fractures in the tunnel have been mapped using various techniques e.g. standard mapping, laser scanning, BIPS TV-logging (unsuccessfully) and Ground Penetrating Radar (GPR)(Patel *et al.*, 1997). All successful mapping techniques picked up similar fractures. Importantly, the hydraulically active features have been identified (Patel *et al.*, 1997). Figure 6.10 shows a section of the standard mapping including identification of water bearing features.

Deposition-holes

The mapping of deposition holes has been undertaken in much the same manner as the tunnel. The hydraulically active features have also been identified and added to the plots. Figure 6.11(a)-(c) shows the maps of the deposition-holes 1, 3 and 5 with the hydraulically active features marked with hatching. The major difference between deposition-hole 1 and deposition-hole 3 goes some way to explain the major differences in inflow, with DH-3 not showing any hydraulically active features. However, deposition-hole 1 does not have more
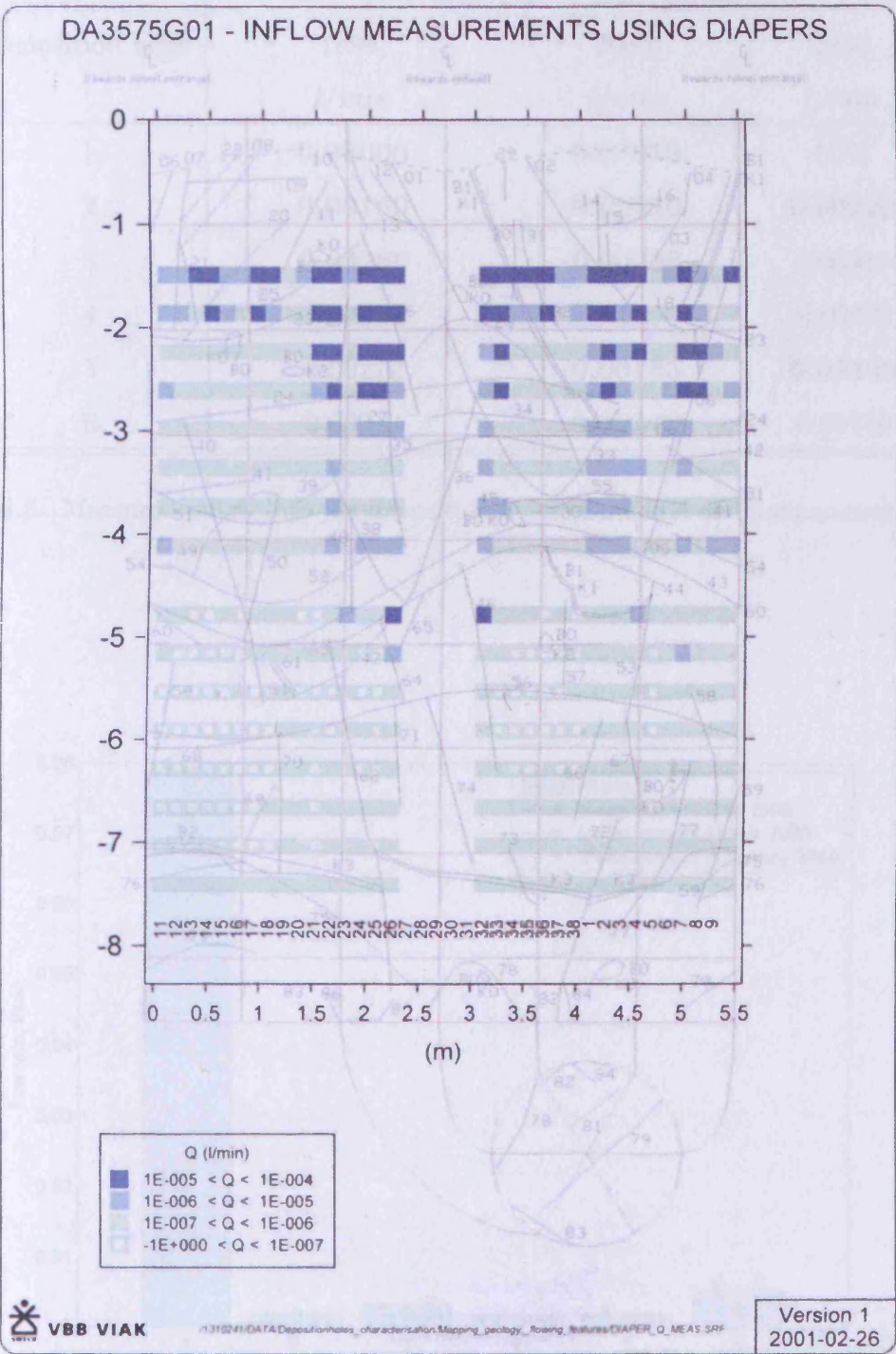
Figure 6.8. Inflow measurement data from diapers, DH3 (Rhén and Forsmark, 2001).

Deposition Hole	$8^{th} - 13^{th}$ December 1999, l/min	$28^{th} - 31^{st}$ March 2000, l/min	June / July 2000, l/min
1	0.08000	0.07870	N/A
2	0.00160	0.00220	0.00220
3	0.00280	0.00310	0.00410
4	0.00072	0	0.00472
5	0.00270	0.00155	0.00160
6	0.00610	0.00270	0.00740

Table 6.3. Measured inflow into the deposition holes (Goudarzi and Johannesson, 2006).
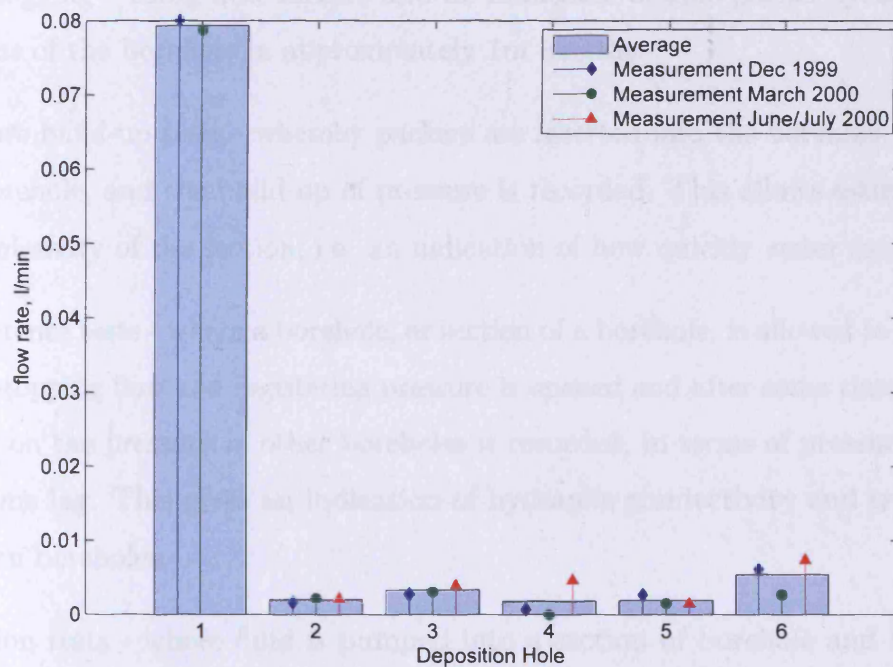
Figure 6.9. Deposition hole inflow measurements (after Rhén and Forsmark, 2001).

hydraulically active features than deposition-holes 5, but has a significantly larger inflow rate. A tentative conclusion can be drawn, that the majority of the flow occurs through these hydraulic features and that the flow generally diffusing through the rock matrix is small in comparison, although the rates through the fractures may highly variable.

6.3.1.3 Borehole data and interference tests

An overview of the drilling and testing can be found by Rhén and Forsmark, 2001. Drilling was carried out first prior to the pre-investigation of the PRP, then in three subsequent campaigns. The boreholes can be seen in a three-dimensional visualisation in figures 6.4 and more precisely in figures 6.12 and 6.13. In each of the boreholes a number of tests were carried out, with the most detailed after drilling campaign 3. A brief summary of these tests is given below. In addition, lead-through holes for instrumentation were drilled, tested, cables installed and then sealed, the location of these can be seen schematically in figure 6.1.

The main tests that were carried out were:

- Flow logging - using flow meters and an inflatable double packer system to isolate sections of the borehole in approximately $1m$ lengths.

- Pressure build-up tests - whereby packers are inserted into the borehole, or section of the borehole, and the build up of pressure is recorded. This allows estimation of the transmissivity of the section, i.e. an indication of how quickly water can flow in.

- Interference tests - where a borehole, or section of a borehole, is allowed to flow, i.e. the valve stopping flow and registering pressure is opened and after some time closed. The effects on the pressure in other boreholes is recorded, in terms of pressure differences and time lag. This gives an indication of hydraulic connectivity and transmissivity between boreholes.

- Injection tests - where fluid is pumped into a section of borehole and the rate and pressures are recorded to estimate the transmissivity.

Drilling tests

A number of drilling campaigns were undertaken to characterise the rock, whereby in each campaign a number of boreholes were drilled and a selection of the hydraulic tests outlined above were completed. Figures 6.12 and 6.13 show the boreholes that were drilled. The key information found from this drilling was the transmissivity of the rock mass and an investigation of the hydraulic connectivity, including the identification of key hydraulic features.

6.3.1.4 Stress conditions

Stress measurements were made after the tunnel was excavated. The data is summarised by Rhén and Forsmark, 2001. Measurements were taken in a vertical borehole to a depth of $22.31m$ below the tunnel. The deepest measurements were assumed to be undisturbed from the tunnel and averaged. Figure 6.14 and table 6.4 show these values and directions. These stresses can be transformed into Cartesian stresses and shears, shown below in the stress vector in table 6.5. It is noted that shear stresses may be present in the original, but these would be minor.
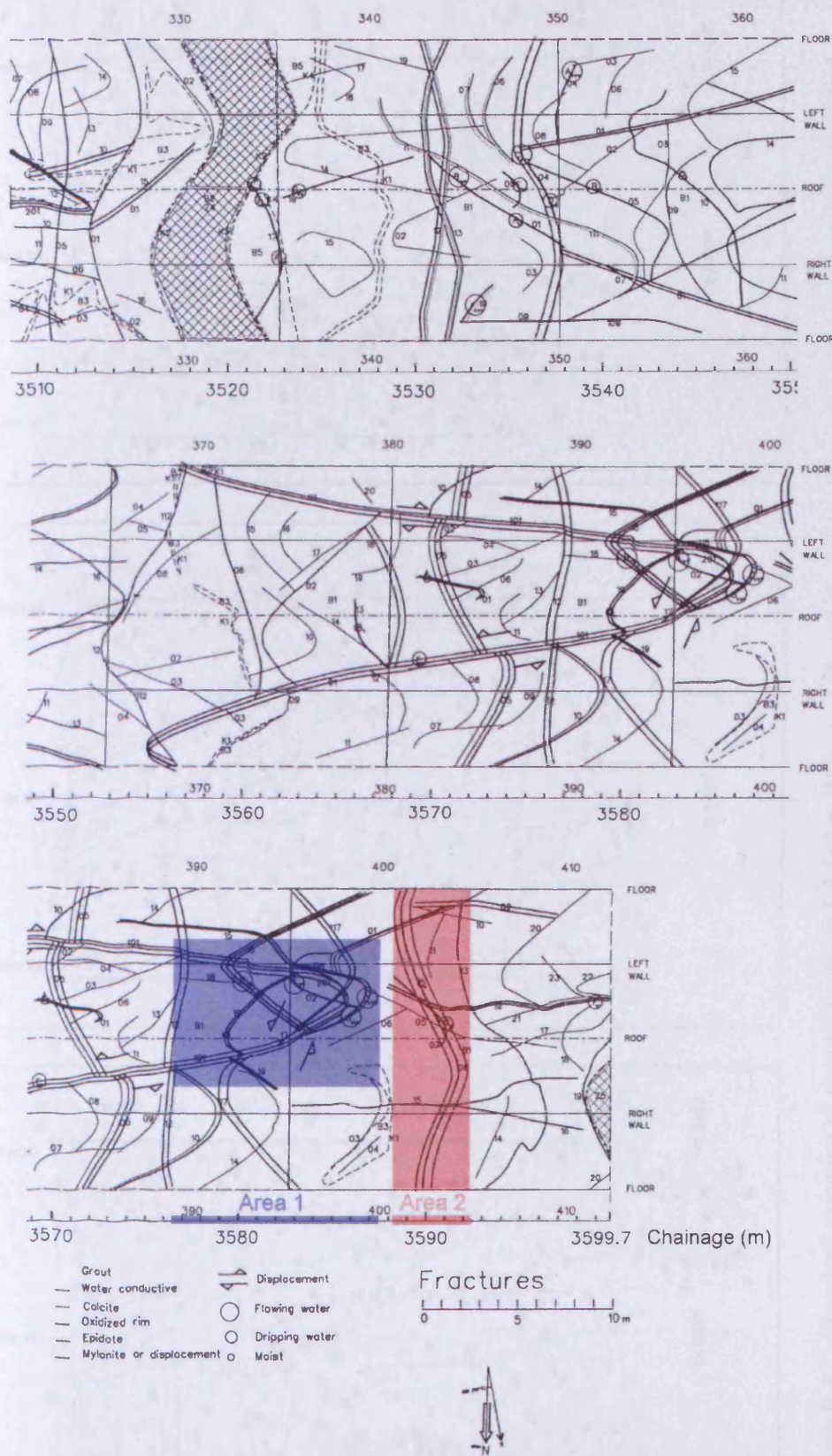
Figure 6.10. Standard mapping of fractures along tunnel, where the centreline is the roof (after Rhén and Forsmark, 2001). Water bearing structures are identified.
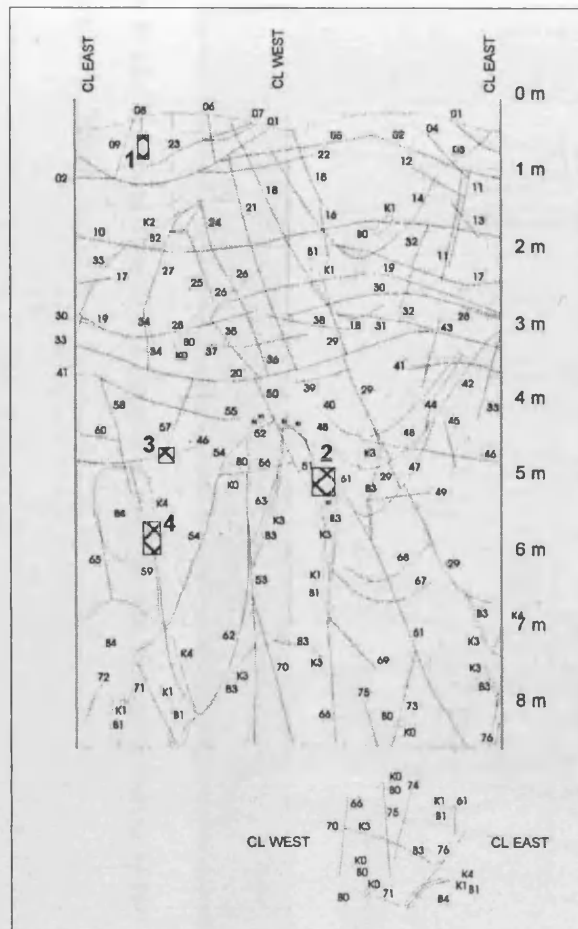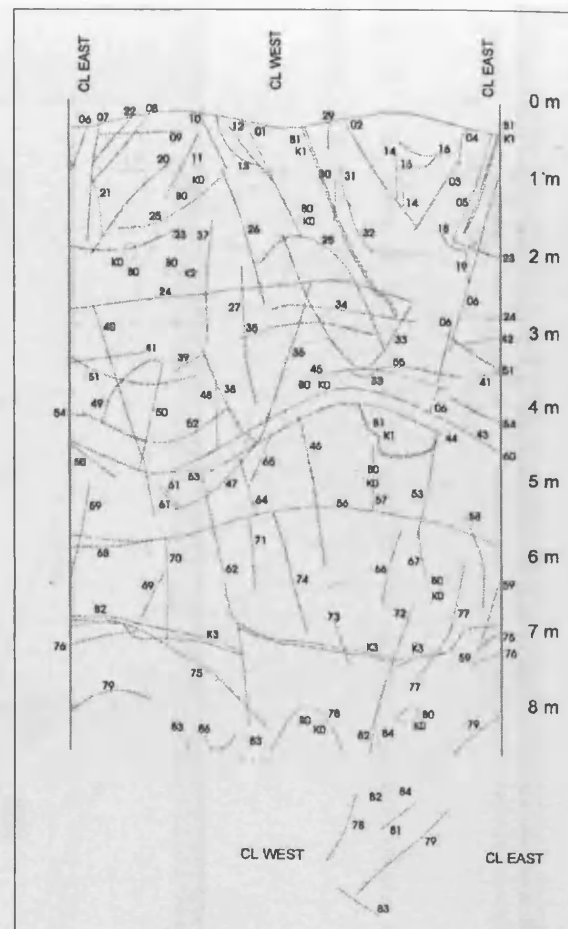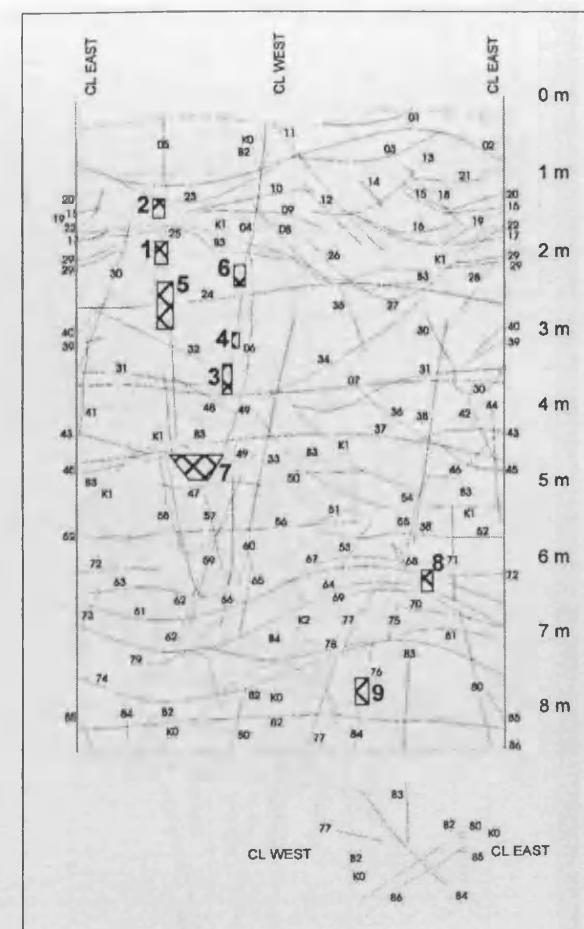
Figure 6.11. Standard mapping of deposition-holes 1-6 (after Rhén and Forsmark, 2001). Water bearing structures are identified.
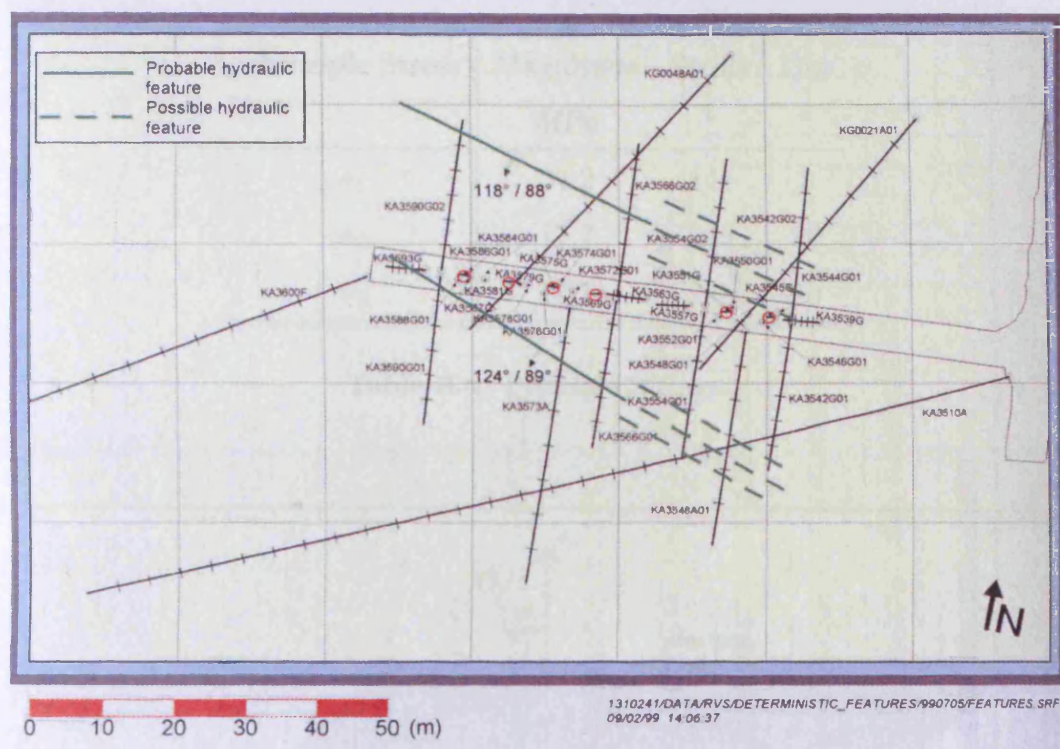
Figure 6.12. Plan view of the boreholes used for the characterisation of the rock mass (Rhén and Forsmark, 2001)
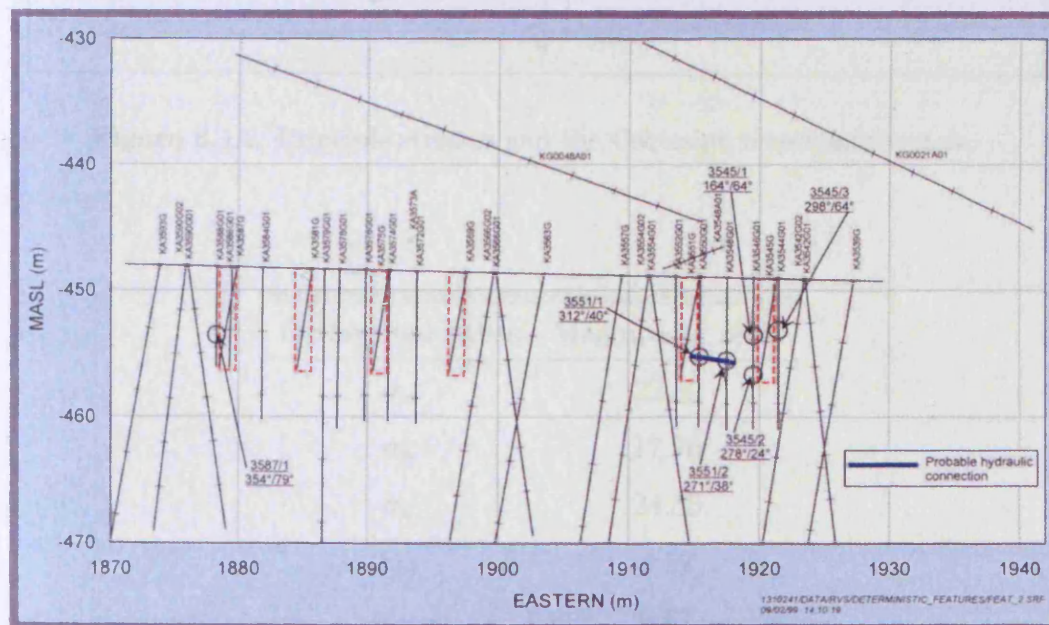
Figure 6.13. Sectional view of the boreholes used for the characterisation of the rock mass (Rhén and Forsmark, 2001)

Principle Stress	Magnitude	Strike	Dip
	MPa	°	°
σ_1	34.2	141	3
σ_2	17.7	245	80
σ_3	13.1	50	10

Table 6.4. Principle Stresses.
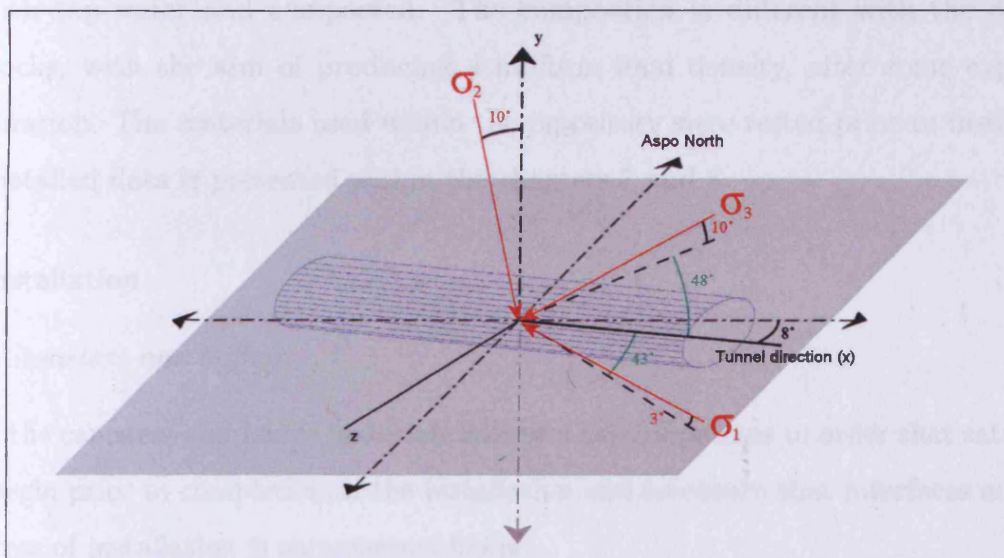
Figure 6.14. Principle stresses and the Cartesian coordinate system.

Orthogonal stress	Magnitude, MPa
σ_x	22.89
σ_y	17.76
σ_z	24.55
τ_{xy}	4.52
τ_{yz}	6.67
τ_{zx}	23.51

Table 6.5. Stresses transformed to orthogonal directions in the rock.

6.4 Placement

The placement of the materials is key to the short term behaviour of the repository and goes some way to illustrating that a real repository could be constructed using similar techniques to that demonstrated here. The placement process is detailed in Börgesson *et al.* (2002) and Johannesson *et al.* (2004) and summarised in Johannesson *et al.* (2007).

6.4.1 Materials used

The buffer material was a highly compacted Na-bentonite, MX-80 as previously described, mixed with tap-water and compacted. The compaction is different with the different shape blocks, with the aim of producing a uniform final density, after some expansion from saturation. The materials used within the repository were tested prior to installation. Further detailed data is presented within the chapters 7 and 8.

6.4.2 Installation

6.4.2.1 Canisters and buffer

Installing the canisters and buffer materials follows a careful process in order that saturation will not begin prior to completion of the installation and to ensure that interfaces are clear. This process of installation is summarised below.

  i. Cleaning the deposition holes - a vacuum cleaner is used to remove any debris from the deposition hole.

  ii. Mounting pumps - a small pump was mounted to remove any water ingress into the deposition hole during the installation.

  iii. Mounting the gantry-crane.

  iv. Installation of water protection sheets.

  v. Deposition of bentonite blocks - the blocks of MX-80 were transported by vehicle into the tunnel and lifted into the deposition holes by use of the gantry crane.

  vi. Instrumentation of the bentonite blocks.

  vii. Transportation of the canisters.

viii. Mounting of the deposition machine - the deposition machine allows the waste canister to be tilted and then lowered into the deposition hole.

ix. Deposition of the canister.

x. Connecting of the canister cables.

xi. Installation of the bentonite bricks - The MX-80 bricks are installed manually and cut to fill gaps at the edges. This is shown in figure 6.15.

xii. Deposition of the final bentonite cylinder

xiii. Removal of plastic sheeting

xiv. Filling with bentonite pellets - The pellets are blown into the gap surrounding the rest of the buffer and the dust is controlled by use of a series of tubes connected to a vacuum cleaner.

xv. Backfilling - The backfill was installed in layers inclined at 35° to the horizontal, that are $20cm$ thick and compacted using a compaction machine. The processes is schematically shown in figure 6.16. The backfill in the tunnel progressed until $30cm$ from the edge of the next deposition hole, when the plastic from this hole was removed and the backfilling process continued. When the edge of the tunnel was reached the first pre-cast concrete beam was placed and the backfilling continued until the location of the next beam was reached. When the compacting machine could no longer be used a mixture of sand and bentonite (80%:20%) was added and the final beam placed.

Figure 6.15. Installation of the bentonite bricks on the top of the canister (Johannesson *et al.*, 2004).
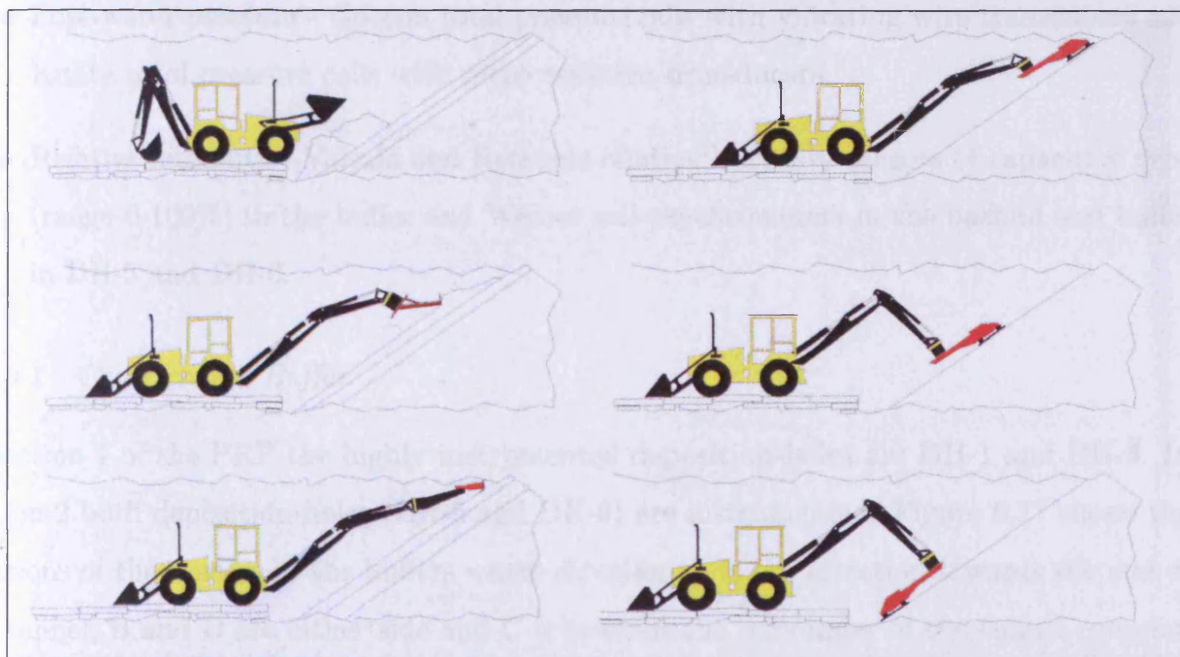
Figure 6.16. Installation of the backfill in layers into the tunnel (Johannesson *et al.*, 2004).

6.4.3 Instrumentation

A summary of sensor data is included in the sensor data reports, the latest of which is Goudarzi and Johannesson, 2007. The majority of the sensors that are included in the PRP measure temperature, total pressure, pore-water-pressure and relative humidity. Most sensors are encapsulated in titanium and the cables are also encapsulated, in titanium tubes in the bentonite buffer and in polyamide tubes in the backfill. The thermocouples were manufactured from cupro-nickel and did not require encapsulation. Cable parcels were taken to lead-through holes and then to the G-tunnel, where data is collected in a 'measuring house'. The lead-through holes must be watertight, to withstand up to $5MPa$ of water-pressure and the materials used to achieve this must have a high degree of long-term stability. The types of the sensors are described in the list below and the locations are given in the following paragraphs.

- Temperature - Pentronic thermocouples have been used in the rock, bentonite and buffer, while optical fiber cables are used on the canister surface.

- Total pressure - Geocon total pressure cells with vibrating wire transducers and Kulite total pressure cells with piezo resistive transducers.

- Pore-water-pressure - Geocon total pressure cells with vibrating wire transducers and Kulite total pressure cells with piezo resistive transducers.

- Relative humidity - Vaisala and Rotronic relative humidity sensors of capacitive type (range 0-100%) in the buffer and Wescor soil psychrometers in the backfill and buffer in DH-5 and DH-6.

6.4.3.1 Canister and Buffer

In section 1 of the PRP the highly instrumented deposition-holes are DH-1 and DH-3. In section 2 both deposition-holes (DH-5 and DH-6) are instrumented. Figure 6.17 shows the locations of the sensors in the buffers where direction A is the direction towards the end of the tunnel, B and D are either side and C is towards the remainder of the tunnel complex. The canister temperature is measured along the surface of the sides of the canister.

6.4.3.2   Backfill

The backfill is mainly instrumented directly above and in between deposition-holes in sections. The locations of the sensors can be seen in figures 6.18 and 6.19.

6.4.3.3   Host Rock

Temperature sensors are placed in the rock, as can be seen in figure 6.20. The sensors are places adjacent to DH-1 and between DH-2 and DH-3 as well as adjacent to DH-4.

6.4.4   Closure

Two plugs have been used the first to isolate the first section and the second to close the project from the remainder of the tunnel. The plugs are designed to withstand a pressure of $4.5MPa$ and to prevent axial water flow. A retaining wall made up of pre-cast concrete planks was first installed and then a reinforced cast concrete plug was formed.

6.5   Post-placement

6.5.1   Data recorded

Just under six years data has been recorded as is presented by Goudarzi and Johannesson (2007) and is summarised and synthesised in section 6.6 below. The measuring system is shown to be performing relatively well. However, more than two thirds of the 363 sensors installed in section 1 have now failed and just less than a quarter of the 394 sensors installed in section 2 have failed. In the majority of cases these are relative humidity sensors that fail at saturation.

Drainage from the inner section and the outer plug was closed-off in November 2004 and damage was observed to canisters 2 and 6 in December 2004. Consequently, power was switched off and drainage opened and then power was restored on December 15th, except in canister 2 which was found to be inoperable. In September 2005 more problems to canister 6 were found. The canister power was switched off for approximately 2 months. In April 2006 a packer in section 1 was broken causing an increase in total and pore-water-pressure in the backfill of section 1.
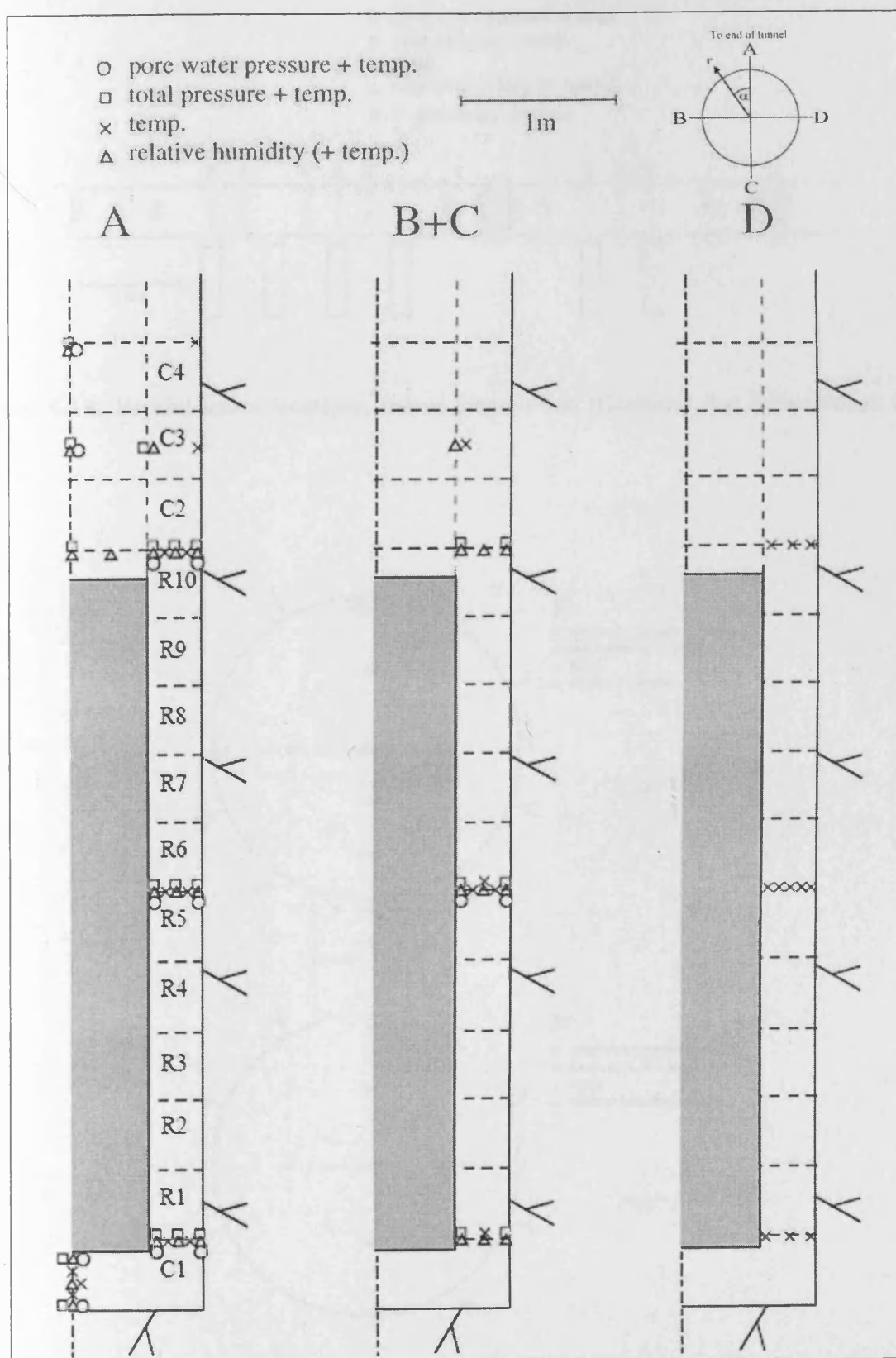
Figure 6.17. Sensor locations in the buffer (Svemar and Pusch, 2000)

O   pore water pressure + temp.
□   total pressure + temp.
×   temp.
△   relative humidity (+ temp.)
E, F measuring sections
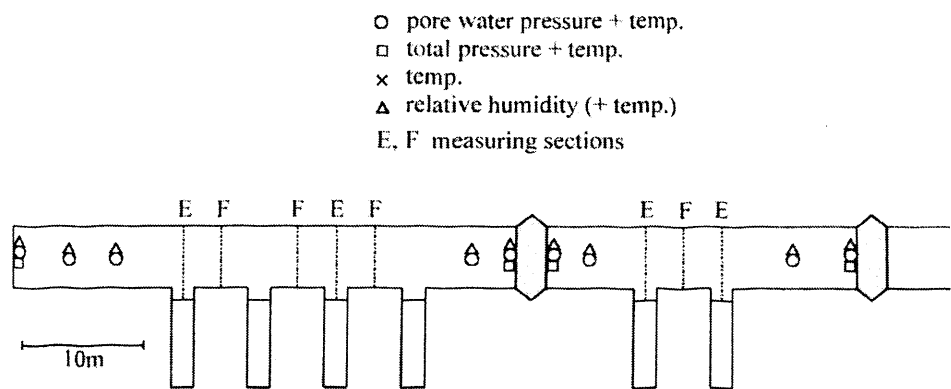
Figure 6.18. Backfill sensor locations, tunnel long section (Goudarzi and Johannesson, 2007).

E

O   pore water pressure + temp.
□   total pressure + temp.
×   temp.
△   relative humidity (+ temp.)

F

O   pore water pressure + temp.
□   total pressure + temp.
×   temp.
△   relative humidity (+ temp.)
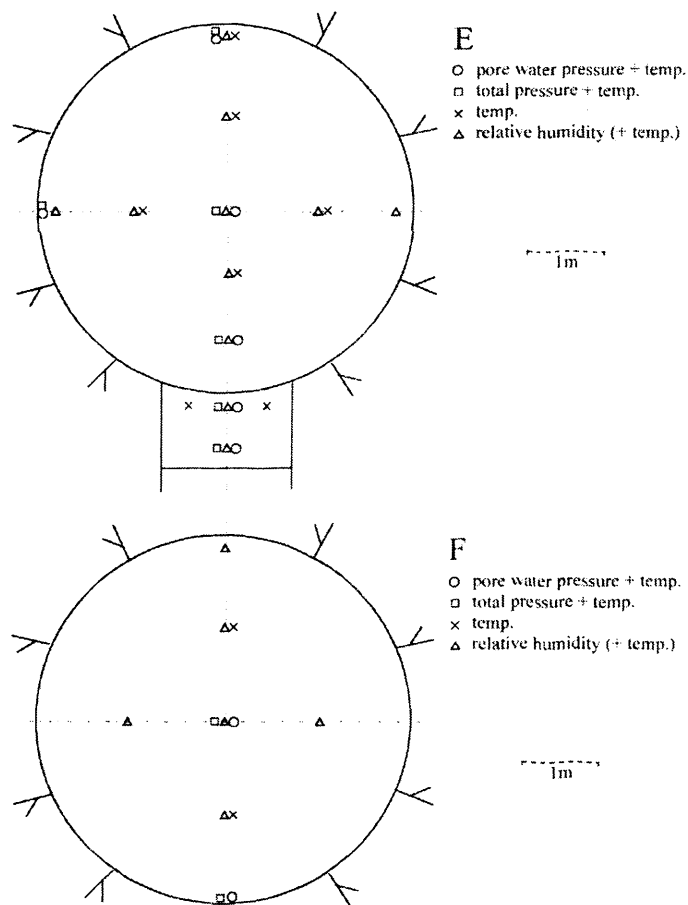
Figure 6.19. Backfill sensor locations, tunnel sections (Goudarzi and Johannesson, 2007).
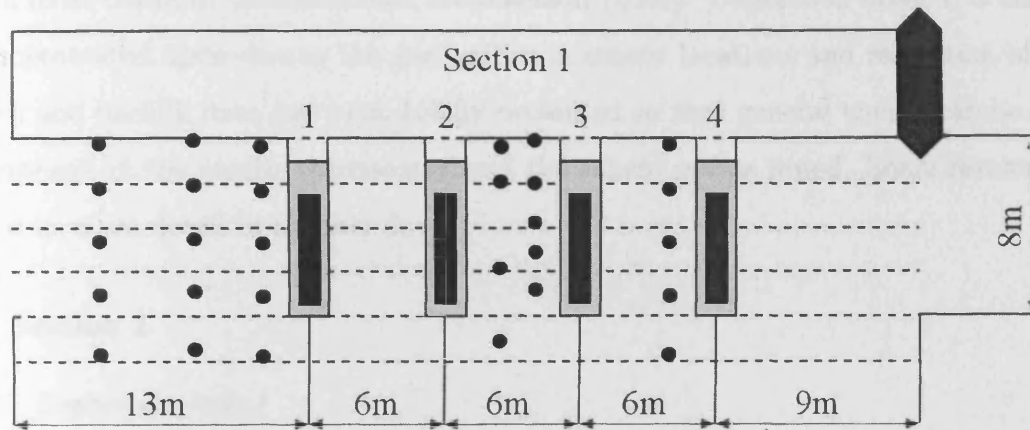
Figure 6.20. Rock sensor locations (Goudarzi and Johannesson, 2007).

6.6   Summary of results

The main findings from the results are presented in this section, while the results can be found in more detail in Goudarzi and Johannesson (2007). Deposition holes 1, 3 and 5 and been concentrated upon due to the similarities in sensor locations and resolution of results. The rock and backfill data has been briefly presented so that general trends can be seen. A brief synthesis of the results is presented and the salient points noted. Some results will be analysed in more detail in chapter 8.

6.6.1   Section 1

6.6.1.1   Deposition-hole 1

Total pressure

Figure 6.21 shows the total pressure, i.e. the swelling pressure and any positive pore-water-pressure. The pressures quickly rise, in under 500 days, to a value over $5MPa$ in most locations, with the value exceeding $7MPa$ in the lower part of the buffer material and approximately $4MPa$ in the upper part. However, in the centre of the MX-80 cylinders, below the heater, this value is much less, only rising to $5MPa$ in the lower cylinder after around 1500 days. In the upper cylinder the value does not rise above $0MPa$, although this could suggest the sensor is not working.

Relative humidity

The relative humidity results are presented in figure 6.22. These clearly show that the buffer largely saturates quickly, under 500 days. There is some uncertainty in the data as some results are shown to jump from under 80% to saturation in the lower sensors. There are some locations in the centre of the cylinders that remain dry and may even undertake some drying from the initial state, see sensor WBU10032. The sensor closer to the heater WBU10022 is clearly shown not to be working, only recording less approximately 20% humidity for a short time.

Temperature

The temperature, as shown in figure 6.23, rises quickly in the first 300 days and then reaches an almost steady state, with a peak at the mid-height of 72.04°C at day 767. This sensor stops working at day 1049, but the trends from the rest of the sensors show a reduction in temperature after this time due to reduction in power to the heaters. The temperatures in the upper section of the buffer are significantly lower than at the mid-height as are the temperatures in the lower region of the buffer. The canister surface temperature is shown by Goudarzi and Johannesson (2007) to be about 75 °C maximum.

Power

The idealised power curve, i.e. the power intended to be delivered, is shown against the measured power for DH-1 in figure 6.24. This gives a good indication that, in general, the power that was expected was delivered was delivered, albeit with a degree of variation.

6.6.1.2   Deposition-hole 3

Total pressure

The total pressure in DH-3 shown in figure 6.25 is much lower than in DH-1 with a maximum of $4MPa$ after 1500 days. The sensors at the mid-height of the canister do not show any significant pressures. At the top of the canister pressures of approximately $2MPa$ after 1500 days are recorded.

Relative humidity

Figure 6.26 shows the relative humidity values for DH-3. At the top of the buffer some saturation occurs in the outer bentonite, with significant drying at the centre of the cylinder just above the heater. At the mid-point and the lower regions a small hydraulic gradient is formed across the sample, but no significant saturation occurs. The sensors have largely stopped working, but are showing an almost steady-state.

Temperature

The temperature results shown in figure 6.27 are largely qualitatively similar to DH-1. The values are higher than in DH-1, at approximately 80 °C in places near the heater. This is likely to be due to the temperature interaction with other deposition-holes. The canister surface temperature is high, approximately 90 °C indicating that the air filled annulus has not been closed by bentonite swelling.

6.6.1.3 Backfill

The temperature results show little of interest with temperatures observed to rise to around 35°C and a small temperature gradient developing. This gradient is negligible compared to the gradients in the buffer material.

The total pressure results show less than $0.5MPa$, except for when pore-water-pressures are shown to increase. This occurs between days 1100 and 1200 and is due to the drainage being switched off and then on again. These are considered to be background results considering the range of pressures for which the sensors were intended to detect, i.e. approximately $20MPa$.

The suction results have been shown in figure 6.28 at the mid point in the tunnel along the section. In general the same trend is followed, a gradual reduction in suction from approximately $3MPa$ to around $0-1MPa$ by the end of the results. Sensors WBA10003 and WBA10006 are shown to be saturating the quickest and are located $3m$ towards the end of the tunnel from DH-1 and directly above DH-1 respectively. The remainder of the tunnel is saturating at a slower rate until near the plug where an increase in saturation is recorded.

6.6.1.4 Rock

Only the results in the rock near to DH-1 are presented here as this gives a good representation of how the temperature field has developed in the rock and the gradients that exist within it. Other measurements have been made and can be found in Goudarzi and Johannesson (2007). Figure 6.29 show the results at the distance of $2m$, $5m$ and $9m$. At a distance of $9m$ there is very little temperature variation in any of the sensors and indeed from the

background temperature. At $5m$ there is approximately a 5 °C variation in temperature and at $2m$ approximately 13 °C.

6.6.2 Section 2

Section 2 was not activated until approximately 600 days after section 1, hence results are only presented from this time.

6.6.2.1 Deposition-hole 5

Total pressure

The total pressures are shown in figure 6.30. In the upper section of the buffer the total pressures quickly reach a value of approximately $2MPa$ after approximately 650 days (50 days after section 2 is activated) and then slowly increases. At the mid-height a value of approximately $6MPa$ is reached by the end of the readings with the gradient remaining approximately constant. The top and bottom trends are similar to that of mid-height but with a slightly lower absolute values of approximately $5MPa$.

Relative humidity

The relative humidity readings shown in figure 6.31. They show saturation being quickest at the top of the deposition-hole, slower in the middle and very slow at the bottom. There is also significant drying at the top of the canister in the centre of the bentonite cylinder.

Temperature

The temperature results are shown in figure 6.32 and are again qualitatively similar to DH-1 and DH-3, reaching a peak value between the two. There is also a high temperature at the centre of the cylinder below the canister.

6.6.3 Results analysis

The results show some similarities and some distinct differences between the deposition-holes. DH-1 saturates quickly, except in areas furthest away from the rock and near heaters where drying occurs. This causes swelling with highest values near the base of the buffer. DH-3 saturates much slower and seems to reach an unsaturated steady state, which may be due to

changes in the bentonite or to an equilibrium in the hydraulic field due to vapour transport due to the temperature gradient and liquid transport due to pore-water pressure gradient. This could indicate that saturation may speed up when the heat flux is reduced.

The variation in the temperature field is limited to a region close to the canister, approximately within $10m$ from the deposition-holes. However, it is large enough that the temperature field from each canister interacts and results in an increase in temperature in the inner deposition-holes. This may be significant for repository design.

There is some uncertainty as to the reliability and quality of readings for some of the sensors. The temperature sensors seem reasonable, with very little data counter to the trends shown by other sensors. There are some results for the relative humidity sensors that indicate they are not as reliable. For example in DH-1 some of the sensors show a dramatic jump from approximately 80% to 100% relative humidity instantaneously. The total pressure sensors also appear to have a large degree of uncertainty. Trends are hard to spot and it is possible that due to the material being a porous medium these sensors are recording local information, which may be different to the overall material response.

A large number of sensors have stopped working. Where sensors have previously been showing steady state, it is possible and reasonable to extrapolate results and gain confidence in modelling. In other cases, for example stress behaviour, there are still large gradients so it is possible to extrapolate results but with much less confidence.

A number of key features are:

- Deposition-hole 1 saturates at a much faster rate than other deposition-holes.

- No deposition-hole becomes fully saturated.

- Temperature fields generally seem reliable.

- Total pressure sensors generally increase as hydration occurs, however patterns in results are difficult to determine and reliability is questionable.

- A large number of sensors have now stopped working.

6.7 Conclusions

The Prototype Repository Project is a full-scale mock-up of a High-Level Nuclear-Waste deep geological repository, using the KBS-3 system, that is designed to investigate the thermo-hydro-mechanical response, among others, of the near-field. This chapter has outlined the background and motivation of the project, including what the project aimed to achieve, highlighted the key dates to the project and specified the geometry and position of the project. In particular, the timeline of the project was presented detailing the emplacement and backfilling timetable integrated with the heating regime.

The pre-placement experimentation and rock characterisation has been discussed with the rock found to be highly characterised in particular the hydraulic behaviour has been tested via a series of tests both inflow tests and tests using boreholes drilled into the rock mass. An indication of fractures existing within the mass can be gained from this data. From the inflow tests it is clear that the flow is highly anisotropic. The flow into deposition-hole 1 is approximately a magnitude greater than the flow into any other deposition-hole. In addition, the flow into the tunnel is also highly anisotropic.

Placement of the materials into the deposition-holes is detailed with the backfill being compacted in-situ highlighted and the method illustrated. The location of sensors in the deposition-holes, rock and backfill was identified, along with the variable that was measured. A salient selection of data has been collated and presented along with a brief description of the behaviour within the project. The results are analysed in conjunction with some of the findings reported in the chapter.

6.8 References

Börgesson, L., Gunnarsson, D., Johannesson, L-E., Sandén, T., (2002) *Äspö Hard Rock Laboratory, Prototype Repository, Installation of buffer, canisters, backfill and instruments in Section 1*, SKB, IPR-02-23, Stockholm.

Johsnnesson, L-E., Gunnarsson, D., Sandén, T., Börgesson, L., (2004) *Äspö Hard Rock Laboratory, Prototype Repository, Installation of buffer, canisters, backfill and instruments in Section II*, SKB, IPR-04-13, Stockholm.

Johannesson, L-E., Börgesson, L., Goudarzi, R., Sandèn, T., Gunnarsson, D., Svemar, C., (2007) "Prototype

repository: A full scale experiment at Äspö HRL", *Physics and Chemistry of the Earth*, **32**, 58-76.

Melhuish, T.A., (2004) "An investigation of the three-dimensional thermo/hydro/mechanical behaviour of large scale in-situ experiments" *PhD Thesis*, Cardiff University.

Goudarzi, R., Johannesson, L-E., (2007) *Äspö Hard Rock Laboratory, Prototype Repository, Sensors data report (Period 010917-070601) Report No:17*, SKB, IPR-07-19, Stockholm.

Patel, S., Dahlström, L-O., Stenberg, L., (1997) *Äspö Hard Rock Laboratory, Characterisation of the rock mass in the prototype repository at Äspö HRL stage 1*, SKB, HRL-97-24, Stockholm.

Rhén, I., Forsmark, T., (2001) "Äspö Hard Rock Laboratory, Prototype Repository, Summary report of investigations before the operation phase" *SKB*, IPR-01-65, Stockholm.

Svemar, C., Pusch, R., (2000) *Äspö Hard Rock Laboratory, Prototype Repository, Project description*, SKB, IPR-00-30, Stockholm.

DH-1
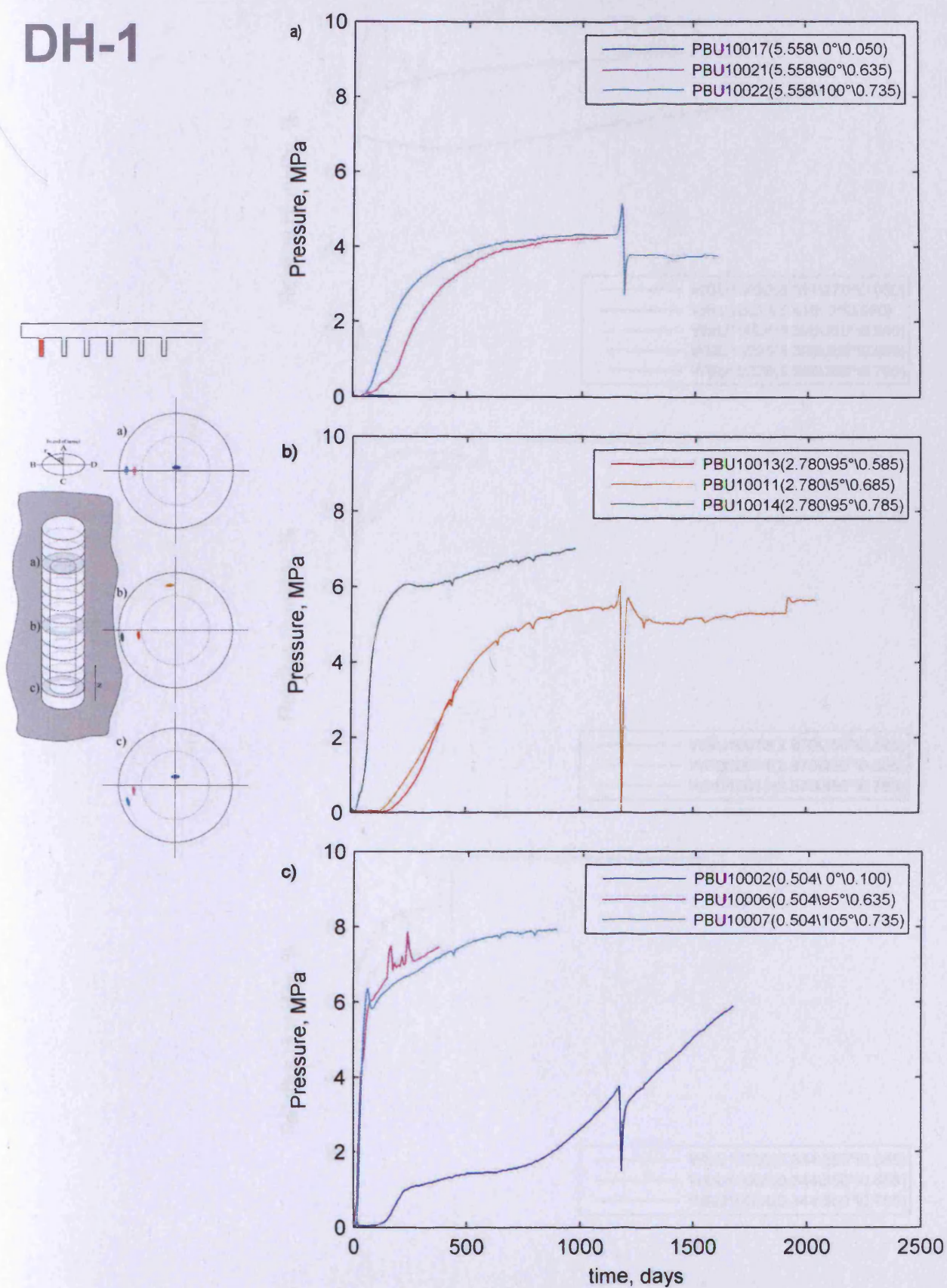
Figure 6.21. Total pressure measurements in DH-1, after Goudarzi and Johannesson (2007).
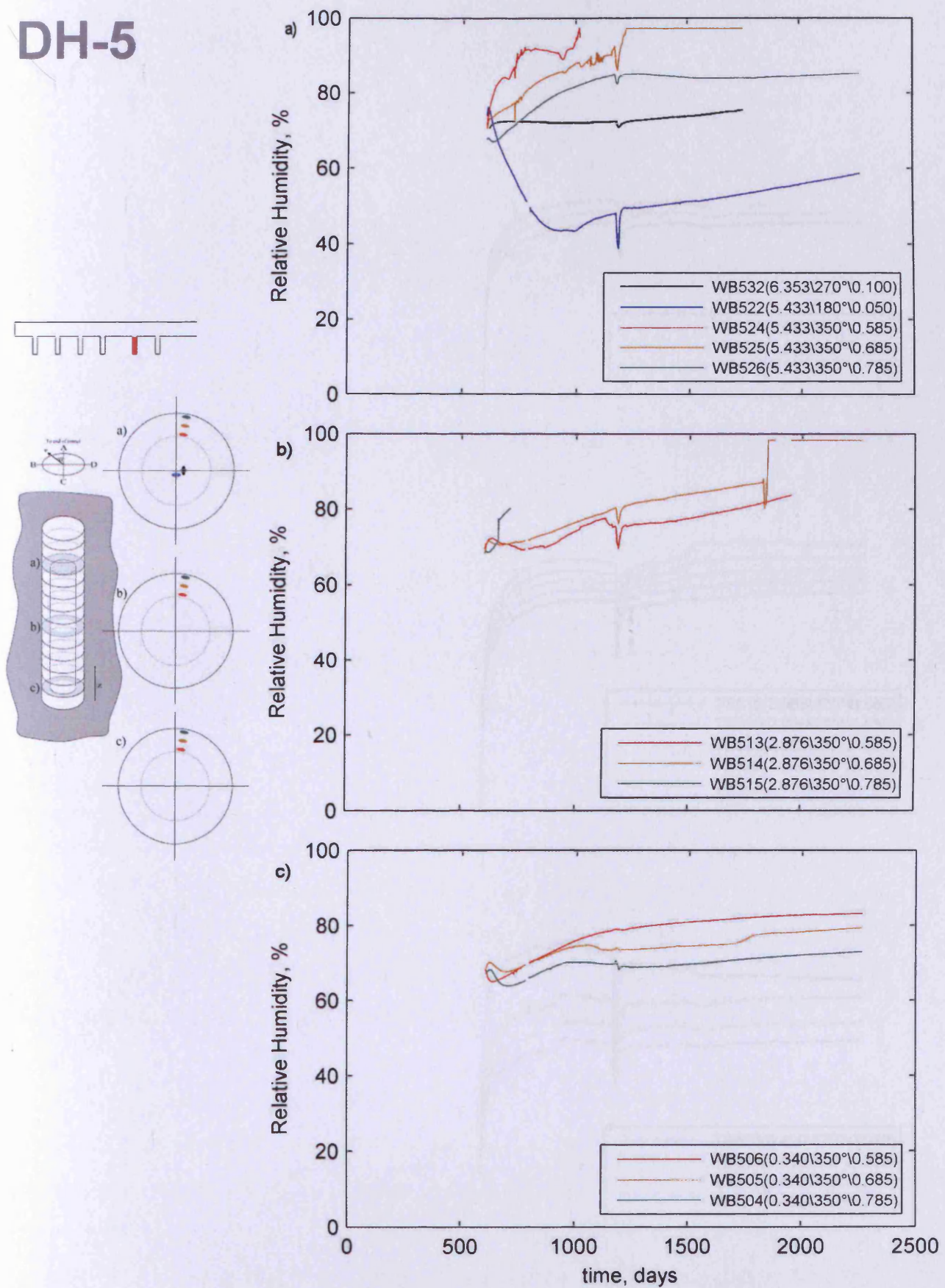
DH-1
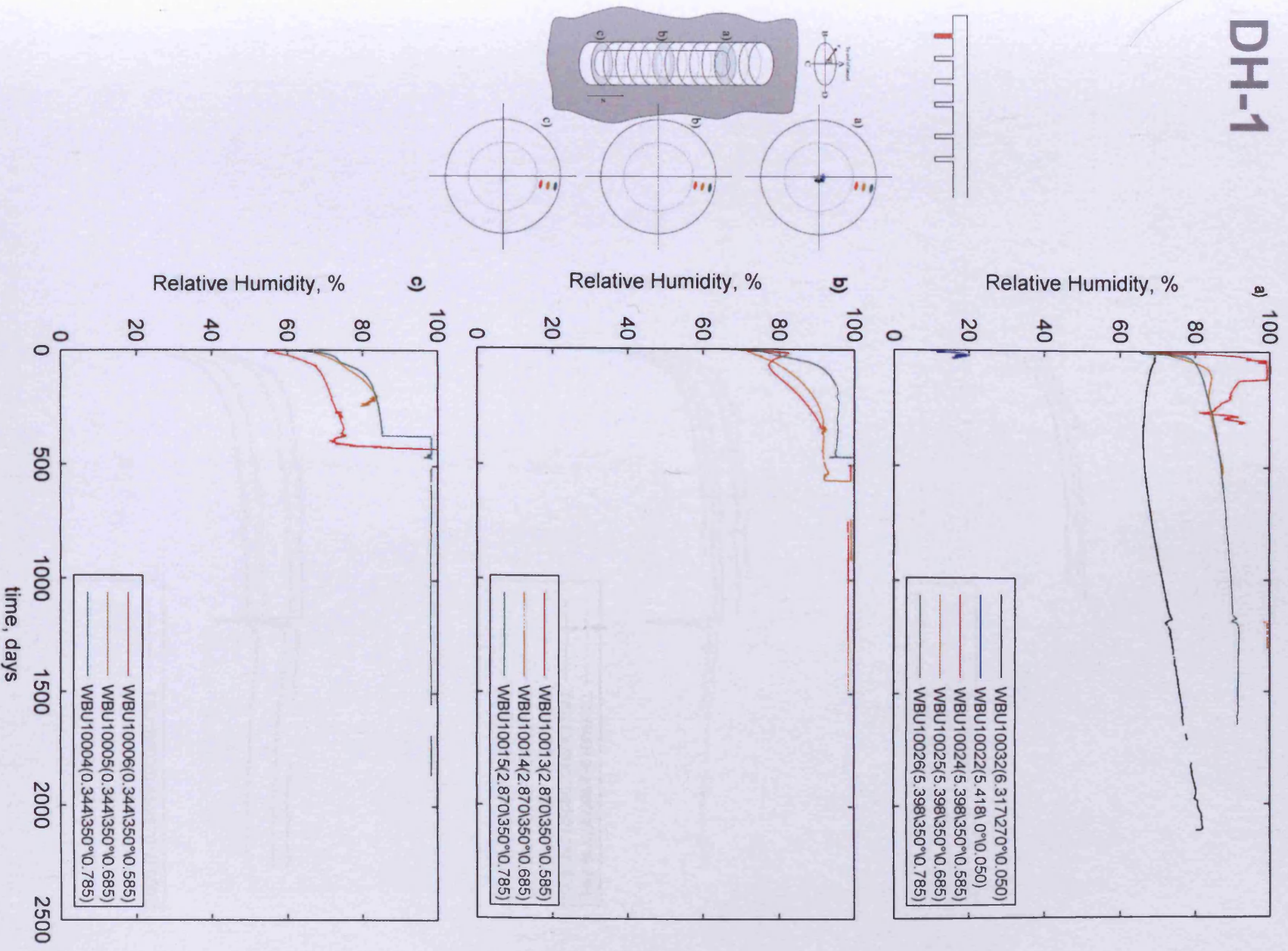
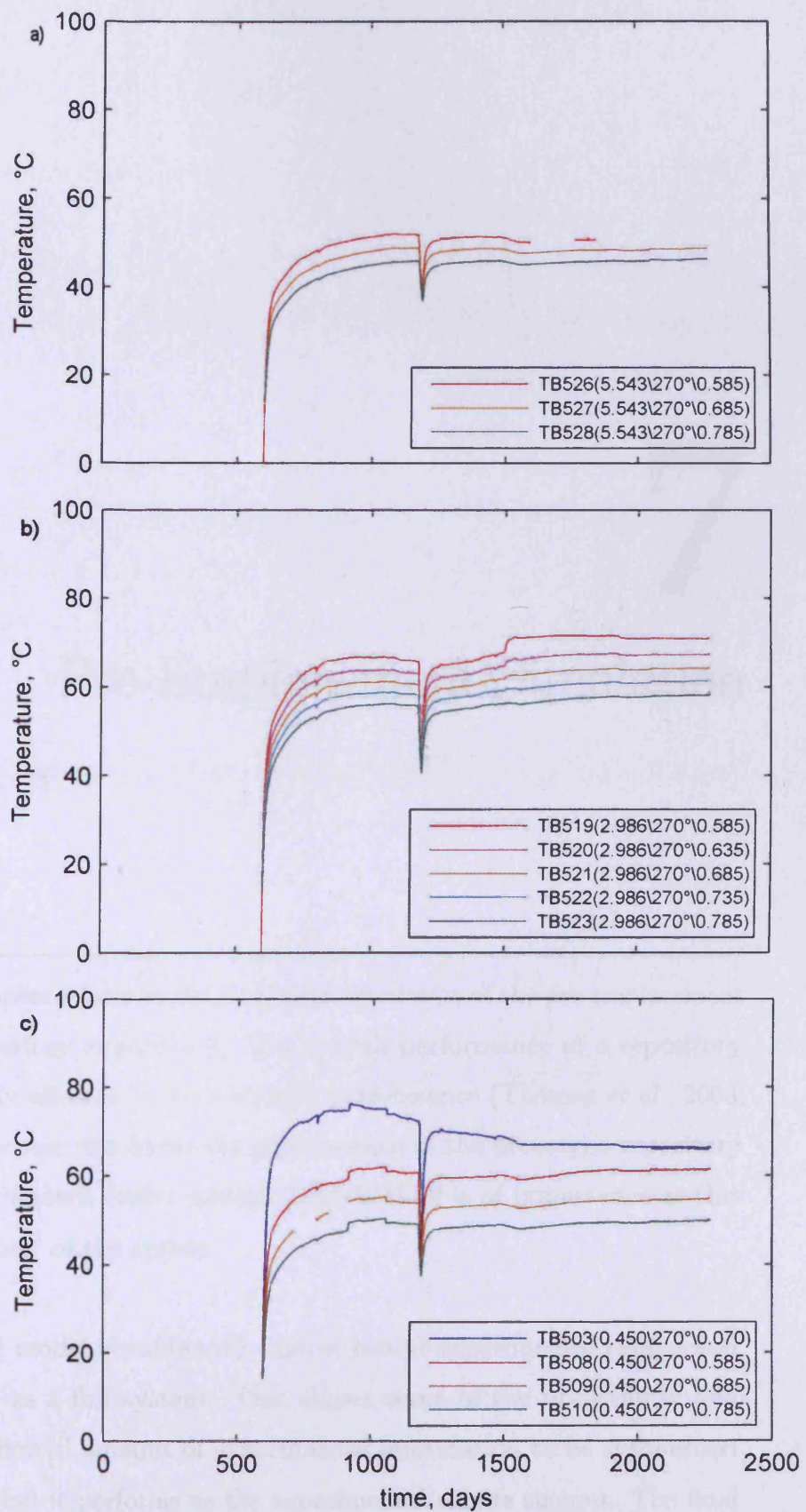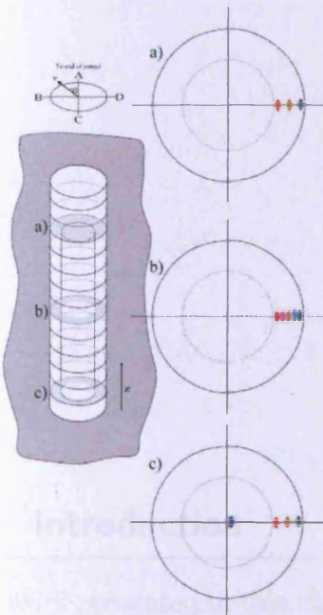**Figure 6.22.** Relative Humidity measurements in DH-1, after Goudarzi and Johannesson (2007).
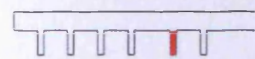
DH-1
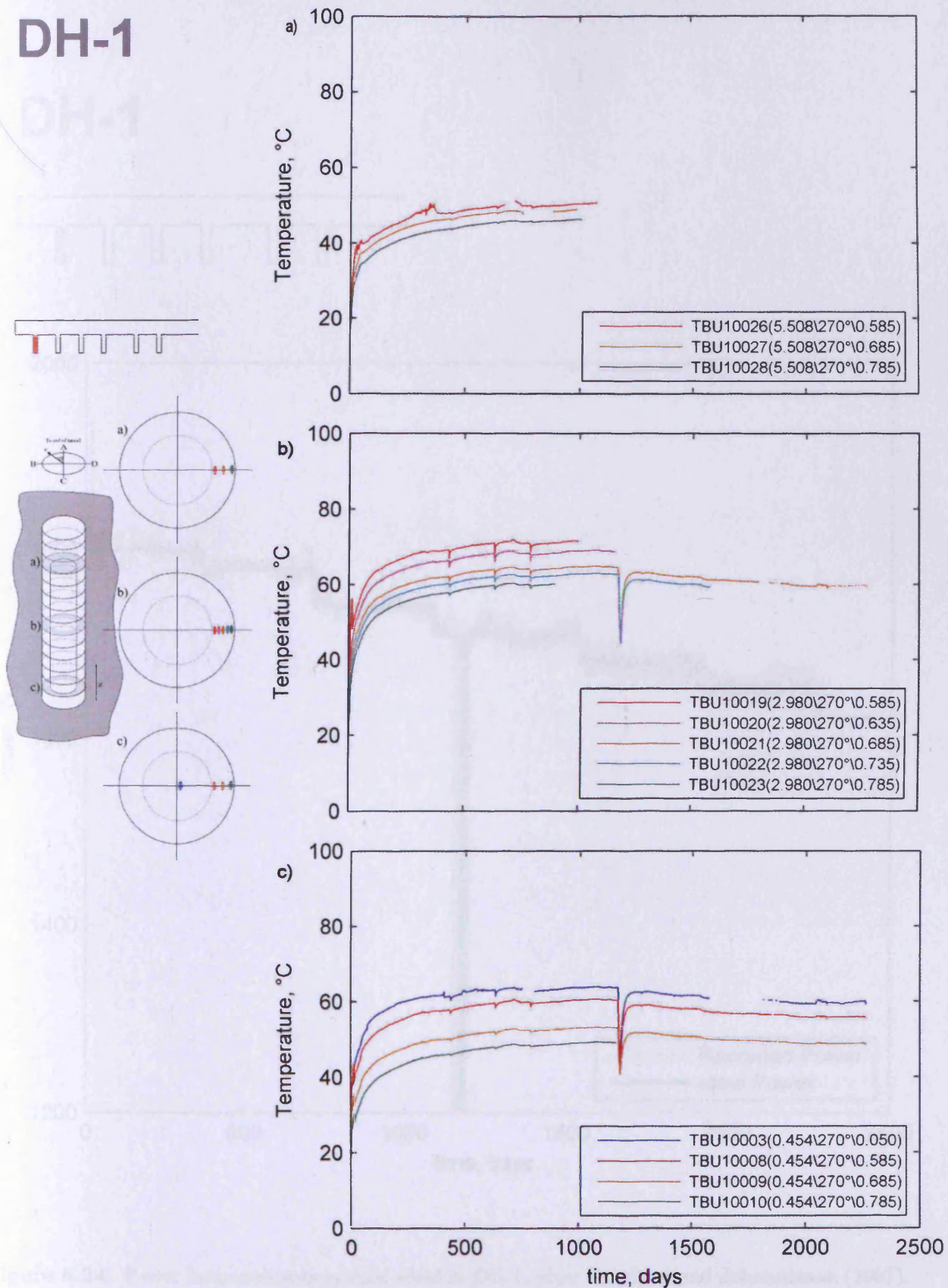
Figure 6.23. Temperature measurements in DH-1, after Goudarzi and Johannesson (2007).
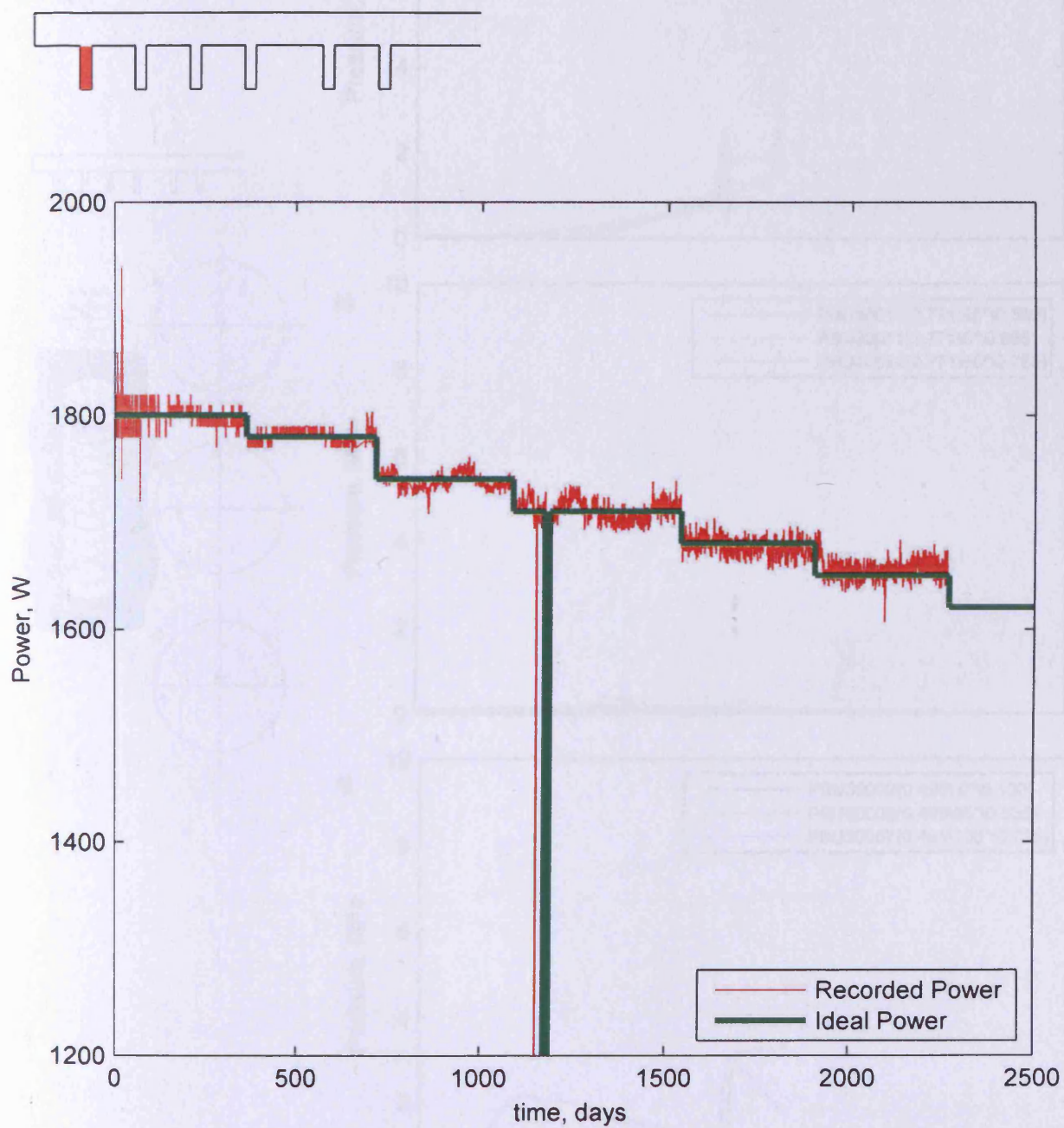
Figure 6.24. Power measurements against ideal in DH-1, after Goudarzi and Johannesson (2007).

DH-3

a)

Legend:
- PBU30017(5.556\ 0°\0.050)
- PBU30021(5.556\90°\0.635)
- PBU30022(5.556\100°\0.735)

b)

Legend:
- PBU30013(2.771\95°\0.585)
- PBU30011(2.771\5°\0.685)
- PBU30014(2.771\95°\0.785)

c)

Legend:
- PBU30002(0.495\ 0°\0.100)
- PBU30006(0.495\95°\0.635)
- PBU30007(0.495\105°\0.735)
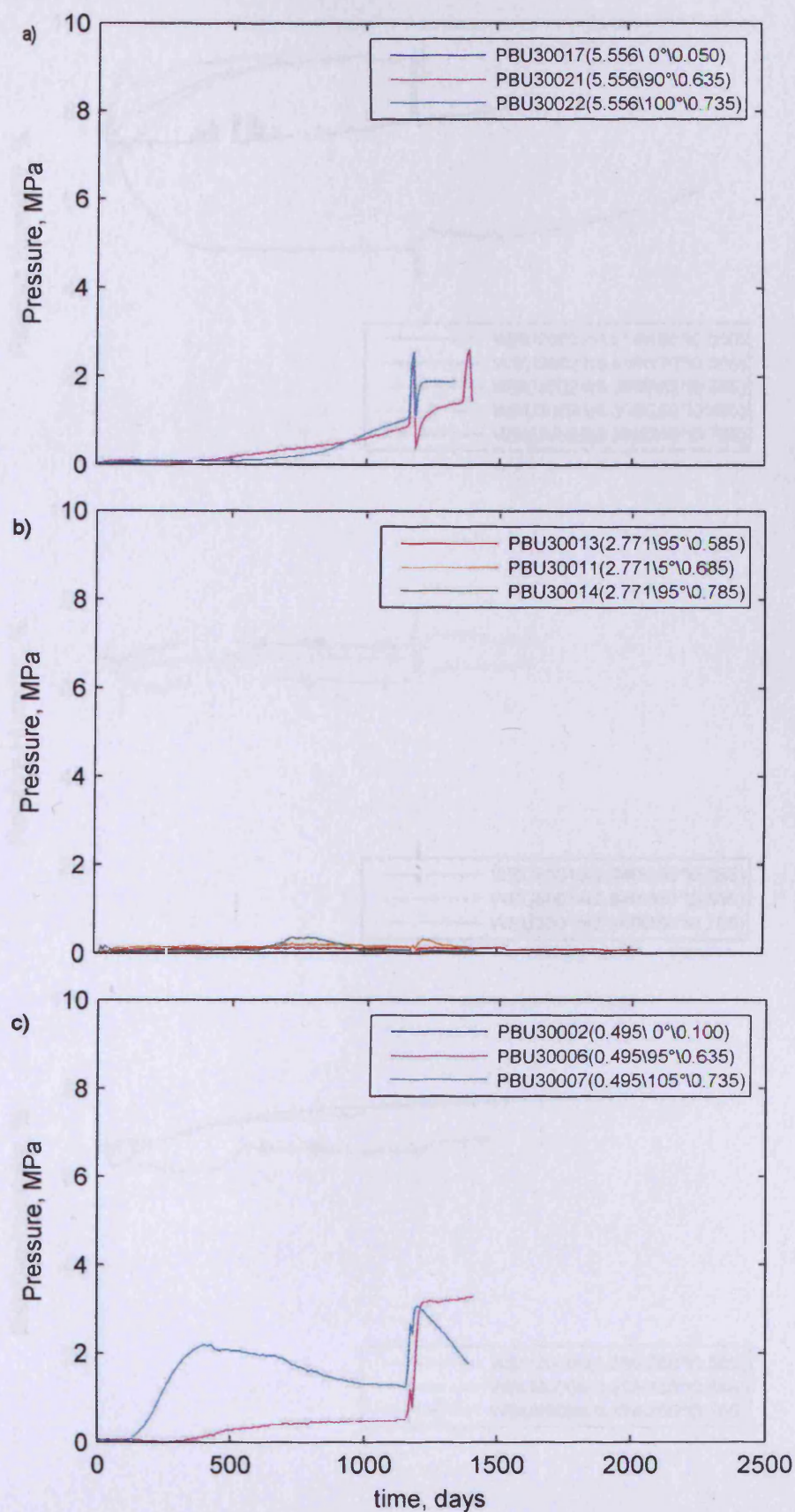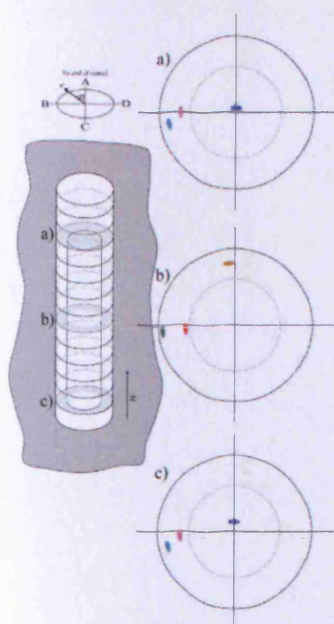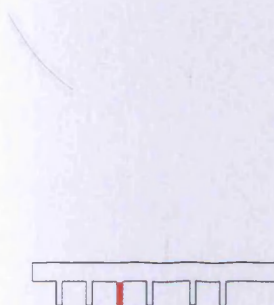
Figure 6.25. Total pressure measurements in DH-3, after Goudarzi and Johannesson (2007).
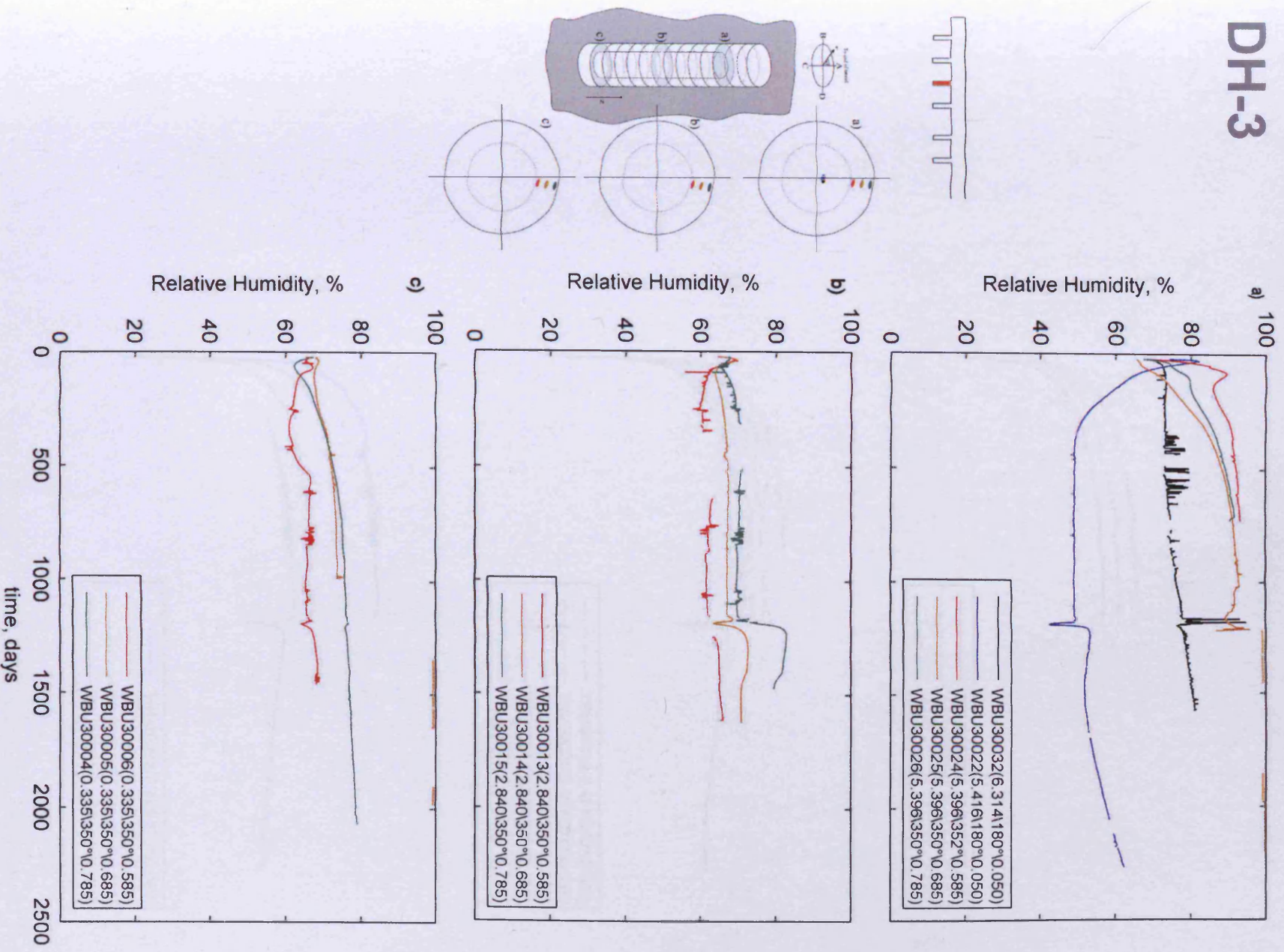
Figure 6.26. Relative Humidity measurements in DH-3, after Goudarzi and Johannesson (2007).
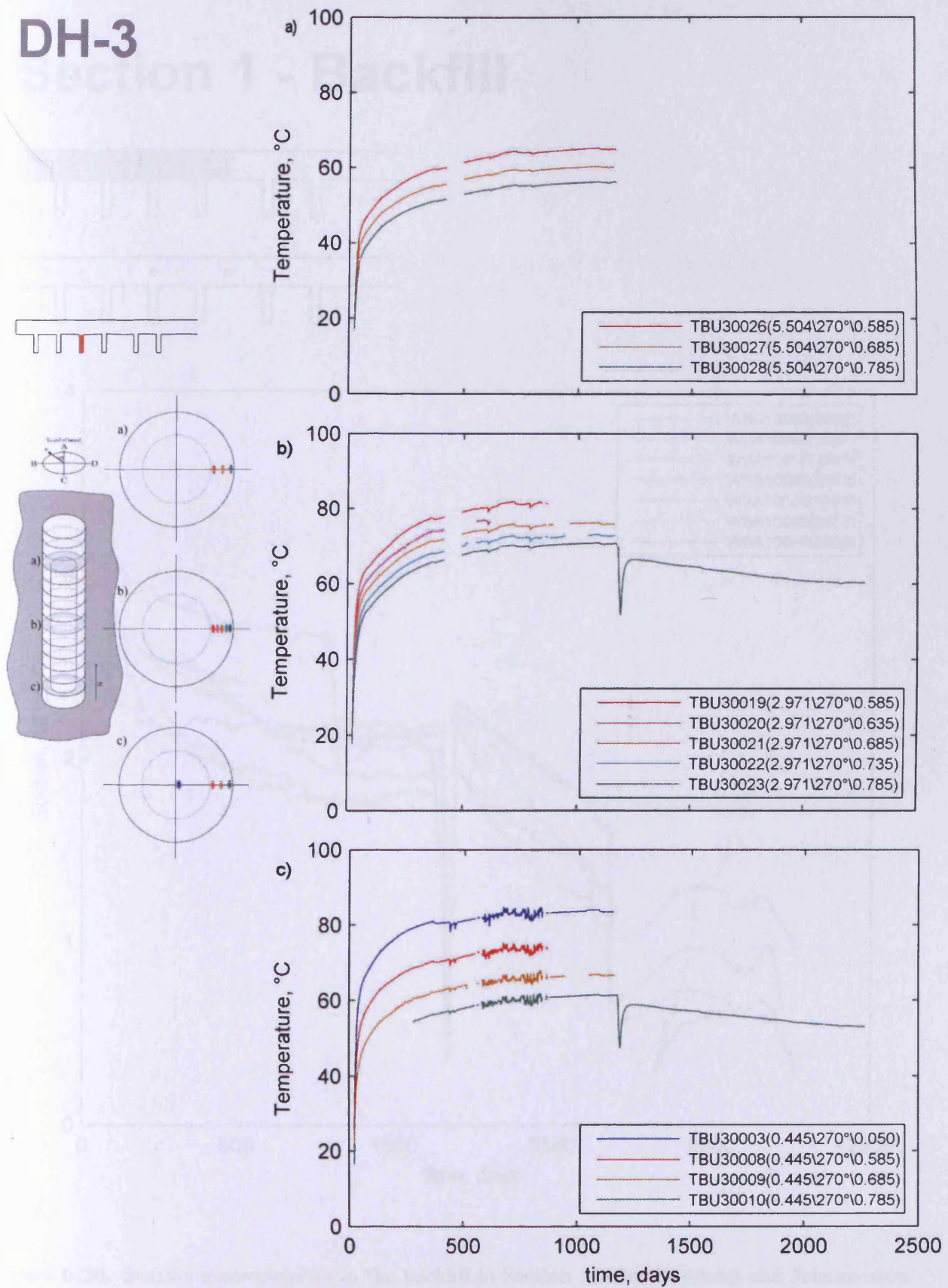
Figure 6.27. Temperature measurements in DH-3, after Goudarzi and Johannesson (2007).

Section 1 - Backfill
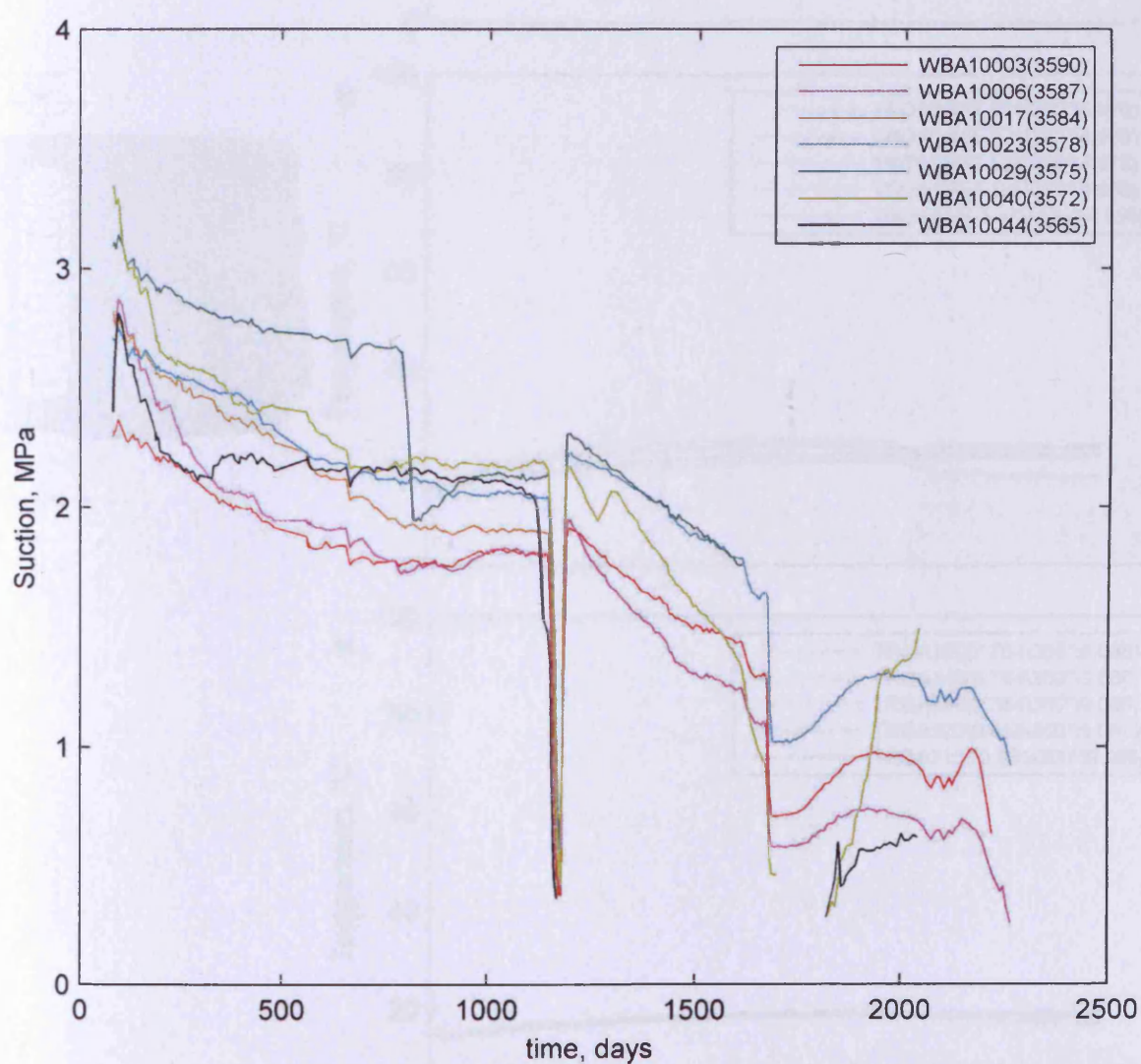
Figure 6.28. Suction measurements in the backfill in Section 1, after Goudarzi and Johannesson (2007).

DH-1
Rock
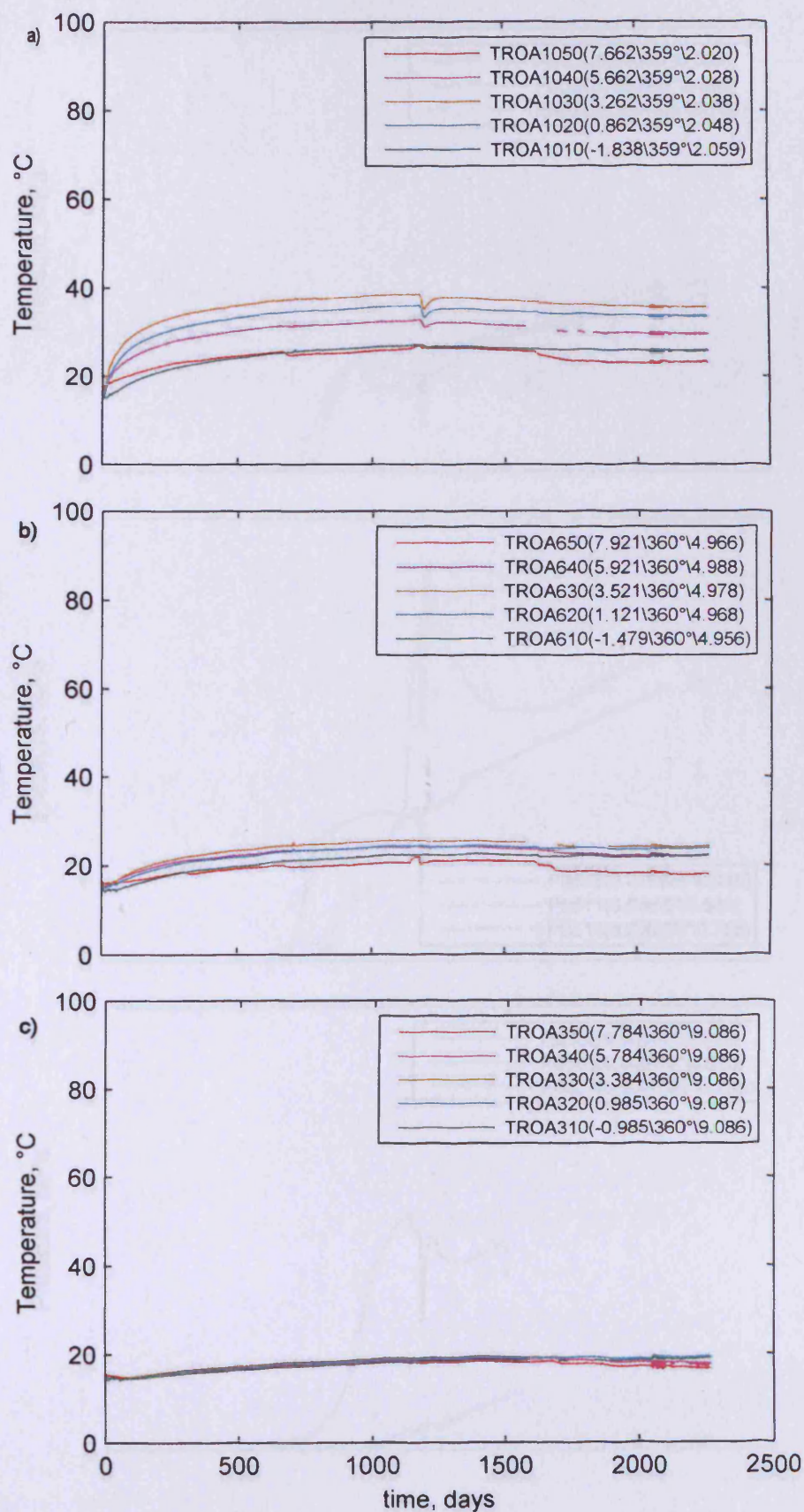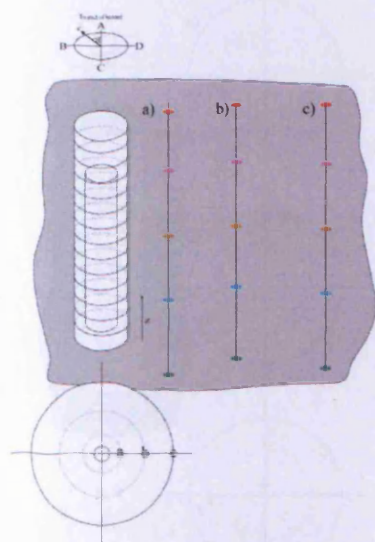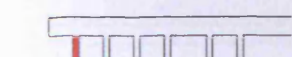
Figure 6.29. Temperature measurements in the rock surrounding DH-1, after Goudarzi and Johannesson (2007).

DH-5
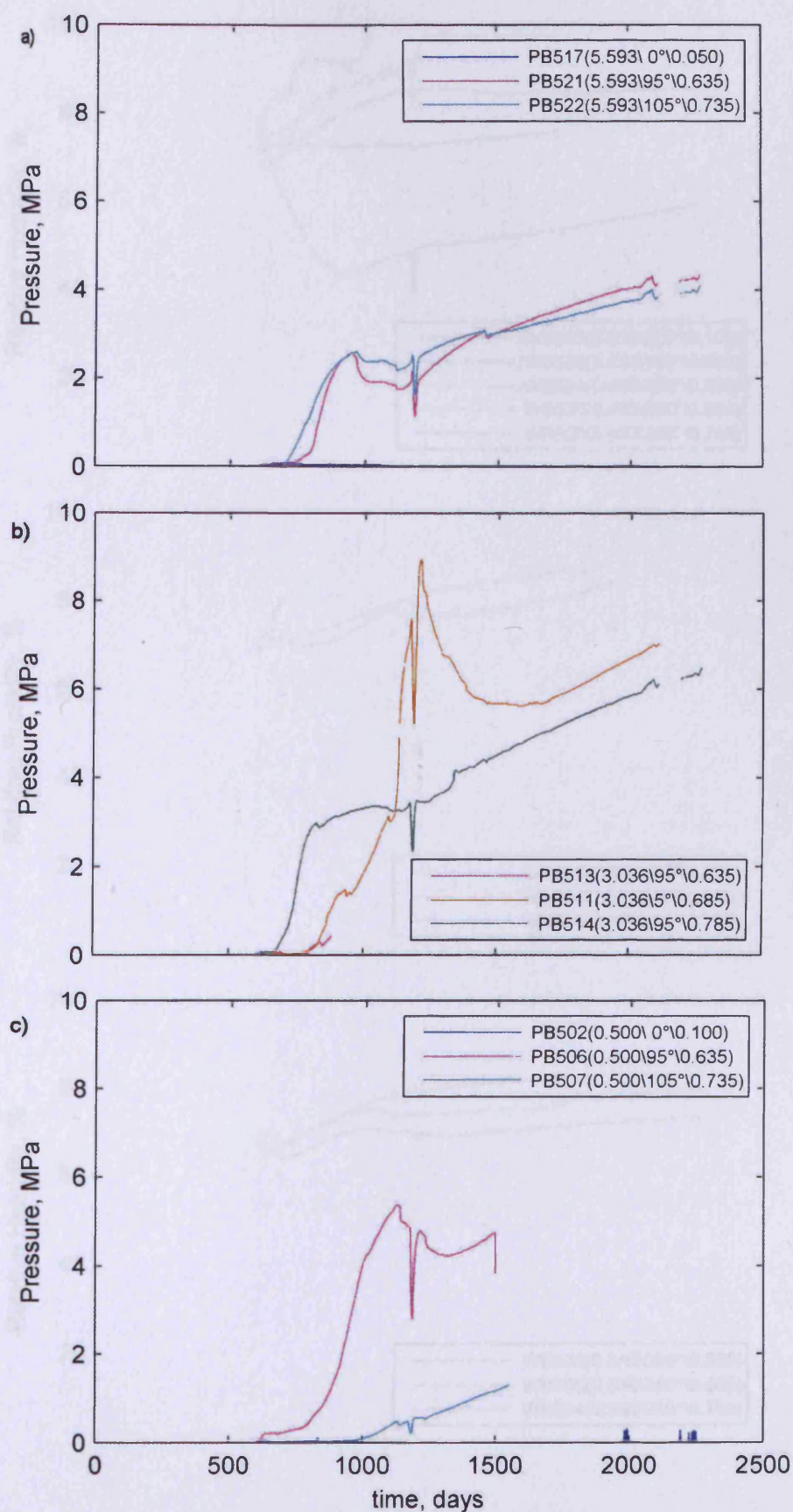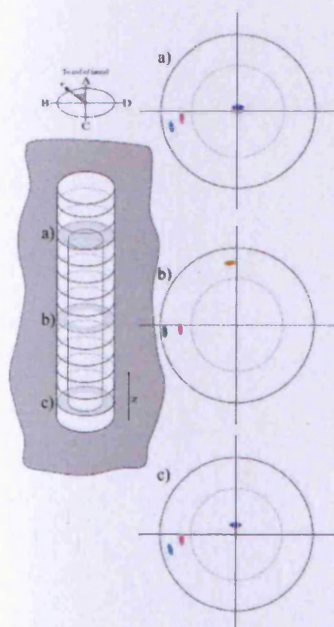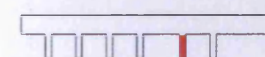
Figure 6.30. Total pressure measurements in DH-5, after Goudarzi and Johannesson (2007).

Figure 6.31. Relative Humidity measurements in DH-5, after Goudarzi and Johannesson (2007).

DH-5

Figure 6.32. Temperature measurements in DH-5, after Goudarzi and Johannesson (2007).

7

Pre-Emplacement Simulation

7.1 Introduction

The work presented in this chapter relates to the numerical simulation of the pre-emplacement stage of the Prototype Repository experiment. The overall performance of a repository structure is likely to be largely affected by its hydraulic performance (Thomas *et al.*, 2003; Vardon *et al.*, 2008). In particular, the hydraulic performance of the prototype repository prior to emplacement of the heaters, buffer material and backfill is of importance as this represents the 'initial conditions' of the system.

In this chapter the numerical model is calibrated against initial experimental results and assessed in three-dimensions as a full system. This allows some of the uncertainty and assumptions yielded from a limited amount of experimental information to be synthesised into the numerical model so that it performs as the experimental results suggest. The final results from this chapter, the calibrated model and simulation output, will be used as input into the post-placement simulations. This then forms a cohesive modelling strategy whereby

a calibration phase is first carried out and then additional simulations are undertaken to verify the model.

The rock characterisation, outlined in chapter 6, produced a number of discrete experimental results. For example, a number of individual fractures, fracture paths and rock masses were characterised. Synthesising these into a single model where all aspects interact can be problematic and calibration is required, particularly as all the experimental results have an implicit degree of uncertainty.

Site data has been collected related to infiltration into the repository (Rhén and Forsmark, 2001) and so can provide a benchmark against which the results of numerical simulation can be validated. The implication of this is that confidence can be gained in the modelling strategy and material parameters used. In such a large analysis this can provide an early indication of correct model calibration.

The proposed modelling strategy is described in section 7.2. The geometric model and material parameters are offered in sections 7.3 and 7.4, with details of the simulations undertaken presented in section 7.5. Results from the simulations are presented in section 7.6 with results from the calibrated model presented in section 7.7. Concluding remarks are given in section 7.8.

Chapter 6 contains information about the project including the available pre-placement hydraulic site data in section 6.3.

7.2 Proposed modelling strategy

In this chapter consideration must be given to how best to simulate the hydraulic field within the rock mass prior to emplacement of the heater and engineered barrier materials. However, consideration must also be given to the later analyses which will include emplaced buffer and backfill material.

The modelling techniques of geomaterials such as soils and rocks have been reviewed in chapter 2. Generally, soils and intact rock can be modelled as a continuum, but for fractured

rock the appropriate modelling technique depends upon the nature of the material and the type and resolution of results required. Continuum models are generally more suited to simplification e.g. by reducing the dimensions of a model, but where important features exist, modelling as an effective continuum or simplification may not be possible. Inherently three-dimensional domains occur with heterogeneous and anisotropic behaviour possible.

In the problem considered here (i.e. a deep geological repository) both large-scale and localised behaviour are of importance. It is also important to link with a fully coupled THM model of the repository, which lends itself to a continuum model. The repository system is considered inherently three-dimensional due to the geometry of the repository structure and the discontinuities in the rock mass. In addition, the data available regarding the discontinuities in the rock mass is limited to that gained during the experimental programme. It is focused close to the repository as that was where fractures could be identified on the surface and boreholes were drilled from. A limited number of key hydraulically conductive fractures have been identified. Therefore, a three-dimensional model has been developed using a continuum finite-element formulation allowing the inclusion of discrete features. This is to enable a high resolution of results around the repository structure, including highly preferential flowpaths, while maintaining reasonable computational performance. The domain is considered as consisting of a number of different regions; the first, generally in the far field, assumes the rock mass is an effective continuum and utilises spatially averaged material properties; and the second, in the near field, considers the rock mass as a combination of intact host rock and known hydraulic features. The domain under investigation is divided into these regions and each part considered as a continuum. This approach allows the consideration of other materials, such as emplaced clay buffer or backfill to be easily included.

This stage is considered to be hydraulic only as no heaters are present in the experiment at this stage, as such only the hydraulic results are presented. The system is considered to be isothermal as there is no major heat differential in the system and no other sources of heat apparent to provide any change. The rock mass is hypothesised to remain largely saturated in this phase, and with no extra applied stress, total stresses will remain constant in this phase.

7.3 Domain and geometric model

The information from the site data and the modelling strategy have been used to create a geometric model of the domain for the pre-emplacement condition i.e. an empty tunnel and deposition-holes within a rock mass, shown in figure 7.3. The domain has been chosen to extend approximately $50m$ away from the repository in all directions, to ensure that the boundary conditions will not unduly effect the results. During the analyses presented in this chapter the hydraulic flux has been monitored at the domain edge to ensure that this assumption is true. In addition, a single analysis has been undertaken with a domain $100m$ away from the repository in all directions with only negligible differences in any results (less than 1%). The total domain size is 100x100x160m with the 160m dimension being along the length of the tunnel.

7.3.1 Proposed fracture model

As a result of the interference tests 1:1-1:6, undertaken after drilling campaign 3, a number of fractures were identified (Rhén and Forsmark, 2001), it is these deterministic features that make up the proposed fracture model. The fact that some deterministic features have been identified does not, by default, suggest that the remainder of the rock mass is not fractured, but only that during the tests, significant identifiable preferential flow directions have not been recognised in those regions. The sampling process uses a discrete number of boreholes to identify these features and as such, some features are likely to be missed, but those of reasonable size and proximity to the tunnels are likely to have been identified. Smaller hydraulic features are less likely to be determined. The radial borehole distribution means that the density of boreholes is reduced as distance from the tunnel increases. The implication of this is that as the distance from the tunnel increases the testing procedure is less likely to determine features and a statistical distribution of features or averaged material properties must be assumed.

Table 7.1 summarises the features identified by Rhén and Forsmark (2001), where T is the transmissivity. It is initially hypothesised that these features have a circular shape, with the coordinates quoting the centre of the feature, in the Äspö coordinate system. Comparing these features with the fracture mapping in figures 6.10 and 6.11 (repeated here in figure

Feature	East (m)	North (m)	Z (mamsl*)	Strike (°)	Dip (°)	Radius (m)	T (m²/s)
North	1892	7289	-449	118	88	20	$5 - 10 \times 10^{-8}$
South	1887	7266	-449	124	89	20	$7 - 9 \times 10^{-8}$
3587/1	1878.28	7275.03	-453.53	354	79	2	8.1×10^{-9}
3551/1	1915.42	7271.06	-455.24	312	40	2	4.7×10^{-9}
3551/2	1917.50	7269.90	-455.56	271	38	2	3.3×10^{-9}
3545/1	1919.55	7268.80	-453.54	164	64	2	2.8×10^{-10}
3545/2	1919.55	7268.80	-456.66	278	24	2	1.7×10^{-9}
3545/3	1921.45	7270.22	-453.14	298	64	2	1.3×10^{-8}

*meters above mean sea level

Table 7.1. Preliminary fracture model data (Rhén and Forsmark, 2001)

7.1 and 7.2) helps build confidence in this model. The minor feature 3587/1 coincides with DH-1 and this can be seen in the fracture mapping (figure 7.2a). The remaining minor features can be shown to be intersecting or surrounding DH-5 and DH-6, which also agrees with the large amount of hydraulically active features observed during surface mapping, e.g. figure 7.2c has a number of water bearing locations.

Area 2, highlighted on the tunnel fracture map, figure 7.1, shows a region with a well defined fracture which is hydraulically active and coincides with the intersection between the tunnel and the South Major fracture. However, area 1, highlighting a large water flow into the tunnel and another well defined fracture does not coincide with any deterministic feature proposed by Rhén and Forsmark (2001), although is close to the South Major fracture and it is possible to have some interaction. A specific volume of the rock in this area has been added to the model to allow the impact of increased permeability in this region to be assessed, for convenience named *Region 1*.
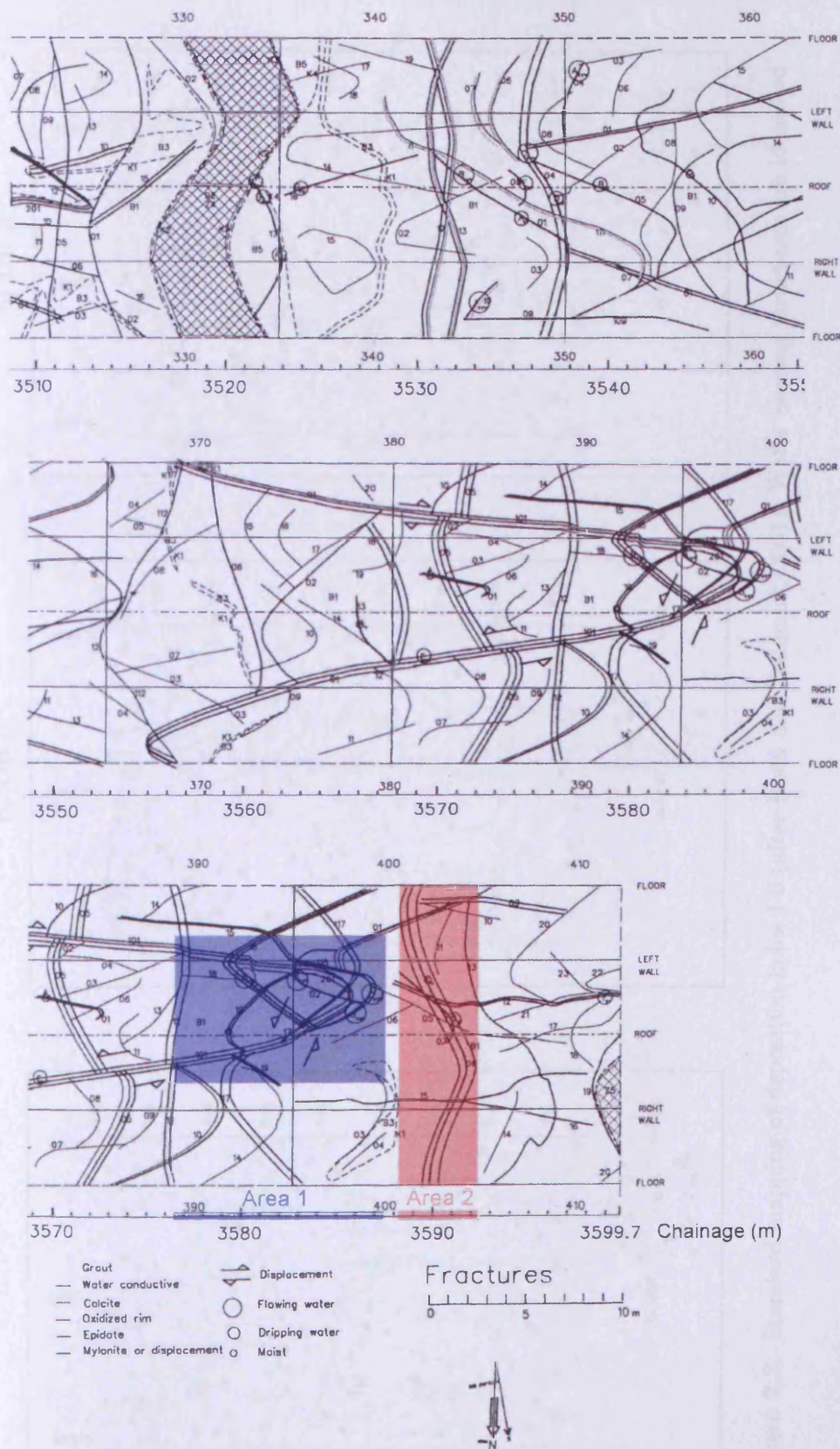
Figure 7.1. Standard mapping of fractures along tunnel, where the centreline is the roof (after Rhén and Forsmark, 2001). Water bearing structures are identified.
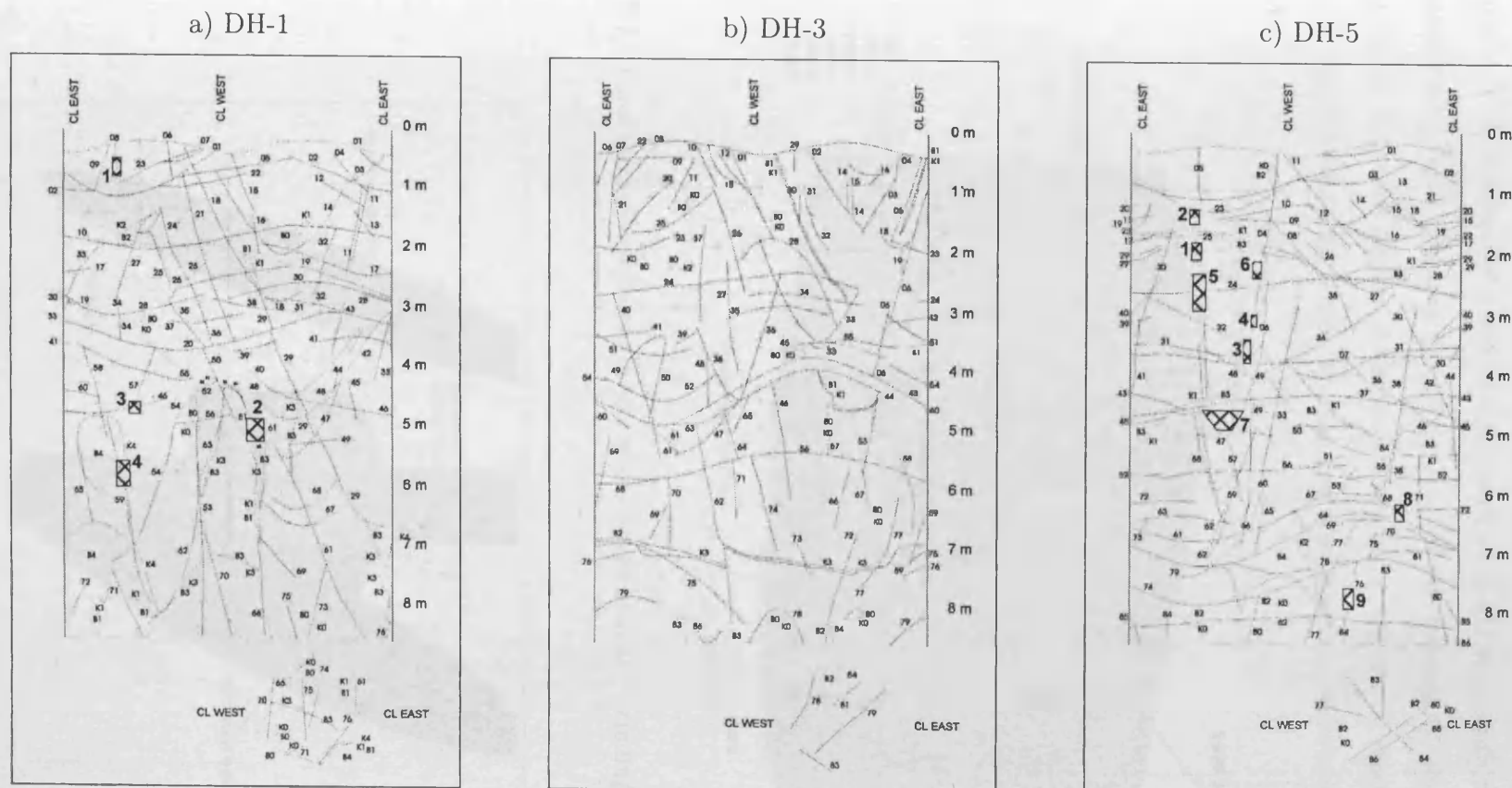
Figure 7.2. Standard mapping of deposition-holes 1-6 (after Rhén and Forsmark, 2001). Water bearing structures are identified.

The mapping of the boreholes and the identified water bearing features (Rhén and Forsmark, 2001) largely correspond to the hydraulic features identified from the inference tests as shown above. This agreement of data builds confidence in the identification of these features. A visualisation of these features in the context of the repository and deposition-holes is shown in figure 7.3; with *Region 1* shown in figure 7.4; the minor fractures shown in detail in figures 7.5 and 7.6 and the water bearing features are shown schematically on figures 6.12 and 6.13.
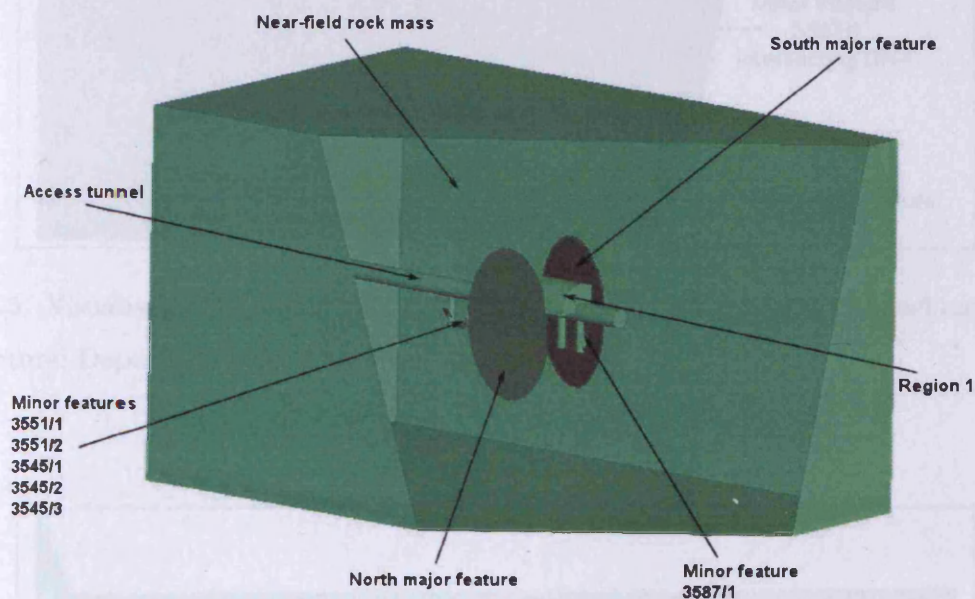
Figure 7.3. Three-dimensional visualisation of the model domain, including the proposed fracture model.
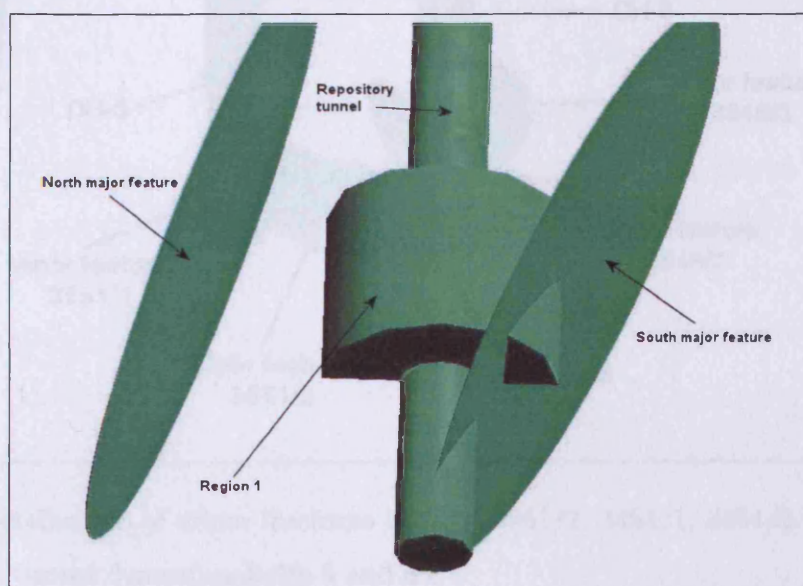
Figure 7.4. Visualisation of *Region 1*, including the repository tunnel and major features.
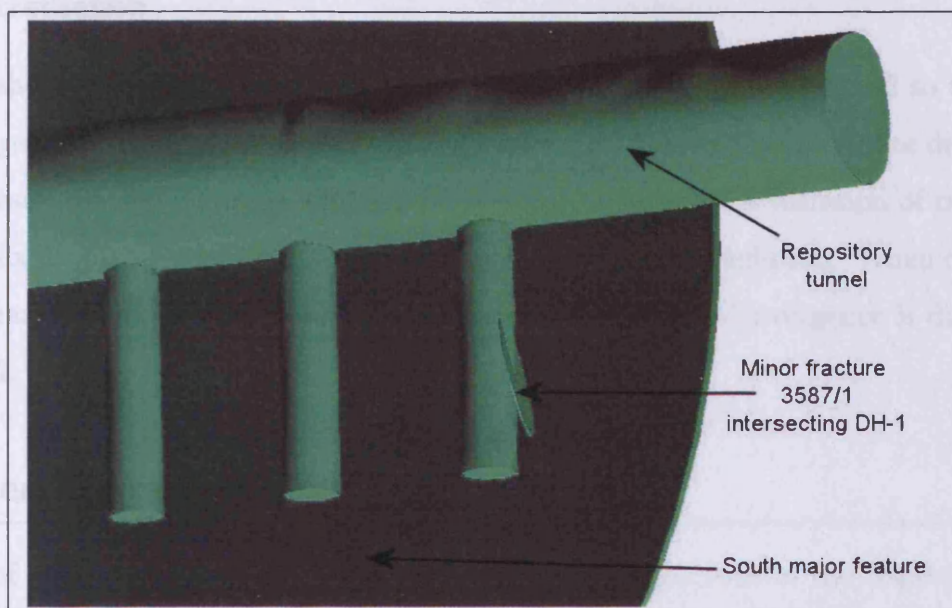
Figure 7.5. Visualisation of minor fracture 3587/1 including the repository tunnel and the South major fracture. Deposition-holes 1 to 3 can also be seen.
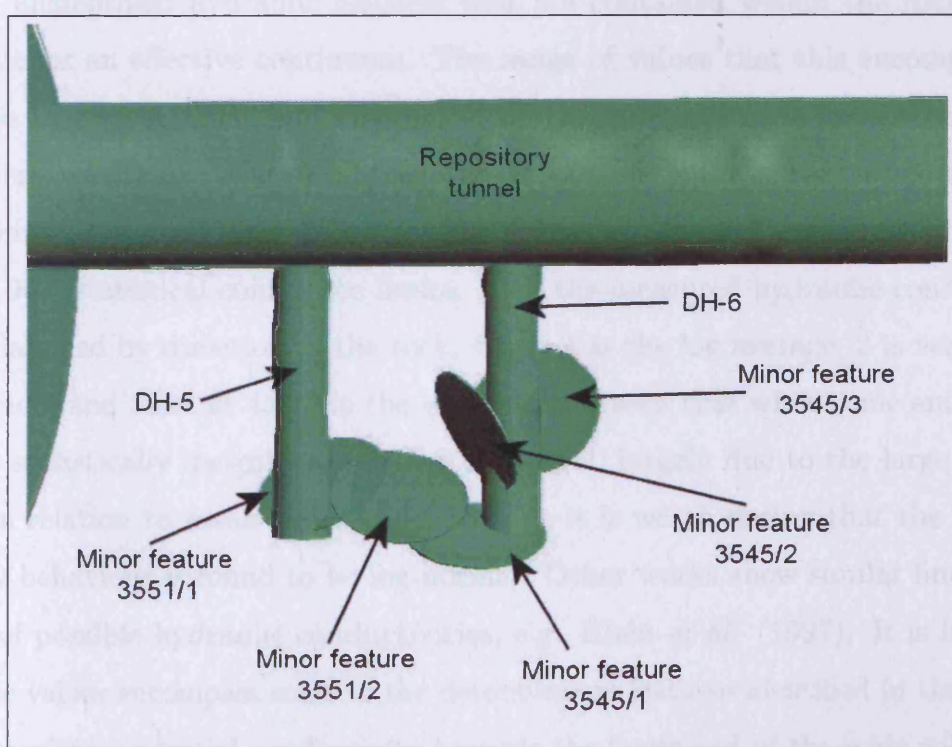
Figure 7.6. Visualisation of minor fractures 3551/1, 3551/2, 3454/1, 3454/2, 3454/3 in context of the repository tunnel deposition-holes 5 and 6.

7.3.2 Discretisation

Linear tetrahedral elements have been used to allow for irregular shapes and so that areas of complex geometry and great spatial variation of results can have appropriate detail and a fine mesh resolution while areas which are expected to have little variation of results and little complex geometry can have a significantly coarser mesh resolution. When discretised the model has 484,954 tetrahedral elements and 86,414 nodes. Convergence is discussed in section 7.5.2.

7.4 Material parameters

Discussion of hydraulic material parameters for the crystalline rock in the Äspö area where the prototype repository experiment is situated is well documented (for example Rhén and Forsmark, 2001; Cleall et al., 2006). The values found during experimentation have a wide range and are spatially variable. In addition, the values adopted for the modelling approach are not the hydraulic conductivities of intact granite rock, but a value encompassing the large set of unidentified hydraulic features that are contained within the rock: i.e. an average value for an effective continuum. The range of values that this encompasses are from 10^{-5} to $10^{-13} m/s$. Rhén and Forsmark (2001) summarise data for a series of tests, although there are others. The results for one set of tests is presented in figure 7.7 with statistical limits, the black lines represent the lowest upper limit and the highest lower limit to the 90% statistical confidence limits. Here the measured hydraulic conductivities have been classified by direction in the rock, where 1 is the log average, 2 is vertical, 3 is horizontal and 4 and 5 are at $45°C$ to the vertical. It is seen that while some anisotropy is seen, this is statistically insignificant at the 90% level, largely due to the large standard deviations in relation to mean value. Additionally, it is worth noting that the hydraulic conductivity behaviour is found to be log-normal. Other works show similar findings and wide range of possible hydraulic conductivities, e.g. Rhén et al. (1997). It is likely that some of these values encompass some of the deterministic features identified in the previous sections. Therefore, an initial conductivity towards the lower end of the scale will be used of $10^{-11} m/s$. Patel et al. (1997) presented a overview of the rock characterisation work for the PRP where the porosity is reported as being 0.005 ± 0.002.
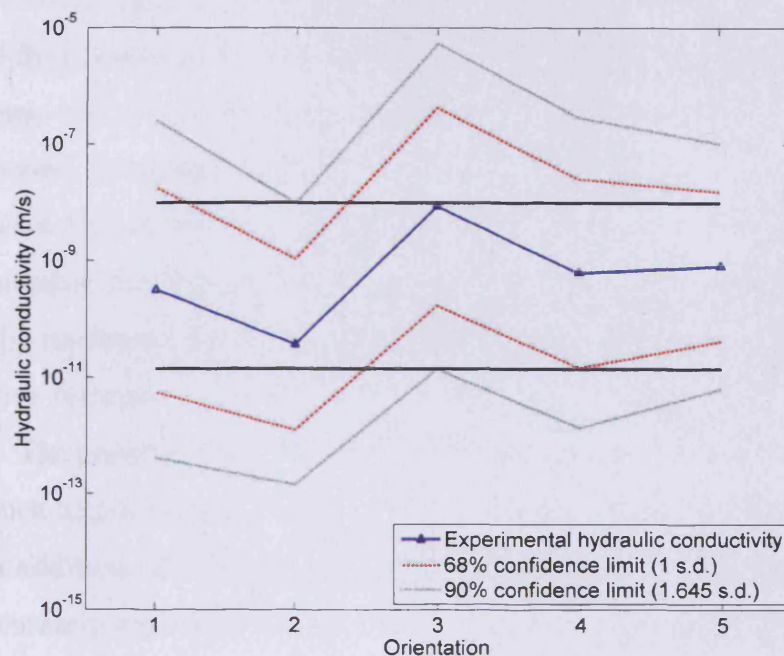
Figure 7.7. Experimental measurement of undisturbed rock mass and statistical limits, after Rhén and Forsmark (2001).

Feature*	Transmissivity* (m^2/s)	Thickness (m)	Hydraulic Conductivity (m/s)
North	$5 - 10 \times 10^{-8}$	0.1	$5 - 10 \times 10^{-7}$
South	$7 - 9 \times 10^{-8}$	0.1	$7 - 9 \times 10^{-7}$
3587/1	8.1×10^{-9}	0.05	1.62×10^{-7}
3551/1	4.7×10^{-9}	0.05	9.4×10^{-8}
3551/2	3.3×10^{-9}	0.05	6.6×10^{-8}
3545/1	2.8×10^{-10}	0.05	5.6×10^{-9}
3545/2	1.7×10^{-9}	0.05	3.4×10^{-8}
3545/3	1.3×10^{-8}	0.05	2.6×10^{-7}

Table 7.2. Initial hydraulic conductivity estimates for the fractures, items marked * after Rhén and Forsmark (2001).

The hydraulic features, discussed in section 7.3, have been represented as areas of higher hydraulic conductivity than the bulk rock mass. These higher hydraulic conductivities has been calculated from transmissivities, shown in table 7.1, where quoted, using a standard fracture thickness, of $0.1m$ for the major fractures and $0.05m$ for the minor fractures, for modelling purposes. It should be noted that these thicknesses (whilst reasonable) are arbitrary and serve only to allow representation of the fracture. As these were established from a limited number of tests and have an assumed shape, they have been taken as a first estimate with the results of the modelling feeding back into sensitivity analysis to provide a more conclusive estimate. It is possible that the fracture aperture is much less than considered here. The porosity of the fracture was considered to be 0.5 as a first estimate as it is likely to be much higher than that of intact rock, but also contains mineral deposits (Patel et al., 1997). In addition, the dimensions of the fractures are not measured therefore this value cannot accurately represent storage, but the overall volume of the fractures compared to that of the rock mass is small. The initial estimate of hydraulic conductivity values for the fractures are summarised in table 7.2. The rock is considered to be saturated throughout the pre-emplacement stage, therefore no relationship between suction and degree of saturation is required.

7.5 Simulation

A range of analyses have been undertaken to understand how the various aspects of the model interact. These analyses are summarised in table 7.3 which includes the key values of hydraulic conductivity used. As a base case *Analysis Set 1* has been undertaken using an average continuum model. These have been undertaken to provide a base for comparison and to investigate the three-dimensional behaviour as a result of the geometrical layout of the repository. The average hydraulic conductivity will be varied from 1×10^{-9} to $1 \times 10^{-13} m/s$.

The second set, *Analysis Set 2*, includes all the identified hydraulic features identified in section 7.3.1, including the region of high hydraulic conductivity. The hydraulic conductivities are as quoted by Rhén and Forsmark (2001), or the central figure when a range is quoted. *Analysis Sets 3, 4, 5 and 6* are sensitivity analyses of the 'intact rock', deterministic hydraulic features, major and minor and the region of high hydraulic conductivity respectively. Where 'intact rock' is quoted this refers to rock including a typical distribution of small fractures

as opposed to an intact non-fissured rock mass.

Each transient analysis was run for 2 years, at which point a pseudo steady-state had been achieved, where the rate of change in inflow results is found to be less than 1%. At these states the results are comparable. It is not assumed that the transient results would match reality but it may be able to gain some appreciation of how long a pseudo steady-state would take to occur.

Analysis	Set 1					Set 2	Set 3		
	1-1	1-2	1-3	1-4	1-5	2-1	3-1	3-2	3-3
Features									
'Intact' rock	1.00×10^{-9}	1.00×10^{-10}	1.00×10^{-11}	1.00×10^{-12}	1.00×10^{-13}	1.00×10^{-11}	1.00×10^{-10}	1.00×10^{-11}	1.00×10^{-12}
North major feature	-	-	-	-	-	8.00×10^{-7}	8.00×10^{-7}	8.00×10^{-7}	8.00×10^{-7}
South major feature	-	-	-	-	-	8.00×10^{-7}	8.00×10^{-7}	8.00×10^{-7}	8.00×10^{-7}
Minor feature 3587/1	-	-	-	-	-	1.62×10^{-7}	1.62×10^{-7}	1.62×10^{-7}	1.62×10^{-7}
Minor feature 3551/1	-	-	-	-	-	9.40×10^{-8}	9.40×10^{-8}	9.40×10^{-8}	9.40×10^{-8}
Minor feature 3551/2	-	-	-	-	-	6.60×10^{-8}	6.60×10^{-8}	6.60×10^{-8}	6.60×10^{-8}
Minor feature 3545/1	-	-	-	-	-	5.60×10^{-9}	5.60×10^{-9}	5.60×10^{-9}	5.60×10^{-9}
Minor feature 3545/2	-	-	-	-	-	3.40×10^{-8}	3.40×10^{-8}	3.40×10^{-8}	3.40×10^{-8}
Minor feature 3545/3	-	-	-	-	-	2.60×10^{-7}	2.60×10^{-7}	2.60×10^{-7}	2.60×10^{-7}
Region 1	-	-	-	-	-	8.00×10^{-7}	8.00×10^{-7}	8.00×10^{-7}	8.00×10^{-7}

Analysis	Set 4						Set 5			Set 6		
	4-1	4-2	4-3	4-4	4-5	4-6	5-1	5-2	5-3	6-1	6-2	6-3
Features												
'Intact' rock	1.00×10^{-11}	1.00×10^{-11}	1.00×10^{-11}	1.00×10^{-11}	1.00×10^{-11}	1.00×10^{-11}	1.00×10^{-11}	1.00×10^{-11}	1.00×10^{-11}	1.00×10^{-11}	1.00×10^{-11}	1.00×10^{-11}
North major feature	8.00×10^{-6}	8.00×10^{-7}	8.00×10^{-8}	8.00×10^{-7}	8.00×10^{-7}	8.00×10^{-7}	8.00×10^{-7}	8.00×10^{-7}	8.00×10^{-7}	8.00×10^{-7}	8.00×10^{-7}	8.00×10^{-7}
South major feature	8.00×10^{-7}	8.00×10^{-7}	8.00×10^{-7}	8.00×10^{-5}	8.00×10^{-6}	8.00×10^{-7}	5.00×10^{-6}	5.00×10^{-6}	5.00×10^{-6}	5.00×10^{-6}	5.00×10^{-6}	5.00×10^{-6}
Minor feature 3587/1	1.62×10^{-7}	1.62×10^{-7}	1.62×10^{-7}	1.62×10^{-7}	1.62×10^{-7}	1.62×10^{-7}	1.62×10^{-6}	1.62×10^{-7}	1.62×10^{-8}	1.62×10^{-7}	1.62×10^{-7}	1.62×10^{-7}
Minor feature 3551/1	9.40×10^{-8}	9.40×10^{-8}	9.40×10^{-8}	9.40×10^{-8}	9.40×10^{-8}	9.40×10^{-8}	9.40×10^{-7}	9.40×10^{-8}	9.40×10^{-9}	9.40×10^{-8}	9.40×10^{-8}	9.40×10^{-8}
Minor feature 3551/2	6.60×10^{-8}	6.60×10^{-8}	6.60×10^{-8}	6.60×10^{-8}	6.60×10^{-8}	6.60×10^{-8}	6.60×10^{-7}	6.60×10^{-8}	6.60×10^{-9}	6.60×10^{-8}	6.60×10^{-8}	6.60×10^{-8}
Minor feature 3545/1	5.60×10^{-9}	5.60×10^{-9}	5.60×10^{-9}	5.60×10^{-9}	5.60×10^{-9}	5.60×10^{-9}	5.60×10^{-8}	5.60×10^{-9}	5.60×10^{-10}	5.60×10^{-9}	5.60×10^{-9}	5.60×10^{-9}
Minor feature 3545/2	3.40×10^{-8}	3.40×10^{-8}	3.40×10^{-8}	3.40×10^{-8}	3.40×10^{-8}	3.40×10^{-8}	3.40×10^{-7}	3.40×10^{-8}	3.40×10^{-9}	3.40×10^{-8}	3.40×10^{-8}	3.40×10^{-8}
Minor feature 3545/3	2.60×10^{-7}	2.60×10^{-7}	2.60×10^{-7}	2.60×10^{-7}	2.60×10^{-7}	2.60×10^{-7}	2.60×10^{-6}	2.60×10^{-7}	2.60×10^{-8}	2.60×10^{-7}	2.60×10^{-7}	2.60×10^{-7}
Region 1	8.00×10^{-7}	8.00×10^{-7}	8.00×10^{-7}	8.00×10^{-7}	8.00×10^{-7}	8.00×10^{-7}	8.00×10^{-7}	8.00×10^{-7}	8.00×10^{-7}	8.00×10^{-6}	8.00×10^{-7}	8.00×10^{-8}

Table 7.3. Analyses undertaken in the pre-placement stage, including the hydraulic conductivity (m/s) of key features.

7.5.1 Initial and boundary conditions

The reported inflow rates, shown in section 6.3 and figures 6.6 and 6.9, show little variation over the time they were recorded for, over 1 year (Rhén and Forsmark, 2001). Although the construction of the tunnel was undertaken over time, the initial conditions for this simulation were assumed to be hydrostatic with the mean sea level. This is likely to be reasonable given the porous nature of the material, although the construction process would have an effect.

The boundary conditions on the far field have been maintained at hydrostatic pore-water pressure and as such it is essential to ensure that the boundary is set far enough away from the repository. As discussed in section 7.3 via monitoring of the boundary fluxes, the distance the boundary is set from the repository has been found not to affect the results. On the interior of the tunnel and deposition-holes following the approach of Thomas *et al.* (2009) the pore-water pressure has been fixed at zero to reflect the atmospheric pressure. In addition, the presence of fractures and anisotropic materials may enable the rock to desaturate locally. There is no experimental evidence of the extent of this behaviour therefore this cannot be accurately included in the model. Moreover the extent is likely to be local to the fracture. Additionally, the approach to model the hydraulic flow into an underground structure by assuming a zero pore-water pressure boundary is well documented, e.g. Potts and Zdravkovic (1999); Melhuish (2004) and found experimentally, e.g. Mishra *et al.* (2008).

7.5.2 Numerical convergence

The mesh has been checked for spatial convergence by running a single analysis with approximately double the number of elements resulting in only negligible result differences, i.e. less than 0.5%. It was found that a temporally converged solution could be found if the timestep started at 1,000 seconds and was allowed to increase, as convergence allowed to a maximum of 10 days. A single analysis was undertaken using a fixed timestep of 1,000 seconds with a negligible difference in results. These analyses were undertaken on the Merlin HPC machine, described in chapter 4, using 16 processors. On average they took 150 timesteps and 2 hours to execute.

7.6 Simulation Results

Large-scale simulations have the potential to generate a large amount of information. Challenges exist in terms of selecting appropriate data and the visualisation of such data. In this work the experimental data is somewhat limited and hence it is this restricted data set that will be used to quantitatively compare the models. This is namely the inflow rate along the repository tunnel, shown in figure 6.6, and the inflow rates in the deposition-holes, shown in figure 6.9. In addition, a contour plot of the pore-water pressure along the centre-line of the PRP will be produced to enable the viewer to qualitatively see differences between various analyses.

The experimental data relating to the inflow into the repository is limited both in time and spatially. Moreover, that which exists exhibits variation over time and the data is taken over a number of years. It is hard to quantify this variation statistically due to the limited amount of data and the variation is hard to attribute to either real variation or uncertainty due to the collection process. It is known, as discussed in section 6.3, that leakage into the deposition-holes occurred during the measurement process. Further uncertainty exists when the flowrates are small, the weir construction and evaporation, for example, may be important. The range of experimental data is shown on numerical figures, but the true range may be higher than this as only limited experimental measurements were made. In addition, qualitative allowances should be made where leakage was known to occur.

7.6.1 Analysis Set 1 - Average continuum model

The results from the simulations of *Analysis Set 1* are shown in the figures 7.8, 7.9 and 7.10. It is seen in figure 7.8 that the inflow into the deposition-holes can be generally simulated by *Analysis 1-3*, with an effective continuum of hydraulic conductivity of approximately $1 \times 10^{-11} m/s$. However, it is clear that this cannot simulate the inflow into DH-1 where the simulated value is only 6% of the experimental results. This inflow is more reasonably simulated by increasing the hydraulic conductivity by a magnitude or more, i.e. *Analysis 1-2*. In addition, the variation among the other deposition-holes is not reflected in *Analysis 1-3*, although this is probably within statistical limits as all values are close to or within the experimental range. It is noted that statistical limits would include zero into DHs 2-6. Note

that this figure does not include results from the wider range of hydraulic conductivities, (i.e. *Analysis 1-1*, where inflows are more than 4 times the largest measured value and *Analysis 1-5* where a lower hydraulic conductivity results in negligible inflows. The general trends in the variation in inflow bewteen each deposition-hole exhibit the same morphology, most easily seen in the hydraulic conductivity of $1 \times 10^{-10} m/s$ line (*Analysis 1-2*), but the scale of variation reduces as the hydraulic conductivity is reduced. In each case the inflows are highest in DH-1, slightly lower in DH-4, 5 and 6, and noticeably reduced in DH-2 and 3. It can be seen that this is a result of the layout of the repository, with the 'interior' DHs, i.e. 2 and 3, effectively being shielded by the outer DHs. The spacing between DHs 4 and 5, however, seems to be large enough for this effect to be hidden. The cause of this effect can be seen in figure 7.10, discussed in more detail below.

Figure 7.9 shows the experimental and simulated results of inflow rate per metre along the tunnel. It should be noted that the area of the bars gives the total sectional inflow and each data-point of the simulated results is calculated for the same length section as the experimental results, and shown as a point for clarity and ease of comparison. It can be seen that the results of the simulation *Analysis 1-1*, with a hydraulic conductivity of $1 \times 10^{-9} m/s$, when compared to experimental results show results of the correct magnitude, but overestimates the inflow rates for the three sections at the end of the tunnel, whereas the results using a hydraulic conductivity of $1 \times 10^{-10} m/s$ to $1 \times 10^{-11} m/s$, *Analyses 1-2 and 1-3* respectively, provide a better representation of the inflows to the tunnel chainages below $3,576m$.

A contour plot of the hydraulic conductivity of *Analysis 1-3* is shown in figure 7.10. The effects of the shape of the repository can clearly be seen. The pore-water-pressure field reduces towards the tunnel and deposition-holes as expected. It can be seen that the position of the deposition-holes in relation to the tunnel and other deposition-holes affects the pore-pressure local to the hole and therefore the inflow rate. The rock adjacent to DH-1, closest to the end of the tunnel, has the steepest gradient of pore-water-pressure, i.e. the colours change the fastest, which reflects the largest inflow. The rock adjacent to DH-2 and the rock adjacent to DH-3 then have a reduced gradient due to the proximity of the adjacent deposition-holes. The rock adjacent to DH-4, DH-5 and DH-6 exhibit similar pore-water
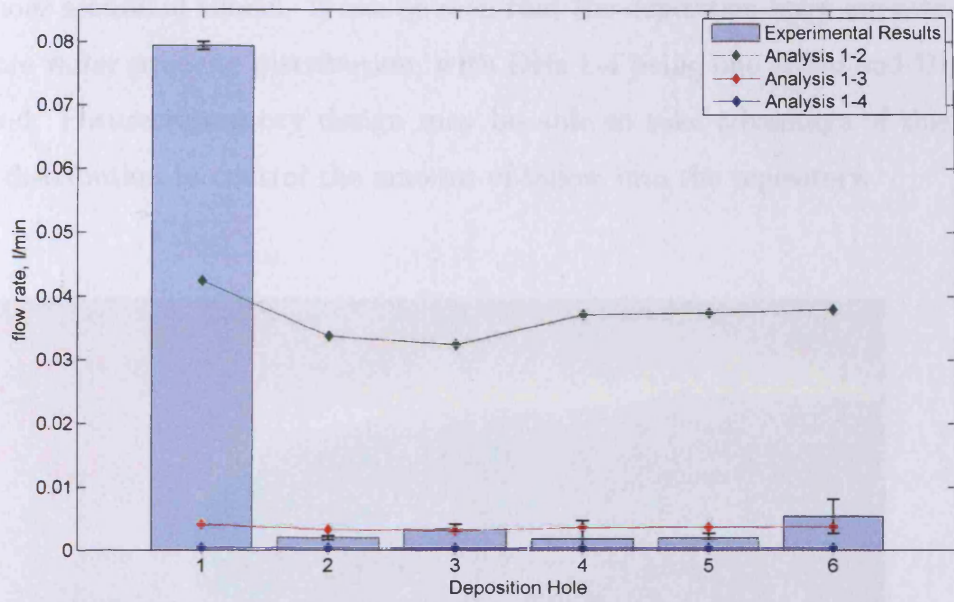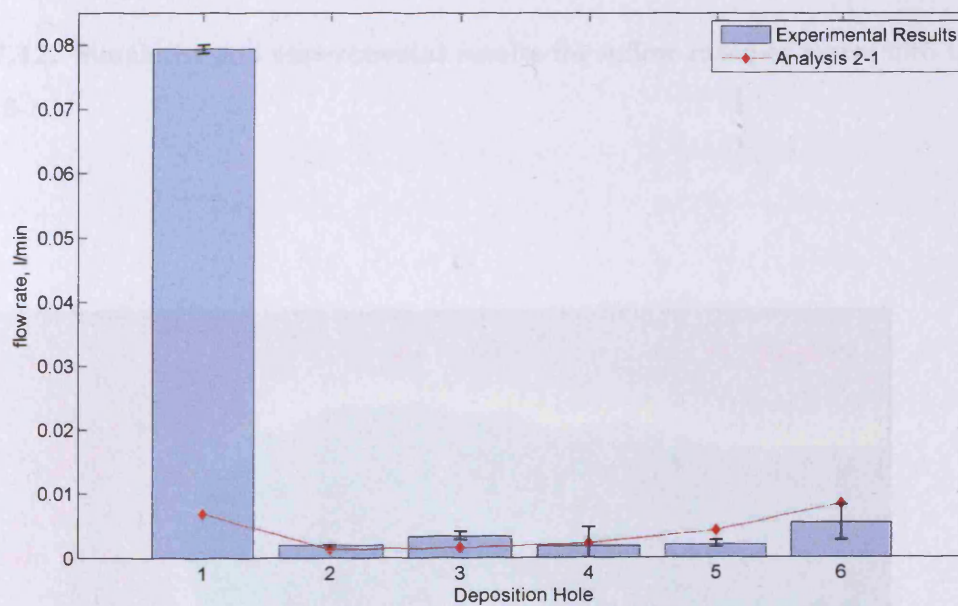
Figure 7.8. Simulated and experimental results for inflow rate into the deposition-holes for *Analysis Set 1* including experimental range.
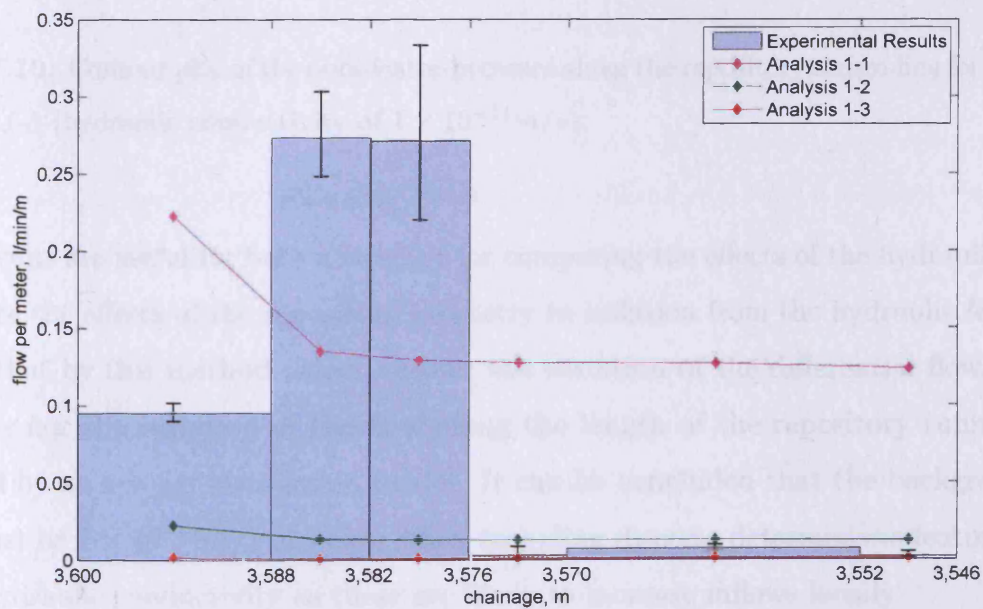
Figure 7.9. Simulated and experimental results for inflow rate per metre into the tunnel for *Analysis Set 1* including experimental range.

pressure gradients, being immediately adjacent to only one other deposition-hole and under a continuous section of tunnel. It can be seen that the deposition-holes are acting as groups in the pore-water pressure distribution, with DHs 1-4 being one group and DHs 5-6 being the second. Future repository design may be able to take advantage of this pore-water pressure distribution to control the amount of inflow into the repository.
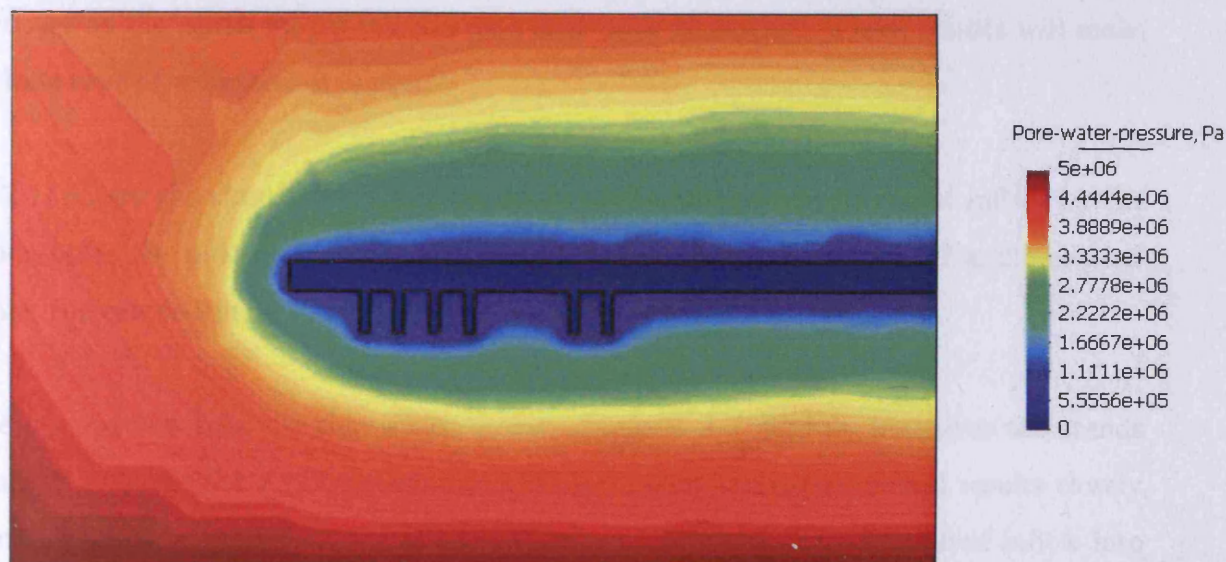
Figure 7.10. Contour plot of the pore-water-pressure along the repository centre-line for simulation *Analysis 1-3* (hydraulic conductivity of $1 \times 10^{-11} m/s$).

These results are useful for both a baseline for comparing the effects of the hydraulic features and to see the effects of the repository geometry in isolation from the hydraulic features. It is clear that by this method alone, neither the variation of the differential flows into the boreholes nor the variation of the flow along the length of the repository tunnel can be captured by an average continuum model. It can be concluded that the background rock mass must be $1 \times 10^{-11} m/s$ or below when including discrete deterministic features with a higher hydraulic conductivity as these are likely to increase inflows locally.

7.6.2   Analysis Set 2 - Fracture model, base case

In this analysis set only a single analysis has been undertaken, *Analysis 2-1*, where the proposed fracture model has been implemented. Eight deterministic features have been added, all features have as a first approximation been allocated hydraulic conductivities and shapes based upon the assumptions and tests reported by Rhén and Forsmark (2001). The region of high hydraulic conductivity identified earlier has been given the same hydraulic conductivity as the north major feature as a first approximation. These results will make up the base case of a fractured model.

Figure 7.11 shows the simulated inflow superimposed onto the experimental inflow for the deposition-holes, the inflow per metre along the tunnel is shown on figure 7.12 and a contour plot along the centre-line is shown in figure 7.13.

Considering the flow into the deposition-holes, *Analysis 2-1* slightly improves the trends exhibited by *Analysis Set 1*. The flows into DHs 2-6 follow the experimental results closely, all falling within reasonable bounds of the experimental results. The simulated inflow into DH-1, however, is only slightly improved, rising from 6% of the experimental value to approximately 12%. However, when considering the inflow into the tunnel the results exhibit closer numerical and experimental correlation, both qualitatively and quantitatively. In addition, in general, where the simulated results show greatest disparity coincides with the greatest experimental range, with the exception of chainage $3,588 - 3,600m$. Recalling that in *Analysis Set 1* the tunnel inflow could be simulated in magnitude only by using an effective continuum with a hydraulic conductivity of $1 \times 10^{-9} m/s$, and the inflow into the deposition-holes by using an effective continuum with a hydraulic conductivity of $1 \times 10^{-11} m/s$, this result shows a much improved simulation method. Moreover, the general qualitative morphology of the inflow rate is much improved with the exception of the inflow into DH-1.

The contour plot of the pore-water pressure, along the centre-line of the repository, shown in figure 7.13, highlights the effects of the major features. The edge of the major fracture can be seen between DH-1 and the end of the tunnel. The effect of this feature on the

pore-water pressure can be seen by the extended contour of around $1MPa$, in blue, extending further vertically than shown by the simulations undertaken in *Analysis Set 1*. Three-dimensional visualisation indicates that the effect of this feature is three-dimensional and figure 7.13 only shows this effect on a single plane where the box above the tunnel is *Region 1*.

It can be seen that by using select deterministic features in addition to a background continuum model, as opposed to using an effective continuum, highly anisotropic inflow rates can be simulated. However, it is noted that some calibration is required to reflect all of the aspects exhibited by the experiment.

Figure 7.11. Simulated and experimental results for inflow rate into the deposition-holes for *Analysis 2-1*.
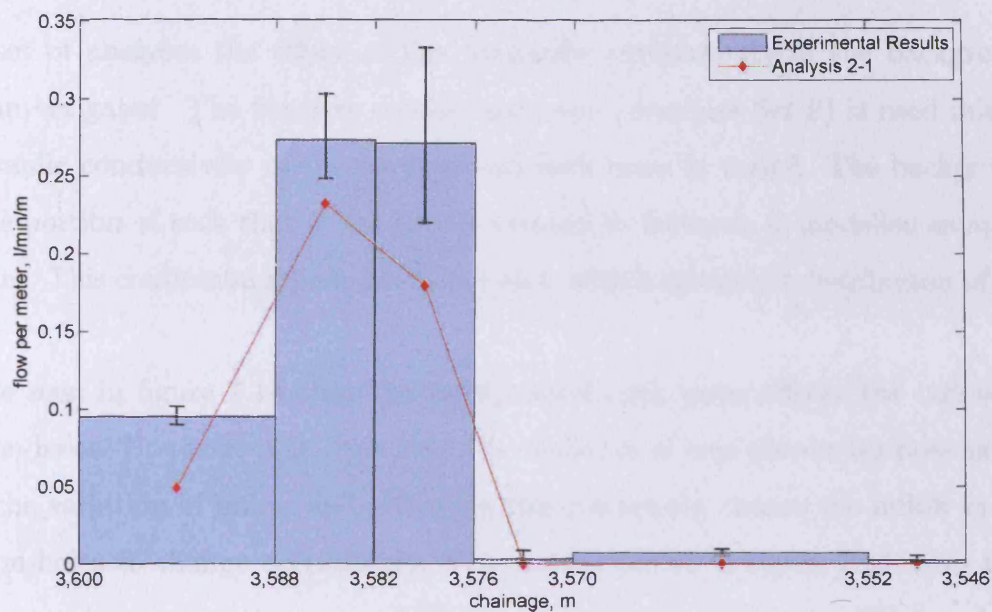
Figure 7.12. Simulated and experimental results for inflow rate per metre into the tunnel for *Analysis 2-1.*
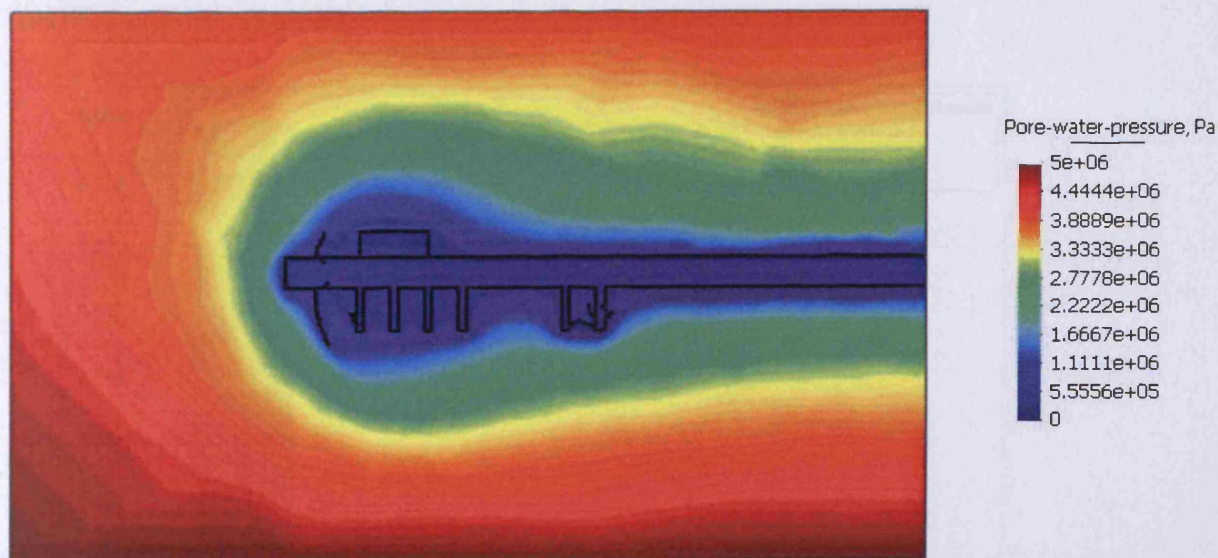
Figure 7.13. Contour plot of the pore-water-pressure along the repository centre-line for *Analysis 2-1.*

7.6.3   Analysis Set 3 - Fracture model, sensitivity to intact rock

In this set of analyses the effect of the hydraulic conductivity of the background rock mass is investigated. The fracture model base case (*Analysis Set 2*) is used initially and the hydraulic conductivity of the background rock mass is varied. The background rock mass, the portion of rock that is not the deterministic features, is modelled as an effective continuum. This continuum represents intact rock with a statistical distribution of fractures.

It can be seen in figure 7.14 that the background rock mass affects the inflow into the deposition-holes. However, it is clear that the variation of this parameter does not in itself explain the variation of inflow as by varying this parameter causes the inflow in all of the deposition-holes to change accordingly. The results shown in figure 7.14 show that these analyses cannot represent the major differences in inflow rate between DH-1 and the other deposition-holes. These results could indicate that the rock surrounding the repository has a variety of hydraulic conductivities; that a number of fractures in addition to the ones already identified exist and are important; or that the deterministic features already identified are not calibrated correctly. However it can be seen that if the hydraulic conductivity is in the region of 1×10^{-11} to $1 \times 10^{-12} m/s$ (i.e. *Analyses 3-2 and 3-3*) generally good results for DH-2 to DH-6 can be obtained.
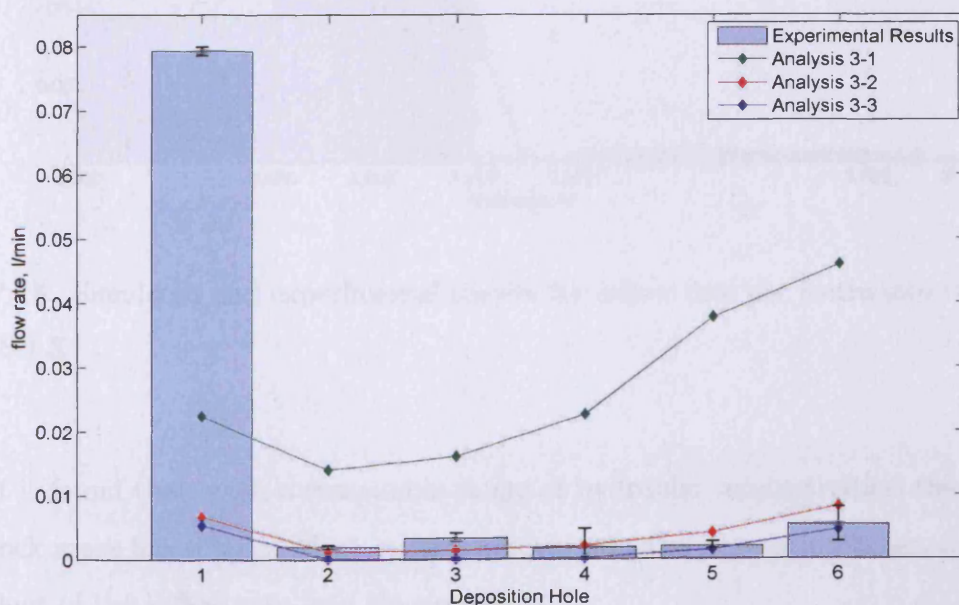
Figure 7.14. Simulated and experimental results for inflow rate into the deposition-holes for *Analysis Set 3*.

The effect of the hydraulic conductivity of the 'intact' rock on the inflow rate into the tunnel is much less than into the deposition-holes. This is shown in figure 7.15 with the flow rate into the tunnel not significantly affected by the variation in hydraulic conductivity. In the low flow rate section, chainage 3,546 to 3,576m, proportionally the flow rate is changed by a large degree, but in real terms all of the variations are small and within the range of uncertainty of both flow rate and measurements. In the high inflow rate section, chainages above 3,576m, the inflow rate does not change significantly. This is largely due to the dominance of the deterministic hydraulic features. This result suggests that the hydraulic features have a large enough surface area in contact with the 'intact' rock to supply water and maintain the pore-water-pressure gradient within the features.
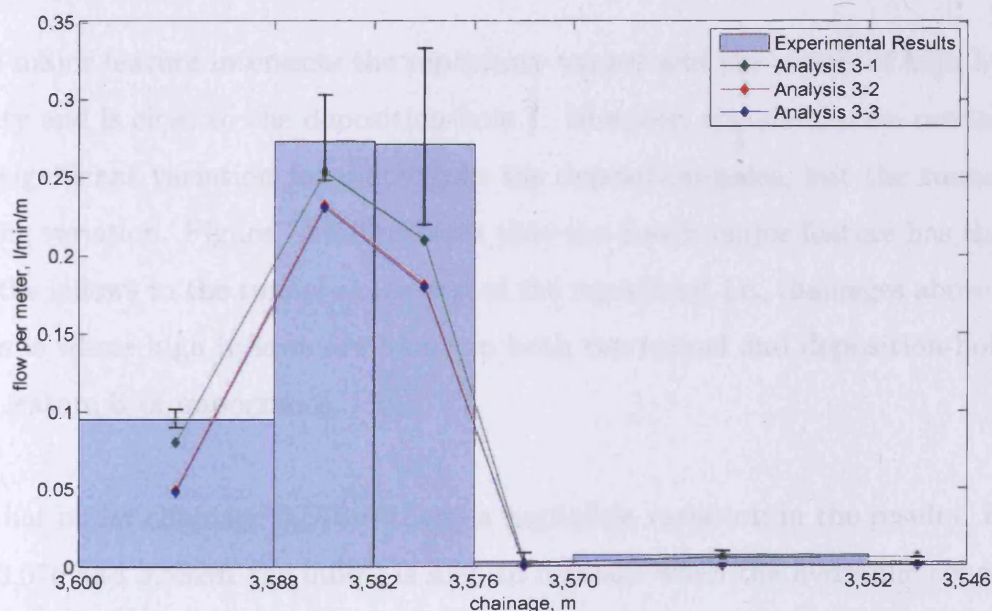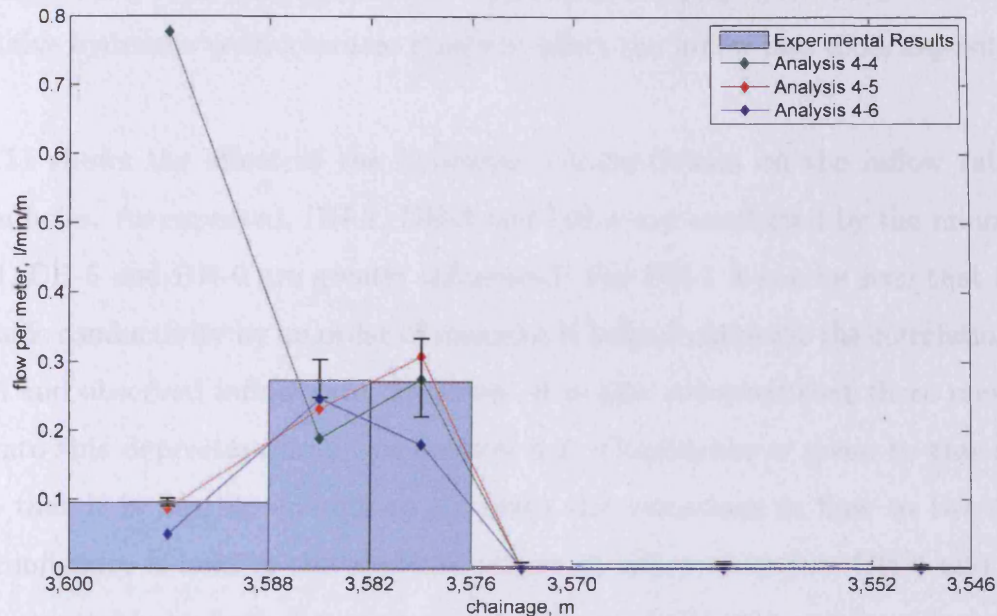

Figure 7.15. Simulated and experimental results for inflow rate per metre into the tunnel for *Analysis Set 3*.

Overall it is found that, with a reasonable range of hydraulic conductivities, the background 'intact' rock mass has a large effect on the inflows into the deposition-holes, but is largely independent of the inflow rate into the tunnel.

7.6.4 Analysis Set 4 - Fracture model, sensitivity to major fractures

In this set of analyses the effect of the major fractures is investigated. The North major feature is investigated in *Analyses 4-1, 4-2 and 4-3*, with the South major fracture investigations in *Analyses 4-4, 4-5 and 4-6*.

Analyses 4-1 to 4-3 showed that the North major feature had a limited effect upon the inflow rates in either the tunnel or the deposition-holes. In particular, there was less than 0.5% difference for the total inflow rate into the deposition-holes over a range of two magnitudes and less than 0.1% difference for the same range on the inflow rate per metre on the tunnel. Therefore, this feature is deemed to have limited overall effect, and hence has not been reported on further.

The South major feature intersects the repository tunnel and the region of high hydraulic conductivity and is close to the deposition-hole 1. However, the simulation results do not show any significant variation for inflow into the deposition-holes, but the tunnel inflow shows strong variation. Figure 7.16 illustrates that the South major feature has the ability to control the inflows to the tunnel at the end of the repository, i.e. chainages above $3,576m$. This region is where high inflows are found in both the tunnel and deposition-hole 1 and hence this feature is of importance.

It is seen that under chainage $3,576m$ there is negligible variation in the results. Between chainages 3,576 and $3,582m$ the inflow is seen to increase when the hydraulic conductivity is increased from $8.00 \times 10^{-7}m/s$ (*Analysis 4-6*) to $8.00 \times 10^{-6}m/s$ (*Analysis 4-5*), but decrease slightly when the hydraulic conductivity is increased from $8.00 \times 10^{-6}m/s$ (*Analysis 4-5*) to $8.00 \times 10^{-5}m/s$ (*Analysis 4-4*). This is due to the interaction between the South major feature and *Region 1*. In particular when the fracture increases hydraulic conductivity up to the hydraulic conductivity of *Region 1* the inflow rate increases. Beyond this hydraulic conductivity the inflow rate decreases with flow instead going through the fracture into the tunnel. The inflow rate at chainage $3,582m$ to $3,588m$ does not change significantly due to the hydraulic conductivity of the South major feature as the intersection between the fracture and the volume of increased hydraulic conductivity is slight at this chainage.
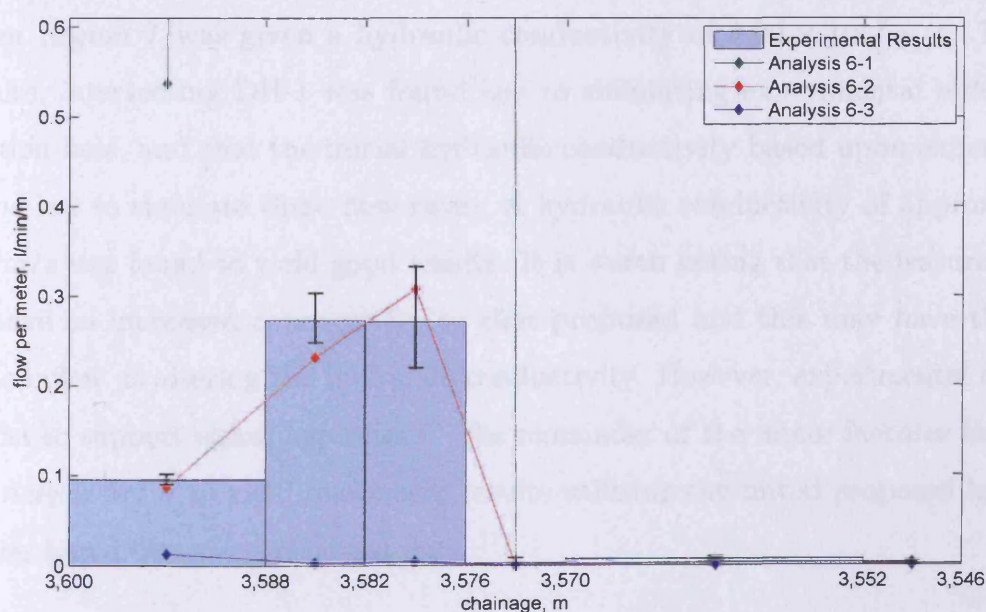
Figure 7.16. Simulated and experimental results for inflow rate per metre into the tunnel for *Analysis Set 4.*

The fracture intersects the tunnel in the chainage $3,588m$ to $3,600m$ and consequently the inflow rate here is highly dependent on the hydraulic conductivity of the South major feature.

The results shown in figure 7.16 indicate that the hydraulic conductivity for the South major feature lies between 8.00×10^{-5} and $8.00 \times 10^{-6}m/s$ (*Analyses 4-4 and 4-5*), albeit closer to $8.00 \times 10^{-6}m/s$. Further sensitivity analyses between these values show that it is likely to lie around $5.00 \times 10^{-6}m/s$ and this value shall be used in further analyses.

7.6.5   Analysis Set 5 - Fracture model, sensitivity to minor features

The minor features as identified in figures 7.3, 7.5 and 7.6 are located intersecting or in close proximity to the deposition-holes. Therefore, it is of no surprise that by changing the hydraulic conductivity there is only a negligible effect on the inflow to the tunnels. To gain knowledge on the general effects of the minor features, all of the hydraulic conductivities have been raised and lowered by an order of magnitude. For the inflow into DH-1, the minor feature 3587/1 intersects the deposition-hole, and the other minor features either

intersect or are in the proximity of DH-5 and DH-6. Therefore, it will be the variation of the respective hydraulic conductivities that will affect the inflow into those deposition-holes.

Figure 7.17 shows the effect of the hydraulic conductivities on the inflow rates to the deposition-holes. As expected, DH-2, DH-3 and DH-4 are unaffected by the minor features and DH-1, DH-5 and DH-6 are greatly influenced. For DH-1 it can be seen that increasing the hydraulic conductivity by an order of magnitude helps to improve the correlation between simulated and observed inflow rate. However, it is also accepted that there may be some seepage into this deposition-hole, see section 6.3. Confidence is given to this modelling approach that it is flexible enough to simulate the variations in flow to the repository, but less confidence is held in the absolute values of inflow recorded. DH-5 and DH-6 are simulated acceptably by both the original hydraulic conductivities and by reducing them by 1 order of magnitude. This gives confidence to the level of robustness within this level of hydraulic conductivity.
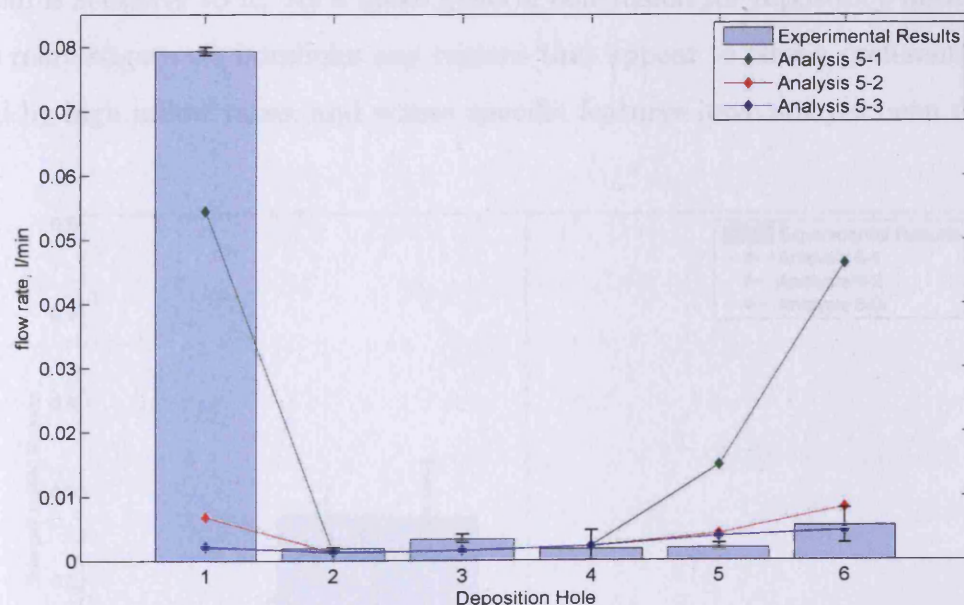
Figure 7.17. Simulated and experimental results for inflow rate into the deposition-holes for *Analysis Set 5.*

7.6.6   Analysis Set 6 - Fracture model, sensitivity to Region 1

Region 1 is a relatively large but a poorly defined quantity. While experimental evidence from inflows and surface fracture mapping exist, unfortunately no experimental evidence via boreholes indicates size or transmissivity. Therefore, a rather large and flexible shape has been included within the geometric model, but little in firm conclusions, with the exception of matching experimental inflow rates can be drawn.

The location of *Region 1*, above the tunnel, means that it is expected to have little or no effect on the inflow to the deposition-holes and this has proven to be the case in the simulations. It is found that along the tunnel at chainages above 3,576m, *Region 1* has a large effect as can be seen in figure 7.18. By varying the hydraulic conductivity the change in inflow rate in sections 3,576 to 3,582m and 3,582 to 3,588m is dramatic with the section 3,588 to 3,600m less so. It can be seen that the initial assumption provides a reasonable fit with experimental data, however it is noted that care must be taken using this parameter as the system is sensitive to it. As a more general conclusion for repository design it may be useful to reinvestigate via boreholes any regions that appear to offer a preferential flow path, indicated by high inflow rates, and where specific features have not yet been determined.

Figure 7.18. Simulated and experimental results for inflow rate per metre into the tunnel for *Analysis Set 6.*

7.7 Results from the calibrated analysis

This analysis set synthesises information yielded from sensitivity analysis sets 1-6 to simulate the experimental conditions. This analysis then forms the calibrated analysis. The numerical data has been compared with experimental data of inflows for both the deposition-holes and for the inflow along the tunnel. The hydraulic conductivities that are used are shown in table 7.4.

The hydraulic conductivity for the 'intact' rock, which is important to remember includes some small non-identifiable fractures, has been determined to be $5.00 \times 10^{-12} m/s$. This was chosen as the conclusions from *Analysis Set 3* was that this value lay between 1.00×10^{-11} and $1.00 \times 10^{-12} m/s$. The North major feature was found to have a negligible effect upon the inflow rate to either the deposition-holes or the tunnel, therefore the value of hydraulic conductivity has been left as that hypothesised based upon experimental data. The South major feature was shown in *Analysis Set 4* to be key to simulating the inflow into the repository tunnel. Moreover it was found likely that this feature had some connectivity with the rock mass above the tunnel near to this location at *Region 1*. The hydraulic conductivity was numerically found to be higher than experimentally determined at approximately $5.00 \times 10^{-6} m/s$ and simulations including *Region 1* were found to yield reasonable numerical results when *Region 1* was given a hydraulic conductivity of $8.00 \times 10^{-7} m/s$. The first minor feature, intersecting DH-1 was found key to simulating experimental inflows into this deposition-hole, and that the initial hydraulic conductivity based upon experimental data was too low to simulate these flow rates. A hydraulic conductivity of approximately $2.50 \times 10^{-6} m/s$ was found to yield good results. It is worth noting that the feature located here may have an increased connectivity to that proposed and this may have the same effect on the inflow as altering the hydraulic conductivity. However, experimental evidence does not exist to support either hypothesis. The remainder of the minor features have been shown in *Analysis Set 5* to yield reasonable results utilising the initial proposed hydraulic conductivities based upon experimental data.

It is worth noting that further calibration of the hydraulic conductivity values may be undertaken so that results may better fit the experimental data. However, given the

uncertainly already discussed within the experimental inflow data, the rock characterisation and resulting proposed conceptual model, the values assigned are deemed reasonable. Where changes have been made to the initially assumed transmissivity of hydraulic features values of hydraulic conductivity have been quoted only to a single significant figure and not to a spurious accuracy.

Region	Hydraulic Conductivity (m/s)
'Intact' rock	5.00×10^{-12}
North major feature	8.00×10^{-7}
South major feature	5.00×10^{-6}
Minor feature 3587/1	2.50×10^{-6}
Minor feature 3551/1	9.40×10^{-8}
Minor feature 3551/2	6.60×10^{-8}
Minor feature 3545/1	5.60×10^{-9}
Minor feature 3545/2	3.40×10^{-8}
Minor feature 3545/3	2.60×10^{-7}
Region of high hydraulic conductivity	8.00×10^{-7}

Table 7.4. Hydraulic conductivities for the *Final analysis*.

Figures 7.19 and 7.20 show the inflow rate into the deposition-holes and inflow rate per metre along the tunnel. It can be seen that these generally fit within the experimental range and almost certainly within reasonable stochastic confidence limits. This indicates that the method proposed, i.e. an effective continuum with the inclusion of discrete hydraulic features, is able to simulate the repository system to the measured resolution, and is a significant improvement in comparison to average continuum model shown in *Analysis Set 1*. It is also indicated that in general the rock characterisation undertaken is sufficient to accurately numerically model the pre-placement behaviour of the repository system.

The results from this analysis will be used as the initial conditions for the post-placement analysis. In addition, the material properties for the saturated hydraulic conductivities shown in table 7.4 will also be used in the post-placement analyses. However, it must be recognised that while the available data has been well matched, there may still be significant

differences in the pore-water-pressure distribution. This is due to the minimal availability of data from within the rock mass, local variations in the pore-water pressure due to fractures and preferential flow paths either connecting to hydraulic fractures identified or others as yet unidentified.

In further should be noted that the calibrated values are within reasonable bounds from the initial propositions based upon experimental data and that reasonable correlation of numerical results with experimental data can be found from the rock characterisation data available.
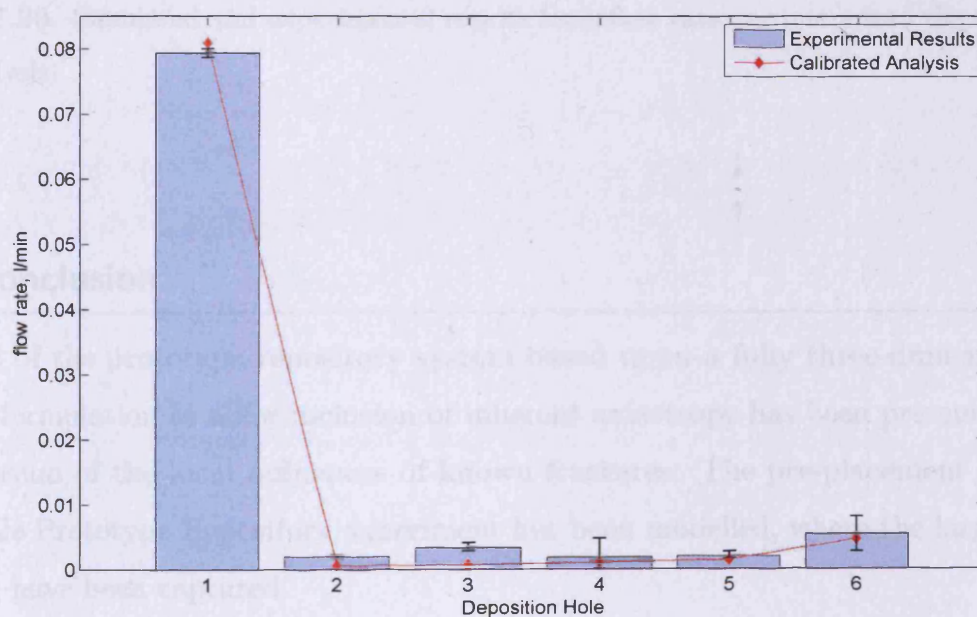
Figure 7.19. Simulated and experimental results for inflow rate into the deposition-holes for the final analysis.
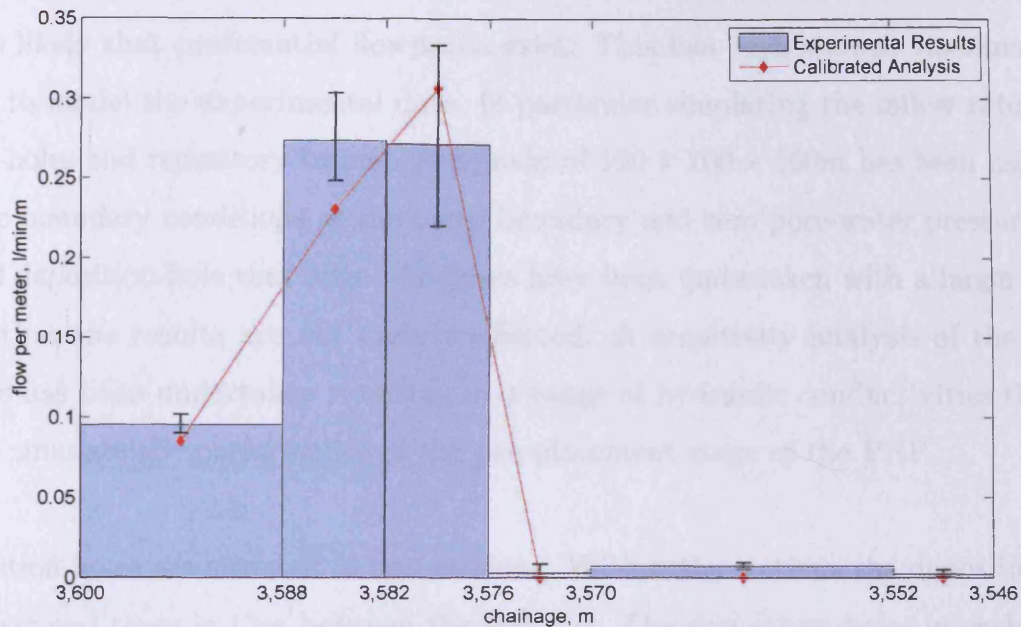
Figure 7.20. Simulated and experimental results for inflow rate per metre into the tunnel for the final analysis.

7.8 Conclusion

A model of the prototype repository system based upon a fully three-dimensional finite-element formulation to allow inclusion of inherent anisotropy has been presented, allowing the inclusion of the local influences of known fractures. The pre-placement stage of the large-scale Prototype Repository experiment has been modelled, where the large variations of inflow have been captured.

It has been demonstrated that the hydraulic performance of this structure is inherently three-dimensional and should be modelled as such to gain meaningful results. In addition a continuum model with the inclusion of discrete deterministic features has been used which provides the required resolution of results while maintaining reasonable computational performance.

The proposed model includes a background 'intact' rock mass, inclusive of small discontinuities, modelled as an effective continuum, with a set of deterministic features.

Two major and eight minor features have been identified and included along with a region where it is likely that preferential flowpaths exist. This has been shown, via simulations, to be able to model the experimental data, in particular simulating the inflow rates in the deposition-holes and repository tunnel. A domain of $100 \times 100 \times 160m$ has been used, with hydrostatic boundary conditions at the outer boundary and zero pore-water pressure at the tunnel and deposition-hole rock edge. Analyses have been undertaken with a larger domain to ensure that the results are not unduly affected. A sensitivity analysis of the various parameters has been undertaken resulting in a range of hydraulic conductivities that may be used to simulate the performance of the pre-placement stage of the PRP.

The deposition-holes are situated in two sections. Within the sections the deposition-holes are $6m$ apart and there is $13m$ between the sections. The deposition-holes in each section are found to be acting as groups in relation to the pore-water pressure distribution, with DHs 1-4 being one group and DHs 5-6 being the second. Future repository design may be able to take advantage of this pore-water pressure distribution to control the amount of inflow into the repository, although it may also be a limiting factor as a certain amount of resaturation is required to allow the bentonite to swell and self-heal.

It was found that the inflow rate in the repository is affected by features that have connectivity to the repository structure or close to the repository structure. Features, even of large size e.g. the North major feature, that are a reasonable distance away from the repository are shown to have little influence. This improves confidence in the modelling approach of using an effective continuum in the far-field and deterministic features in the near-field.

The analysis of various experimental data allowed the identification of a region where inflow into the tunnel occurred preferentially. It was hypothesised that in this location the rock may have a number of unidentified hydraulic features. To allow for this a region of high hydraulic conductivity, *Region 1*, was included and it has been found to deliver improved numerical results. However, it was found that the system response was quite sensitive to this region, therefore care must be taken for subsequent analyses.

Confidence can be placed on the ability of the proposed model to represent the behaviour found experimentally. The proposed fracture model based upon the approach of an effective

continuum model with the inclusion of specific deterministic hydraulic features has been shown to be able to numerically replicate experimental data, with little calibration required.

Finally it can be noted that the model presented is able to provide suitable initial and boundary conditions for a fully coupled Thermo-Hydraulic-Mechanical analysis of the post emplacement phase of a repository.

7.9 References

Berkowitz, B., (2002) "Characterizing flow and transport in fractured geological media: A review", *Advances in Water Resources*, **25**, 861-884.

Cleall, P.J., Melhuish, T.A., Thomas, H.R., (2006) "Modelling the three-dimensional behaviour of a prototype nuclear waste repository", *Engineering Geology*, **85**(2), 212-220.

Melhuish, T.A., (2004) "An investigation of the three-dimensional thermo/hydro/mechanical behaviour of large scale in-situ experiments", *PhD Thesis*, Cardiff University, Cardiff.

Mishra, S.B., Nagaraj, C., Venkateswarlu, V., Adhikari, G.R., (2008) "Measurement and analysis of pore water pressure in large caverns and shafts in a hydro-electric project", *Geotechnical and Geological Engineering*, **26**, 367-374.

Neretnieks, I., (1993) "Solute transport in fractured rock: applications to radionuclide waste repositories.", *Flow and contaminant transport in fractured rock*, Bear, J., Tsang, C-F., de Marsily, G., (eds.) Academic Press, San Diego, 39-127.

Patel, S., Dahlström, L-O., Stenberg, L., (1997) *Äspö Hard Rock Laboratory, Characterisation of the rock mass in the Prototype Repository at Äspö HRL Stage 1*, SKB, HRL-97-24, Stockholm.

Potts, D.M., Zdravkovic, L., (1999) *Finite Element Analysis in Geotechnical Engineering: application*, Thomas Telford, London.

Rhén, I., Forsmark, T., (2001) *Äspö Hard Rock Laboratory, Prototype Repository, Summary report of investigations before the operation phase*, SKB, IPR-01-65, Stockholm.

Rhén, I., Gustafson, G., Stanfors, R., Wikberg, P., (1997) *Äspö HRL - Geoscientific evaluation 1997/5, Models based on site characterization 1986-1995*, SKB, TR-97-06, Stockholm.

Thomas, H.R., Cleall, P.J., Chandler, N., Dixon, D., Mitchell, H.P., (2003) "Water infiltration into a large-scale in-situ experiment in an underground research laboratory", *Géotechnique*, **53**(2), 207-224.

Thomas, H.R., Cleall, P.J., Dixon, D., Mitchell, H.P., (2009) "The coupled thermal-hydraulic-mechanical behaviour of a large-scale in situ heating experiment", *Géotechnique*, **59**(4), 401-413.

Vardon, P., Thomas, H.R. and Cleall, P., (2008) "Modeling the Three-Dimensional Hydraulic Performance of a Prototype Repository System within Fractured Crystalline Rock", *Proceedings of the 3rd International Symposium GeoProc'2008*, Lille, France, 2008, edited by Shao, J-F., Burlion, N., Wiley, ISTE, pp. 517-524, ISBN 978-1-84821-043-1.

8

Post-Emplacement Simulation

8.1 Introduction

In this chapter the post-emplacement stage of the Prototype Repository Project (PRP) is modelled. The modelling commences with the placement of the canisters and buffer material and includes the section of time where experimental results are available and also includes calculated future results for some analyses. These results are of importance so that this work may be reviewed and hence the theory and approach tested against future experimental results, e.g. results found when the experiment is dismantled. This validation test would be the final stage of the modelling process and the findings fed into any future predictive effort.

A modelling strategy is followed that includes a number of analyses being undertaken, each with a differing amount of realism and detail, increasing in order of complexity, hence taking differing execution times. Not only will this provide information on whether the theory used accurately describes the processes occurring in the PRP, information will be gained on the importance and validity of various simplifications.

A considerable amount of effort is spent in allocating appropriate material parameters and material models so that the complex behaviour of the materials emplaced in the repository can be simulated. Where available experimental results for the exact materials used in the repository have been found and appropriate material parameters derived. Where experimental results have not been available, experiments on similar materials have been used and where no data exists engineering judgement and numerical simulation have been used to establish appropriate numerical parameters.

This chapter first describes the modelling strategy in section 8.2, then describes the geometric aspects of the model in section 8.3 and defines material parameters for all the materials used in section 8.4. The initial and boundary conditions are discussed in sections 8.5 and 8.6 respectively. The various simulations outlined in the modelling strategy are presented in sections 8.7 to 8.11 with long term simulations contained in section 8.12. Finally, concluding remarks are given in section 8.13.

8.2 Proposed modelling strategy

The proposed strategy uses a variety of scales and simplifications, increasing in order of complexity, to simulate the PRP. The aim is to restrict the number of large-scale three-dimensional simulations that are required due to the prohibitive execution times. These simplifications were not undertaken for the pre-emplacement stage as the simulation time requirements were less arduous. However, it is recognised that to simulate the THM behaviour of the PRP three-dimensional analyses are essential.

The strategy begins with smaller scale two dimensional (axi-symmetric) simulations of a single deposition-hole to investigate the key processes, material parameters and conditions and finishes with large scale, three-dimensional THM simulations. These are summarised with key details in table 8.1. Smaller scale simulations to support the theoretical formulation and model developments have been undertaken in chapter 5 and previously elsewhere (e.g. Thomas and He, 1998).

Analysis Set	Analysis Geometry	Processes	Number of finite-elements	Comments
1	2D axi-sym.	T-H	2,197 - unfractured 2,421 - fractured	Including looking at the different types of hydraulic conductivity. Only post-placement for simplicity.
2	2D axi-sym.	T-H	2,197 - unfractured 2,421 - fractured	Two stages of simulation, a) pre- and b) post-placement.
3	2D axi-sym	T-H-M	2,197 - unfractured 2,421 - fractured	
4	3D	T-H	551,444 - unfractured 920,983 - fractured	
5	3D	T-H-M	551,444 - unfractured 920,983 - fractured	

Table 8.1. Modelling strategy for post-emplacement.

8.3 Domain and geometric model

The rock mass contains a number of fractures and these have been mapped and the rock mass hydraulically tested via the use of boreholes, as described in chapter 6. A geometric model has been developed in chapter 7 which includes key hydraulic fractures and shown to be able to reasonably simulate the highly anisotropic inflow into the tunnel and the deposition holes.

As discussed in chapters 6 and 7 deposition-holes DH-1 and DH-3 have been found to behave very differently and in addition are highly instrumented in the buffer material. A highly hydraulically active fracture of approximately $2m$ in radius has been identified, intersecting DH-1 at approximately mid-height. This fracture allows a large amount of water to flow into this deposition-hole. In contrast, the rock in which DH-3 is situated is largely intact, i.e. does not intersect any hydraulically active fractures and the inflow rate into this deposition-hole is significantly less than into DH-1, both pre and post-emplacement.

For the two-dimensional axi-symmetric simulations two separate geometries have been created, one with and one without a fracture. The domain with a fracture can be seen in figure 8.1, with the other domain identical with the exception of the fracture. It is noted that while the idealised fracture does not describe the fracture geometry accurately it is a good approximation which will aid general understanding of the processes occurring and the influence of a fracture on the buffer resaturation. In fact, the shape and location of the fracture that have been developed in chapter 7 from the borehole tests are themselves an approximation. This model contain 1178 nodes and 2197 3-noded triangular elements for the unfractured domain and 1290 nodes and 2421 3-noded triangular elements for the fractured.
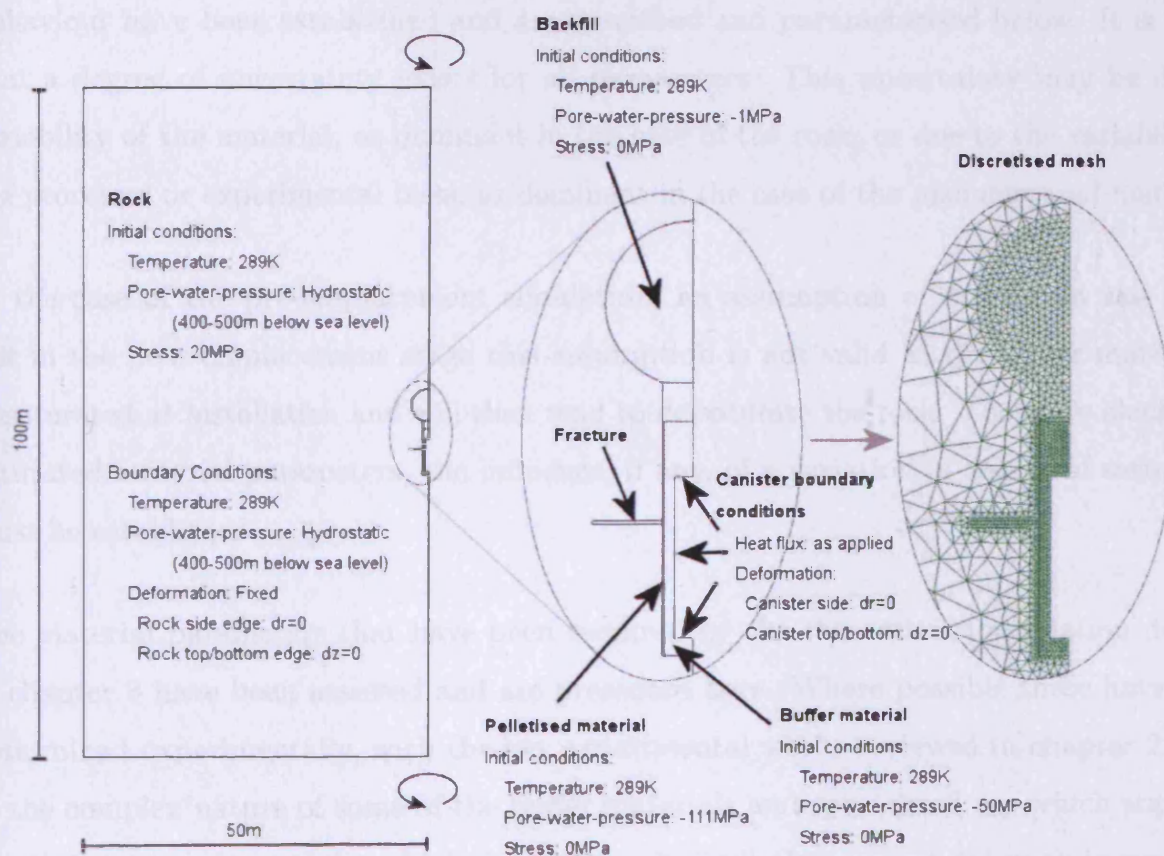
Figure 8.1. Domain of the axi-symmetric model shown with the idealised fracture. Boundary and initial conditions are shown for the thermal, hydraulic and mechanical fields.

The initial and boundary conditions that have been applied are discussed later for the particular analyses. To investigate the difference in behaviour using the pre-placement simulations a matching pre-placement analysis was undertaken. The domain was similar to the one shown in figure 8.1 but without any buffer material. The edges of the rock at the

tunnel interface had a zero pore-water-pressure condition applied to them. The domain had 492/604 nodes and 815/1039 elements for the unfractured/fractured models respectively.

The three dimensional geometry includes the major and minor fractures described in section 7.3, the background rock mass and the emplaced materials. The host rock domain is visualised in figures 7.3, 7.4, 7.5 and 7.6 with the emplaced materials indicatively shown in figure 8.2.

8.4 Material parameters

The properties describing the materials in respect to the hydraulic, thermal and mechanical behaviour have been established and are described and parameterised below. It is noted that a degree of uncertainty exists for all parameters. This uncertainty may be due to variability of the material, as dominant in the case of the rock, or due to the variability in the processes or experimental tests, as dominant in the case of the manufactured materials.

In the case of the pre-emplacement simulation, an assumption of saturation was made, but in the post-emplacement stage this assumption is not valid as the buffer material is unsaturated at installation and will then tend to de-saturate the rock. Therefore along with saturated material parameters, the influence, if any, of a variation in degree of saturation must be established.

The material parameters that have been required by the theoretical formulation defined in chapter 3 have been assessed and are presented here. Where possible these have been determined experimentally, with the key experimental works reviewed in chapter 2. Due to the complex nature of some of the buffer materials and specialised use which stipulate particular properties, such as high densities, only limited experimental work is available. Where this is the case, numerical investigations have been used and assumptions have been made. The saturated hydraulic material parameters of the host rock and fractures within the rock are consistent with the pre-emplacement analysis.

Figure 8.2 highlights the materials that have been identified for use in the models. Each of the materials will need material parameters where the theoretical formulation requires. In addition the rock is made up of intact granite including a series of fractures.
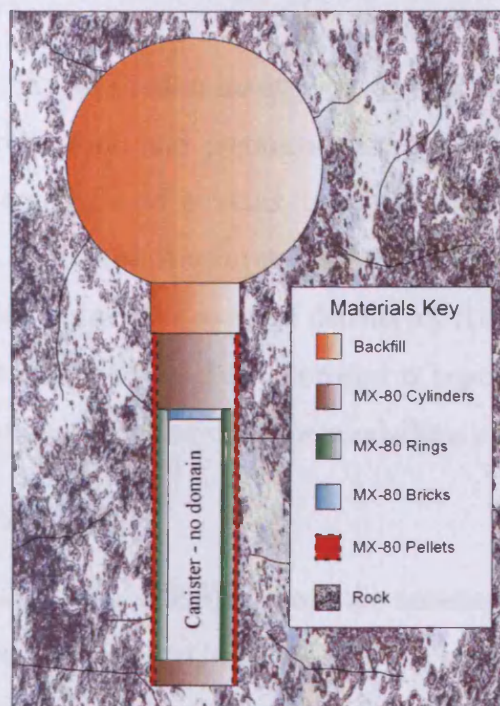
Figure 8.2. Materials defined for use within the model.

8.4.1 Rock

The host rock, as discussed previously in chapters 6 and 7, contains many discontinuities and in particular a number of discrete fractures have been identified. These fractures have been identified through hydraulic investigation and the hydraulic properties have been assessed earlier in chapter 7. The parameter used to define the ability of a fracture to conduct water was the transmissivity. To convert this into a hydraulic conductivity, as required by a spatial discretisation, a width has been assumed (see table 7.2). This allows for easy inclusion into the finite-element mesh. However, these fractures are unlikely to be this dimension and certainty not as uniform as assumed. For other, non-hydraulic, processes the rock mass is modelled as a continuum and the material parameters used for the fractures are identical to the rock mass, due to a lack of other data. Where moisture transfer impacts other processes, e.g. the liquid advective component of heat transfer (convection), the fractures will impact upon this process.

8.4.1.1 General Parameters

Äspö Diorite was found to be the predominant type of rock in the location of the PRP, but fine-grained granite, greenstone and pegmatite are all also found. The fine-grained granite and greenstone are largely found in veins, bands or inclusions. Some rock alteration is noted near to fractures. Joints and fractures are commonly filled with chlorite, calcite and epidote and are generally tight. The average density of the diorite granite is reported as being $2770 kg/m^3$ (Dahlström, 1998) and the porosity is reported as being 0.005 ± 0.002 (Patel et al., 1997), with the central value used for modelling purposes.

8.4.1.2 Hydraulic Parameters

The approach presented by Gens et al. (1998) for both the unsaturated hydraulic conductivity relationship and the Soil Water Retention Curve (SWRC) of granite has been followed. This work was undertaken for the granite found at the Grimsel URL in Switzerland, but has been utilised to simulate the PRP previously (e.g. Melhuish, 2004). The relationship for the hydraulic conductivity is:

for $S_l \leq 1$

$$K_l = K_{sat} S_l^{1/2} \left(1 - \left(1 - S_l^{1/\beta_l} \right)^{\beta_l} \right)^2 \qquad (m/s) \qquad (8.1)$$

where K_l is the unsaturated hydraulic conductivity, K_{sat} is the saturated hydraulic conductivity, S_l is the degree of saturation and β_l is a material parameter. The value of K_{sat} used is that used in the final analysis of chapter 7, i.e. $5 \times 10^{-12} m/s$ for the intact rock, and the value of β_l found by Gens et al. (1998) to be 0.33. This is shown on figure 8.3.

The relationship for the SWRC is stated by Gens et al. (1998) as;

for $s \geq 0$

$$S_l = \left(1 + \left(\frac{s}{P_0} \right)^{1/(1-\beta_l)} \right)^{-\beta_l} \qquad (8.2)$$

where s is the suction, β_l is the same material parameter used in equation (8.1) and P_0 is a material parameter close to the air entry value. Following the approach of Davies (1991) and Melhuish (2004) linking the threshold pressure to the air entry value and in turn the intrinsic permeability and threshold pressure, a value of $0.33 MPa$ is used for P_0. This relationship is shown on figure 8.4.
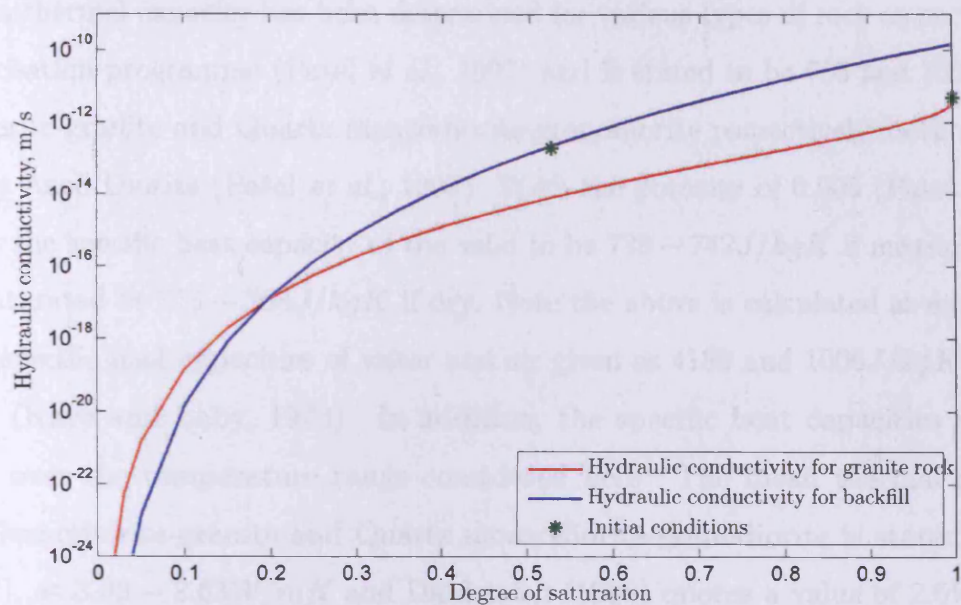
Figure 8.3. Hydraulic conductivity relationship for the granite rock found at Äspö HRL, including initial condition prior to material emplacement.
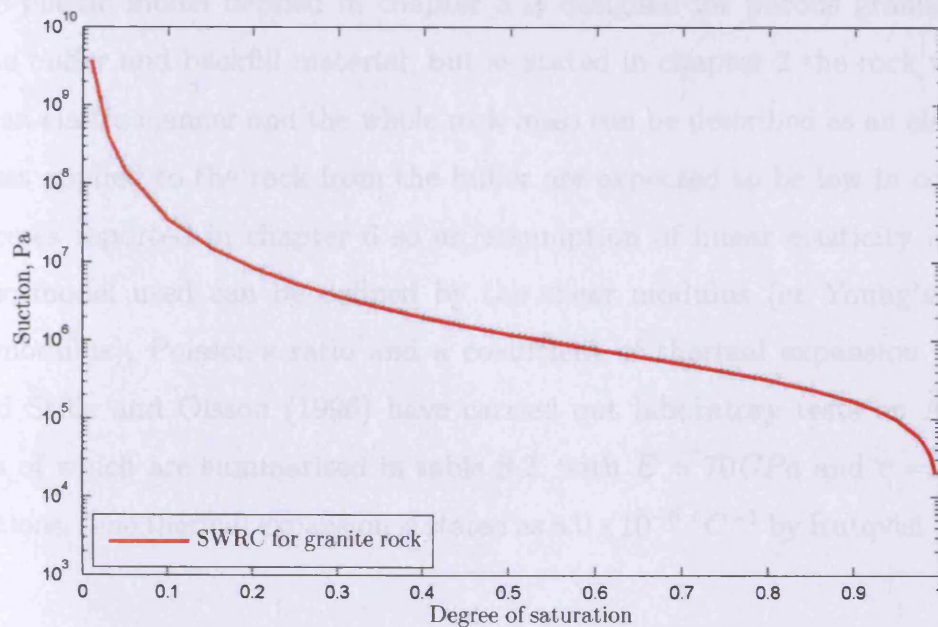
Figure 8.4. The soil water retention curve for Äspö HRL granite rock.

8.4.1.3   Thermal Parameters

The mean thermal capacity has been determined for various types of rock as part of the rock characterisation programme (Patel *et al.*, 1997) and is stated to be 755 and $760J/kg/K$ for Granodiorite-granite and Quartz monzodiorite-granodiorite respectively, both of which are similar to Äspö Diorite (Patel *et al.*, 1997). With the porosity of 0.005 (Patel *et al.*, 1997) this gives the specific heat capacity of the solid to be $738 - 742J/kgK$ if measured when the rock is saturated or $753 - 758J/kgK$ if dry. Note the above is calculated as equation (3.75) with the specific heat capacities of water and air given as 4180 and $1006J/kgK$ respectively at $293K$ (Kaye and Laby, 1973). In addition, the specific heat capacities are assumed constant over the temperature range considered here. The mean thermal conductivity for the Granodiorite-granite and Quartz monzodiorite-granodiorite is stated by Patel *et al.* (1997), as $3.03 - 2.63W/mK$ and Dahlström (1998) quotes a value of $2.5W/mK$ from Sundberg (1991). It is assumed to be constant due to the very low porosity, hence small changes in water content. In the fractures this is used as a first approximation, although it is noted that the water content change may be much greater.

8.4.1.4   Mechanical Parameters

The elasto-plastic model defined in chapter 3 is designed for porous granular materials such as the buffer and backfill material, but as stated in chapter 2 the rock will generally behave in an elastic manner and the whole rock mass can be described as an elastic medium. The stresses applied to the rock from the buffer are expected to be low in comparison to initial stresses reported in chapter 6 so an assumption of linear elasticity is reasonable. The elastic model used can be defined by the shear modulus (or Young's modulus or the bulk modulus), Poisson's ratio and a coefficient of thermal expansion. Delin *et al.* (1995) and Stille and Olsson (1996) have carried out laboratory tests on Äspö Diorite, the results of which are summarised in table 8.2, with $E = 70GPa$ and $v = 0.25$ used in the simulations. The thermal expansion is stated as $8.0 \times 10^{-6} \, °C^{-1}$ by Rutqvist *et al.* (2005).

The fractures have been found to be tight (Patel *et al.*, 1997) which suggests that even with increased stresses from the expansive clays the fracture apertures will remain constant at a minimum.

Uniaxial Compressive Strength, MPa	Young's modulus, GPa	Poisson's Ratio, v	Reference
195	69	0.25	Delin *et al.* (1995)
171	73	0.24	Stille and Olsson (1996)

Table 8.2. Mechanical parameters for Äspö Diorite as determined by Delin *et al.* (1995) and Stille and Olsson (1996).

8.4.2 Buffer Material

The buffer material, as previously described, is a highly compacted manufactured sodium bentonite clay, known as MX-80. The material is manufactured into the blocks and pellets that are used within the repository and, as such, a degree of confidence higher than that given to natural materials can be given to the material parameters. In addition, a comprehensive test regime was undertaken during manufacture and installation of this material in the PRP.

8.4.2.1   General Parameters

The measured average bulk densities of the emplaced buffer material are shown in table 8.3 below, along with the corresponding porosities and water contents by percentage weight. These values are used in the simulations unless stated otherwise, e.g. where average buffer values are used.

MX-80 block	Average Bulk Density, kg/m^3	Porosity	Water Content, %
Cylinder	2018	0.4	17.6
Ring	2085	0.36	17.2
Bricks	1950	0.38	14.4
Pellets	1200	0.62	13.1

Table 8.3. Installed buffer average material data, after Börgesson *et al.* (2002) and Johannesson *et al.* (2004).

The production of the bentonite for the PRP is detailed by Johannesson (2002). The bentonite is delivered in powder form and mixed to the required water content in an

industrial mixer. All the buffer materials described here, with the exception of the pellets, are compacted, on average, to the density shown in table 8.3 and then installed in the repository. A maximum compaction force of $100MPa$ is used to achieve this. Each block is manually checked for damage, measured and weighed.

The pelletised material is made of compacted pellets, which are each approximately $2000kg/m^3$ and measure $16.3mm$ in length and width and a maximum of $8.3mm$ in thickness. They are installed into the gap between the buffer material and the rock by the use of a pneumatic machine (Börgesson et al., 2002; Johannesson et al., 2004). This means that while the main bulk of the buffer material, the cylinders, rings and bricks, are a continuous material the pelletised region is not. The density quoted in table 8.3 is the overall average density for the volume filled with pellets, including the inter-pellet pores as well as the internal pore-structure.

8.4.2.2   Hydraulic Parameters

Cylinders, Rings and Bricks

The unsaturated hydraulic conductivity of the bentonite is discussed in detail in chapter 5 and consequently only briefly mentioned here. The values used for the parameters δ and K_{sat} of equation 5.1, the original hydraulic conductivity relationship, are 3 and $1.9 \times 10^{-14} m/s$ based upon the work of Börgesson and Hernelind (1999) and Villar et al. (2005). The additional parameters required for the modified hydraulic conductivity relationship, equations 5.4 and 5.8, have been taken as $\alpha = 5.0 \times 10^{-8}$ and $\omega_{abs}^{max} = 0.94$. It is noted that the value of K_{sat} for the modified hydraulic conductivity relationship may change depending upon the initial saturation and the initial assumed absorbed moisture. The full range of hydraulic conductivities with respect to degree of saturation and time are shown in figure 5.5, with the 'standard' relationship identified.

The SWRC used is a van Genutchen relationship that was fitted to experimental data from Börgesson and Hernelind (1999). The van Genutchen relationhip is:

$$\theta_l = nS_l = \theta_{res} + \frac{\theta_{sat} - \theta_{res}}{\left[1 + \left(\frac{1000as}{\rho_l g}\right)^b\right]^{(1-1/b)}} \tag{8.3}$$

where θ_{res} and θ_{sat} are the residual and saturated water contents, s is the suction, a and b are material parameters. It was found by Melhuish (2004) that to fit the experimental data a value of $a = 4.5 \times 10^{-7} m^{-1}$ was appropriate. However, Melhuish found that the emplaced bentonite and the recorded initial experimental data did not fit the experimental data provided by Börgesson and Hernelind (1999) and suggested the following material parameters:

$$a = 1.25 \times 10^{-7} m^{-1}, \ b = 1.75, \ \theta_{res} = 0.0001, \ \theta_{sat} = n$$

The experimental results and fitted relationships are shown in figure 8.5.

Pellets

Again, the unsaturated hydraulic conductivity of the bentonite pellets is discussed in detail in chapter 5 and therefore not repeated in detail here. The relationship suggested by Melhuish (2004) is identical to the relationship for the buffer blocks as given by Börgesson and Hernelind (1999), equation (5.1), referred to here at the 'standard' unsaturated hydraulic conductivity relationship. The material parameters for the 'standard' unsaturated hydraulic conductivity relationship are $K_{sat} = 1 \times 10^{-12} m/s$ and $\delta = 2$ for a well graded compacted pelletised bentonite (Hoffmann et al., 2007).

A modified hydraulic conductivity has been proposed in chapter 5, equation (5.13), and includes some of the observations made by Hoffmann et al. (2007). Following from chapter 5 values of $\beta_p = 1 \times 10^{-7} m/s$, $k_{init} = 1 \times 10^{-10} m/s$ and $k_{inf} = 1 \times 10^{-16} m/s$ have been used.

Only limited test data on pelletised bentonite is available for the SWRC some of which is presented by Hoffmann et al. (2007). For an individual pellet the SWRC is likely to be similar to that of compacted bentonite blocks, but for a pelletised region which includes pellets and large inter-pellet pores, the relationship may be much different. Hoffmann et al. (2007) suggest a modified van Genutchen relationship which only differs significantly from the standard van Genutchen, equation (8.3), for very low water contents, i.e. degree of saturation of below 0.2, which are unlikely to be achieved. Therefore, using the same relationship as for the bentonite blocks, equation (8.3), and matching the relationship from Hoffmann et al. (2007) the fitted material parameters are:

$$a = 7.00 \times 10^{-7} m^{-1}, \ b = 1.3, \ \theta_{res} = 0.0001, \ \theta_{sat} = n$$

Figure 8.5 shows the relationship for the SWRC for pellets, using the relationship suggested by Hoffmann *et al.* (2007) along with the SWRC for the bentonite blocks.

8.4.2.3 Thermal Parameters

Cylinders/Rings/Bricks

The heat capacity of the solid particles of MX-80 has been found to be $800 J/kg/K$ (Börgesson and Hernelind, 1999). The thermal conductivity was determined by Börgesson and Hernelind (1999) where experimental data has been matched to a series of points, as shown in table 8.4, whereby linear interpolation is undertaken between the values. This relationship along with experimental data are shown in figure 8.6.

Degree of saturation, S_l	Thermal conductivity, λ, $W/m/K$
0	0.3
0.2	0.3
0.8	1.2
1.0	1.3

Table 8.4. Thermal conductivity of MX-80 as a function of degree of saturation, after Börgesson and Hernelind (1999).

Pellets

No experimental data was available for the thermal conductivity of the pellets. It has been assumed that the pelletised region has the same thermal conductivity relationship as that of bentonite blocks. However, it is noted that extra pores between the pellets may have an effect in the short term, probably lowering the thermal conductivity. In the long term it is hoped that the pellets and the remaining bentonite will become homogenised, therefore supporting the assumption of equal thermal conductivity. However, due to the SWRCs shown in figure 8.5 a lower degree of saturation is calculated for the same suction in the pellets as the main bentonite blocks, therefore resulting in a lower thermal conductivity until saturation. However, this is not based upon experimental data and there may be a quantitative error associated in this parameter.
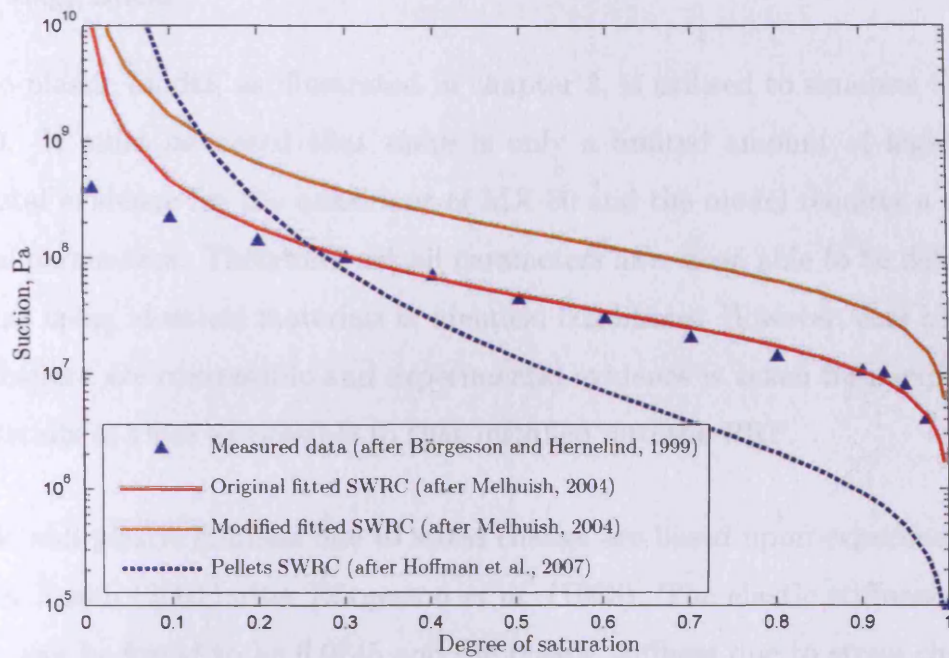
Figure 8.5. The soil water retention curves for MX-80 compacted blocks and pellets.
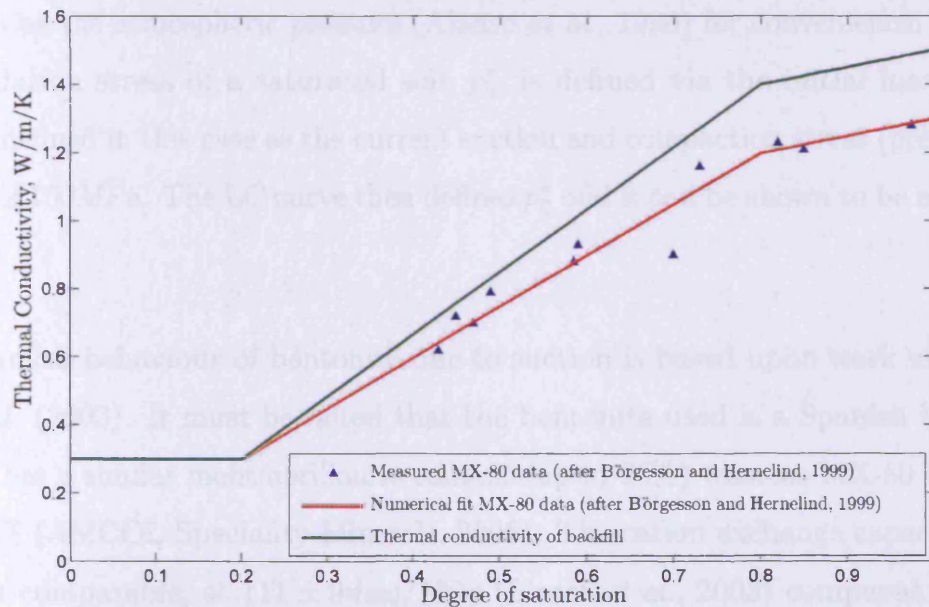
Figure 8.6. The unsaturated thermal conductivity relationship for MX-80 compacted blocks and pellets.

8.4.2.4   Mechanical Parameters

Cylinders/Rings/Bricks

The elasto-plastic model, as illustrated in chapter 3, is utilised to simulate the behaviour of MX-80. It must be noted that there is only a limited amount of highly controlled experimental evidence for the behaviour of MX-80 and the model requires a large number of material parameters. Therefore, not all parameters have been able to be defined based on experiments using identical materials in identical conditions. However, care has been taken that parameters are compatible and experimental evidence is taken from experiment work using materials as close as possible to that installed into the PRP.

The elastic and plastic stiffness due to stress change are based upon experimental evidence collated by Pusch (2001) after Börgesson *et al.* (1993). The elastic stiffness due to stress change, κ, can be found to be 0.0245 and the plastic stiffness due to stress change, $\lambda(0)$ to be 0.238. The relationship defining the plastic stiffness at any suction, equation (3.120), is defined by means of two parameters, r and β. These have been found experimentally by Lloret *et al.* (2003) to be 0.9 and 1.0 respectively for compacted bentonite.

The reference stress, p_c, used in equation (3.119) to define the load collapse (LC) is assumed to be the atmospheric pressure (Alonso *et al.*, 1990) for convenience. The effective preconsolidation stress of a saturated soil, p_0^*, is defined via the initial maximum stress conditions defined in this case as the current suction and compaction stress (preconsolidation stress, p_0) of $100MPa$. The LC curve then defines p_0^* and it can be shown to be approximately $45MPa$.

The mechanical behaviour of bentonite due to suction is based upon work undertaken by Lloret *et al.* (2003). It must be noted that the bentonite used is a Spanish bentonite not MX-80. It has a similar montmorillonite content (up to 90%) whereas MX-80 bentonite has at least 90% (AMCOL Speciality Minerals, 2006). The cation exchange capacity is slightly higher, but comparable, at $111 \pm 9meq/100g$ (Lloret *et al.*, 2003) compared to MX-80 at $79 \pm 5meq/100g$. However, in the MX-80 the majority of the cation exchange capacity is made up of sodium (Bradbury and Baeyens, 2003, after Bradbury and Baeyens, 2002) and only 23% of the Spanish bentonite's exchangeable cations are sodium (Lloret *et al.*, 2003),

which may suggest an underestimation of swelling behaviour.

Lloret *et al.* (2003) describe a series of tests on compacted bentonite with initial dry densities of approximately $1.7g/cm^3$ and water contents of approximately 13% therefore directly comparable to the material installed in the PRP. These yield values of κ_s of 0.075 under $100MPa$ and 0.0064 above. It must also be noted that the experiments indicated that the effects of suction were reduced at higher levels of stress, up to $10MPa$, which the model outlined in chapter 3 does not have the capacity to reproduce. The tests also indicated no significant plastic strain had developed and therefore a highest value achieved in the tests ($500MPa$) for s_0 has been assumed.

The shear modulus is taken from assumptions made by Mitchell (2002) and Gens *et al.* (1998) as $10MPa$ which is consistent given the values of κ to a Poisson's ratio of approximately 0.4 given low suction. Standard triaxial tests carried out on MX-80 and reported by Börgesson *et al.* (1995) yielded the slope of the critical state line, M of approximately 0.358. Given that some of the tests are drained and others undrained no real assessment of the variation of cohesion with suction can be made. However, some cohesion is apparant and as the samples carried out by Börgesson *et al.* (1995) had a degree of saturation of 0.99 (approximately $1 \times 10^7 Pa$ suction) and a cohesion of approximately $56kPa$ a first approximation for the cohesion property k, 5.6×10^{-3} will be used.

Börgesson *et al.* (1995) state that the thermal expansion, α_T, of MX-80 is largely governed by the water content, therefore this parameter will change over time as the buffer material saturates or de-saturates. Two approaches are possible, an average expansion based upon the average water content expected during the period of elevated temperature, or an explicit calculation of water density change. As a first approximation a constant of $1 \times 10^{-4} K^{-1}$ will be used.

Pellets

There is only very limited experimental data available for the pelletised region, however this is a critical region in terms of development of stresses within the deposition holes and one of the most complex due to the pelletised, non-homogenous, nature. Hoffmann *et al.* (2007) have undertaken some experimentation, although both the pellets and samples

are somewhat different, an indication of material parameters may be gained. In addition, Melhuish (2004) completed a numerical sensitivity analysis and the results also give an indication of appropriate parameters. Both of these authors recommend an increase of the κ value so that more deformation occurs with the application of stress, consequently the value of shear modulus would be decreased. In general, the approach for parameters follows the data given above for the buffer blocks. The first estimate for the parameters is given in table 8.5. Analyses undertaken later in this chapter will examine these assumptions and compare the results to experimental, post-mortem results of a similar experiment, the CRT, in the buffer and pelletised region, in terms of dry density, to give confidence in a final parameter selection.

κ	$\lambda(0)$	r	β	p_c	p_0^*	κ_s	λ_s	s_0	G	k	M	α_T
0.25	1.00	0.9	1.0	$0.1 MPa$	$45 MPa$	0.075	0.075	$500 MPa$	$1 MPa$	0	0.358	$0 K^{-1}$

Table 8.5. First estimate of material parameters for pelletised bentonite.

8.4.3 Backfill Material

The backfill material used for the PRP is a mixture of crushed rock from the excavation of the tunnel (70%) and bentonite (30%). The bentonite used was a converted sodium bentonite originating from Milos, Greece. This was used as opposed to MX-80 to reduce costs. Water was added to yield a water content of 12% and it was mixed and added in compacted layers (Johannesson et al., 2007).

8.4.3.1 General Parameters

The backfill was compacted on site and as such the dry density of the backfill varies across layers due to the influence of the walls and accessibility. On average a nuclear gauge measured the dry density to be $1.7 g/cm^3$ (Börgesson et al., 2002), although another estimate based upon the amount of material that entered the PRP calculated the dry density to be $1.58 g/cm^3$. A value of $1.65 g/cm^3$ will be used in this study, consistent with the conclusion of Börgesson et al. (2002). This corresponds to a porosity of approximately 0.4.

8.4.3.2 Hydraulic Parameters

The saturated hydraulic conductivity of backfill has been found to be $1.5 \times 10^{-10} m/s$ by Johannesson *et al.* (1999) and corroborated by Pusch (2001). The relationship used for the unsaturated variation of hydraulic conductivity proposed for use in MX-80 by Börgesson and Hernelind (1999), equation (5.1), was used for backfill by the same authors (Börgesson and Hernelind, 1998) with the value of $\delta = 10$ found to match the relationship to experimental data. This is seen in figure 8.3. The same reduction in hydraulic conductivity reported for compacted bentonite has not been reported for backfill. It is anticipated that the flow takes place in macro-pores which are not able to be filled by the swelling bentonite. This approach has been used with success elsewhere (e.g. Thomas *et al.*, 2009a).

Experimental data for the SWRC is presented by Börgesson and Hernelind (1999) as a set of discrete points. These points are shown along with the numerical fit of the van Genutchen relationship, equation (8.3), in figure 8.7. In addition, experimental work undertaken by Clay Technology (2000) cited by Mata (2003) agrees in general with the results presented by Börgesson and Hernelind (1999), although it is noted that the results show a large spread. It is again noted that the van Genutchen equation fit deviates from the experimental results at very low water content, but that in this experiment it is very unlikely that these low water contents will be achieved. It is also noted by Mata (2003) that a large variation in experimental data, of up to two magnitudes, was apparent. The material parameters used are:
$$a = 1.0 \times 10^{-4} m^{-1}, \; b = 1.23, \; \theta_{res} = 0.0001, \; \theta_{sat} = n$$

8.4.3.3 Thermal Parameters

The saturated thermal conductivity is stated by Börgesson and Hernelind (1999) as $1.5 W/m/K$ and as there is no experimental evidence of its variation with respect to water saturation a similar relation to that of MX-80 is assumed (Melhuish, 2004). This is logical due to the similar variation in moisture content that may occur and that the material is a mixture of bentonite and crushed rock. This is shown in figure 8.6. The heat capacity of the backfill is given by Börgesson and Hernelind (1999) as $1200 J/kg/K$. Utilising equation (3.75) the heat capacity of the solid is $842 J/kg/K$.
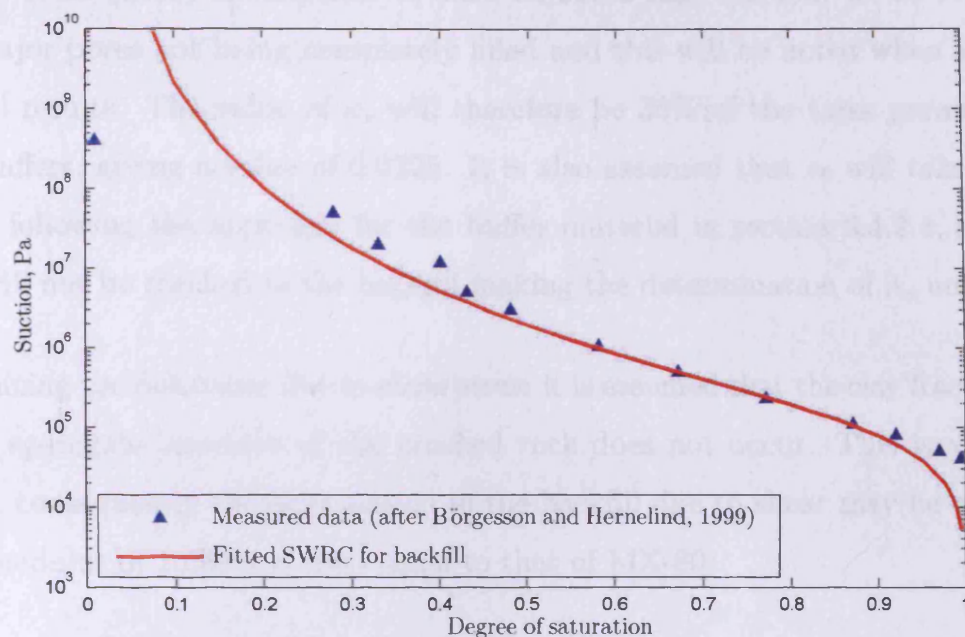
Figure 8.7. The soil water retention curve for the backfill.

8.4.3.4 Mechanical Parameters

Only very limited experimental data is available for the mechanical parameters of the backfill. However a thesis by Mata (2003) does contain the results of a number of experimental tests on the backfill used in the Backfill and Plug Test Project (BPTP) at the HRL. The proportions of crushed rock and bentonite are the same 70/30, but the bentonite is MX-80 in this case. The tests performed show an initial elastic response, most likely from the compaction gained during sample preparation, then a plastic deformation including an unload-load loop during the test. The gradients of the lines in natural log of vertical stress against void ratio give κ and $\lambda(0)$, being 0.016 and 0.102 respectively.

Due to a lack of similar experimental evidence in suction controlled conditions the values of r and β will be assumed to be consistent with the MX-80. To establish the mechanical behaviour in response to suction change it is assumed that the crushed rock is inert to changes in suction and further it is suggested by Börgesson *et al.* (2003) that the constant volume swelling pressures would be equal to that of MX-80 should all the major pores be filled, synonymous to pore-pressure behaviour. However, it is the volume change in response to suction change that is required for this formulation. Assuming that all the major pores are filled the volume change response would be proportional to the clay fraction, adopting the

Börgesson *et al.* (2003) assumption. It must be noted that this may be an over-prediction due to major pores not being completely filled and this will be noted when analysing the numerical results. The value of κ_s will therefore be 30% of the same parameter for the MX-80 buffers, giving a value of 0.0225. It is also assumed that s_0 will take the value of $500MPa$, following the approach for the buffer material in section 8.4.2.4, and that this suction will not be reached in the backfill making the determination of λ_s unnecessary.

In determining the behaviour due to shear stress it is assumed that the clay fraction is critical and that aggregate interlock of the crushed rock does not occur. This is a conservative approach, consequently the deformation in the backfill due to shear may be overestimated. A shear modulus of $10MPa$ is used equal to that of MX-80.

Again, with no evidence to support cohesion gain with suction, k is assumed consistent with that of the buffer blocks and proportional to the amount of clay in the mixture, therefore as a first approximation 1.7×10^{-3}; the slope of the critical state line, M, is assumed the same as that of MX-80; and the reference stress, p_c, is the atmospheric pressure. The effective preconsolidation stress of a saturated soil, p_0^*, is calculated in the same manner as for the MX-80 and yields a value of $44MPa$. The coefficient of thermal expansion, α_T, will be assumed to be proportional of the material mixture, yielding $3.56 \times 10^{-5}K^{-1}$.

8.4.4   Concrete Plugs

In general concrete is only used in any substantial volume in the plug structures that seal the sections. It is designed to resist the pressures that are placed upon it and as such is assumed to be undeformable and fixed. It is also designed to seal the sections hydraulically so a very low permeability and low porosity has been assumed. The density of the concrete plug, including reinforcement was approximately $2350kg/m^3$.

The variation of suction with moisture content is assumed to be the same as the rock as is the hydraulic conductivity relationship. However, a saturated hydraulic conductivity, K_{sat}, is assumed to be lower than the rock at, $1 \times 10^{-14}m/s$. Due to a lack of data the thermal properties are assumed to be the same as for the rock.

8.4.5   Summary of material parameters

A summary of all of the material parameters is presented in table 8.6.

Properties	Rock	Fractures	MX-80 cylinders	MX-80 rings	MX-80 bricks	MX-80 pellets	Backfill	Concrete
porosity, n	0.005	0.1	0.4	0.36	0.384	0.61	0.363	0.005
ρ_s (kg/m^3)	2770	2770	2770	2770	2770	2770	2770	2770
C_{ps}	750	750	800	800	800	800	850	750
λ_T (W/mK)	2.4	2.4	as figure 8.6	as figure 8.6	as figure 8.6	as figure 8.6	as figure 8.6	2.4
K_l (m/s) constants	equation (8.1) $\beta = 0.33$ $K_{sat} = 5.0 \times 10^{-12}$	equation (8.1) $\beta = 0.33$ $K_{sat} = various$	equation (5.4) $\delta = 3$ $K_{sat} = 1.9 \times 10^{-14}$ $\alpha = 5.0 \times 10^{-8}$	equation (5.4) $\delta = 3$ $K_{sat} = 1.9 \times 10^{-14}$ $\alpha = 5.0 \times 10^{-8}$	equation (5.4) $\delta = 3$ $K_{sat} = 1.9 \times 10^{-14}$ $\alpha = 5.0 \times 10^{-8}$	equation (5.13) $k_{init} = 1.0 \times 10^{-10}$ $k_{inf} = 1.0 \times 10^{-16}$ $\beta_p = 1.0 \times 10^{-7}$	equation (5.1) $\delta = 10$ $K_{sat} = 1.5 \times 10^{-10}$	equation (8.1) $\beta = 0.33$ $K_{sat} = 1.0 \times 10^{-14}$
S_l constants	equation (8.2) $\beta = 0.33$ $P_0 = 0.33$	equation (8.2) $\beta = 0.33$ $P_0 = 0.33$	equation (8.3) $a = 1.25 \times 10^{-7}$ $b = 1.75$ $\theta_{res} = 0.0001$ $\theta_{sat} = n$	equation (8.3) $a = 1.25 \times 10^{-7}$ $b = 1.75$ $\theta_{res} = 0.0001$ $\theta_{sat} = n$	equation (8.3) $a = 1.25 \times 10^{-7}$ $b = 1.75$ $\theta_{res} = 0.0001$ $\theta_{sat} = n$	equation (8.3) $a = 7.00 \times 10^{-6}$ $b = 1.3$ $\theta_{res} = 0.0001$ $\theta_{sat} = n$	equation (8.3) $a = 1.00 \times 10^{-4}$ $b = 1.23$ $\theta_{res} = 0.0001$ $\theta_{sat} = n$	equation (8.2) $\beta = 0.33$ $P_0 = 0.33$
G (MPa)	27600	27600	10	10	10	1	10	27600
v	0.25	0.25	-	-	-	-	-	0.25
κ	-	-	0.0245	0.0245	0.0245	0.25	0.016	-
$\lambda(0)$	-	-	0.238	0.238	0.238	1.0	0.102	-
p_c	-	-	1.0×10^5	1.0×10^5	1.0×10^5	1.0×10^5	1.0×10^5	-
p_0^* (MPa)	-	-	45	45	45	45	45	-
β	-	-	1.0	1.0	1.0	1.0	1.0	-
r	-	-	0.9	0.9	0.9	0.9	0.9	-
M	-	-	0.358	0.358	0.358	0.358	0.358	-
k	-	-	5.6×10^{-3}	5.6×10^{-3}	5.6×10^{-3}	5.6×10^{-3}	1.7×10^{-3}	-
κ_s	-	-	0.075	0.075	0.075	0.075	0.0225	-
λ_s	-	-	0.075	0.075	0.075	0.075	0.0225	-
s_0 (MPa)	-	-	500	500	500	500	100	-
$\alpha_T K^{-1}$	8×10^{-6}	8×10^{-6}	1×10^{-4}	1×10^{-4}	1×10^{-4}	0	3.56×10^{-5}	8×10^{-6}

Table 8.6. Summary of material properties.

8.5 Initial conditions

The initial conditions of the system must be defined as the starting point of the analysis when undertaking a transient analysis. For THM analyses the primary variables must be defined, with the exception of the displacement whereby the displacements are calculated relative to the initial position. In this case the initial stresses must be defined.

8.5.1 Rock

The initial pore-pressures in the rock are discussed in detail in chapter 7. In general, the results from the pre-placement simulations will be used for the initial conditions, but in some analyses hydrostatic pressure will be used for convenience. The impact of these different initial conditions is assessed in section 8.8. The initial thermal conditions are assumed to be of $288K$ based upon the initial experimental results. The initial stresses in the rock mass have been taken as the undisturbed stresses discussed and transformed into orthogonal stresses in section 6.3.1. For ease of use they have been averaged and rounded to $20MPa$ for the axisymmetric analyses. With the elastic model used for the rock this will have no impact as the stress increment determines the deformation.

8.5.2 Buffer

The initial hydraulic conditions are determined from the water content reported by Börgesson *et al.* (2002) and Johannesson *et al.* (2004) and equation (8.3). Agreement is also found utilising the psychrometric law and the initial results from the relative humidity sensor results reported by Goudarzi and Johannesson (2007). The degree of saturation along with the initial pore-water-pressures for the different buffer materials are reported in table 8.7 below. Initially, the air-pressure is assumed to be atmospheric and as the temperatures are not anticipated to be above $100°C$ it is assumed that they are fixed (Thomas *et al.*, 2009b). The thermal initial conditions are assumed to be the same as the rock, $288K$. This is due to no initial heating and a period of time in the tunnel prior to installation. The compacted bentonite buffer is installed with zero external stress applied. However, a residual stress from the compaction process may hold parts of the blocks under stress. An initial condition of $0.05MPa$ was applied which is reasonable when looking at experimental results.

MX–80 material	Suction, s, MPa	Degree of saturation
Cylinder	-64.7	0.79
Ring	-49.2	0.86
Bricks	-112	0.64
Pellets	-111	0.25

Table 8.7. Initial pore-water-pressures for the buffer materials.

8.5.3 Backfill

The initial degree of saturation for the backfill material was found to be 0.524, from the water content and porosity. This leads to the calculation of initial suction of $1.04 MPa$ via equation (8.3). The initial temperature is as for the bentonite buffer. During installation the backfill material is compacted. However, this load is removed and therefore initially the backfill has zero applied stress, but an initial stress of $0.05 MPa$ was applied to allow for some residual stress.

8.6 Boundary conditions

The domain has been chosen specifically so that the outer boundary will be far enough away from the repository that the variable fields in the region of interest will not be disturbed. Additional checks have been made with boundaries further away from the repository with negligible difference in the results and the fluxes at the boundaries have been monitored to ensure that they are negligible, as discussed in section 7.5.1. The outer boundary, away from the repository, is considered to maintain hydrostatic pore-water pressure, be fixed at the initial temperature of $288K$ and have zero deformation in the direction normal to the boundary surface.

The canisters are not modelled and therefore there is a model boundary at the buffer edge adjacent to the canister. Hydraulically a zero-flux condition is applied, the idealised heat output from the canisters, shown in figure 6.24 for DH-1, divided by the surface area forms a heat flux boundary condition and deformation is fixed for the direction normal to the canister surface. The canisters, including the steel overpack, are likely to be virtually undeformable at the expected stresses, but in reality the whole canister may be displaced. This, however, cannot be reproduced with this boundary condition and is a limitation of the model.

8.7 Results - Analysis Set 1

The simulations presented in this section are two-dimensional, axi-symmetric analyses and are entitled *Analysis Set 1* in table 8.1. Figure 8.1 illustrates the domain, the discretisation and the initial conditions. The materials included are shown in figure 8.2 and the idealised fracture in the fractured domain is given the hydraulic conductivity and width, therefore the same transmissivity, of the minor fracture calibrated in chapter 7. As discussed in section 8.3, the fractured domain is an idealised version of DH-1 and the unfractured an idealised version of DH-3. The initial conditions in the rock for this analysis set are hydrostatic. The mesh has been produced using linear triangular elements to enable the ease of changing the size of the elements and fitting complex shapes. To check spatial convergence a single analysis where the density of elements has been approximately doubled has been undertaken resulting in only negligible differences in the results. The analyses that have been undertaken as a subset of *Analysis Set 1*, including some salient details, are shown in table 8.8.

Analysis Name	Analysis Geometry and Type	Fractured/ Unfractured	Hydraulic conductivity relationships for MX-80 buffer and pellets
1-1-TH2D-UnF-st	2D axi-sym. T-H	Unfractured	Standard
1-2-TH2D-F-st	2D axi-sym. T-H	Fractured	Standard
1-3-TH2D-UnF-mod	2D axi-sym. T-H	Unfractured	Modified
1-4-TH2D-F-mod	2D axi-sym. T-H	Fractured	Modified

Table 8.8. Analyses undertaken in *Analysis Set 1*.

8.7.1   Numerical conditions

For the fractured analyses the timestep was initially 1 second and allowed to increase up to 100 days utilising a multiplier of 1.15 when convergence allowed. Due to the relatively small scale of these analyses, they were undertaken on a 'standard' desktop personal computer, with an Intel Pentium 4 $3.0GHz$ single core processor and $2GB$ of RAM. Typically a 10 year analysis could be undertaken in 15 minutes, requiring 400 timesteps and a 1,000 year analysis was completed in approximately 43 minutes and required approximately 3,800 timesteps. The unfractured analysis was undertaken in the same manner and a 1,000 year analysis could be undertaken in approximately 30 minutes and similarly required approximately 3.800 timesteps.

8.7.2   Results

The results are presented here for the initial operation phase, that is less than 10 years, when the thermal and hydraulic gradients are at their greatest. In this time the peak temperature is likely to be found and the moisture regime will be greatly influenced by the heat distribution. In general, the analyses are run until the point of saturation with the time reported; this is important in terms of performance assessment as this is when corrosion of the canister and therefore gas generation will begin to occur.

A selection of representative sensor locations have been identified, allowing the spatial variation of variables through the buffer to be captured as well as groups of sensors where more detailed knowledge of the hydraulic and temperature variation through the buffer material is made. These are shown in all figures with the results along with coordinates and locations specified in the figure legends.

Figure 8.8 shows the hydraulic results in the form of relative humidity for the 'standard' unsaturated hydraulic conductivity relationship for the fractured domain, i.e. analysis 1-1-TH2D-F-st defined in table 8.8. The results are both qualitatively and quantitatively reasonable, albeit with some definite deviation from experimental data.

The morphology of the numerical results compare to the experimental results within the first approximately 1,000 days is reasonable, with a general quantitative underestimation of saturation in the lower and mid-height sections and a more complex pattern of both under

and over estimation in the upper section. The underestimation at the start can be attributed to the hydraulic conductivity relationship of the pellets. No allowance is made within the 'standard' relationship for the granular behaviour including the large inter-granular pores. As discussed in chapter 6, in the lower section experimentally the sensors show a large increase in relative humidity at approximately 500 days which in reality is unlikely and hence indicates that the sensors are not functioning after this time.

After 1,000 days both the mid-height and bottom of the buffer is saturated and the relative humidity for experimental and numerical results match well, although only a limited number of sensors are working. In the upper section correlation of the gradients of the lines and quantitative results between 1,000 and 1,500 days is good, but post 1,500 days the gradients of the numerical results increase and quickly saturate. This is opposed to the experimental results where the gradients are either maintained or decrease to an almost steady-state. This can possibly be attributed to macro/micro-structural change within the bentonite, reducing the available pores for flow. The sharp change of gradient in the results from sensor WBU10026 at approximately 500 days is due to the hydration effect of the fracture reaching this location.

The results for the modified unsaturated hydraulic conductivity relationship also for the fractured domain, i.e. analysis 1-4-TH2D-F-mod, are shown in figure 8.9. The results are significantly improved in the upper and mid-height location both quantitatively and qualitatively. In particular, the long-term gradients are significantly improved, suggesting that the capability of this relationship to predict long-term behaviour would be improved. The numerical results in the location of sensor WBU10026 in the upper region still exhibit an initial underestimation of relative humidity although the qualitative behaviour is good. This can be attributed to either the inability of the pellets to efficiently transfer suction as the material is not continuous, or a initial wetting of this region during installation. In the lower region the behaviour before 500 days is similar to that of the analysis 1-2-TH2D-F-st, but subsequent to that the saturation rate is slower. As mentioned above, in the lower region experimentally the sensors show a large increase in relative humidity at approximately 500 days possibly indicating that the sensors are largely saturated which is the case in either analysis.

The temperature results for both analyses are presented in figures 8.10 and 8.11 respectively. These results are almost identical to within $0.5°C$ at all locations. Throughout the general shape of the results is reasonable to the experimental data with an underestimation of temperature after approximately 100 days. This is probably due to the interaction of the temperature fields of the adjacent deposition-holes not being considered. Therefore, this pattern is expected for all analyses of single deposition-holes. It is noted that the kink in the simulation results coincides with the period of time in which the power to all canisters was switched off.

For the unfractured domains, analyses 1-1-TH2D-UnF-st and 1-3-TH2D-UnF-mod consider the standard and modified unsaturated hydraulic conductivity relationship respectively. Relative humidity results for these two analyses are presented in figures 8.12 and 8.13.

In analysis 1-1-TH2D-UnF-st, figure 8.12, it is clear that the rate of saturation at the mid-height and bottom of the buffer is much faster than found experimentally, this is especially obvious after 500 days. In the upper region there is both more extreme drying and wetting exhibited experimentally than calculated numerically in the short term, however in all locations the point of saturation is calculated as occurring before the experimentally observed point.

In figure 8.13 the behaviour at the mid-height and base of the buffer is much improved when the modified unsaturated hydraulic conductivity relationships are used, albeit with an overestimation of the quantitative saturation. However, importantly, the gradients of the rate of saturation when experimental data finishes are similar, this indicates that the modified unsaturated hydraulic conductivity relationship is likely to be more suited to predicting long-term behaviour.

The temperature results have been omitted for brevity as they too are within $0.5°C$ at all sensor locations of analyses 1-2-TH2D-F-st and 1-4-TH2D-F-mod.

Contour plots of the temperature and pore-water pressure at various times for the modified unsaturated hydraulic conductivity relationship both for the fractured and unfractured domains are presented in figures 8.14 and 8.15 respectively. It is clear that the temperature

evolution is largely independent of the presence of the fracture. For the pore-water pressure the effect of the fracture can be clearly seen and it is noticed that the hydraulic behaviour is local to the fracture. In particular it can been seen that at the locality of the fracture the material quickly becomes saturated through the entire thickness of the buffer. This is important for the performance assessment process and predicting how the canister may corrode. It is worth noting the spatial gradients in variables at various locations. For the mid-section the vertical gradients are low and the horizontal gradients high for both the temperture and the pore-water pressure. However, at the upper and lower sections there is both a vertical and horizontal gradient, which means that results will have a large sensitivity on the exact position of the sensor. This phenomenon should be noted when analysing further results.

8.7.3 Summary

The temperature evolution has been reasonably simulated in these analyses, particularly in the first 100 days, although a definite underestimation is found after approximately 100 days, due to the interaction of heat output from other heat canisters in the experiment affecting the results after this time. It is found that there are only negligible differences between the simulations of a fractured and unfractured domain.

The hydraulic behaviour of DH-1 was seen to be reasonably simulated with either of the hydraulic conductivity relationships used, as effectively they are the same in the short term, although some overestimation of the hydration rate is found after approximately 1500 days for the original approach. The simulations results for DH-3 where experimentally the saturation rate is much slower, show an increasing overestimation with time, when using the original hydraulic conductivity. Using the modified hydraulic conductivity the results for this deposition-hole are much improved, with particular emphasis on the final gradients indicating that long term behaviour may be much better simulated. Therefore, it is concluded that as a first estimate of predicting the micro-structural change observed in a bentonite buffer, a time/degree-of-saturation dependant unsaturated hydraulic relationship can be used to achieve significantly improved results. In particular, the long-term behaviour, especially the rate of re-saturation, is significantly closer to experimental results. This in turn is likely to yield a much improved estimate of time of saturation.

DH-1
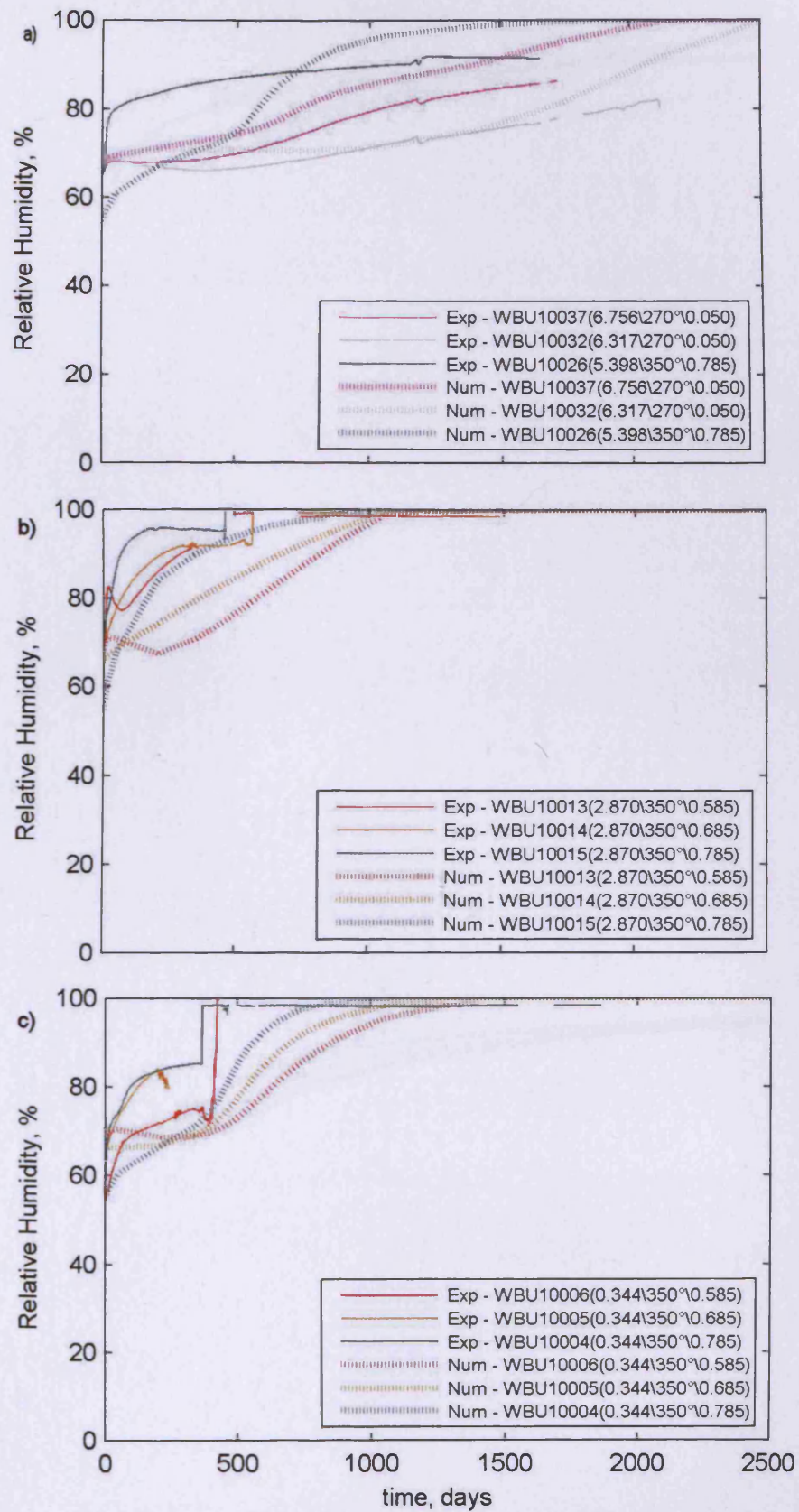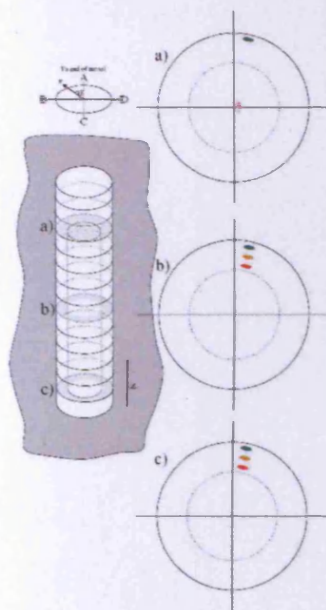
Figure 8.8. Relative Humidity measurements in DH-1 experimental against numerical (1-1-TH2D-F-st) with standard unsaturated hydraulic conductivity relationship, experimental results after Goudarzi and Johannesson (2007).

DH-1
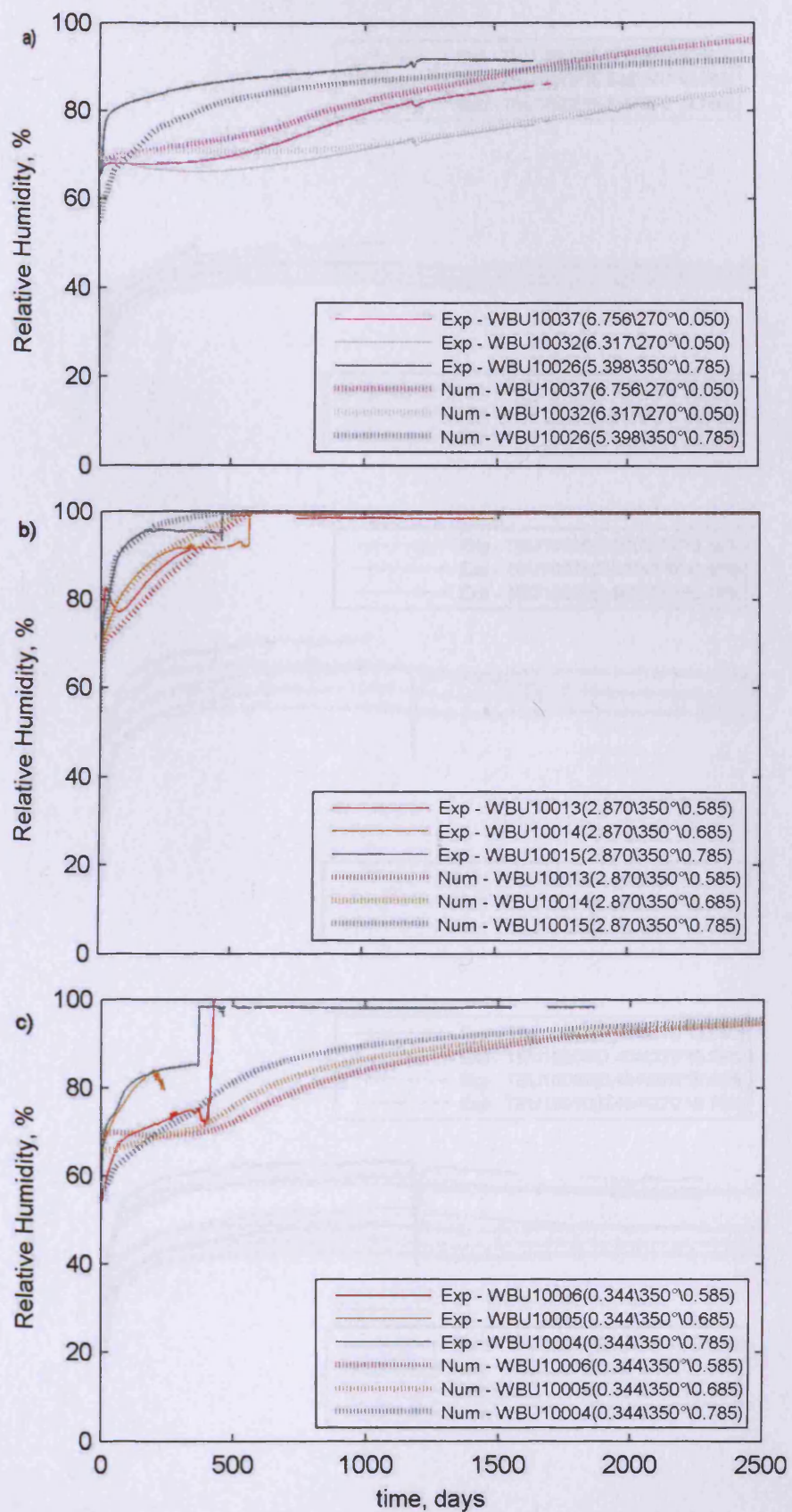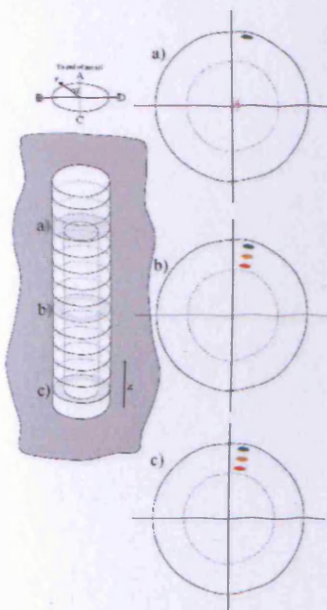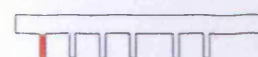
Figure 8.9. Relative Humidity measurements in DH-1 experimental against numerical (1-3-TH2D-F-mod) with modified unsaturated hydraulic conductivity relationship, experimental results after Goudarzi and Johannesson (2007).

DH-1
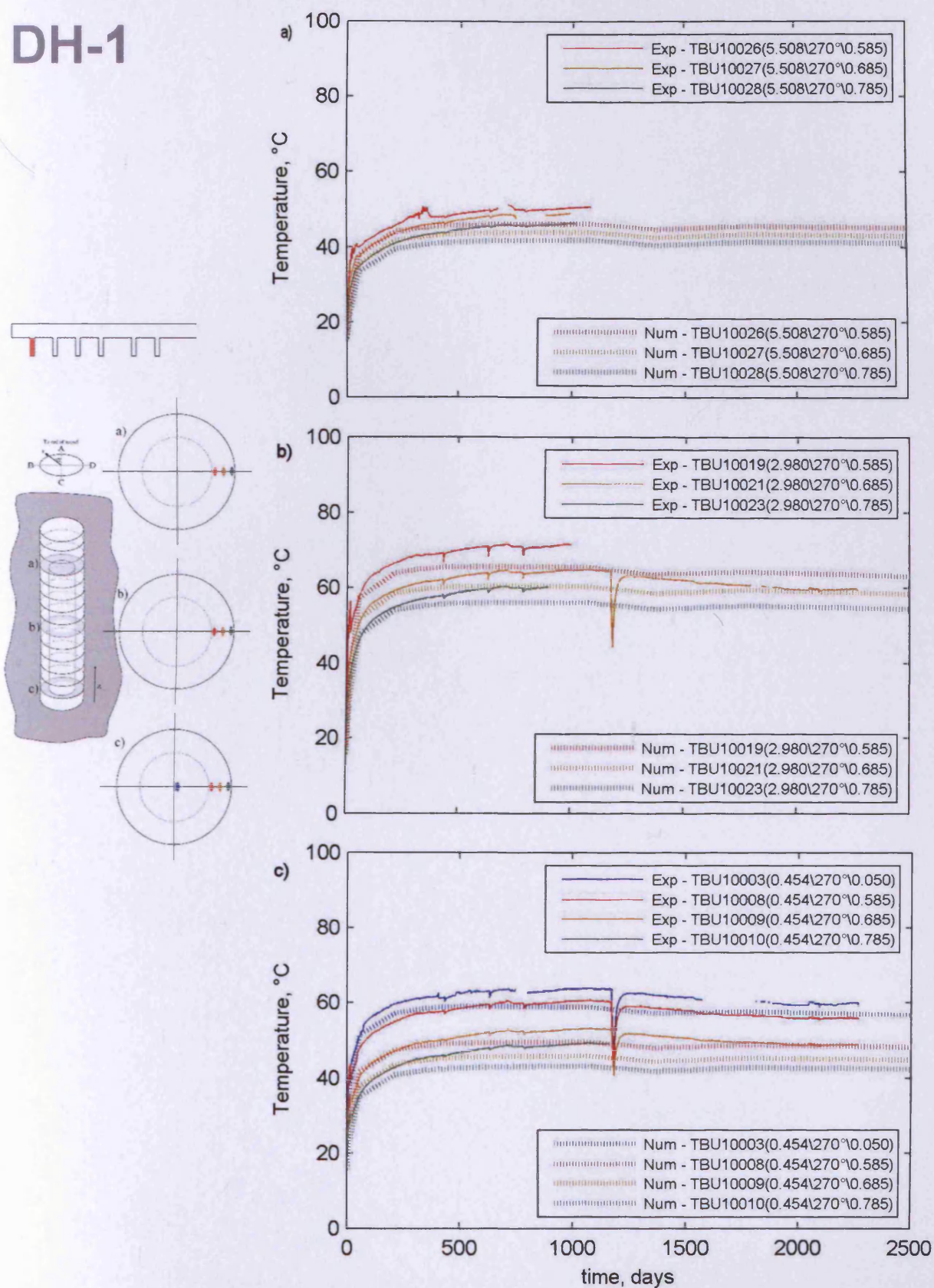
Figure 8.10. Temperature measurements in DH-1 experimental against numerical (1-1-TH2D-F-st) with standard unsaturated hydraulic conductivity relationship, experimental results after Goudarzi and Johannesson (2007).

DH-1
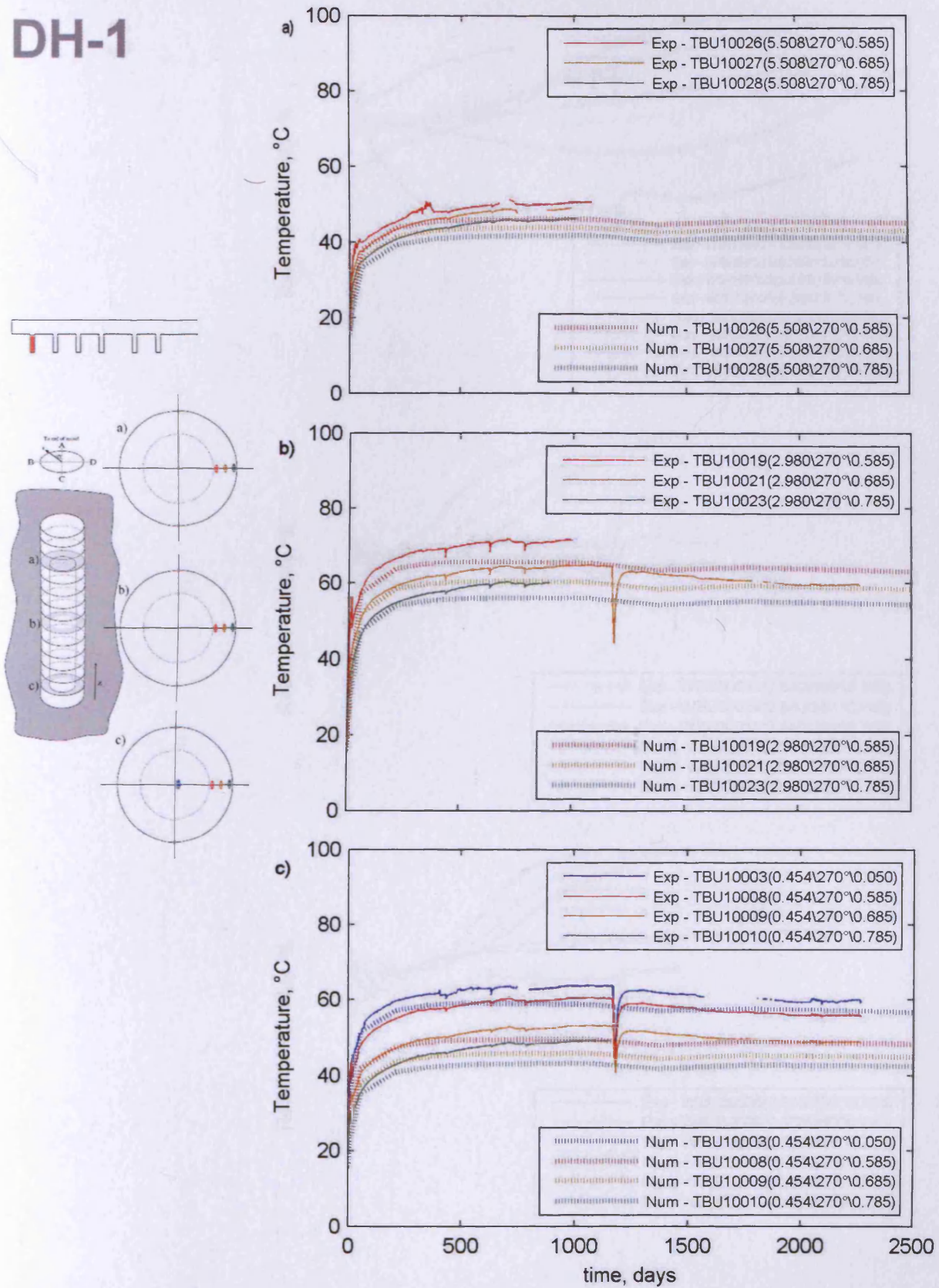
Figure 8.11. Temperature measurements in DH-1 experimental against numerical (1-3-TH2D-F-mod) with modified unsaturated hydraulic conductivity relationship, experimental results after Goudarzi and Johannesson (2007).
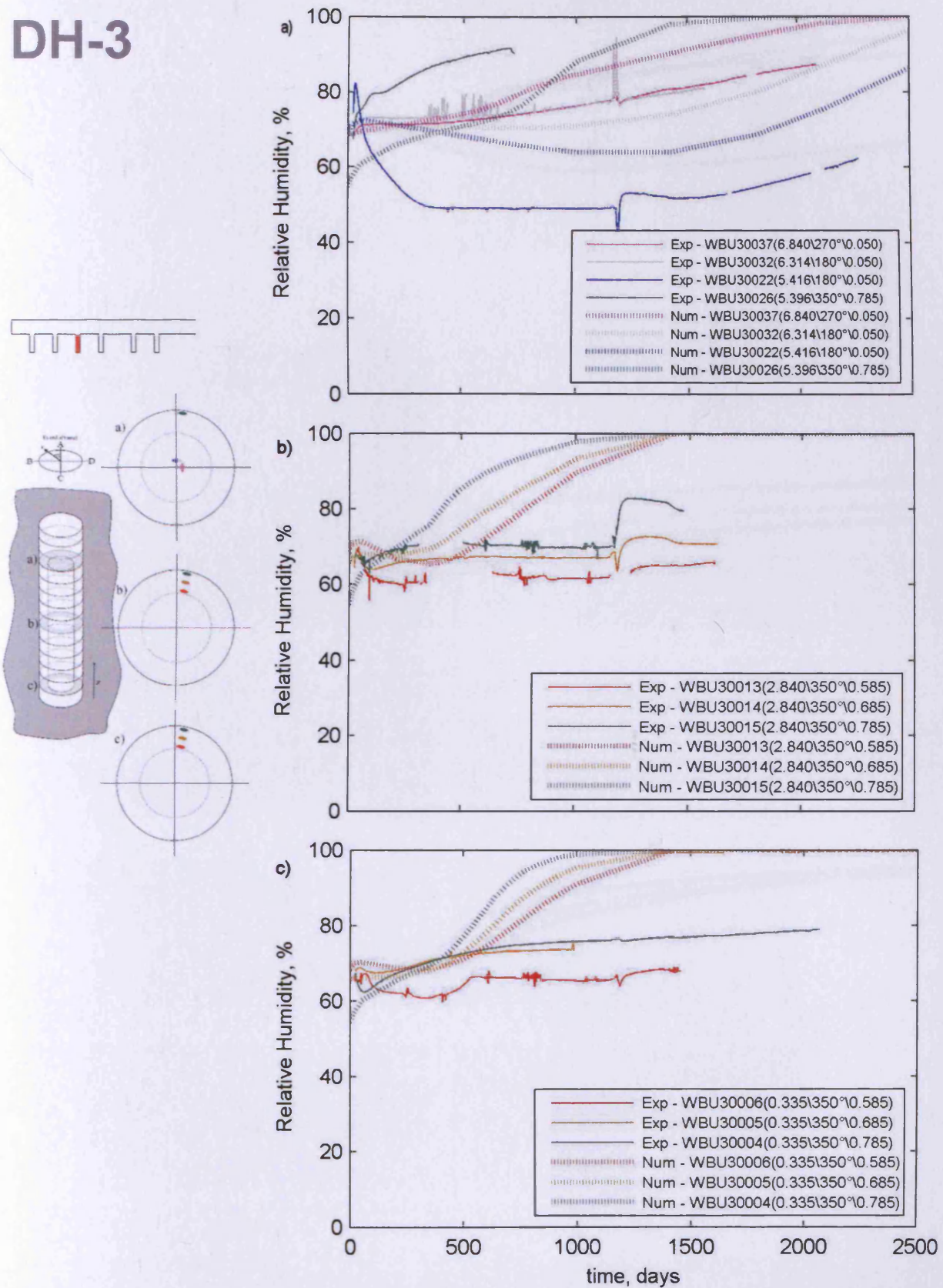
Figure 8.12. Relative Humidity measurements in DH-3 experimental against numerical (1-2-TH2D-UnF-st) with standard unsaturated hydraulic conductivity relationship, experimental results after Goudarzi and Johannesson (2007).

DH-3
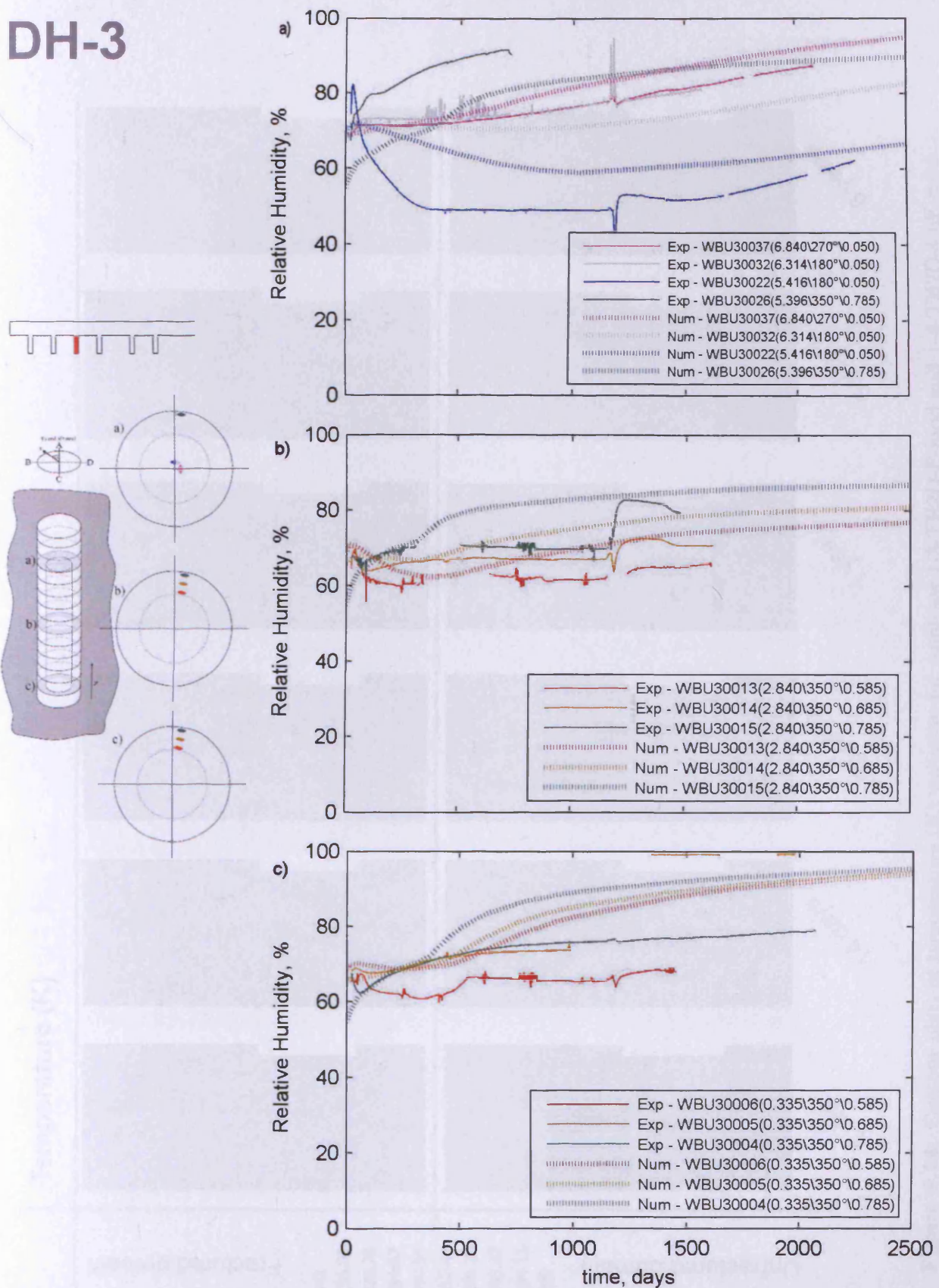
Figure 8.13. Relative Humidity measurements in DH-3 experimental against numerical (1-4-TH2D-UnF-mod) with modified unsaturated hydraulic conductivity relationship, experimental results after Goudarzi and Johannesson (2007).
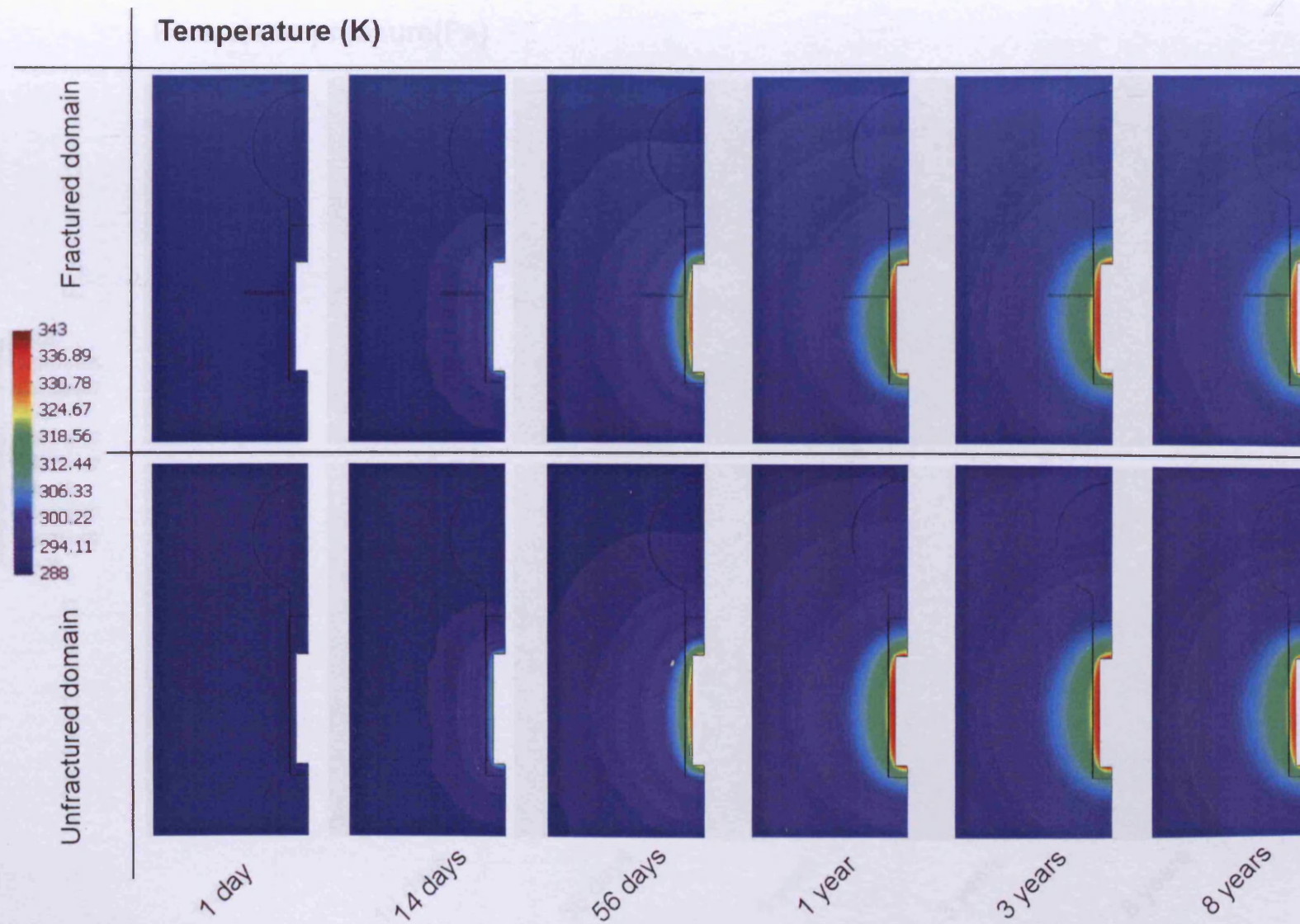
Figure 8.14. Contour plots of temperature (K) variation for Analyses 1-3-TH2D-F-mod and 1-4-TH2D-UnF-mod.

Pore-water pressure(Pa)
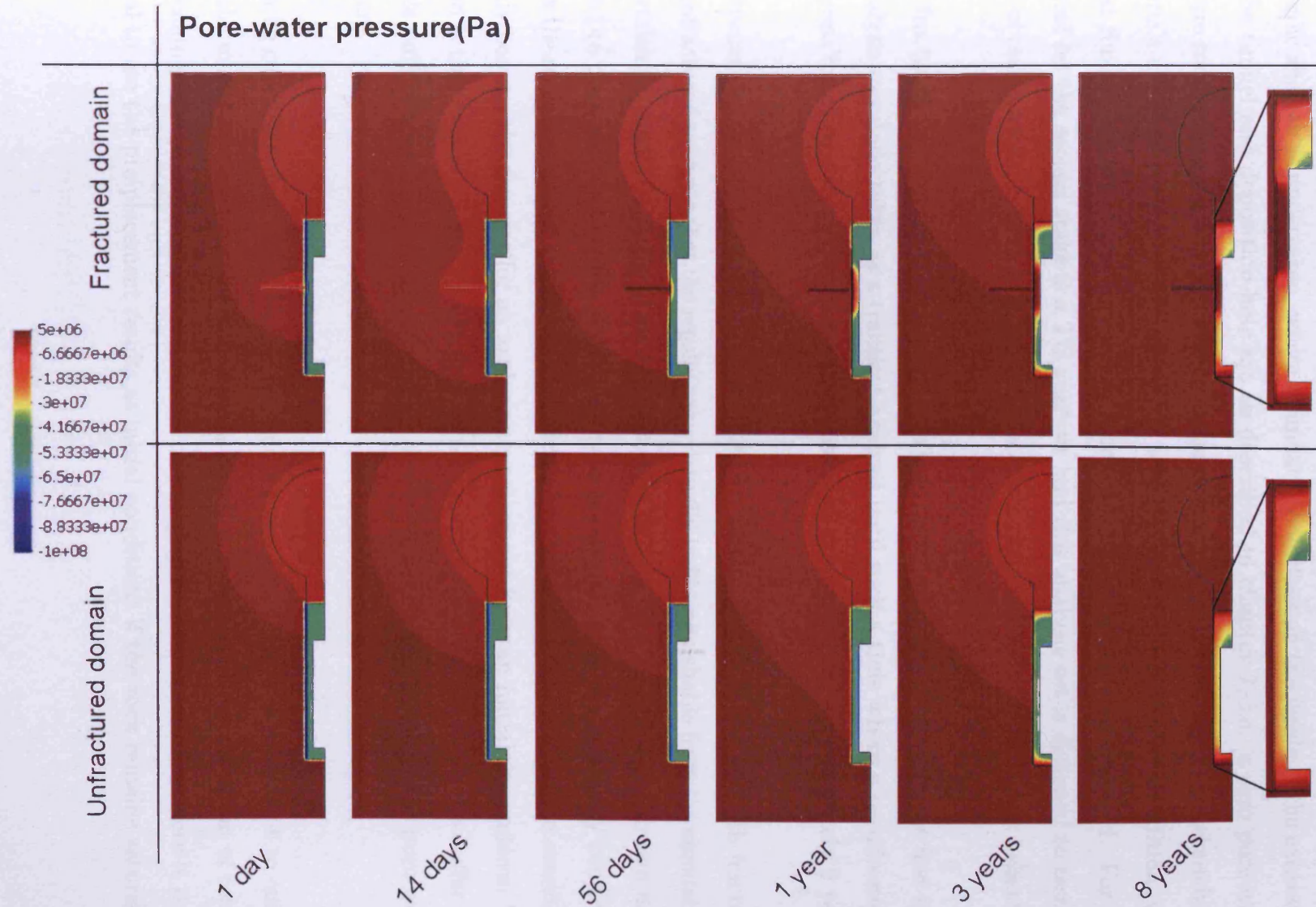
Figure 8.15. Contour plots of pore-water pressure (Pa) variation for Analyses 1-3-TH2D-F-mod and 1-4-TH2D-UnF-mod.

8.8 Results - Analysis Set 2

In this set of analyses, two-stage analyses are undertaken. In the first stage a pre-placement hydraulic analysis is undertaken, where boundary conditions on the inside of the excavation for the tunnel and deposition-hole are as described in chapter 7, i.e. a zero pore-water pressure condition is applied. The second stage of analysis is post-emplacement where buffer materials are included in the domain and a zero-flux hydraulic boundary condition, with a heat flux is applied to the edge of the domain where the canister is placed. For this analysis set the second stage is a TH analysis and this analysis set is designed to test the effect of the hydraulic behaviour in the pre-placement stage on the post-placement behaviour.

Both fractured and unfractured two-stage analyses have been carried out with the first stage of analysis was undertaken as a transient analysis until such a time where a pseudo-steady-state was found to occur. This time, as discussed in chapter 7, was approximately 2 years.

The results have not been presented graphically for brevity. It was found for both fractured and unfractured analyses that the results were virtually indistinguishable from the simulations undertaken in *Analysis Set 1*. This is due to two factors, the first that the drawn down in the pre-placement behaviour, due to the zero pore-water pressure boundary condition, allows the rock to maintain saturation hence transfer pressure quickly, so that the conditions quickly become the same as for an analysis that does not have an initial drawndown. The second is that the initial gradient in pore-water pressure between the bentonite buffer and rock is only changed by approximately 5% due to the reduction in the rock pore-water pressure.

It can be concluded that while the pre-placement stage of modelling is important to ensure that the model proposed for the rock mass is giving a reasonable representation of reality, the results in the post-placement stage show only negligible differences. Therefore it is not critical to use the pre-placement results as initial conditions if the rock remains saturated.

8.9 Results - Analysis Set 3

In *Analysis Set 3* simulations are undertaken of the THM behaviour of single axisymmetric deposition-holes. The same domains as used in *Analysis Set 1 and 2* are used. In addition, as there is a degree of uncertainty of the mechanical behaviour of the pelletised bentonite a brief sensitivity analysis is undertaken. The analyses that have been undertaken are detailed in table 8.9.

Analysis Name	Analysis Type	Fractured/ Unfractured	Hydraulic conductivity relationships	Comments
3-1-THM2D-UnF	2D axi-sym. T-H-M	Unfractured	Modified	
3-2-THM2D-F	2D axi-sym. T-H-M	Fractured	Modified	
3-3-THM2D-UnF-Sens	2D axi-sym. T-H-M	Unfractured	Modified	Sensitivity analysis of the pelletised region.
3-4-THM2D-F-Sens	2D axi-sym. T-H-M	Fractured	Modified	Sensitivity analysis of the pelletised region.

Table 8.9. Analyses undertaken in *Analysis Set 3*.

8.9.1 Numerical conditions

These analyses, as for both *Analysis Set 1 and 2*, were undertaken on a desktop computer for convenience, as they are small scale and therefore execution time was not unduly prohibitive. For a 10 year analysis the number of timesteps varied between 300 and 1,000 dependent upon conditions and whether yield occurred. The execution time depended not only on the number of timesteps but on the numerical stability which was also affected by yielding. However, most simulations were undertaken in approximately 30 minutes with a 1,000 year simulation taking approximately 2.5 hours.

8.9.2   Results

The results for *Analysis set 3* are presented below. The temperature results have been omitted for brevity as no significant difference is found from this analysis set and the first or second. This is due to the main process of heat transfer being conduction and convection which are not largely affected by material deformation in a small strain problem.

The relative humidity results are also largely similar and therefore have not been shown for succinctness. However, an important difference worth noting is that where resaturation occurs faster than in other locations, i.e. near to the location of the fracture, the void ratio increases and consequently more water is required to reach full saturation, therefore at the location of the sensor closest to the canister an increase in time to full saturation is calculated. However, this occurs at about 95% relative humidity when the sensor in question has stopped working, therefore no comparison with experimental data is possible.

The results for net mean stress are presented for the unfractured and fractured domains respectively in figures 8.16 and 8.17. For the unfractured domain, analysis 3-1-THM2D-UnF, the numerical results exhibit a good match, both qualitatively and quantitatively, in comparison to experimental results. The results in the upper section of the buffer are qualitatively good with a slight underestimation especially between 1,000 and 1,500 days before the sensors stop working. The results at mid-height show slightly increased values compared to the experimental results. This is unsurprising, as the calculated resaturation rates and therefore the swelling pressures are slightly higher than the observed behaviour as can be seen in figure 8.12. In the lower section of the buffer the results can be seen to be quantitatively good although there are certain qualitative differences that cannot be easily explained by measured physical processes.

For the fractured domain, analysis 3-2-THM2D-F, the numerical results generally exhibit a reasonable correlation, in all cases reasonable quantitative results are found, however the morphology of the stress results does not always show as close a correlation. This finding was partially expected as the fractured deposition-hole has highly anisotropic resaturation. In addition, the fracture included is highly idealised for the sake of undertaking axisymmetric

analyses. Moreover, some experimental results do not reflect other processes recorded, for example sensors PBU10006 and PBU10007 in the base of buffer exhibit an almost instantaneous stress increase to $6MPa$; this is not reflected in the hydraulic or thermal results as would be expected. It is possible that this stress result to be very local to the sensors where a preferential hydraulic pathway may have been created by the inclusion of the sensors.

It is of interest to note an important qualitative feature in the experimental results that the sensors show a reduction in stress gradient between 4 and $6MPa$ in all locations where this value is reached, possibly suggesting plastic yield. Significantly, when reducing the effective saturated preconsolidation pressure to $5MPa$ in the buffer this feature is observed in the simulation. These results are shown in figure 8.18. It is noted that in this simulation displacements are reduced. This assumption of plastic deformation is supported by the unsmooth lines in the experimental stress sensor results at these locations from the granular material plastic behaviour.

At the mid-section of analysis 3-2-THM2D-F, the fractured analysis, when including the reduction of preconsolidation stress to $5MPa$, the qualitative shape of the stress results, shown in figure 8.18, is well simulated although quantitative differences remain. There are significant gradients in the stress level in the vertical direction due to the anisotropic saturation. Again results that are not reflected in the hydraulic behaviour cannot be simulated. For a similar analysis in the unfractured domain, reducing the effective pre-consolidation stress to $5MPa$, there is little difference in any of the sensors, except a reduction in the final stress of the sensor PBU30002 due to plastic yield and a corresponding reduction in deformation.

By reducing the effective pre-consolidation pressure of the buffer, the stress behaviour is qualitatively better represented, but this does not correlate with the compaction pressure to which the buffer material was exposed, i.e. $100MPa$. However, alternatively if the effective pre-consolidation of the region of bentonite pellets is reduced to $5MPa$ which may represent the collapse of the macro-structure reported by Imbert and Villar (2006) the stress evolution is similar. However, importantly, the deformation behaviour is very different. The deformation in the radial direction is increased over the both previous analyses and the

vertical displacement is reduced in comparison to the previous analysis 3-2-THM2D-F. This is significant in terms of backfill design and performance assessment. Where the buffer and pellets become saturated, the pelletised region and buffer become mostly homogenised in terms of density and void ratio. This is as found experimentally in large scale experiments such as the CRT (THERESA, 2008, cites Johannesson, 2007) where post-mortem analyses have been carried out. This data is shown in figure 8.19 along with numerical sensitivity data from analysis 3-4-THM2D-F-Sens for the coefficient of deformation for a virgin soil, $\lambda(0)$, for the pellets, showing that it is likely that this value lies between 0.4 and 0.6. It is noted that the CRT yielded a high final water content due to the hydration regime, therefore is not completely indicative of the results for this experiment. However, the test set-up of a single deposition-hole is the same in terms of materials and dimensions. By comparison the dry density results for the unfractured analysis is shown in figure 8.20 but do not enter the plastic phase at mid-height so only a single result is shown. The lack of re-hydration of the main buffer blocks consequently means that the stress levels produced do not yield a large degree of homogenisation.

A contour plot of displacements both in the vertical and radial (horizontal) directions, from analyses undertaken with the original effective pre-consolidation stresses, is shown in figure 8.21 for both the fractured and unfractured analyses. The scales are shown along with the figure and it is worth noting that the vertical displacement scale contains values up to 5 times higher than the radial displacement. The qualitative deformations are the same for the subsequent analyses with a reduced effective pre-consolidation stress, but quantitatively lower. Predictably from the hydraulic behaviour, the displacements are greater for the simulation containing a fracture due to increased resaturation. The fracture is seen to clearly cause deformation to the buffer in close proximity with positive vertical deformation above the fracture location in the buffer and negative vertical deformation below. The buffer material is also seen to be deforming, lifting towards the tunnel, although buffer material is not simulated to leave the deposition-hole. The unfractured simulation also exhibits this phenomenon with a lower magnitude. In the radial (horizontal) direction, displacement is seen at the location of the pellets, which is consistent with other experiments which show a homogenisation between the pelletised region and the buffer. Interestingly, at the base of the buffer material negative radial displacement is shown as the buffer saturates and

expands into the pelletised region. However, at the top this deformation does not occur to the same magnitude, most likely as the buffer is not as well restrained vertically at this location.

8.9.3   Summary

Both the temperature and relative humidity results were almost identical to that in the thermo-hydraulic analyses from section 8.7 with slightly increased saturation times closest to the canister due to porosity redistribution.

Deformation and stress results are intrinsically highly coupled to the hydraulic behaviour and reflect the physical behaviour. In all locations the quantitative results are a good match to the experimental results as is generally the qualitative behaviour. There is some definite deviation of the numerical results from the experimental data possibly due to local stress behaviour and anisotropic heterogeneous saturation in the experiment.

It is seen experimentally that where stress values reach approximately $5MPa$ a reduction in the rate of stress development is seen with the cause determined to be plastic deformation. To be consistent with initial compaction it is likely that this occurs in the pelletised region and via sensitivity analysis the coefficient of deformation for a virgin soil for the pellets is investigated. Both stress gradient reduction and homogenisation of density between the pellets and bentonite buffer, as found in post-mortem analyses of other experiments, is found. Significantly, vertical displacement is reduced which may impact upon backfill design criteria and performance assessment.

DH-3
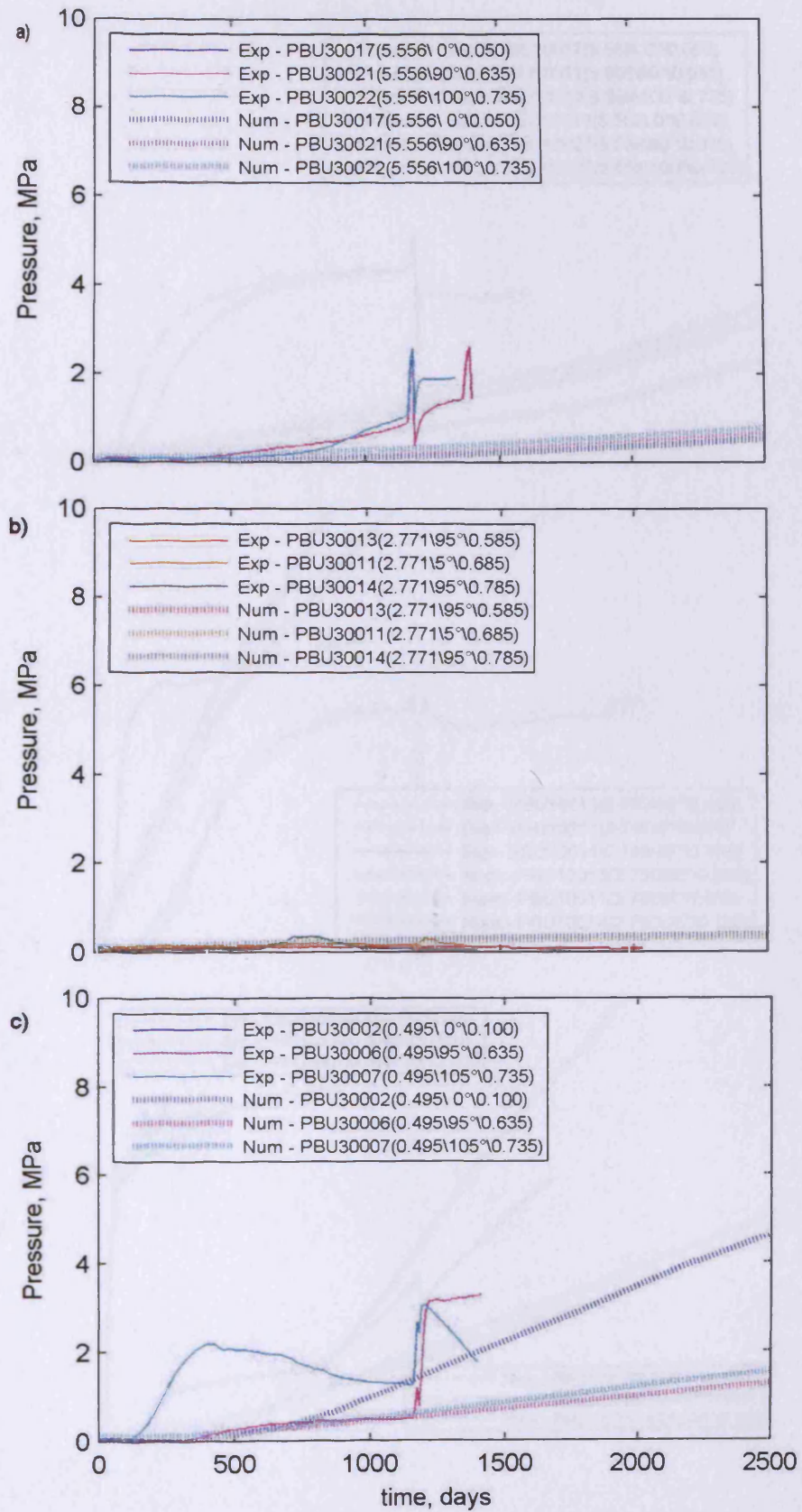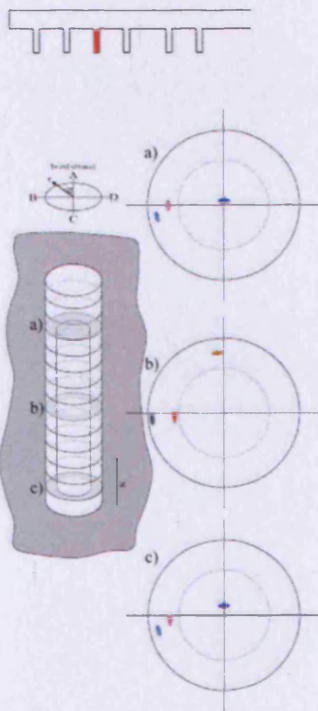
Figure 8.16. Net mean stress measurements in DH-3 experimental against numerical (3-1-THM2D-UnF), experimental results after Goudarzi and Johannesson (2007).
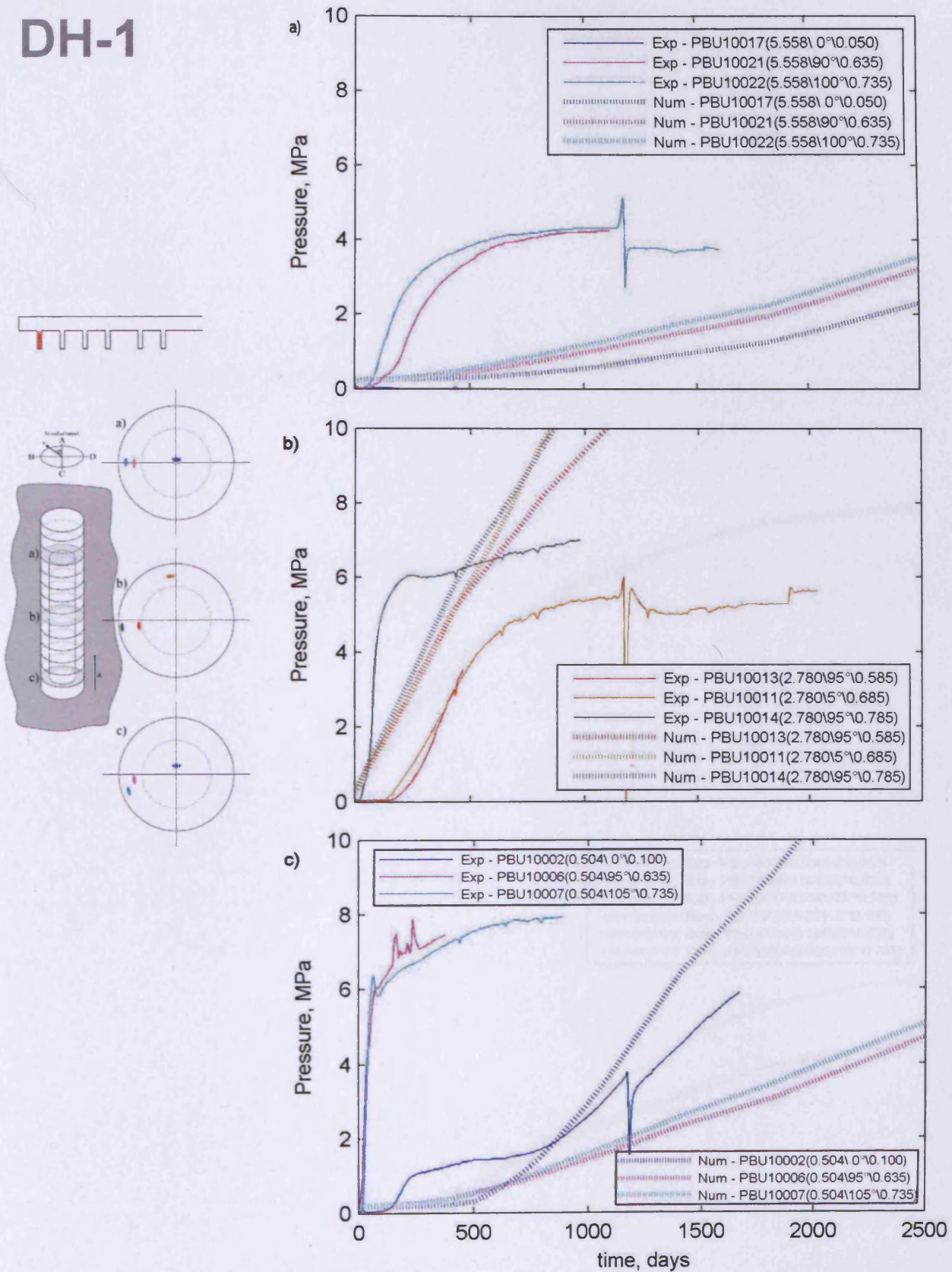
Figure 8.17. Net mean stress measurements in DH-1 experimental against numerical (3-2-THM2D-F), experimental results after Goudarzi and Johannesson (2007).

DH-1
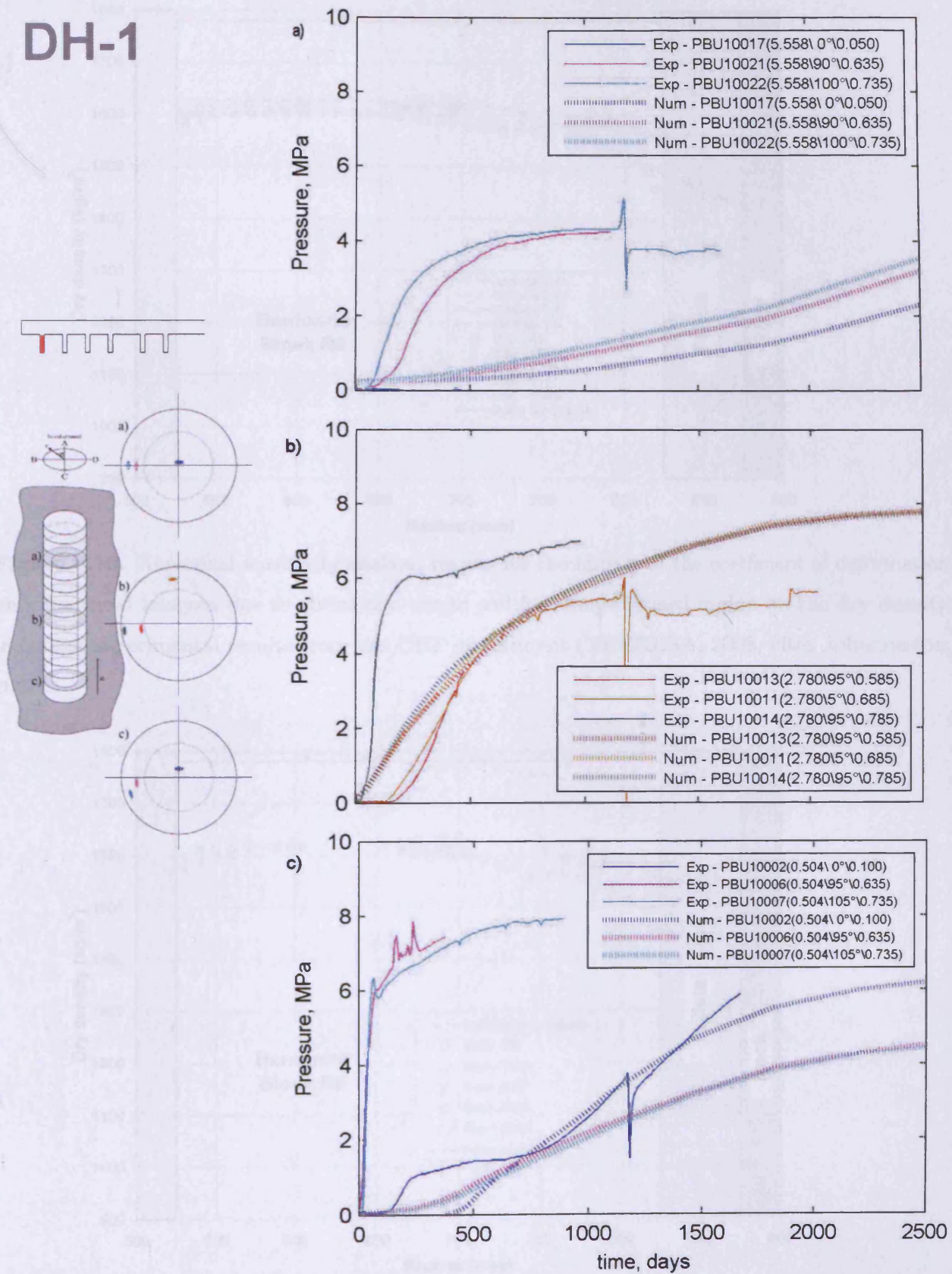
Figure 8.18. Net mean stress measurements in DH-1 experimental against numerical (3-2-THM2D-F) with a reduced pre-consolidation stress, experimental results after Goudarzi and Johannesson (2007).
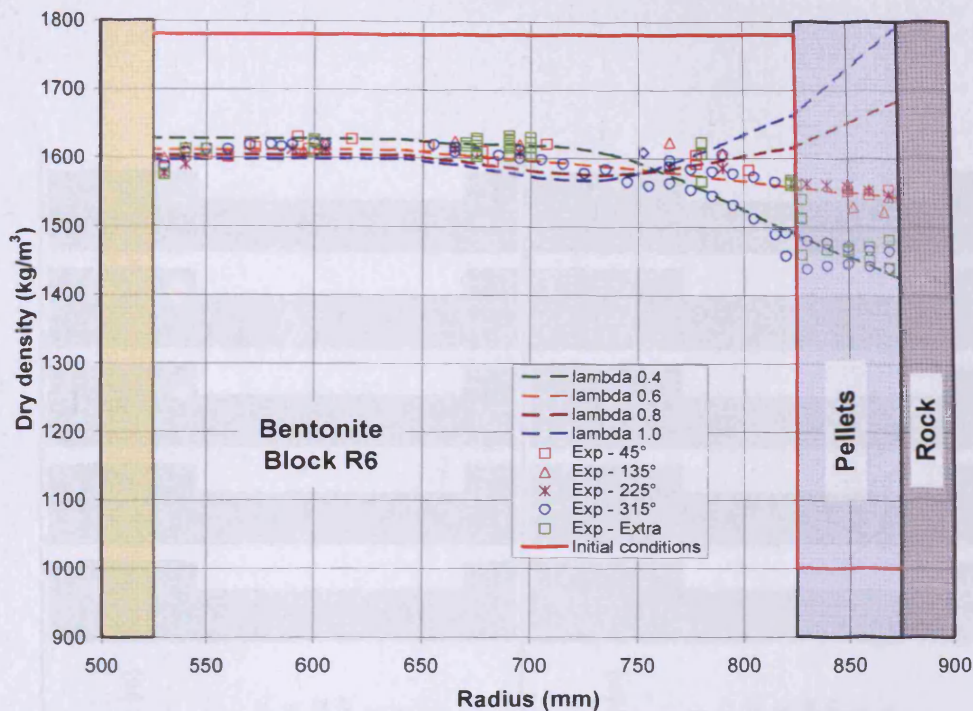
Figure 8.19. Numerical sensitivity analysis results for the impact of the coefficient of deformation on a fractured analysis due to stress of a virgin soil for the pelletised region on the dry density, including experimental results from the CRT experiment (THERESA, 2008, cites Johannesson, 2007).
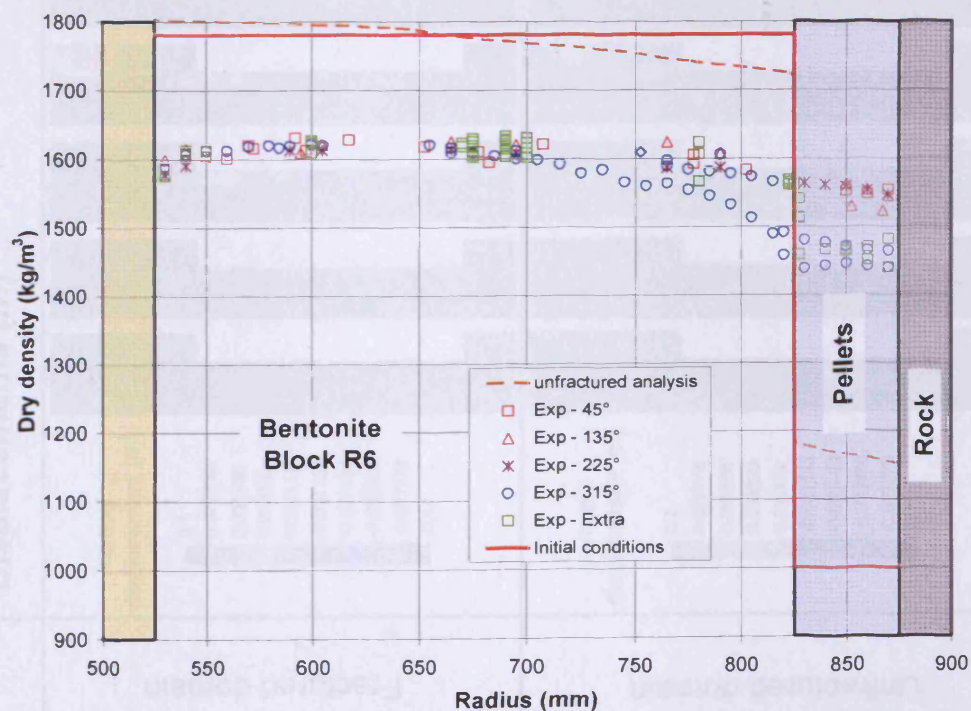
Figure 8.20. Numerical results for the dry density for an unfractured analysis, including experimental results from the CRT experiment (THERESA, 2008, cites Johannesson, 2007).
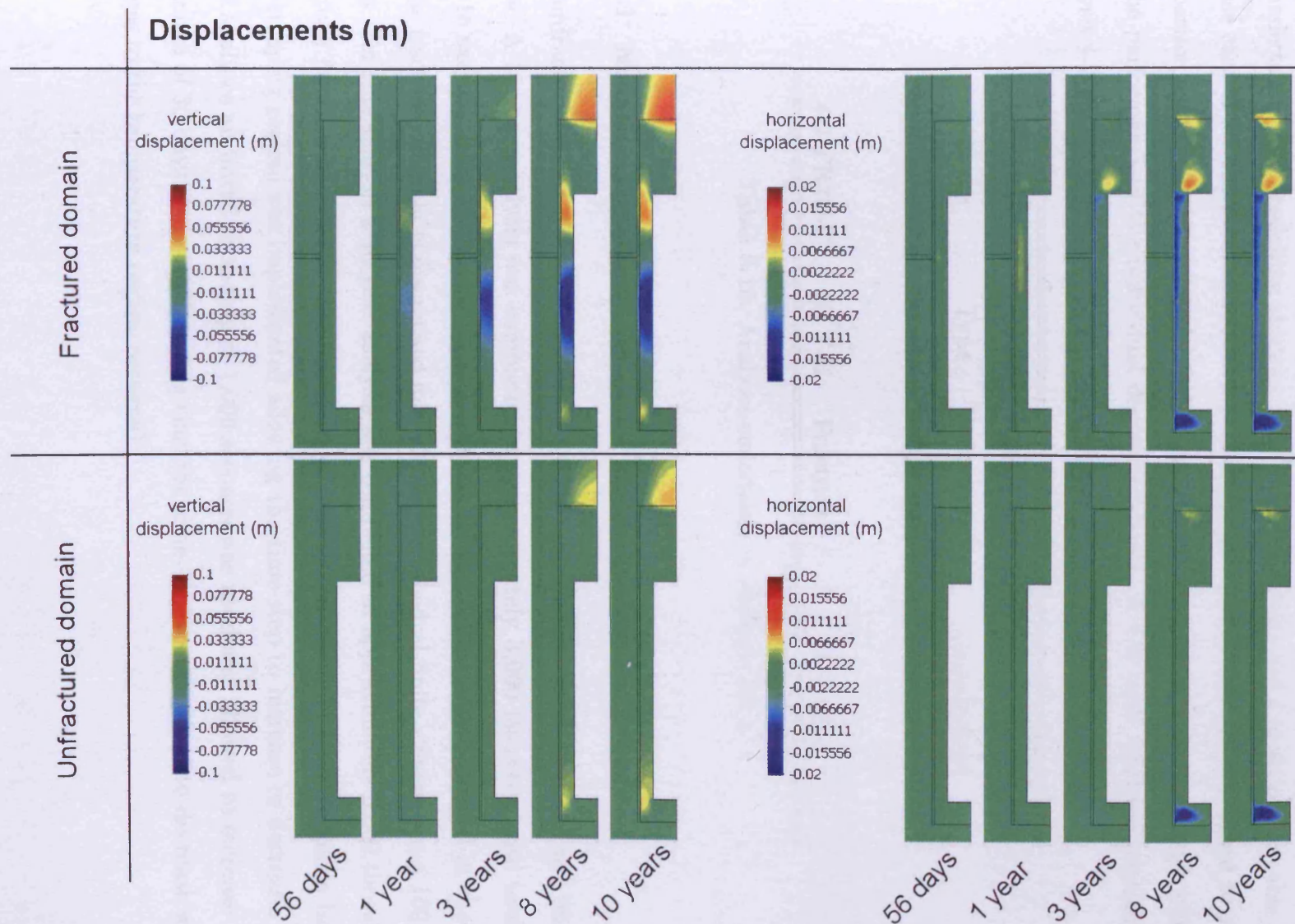
Displacements (m)

Figure 8.21. Contour plots of displacement for Analyses 3-1-THM2D-UnF and 3-2-THM2D-F.

8.10 Results - Analysis Set 4

In *Analysis Set 4* coupled three-dimensional thermo-hydraulic simulations of the whole PRP are undertaken. The modelling strategy followed for *Analysis Set 4* is set out in table 8.10. A base case of an unfractured repository, analysis 4-1-TH3D-UnF, is performed to allow comparison with the fractured model and to investigate the influence of the repository shape on the performance of the individual deposition holes. A full scale fractured simulation, analysis 4-2-TH3D-F, is carried out and compared with experimental data.

Analysis Name	Analysis Type	Fractured/ Unfractured	Hydraulic conductivity relationships
4-1-TH3D-UnF	3D T-H	Unfractured	Modified
4-2-TH3D-F	3D T-H	Fractured	Modified

Table 8.10. Analyses undertaken in *Analysis Set 4*.

8.10.1 Numerical conditions

The unfractured domain is discretised into 551,444 tetrahedral finite-elements and 96,258 nodes. A 10 year analysis was completed in approximately 3,000 timesteps and took 30 days to execute using 16 processors on Merlin, an HPC machine fully described in chapter 4. The fractured domain is discretised into 920,983 tetrahedral finite-elements and 160,273 nodes. For this analysis a 10 year analysis was completed in approximately 3,000 timesteps and took 60 days to execute, also using 16 processors on Merlin. A convergence based time-stepping regime was implemented allowing the time-step to increase or decrease. For these analyses an initial time-step of 1,000 seconds was used and allowed to increase to a maximum of 30 days. It is worth noting that the time-step was required to decrease when changes to the temperature regime occurred.

8.10.2 Results

8.10.2.1 Analysis 4-1-TH3D-UnF

Contour plots of the numerical results of the temperature and pore-water pressure fields for the PRP and surrounding rock of the unfractured analysis, 4-1-TH3D-UnF, can be seen in figures 8.22, 8.23 and 8.24, for the temperature, the pore-water pressure and a detailed view of DH1-4 for the pore-water pressure respectively. A number of key points can be made:

- The regions of increased temperature resulting from the heat output of each of the canisters interact with each other resulting in a single more complex temperature regime. This field is also clearly three-dimensional validating the three-dimensional modelling approach.

- When the heat output of DH-2 is switched-off the hydration rate increases, signifying the importance of temperature driven water-vapour flow.

- Within each deposition hole, drying occurs adjacent to the canister. In particular a locally dry region occurs at the top and bottom of each canister and high spatial gradients exist in these localities.

- The backfill remains unsaturated at the end of the 10 years analysis and seems to dominate the draw-down in the granite rock.

- Qualitatively there is little difference between any of the deposition-holes which have a similar thermal regime, i.e. DH-1, DH-3 and DH-4.

The temperature at the select sensor locations for DH-1 and DH-3 are shown in figures 8.25 and 8.26 respectively. It is noted that the temperature profiles generally match the experimental results very well. The early evolution is similar to that shown in the two-dimensional analyses, but after a few hundred days the underestimation exhibited by the two-dimensional analyses, shown for example in figure 8.10, does not appear and the morphology of the temperature evolution is almost identical to that of the experimental results.

In DH-1 there is a slight over estimation of the temperature at the centre of the buffer immediately below the canister. It is noted that at this location large spatial gradients occur

in the temperature field at this location and the error is within these bounds. For DH-3 the temperatures are underestimated in the lower region of the buffer, where experimentally the highest temperatures are recorded. It is possible that with the low rate of hydration shown experimentally the buffer material is not touching the canister, due to shrinkage, or the buffer has cracked, due to desiccation, either possibility would make the model assumptions of continuity locally invalid. In the temperature results for both deposition-holes a sharp decline is noted at around 1200 days due to the power to all the canisters being switched off and then all but DH-2 being switched back on. This decline is greater than that seen in the two-dimensional analyses as the effect of DH-2 is included.

The relative humidity results for DH-1 and DH-3 are shown in figures 8.27 and 8.28 respectively. In DH-1 the numerical simulation results compare well with the experimental results in the upper and lower sections of the buffer both qualitatively and quantitatively. There is a discrepancy in sensor WBU10028 at times before approximately 750 days where initially the rate of saturation is much lower than that shown experimentally. This is likely to be due to the influence of the pelletised region as this sensor is immediately adjacent to this region. It is possible that in reality the pelletised region allows more moisture through in the early stages than numerically calculated due to the existence of inter-pellet pores which are formed at the time of installation, therefore not easily quantifiable and highly heterogeneous. It is also the sensors closest to the rock that are likely to be most affected by the presence of any preferential pathways from the installation of the buffer and sensor connectors. However, in the longer term this sensor matches the experimental data well in both the gradient and quantity. The final dip in relative humidity is due to a moisture redistribution in the buffer due to a reduced temperature gradient, therefore a reduction in water-vapour transport. The process at this location is particularly complex with the geological supply/bentonite hydraulic conductivity, both pellets and blocks/temperature induced vapour transport all playing important roles.

The relative humidities in the lower region converge to an almost identical value due to a combination of effects. The first is the direction of hydration which is two-dimensional, from both the side of the buffer and through the base. The second is the reduced effect of vapour transport due to a lower temperature gradient, approximately $10K$ less than at the

mid-height and greater volume of bentonite for the vapour to move through/condense in, due to the location near the canister corner.

The mid-height region, where a minor fracture is hypothesised to intersect, shows a much reduced initial re-saturation rate, compared to experimental results. The general trend is of slow re-saturation although many times slower than shown experimentally with the relative humidity after 10 years being between 80 and 92%.

In DH-3 the buffer simulation in the upper region also matches the experimental results reasonably, especially considering the long term gradients. Significantly the drying and subsequent re-hydration shown by sensor WBU30022 is well simulated, with the exception of a very early increase in relative humidity, most likely due to a water-vapour front. Again the sensor located closest to the pellets experimentally shows more early hydration than is simulated, although the subsequent gradients are similar. The long term behaviour cannot be compared, however, as the sensor has stopped working. The mid-height results show reasonable correlation with the experimental results and are lower than that simulated by DH-1 due to location in the repository. The lower regions of the buffer show similar simulated results to DH-1 which are higher than that shown experimentally in DH-3.
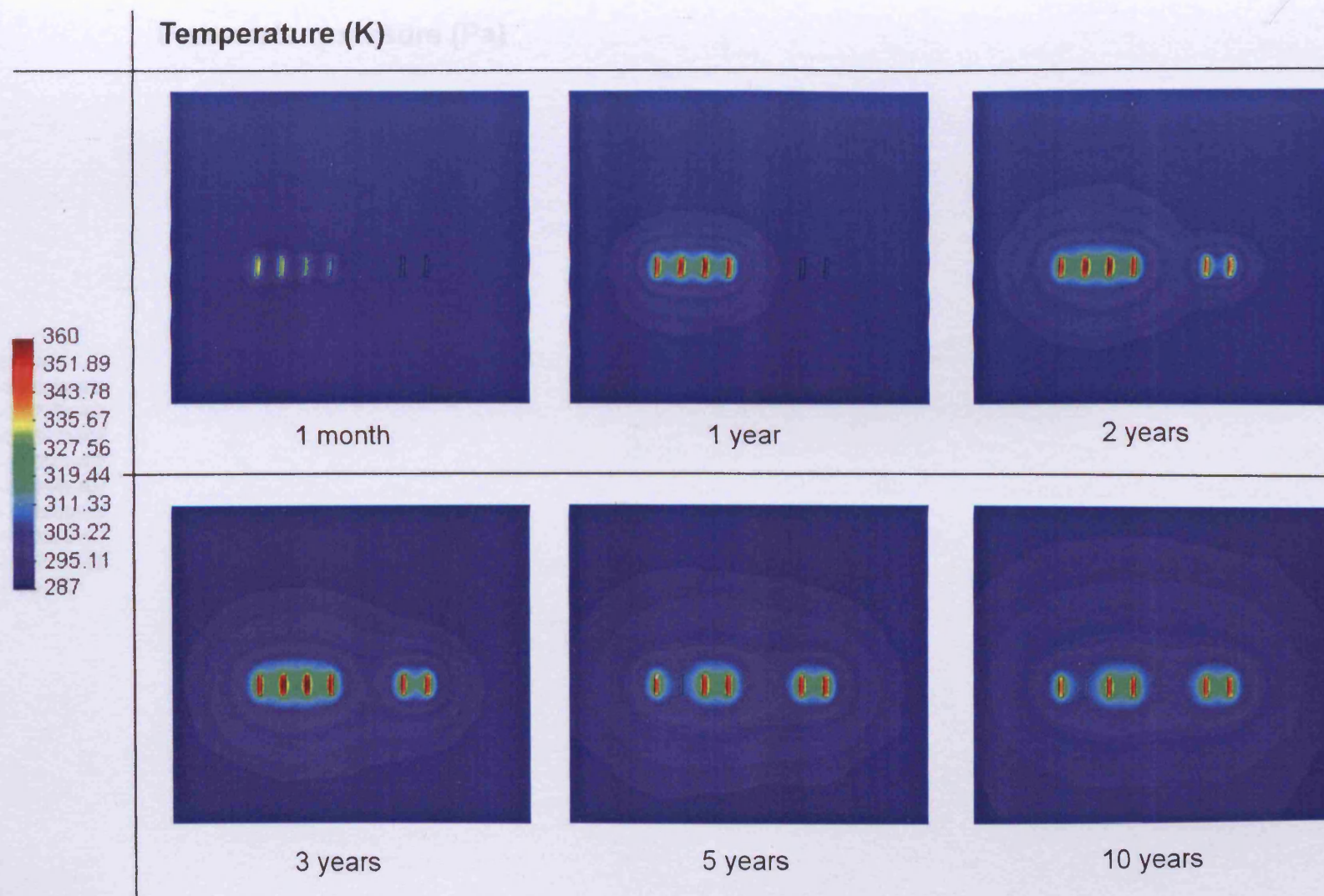
Temperature (K)

Figure 8.22. Contour plots of temperature for Analysis 4-1-TH3D-UnF.

Pore-water pressure (Pa)
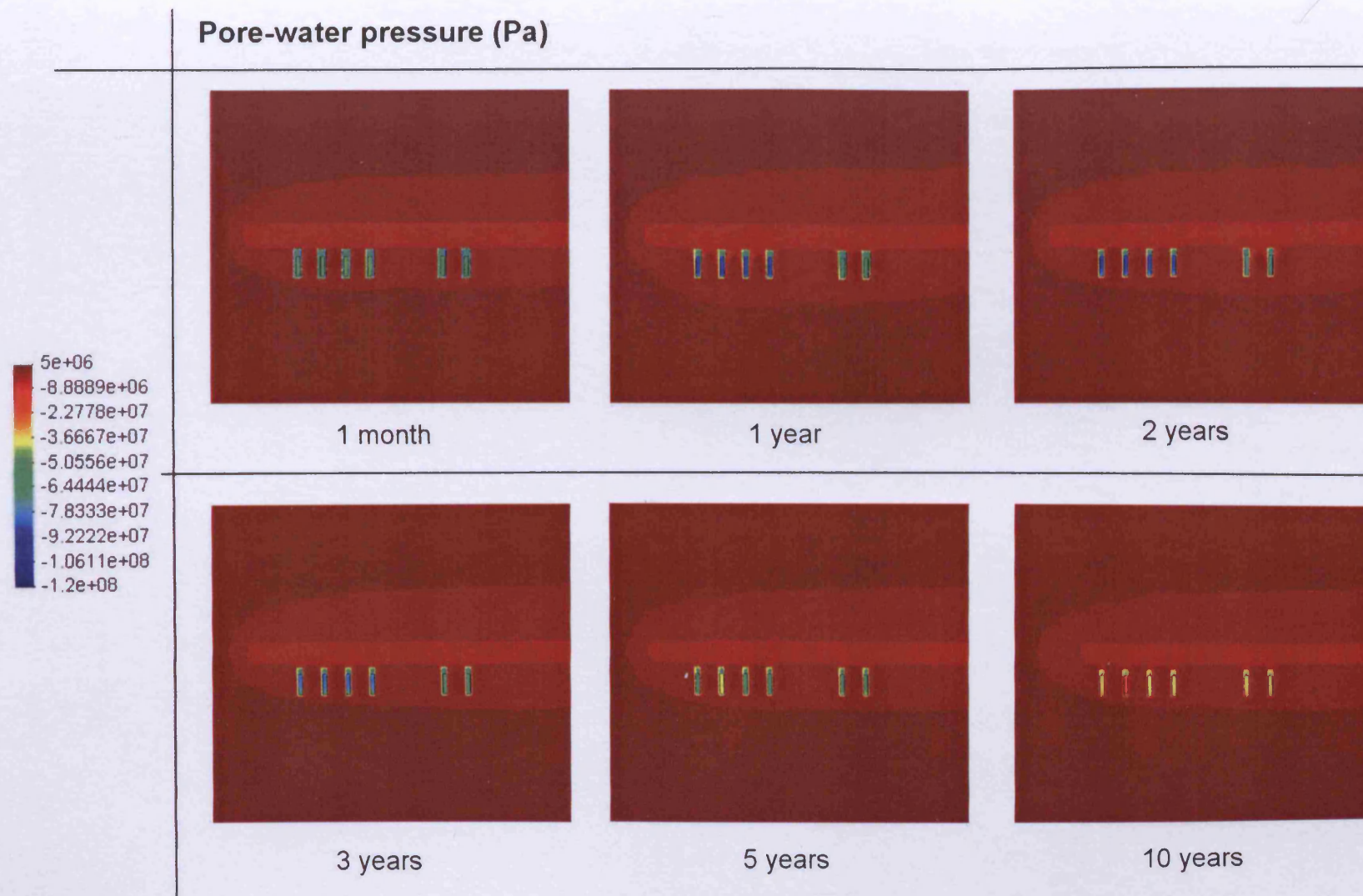
Figure 8.23. Contour plots of pore-water pressure for Analysis 4-1-TH3D-UnF.

Pore-water pressure (Pa)
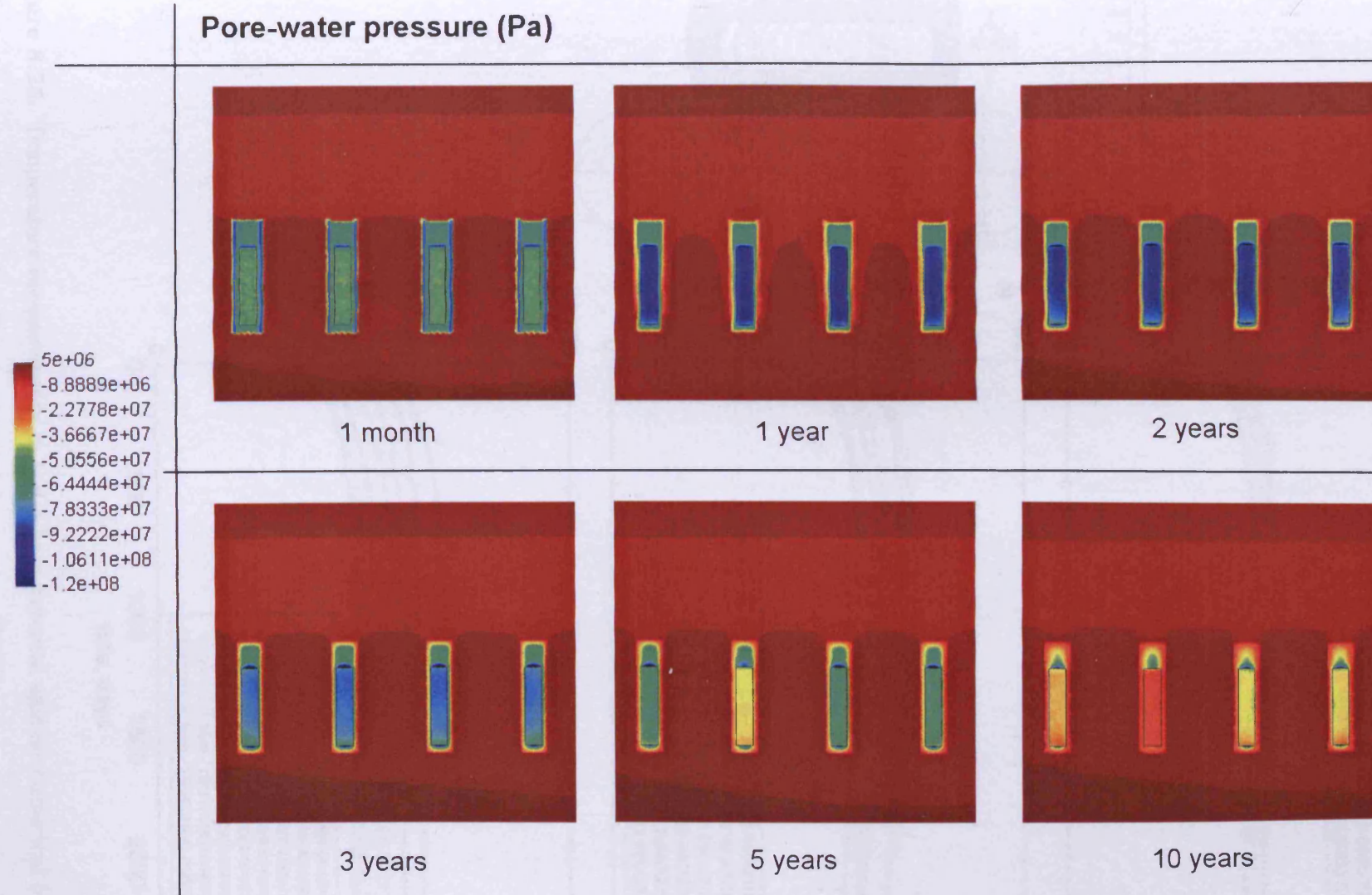
**Figure 8.24.** Contour plots of pore-water pressure of DH-1 to DH-4 for Analysis 4-1-TH3D-UnF.
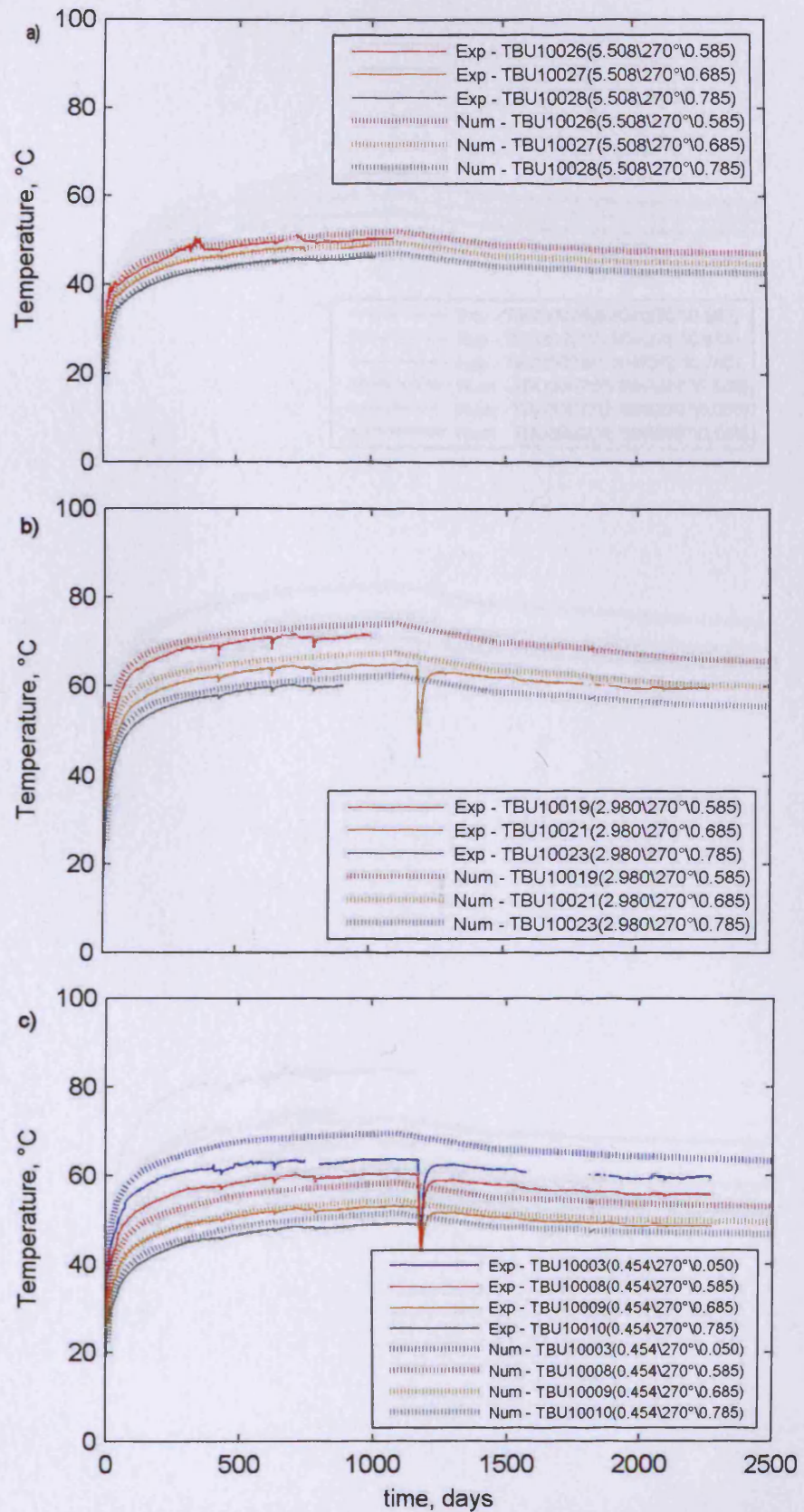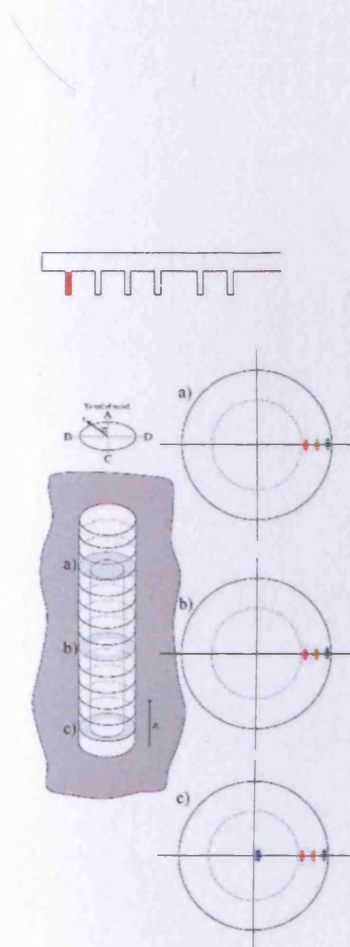
Figure 8.25. Temperature measurements in DH-1 experimental against numerical (4-1-TH3D-unF), experimental results after Goudarzi and Johannesson (2007).

DH-3
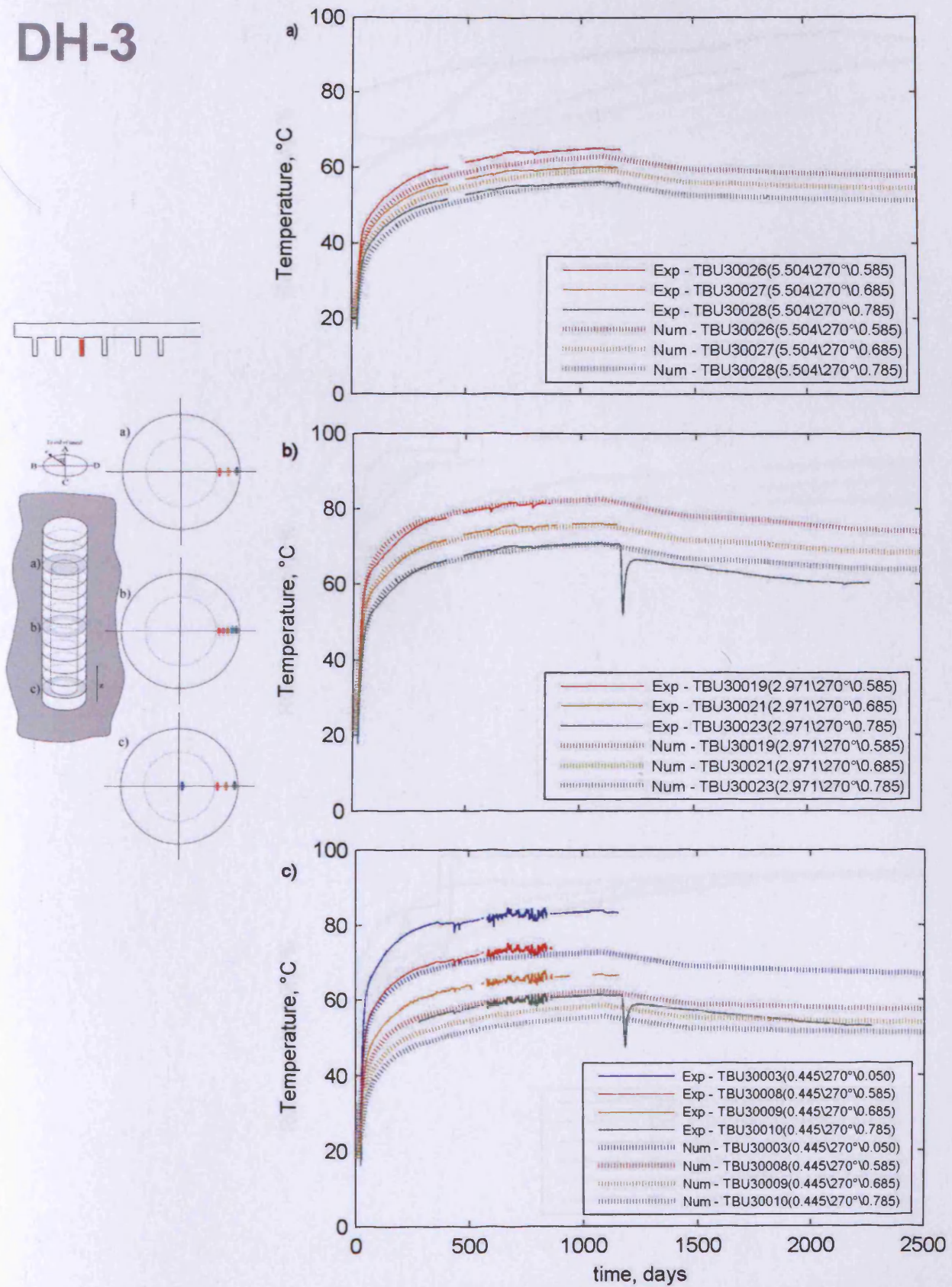
Figure 8.26. Temperature measurements in DH-3 experimental against numerical (4-1-TH3D-unF), experimental results after Goudarzi and Johannesson (2007).
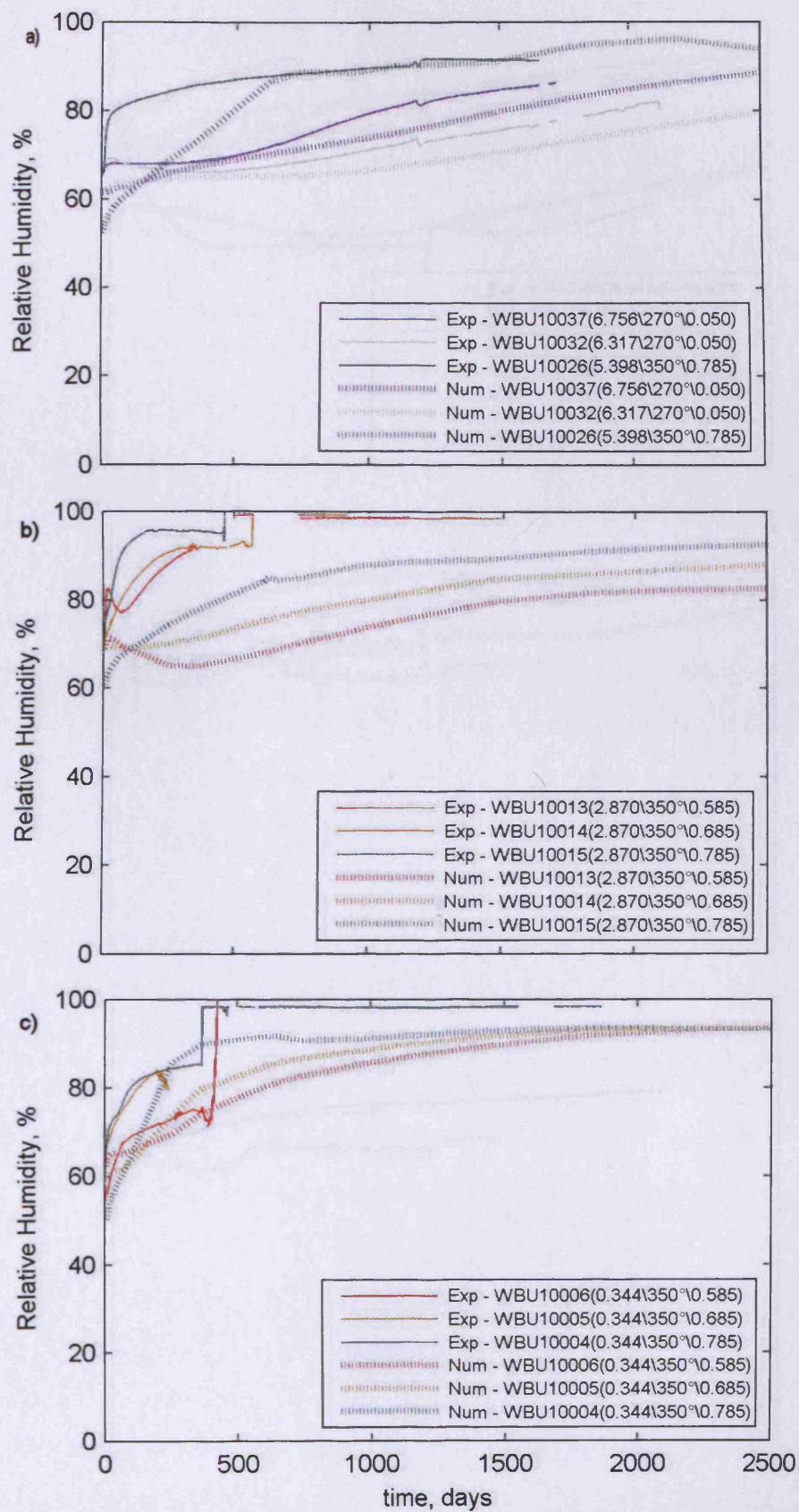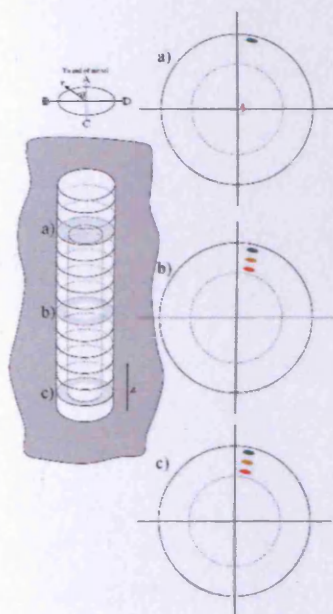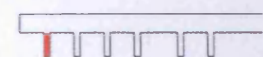
Figure 8.27. Relative Humidity measurements in DH-1 experimental against numerical (4-2-TH3D-UnF), experimental results after Goudarzi and Johannesson (2007).
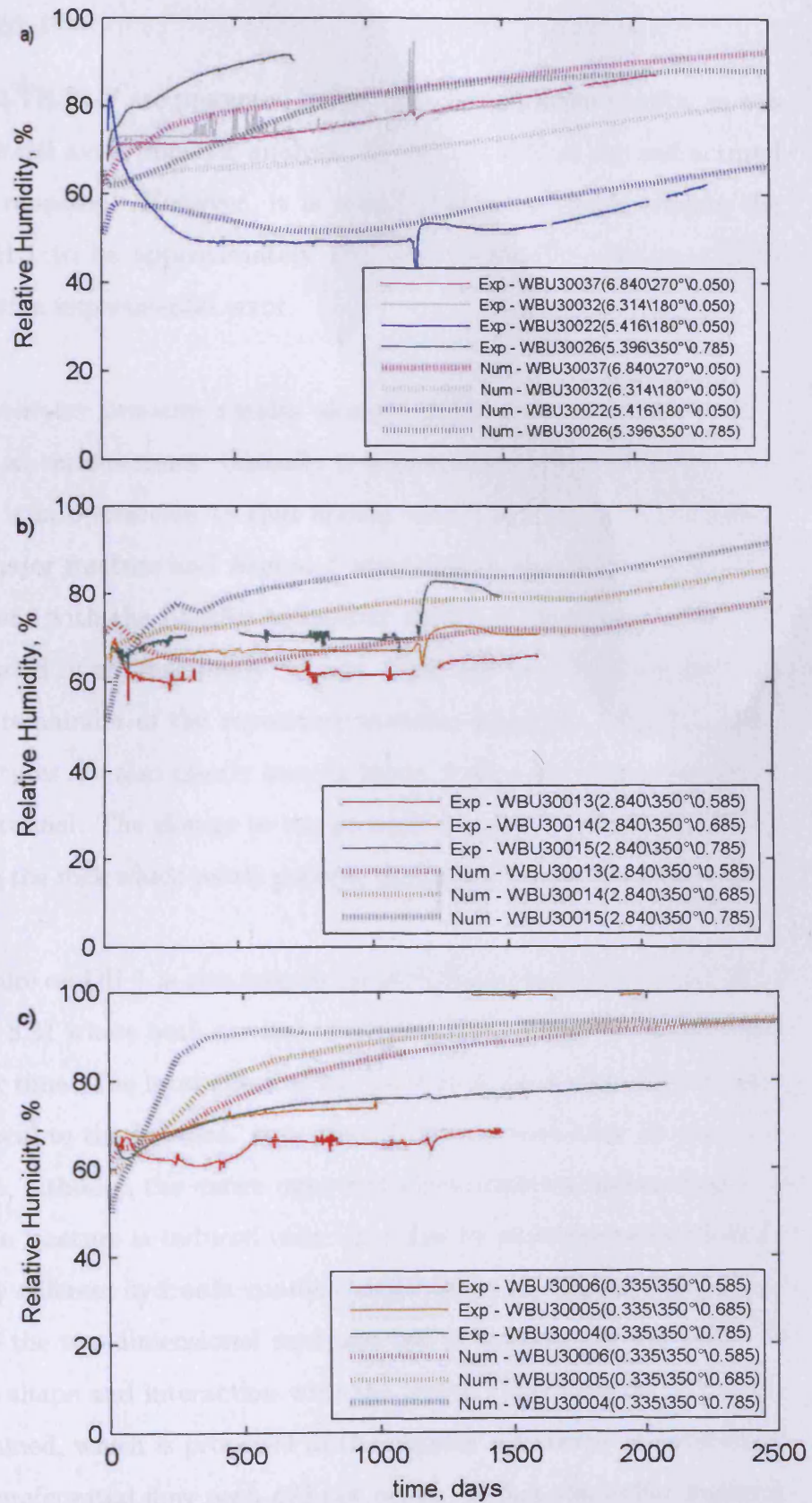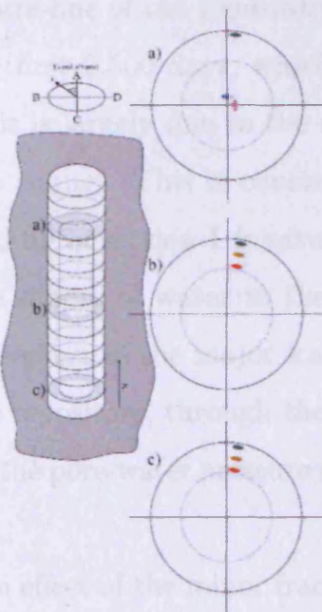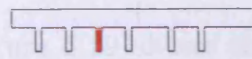
Figure 8.28. Relative Humidity measurements in DH-3 experimental against numerical (4-2-TH3D-UnF), experimental results after Goudarzi and Johannesson (2007).

8.10.2.2   Analysis 4-2-TH3D-F

The results from analysis 4-2-TH3D-F are presented below. The temperature results, as was the case for the two-dimensional axi-symmetric analysis, are within $1°C$ of the unfractured analysis so have not been repeated. However, it is noted that the fracture causes the mid-height results from DH-1 to be approximately $1°C$ lower which is consistent with experimental results but within experimental error.

Figure 8.29 shows the pore-water pressure results along a vertical section through the centre-line of the repository at various times. Globally it is seen that backfill saturates over the first 2,500 days, which is in opposition to that shown with the unfractured analysis. This is largely due to the major fracture and *Region 1* identified in chapter 7 intersecting the tunnel. This is consistent with the backfill behaviour shown in chapter 6 where the backfill in section 1 is saturated in approximately 7 years. This will have a major effect on the supply of water to the remainder of the repository system, especially after this time. The effect of the major fractures are also clearly seen in figure 8.30, a horizontal section of the repository, through the tunnel. The change in the geological water supply has an effect on the pore-water pressure in the rock which partly governs the resaturation rate of the buffer.

The effect of the minor fracture on DH-1 is also seen in figure 8.29 and both DH-1 and DH-3 are shown in detail in figure 8.31 where both vertical and horizontal sections show the pore-water pressure variation over time. The local effect of the fracture is clear with re-saturation occurring at a higher rate local to the fracture. It is noted however, that after 10 years the local effect is less noticeable, although the entire deposition-hole shows a higher degree of saturation. The effect of the fracture is reduced over time due to moisture redistribution occurring due to the spatially different hydraulic conductivities due to macro/micro-structure changes. In this case, unlike the two-dimensional analyses, full saturation was not achieved due to the assumed fracture shape and interaction with the buffer. Therefore the hydraulic conductivity was not maintained, which is proposed in the chapter 5 to occur at saturation, and therefore a permanent preferential flow path did not occur. In fact the buffer material in this area swelled and the hydraulic conductivity reduced over time creating an area of lower hydraulic conductivity. For a non-isotropically saturating material, higher flow-rates

will initially cause higher hydraulic conductivities but depending upon the exact flow regime the bentonite may either swell causing micro-structural choking or if saturation is reached at an early stage, cause preferential flow. However, more experimentation is required to confirm this numerically predicted behaviour. Additionally, if saturation is reached from the buffer/rock interface to the buffer/canister interface no vapour will be able to flow. However, should this not occur diffusive moisture-vapour transport due to the thermal gradient will occur and as the hydraulic conductivity reduces, due to micro/macro-structure effects, a moisture redistribution in the buffer is likely. The pelletised material also is numerically considered to reduce in hydraulic conductivity as re-saturation occurs. It is possible that preferential pathways may form due to the flow of water and influenced by the strongly heterogeneous pore structure. Additionally, if boundary conditions develop, such as a reduction in temperature fluxes as found here, and the material is anisotropically saturated the hydraulic conductivity may be a function of previous saturation, current saturation, time and pore-pressure gradient which may create unpredictable results, especially at high degrees of saturation where the hydraulic conductivity can vary the most.

The relative humidity results for DH-1 ad DH-3 are shown in figures 8.32 and 8.33 respectively. In figure 8.32, for DH-1, it is seen that in all locations the numerical results simulate the experimental results reasonably. In the upper section the simulation output in the location of the sensors WBU10037 and WBU10032 match the experimental results in both quantity and gradient throughout. Some deviation is shown in sensor WBU10026 in the upper section of the buffer at $0.785m$ radius from the centre of the deposition-hole, adjacent to the pellets. As discussed for analysis 4-1-TH3D-UnF, this is possibly due to the initial conditions and initial availability of water due to the installation process, moreover it is possible that the effect of the fracture as implemented within the simulation is to direct water away from this location initially, and that a more complex fracture network exists. However, the rate of re-saturation after the first approximately 300 days is almost identical to that exhibited experimentally. In the mid-section the numerical results match the experimental results well. It is noted that the effect of the fracture seen in the contour plots creates a large spatial gradient and the results are therefore sensitive to the exact sensor location and subtleties of the fracture - deposition-hole interaction. A possibly significant difference is that the inner-most sensor location, sensor WBU10013 at $0.585m$ radius, does not saturate

as much as is shown experimentally and therefore allows vapour transport to continue. It is not clear if this location is saturated experimentally as the sensor has stopped working. In the two-dimensional analyses this location was shown to saturate although the fracture geometry was further idealised and the backfill behaviour and major fracture interaction was not able to be considered. In the lower section of the buffer, the behaviour is well simulated when compared to experimental results for the first 500 days. After this time, as previously discussed in section 8.7.2, a large instantaneous increase in relative humidity is shown experimentally indicating sensor failure. Therefore, it is impossible to assess the behaviour beyond this point. In addition, the sensor closest to the pellets shows a slightly lower re-saturation than the experimental results. This perhaps indicates that the water is being directed away from this location by the fracture initially, and that the water supply by the fracture is not as great as occurs in reality. This could suggest that this fracture has a connectivity greater than suggested by the proposed fracture model. Significant for long term simulations the gradients of re-saturation shown in the simulations are almost identical to that shown by all the sensors experimentally when they fail or at the current final recording.

In figure 8.33, for DH-3, the results are much improved over the previous analyses. The upper section matches experimental results well, with again underestimation in the sensor closest the pelletised region. The gradients and approximate magnitudes shown in sensors WBU30037 and WBU30032 are reasonable, although the numerical results show that sensor WBU30037 has a higher relative humidity in fitting with the location further away from the canister and closer to a hydrating surface. In the mid-height the results are significantly improved with only a slight overestimation of the re-hydration. The final gradients shown experimentally are also matched well in the simulation. This location is also affected greatly by the change in temperature and flux and backfill re-saturation is the time period 1,700-2,200 showing an increase in hydration. This cannot be confirmed experimentally as the appropriate sensors have already failed. However, this behaviour is in fitting with the conceptual hydraulic conductivity model as significant micro-structural change would not have occured due to low re-saturation. In the base of the buffer section the numerical results are not improved. It is likely that the model does not reflect some aspect of reality, possibly local lower permeability rock, or water is transferred elsewhere by fractures that have not been identified. This overestimation of hydration is likely to have some impact of

the numerical underestimation of the temperature results in this location.

8.10.3 Summary

A number of key points have been found in this set of analyses and these are listed below:

- The behaviour of the repository is inherently three-dimensional.

- The thermal results are well simulated and inherently three-dimensional.

- The fractured model behaves significantly better in comparison with the unfractured model considering the hydraulic results.

- Behaviour of both major and minor fractures is important and while the proposed model captures a number of key behaviours of the PRP, some are not captured and a significantly more complex fracture model may be required.

- Behaviour of the backfill as a water sink is possibly significant.

- Pelletised region requires more experimental evidence to allow good simulation of the behaviour of the pellets and the buffer in close proximity to the pelletised region.

- The initial availability of water due to the installation process could be investigated more fully to capture some initial uncertainty.

- More complex fracture networks in close proximity to the deposition-holes, especially if intersecting more important fracture, may have an important effect.
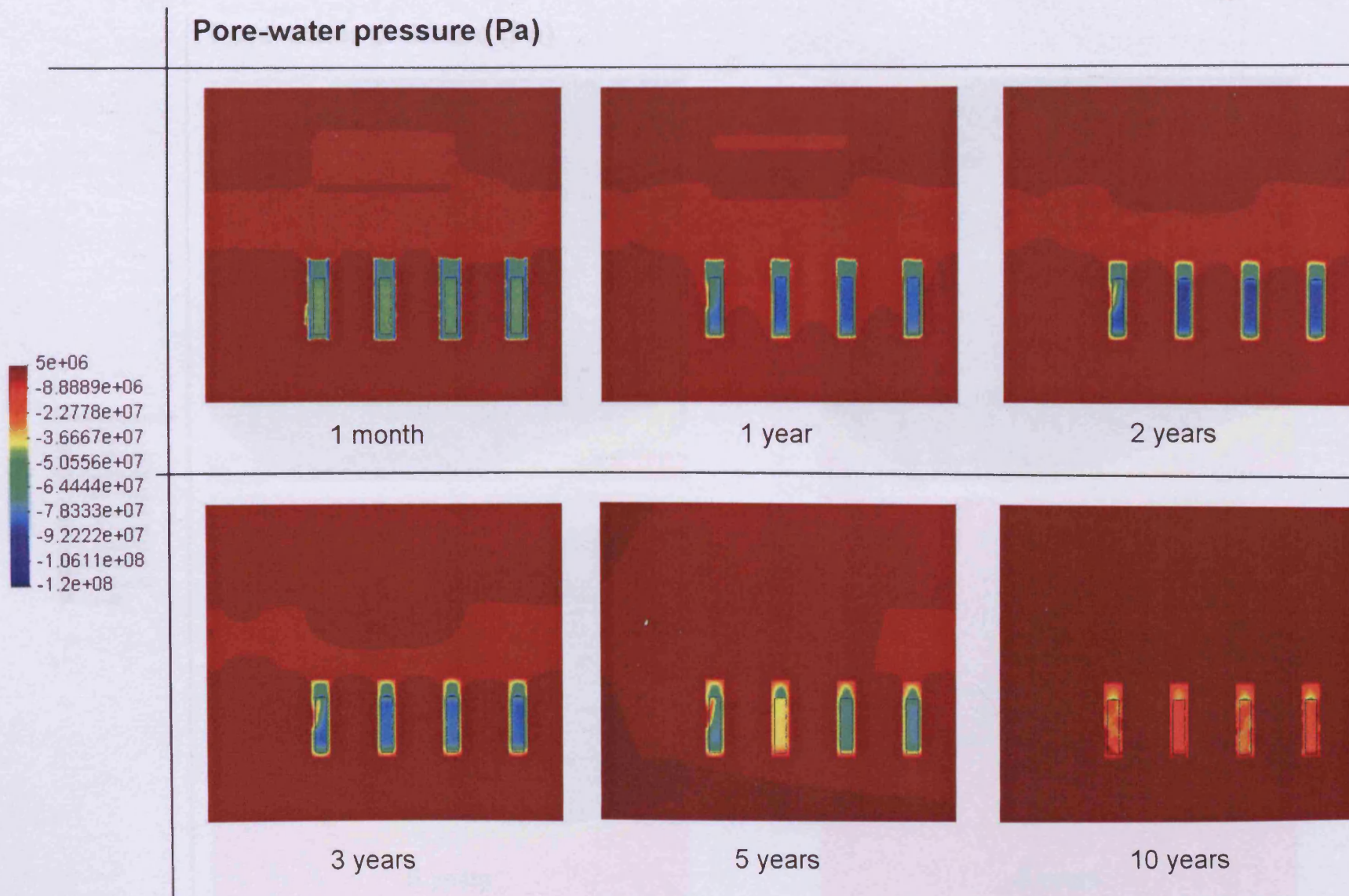
Figure 8.29. Contour plots in section along repository of pore-water pressure for Analysis 4-2-TH3D-F.
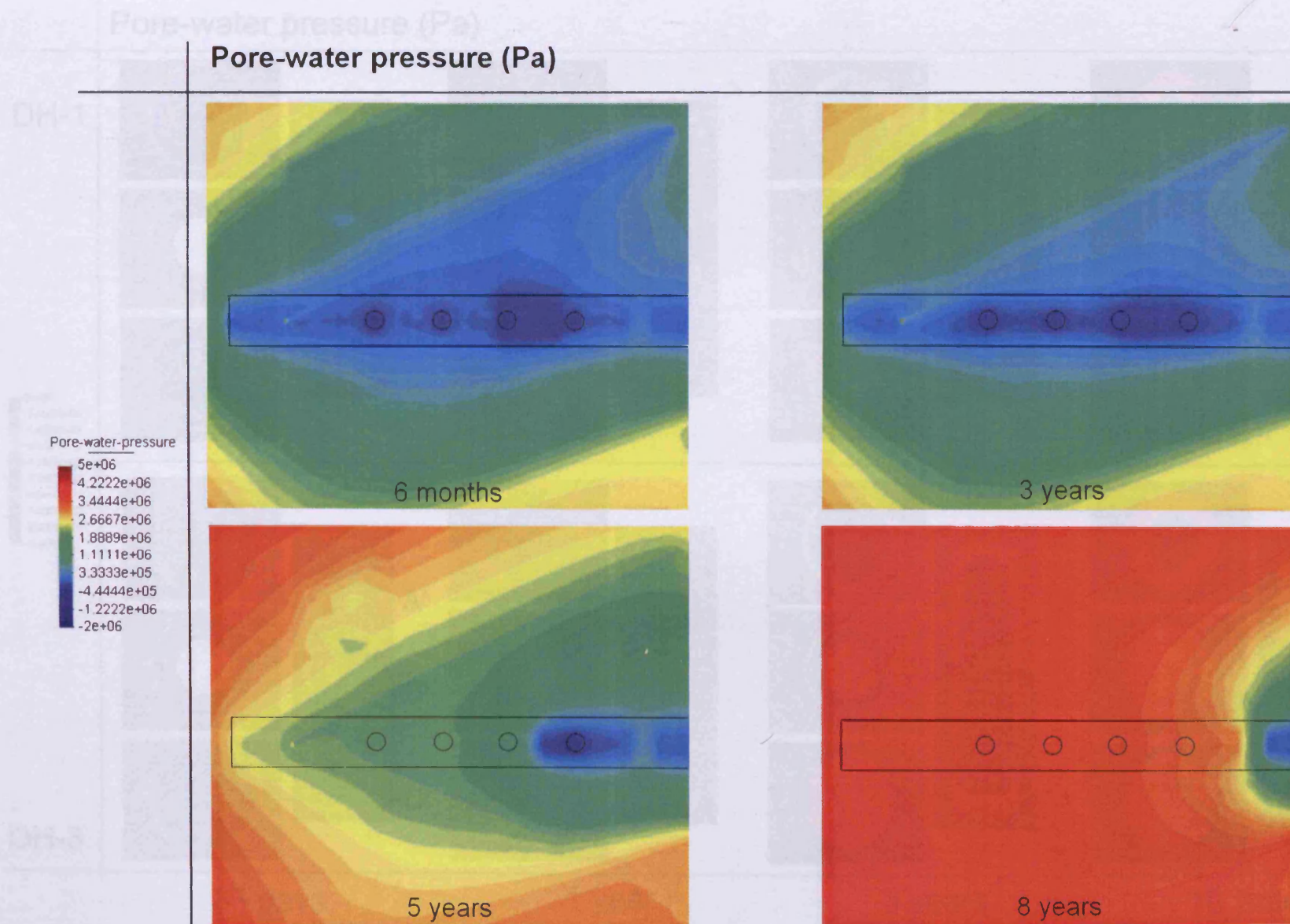
Figure 8.30. Contour plots in horizontal section through repository tunnel and rock mass of pore-water pressure for Analysis 4-2-TH3D-F.
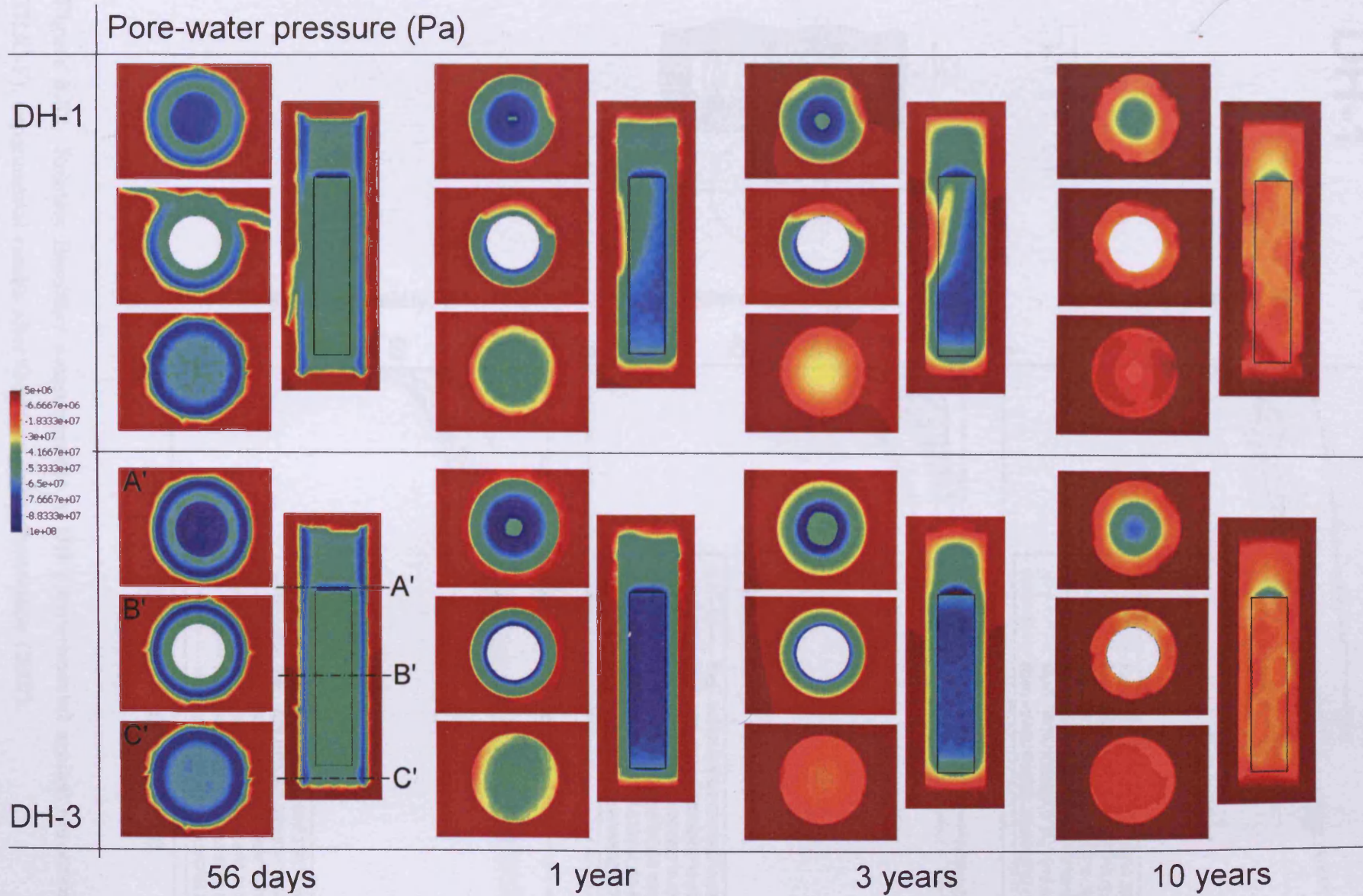
Figure 8.31. Contour plots in section of pore-water pressure of DH-1 and DH-3 for Analysis 4-2-TH3D-F. Slices through deposition-holes are taken at A', B' and C' throughout.
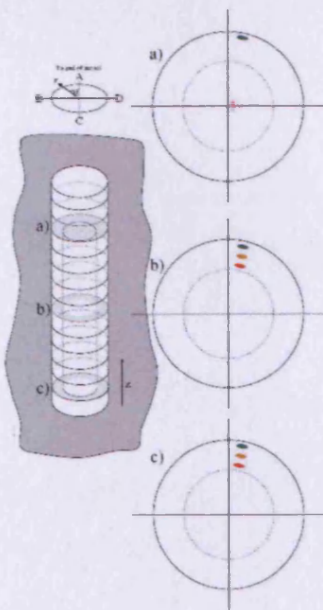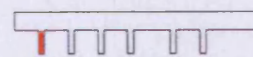
DH-1

a)

b)

c)

Legend panel a):
- Exp - WBU10037(6.756\270°\0.050)
- Exp - WBU10032(6.317\270°\0.050)
- Exp - WBU10026(5.398\350°\0.785)
- Num - WBU10037(6.756\270°\0.050)
- Num - WBU10032(6.317\270°\0.050)
- Num - WBU10026(5.398\350°\0.785)

Legend panel b):
- Exp - WBU10013(2.870\350°\0.585)
- Exp - WBU10014(2.870\350°\0.685)
- Exp - WBU10015(2.870\350°\0.785)
- Num - WBU10013(2.870\350°\0.585)
- Num - WBU10014(2.870\350°\0.685)
- Num - WBU10015(2.870\350°\0.785)

Legend panel c):
- Exp - WBU10006(0.344\350°\0.585)
- Exp - WBU10005(0.344\350°\0.685)
- Exp - WBU10004(0.344\350°\0.785)
- Num - WBU10006(0.344\350°\0.585)
- Num - WBU10005(0.344\350°\0.685)
- Num - WBU10004(0.344\350°\0.785)

Figure 8.32. Relative Humidity measurements in DH-1 experimental against numerical (4-2-TH3D-F), experimental results after Goudarzi and Johannesson (2007).

DH-3
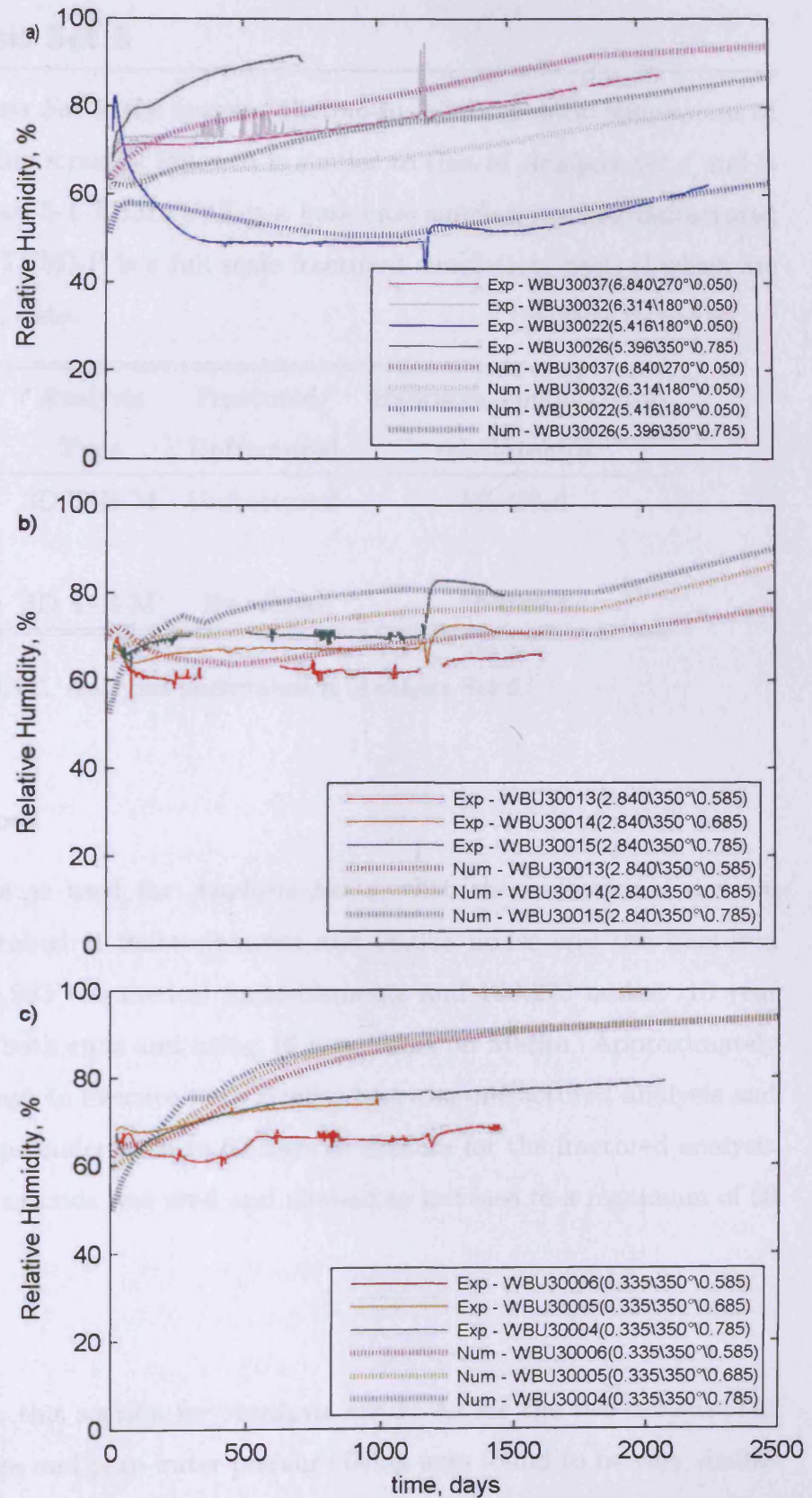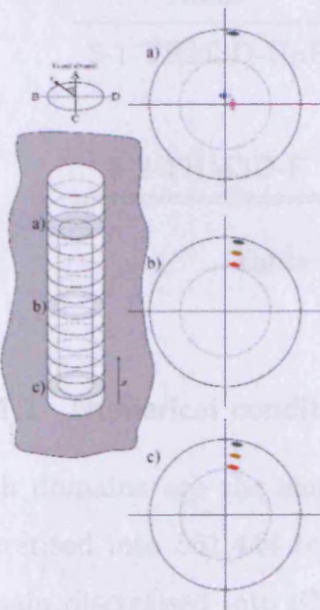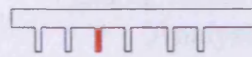
Figure 8.33. Relative Humidity measurements in DH-3 experimental against numerical (4-2-TH3D-F), experimental results after Goudarzi and Johannesson (2007).

8.11   Results - Analysis Set 5

This section presents *Analysis Set 5*, the coupled thermo-hydro-mechanical simulations of the entire PRP. The modelling strategy followed is similar to that of *Analysis Set 4* and is set out in table 8.11. Analysis 5-1-TH3D-UnF is a base case simulation of an unfractured repository and analysis 5-2-TH3D-F is a full scale fractured simulation, both of which are compared with experimental data.

Analysis Name	Analysis Type	Fractured/ Unfractured	Hydraulic conductivity relationships
5-1-THM3D-UnF	3D T-H-M	Unfractured	Modified
5-2-THM3D-F	3D T-H-M	Fractured	Modified

Table 8.11. Analyses undertaken in *Analysis Set 5*.

8.11.1   Numerical conditions

Both domains are the same as used for *Analysis Set 4*, with the unfractured domain discretised into 551,444 tetrahedral finite-elements and 96,258 nodes and the fractured domain discretised into 920,983 tetrahedral finite-elements and 160,273 nodes. 10 year analyses was completed for both runs and using 16 processors on Merlin. Approximately 3,500 timesteps taking 40 days to execute were required for the unfractured analysis and approximately 5,000 timesteps undertaken in 60 days to execute for the fractured analysis. An initial time-step of 1,000 seconds was used and allowed to increase to a maximum of 30 days.

8.11.2   Results

The results are presented in this section for *Analysis set 5*. As for the two-dimensional analyses both the temperature and pore-water pressure fields were found to be very similar to that of the thermo-hydraulic analyses due to the confined nature of the bentonite. The micro-structural swelling behaviour of both the buffer blocks and pellets have a major effect, which could be considered mechanical, but due to lack of experimental data these

have been accounted for directly in the hydraulic conductivity. Further experimentation and constitutive model development would be required for this to be included within a mechanical model.

It is worth noting that the amount of data produced for these analyses is significant, i.e. many Giga-Bytes; even for a single timestep many hundreds of Mega-Bytes were produced which can cause problems in terms of memory capacity when interrorgating the data. Consequently significant problems exist in terms of visualisation and investigation of results. Further work in terms of the use of parallel computation, both processing and data parallelism, to view and manipulate this data would be required to make the investigation of results simpler and of a greater value, especially if increasing the size of models where viewing the results in a useful fashion could become the overriding difficulty.

8.11.2.1   Analysis 5-1-THM3D-UnF

The first analysis, 5-1-THM3D-UnF, is an unfractured full three-dimensional repository simulation. A contour plot of the displacements is shown in figure 8.34. It can be seen that the displacements are restricted, to any major degree, to within each deposition-hole. And where displacement occurs in the backfill, due to the bentonite swelling and causing deformation, the effects of each deposition-hole do not interact. It is also seen in comparison with figure 8.21 that the displacements are similar in both quantity and quality of the unfractured analysis, which would be expected if the deformation is isolated. The rock mass is displaced by a negligible amount due to the high stiffness.

The vertical and horizontal displacements are presented graphically in figure 8.34. It can be seen that the displacements are largely contained within the deposition holes and are of equal magnitudes to that exhibited in the two-dimensional analyses. There is little difference between the deposition-holes due to the limited differences in the re-saturation in this simulation, with DH-1 exhibiting slightly more vertical deformation at the top of the buffer due to the slightly higher saturation.

Plots of the simulated and experimental results for the net mean stress for both DH-1 and DH-3 are shown in figures 8.35 and 8.36. Both sets of numerical data are similar

highlighting the similar saturation rate for both deposition-holes in this simulation, unlike reality where DH-1 saturates generally faster. The only real difference is in the lower buffer where the stresses are higher for DH-1 which is as a consequence of slightly higher saturation due to its relative location in the repository. The similarity of the stress evolution in the deposition-holes is also made possible by the lack of interaction of the mechanical effects from other deposition-holes. The numerical response is similar to that of the two-dimensional analysis for the unfractured analysis and consequently the comparison with experimental results is favourable with DH-3, shown in figure 8.36. The numerical results at the mid-section show little deviation from the initial numerical value until approximately 2,000 days where a change in gradient shows an increase, this is due to the decreasing heat-flux and consequential swelling from re-saturation. In the upper section of the buffer the numerical and experimental behaviour show a slowly increasing gradient of stress increase. In the stages immediately before the sensors fail, at approximately 1,400 days the experimental data is seen to increase sharply, which is not reflected in the numerical results. In the lower section of the buffer, the numerical results match in quantity, but the morphology of the experimental results is not reflected. No measured underlying physical process seems able to explain the stress evolution in these times. It is conjectured that local stress evolution due to the non-homogenous nature of the material may be responsible.
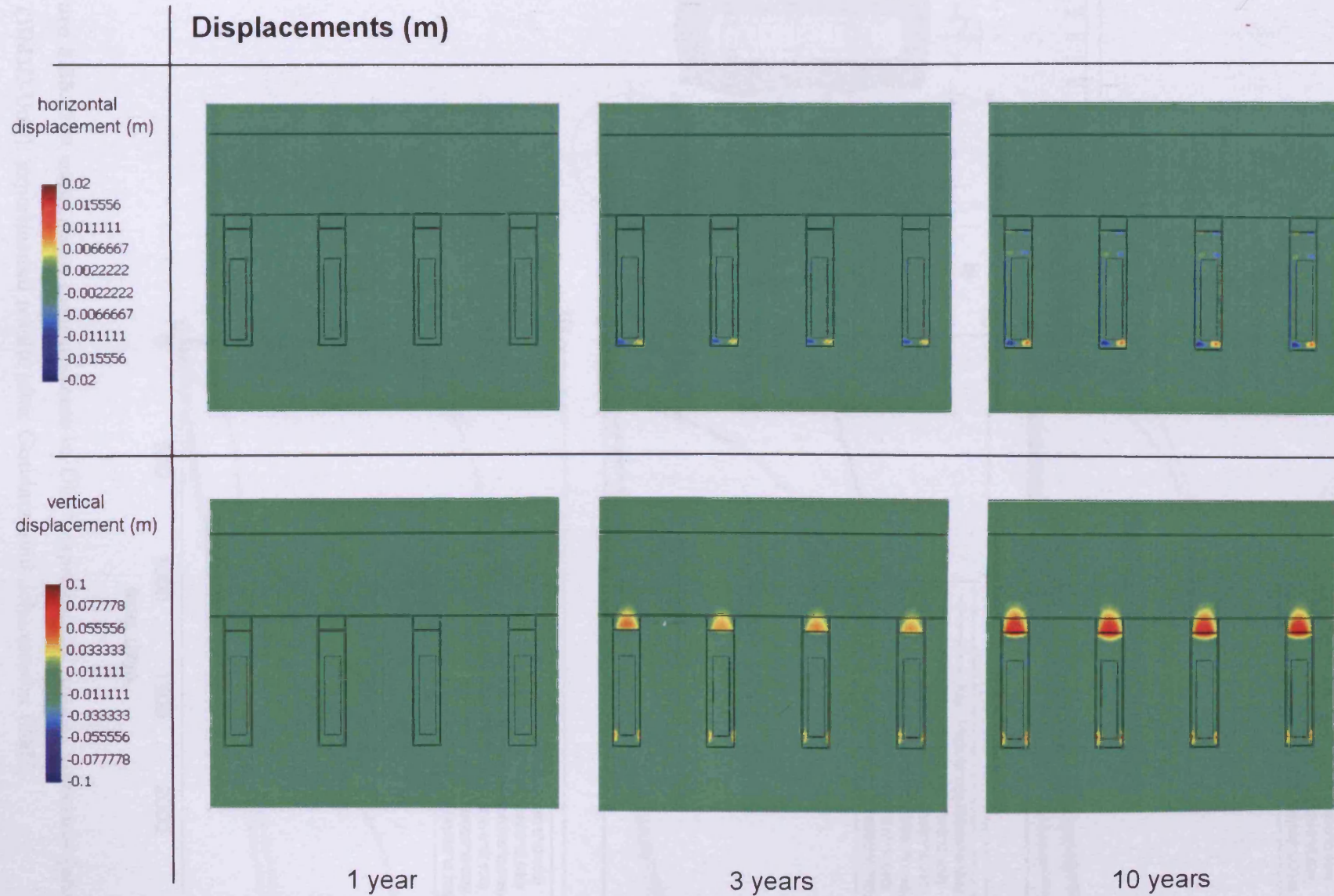
Figure 8.34. Contour plots of deformation along a vertical section through repository centre-line for Analysis 5-1-THM3D-UnF.
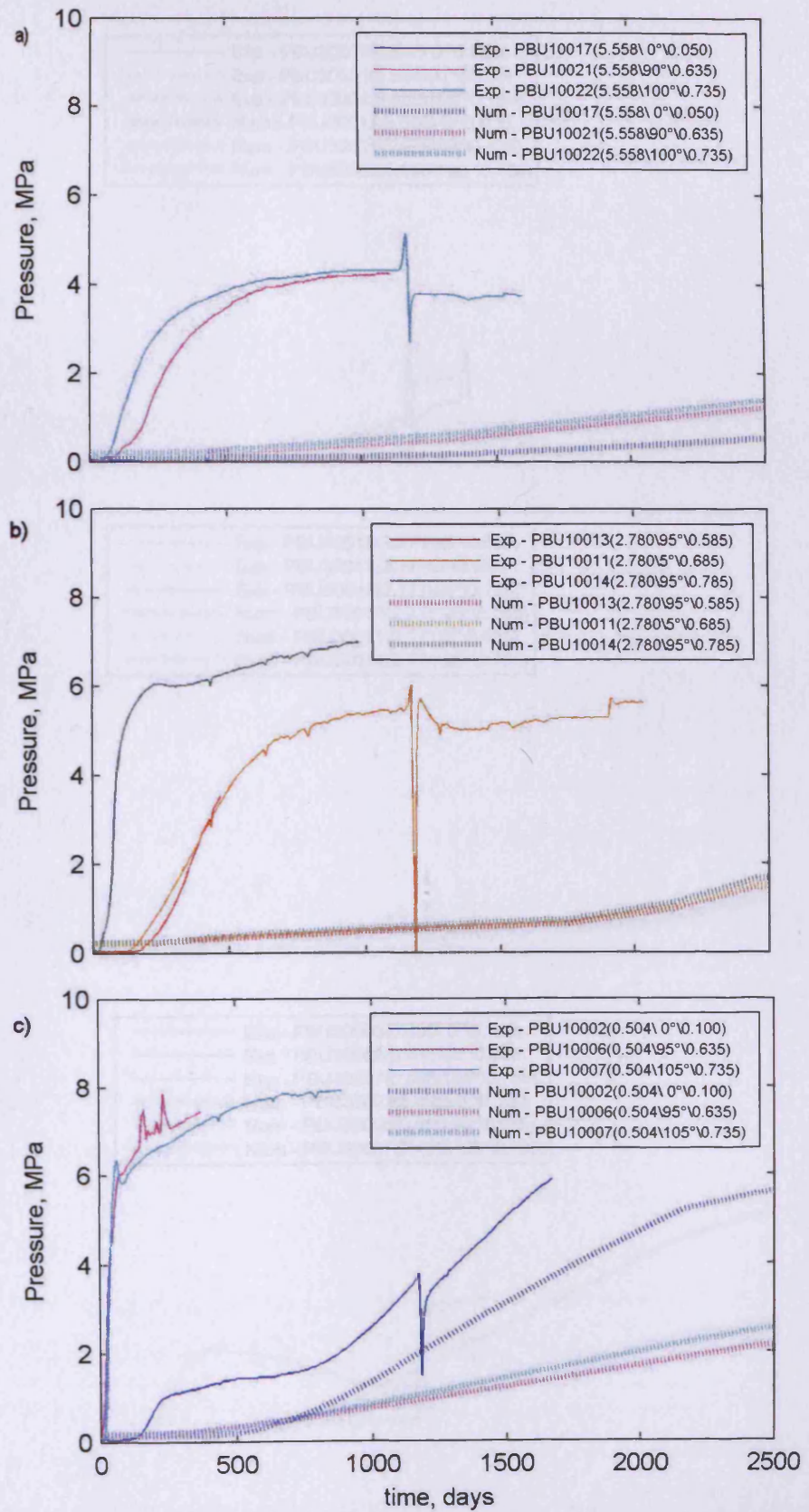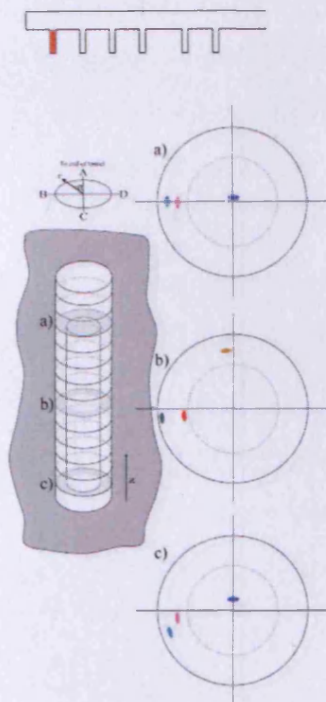
DH-1

Figure 8.35. Net mean stress measurements in DH-1 experimental against numerical (analysis 5-1-THM3D-UnF), experimental results after Goudarzi and Johannesson (2007).
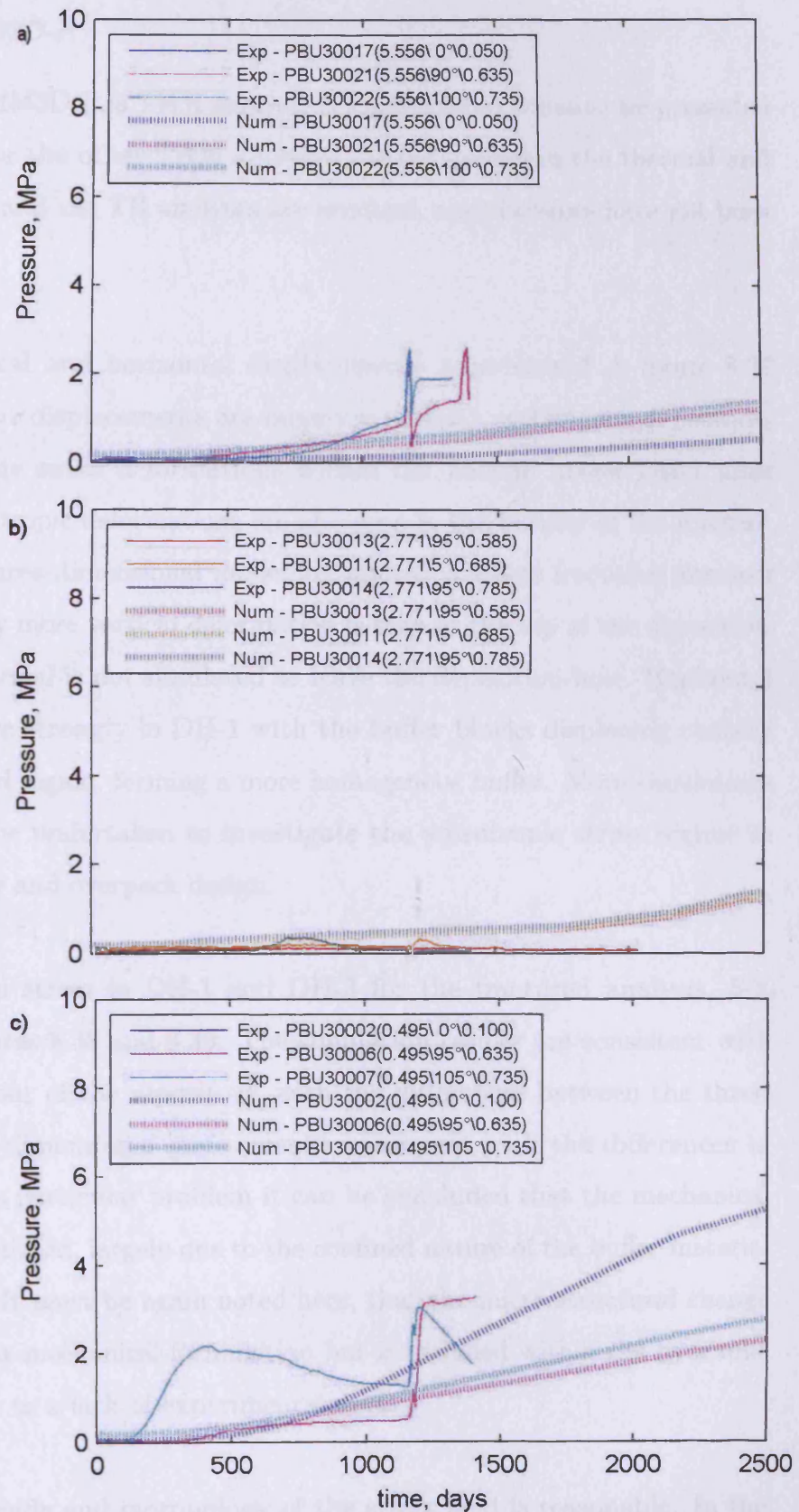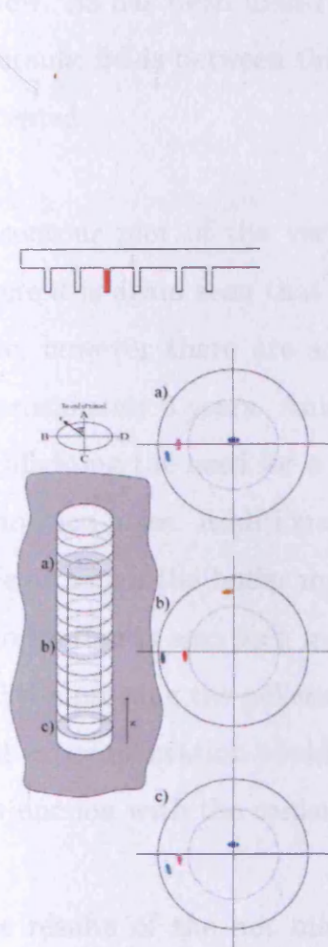
DH-3

Figure 8.36. Net mean stress measurements in DH-3 experimental against numerical (analysis 5-1-THM3D-UnF), experimental results after Goudarzi and Johannesson (2007).

8.11.2.2   Analysis 5-2-THM3D-F

The results of analysis 5-2-THM3D-F, a THM analysis of the fractured domain, are presented below. As has been found for the other THM analyses the differences in the thermal and hydraulic fields between this and the TH analyses are minimal, and therefore have not been repeated.

A contour plot of the vertical and horizontal displacements is presented in figure 8.37 where it is again seen that the displacements are largely contained within each deposition-hole, however there are some small deformations within the backfill above DH-1 after approximately 3 years. Anisotropic deformations are also seen in the locality of the fracture, highlighting the need for a three-dimensional modelling approach where fractures intersect deposition-holes. Additionally more vertical deformation is seen at the top of the deposition-hole although the buffer material is not simulated to leave the deposition-hole. Horizontal deformation is also seen more strongly in DH-1 with the buffer blocks displacing radially and compressing the pelletised region, forming a more homogenous buffer. More simulations and experimentation could be undertaken to investigate the anisotropic stress regime in conjunction with the canister and overpack design.

The results of the net mean stress in DH-1 and DH-3 for the fractured analysis, 5-2-THM3D-F, are shown in figures 8.38 and 8.39. The simulation results are consistent with the overall hydraulic behaviour of the repository, with the differences between the three-dimensional results and two-dimensional stress results consistent with the differences in hydraulic behaviour. For this particular problem it can be concluded that the mechanical influence on the hydraulic is limited, largely due to the confined nature of the buffer material and limited porosity change. It must be again noted here, that the micro-structural change has not been considered in the mechanical formulation but is included within the hydraulic conductivity relationship due to a lack of experimental data.

For DH-1 the general magnitude and morphology of the stress field is reasonable. In the upper section of the buffer the early evolution is not reflected, this may be explained by either local stresses being generated and not equilibrated with the remainder of the buffer

or the high hydraulic and thermal gradients, therefore sensitivity to sensor location. In the mid-section both the quantity and quality of the simulation results match the experimental results well. It is noted that in this location the level of mean stress is sensitive to exact sensor placement, in vertical and both horizontal directions. This is due to the anisotropic hydration behaviour caused by the fracture. Therefore, these results are deemed to represent the behaviour well. In the lower region, the stresses in the centre of the cylinder is well simulated in both evolution and value, and the stresses in the outer area show a very high gradient early in the experiment. Neither the temperataure or the hydraulic field show any behaviour that may cause this effect. In DH-3 the stress evolution is similar to that shown in the unfractured analysis, albeit slightly reduced matching the slightly reduced hydration, and therefore significantly different to that of DH-1.

The key differences between the stress evolution between DH-1 and DH-3 are reflected in the simulation with reasonable correlation with experimental evidence. However, some differences between the numerical and experimental evolution still exist. It is possible that some of these differences are due to heterogeneity and local effects as well as unknowns in the underlying phenomena. It is seen that the stress field is dependant largely upon the hydraulic field in these simulations, which in turn is strongly coupled with the temperature field.

8.11.3 Summary

Three-dimensional THM analyses were carried out in this section, both with and without the inclusion of fractures. The deformation and stress evolution is consistent with the thermo-hydraulic physics of the problem and in general yields a good quantitative and qualitative correlation with experimental results. The fractured analysis allows improved simulation of the hydraulic behaviour which is shown in section 8.10 as consequentially improved stress-deformation behaviour, in particular when comparing DH-1 and DH-3 which hydrate at significantly different rates.

Deformation was largely found to be isolated within individual deposition-holes but the hydraulic and thermal regimes governing the swelling behaviour are not, so three-dimensional simulations are required. A number of differences exist between the simulated and

experimental mechanical behaviour that cannot be explained by differences in the hydraulic regimes. Local stress behaviour partly influenced by preferential hydraulic pathways and the behaviour of the pellets are possible reasons along with some degree of experimental error.

Generally, the thermo-hydraulic-mechanical behaviour of the PRP project can be well simulated with the key aspects shown. A number of difficulties exist due to the three-dimensional nature of the problem and the fractured rock. More experimentation on buffer materials are key to understanding the behaviour of the buffer, particularly in the long term due to the micro-structural evolution in both the buffer blocks and the pellets.
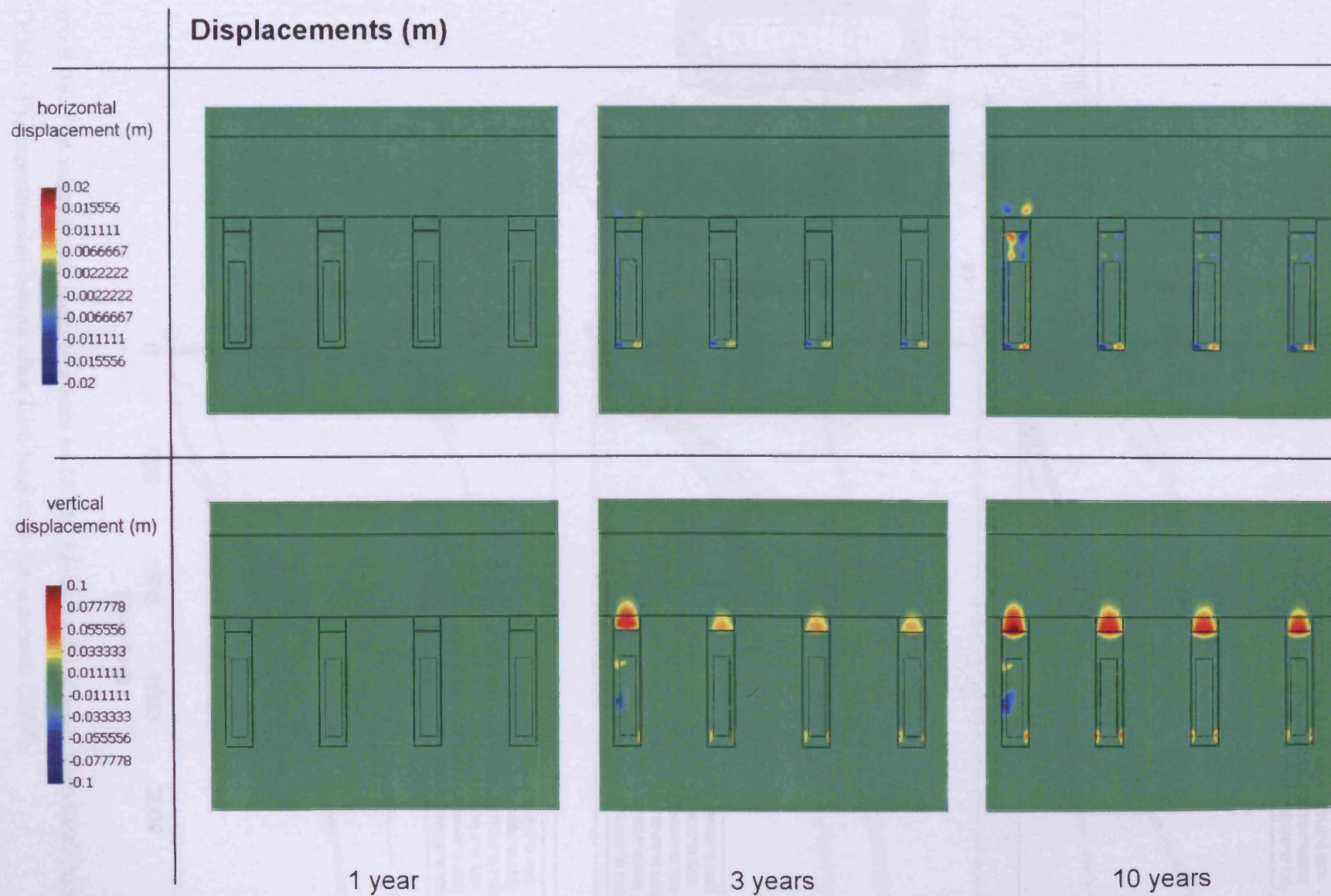
Figure 8.37. Contour plots of deformation along a vertical section through repository centre-line for Analysis 5-1-THM3D-UnF.
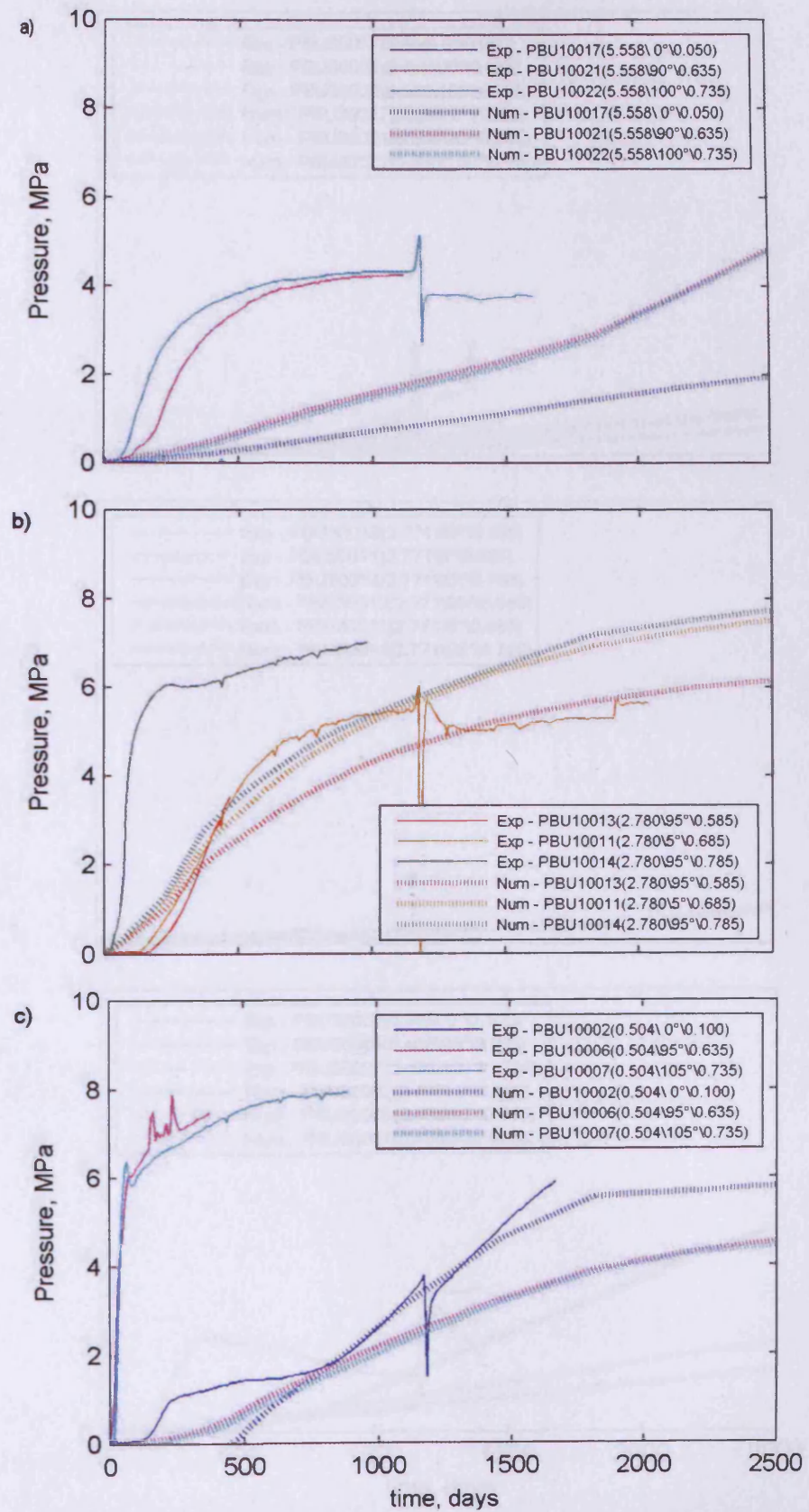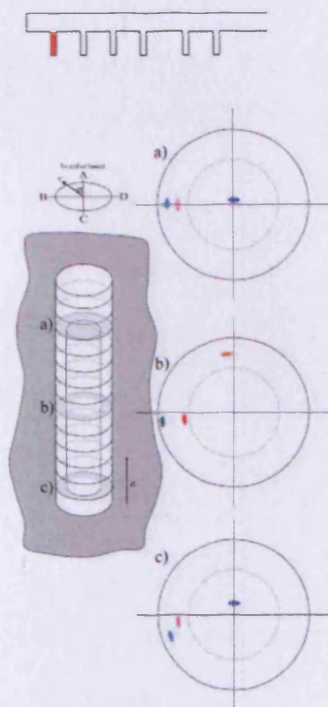
Figure 8.38. Net mean stress measurements in DH-1 experimental against numerical (analysis 5-2-THM3D-F), experimental results after Goudarzi and Johannesson (2007).
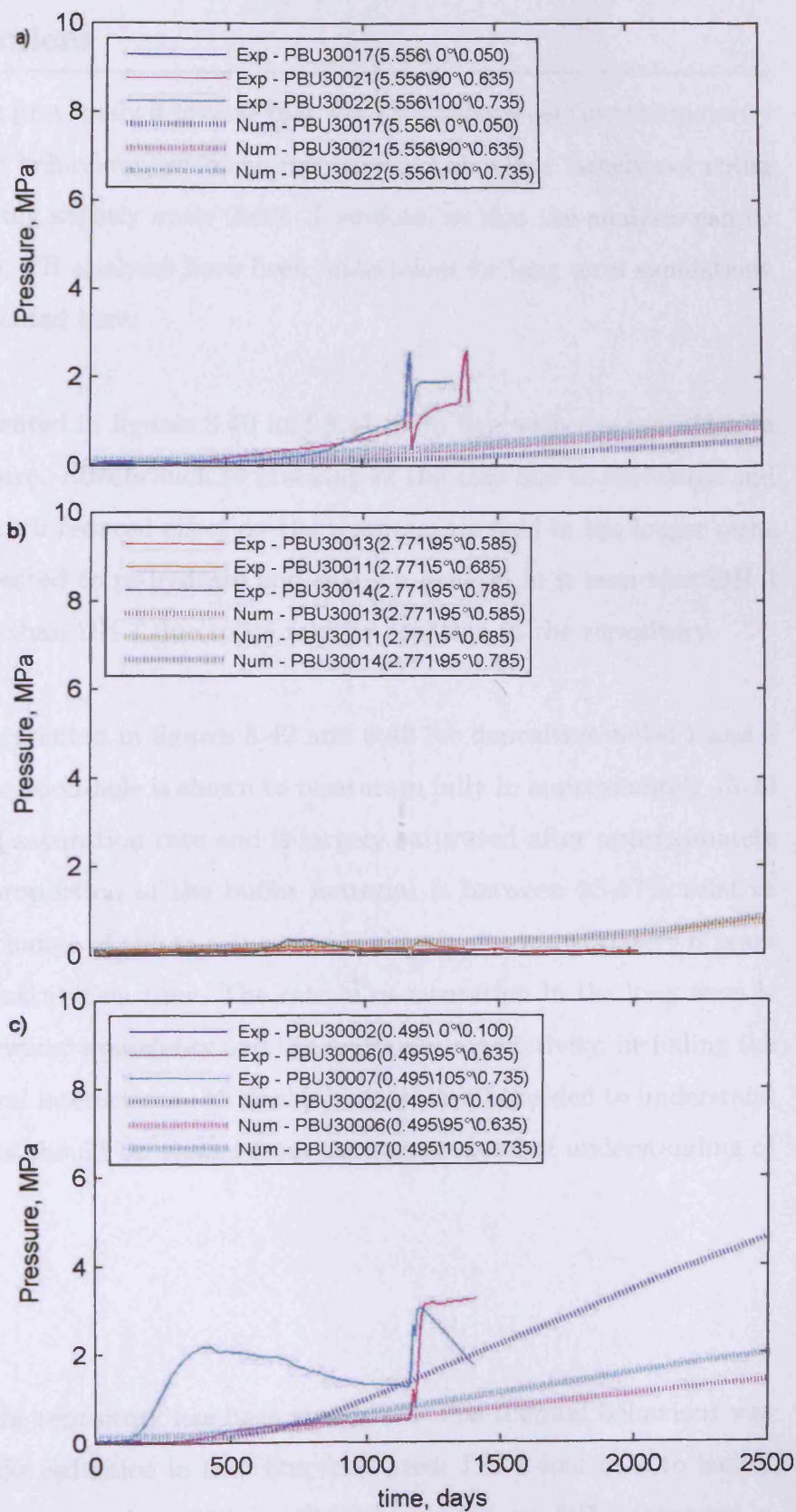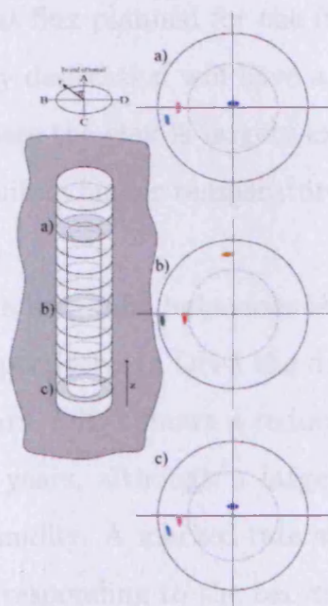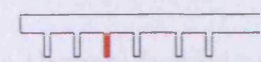
DH-3

Figure 8.39. Net mean stress measurements in DH-3 experimental against numerical (analysis 5-2-THM3D-F), experimental results after Goudarzi and Johannesson (2007).

8.12 Long term predictions

From the analyses undertaken previously it is clear that the TH analyses capture the majority of the thermal and hydraulic behaviour, with the mechanical behaviour largely occurring due to these and only impacting slightly upon them. Therefore, so that the analyses can be undertaken in a reduced time, TH analyses have been undertaken for long term simulations, i.e. predictions, and are presented here.

The thermal behaviour, presented in figures 8.40 and 8.41, is in line with the reduction in heat flux planned for the future. Effects such as cracking of the clay due to shrinkage and clay desiccation will have a much reduced effect on the temperature field in the longer term, where the clay is largely expected to re-hydrate and seal. In general in it seen that DH-3 exhibits higher temperatures than DH-1 due to its relative location in the repository.

The hydraulic behaviour is presented in figures 8.42 and 8.43 for deposition-holes 1 and 3 respectively. In DH-1 the deposition-hole is shown to resaturate fully in approxiamtely 15-20 years. DH-3 shows a reduced saturation rate and is largely saturated after approximately 30 years, although a large proportion of the buffer material is between 95-97% relative humidity. A marked rate of change of the re-saturation is shown at approximately 6 years corresponding to the backfill saturation time. The rate of re-saturation in the long term is governed by a combination of water availability and the hydraulic conductivity, including the effect of micro/macro-structural interactions. More experimentation is needed to understand these aspects and these results should be viewed from the current level of understanding of this phenomena.

8.12.1 Summary

The long term behaviour of the repository has been simulated. The thermal behaviour was found to reduce in line with the reduction in heat flux simulated. DH-3 continues to have a higher temperature than DH-1 due to the position within the repository. DH-1 saturates in approximately 15-20 years whereas DH-3 takes over 30 years to fully saturate. This different behaviour is likely to impact upon the performance assessment.
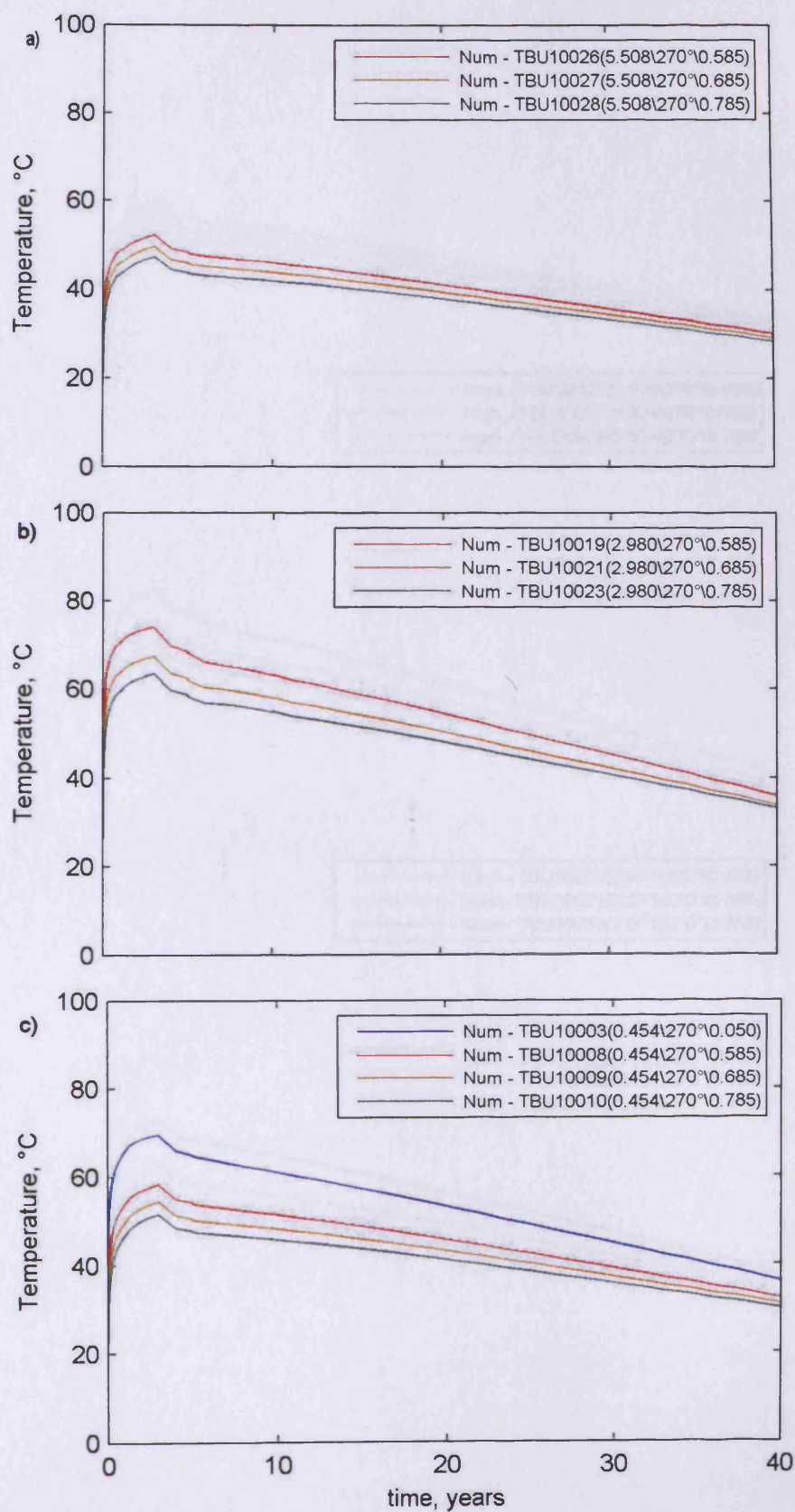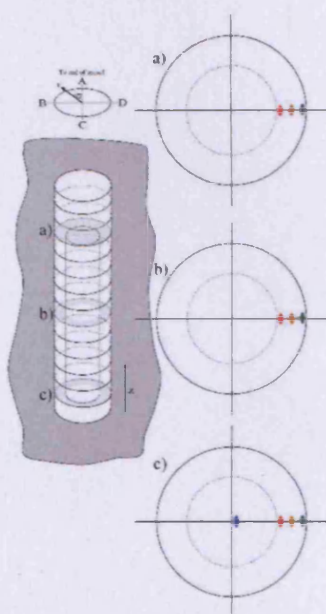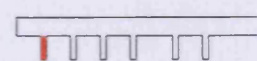
DH-1

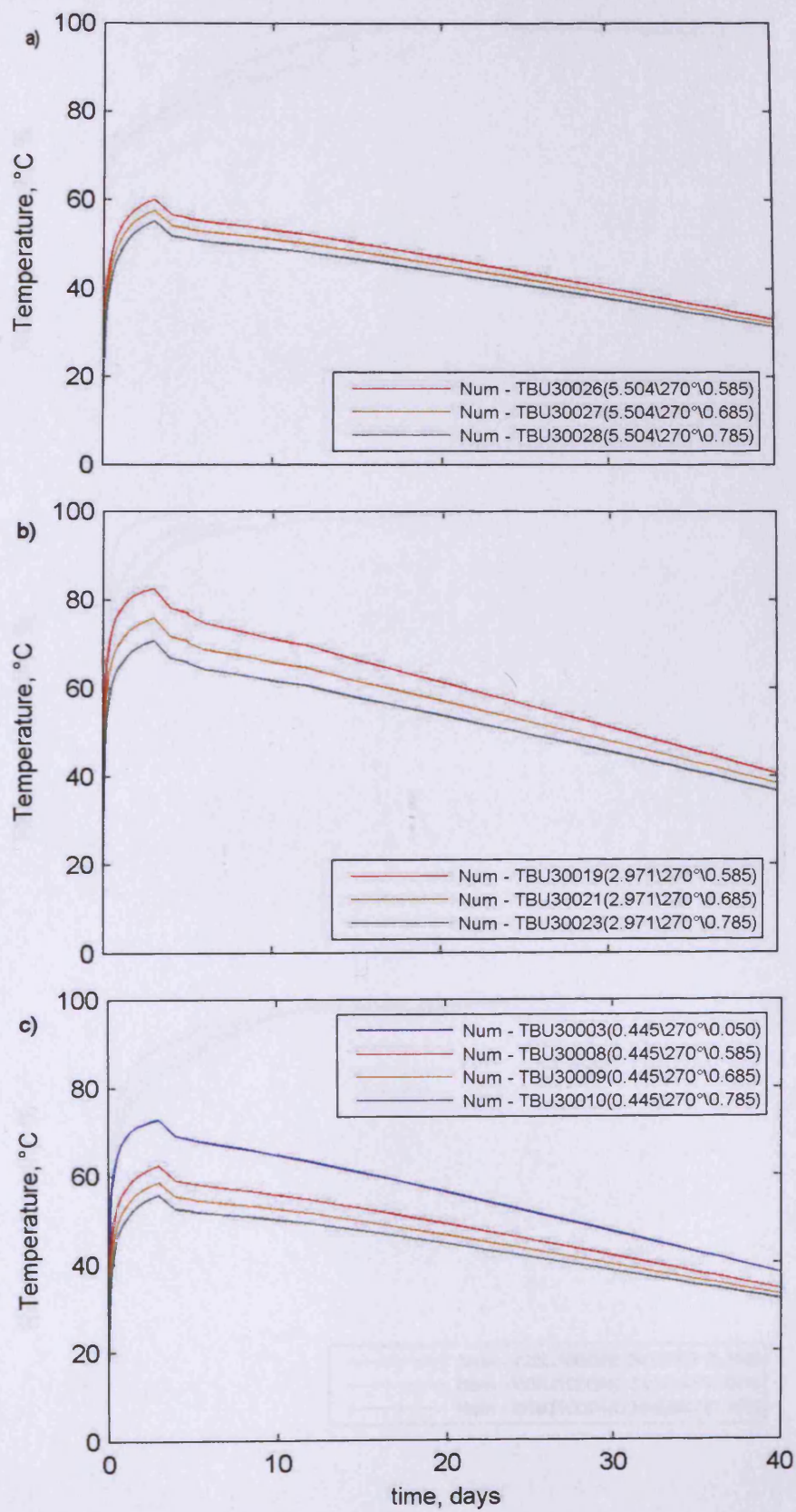**Figure 8.40.** Temperature simulation results for long term predictions in DH-1.
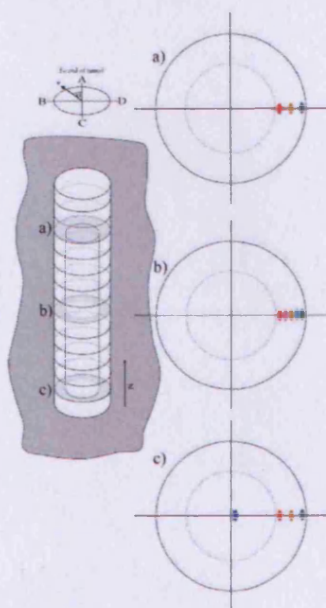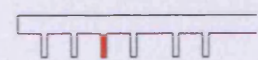
DH-3

Figure 8.41. Temperature simulation results for long term predictions in DH-3.
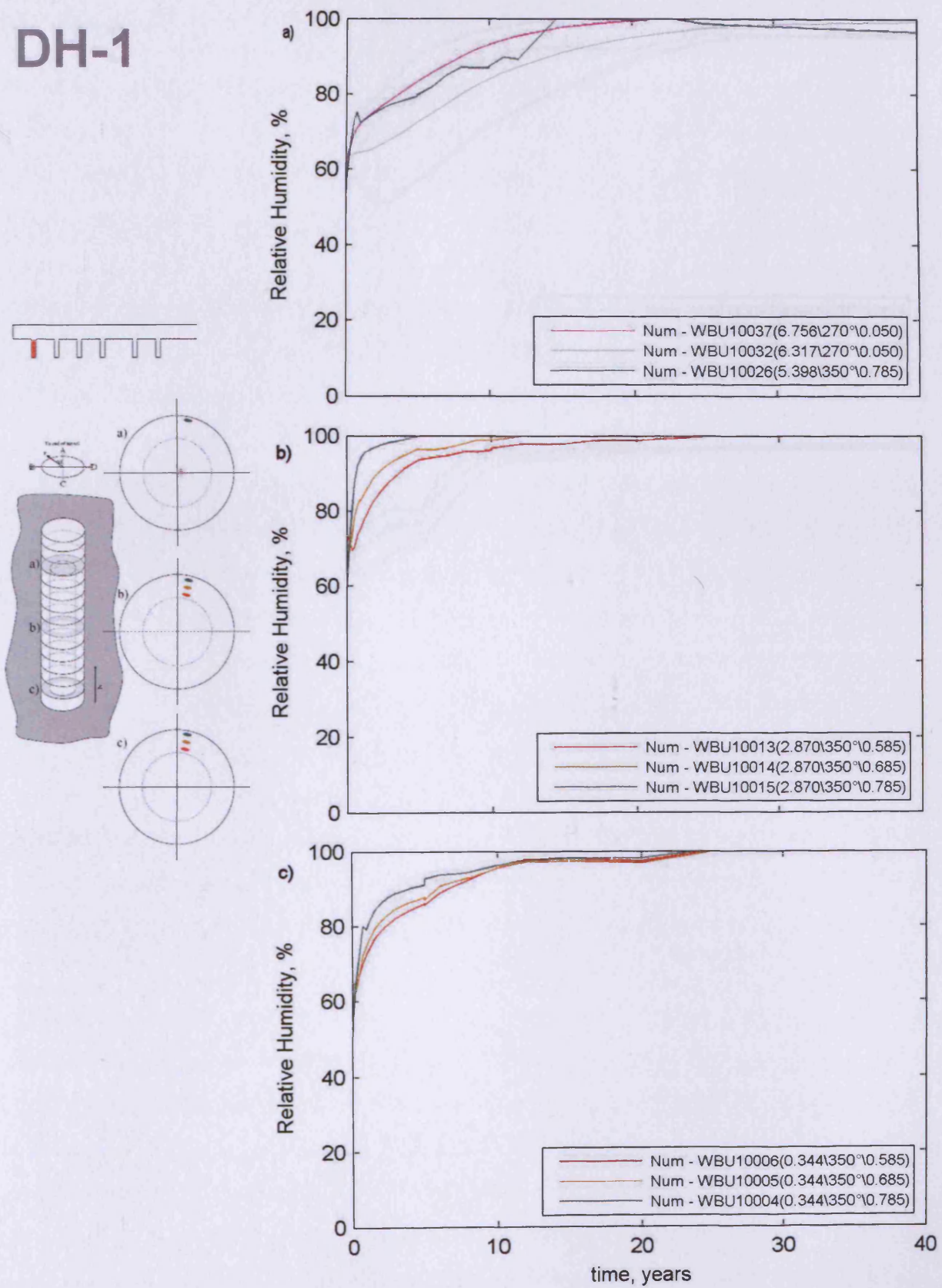
Figure 8.42. Relative Humidity simulation results for long term predictions in DH-1.
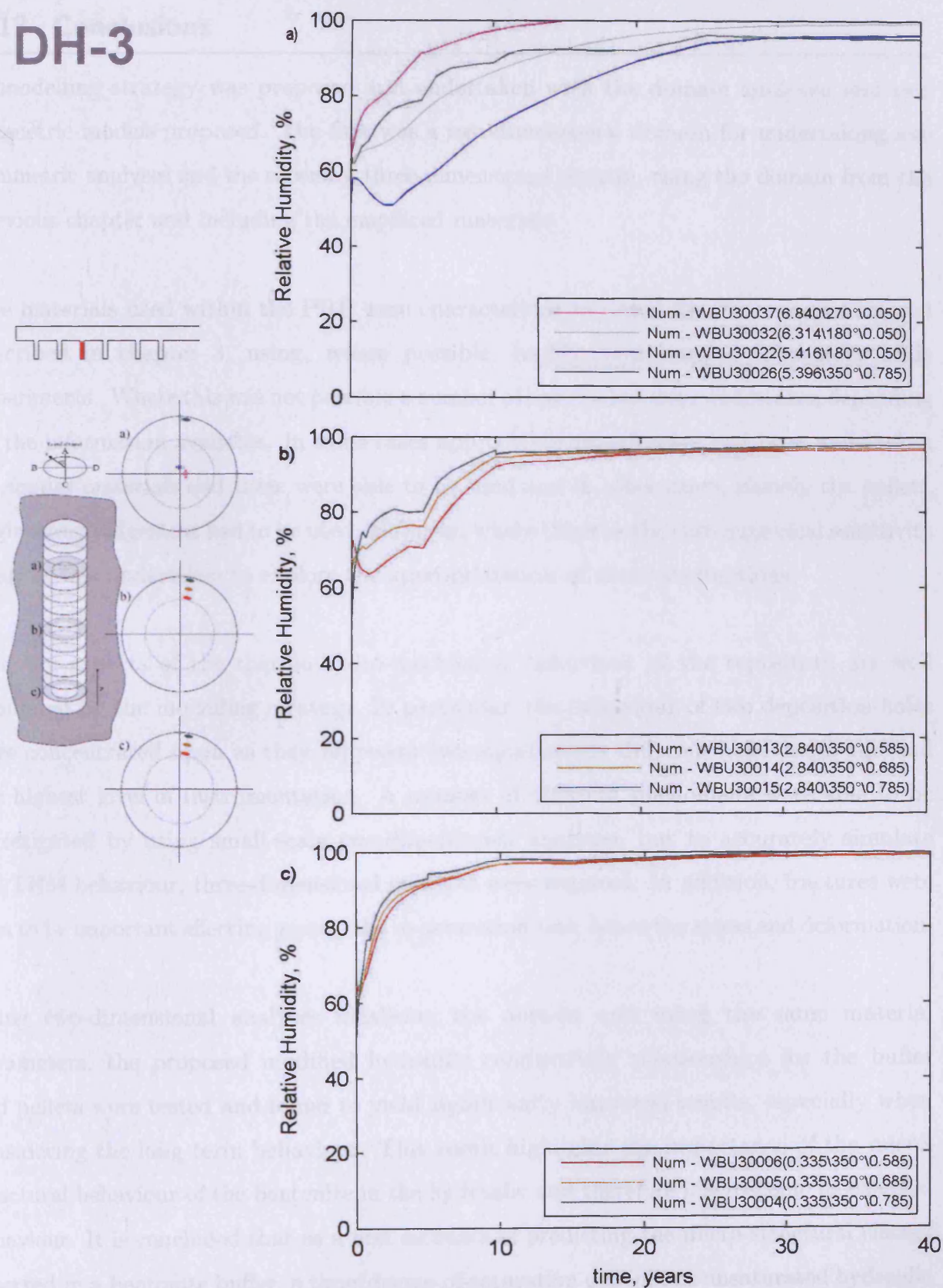
Figure 8.43. Relative Humidity simulation results for long term predictions in DH-3.

8.13 Conclusions

A modelling strategy was proposed and undertaken with the domain analysed and two geometric models proposed. The first was a two dimensional domain for undertaking axi-symmetric analyses and the second a three-dimensional domain, using the domain from the previous chapter and including the emplaced materials.

The materials used within the PRP were characterised in detail for the numerical model described in chapter 3, using, where possible, highly instrumented laboratory scale experiments. Where this was not possible a number of approaches were undertaken depending on the information available. In some cases appropriate experiments had been undertaken on similar materials and these were able to be used and in other cases, namely the pellets, engineering judgement had to be used. However, where this was the case numerical sensitivity analysis was undertaken to explore the appropriateness of these assumptions.

The key aspects of the thermo-hydro-mechanical behaviour of the repository are well simulated by the modelling strategy. In particular, the behaviour of two deposition-holes were concentrated upon as they represent two significantly different behaviours and had the highest level of instrumentation. A number of different phenomena were able to be investigated by using small-scale two-dimensional analyses, but to accurately simulate the THM behaviour, three-dimensional analyses were required. In addition, fractures were seen to be important effecting greatly the re-saturation rate, hence the stress and deformation.

Using two-dimensional analyses idealising the domain and using the same material parameters, the proposed modified hydraulic conductivity relationships for the buffer and pellets were tested and found to yield significantly improved results, especially when considering the long term behaviour. This result highlights the importance of the micro-structural behaviour of the bentonite in the hydraulic and therefore macroscopic mechanical behaviour. It is concluded that as a first estimate of predicting the micro-structural change observed in a bentonite buffer, a time/degree-of-saturation dependant unsaturated hydraulic relationship can be used to achieve significantly improved results. In particular, the long-term behaviour, especially the rate of re-saturation, is significantly closer to experimental

results. This in turn is likely to yield a much improved estimate of time of saturation.

An investigation of the impact on using the results of a pre-placement analysis as the initial conditions against using hydrostatic pressure as initial conditions was carried out and only a negligible impact was found. This was due to the rock remaining saturated due to the boundary conditions and the limited impact upon the pore-water pressure gradient.

Mechanical deformation was seen to be able to be quantitively well simulated in two-dimensional analyses and that deformation was generally limited to the material within the deposition-holes. Some qualitative differences are seen that cannot be explained by the hydration or thermal effects. The swelling pressures generated were seen to be able to be simulated with a few differences such as where an almost instantaneous stress increase was recorded. Notably the rate of stress increase reduced in all cases if the stress exceeded approximately $5MPa$. This behaviour could be well reproduced if the stress level where yield occurs in the pellets was reduced to this level. Additionally, when doing this vertical displacement of the buffer material reduced, which may have significant implications for the design of the backfill and performance assessment. Through numerical sensitivity analyses the deformation occuring at yield of the pellets was investigated, as experimental evidence was not available. A value of $\lambda(0)$ between 0.4 and 0.6 was shown is match post-mortem analyses of a similar test.

In three-dimensional analyses the behaviour of these two deposition-holes was also concentrated upon, with the key differences noted in the simulations when using a domain including fractures. The temperature field was noted to be intrinsically three-dimensional, with the effects of adjacent canisters heat output influencing the temperature within other deposition-holes. The simulation results of the temperature field in comparison with the experimental data was good for the three-dimensional analyses. The temperature behaviour was found not to be greatly influenced by the use of a fractured domain.

The importance of the fracture intersecting DH-1 was highlighted and the highly three-dimensional anisotropic hydration behaviour noted. The saturation of DH-1 at the mid-height in the three-dimensional analysis matched the experimental behaviour well, but was seen

to be slower than that shown experimentally, especially at the hot buffer surface, i.e. the surface adjacent to the canister. This may be due to preferential pathways developing in the buffer, or that the assumptions made on the connectivity and size of the fracture intersecting DH-1 may be too conservative. Post-mortem investigation of the bentonite and of the fracture may be possible to confirm these hypotheses.

The significance of the backfill was also established when examining the three-dimensional analyses. The backfill was not able to saturate due to the supply of water from the rock in the unfractured analysis and therefore affected the supply of water to the deposition-holes. In the fractured analysis the backfill was shown to saturate in a similar time to that exhibited experimentally therefore significantly altering the pore-water pressure gradients in the rock. The geological supply of water is critical to the hydration rate of various aspects of the repository.

Geological conditions, backfill and buffer saturation and bentonite micro-structural behaviour all link to form the hydraulic regime and this along with the temperature effects govern the re-saturation. The accurate capturing of these phenomena will enable accurate prediction and simulation of a repository system.

The long term behaviour of the repository is simulated with results presented. The thermal behaviour is found to be in line with the reducing temperature fluxes. DH-1 is found to saturate fully in approximately 15-20 years whereas DH-3 is found to be almost fully saturated after 30 years.

Computational performance was key to enabling these simulations to be undertaken, with an estimated speed-up of over 5 times still meaning simulations took up to 2 months to complete. Undertaking small-scale analyses to investigate certain key features enabled material behaviour and model response to be investigated in a reasonable time-scale. However, it is noted that a number of key features could not be investigated using small scale, simplified models. The large quantities of data yielded also meant that visualisation and comparison with experimental results was not trivial. Further work in data parallel visualisation coupled with parallel computation will be necessary for future work.

8.14 References

Alonso, E.E., Gens, A., and Josa, A., (1990) "A constitutive model for partially saturated soils", *Géotechnique*, **40**(3), 405-430.

AMCOL Speciality Minerals, (2006) *Fine Granular Industrial Sodium Bentonite, MX-80*, AMCOL Speciality Minerals, Winsford.

Börgesson, L., Gunnarsson, D., Johannesson, L-E., Sandén, T., (2002) *Äspö Hard Rock Laboratory, Prototype Repository, Installation of buffer, canisters, backfill and instruments in section 1*, SKB, IPR-02-23, Stockholm.

Börgesson, L., Hernelind, J., (1998) *Preparatory modelling for the backfill and plug test - Scoping calculations of H-M processes*, SKB, IPR-99-11, Stockholm.

Börgesson, L., Hernelind, J., (1999) *Preliminary modelling of the water saturation phase of the buffer and backfill materials*, SKB, IPR-00-11, Stockholm.

Börgesson, L., Johannesson, L-E., Fredrikson, A., (1993) *Laboratory investigations of highly compacted bentonite blocks for buffer material Compaction technique and material composition*, SKB, PR 44-93-010, Stockholm.

Börgesson, L., Johannesson, L-E., Gunnarsson, D., (2003) "Influence of soil structure heterogeneities on the behaviour of backfill materials based on mixtures of bentonite and crushed rock", *Applied Clay Science*, **23**, 121-131.

Börgesson, L., Johannesson, L-E., Sandén, T., Hernelind, J., (1995) *Modelling of the physical behaviour of water saturated clay barriers, Laboratory tests, material models and finite element application*, SKB, TR-95-20, Stockholm.

Bradbury, M.H., Baeyens, B., (2002) "Porewater chemistry in compacted re-saturated MX-80 bentonite: physicochemical characterisation and geochemical modelling", *PSI Bericht 0210, Villigen PSI and NTB 01 08*, Nagra, Wettingen.

Bradbury, M.H., Baeyens, B., (2003) "Porewater chemistry in compacted re-saturated MX-80 bentonite", *Journal of Contaminant Hydrology*, **61**, 329-338.

Clay Technology, (2000) Personnal Communication cited in Mata (2003).

Dahlström, L-O., (1998) *Äspö HRL - Test plan for the Prototype Repository*, SKB, HRL-98-24, Stockholm.

Davies, P.B., (1991) *Evaluation of the role of threshold pressure in controlling flow of waste-generated gas into bedded salt at the waste isolation pilot plant*, Technical Report, SAND-90-3246, Sandia National Laboratories, Albuquerque, New Mexico.

Delin, P., Sturk, R., Stille, H., (1995) *Laboratory testing of rock*, SKB, Technical note 25-95-08v.

Gens, A., Garcia-Molina, A.J., Olivella, S., Alonso, E.E., and Huertas, F., (1998) "Analysis of a full scale in situ test simulating repository conditions", *International Journal for Numerical and Analytical Methods in Geomechanics*, **22**, 515-548.

Goudarzi, R., Johannesson, L-E., (2007) *Äspö Hard Rock Laboratory, Prototype Repository, Sensors data report (Period 010917-070601) Report No:17*, SKB, IPR-07-19, Stockholm.

Hoffmann, C., Alonso E.E., Romero, E., (2007) "Hydro-mechanical behaviour of bentonite pellet mixtures", *Physics and Chemistry of the Earth*, **32**, 832-849.

Imbert, C., Villar, M.V., (2006) "Hydro-mechanical response of a bentonite pellets/powder mixture upon infiltration", *Applied Clay Science*, **32**, 197-209.

Johannesson, L-E., (2002) *Äspö Hard Rock Laboratory, Manufacturing of bentonite buffer for the Prototype Repository*, SKB, IPR-02-19, Stockholm.

Johannesson, L-E., (2007) *Testing of a retrieval technique, Dismantling and sampling of buffer and determination of density and water ratio*, Unpublished report.

Johannesson, L-E., Börgesson, L., Sandén, T., (1999) *Äspö HRL - Backfill materials based on crushed rock (part 2). Geotechnical properties determined in laboratory*, SKB, IPR-99-23, Stockholm.

Johannesson, L-E., Gunnarsson, D., Sandén, T., Börgesson, L., Karlzén, R., (2004) *Äspö Hard Rock Laboratory, Prototype Repository, Installation of buffer, canisters, backfill and instruments in section II*, SKB, IPR-04-13, Stockholm.

Johannesson, L-E., Börgesson, L., Goudarzi, R., Sandèn, T., Gunnarsson, D., Svemar, C., (2007) "Prototype repository: A full scale experiment at Äspö HRL", *Physics and Chemistry of the Earth*, **32**, 58-76.

Kaye, G.W.C., Laby, T.M., (1973) *Tables of physical and chemical constants*, 14th Edition, Longmans, London.

Lloret, A., Villar, M.V., Sánchez, M., Gens, A., Pintado, X., Alonso, E.E., (2003) "Mechanical behaviour of heavily compacted bentonite under high suction changes", *Géotechnique*, **53**(1), 27-40.

Mata, C., (2003) "Hydraulic behaviour of bentonite based mixtures in engineered barriers: The Backfill and Plug Test at the Äspö HRL (Sweden)", *PhD Thesis*, Technical University of Catalonia.

Melhuish, T.A., (2004) "An investigation of the three-dimensional thermo/hydro/mechanical behaviour of large scale in-situ experiments", *PhD Thesis*, Cardiff University, Cardiff.

Mitchell, H.P., (2002) "An investigation into the thermo/hydro/mechanical interactions involved in high level nuclear waste disposal", *Ph.D Thesis*, University of Wales, Cardiff.

Patel, S., Dahlström, L-O., Stenberg, L., (1997) *Äspö Hard Rock Laboratory, Characterisation of the rock mass in the Prototype Repository at Äspö HRL Stage 1*, SKB, HRL-97-24, Stockholm.

Pusch, R., (2001) *The buffer and backfill handbook, Part 2: Materials and techniques*, SKB, TR-02-12, Stockholm.

Rutqvist, J., Chijimatsu, M., Jing, L., Millard, A., Nguyen, T.S., Rejeb, A., Sugita, Y., Tsang, C.F., (2005) "A numerical study of THM effects on the near-field safety of a hypothetical nuclear waste repositoryBMT1 of the DECOVALEX III project. Part 3: Effects of THM coupling in sparsely fractured rocks", *International Journal of Rock Mechanics & Mining Sciences*, **42**, 745755.

Stille, H., Olsson, P., (1996) *Summary of rock mechanical results from the construction of Äspö Hard Rock Laboratory*, SKB, HRL-96-07.

Sundberg, J., (1991) *Thermal properties of the rock on Äspö island. Thermal conductivity, heat capacity, geothermal gradient and heat flow*, SKB, Äspö Hard Rock Laboratory Progress Report 25-91-09, Stockholm.

THERESA, (2008) *THERESA project, Interface benchmark (1-D), Large scale test case, Description of the Canister Retrieval Test (CRT)*, Unpublished report.

Thomas, H.R., Cleall, P.J., Dixon, D., Mitchell, H.P., (2009a) "The coupled thermal-hydraulic-mechanical behaviour of a large-scale in situ heating experiment", *Géotechnique*, **59**(4), 401-413.

Thomas, H.R., Siddiqua, S., Seetharam, S.C., (2009b) "Inclusion of higher-temperature effects in a soil behaviour model", *Géotechnique*, **59**(3), 279-282.

Thomas, H.R., He, Y., (1998) "Modelling the behaviour of unsaturated soil using an elasto plastic constitutive relationship", *Géotechnique*, **48**(5), 589-603.

Villar, M.V., Martín, P.L., Barcala, J.M., (2005) *Infiltration tests at isothermal conditions and under thermal gradient*, CIEMAT, Technical Report CIEMAT/DMA /M2140/1/05, Madrid.

G
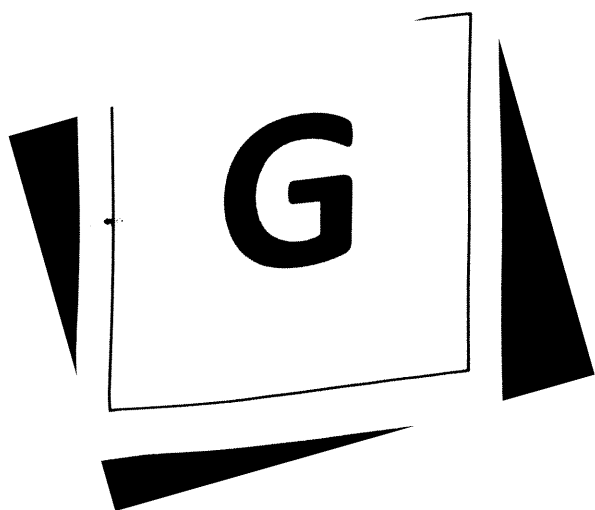
9

Conclusions and Suggestions for Further Work

9.1 Introduction

Specific conclusions pertinent to each chapter have been presented at the end of each chapter. This chapter aims to synthesise those conclusions and relate them to the objectives presented at the start of this work. Key contributions and advancements will be highlighted throughout this chapter along with opportunities for further work.

The work presented in this thesis aimed in general to simulate in three-dimensions the thermo-hydro-mechanical behaviour of the Prototype Repository Project undertaken in the Hard Rock Laboratory in Äspö, Sweden. Specifically the objectives as stated in the introduction were to:

i. Produce a three-dimensional thermo-hydro-mechanical model of the Prototype Repository Project.

  • Formulate a computational algorithm so that large-scale long-term simulations

may be undertaken in a reasonable time. High-performance computer facilities may be used if appropriate.

- Develop existing material models to take account of rock fractures;

- Develop existing material models to take account of time dependent micro-structural behaviour of buffer materials;

   ii. Compare with experimental field data.

   iii. Evaluate numerical and experimental results.

It is claimed that these objectives have been successfully achieved and a more thorough analysis is presented below.

9.2 Summary of work

A brief outline of the nuclear industry in the UK was presented showing that the majority of current sites in the UK are due to be decommissioned within the next 15 years. Additionally, it was seen that within the context of low carbon energy production and renewed interest in energy security new nuclear build is likely. The problem of nuclear waste and in particular High-Level Nuclear Waste (HLW) was outlined along with proposed disposal concepts and the concept of deep geological disposal was discussed along with the use of a safety case with performance assessment to ensure the safety of a complete repository system.

A selective literature review into the simulation of nuclear waste repositories was carried out. Due to the vast quantity of work already carried out in this field only the most important and most recent works were reviewed. Representing the coupled thermo-hydro-mechanical behaviour of unsaturated porous media and fractured rock was discussed with the two basic approaches of thermodynamics and mechanistic models introduced. It was concluded that mechanistic models were generally found to have more easily determined and directly measured material parameters. Preferential flowpaths were seen to alter the hydraulic regime considerably in fractured rock, with a number of approaches available to simulate fractured rock dependant on the scale and resolution of results required.

A review of key experimental work, both in a laboratory and in-situ, was undertaken. Both sets of experimentation give useful results with a range of timescales, size and isolation and all lead towards building knowledge and confidence in the performance of the engineered barrier system. A number of key underground laboratories were highlighted including the Hard Rock Laboratory in Äspö, Sweden where the Prototype Repository Project is located.

Both the theoretical and numerical formulations were presented in chapter 3. In general an approach for modelling the behaviour of the Thermo-Hydro-Mechanical behaviour of an unsaturated soil based upon a porous media approach. The governing equations of the flow variables were developed via a mass balance approach and the mechanical formulation was based upon stress equilibrium. Numerically a finite-element scheme was utilised spatially and a finite-difference scheme temporally.

The computational algorithm to solve initial value problems for the theory presented in chapter 3 was considered in chapter 4. An existing serial computational algorithm was analysed and optimised yielding approximately a 30% time saving in executing analyses. High Performance Computing (HPC) was considered to further reduce analyses run time, especially considering large scale analyses. A new HPC algorithm was established for both the matrix build and solver of the computer code, using a multi-level parallelisation technique. This yielded significantly improved results over an existing parallel implementation. The numerical implementation of the model, COMPASS, was fully integrated with pre and post-processing software allowing complex three-dimensional geometries, meshes and conditions to be discretised and the results visualised.

The development of existing material models for bentonite blocks and pellets were presented in chapter 5. These developments related to the time dependent micro-structural behaviour of both compacted bentonite blocks and compacted bentonite pellets. A first estimate of a time dependent material model for both bentonite blocks and pelletised bentonite when swelling is restrained were presented. These were tested against small scale controlled laboratory tests where possible and also against a large-scale test. Comparable results were found in the short term to existing material models but significantly improved qualitative and quantitative results were found in the long term, which may produce improved predictions of long term behaviour.

The Prototype Repository Project (PRP) was introduced in detail in chapter 6 with the salient features of the project including experimental results indicated. In particular, the PRP is a full-scale mock-up of a High-Level Nuclear-Waste deep geological repository, using the KBS-3 system, that was designed to investigate the thermo-hydro-mechanical response, among others, of the near-field. Two major stages of the project were identified: the pre-placement, where the repository tunnel has been constructed but no buffer material has been emplaced; and post-placement, where buffer material and canisters have been installed. In both stages a considerable amount of experimental data has been recorded and a synthesis of this information was included. A key finding was that in both phases of the experiment highly anisotropic flow conditions exist.

Two chapters of simulations are presented correlating to the two stages of the PRP identified. Chapter 7 contains simulations of the pre-placement phase of the PRP and chapter 8 contains simulations of the post-placement phase. In both cases three-dimensional simulations were undertaken.

9.3 Pre-placement simulation of the Prototype Repository Project

Modelling considerations for fractured rock were discussed in chapter 2 and it was stated that the appropriate modelling technique depends upon the specific material considered, the information available, the required resolution of results and the use of the results. A proposed technique was outlined in chapter 7 based upon these considerations and a series of analyses undertaken. This model was shown to be able to reproduce the experimental results within the bounds of reasonable error.

Within chapter 7 the pre-placement stage of the PRP was simulated allowing for the proposed model for the rock mass to be calibrated. The results of this chapter demonstrated that the hydraulic performance of the PRP is inherently three-dimensional. First, an effective continuum model was undertaken as a base-case and the results of this simulation clearly showed that the heterogeneity and anisotropy within the rock mass were critical for the performance of the repository system. A geometric model was proposed including a continuum model of the background rock mass, inclusive of small discontinuities. A

number of key discontinuities and a region of high hydraulic conductivity were also included based upon experimental evidence. It was shown that this model was able to reproduce the experimental data in particular being able to include the highly anisotropic flow regime, with only limited calibration required.

A sensitivity analysis of the various aspects was undertaken to identify the relative importance of each feature. It was found that discontinuities close to and interacting with the repository have the greatest effect, which supports the modelling technique of including only the key features that were identified.

9.4 Post-placement simulation of the Prototype Repository Project

Three-dimensional thermo-hydro-mechanical simulations were undertaken of the post-placement stage of the Prototype Repository Project. The THM behaviour was able to be generally well represented. These simulations were able to simulate a number of key features, including importantly the anisotropic hydraulic behaviour. Long term simulations are reported and may be compared to future experimental results. To the author's knowledge this is the first time this has been achieved.

Two sets of three-dimensional models were undertaken, the first without fractures to act as a base case, and the second including the set of discontinuities proposed in chapter 7. The importance of the fracture intersecting the first deposition-hole was highlighted as was the behaviour of the backfill which saturated at a significantly faster rate during the simulation including the fractures. The behaviour of the thermal field was simulated well, with only minor discrepancies between the experimental and numerical results. The hydraulic field was generally well simulated throughout, and in all cases a good rate of resaturation simulated at the end of the simulation or when the sensor failed. It was concluded that the geological conditions, backfill re-saturation and buffer re-saturation, including the micro-structural effects of the bentonite, are all important to the simulation of a HLW repository. Long term analyses where carried out and the overall effects of the anisotropic hydration investigated. It was found that in the simulations DH-1 was saturated in 15-20 years and DH-3 was nearly saturated after 30 years. This may be significant in performance assessment. It is noted that good use of computational facilities is key to the completion of these simulations, with

High-Performance-Computing required to undertake the simulations and data processing and visualisation of the results being non-trivial.

The HPC algorithm developed in chapter 4 enabled these analyses to be undertaken. The ability to handle large, three-dimensional, complex geometries and undertake such analyses in reasonable time allows more realistic simulations, such as the simulations considered in this thesis, to be undertaken that otherwise would be beyond computing capabilities.

A number of two-dimensional axi-symmetric analyses were undertaken for single deposition-holes to investigate a number of key features prior to the three-dimensional analyses. Two idealised domains were used for the two-dimensional analyses, one with all the rock simulated as an effective continuum, representing an absence of large fractures, and one with the inclusion of a single fracture intersecting the deposition-hole. This fracture was seen to be critical to simulate the re-saturation rate of the buffer. Moreover, it was seen that this response could be local to the fracture hence supporting the modelling strategy of including discrete fractures. An investigation of the proposed time-dependent hydraulic conductivity relationship was carried out, with the results being similar to the results using the original relationship in the short term, but significantly improved in the long term. This is important for long term predictive behaviour.

The thermal results were shown to be inherently three-dimensional and underestimated the temperatures after approximately 100 days in two-dimensional analyses. Hydraulic results showed a good correlation with experimental results in the short term and required the use of a time-dependent hydraulic conductivity, representing micro-structural change, for good long term numerical and experimental correlation. The mechanical results were shown to be show reasonable quantitative and qualitative correlation, in fitting with the simulated hydraulic and thermal fields, although some aspects could not be reproduced. Importantly, it was seen that experimentally the rate of stress development reduced when values reached $5MPa$ and this could be reproduced by reducing the stress where yield occurs for the pellets. A reduction in simulated vertical deformation was then also found, which is significant for the design of the backfill and performance assessment.

9.5 Suggestions for further work

The work presented in this thesis has indicated that, in general, the three-dimensional THM behaviour of a nuclear waste repository structure can be numerically simulated. However, limitations exist, some of which were described in the introduction and others have been found during this work. In addition, simulation work, such as that presented in this work, must be incorporated into performance assessment and the design processes to develop an acceptable proposition for deep geological disposal.

The host rock is a highly heterogeneous material which affects the repository behaviour. Inclusion of more heterogeneity into numerical models is required to be able to fully predict the behaviour of repositories. Statistical analyses may be required and the results of these may aid generic design and performance assessment.

The buffer materials, generally compacted bentonite either installed as blocks or pelletised, require further experimentation, particularly into the micro-structural change and long term behaviour. It is acknowledged that this experimentation can be expensive due to the timescales required, high densities and pressures and the temporal behaviour. The micro/macro-structure change must be quantified for models to be able to predict the long term behaviour. Other aspects that are not well understood include vapour transport and additionally many aspects of the behaviour of bentonite pellets require investigation.

The macro/micro-structure interactions of highly-compacted bentonitic materials occur when these materials are hydrated in confined conditions as discussed in chapter 5. The expansive nature of the materials means that while the total volume of pores remains relatively constant the pore-size distribution changes significantly and gels form within the micro-structure. Detailed characterisation of this process would be useful, possibly using high resolution non-destructive visualisation techniques such as nanotomography, as well as observing macroscopic behaviour. Analysis of the micro/macro-structure interactions will also inform the simulation of the swelling behaviour. Building multi-scale models such as atomic/micro-structural/macro-structural may also aid conceptual understanding of macroscopic behaviour.

Non-homogeneous materials, e.g. the pelletised bentonite, must be characterised especially as these materials proposed for use in repositories are not inert granular materials. For example the collapse of the macro-structure should be studied as it has the potential to change the deformation characteristics of the buffer material. The effect of gaps between blocks of bentonite, fractures that may occur due to temperature effects or gas build-up must be considered. These discontinuities have the potential to dominate flow behaviour in the long term, but must be examined in conjunction with understanding more about the micro-structural behaviour.

The variability of material parameters is also not well known. This is possibly due to the time and expense required to undertake multiple experiments, however, this is key to understanding the predictive capabilities of numerical simulation. Only when the reliability of models and the material variability has been established and quantified may the models be used in a truly predictive capacity.

Thermo-hydro-mechanical simulations, such as undertaken within this work, need to be integrated with the design process of various other constitutive parts of the repository concept. For example, the anisotropic stress regime could be further investigated in conjunction with the design of the canister and overpack.

Processes other than thermo-hydro-mechanical processes occur in repository structures such as considered in this work. For example the chemical and biological processes occurring may cause the generation of gas from the corrosion of the metal canisters and the breakdown of clay minerals. These processes are required to be understood for a full understanding of the behaviour of the repository and an assessment of the safety to be undertaken.

Computer technology that enables the simulations to be undertaken is transient and as such the ability to undertake large scale or complex analyses generally increases with time. However, as stated in chapter 4 the trend is to move to having more processing elements, therefore access to a higher total processing power, but new algorithms must be developed to take advantage of this. Techniques should in general follow the development of technology

so that full advantage can be taken of developments at any time. Domain-decomposition or distributed memory-storage, for example, may be examined which may enable analyses to be undertaken faster and allow analyses that have large memory storage requirements to be undertaken.

When executing large models, challenges in terms of forming the output data into useful output can be challenging both in terms of the computation required and the techniques used. Parallel data storage and processing will be required in the future and more advanced visualisation will need to be used.